Fifteen years of progress on Neutrino Cosmology

Julien Lesgourgues

Fifteen years of progress on Neutrino Cosmology

Dossier de candidature
pour le diplôme
d'Habilitation à diriger des recherches

Julien Lesgourgues

18th January 2014

Contents

Part I
Front Matter

1 Introduction

1.1 What is special about neutrino cosmology?

In order to apply for the "Habilitation à diriger des recherches", I was expected to present a compilation of my work on a given topic. I hesitated between my main three lines of research:

1. **Cosmological Inflation:** Can we understand the quantum-to-classical transition of perturbations? What are the signatures of multiple inflation? Can we reconstruct the scalar potential, detect features in the primordial spectrum, and bound isocurvature modes?

2. **Dark Matter Cosmology:** Is dark matter cold or warm, made of particles or a scalar field, decaying or annihilating, totally decoupled or slightly interacting?

3. **Neutrino Cosmology:** What are the possible signatures of neutrinos in cosmology? How can we measure neutrino-related parameters?

I actually like very much all these topics, opening windows on particle physics. The interplay between cosmology and particle physics always sounded fascinating to me. The third topic is however the one to which I devoted more times, and through which I am best known in the community. Indeed, I feel that working on this topic was, in a way, the safest investment that I could make.

Indeed, we know that cosmology will give us access to at least one neutrino-related parameter: the total neutrino mass M_ν. Thanks to neutrino oscillation experiments, this mass is known to be equal to or larger than 0.06 eV. We have very strong reasons to believe that there is a cosmic neutrino background in the universe, thanks to measurements of the so-called effective neutrino number $N_{\rm eff}$. Current data exclude $N_{\rm eff} = 0$ at the ten-sigma level, and confirm that $N_{\rm eff}$ is at least equal to three (the value corresponding to the standard model of neutrino decoupling in the early universe, for three families of neutrinos). Finally, cosmic neutrinos with a mass of 0.06 eV are expected to affect cosmological observables at the five per cent level, and future surveys will measure these observables with per cent precision. Hence, neutrinos can be expected to play the same role in modern cosmology as the Higgs boson at the LHC: we have very strong reasons to believe that we will detect their mass. Even a null detection would have crucial consequences: it would be in such contradiction with theoretical expectations that it would signal the discovery of physics beyond the standard model. In addition, since the cosmic neutrino background exists, many non-minimal assumptions concerning neutrino physics and early universe physics can be tested (deviations from the standard model of neutrino decoupling, large leptonic asymmetry, non-standard neutrino interactions, existence of sterile neutrinos, etc.)

For these reasons, the study of neutrinos is one of the most rewarding topics for cosmologists. New constraints are immediately important and concretely applicable to model-building in particle physics. We wish that the same will become true for other topics. We hope to understand when and how inflation took place. We are ready to do everything possible for learning something on the nature of dark energy (or the origin of the cosmological constant) from future observations. As far as the nature of dark matter is concerned, it would be fantastic if cosmological data was measuring something more than just the relic density. We have ideas for probing phase transitions in the early universe, understanding the role of cosmological magnetic fields, testing the invariance of fundamental constants. But in none of these directions we can be sure that future data will tell us something new. As far as neutrinos are concerned, we know that the measurement of the neutrino mass scale can happen at any time from now, and that in at most ten years, it will be detected. If ever the effect of neutrino masses on cosmological observables remained invisible, some radical departure from the standard model of cosmology and/or particle physics

would have to be invoked (decay of active neutrinos at late times, non-standard neutrino interactions, etc.)

Neutrino cosmology is an interdisciplinary topic in which it is important to take into account results from laboratory experiments, neutrino telescopes and cosmological observations. The complementarity between these different techniques is remarkable. Some parameters like the total neutrino mass are much easier to access with cosmology: the next generation of tritium decay experiments will still not compete with the current generation of cosmological observations. On the other hand, laboratory experiments have access to mixing angles, CP violating phases, or the fact that neutrino have a Dirac or Majorana mass term, while cosmology is essentially insensitive to these properties. To summarise the situation, neutrinos are such elusive particles that they can only be understood by confronting very different techniques. Laboratory experiments rely on huge, ultra-sensitive detectors. Neutrino telescopes take advantage of the high energy of neutrinos produced by cosmic rays. Cosmology gains from the fact that the number density of neutrinos produced in the early universe is amazingly large, with still 336 neutrinos per centimetre cube today. Neutrinos are actually the most abundant particles in the universe.

1.2 Outline of this manuscript

In section 1.3, I present the list of my publications directly related to neutrino cosmology.

Section 2 summarises and explains the structure of these publications. I did not want to write here one more review on neutrino cosmology: it would have overlapped with my previous review articles, and with some chapters of the book "Neutrino Cosmology", presented this manuscript in section 3.1, pages 25-179. For that reason, **I kept section 2 as concise as possible, and wrote it in an informal and personal style.** For each sub-topic, I present my papers in chronological order, like a little story, insisting on what was the status of the topic when I started, what was new in my papers, what was my role, when I was scooped, etc. I don't present a self-contained summary of physical concepts, since they are all defined and developed in the papers included in Part II. I hope that with such a choice, section 2 is not too heavy to digest.

In Part II, sections 3-5, I present the most representative publications within the list of section 1.3. The papers are grouped by theme, following the same structure as the discussion in section 2. Section 3 contains papers focused mainly on theoretical aspects, explaining in details the effect of neutrinos on cosmological observables. Section 4 is devoted to detectability issues, and presents sensitivity forecasts for future experiments. Papers deriving new bounds on neutrino physics from cosmological observations are grouped in section 5.

1.3 List of publications directly related to neutrino cosmology

- **"Cosmological implications of a relic neutrino asymmetry"**
  J. Lesgourgues and S. Pastor.
  hep-ph/9904411
  Phys. Rev. D **60**, 103521 (1999)
  Presented in section 3.2, pages 181-194

- **"Cosmological measurement of neutrino mass in the presence of leptonic asymmetry"**
  J. Lesgourgues, S. Pastor and S. Prunet.
  hep-ph/9912363
  Phys. Rev. D **62**, 023001 (2000)

- **"Remarks on the Boomerang results, the baryon density, and the leptonic asymmetry"**
  J. Lesgourgues and M. Peloso.
  astro-ph/0004412
  Phys. Rev. D **62**, 081301 (2000)

- **"The Lepton asymmetry: The Last chance for a critical-density cosmology?"**
  J. Lesgourgues and A. R. Liddle.
  astro-ph/0105361
  Mon. Not. Roy. Astron. Soc. **327**, 1307 (2001)

- **"Constraining the window on sterile neutrinos as warm dark matter"**
  S. H. Hansen, J. Lesgourgues, S. Pastor and J. Silk.
  astro-ph/0106108
  Mon. Not. Roy. Astron. Soc. **333**, 544 (2002)

- **"Measuring the cosmological background of relativistic particles with WMAP"**
  P. Crotty, J. Lesgourgues and S. Pastor.
  astro-ph/0302337
  Phys. Rev. D **67**, 123005 (2003)

- **"Current cosmological bounds on neutrino masses and relativistic relics"**
  P. Crotty, J. Lesgourgues and S. Pastor.
  hep-ph/0402049
  Phys. Rev. D **69**, 123007 (2004)
  Presented in section 5.1, pages 285-297

- **"Probing neutrino masses with future galaxy redshift surveys"**
  J. Lesgourgues, S. Pastor and L. Perotto.
  hep-ph/0403296
  Phys. Rev. D **70**, 045016 (2004)
  Presented in section 4.1, pages 219-232

- **"Constraining warm dark matter candidates including sterile neutrinos and light gravitinos with WMAP and the Lyman-alpha forest"**
  M. Viel, J. Lesgourgues, M. G. Haehnelt, S. Matarrese and A. Riotto.
  astro-ph/0501562
  Phys. Rev. D **71**, 063534 (2005)

- **"Probing neutrino masses with cmb lensing extraction"**
  J. Lesgourgues, L. Perotto, S. Pastor and M. Piat.
  astro-ph/0511735
  Phys. Rev. D **73**, 045021 (2006)
  Presented in section 4.2, pages 233-245

- **"Massive neutrinos and cosmology"**
  J. Lesgourgues and S. Pastor.
  astro-ph/0603494
  Phys. Rept. **429**, 307 (2006)

- **"Can sterile neutrinos be ruled out as warm dark matter candidates?"**
  M. Viel, J. Lesgourgues, M. G. Haehnelt, S. Matarrese and A. Riotto.
  astro-ph/0605706
  Phys. Rev. Lett. **97**, 071301 (2006)
  Presented in section 5.5, pages 343-346

- **"Probing cosmological parameters with the CMB: Forecasts from full Monte Carlo simulations"**
  L. Perotto, J. Lesgourgues, S. Hannestad, H. Tu and Y. Y. Y. Wong.
  astro-ph/0606227
  JCAP **0610**, 013 (2006)

- **"Physics at a future Neutrino Factory and super-beam facility"**
  A. Bandyopadhyay *et al.* [ISS Physics Working Group Collaboration].
  arXiv:0710.4947 [hep-ph]
  Rept. Prog. Phys. **72**, 106201 (2009)

- **"Constraining neutrino masses with the ISW-galaxy correlation function"**
  J. Lesgourgues, W. Valkenburg and E. Gaztanaga.
  arXiv:0710.5525 [astro-ph]

Phys. Rev. D **77**, 063505 (2008)
Presented in section 4.3, pages 247-256

- **"Using BBN in cosmological parameter extraction from CMB: A Forecast for PLANCK"**
J. Hamann, J. Lesgourgues and G. Mangano.
arXiv:0712.2826 [astro-ph]
JCAP **0803**, 004 (2008)

- **"Lyman-alpha constraints on warm and on warm-plus-cold dark matter models"**
A. Boyarsky, J. Lesgourgues, O. Ruchayskiy and M. Viel.
arXiv:0812.0010 [astro-ph]
JCAP **0905**, 012 (2009)

- **"Cosmological constraints on a light non-thermal sterile neutrino"**
M. A. Acero and J. Lesgourgues.
arXiv:0812.2249 [astro-ph]
Phys. Rev. D **79**, 045026 (2009)
Presented in section 5.2, pages 299-316

- **"Realistic sterile neutrino dark matter with keV mass does not contradict cosmological bounds"**
A. Boyarsky, J. Lesgourgues, O. Ruchayskiy and M. Viel.
arXiv:0812.3256 [hep-ph]
Phys. Rev. Lett. **102**, 201304 (2009)
Presented in section 5.6, pages 347-350

- **"Non-linear Power Spectrum including Massive Neutrinos: the Time-RG Flow Approach"**
J. Lesgourgues, S. Matarrese, M. Pietroni and A. Riotto.
arXiv:0901.4550 [astro-ph.CO]
JCAP **0906**, 017 (2009)

- **"Model independent constraints on mass-varying neutrino scenarios"**
U. Franca, M. Lattanzi, J. Lesgourgues and S. Pastor.
arXiv:0908.0534 [astro-ph.CO]
Phys. Rev. D **80**, 083506 (2009)

- **"Cosmological parameters from large scale structure - geometric versus shape information"**
J. Hamann, S. Hannestad, J. Lesgourgues, C. Rampf and Y. Y. Y. Wong.
arXiv:1003.3999 [astro-ph.CO]
JCAP **1007**, 022 (2010)

- **"The Cosmic Linear Anisotropy Solving System (CLASS) II: Approximation schemes"**
D. Blas, J. Lesgourgues and T. Tram.
arXiv:1104.2933 [astro-ph.CO]
JCAP **1107**, 034 (2011)

- **"The Cosmic Linear Anisotropy Solving System (CLASS) IV: efficient implementation of non-cold relics"**
J. Lesgourgues and T. Tram.
arXiv:1104.2935 [astro-ph.CO]
JCAP **1109**, 032 (2011)
Presented in section 3.3, pages 195-218

- **"Cosmological lepton asymmetry with a nonzero mixing angle θ_{13}"**
E. Castorina, U. Franca, M. Lattanzi, J. Lesgourgues, G. Mangano, A. Melchiorri and S. Pastor.
arXiv:1204.2510 [astro-ph.CO]
Phys. Rev. D **86**, 023517 (2012)
Presented in section 5.3, pages 317-327

- **"Neutrino masses and cosmological parameters from a Euclid-like survey: Markov Chain Monte Carlo forecasts including theoretical errors"**
  B. Audren, J. Lesgourgues, S. Bird, M. G. Haehnelt and M. Viel.
  arXiv:1210.2194 [astro-ph.CO]
  JCAP **1301**, 026 (2013)
  Presented in section 4.4, pages 257-283

- **"Neutrino mass from Cosmology"**
  J. Lesgourgues and S. Pastor.
  arXiv:1212.6154 [hep-ph]
  Adv. High Energy Phys. **2012**, 608515 (2012)

- **"Neutrino cosmology"**
  J. Lesgourgues, G. Mangano, R. Miele, S. Pastor
  Cambridge University Press, 400 pages, April 2013
  http://www.cambridge.org/gb/knowledge/isbn/item6947425/
  Presented in section 3.1, pages 25-179 (only chapters 5 and 6)

- **"Planck 2013 results. XVI. Cosmological parameters"**
  P. A. R. Ade *et al.* [Planck Collaboration].
  arXiv:1303.5076 [astro-ph.CO].
  In press.
  Presented in section 5.4, pages 329-342 (only sections 6.3 and 6.4)

2 Summary and structure of my publications on neutrino cosmology

When I started woking on neutrino cosmology, this field was still in its infancy. Cosmologists knew that neutrino masses slow down structure formation in the universe, and that for this reason, most dark matter must be cold. However, actual constraints on the total neutrino mass were extremely weak. As far as non-standard neutrino properties are concerned, there were no bounds at all (on the leptonic asymmetry, on non-standard interactions, on sterile neutrinos, etc.)

In 1998, the Super Kamiokande experiment discovered neutrino flavour oscillations. It then became clear that the neutrino sector had some rich phenomenology, with many uncertainties and several parameters to be measured. Because of the weak neutrino interaction rate, it appeared that cosmological surveys were one of the few relevant tools for measuring some of these parameters. This fascinating topic, at the interface between cosmology and particle physics, became my primary field of research precisely on that year.

2.1 Investigations on the fundamental role of neutrinos in cosmology

2.1.1 Impact of neutrino asymmetry on the CMB and LSS

The matter-antimatter asymmetry in the baryon sector, or baryon asymmetry, is known to be very small in our universe, of the order of 10^{-9}. This small number plays a key role in our understanding of baryogenesis. The matter-antimatter asymmetry in the uncharged lepton sector (often called for simplicity the lepton asymmetry) is much less constrained (unless one refers to very specific models of baryogenesis through leptogenesis). In principle, the quantity $(n_\nu - n_{\bar{\nu}})/(n_\nu + n_{\bar{\nu}})$ could even be of order one for each family of neutrinos. A large asymmetry can be generated in various ways (resonant oscillations with sterile neutrinos, Affleck-Dine mechanism) without conflicting with our basic understanding of the early universe. During epochs when oscillations between cosmic neutrinos can be neglected, and assuming that cosmic neutrinos have a Fermi-Dirac distribution (because they were in thermal equilibrium until decoupling), a convenient parameter for characterising the lepton asymmetry of each family i is $\xi_i = \mu_i/T$, where μ_i is the chemical potential and T is the neutrino temperature. As soon as neutrino oscillations in the cosmic neutrino background become negligible, this parameter is conserved for each family. An increasing asymmetry implies an increasing total density of neutrinos, explaining why a large asymmetry is often called a "neutrino degeneracy".

The role of a large lepton asymmetry on Big Bang Nucleosynthesis (BBN) has been thoroughly investigated in the 1970's, allowing people to infer limits on the chemical potentials from the observation of light element abundances. It was shown that BBN cannot exclude a large lepton asymmetry, provided that the chemical potential in the electron sector and in the μ, τ sector are related in a precise way: indeed, a cancellation between two antagonist effects associated respectively to μ_e and $(\mu_e + \mu_\nu + \mu_\tau)$ can then lead to roughly the same amount of primordial Helium and Deuterium as if all chemical potentials were negligible. BBN models with large leptonic asymmetries are called "degenerate BBN" models.

The role of a large lepton asymmetry on the Cosmic Microwave Background (CMB) and Large Scale Structure (LSS) spectra was calculated much later. Together with Sergio Pastor, who did his first postdoc at SISSA exactly at the same time as me, we wrote the third paper on this topic: **"Cosmological implications of a relic neutrino asymmetry", Phys. Rev. D 1999** (presented in section 3.2, pages 181-194). A first paper had discussed only the case of degenerate massless neutrinos. We started to modify the public code CMBFAST in order to incorporate a chemical potential in the neutrino phase-space distribution. We were scooped by a second paper, that was however obtaining an incorrect CMB spectrum, due to incomplete modifications of the same code. Hence our paper was the first one featuring the correct calculation, and showing the impact on the CMB and LSS spectra of light active neutrinos with a large asymmetry.

Note that in the limit of massless neutrinos, increasing the lepton asymmetry is equivalent to increasing the effective neutrino number $N_{\rm eff}$ accounting for the total density of ultra-relativistic relics in the universe. Our work was not trivial in the sense that we studied the more realistic case of active neutrinos with a small mass. In that case, in order to compute the correct CMB and LSS spectra, a neutrino phase-space distribution function with non-zero chemical potential needs to be implemented explicitly in the Boltzmann code. We also provided in the paper a physical explanation of our numerical results.

2.1.2 Impact of neutrino mass on the CMB and LSS

During my first years of research in the field, the physical explanation for the signature of neutrino masses on the CMB and LSS power spectra was not very clear in the mind of most people.

As far as the matter power spectrum is concerned, it was well-known since Bond, Efstathiou and Silk (1980) that neutrino masses produce a step-like suppression on small scales. The maximum suppression was known to be of the order of $\Delta P/P = -8f_\nu$, thanks to a first-order fit of numerical results performed by Hu and Eisenstein in 1998 (a fit of the full matter power spectrum was presented on the same year by Novosyadlyj, Durrer and Lukash). The literature was also containing a few attempts to explain this result on the basis of purely analytical solutions, but they were misleading or incorrect.

Concerning the CMB spectrum, the following reasoning could be found in several papers: if neutrinos have a mass smaller than about 0.6 eV, they are still relativistic at the time of photon decoupling; then, the CMB does not know about this mass, and it has no impact on the CMB spectrum. This reasoning is wrong, as will be explained in the next sections.

Impact on LSS. After collaborating on a several projects related to various aspects of neutrino cosmology, Sergio Pastor and myself decided to write the review **"Massive neutrinos and cosmology", Phys. Rept. 2006**. I was in charge of the CMB and LSS chapters, and I wanted to explain the effect of neutrino masses in a better way than previous papers. In the review, after recalling the analytic results of Bond, Efstathiou and Silk concerning the scale-dependent growth factor of CDM induced by neutrino masses, I showed how to calculate the suppression factor analytically. Actually, my derivation was only semi-analytic, because one intermediate step had to be matched to simulations. However the result was doing a correct prediction for the suppression factor, corresponding roughly to $\Delta P/P = -8f_\nu$ in the limit of degenerate neutrinos with $f_\nu < 0.05$, but remaining much closer to exact numerical results for larger f_ν and/or when the mass is split differently among neutrino families. I revisited the same issue six years later, when writing the book **"Neutrino cosmology" (Cambridge University Press, 2013,** partially reproduced in section 3.1, pages 25-179) in collaboration with G. Mangano, G. Miele and S. Pastor. In chapter 6 on Large Scale Structure, I presented a more complicated but entirely analytic derivation of an accurate formula for the suppression factor (in pages 297-305 of the book, or 129-137 of this manuscript). Note that obtaining accurate analytical formulas is not important for the purpose of making use of them, because numerical results are anyway quick and easy to obtain with a Boltzmann code. These results are more important as a conceptual proof that we understand fully the effect of neutrino masses on the matter power spectrum, as well as the way it depends on the splitting of the total mass between different species. In summary, I believe that the discussion presented in the Physics Reports and in Chapter 6 of the book clarified the understanding of the role of neutrino masses in structure formation within the community.

Impact on the CMB. On the same two occasions, I tried to clarify the effect of neutrino masses on the CMB. In the Physics Report, we showed that the claim concerning the null impact of small neutrino masses ($m_\nu < 0.6$ eV) on the CMB is wrong for at least two reasons. (i) First, provided that neutrinos are non-relativistic today (i.e. $m_\nu > 6 \times 10^{-4}$ eV), the cosmological background evolution is sensitive to their mass, since neutrinos behave like radiation in the past, and like non-relativistic matter at late times. Depending on which cosmological parameters are kept fixed when the neutrino mass varies, this modified background evolution affects either the time of equality between matter and radiation, or that of equality between matter and a cosmological constant, or the angular scale of the sound horizon at recombination, or the angular scale of the Silk damping length. (ii) The second reason is that CMB anisotropies are weakly lensed by large scale structure. The neutrino mass (even if smaller than 0.6 eV) affects the matter power spectrum, and hence also on the observable CMB spectrum.

In summary, in the reasoning presented in our Physics Reports, the conclusion was that the effect of neutrino masses on the CMB cannot be summarised in one sentence, because effect (i) depends on which cosmological parameters one decides to keep fixed while varying m_ν. The important point is that for whatever choice, there is always a non-zero effect (even at the level of the unlensed CMB spectrum), due to the variation of at least one characteristic time or scale.

However, there is an even clearer way to understand the role of neutrino masses, that I first pointed out in chapter 5 of our book on **"Neutrino Cosmology" (Cambridge University Press, 2013,** in pages 262-266 of the book, or 94-98 of this manuscript). The point is the following. Among the characteristic times and scales mentioned above, three have a very distinct and well-constrained effect on the CMB: the time of equality between matter and radiation, the angular scale of the sound horizon at

recombination, and the angular scale of the Silk damping length. Instead, the time of equality between matter and a cosmological constant is loosely constrained, because it only affects very large angular scales, through the Late Integrated Sachs-Wolfe (LISW) effect, for which cosmic variance is large. Hence, when discussing the effect of neutrino masses on the CMB, it is useful to vary m_ν while keeping fixed the first three quantities, in order to see whether there is a residual effect, on top of a trivial modification of the LISW effect for multipoles $l < 50$. In other words, if one varies the neutrino mass while adjusting other cosmological parameters in order to fix the time of equality, the peak scale and the Silk damping scale, one can "neutralise" the effect of the neutrino mass on the CMB induced at the level of the background evolution (appart from an irrelevant LISW effect), and isolate the effect induced at the level of cosmological perturbations, caused by the gravitational coupling between neutrinos and photons.

In 2012, I followed exactly this approach when writing chapter 5 of the book, and to my surprise, the plot showing the variation of the CMB temperature spectrum under this transformation revealed a very characteristic impact of neutrino masses (see Figure 5.6, page 265 of the book, 97 of this manuscript). The mass creates a small depression in the C_l^{TT}'s for multipoles in the range $20 < l < 200$. The precise amplitude and position of this depression depends on the value of individual neutrino masses (rather than on the total one). This dip can be interpreted physically as a consequence of the Early Integrated Sachs-Wolfe (EISW) effect. When neutrinos become non-relativistic *after* photon decoupling, they have a characteristic effect on the evolution of metric fluctuations on intermediate scales. Since the observed temperature of CMB photons depends on the time derivative of metric fluctuations along the line of sight, the effect induced by the mass is visible in the final CMB spectra. This effect was always implicitly included in previous numerical calculations of the CMB spectrum. But it had never been identified and discussed physically. What particularly impressed me is that I remember discussions with Alexei Starobinsky several years ago, in which he said that there should be such an effect, and that nobody ever discussed it. Hence my numerical results confirmed a thought of Alexei, coming from his outstanding physical intuition. I still have in project to write an analytic paper that would better explain this effect, in collaboration with him.

Another paper arrived independently to the same conclusion, by Hou et al. (arXiv:1212.6267). When this paper came out, our book was still in production stage with the editor. Fortunately, we were not scooped by this paper, because while the book was being processed, we wrote a short review in which our main new results were summarised, including this discussion of the neutrino-induced feature (**"Neutrino mass from Cosmology", Adv. High Energy Phys. 2012**). By chance, this review appeared one week before the preprint of Hou et al.

There is now wide agreement that the dip that we identified explains the sensitivity of the WMAP data to neutrino masses. WMAP is not very sensitive to lensing due to its poor angular resolution, and still it give a constraint $M_\nu < 1.3$ eV (95% CL), or $m_\nu < 0.43$ eV for each family. When using Planck data alone, the neutrino mass constraint comes from both lensing and the EISW effect. In the future, one may expect that the constraint from lensing will be stronger than that from the EISW effect.

Impact of the mass splitting. Another interesting question is: do the CMB and LSS spectra depend only on the total neutrino mass $M_\nu = \sum_i m_{\nu i}$, that controls the neutrino density today ($\omega_\nu \propto M_\nu$), or is it also sensitive to individual masses, or in other words, to the splitting of the total mass between different species?

Individual masses are actually expected to play a role, because they control the time of the non-relativistic transition for each species, and the free-streaming scale associated with each of them. A simple reasoning shows that the mass splitting should hence affect the position of the step-like feature in the matter power spectrum, and to a lesser extent, the amplitude of the step. It should also affect the CMB through the detail of the EISW-induced depression in the C_l's. Until 2004, these effects had never been computed, because the two Boltzmann codes available at that time (CMBFAST and CAMB) included a single family of massive neutrinos. For the paper **"Probing neutrino masses with future galaxy redshift surveys", Phys. Rev. D 2004,** presented in section 4.1, pages 219-232, I modified CMBFAST in order to simulate several massive species at the same time. We showed that the difference between the CMB and matter power spectra of several models with the same total mass M_ν but different mass splittings (equal mass, mass concentrated in one species, realistic normal hierarchy, realistic inverted hierarchy scenarii). The difference was found to be very small, but matching physical expectations.

Apart from the papers and review articles mentioned above, I have developed these results in several review articles and conference proceedings, including a few sections in **"Physics at a future Neutrino Factory and super-beam facility", Rept. Prog. Phys. 2009**.

2.1.3 Impact of neutrino density (and higher momenta) on the CMB and LSS

I also worked on the role of the density of neutrinos (and/or of other ultra-relativistic relics) on cosmological observables, and on the degeneracy between its effect and that of other cosmological parameters. The parameter playing a key role in this case is the effective neutrino number $N_{\rm eff}$, i.e. the density of radiation beyond the contribution of photons, normalised to the contribution of one standard neutrino in the instantaneous decoupling limit. Indeed:

- In any cosmological model in which the mass of neutrinos (and of possible other light relics) is negligible, the equations governing cosmological perturbations can all be integrated over the momentum of these species, and $N_{\rm eff}$ is the only parameter accounting for the density of neutrinos and extra relics. In particular, $N_{\rm eff}$ will encode the effect of a non-standard temperature, a chemical potential and possible non-thermal distorsions for each family of active neutrinos and possibly of light sterile neutrinos.

- Instead, when neutrinos or other relics have a sizeable mass, the momentum of massive species cannot be integrated out. In that case, $N_{\rm eff}$ can still be defined at early times, when all species are relativistic. However, the observable CMB and LSS spectra will depend on a combination of $N_{\rm eff}$, of the masses, and possibly of other parameters describing chemical potentials, non-thermal distorsions, etc.

We presented a discussion of the degeneracy between the total neutrino mass and $N_{\rm eff}$ for a few simple models in **"Current cosmological bounds on neutrino masses and relativistic relics", Phys. Rev. D 2004**, presented in section 5.1 of this manuscript, pages 285-297. We were scooped by a paper by Hannestd and Raffaelt on the same topic, that appeared slightly before ours, but we gave more details on the physical explanation of the degeneracy, and both papers are usually acknowledged when one refers to this well-known degeneracy. Actually, this degeneracy was problematic a few years ago, when the data had large error bars, but with the precision level of Planck, the two effects of $N_{\rm eff}$ and M_ν can be clearly separated.

The role of $N_{\rm eff}$ in the CMB and matter power spectra has given rise to some confusions. Just like for the neutrino mass, the discussions presented in the literature until recently concluded that the effect of $N_{\rm eff}$ depends very much on which parameters are kept fixed. We illustrated this in our Physics Report. These discussions were not incorrect, but they could be pushed further. A paper by Hou et al., arXiv:1104.2333 (different from the one mentionned in section 2.1.2), was very useful in that respect. For the first time, these authors decided to study the effect of $N_{\rm eff}$ when all characteristic redshifts in the cosmological background evolution are kept fixed. This can be done by increasing the radiation, matter and cosmological constant densities in exactly the same proportion. The result is quite illuminating: all "background effects" of $N_{\rm eff}$ are "neutralised", excepted an increase in the Silk damping length affecting very large l's. On top of that, additional effects of $N_{\rm eff}$ induced at the level of perturbations (i.e. by the gravitational coupling between neutrinos and light species) appear clearly. The latter effects had been studied earlier by Bashinksy and Seljak (astro-ph/0310198) and dubbed "neutrino drag" effects. They result in a small shift in the amplitude and position of the peaks.

In chapter 6 of the book **"Neutrino cosmology" (Cambridge University Press, 2013,** pages 255-262 of the book, or 87-94 of this manuscript), I wrote an updated discussion of these various effects, taking advantage of the point of view promoted by Hou et al., and extending it to the discussion of the effect of $N_{\rm eff}$ on the matter power spectrum. This discussion shows in particular that $N_{\rm eff}$ can be probed through the scale of BAO oscillations, provided that the latter are measured with high accuracy.

We just mentioned that for massive species, the momentum dependence of the phase-space distribution $f(p)$ cannot be integrated out in the set of equations governing the evolution of cosmological perturbations. Hence the results may depend on all details in $f(p)$. Since the properties of a distribution can be reconstructed from the set of its momenta, $a_n \equiv \int p^n f(p) dp$, it is interesting to investigate whether the cosmological data can probe independently several momenta. In minimal models with massive neutrinos (or extra light relics with a thermal distribution), everything can be described in terms of two independent momenta, encoding respectively the value of the density before the non-relativistic transition (parametrised by $N_{\rm eff}$), and the value of the density at later times ($\rho_i = m_i n_i$). For more complicated scenarii featuring non-thermal corrections, the number of independent momenta can be arbitrarily large.

To illustrate this problem, in **"Do observations prove that cosmological neutrinos are thermally distributed?", Phys. Rev. D 2005,** we studied the case of active neutrinos produced in two

stages: at early times from thermal equilibrium (when $T \geq 1$ MeV), and at late time from the decay of an hypothetical unstable relic. This model leads to non-thermal distorsions, and we used it to show the effect of higher momenta in the distribution, for fixed mass and fixed $N_{\rm eff}$. We showed that these effects are very small (at least at the level of linear perturbations), making it difficult to measure more than three independent momenta, even with future high-precision data.

2.1.4 Impact of sterile neutrinos

The idea of sterile neutrinos, insensitive to weak interactions but sharing their mass mixing matrix with active neutrinos, has been introduced early on by Sciama. In presence of N sterile neutrinos, the number of neutrino mass eigenstates is $3 + N$ instead of just 3. To be rigorous, one should only call "sterile neutrinos" the flavour eigenstates that are gauge singlets. By extension, the expression often refers to the mass eigenstates that are dominated by sterile components. This is why people often refer to the decay of sterile neutrinos: the probability of such a decay is always small, because in reality, it is triggered by the decay of the small active component of a such a mass eigenstate. In the past fifteen years, sterile neutrinos have often been invoked in two contexts: light sterile neutrinos with a mass in the eV range, and heavy sterile neutrinos with a mass in the keV range. These two cases are interesting because they may provide, respectively, an explanation to anomalies in short baseline neutrino oscillation experiments (LSND, MiniBoone, reactor experiments), and an interesting dark matter candidate that would be an alternative to the WIMP paradigm.

In papers like **"Cosmological constraints on a light non-thermal sterile neutrino", Phys. Rev. D 2009,** presented in section 5.2, pages 299-316, and **"Lyman-alpha constraints on warm and on warm-plus-cold dark matter models", JCAP 20009,** we calculated and discussed the matter power spectrum of models with light or heavy sterile neutrinos. In the former paper, we showed that for sterile neutrinos produced through non-resonant oscillations with active neutrinos, the quantity really constrained by the data is the ratio of average momentum over mass, controlled by T/m. In the latter paper, together with the numerical calculation of the matter power spectrum, I presented an analytic estimate of the steplike suppression induced in the matter power spectrum by heavy sterile neutrinos becoming non-relativistic during radiation domination.

2.1.5 Progress on the side of numerical calculations

Analytic approaches are nice for understanding physically the effect of parameters. When it comes to constraining models with cosmological data, or perform sensitivity forecasts, people use numerical codes simulating the evolution of linear perturbations and computing the observable spectrum of CMB anisotropies and matter density fluctuations. Since the main equation of evolution integrated by these codes is the Boltzmann equation of photons, they are called Boltzmann codes. I started my PhD precisely at the time at which the first efficient Boltzmann code, CMBFAST (Seljak and Zaldarriaga 1996), was made publicly available. In many occasions, I modified this code in order to incorporate new effects related to neutrino cosmology (neutrino chemical potential, different masses, etc.) Later on, another Boltzmann code, CAMB (Challinor and Lewis 2001), took the leadership, because it was faster and more accurate. I worked a lot with CAMB e.g. to implement warm dark matter (e.g. heavy sterile neutrinos), mass-varying neutrinos (see the next sections), etc.

At some point, I became convinced that even better codes could be written, achieving better speed, flexibility, user-friendliness, and covering more general cases. One of the leaders of the Planck team, François Bouchet, encouraged me to go in that direction, in order to establish the validity of Planck results on a more robust ground than just trusting a single code (namely, CAMB). I then started to develop the Cosmic Linear Anisotropy Solving System (CLASS, `http://class-code.net`). The code was released in April 2011. Both CAMB and CLASS have been used for the official analysis of Planck data released in March 2013 and later. The comparison of the results of the two codes has also benefited to the speed and accuracy of CAMB, and triggered general progress in the field of cosmological Boltzmann codes.

The code CLASS does not only feature an independent rewriting of other codes. In order to make it efficient, we found some new physical approximations and new algorithms. As far as neutrinos are concerned, in collaboration with Thomas Tram, we implemented a new scheme for sampling the momentum space of neutrinos. This approach, described in **"The Cosmic Linear Anisotropy Solving System (CLASS) IV: efficient implementation of non-cold relics", JCAP 2011,** and presented in section

3.3, pages 195-218, is based on an adaptative quadrature scheme. For a general phase-space distribution function passed by the user, the code automatically finds the optimal discretisation of momentum space that will lead to a given precision for a minimum amount of computing time. If the phase-space distribution is modified by the user (e.g. to feature a chemical potential or non-thermal distorsions), the code will immediately recalculate a new optimal sampling at a given precision level. This approach allows to make the code much faster in presence of massive neutrinos. A simplified version of our approach has been implemented in CAMB by Antony Lewis.

We also derived and tested a new approximation scheme allowing to replace the collisionless Boltzmann equation describing massless neutrino perturbations by a much simpler pair of equations describing an imperfect fluid with shear viscosity. This approximation, described in **"The Cosmic Linear Anisotropy Solving System (CLASS) II: Approximation schemes", JCAP 2011,** is switched on automatically by the code in a range of time and scales such that it leads to a negligible error. This new approximation scheme is called the "ultra-relativistic fluid approximation" in the code. In the previously mentioned CLASS IV paper, we extended it to massive neutrinos.

Finally, CLASS incorporates a wide range of possibilities for modelling the active/sterile neutrino sector. Unlike in CAMB, the user can pass in input several types of analytic phase-space distributions associated to different temperatures, chemical potentials, normalisation factors or masses; the input can also consist in a set of tabulated values for the phase-space distribution function. The number of distinct neutrino-like species (called generically "non-cold dark matter species" in the code) is arbitrary. In that sense, CLASS is a dedicated numerical tool for neutrino cosmology. The code is more and more diffused and used throughout the CMB and LSS community.

2.2 Sensitivity of future cosmological data

Both observers and theorists are usually very interested in sensitivity forecasts of future experiments to cosmological parameters. For observers, this provides a guideline for designing and planning experiments. For theorists, it is useful to know which physical assumptions can be tested observationally, and on which time scale.

2.2.1 CMB and Galaxy surveys

A simple way to make forecasts is to compute the so-called Fisher matrix, accounting for the curvature of a likelihood associated to a given set of experiments, in the vicinity of the model assumed to be the best fit to the data. I first learnt how to implement and use the Fisher matrix machinery in **"Cosmological measurement of neutrino mass in the presence of leptonic asymmetry", Phys. Rev. D 2000**. This paper was following my first work on the cosmological effects of a leptonic asymmetry. We forecasted the precision with which the combination of the Planck and SDSS data sets would enable to reconstruct the neutrino mass, if the leptonic asymmetry turned out to be large (an assumption which is now ruled out).

In **"Probing neutrino masses with future galaxy redshift surveys", Phys. Rev. D 2004**, presented in section 4.1, pages 219-232, we extended Fisher matrix forecasts to several combination of CMB and LSS experiments. We showed in particular how the sensitivity to neutrino masses depends on the volume of a given galaxy redshift survey, and we proved that the best surveys planned on the long term would be able to detect even the minimal allowed total neutrino mass (of the order of $M_\nu \sim 0.06$ eV). The conclusions of this paper still apply. We also showed that the most optimistic combination of experiments would never reach such a sensitivity that one could discriminate between the Normal Hierarchy and Inverted Hierarchy model, for a given total mass of e.g. $M_\nu \sim 0.1$ eV. This was the first forecast addressing this issue. Our pessimistic conclusion on this particular point has been reconsidered in forecasts based on a new futuristic observational technique, that of 21cm surveys, which might be able to remove such a degeneracy, although this is still not quite clear.

In **"Do observations prove that cosmological neutrinos are thermally distributed?", Phys. Rev. D 2005**, we considered the case of neutrinos with non-thermal corrections, and investigated the sensitivity of future CMB and LSS experiments to such corrections. We concluded that future cosmological data could at best measure independently three momenta of the phase-space distribution (this is enough for concluding that non-thermal corrections exist, but not for characterising them precisely).

Finally, in **"Using BBN in cosmological parameter extraction from CMB: A Forecast for PLANCK", JCAP 2008**, we showed that in order to extract the correct value of cosmological

parameters from Planck data, it is crucial to make correct assumptions concerning the primordial Helium fraction $Y_{\rm He}$. We showed that one can either consider this abundance as an extra free cosmological parameter, or infer it from $(\omega_b, N_{\rm eff})$ under the assumption that the standard BBN model applies. Instead, the method used until that point (and still used in the WMAP analysis), consisting in fixing arbitrarily $Y_{\rm He}$ to 0.24, could significantly bias Planck results for other parameters. Our analysis has met consensus and has been adopted in the baseline analysis of Planck data by the whole collaboration.

2.2.2 CMB lensing

The CMB fluctuations observed on the last scattering surface are affected by weak gravitational lensing by neighbouring large scale structures. The spectra of CMB anisotropies inferred directly from CMB maps are called the "lensed power spectra". Using the fact that lensing introduces particular types of correlations between CMB multipoles, that would vanish in the case of a gaussian CMB with zero lensing effects, Hu and Okamoto introduced in 2000 a technique called "lensing extraction with quadratic estimators", allowing to reconstruct the map of lenses, and to compute the power spectrum of the lensing potential. With very precise CMB observations, this technique could even allow to reconstruct the unlensed CMB map, and to compute the unlensed spectrum. In complement, in Phys.Rev. D71 (2005) 103514 [astro-ph/0412551], I showed that for cosmological models with non-zero primordial non-gaussianity, this technique can still be used. The reason is that weak lensing and primordial non-gaussianity introduce very different types of correlations in the sky.

Thanks to lensing extraction, CMB experiments can be used to measure the matter power spectrum in the redshift range $1 < z < 3$ (the lensing potential gets significant contributions from structures up to $z \sim 3$), and hence to constrain the total neutrino mass through its effect on LSS (on top of its effect on the CMB). This was first pointed out in a forecast by Kaplinghat et al. (astro-ph/0303344) showing that Planck and a post-Planck CMB satellite would be much more sensitive to neutrino masses than previously expected. Then, in **"Probing neutrino masses with cmb lensing extraction", Phys. Rev. D 2006**, presented in section 4.2, pages 233-245, we pushed this analysis further, and studied the sensitivity to the total neutrino mass of several future CMB experiments, considering more assumptions on the underlying cosmological model, and on the level of foreground contamination of CMB maps. We released our code FutureCMB for doing such forecasts; it has been used by many authors. Moreover, the most sophisticated part of this code (in charge of computing the theoretical limit up to which lensing extraction can be performed) has no equivalent in the community, and is used in every work involving CMB lensing extraction.

Shortly after, we published in **"Probing cosmological parameters with the CMB: Forecasts from full Monte Carlo simulations", JCAP 2006,** the best possible forecast that we could make of the Planck sensitivity to cosmological parameters, including the total neutrino mass. This analysis differed from previous ones in essentially two ways: it included lensing extraction, with realistic assumptions concerning the error on this process; and it was based on a Monte Carlo Markhov Chain (MCMC) analysis of mock data, instead of a simple Fisher matrix analysis. MCMC forecasts are more robust than Fisher matrix forecasts, and make no assumption on the shape of the likelihood with respect to model parameters. For all these reasons, this work became the most cited Planck forecast paper. A few years later, we were pleased to check that the error bars obtained in the real Planck data analysis (with and without lensing extraction) match our predictions fairly well.

2.2.3 Cross-correlation between CMB and LSS

CMB maps are affected by the gravitational redshifting/blueshifting of CMB photons going through gravitational potential wells at late time: this is called the Late Integrated Sachs-Wolfe (LISW) effect. This effect is generated by the time derivative of the gravitational potential along the line-of-sight. In a purely matter-dominated universe, this derivative vanishes on large scales as long as linear perturbation theory is valid. Indeed, in that case, matter fluctuation grow exactly like the scale factor, $\delta \propto a$. The Poisson equation then implies that the gravitational potential ϕ is constant. In a universe with Λ or dark energy domination at late times, matter fluctuations grow at a slower rate, and metric fluctuations decay, inducing a non-zero LISW effect. The same gravitational potential distribution responsible for this LISW effect can be inferred from the distribution of matter on large scales. Hence, the LISW effect is responsible for a statistical correlation between CMB maps and LSS maps. Measuring this correlation probes the presence of Λ or dark energy. This technique has already been applied successfully, although

with large error bars.

We know that neutrino masses also slow down the formation of structure. During matter domination, one has $\delta \propto a^{1-\epsilon}$, where ϵ is a small number related to the total neutrino mass. Hence, massive neutrinos give an extra contribution to the LISW effect, starting at a higher redshift. This had never been considered before our paper **"Constraining neutrino masses with the ISW-galaxy correlation function", Phys. Rev. D 2007**, presented in section 4.3, pages 247-256. In this work, we calculed (both analytically and numerically) the neutrino-induced LISW effect, and showed to which extent it could be reconstructed by cross-correlating the CMB and LSS data at high redshift. Our results show that this technique, applied to future LSS experiments such as LSST or Euclid (in combination with Planck), will have some sensitivity to neutrino masses. It will be less sensitive than just measuring neutrino masses from the step-like suppression induced in the LSS spectrum alone, but it may still be useful because it will provide independent evidence on the total neutrino mass, with a different dependence on systematic effects.

2.2.4 Role of non-linear corrections

In section 2.1.2, we discussed the impact of neutrino masses on the matter power spectrum within the theory of linear cosmological perturbations. LSS observations do probe the linear matter power spectrum on very large scale (up to some bias factor), but on smaller scales, they are sensitive to the non-linear evolution of matter perturbations, caused by gravitational collapse. Predicting the matter power spectrum on non-linear scales is technically difficult, and in presence of neutrino masses the difficulty is even larger. In N-body simulations, it is only since a few years that people are able to include neutrinos with a small realistic mass. N-body simulations are computationally very heavy, and for parameter extraction from future data, it would be much more convenient to have a fast way to calculate the non-linear power spectrum analytically, at least on mildly non-linear scales. Such approaches are currently being developed. They are usually inspired from renormalisation techniques in quantum field theory. In **"Non-linear Power Spectrum including Massive Neutrinos: the Time-RG Flow Approach", JCAP 2009,** we generalised one of these techniques (called the Time Renormalisation Group approach) to models with massive neutrinos.

A big step for unveiling the neutrino mass will be taken by the Euclid satellite. Euclid will produce a galaxy survey and a weak lensing survey that will be large and accurate enough to detect the total neutrino mass, even if it has the minimal value predicted by oscillation experiments, $M_\nu \sim 0.06$ eV. However, the significance with which such a mass will be measured is still debated. This has to do with the difficulty to make precise predictions on non-linear scales, for which one should take into account not only the non-linear evolution of total matter perturbations, but also non-linear biasing and redshift space distorsions. In forecasts, people usually include data only on linear scales, up to a cut-off wavenumber $k_{\rm NL}$. This scale is not obvious to calculate, since in reality non-linear corrections affect the power spectrum in a very progressive way as a function of k. In **"Neutrino masses and cosmological parameters from a Euclid-like survey: Markov Chain Monte Carlo forecasts including theoretical errors", JCAP 2013,** presented in section 4.4, pages 257-283, we introduced a new way to do forecasts. We implemented in the experimental likelihood that we use to fit mock Euclid data a theoretical error, depending on redshift z and on wavenumber k. This error is supposed to account for uncertainties in the prediction of non-linear corrections. It leads to a forecast which is very conservative and robust, while at the same time one does not throw way all the information above $k_{\rm NL}$, since the presence of the theoretical error allows to include data up to higher k's. In addition, our work is one of the first Euclid forecasts based on an MCMC analysis of mock data, rather than an approximate Fisher matrix approach. I am a member of the Euclid theory group, and this forecast is part of the effort for preparing the optimal way to analyse the future data.

2.3 Model comparison with the data

In cosmology, bounds on model parameters are often derived by theorists (like myself) rather than by observers. Indeed, parameter estimation from cosmological data requires some very specific and non-trivial numerical tools, and a wide knowledge of cosmological parameters and models. There is almost no limit to the number of alternative cosmological scenarios than one can consider and compare to the data. Observers have to deal with complicated problems related to the raw data analysis, and have time to publish only basic analyses of their data for the simplest cosmological models.

I derived many new bounds on cosmological parameters (including neutrino-related parameters), using three different tools for parameter extraction. When I started working in the field, there was no public code available for doing parameter extraction from the data. In 2002, with my post-doc Patrick Crotty, we developed our own parameter extraction code (using CMBFAST and performing likelihood interpolation in a grid in parameter space). My papers between 2002 and 2004 are based on this code. Then, I started to use the public codes COSMOMC and CAMB of Antony Lewis et al., modifying them for the purpose of each new paper. My publications from 2005 to 2010 are based on these codes. Finally, my students and postdocs B. Audren, T. Tram, D. Blas and myself released CLASS, and the associated parameter extraction code MONTE PYTHON. Since 2011, all my papers are based on these public codes, developed by my group but used by a growing fraction of the community.

2.3.1 Standard active neutrinos

I published constraints on the parameters related to active neutrinos (mass, number density, chemical potential, etc.) after the major data releases of the last fifteen years:

- The data of the first Boomerang ballon, release in 2000, showed an anomalous third CMB peak, that could be interpreted in terms of a large leptonic asymmetry. We were the first to propose this explanation (just 4 days after the data release) in **"Remarks on the Boomerang results, the baryon density, and the leptonic asymmetry", Phys. Rev. D 2000.** One year later, in **"The Lepton asymmetry: The Last chance for a critical-density cosmology?", Mon. Not. Roy. Astron. Soc. 2001,** we showed that when taking into account other recent cosmological data sets, this explanation started to be very constrained. Later on, it was understood that the third peak anomaly in Boomerang data was due to systematic errors.

- After the first WMAP release, we worked hard in order to be the first to publish constraints on the radiation density parameter $N_{\rm eff}$, that had not been considered by the WMAP collaboration itself. Our paper **"Measuring the cosmological background of relativistic particles with WMAP", Phys. Rev. D 2003,** was put on-line one week only after the data release. This was the last major cosmological data release in which $N_{\rm eff}$ bounds were not published by the collaboration itself... Soon after, we published joint bounds on $N_{\rm eff}$ and on the total neutrino mass in **"Current cosmological bounds on neutrino masses and relativistic relics", Phys. Rev. D 2004,** presented in section 5.1, pages 285-297, stressing that there was a degeneracy between these parameters (which is not true anymore with Planck accuracy).

- We analysed the sensitivity of new SDSS galaxy redshift data to neutrino masses in **"Cosmological parameters from large scale structure - geometric versus shape information", JCAP 2010,** with a new approach showing how much information is contained in the baryonic oscillation features compared to the smooth overall shape of the matter power spectrum.

- I spend a majority of my research time in 2012-2013 working on the analysis of the Planck satellite data. I played a major role in the writing of the neutrino sections in the main cosmology paper, **"Planck 2013 results. XVI. Cosmological parameters", arXiv:1303.5076 [astro-ph.CO].** In this work, we published unprecedentedly strong and robust constraints on neutrino mass and density. The neutrino section (and its companion BBN section) are presented in section 5.4 of this manuscript, pages 329-342.

Also, before the Planck release, we derived in **"Cosmological lepton asymmetry with a nonzero mixing angle θ_{13}", Phys. Rev. D 2012,** presented in section 5.3, pages 317-327, the strongest limit ever found on the neutrino asymmetry and chemical potentials. This progress was triggered mainly not by WMAP data, but by new data on the particle physics side, especially the measurement of the mixing angle θ_{13} by the RENO and Daya Bay experiments. The existence of such large mixing proves that neutrino oscillations in the early universe were very efficient, and tended to equalise the phase-space distribution function of the three mass eigenstates. As a result, the degeneracy between the parameters μ_e and $(\mu_e + \mu_\nu + \mu_\tau)$ known to exist in the "degenerate BBN scenario" cannot work, and measurements of the primordial deuterium abondance provide very strong bounds on the initial chemical potential of all three flavour eigenstates.

2.3.2 Non-standard active neutrinos

Standard active neutrinos are assumed to be fully decoupled below a temperature of 1 MeV. This assumption can be relaxed in several ways. I have already explored some of them, but much more work remains to be done in this field.

A relic particle with a lifetime of the same order of magnitude as the age of the universe could decay and produce extra neutrinos below $T \sim 1$ MeV. Since the newly produced neutrinos could not thermalise, this scenario would induce non-thermal corrections in the neutrino phase-space distribution. As already mentioned in some of the previous sections, we considered this case in **"Do observations prove that cosmological neutrinos are thermally distributed?", Phys. Rev. D 2005.** Besides a discussion of the underlying model and a forecast of future experimental sensitivity to its parameters, we showed that the cosmological data available at that time were not in favour of such non-thermal distorsions.

Neutrino masses could be induced by a coupling term between neutrinos and a scalar field. If this field plays the role of dark energy, its vacuum expectation value generates an effective neutrino mass. In this class of models, the neutrino mass depends on time and location. This idea has given rise to a very large number of publication. In **"Model independent constraints on mass-varying neutrino scenarios", Phys. Rev. D 2009,** we updated constraints on this scenario with recent cosmological data, and obtained very strong bounds. It should however be noted that our paper was relying on the assumption that the formation of non-linear neutrino clumps, that may result from the fifth force generated by the coupling with a light scalar field, would contradict observations. This assumption is not necessarily valid (but is very difficult to test).

2.3.3 Light sterile neutrinos

The possibility of active-sterile neutrino oscillations is very intriguing, especially given the few anomalies claimed to exist in LSND, MiniBoone and reactor data. Although far from being conclusive, these anomalies suggest that there might be at least one sterile neutrino with a mass of the order of one eV. The cosmological signature of such sterile neutrinos depends on their production mechanism (since they do not necessarily thermalise). With a PhD student, I confronted various assumptions to existing data in **"Cosmological constraints on a light non-thermal sterile neutrino", Phys. Rev. D 2009,** presented in section 5.2, pages 299-316. This analysis was updated in the Planck paper **"Planck 2013 results. XVI. Cosmological parameters", arXiv:1303.5076 [astro-ph.CO],** pages 329-342, in section 6.3.3., for which I was a leading author. Using Planck alone, it is not possible to exclude any kind of sterile neutrinos with a mass in the eV range, but joint constraints from particle physics and cosmology are now putting this scenario under considerable tension.

2.3.4 Heavy sterile neutrinos

Heavy sterile neutrinos with a mass in the keV range are very interesting dark matter candidates for two reasons: first, their existence and their production are easy to motivate in simple extensions of the standard model of particle physics; second, they can leave distinct signatures, since they would be warm and decaying dark matter particles.

In **"Constraining the window on sterile neutrinos as warm dark matter", Mon. Not. Roy. Astron. Soc. 2002,** we showed that sterile neutrinos produced through non-resonant oscillations with active neutrinos can in principle be completely ruled out. Indeed, the analysis of Lyman-alpha forests in quasar spectra provides information on structure formation at small scales and high redshift. Warm dark matter tends to slow down structure formation on small scales. Hence, Lyman-alpha data have the potential to rule out warm dark matter with a large velocity dispersion, i.e., with a small mass. On the other hand, if dark matter is made of sterile neutrinos and if their mass is too large, we should see their decay line in X-ray observations of galactic and sub-galactic halos. In this MNRAS paper, we showed that the window on the mass of *non-resonantly-produced sterile neutrino dark matter* could be closed soon, when bounds from Lyman-alpha and X-ray data would cross each other.

I then collaborated with Lyman-alpha experts (in particular, Matteo Viel) in order to improve lower bounds on the warm dark matter mass (for different warm dark matter candidates, including a sterile neutrino). As Lyman-alpha data was improving, we published updated bounds first in **"Constraining warm dark matter candidates including sterile neutrinos and light gravitinos with WMAP and the Lyman-alpha forest", Phys. Rev. D 2005,** and then in **"Can sterile neutrinos be ruled out as warm dark matter candidates?", Phys. Rev. Lett. 2006,** presented in section 5.5, pages

343-346. These works did achieve the goal of closing the window on the mass of non-resonantly-produced sterile neutrino dark matter.

A few years later, we extended our analysis to the more general case of cosmological models with a mixture of cold and warm dark matter: **"Lyman-alpha constraints on warm and on warm-plus-cold dark matter models", JCAP 2009.** Our motivation was twofold. The less natural motivation comes from the fact that, in principle, several dark matter particles could co-exist in the universe, with different masses and velocity dispersions. Hence there could be at the same time a cold component and a warm component. However, the most natural motivation comes from sterile neutrinos produced through resonant oscillations with active neutrinos. In that case, it was shown by Laine & Shaposhnikov (2008) that the phase-space distribution of sterile neutrinos is very peculiar, with a strong enhancement of low-momentum particles. Then, one would have a single dark matter particle in the universe, but this single species would behave effectively like the superposition of a cold component and a warm component. In **"Realistic sterile neutrino dark matter with keV mass does not contradict cosmological bounds", Phys. Rev. Lett. 2009,** presented in section 5.6, pages 347-350, we explicitly considered a model of this type, and showed that mass bounds from Lyman-alpha data are much weaker in this case than for non-resonantly produced sterile neutrinos. The conclusion is that resonantly produced sterile neutrinos are still valid dark matter candidates. This category of models could still be excluded or discovered in the near future thanks to better X-ray observations.

Part II
Choice of most representative publications

3 Neutrino effects on cosmological observables

3.1 Neutrinos, CMB and LSS, chapters 5 and 6 of "Neutrino Cosmology", CUP 2013

NEUTRINO COSMOLOGY

JULIEN LESGOURGUES
École Polytechnique Fédérale de Lausanne (EPFL), Switzerland
CERN, Switzerland
CNRS – Université de Savoie, France

GIANPIERO MANGANO
Istituto Nazionale di Fisica Nucleare (INFN), Italy

GENNARO MIELE
University of Naples Federico II, Italy

SERGIO PASTOR
IFIC, CSIC – Universitat de València, Spain

CAMBRIDGE
UNIVERSITY PRESS

Contents

5

Neutrinos in the cosmic microwave background epoch

The statistical properties of CMB temperature and polarization anisotropy maps encode very precise information on the history and composition of our universe. They depend primarily on the behaviour of inhomogeneities in the photon and baryon medium until photon decoupling, which *feels* all other species in two ways: through their impact on the cosmological background evolution, and via their contribution to the local gravitational forces. This is why neutrinos play an indirect yet important role in the physics of CMB anisotropies, and why present (and future) data on these observables give us quite remarkable pieces of information on neutrino properties.

To understand this point quantitatively, we need to follow photon decoupling at a much more detailed level than in Section 2.4.1. This is the subject of Section 5.1, where we overview the main features of CMB physics, of cosmological perturbation equations, the different contributions to the spectrum of CMB temperature anisotropies, and the effect of each cosmological parameter on the CMB spectrum. Neutrinos will appear on stage in Section 5.2, where we focus on the evolution of their perturbations until photon decoupling, and in Section 5.3, where we infer the effect of neutrino abundance, masses and properties on CMB anisotropies. Finally, Section 5.4 is a brief summary of recent constraints on neutrino properties, exploiting CMB data alone.

In the following pages, physical quantities are written as the sums of their spatial averages, denoted by an overline, and their fluctuations in real or Fourier space. For instance, the density of a given species i will read $\rho_i(\eta, \vec{x}) = \overline{\rho}_i(\eta) + \delta\rho_i(\eta, \vec{x})$, where η stands for conformal time and $\vec{x}$ for comoving coordinate. To simplify the notation, we will use the same symbol for the perturbation in real space (e.g., $\delta\rho_i(\eta, \vec{x})$) and in Fourier space ($\delta\rho_i(\eta, \vec{k})$).

5.1 Cosmic microwave background anisotropies

5.1.1 Overview

CMB physics mainly depends on the behaviour of three species until recombination: baryons, electrons and, of course, photons.

Baryons and electrons remain strongly coupled throughout recombination via Coulomb scattering. Electric neutrality ensures that their density contrasts $\delta\rho_{\rm B}/\overline{\rho}_{\rm B}$ and $\delta\rho_e/\overline{\rho}_e$ are equal to each other, everywhere in the perturbed universe. They can be considered as a single fluid, whose energy density is dominated by baryons, because they are considerably more massive. For convenience, in the context of CMB physics, the tightly coupled baryon–electron medium is often referred as "baryons" only.

Photons and electrons interact through Compton scattering, which becomes inefficient around the time of recombination, as we saw in Section 2.4.1. At much higher redshift, the tightly coupled photon–baryon(–electron) plasma can be described as a single fluid. This approximation is accurate enough to understand the basics of acoustic oscillations, as we shall do in Section 5.1.5. As long as tight coupling holds, thermal equilibrium imposes a blackbody spectrum locally. Photons can then be described at each point by their temperature (plus some Stokes parameters specifying their polarization state). However, an observer at rest with respect to the coordinate frame but not to the fluid will see a Doppler shift. Hence, in a spherical harmonic expansion of the local temperature distribution, the perturbation at any given point is characterized by a monopole and a dipole.

When photons decouple, we could expect a priori that their distribution function becomes gradually nonthermally distorted, at least at the level of perturbations (we saw in Section 2.4.1 that the background distribution remains of the Bose–Einstein type). However, as long as photons interact only gravitationally, the equivalence principle implies that photons of different energy travelling along a given geodesic are redshifted by the same amount at each point, in such a way that the distribution of photons along this geodesic can experience a temperature shift, but no nonthermal distortions. Hence, after decoupling, photons can be described by a local value of temperature $\overline{T}(\eta) + \delta T(\eta, \vec{x}, \hat{n})$ (and of Stokes parameters for polarization), with extra dependence on the direction of propagation $\hat{n}$, unlike in thermal equilibrium. The same holds for standard decoupled relativistic neutrinos, described by $\overline{T}_\nu(\eta) + \delta T_\nu(\eta, \vec{x}, \hat{n})$. The same arguments cannot be extended to nonrelativistic neutrinos, for which gravitational interactions lead to some distortions in their momentum distribution. Such neutrinos will be described by a more complicated distribution function, depending also on momentum. We will review in Section 5.2.1 the evolution equation for these degrees of freedom.

The tightly coupled photon–baryon fluid experiences pressure forces due to photon pressure $P_\gamma = \rho_\gamma/3$. Any inhomogeneity propagates in the form of acoustic waves. Acoustic oscillations are affected by

- the baryon-to-photon ratio $\eta_{\rm B}$ (defined in Eq. (2.160)), which controls the effective pressure and sound speed of the photon–baryon fluid, and
- gravitational forces, caused by the self-gravity of the fluid and by gravitational interactions with other species.

The dispersion relation of these acoustic waves is such that a given perturbation propagates with only one wavefront, instead of multiple wavefronts as for waves on a water surface. This means that at a given time, a single correlation length appears in the spatial temperature distribution of the fluid. This correlation length is given simply by the distance travelled by a wavefront since some initial time, called the sound horizon. Because of the expansion of the universe, the value of the sound horizon at a given conformal time η is almost insensitive to the choice of initial time η_i, provided that $\eta_i \ll \eta$: the sound horizon does not depend on the early cosmological evolution close to the Big Bang, but rather on the late evolution around the recombination epoch.

After decoupling, free-streaming photons carry information on the local temperature and velocity of the fluid at recombination, near their last scattering point (with minor distortions acquired after decoupling and called secondary anisotropies). We will briefly comment on the fact that they also carry extra information encoded in their polarization state. Hence, to some extent we can reconstruct the map of temperature and polarization fluctuations on the last scattering surface, and extract the correlation length given by the sound horizon at decoupling, projected along a given angle. Indeed, the observed angular correlation function of CMB maps contains one characteristic feature, whose angular scale, shape and amplitude depend on the details of the photon–baryon plasma, the cosmological background evolution, and the presence of any other fluid interacting gravitationally with this plasma.

The correlation function can also be computed in multipole space after expanding CMB maps in spherical harmonics. The angular correlation function is usually noted $C(\theta)$, and its counterpart in harmonic space C_l is called the CMB (temperature or polarization) power spectrum. Strictly speaking, the angular correlation function $C(\theta)$ and the power spectrum C_l contain the same amount of information. However, the dependence of the C_l power spectrum on the underlying cosmological model is more transparent and easy to interpret. As in most of the literature, we will focus on this observable. The power spectrum contains several regularly spaced peaks, corresponding to the various harmonics of the single characteristic feature in $C(\theta)$. A large amount of cosmological information is encoded in the amplitude of each of these peaks.

5.1.2 Perturbation equations

The linearly perturbed universe can be described by a perturbed metric tensor $\overline{g}_{\mu\nu} + \delta g_{\mu\nu}$ and a set of dynamical variables for each species that we will review in this section. Perturbations can be described in several gauges, i.e., using several possible definitions of equal-time hypersurfaces on which spatial averaging is performed, all compatible with the assumption of a homogeneous background. We do not provide details here on the gauge issue, which is well described throughout the literature (see, e.g., Ma and Bertschinger, 1995). For simplicity, we restrict the following presentation to the Newtonian gauge in a spatially flat background spacetime, where the perturbed line element reads

$$ds^2 = a^2(\eta)\left[-(1+2\psi(\eta,\vec{x}))d\eta^2 + (1-2\phi(\eta,\vec{x}))d\vec{x}^2\right] \tag{5.1}$$

and ψ plays the role of the Newtonian gravitational potential on scales much smaller than the Hubble radius. Any other gauge choice would be equally good, because truly observable quantities are always gauge-invariant. We will occasionally refer to the impact of a nonzero spatial curvature, without introducing the full equations of evolution in that case. The whole system of evolution equations for first-order cosmological perturbations in a spatially flat background spacetime is presented in the seminal paper by Ma and Bertschinger (1995). This section contains a pedagogical summary of this reference, sufficient for the purposes of this book. It can also be used to make first contact with cosmological perturbations, before investigating more technical aspects in the original papers.

Energy–momentum vector in the perturbed universe

Let us consider a particle of mass m, of physical momentum p^i (defined in 2.18), and of energy $E = \sqrt{p^2 + m^2}$. As in Chapter 2, we define $y = ap$, and similarly rescale the energy as

$$\epsilon \equiv a\ E = \sqrt{y^2 + a^2 m^2}. \tag{5.2}$$

We will use circumflexes to denote unit vectors, so that the proper momentum can be written as $\vec{p} = p\,\hat{n}$, with components $p^i = p_i = p\,n_i$. In the linearly perturbed universe and in the Newtonian gauge, the components of the comoving energy–momentum vector P_μ can be shown to be related to metric perturbations and to (y, ϵ) through

$$P_0 = -(1+\psi)\epsilon, \qquad P_i = (1-\phi)y\,n_i. \tag{5.3}$$

The geodesic equation can be written in terms of the above variables, and gives the time variation of y for a freely falling particle in the linearly perturbed universe,

$$\frac{dy}{d\eta} = -y\,\phi' - \epsilon\,\hat{n}\cdot\vec{\nabla}\psi, \tag{5.4}$$

with $'$ denoting the derivative with respect to conformal time. The geodesic equation also gives the variation of the direction of propagation $d\hat{n}/d\eta$, accounting for gravitational lensing effects. Both $dy/d\eta$ and $d\hat{n}/d\eta$ are of order one in perturbations, because in a homogeneous universe particles would propagate along straight lines with fixed comoving momentum. A crucial point is that for relativistic particles, we can use $\epsilon = y$ and rewrite the momentum evolution as

$$\frac{d\ln y}{d\eta} = -\phi' - \hat{n}\cdot\vec{\nabla}\psi. \tag{5.5}$$

This equation shows that when travelling across metric perturbations, relativistic decoupled particles experience a relative momentum shift which does not depend on the momentum itself. Hence, for any relativistic free-streaming species which attained an equilibrium distribution, the phase-space distribution keeps the functional form of a Fermi–Dirac or Bose–Einstein function, with the temperature now becoming a function not only of time and space, but also of direction. For these species, nonthermal distortions can be generated only through nongravitational couplings. On the other hand, for nonrelativistic decoupled particles, gravitational interactions do produce nonthermal distortions at the level of perturbations, because the momentum dependence cannot be eliminated from the r.h.s. of (5.4).

Perturbed stress–energy tensor

It is useful to classify the 10 degrees of freedom of the perturbed stress–energy tensor $\delta T_{\mu\nu}$ of each species as scalars, vectors and tensors under spatial rotations (Bardeen, 1980). In fact, in linear perturbation theory, the scalar, vector and tensor sectors are decoupled from each other. In this book, we will focus only on the scalar degrees of freedom. Indeed, the vectors describe vorticity, which quickly decays on all cosmologically interesting scales, at least in the standard picture. The tensors, briefly mentioned in Section 5.1.8, describe gravitational waves. These can be excited by inflation and lead to a signature in the CMB, but in our current understanding, they cannot be observed with a precision sufficient to probe any neutrino effect.

For every perturbed stress–energy tensor, there are four scalar degrees of freedom. They are usually defined as the relative density fluctuation $\delta \equiv \delta\rho/\overline{\rho}$, a function θ related to the bulk velocity divergence (or energy flux divergence), the pressure perturbations δP and a dimensionless potential σ associated to anisotropic

stress (i.e., anisotropic pressure). These four degrees of freedom are related to δT^μ_ν through

$$\overline{\rho}\,\delta = -\delta T^0_0 \tag{5.6}$$

$$(\overline{\rho} + \overline{P})\,\theta = \sum_i \partial_i \delta T^0_i \tag{5.7}$$

$$\delta P = \frac{1}{3}\sum_i \delta T^i_i \tag{5.8}$$

$$(\overline{\rho} + \overline{P})\nabla^2\sigma = -\sum_{i,j}\left(\partial_i\partial_j\frac{1}{3}\nabla^2\delta_{ij}\right)\delta T^i_j. \tag{5.9}$$

The total stress–energy tensor of the multicomponent universe is obtained by summing over quantitites on the l.h.s. in the above equations (for instance, the total δT^0_0 is given by $-\sum_i \overline{\rho}_i\delta_i$, and leads to a total density fluctuation $\delta_{\rm tot} = \sum_i \overline{\rho}_i\delta_i/\overline{\rho}_{\rm tot}$).

The conservation equation $\nabla_\mu T^\mu_\nu = 0$ leads to two equations of motion for the scalar sector, the energy conservation equation and the Euler equation. We see that two more relations would be needed to close the four-variable system. One of these relations is often provided by knowledge of the equation of state or, in the case of fluids with nonadiabatic perturbations, by knowledge of the sound speed. This makes it possible to replace δP as a function of δ. For a perfect fluid, microscopic interactions enforce isotropic pressure and the anisotropic stress vanishes, so that the system is closed. For some classes of imperfect fluids, the anisotropic stress can still be expressed as a function of other variables. In more general cases, and in particular for weakly coupled or collisionless species, the stress–energy tensor and its conservation equations are not sufficient for describing the perturbation evolution.

We will mainly be interested in species that can be characterized by their phase-space distribution function f obeying the (perturbed) Boltzmann equation. This distribution can be decomposed into a background term f_0 depending on y and occasionally on η (as already seen in Section 2.2), plus a perturbation $\delta f(\eta, \vec{x}, \vec{p})$ or $\delta f(\eta, \vec{x}, y, \hat{n})$, depending explicitly on time and on the full phase-space coordinates. For such systems, the stress–energy tensor and the scalar degrees of freedom (δ, θ, δp, σ) can be extracted from f_0 and δf using the perturbed version of Eq. (2.42),

$$T^\mu_\nu = g\int \frac{d^3p}{(2\pi)^3}\frac{P^\mu P_\nu}{E} f(\eta, \vec{x}, \vec{p}). \tag{5.10}$$

This relation can be combined with the Boltzmann equation in order to derive the energy conservation and Euler equations in a different way than from $\nabla_\mu T^\mu_\nu = 0$.

Photons

Before decoupling, the dominant photon interaction is Compton scattering off electrons. CMB physics can be studied in the Thomson limit of Compton scattering, in which the photon energy is assumed to be much smaller than the electron rest energy. The evolution is described by the perturbed version of the Boltzmann equation (2.92). This means that the Liouville operator on the l.h.s. of (2.92) now includes partial derivatives with respect to each phase-space coordinate x^i and p^i. The collisional integral $\mathbf{C}(f_\gamma(\eta, \vec{x}, \vec{p}); f_i)$ on the r.h.s. should be chosen to describe Thomson scattering, and can be simplified by noticing that Pauli blocking and stimulated emission play a negligible role in this context (see Section 2.2.1).

We learned from Eq. (5.5) that even when photons decouple, their phase-space distribution keeps the functional form of a Bose–Einstein distribution, but with a direction-dependent temperature. We can then write the full photon phase-space distribution at any time (before, during and after recombination) as

$$f_\gamma(\eta, \vec{x}, \vec{p}) = \left[\exp\left(\frac{y}{a(\eta)\,\overline{T}(\eta)\left\{1 + \Theta_\gamma(\eta, \vec{x}, \hat{n})\right\}} \right) - 1 \right]^{-1}, \tag{5.11}$$

where $\Theta_\gamma \equiv \delta T/\overline{T}$ stands for the relative photon temperature shift. We recall that after electron–positron annihilation and until today, the product $a(\eta)\,\overline{T}(\eta)$ remains constant in time (see Section 2.4.1). In the absence of temperature fluctuations, we recover the expected background distribution

$$f_{\gamma 0}(y) = \left[\exp\left(\frac{y}{a\,\overline{T}} \right) - 1 \right]^{-1} = \left[\exp\left(\frac{p}{\overline{T}} \right) - 1 \right]^{-1}. \tag{5.12}$$

One can replace f_γ in the Boltzmann equation, expand it at first order in perturbations and turn it into a linear equation of evolution for Θ_γ. After the Liouville operator is expanded, $d\vec{x}/d\eta$ can be replaced by $\hat{n}$ and $dy/d\eta$ by its expression in Eq. (5.4). The expression for $d\hat{n}/d\eta$ is not needed because this vector is contracted with the spatial gradient of f_γ with respect to the direction $\hat{n}$ and the product vanishes at first order in perturbations. After some algebra and simplifications, the Boltzmann equation reduces to

$$\Theta_\gamma{}' + \hat{n} \cdot \vec{\nabla}\Theta_\gamma - \phi' + \hat{n} \cdot \vec{\nabla}\psi = a n_e \sigma_{\rm T}(\Theta_{\gamma 0} - \Theta_\gamma + \hat{n} \cdot \vec{v}_{\rm B}), \tag{5.13}$$

where n_e is the number density of free electrons and $\sigma_{\rm T}$ the Thomson cross section (both previously defined in Section 2.4.1). $\Theta_{\gamma 0}$ is the temperature perturbation monopole, i.e., the average of Θ_γ over all directions $\hat{n}$, whereas $\vec{v}_{\rm B}$ is the (common) bulk velocity of baryons and electrons, as these particles are tightly coupled by Coulomb interactions. Because we are studying scalar perturbations, we only

need to consider the irrotational part of $\vec{v}_{\rm B}$, which is fully given in terms of its divergence $\theta_{\rm B}$.

The interaction term on the r.h.s. of (5.13) is rather intuitive. In the tightly coupled limit, Thomson scattering forces Θ_γ to be equal to $\Theta_{\gamma 0} + \hat{n}\cdot\vec{v}_{\rm B}$, i.e., to be independent of direction apart from a dipole term due to the Doppler effect, or in other words to the motion of the photon–baryon fluid with respect to an observer with fixed coordinates. Indeed, in a particular frame comoving with the baryons, $\vec{v}_{\rm B}$ would vanish, and the role of Thomson scattering would be to enforce an isotropic temperature distribution such that $\Theta_\gamma = \Theta_{\gamma 0}$. This is what we expect in a fluid in thermal equilibrium.

The role of a CMB Boltzmann code such as CMBFAST (Seljak and Zaldarriaga, 1996), CAMB (Lewis *et al.*, 2000), CMBEASY (Doran, 2005) or CLASS (Blas *et al.*, 2011) is precisely to solve Eq. (5.13) coupled with other equations of evolution for baryons, dark matter or neutrinos (the latter two being coupled only gravitationally). This linear system of differential equations describes the probability evolution in the stochastic theory of cosmological perturbations (as we shall see in more detail in Section 5.1.4). The system can be more conveniently solved in Fourier space. It is also more practical to reduce the dimensionality of the problem by expanding $\Theta_\gamma(\eta,\vec{k},\hat{n})$ in spherical harmonics. We note that in the Fourier transform of Eq. (5.13), $\hat{n}$ enters only through the combination $\mu\equiv\hat{n}\cdot\hat{k}$, i.e., the cosine of the angle between the direction of propagation and the wavevector. This rotational symmetry of the equation around the axis defined by $\hat{n}$ is a consequence of the isotropy of the Friedmann background. Moreover, initial conditions respect the same symmetry, because the temperature of tightly coupled photons can only depend on direction through a monopole and a dipole oriented along $\hat{n}$. Hence, we can consider Θ_γ as a function of $(\eta,\vec{k},\mu)$ only and perform a one-dimensional Legendre transformation with respect to μ, instead of a two-dimensional transformation with respect to $\hat{n}$,

$$\Theta_\gamma(\eta,\vec{k},\mu) = \sum_l (-i)^l (2l+1)\Theta_{\gamma l}(\eta,\vec{k})P_l(\mu), \tag{5.14}$$

where $\Theta_{\gamma 0}(\eta,\vec{k})$ is just the Fourier transform of the monopole which already appeared in Eq. (5.13). After these transformations, the Boltzmann equation leads to an infinite hierarchy of coupled equations for the multipole moments of Θ_γ:

$$\begin{aligned}
\Theta_{\gamma 0}{}' &= -k\Theta_{\gamma 1} + \phi' \\
\Theta_{\gamma 1}{}' &= \frac{k}{3}\left(\Theta_{\gamma 0} - 2\Theta_{\gamma 2} + \psi\right) + a n_e \sigma_{\rm T}\left(\frac{\theta_{\rm B}}{3k} - \Theta_{\gamma 1}\right) \\
\Theta_{\gamma l}{}' &= \frac{k}{(2l+1)}\left[l\Theta_{\gamma(l-1)} - (l+1)\Theta_{\gamma(l+1)}\right] - a n_e \sigma_{\rm T}\Theta_{\gamma l}, \qquad \forall\, l \geq 2.
\end{aligned} \tag{5.15}$$

One can show that the first three momenta are related to the scalar degrees of freedom introduced in the previous subsection through

$$\delta_\gamma = 4\Theta_{\gamma 0}, \qquad \theta_\gamma = 3k\Theta_{\gamma 1}, \qquad \sigma_\gamma = 2\Theta_{\gamma 2}. \tag{5.16}$$

We notice that in the tightly coupled regime, $\Theta_\gamma(\eta, \vec{k}, \mu)$ is the sum of an isotropic term and a Doppler term. This means that all multipoles $\Theta_{\gamma l}(\eta, \vec{k})$ with $l \geq 2$ are negligible in this limit.

Baryons

Baryons (or, as we mentioned previously, the tightly coupled baryon–electron fluid) can be described by exactly the same Boltzmann equation as photons, maintaining their phase space density $f_{\rm B}$, with a coupling term opposite to the one in the photon equation. As for photons, it reduces to an equation for the baryon temperature fluctuation $\Theta_{\rm B}$. However, further simplifications arise in the limit of nonrelativistic baryons, because all Legendre momenta $\Theta_{{\rm B}l}$ can be neglected apart from the monopole, related to the density fluctuation $\delta_{\rm B}$, and the dipole, which gives the bulk velocity divergence $\theta_{\rm B}$. After some algebra, the full Boltzmann equation eventually reduces to the energy conservation equation and the Euler equation sourced by Thomson scattering,

$$\begin{aligned} \delta_{\rm B}' &= -\theta_{\rm B} + 3\phi' \\ \theta_{\rm B}' &= -\frac{a'}{a}\theta_{\rm B} + k^2\psi + R^{-1}\, a n_e \sigma_{\rm T}(\theta_\gamma - \theta_{\rm B}), \end{aligned} \tag{5.17}$$

where we have defined the baryon-to-photon ratio R, rescaled by a factor of $3/4$ to get simpler equations in the following:

$$R(\eta) \equiv \frac{3}{4}\frac{\overline{\rho}_{\rm B}(\eta)}{\overline{\rho}_\gamma(\eta)}. \tag{5.18}$$

The factor $\overline{\rho}_{\rm B}$ appearing in the denominator in the baryon Boltzmann equation (5.17) should not be a surprise. The limit $\overline{\rho}_{\rm B} \to \infty$ corresponds to an infinite average baryon mass, i.e., to the limit where no photon carries enough energy to transfer momentum to the baryon–electron fluid in each Thomson scattering process. In this case, the coupling term does not affect the bulk velocity of baryons. Note that in Eqs. (5.17), we neglected any pressure term (i.e., any particle velocity dispersion) for the baryons. This approximation is valid for the large cosmological scales in which we are interested in this book. It would be incorrect on scales smaller than the baryon Jeans length, which is today in the range of galactic scales, i.e., deep in the nonlinear regime.

Cold dark matter

Cold dark matter (CDM) is assumed to have decoupled from other species when already nonrelativistic and well before the CMB formation epoch. Its Boltzmann equation reduces to the same equations as for baryons but without the coupling term:

$$\delta'_{\rm C} = -\theta_{\rm C} + 3\phi'$$
$$\theta'_{\rm C} = -\frac{a'}{a}\theta_{\rm C} + k^2\psi. \tag{5.19}$$

Another way to derive these equations is to write the energy conservation and Euler equations for a species such that the pressure $\overline{P}$, pressure perturbation δP, and anisotropic pressure potential σ all vanish.

Neutrinos

Because the impact of neutrinos on the CMB is the main topic of this chapter, we will present and discuss neutrino equations separately in Section 5.2. In the current section, we limit our description of CMB physics to the case of a neutrinoless universe.

Einstein equations

The list of evolution equations introduced up to now would form a closed system if metric perturbations ϕ and ψ were known. These functions can be inferred from the total perturbed stress–energy tensor through Einstein equations. For scalar perturbations, Einstein equations provide four independent relations which, along with the previous equations of motion, would lead to a redundant system. The reason is that through Bianchi identities, Einstein equations imply two equations of conservation for the scalar part of the total stress–energy tensor. The same equations could be derived by combining the equations of motion of individual species. Hence, a practical way to solve the full system in the Newtonian gauge without redundancy is to use the equation of motion of each species, plus two Einstein equations playing the role of constraint equations, and providing ϕ and ψ at each step as a function of total matter perturbations. The first can be found from $\delta G^0_0 = 8\pi G\ \delta T^0_0$:

$$k^2\phi + 3\frac{a'}{a}\left(\phi' + \frac{a'}{a}\psi\right) = -4\pi G\ a^2 \sum_i \delta\rho_i. \tag{5.20}$$

Deep inside the Hubble length, this equation gives the Poisson equation, because for $k \gg \frac{a'}{a}$ one gets

$$-\frac{k^2}{a^2}\phi = 4\pi G\ \delta\rho_{\rm tot}. \tag{5.21}$$

On the l.h.s., we recognize the Fourier transform of $a^{-2}\Delta\phi$, where Δ is the Laplacian defined with respect to comoving coordinates, such that $a^{-2}\Delta$ is the physical Laplacian. The r.h.s. is the usual source term in the Poisson equation (in the context of general relativity, the energy density fluctuation plays the role of the total mass density in the Newtonian version of the Poisson equation). To close the system, we need one more component of the Einstein equations, for instance, the one corresponding to the anisotropic stress component of the stress–energy tensor:

$$k^2(\phi - \psi) = 12\pi G a^2 \sum_i (\overline{\rho}_i + \overline{p}_i)\sigma_i . \tag{5.22}$$

We see that as long as the total anisotropic stress can be neglected, the two metric fluctuations coincide. Strictly speaking, it is the gradient of $\phi - \psi$ which vanishes, but $\phi = \psi$ is the only solution of $\Delta(\phi - \psi) = 0$ which is regular everywhere, does not diverge at infinity, and remains compatible with linear perturbation theory.

5.1.3 Adiabatic and isocurvature modes

The full system of coupled differential equations describing linear perturbations that we introduced in the last subsection includes two first-order equations for baryons, two for CDM, and an infinite hierarchy of equations for photons. However, we should keep in mind that as long as photons are tightly coupled, or for wavelengths greater than the Hubble scale, all multipoles above $l = 0$ (the monopole accounting for local density fluctuations) and $l = 1$ (the dipole due to the relative motion between the tightly coupled fluid and the coordinate frame) are negligible. We have seen in the last section how the coupling term in the Boltzmann equation enforces such a simplification, which is a natural consequence of the fact that in a strongly interacting fluid, the kinetics can be entirely described by a bulk velocity. This reduces the effective number of equations of evolution for photons to two, as for baryons. When computing the CMB or the large scale structure (LSS) power spectra, one always chooses initial conditions deep in the super-Hubble and tightly coupled regime, in which this simplification holds. In summary, on super-Hubble scales, all perturbations in a universe with three species (photons, baryons, CDM) can be described by six first-order equations. More generally, for N species, one would get $2N$ first-order equations.[1]

Such a system admits $2N$ independent initial conditions. Half of them can be shown to seed decaying modes that we cannot observe today, because the other half lead to much larger fluctuations. In studying possible mechanisms for the generation

[1] We will see in Section 5.2.2, where we introduce the so-called neutrino velocity isocurvature mode, that collisionless species such as neutrinos constitute a small exception to this rule.

of initial conditions (inflation, dynamics of spontaneous symmetry breaking, etc.), one task consists of identifying which combination of the N nondecaying solutions gets excited. Eventually, in complicated mechanisms in which the generation of initial conditions arises from a superposition of random processes, more than one combination can be excited, with or without statistical correlations between the various initial modes (e.g., in multiple-field inflation).

One particular combination has a particularly simple physical interpretation. In a perfectly homogeneous universe, the Friedmann law combined with our knowledge of particle physics and thermodynamics allows us to predict the evolution of homogeneous densities and pressures $\overline{\rho}_i(t)$ and $\overline{P}_i(t)$ for each species (here t stands for whatever definition of time we are adopting in the Friedmann universe). The simplest realization of an inhomogeneous universe that we can think of is the following: assume that some mechanism introduces a local time-shift (accounting, for instance, for inflationary fluctuations: in single-field inflation, the inflaton is the only clock in the quasi-De Sitter universe, and its fluctuations can be seen as local shifts with respect to average time). In such a hypothetical universe, densities and pressures would be described by functions

$$\begin{aligned} \rho_i(t,\vec{x}) &= \overline{\rho}_i(t+\delta t(\vec{x})) \simeq \overline{\rho}_i(t) + \dot{\overline{\rho}}_i(t)\,\delta t(\vec{x}) \\ P_i(t,\vec{x}) &= \overline{P}_i(t+\delta t(\vec{x})) \simeq \overline{P}_i(t) + \dot{\overline{P}}_i(t)\,\delta t(\vec{x}), \end{aligned} \tag{5.23}$$

where the time-shift function $\delta t(\vec{x})$ (assumed to be of order one in perturbations) would be the same for all species. This assumption makes sense and is preserved by the time evolution, at least on super-Hubble wavelengths, for which different worldlines can be thought to have independent histories. This singles out a specific subclass of initial conditions subject to

$$\frac{\delta\rho_i}{\overline{\rho}_i + \overline{P}_i} = \frac{\dot{\overline{\rho}}_i(t)}{\overline{\rho}_i + \overline{P}_i}\delta t(\vec{x}) = -3\frac{\dot{a}(t)}{a(t)}\delta t(\vec{x}), \tag{5.24}$$

which *does not* depend on the species i (for the last equality, we have used the energy conservation equation (2.48)). In such a perturbed universe, some remarkable properties would emerge. First, each species would have an adiabatic sound speed at least on super-Hubble scales; i.e., the ratio $\delta P_i/\delta\rho_i$ would be given by

$$\frac{\delta P_i(t,\vec{x})}{\delta\rho_i(t,\vec{x})} = \frac{\dot{\overline{P}}_i(t)}{\dot{\overline{\rho}}_i(t)} \equiv c^2_{a,i}(t). \tag{5.25}$$

In addition, the total perturbations (summed over all species) would also be described by an effective sound speed:

$$\delta P(t,\vec{x}) = c^2_{\rm s}(t)\delta\rho(t,\vec{x}), \qquad \text{with } c^2_{\rm s}(t) \equiv \frac{\sum_i \dot{\overline{\rho}}_i(t) c^2_{a,i}(t)}{\sum_i \dot{\overline{\rho}}_i(t)}. \tag{5.26}$$

This property is not true in the general case. Without assuming Eq. (5.23), we could write the total pressure perturbation only as a sum over N independent functions of $\vec{x}$, which could eventually be arranged as

$$\delta P(t,\vec{x}) = \sum_i c^2_{\mathrm{s},i}(t)\delta\rho_i(t,\vec{x}) \\ = c^2_{\mathrm{s}}(t)\delta\rho(t,\vec{x}) + \sum_{i\neq j} d_{ij}(t)\left[\frac{\delta\rho_i}{\overline{\rho}_i+\overline{P}_i} - \frac{\delta\rho_j}{\overline{\rho}_j+\overline{P}_j}\right], \quad (5.27)$$

where the term between brackets stands for the entropy perturbation δS_{ij} of the fluid i compared to another fluid j (chosen arbitrarily as a reference), and the coefficients $d_{ij}(t)$ correspond to the partial derivatives of total pressure P with respect to S_{ij}. Hence, any set of perturbations satisfying Eq. (5.23) is such that the fluctuations of the total effective fluid have adiabatic properties. These solutions of the perturbation equations are called *isentropic* or *adiabatic* modes, whereas any other solution would feature entropy perturbations.

In order to define actual adiabatic initial conditions, one should impose Eq. (5.23) and solve the remaining system of differential equations, composed of only two independent equations. This leads to a basis of two independent initial conditions. When this basis is chosen appropriately, one of the solutions becomes quickly negligible with respect to the other one as time evolves. These two solutions (defined up to an arbitrary normalization constant) are called the decaying and growing *adiabatic modes*. Without Eq. (5.23) being imposed, the full system would have a basis of initial conditions including these two modes plus $2N-2$ entropy modes. A customary way to fix the basis of nonadiabatic modes consists of picking up linear combinations such that all perturbations vanish, except for two fluids with opposite density fluctuations exactly cancelling each other in the expression of spatial curvature fluctuations (at least, in the asymptotic super-Hubble limit). These combinations are called *isocurvature modes*. Any general initial condition can be decomposed on the basis of solutions formed by one growing adiabatic mode, $(N-1)$ growing isocurvature modes, and N decaying modes. Nonadiabatic modes include CDM isocurvature modes (with entropy perturbations between CDM and photons), baryon isocurvature modes, plus other modes if there are more species present in the universe (neutrino isocurvature modes will be mentioned in Section 5.2.2).

Although the simplest mechanisms for the generation of primordial perturbations can be formulated as a unique time-shift effect, and lead to adiabatic perturbations, isocurvature modes might be excited by more complicated mechanisms such as multiple-field inflation in the early universe, leading to a superposition of several independent time-shift functions. However, even when some isocurvature modes

are excited at early times, the assumption that all species were once in thermal equilibrium implies that they share the same local fluctuations in number density, i.e., that any entropy perturbation has been erased. Hence, isocurvature modes should be taken into account only if they are attached to an always decoupled species. A known exception to this rule applies to particles with a sizeable chemical potential, as discussed by Malik and Wands, 2009. Even in thermal equilibrium, such particles can have a chemical potential $\mu(t, \vec{x})$, which could in principle fluctuate spatially, in such a way as to break the adiabaticity condition. This cannot be the case for the photons, baryons and CDM particles discussed here, but we will come back to this issue in the case of neutrinos.

In summary, isocurvature modes require some very specific assumptions and are not expected to be relevant in the simplest cosmological models. Of course, this conclusion is based on theoretical priors. Ultimately, the data should tell us whether isocurvature modes are present or not. So far, all CMB and LSS observations are compatible with purely adiabatic initial conditions, and put strong limits on the amplitude of isocurvature modes which, if any, should be small with respect to the dominant adiabatic contribution. Whenever more precise data become available, these limits will become stronger, or on the contrary we might discover a tiny isocurvature contribution. In the rest of this book, we will assume for simplicity that the universe can be described in terms of purely adiabatic initial conditions.

5.1.4 Power spectra and transfer functions

Power spectrum

The theory of cosmological perturbations is a stochastic theory, whose goal is to predict the statistical properties of perturbations at some arbitrary time η, given the statistical properties of perturbations at initial time $\eta_{\rm in}$ (inferred from quantum field theory in the case of inflationary cosmology). The simplest possible assumption compatible with all observations at the time of writing is that the early universe features gaussian fluctuations. As long as perturbations remain linear, gaussianity is preserved and all fluctuations can be described entirely by their two-point correlation function in real or in Fourier space, for instance, $\langle A(\eta, \vec{k}) A^*(\eta, \vec{k}')\rangle$ for an arbitrary quantity A. For a stochastic gaussian field, different wavevectors are uncorrelated, and the Fourier two-point correlation function is proportional to the Dirac distribution $\delta^{(3)}(\vec{k} - \vec{k}')$. The coefficient of proportionality is called the power spectrum P_A. In a statistically isotropic universe such as the Friedmann universe, the power spectrum can be a function of only the wavenumber k, not of the direction $\hat{k}$. Finally, many authors use the notation $\mathcal{P}_A$ for the power spectrum

rescaled by a factor $k^3/(2\pi^2)$:

$$\mathcal{P}_A(k) = \frac{k^3}{2\pi^2} P_A(k). \tag{5.28}$$

The technical reason for this redefinition is that $\mathcal{P}_A(k)$ represents the contribution of each logarithmic interval in wavenumber space to the two-point correlation function in real space.

The goal of the theory of linear cosmological perturbations is to predict the power spectrum of all quantities at any time, given some primordial power spectrum accounting for initial conditions, e.g., at the end of inflation.

Transfer functions

Like the power spectrum, the system of linear differential equations for cosmological perturbations does not depend on the wavevector direction $\hat{k}$ in the Friedmann universe. Hence this system can be solved only once for each wavenumber k, starting from an arbitrary initial condition. Let us assume, for instance, that we normalize the solution to $\Theta_{\gamma 0}(\eta_{\rm in}, \vec{k}) = 1$; the power spectrum of $\Theta_{\gamma l}$ at a given time would then be given by the actual power spectrum of $\Theta_{\gamma 0}$ at initial time, multiplied by the square of such a solution $\Theta_{\gamma l}(\eta, \vec{k})$.

By convention, in a universe with only adiabatic initial conditions, the initial normalization often refers to a quantity $\mathcal{R}$, called the comoving curvature perturbation. Indeed, in the comoving gauge (in which equal-time hypersurfaces are orthogonal at each point to the total velocity of the cosmic fluid), the dimensionless quantity $\mathcal{R}$ represents the local fluctuation of the spatial curvature in comoving units. In the Newtonian gauge, the curvature perturbation is given by

$$\mathcal{R} = \psi - \frac{1}{3}\frac{\delta\rho_{\rm tot}}{\overline{\rho}_{\rm tot} + \overline{P}_{\rm tot}}. \tag{5.29}$$

All equations can be solved starting from the arbitrary initial condition $\mathcal{R}(\eta, \vec{k}) = 1$. The power spectrum of a given quantity at time η will then be given by the square of the solution multiplied by the initial power spectrum of $\mathcal{R}$.

Equivalently, we could say that all equations of evolution can be divided by a normalizing quantity, namely $\mathcal{R}(\eta_{\rm in}, \vec{k})$ in the usual case. We can then solve the system and find the solution for

$$\Theta_{\gamma l}(\eta, k) \equiv [\Theta_{\gamma l}(\eta, \vec{k})/\mathcal{R}(\eta_{\rm in}, \vec{k})] \tag{5.30}$$

$$\delta_{\rm B}(\eta, k) \equiv [\delta_{\rm B}(\eta, \vec{k})/\mathcal{R}(\eta_{\rm in}, \vec{k})] \tag{5.31}$$

and similar rescaled variables for other perturbations. The quantities on the l.h.s., depending on k rather than $\vec{k}$, are called transfer functions. Their square multiplied by the initial curvature power spectrum gives the power spectrum of the

corresponding quantity at time η. In the following, any perturbation of photons, baryons, CDM, etc., written as a function of a wavenumber instead of a wavevector, will stand for a transfer function normalized with respect to curvature: $f(\eta, k) \equiv [f(\eta, \vec{k})/\mathcal{R}(\eta_{\rm in}, \vec{k})]$.

Primordial spectrum

The primordial curvature spectrum $\mathcal{P}_\mathcal{R}(k)$ is not a function of time, because comoving curvature is conserved on super-Hubble scales (at least in the absence of isocurvature modes). According to the previous definitions, we have

$$\langle \mathcal{R}(\eta_{\rm in}, \vec{k})\, \mathcal{R}^*(\eta_{\rm in}, \vec{k}')\rangle = \frac{2\pi^2}{k^3}\mathcal{P}_\mathcal{R}(k)\, \delta^{(3)}(\vec{k} - \vec{k}'). \tag{5.32}$$

This spectrum can be used to express all other spectra at any time; for instance,

$$\langle \Theta_{\gamma l}(\eta, \vec{k})\, \Theta^*_{\gamma l}(\eta, \vec{k}')\rangle = \frac{2\pi^2}{k^3}\mathcal{P}_\mathcal{R}(k)\, [\Theta_{\gamma l}(\eta, k)]^2\, \delta^{(3)}(\vec{k} - \vec{k}') \tag{5.33}$$

for all η.

Inflation predicts a nearly scale-invariant power spectrum (i.e., a nearly flat $\mathcal{P}_\mathcal{R}(k)$), as a consequence of the nearly constant energy density of the universe during the inflation stage. At first order, deviations from scale-invariance are accounted for by a tilt $n_{\rm s}$ close to unity,

$$\mathcal{P}_\mathcal{R}(k) = A_{\rm s}(k/k_0)^{n_{\rm s}-1}, \tag{5.34}$$

where $A_{\rm s}$ stands for the primordial spectrum amplitude at the arbitrary pivot scale k_0. Beyond leading order, one could consider the running of the tilt with k, the running of the running, etc. A detailed study of quantum scalar perturbations during inflation shows that the tilt running and higher terms in the expansion are negligible (unless in very specific, nonminimal models), and makes it possible to relate $A_{\rm s}$ and $n_{\rm s}$ to the amplitude and shape of the inflaton potential $V(\phi)$ within a small range of field values $\Delta\phi$, called the observable window of inflation.

5.1.5 Acoustic oscillations

Sound speed

A precise solution of the system of differential equations describing cosmological perturbations can only be obtained numerically. Many analytic approximations have been discussed in the literature, at different levels of precision (see, e.g., Hu, 1995). Here, we will remain at the level of a qualitative discussion.

On times and scales for which the baryons and photons can be considered a single tightly coupled fluid, we can compute the sound speed of perturbations in

this fluid as

$$c_{\rm s}^2 = \frac{\delta P_\gamma + \delta P_{\rm B}}{\delta\rho_\gamma + \delta\rho_{\rm B}}. \tag{5.35}$$

Photons and baryons are then in thermal equilibrium with a temperature $T(\eta, \vec{x})$. Relativistic photons satisfy $\delta_\gamma = 4\,\delta T/\overline{T}$ and $\delta P_\gamma = \delta\rho_\gamma/3$, whereas for nonrelativistic baryons we can use $\delta_b = 3\,\delta T/\overline{T}$ and neglect $\delta P_{\rm B}$. The sound speed is then equal to

$$c_{\rm s}^2 = \frac{1}{3(1+R)}, \tag{5.36}$$

where we recall that $R \equiv 3\overline{\rho}_{\rm B}/(4\overline{\rho}_\gamma)$. This ratio increases like the scale factor. It remains much smaller than one during radiation domination, and becomes of order one at the beginning of matter domination, i.e., near the recombination time. Hence, the sound speed in the fluid remains equal to $1/\sqrt{3}$ during radiation domination (or $c/\sqrt{3}$ in physical units), and then drops slowly down to zero. As long as the sound speed is nonzero, acoustic waves propagate in the fluid with a velocity $c_{\rm s}$.

Sound horizon

If initial gravitational and pressure forces would compensate for each other exactly at each point, the tightly coupled fluid would be in equilibrium, with no propagation of acoustic waves. However, primordial perturbations (seeded by inflation, and/or eventually by some alternative mechanism) drive the system locally out of equilibrium at the initial time, for both adiabatic and nonadiabatic initial conditions. Starting from such perturbations, acoustic waves propagate causally, within a distance called the sound horizon. The comoving sound horizon (i.e., the comoving distance travelled by a wavefront since some arbitrary time deep inside the radiation-dominated regime) is given simply by

$$r_{\rm s}(\eta) = \int_{t_{\rm in}}^{t} \frac{c_{\rm s}(t)dt}{a(t)} = \int_{\eta_{\rm in}}^{\eta} c_{\rm s}(\eta')d\eta'. \tag{5.37}$$

This quantity is indeed independent of $\eta_{\rm in}$ as long as it is much smaller than η. During radiation domination, $r_{\rm s}$ is equal to the comoving causal horizon η divided by $\sqrt{3}$.

A driven oscillator

Acoustic waves are density waves in the photon–baryon fluid. They can be represented by the variable $\Theta_{\gamma 0}(\eta, k)$, which remains equal to $\frac{1}{4}\delta_\gamma(t, k)$ and $\frac{1}{3}\delta_{\rm B}(\eta, k)$ as a consequence of thermal equilibrium as long as the tight-coupling approximation holds. The most naive expectation would be that in Fourier space, this variable evolves like $\Theta_{\gamma 0}(\eta, k) \sim \cos[kr_{\rm s}(\eta) + \varphi]$. In particular, for $kr_s(\eta) \ll 1$,

i.e., for wavelengths much larger than the sound horizon, perturbations should still be frozen.

Such solutions indeed emerge from tight-coupling approximations to the full differential system, but not in such a trivial form. Indeed, the equation governing the evolution of $\Theta_{\gamma 0}(\eta, k)$ differs form that of a harmonic oscillator for essentially three reasons:

- The sound speed depends on time, so the oscillator equation for $\Theta_{\gamma 0}(\eta, k)$ has a time-dependent mass.
- The photon–baryon fluid feels gravitational forces, seeded by its own overdensities, and by gravitational interactions with other species (CDM, or neutrinos, as we will see in the next sections). It is also affected by other general relativity effects, such as local time dilation. These effects are accounted for by gradients and time derivatives of metric fluctuations, which act as a driving term in the oscillator equation for $\Theta_{\gamma 0}(\eta, k)$. Because baryons are nonrelativistic, this driving term also evolves when the baryon-to-photon ratio R increases.
- The increasing value of R also changes other properties of the baryon–photon fluid, such as its inertia.

We can track these different effects in the equation governing the evolution of $\Theta_{\gamma 0}(\eta, k)$ at leading order in the tight-coupling limit, which is easy to obtain from Eqs. (5.15) and (5.17). In the limit $\sigma_{\rm T} \to \infty$, we have already seen that Eq. (5.15) implies $\theta_{\rm B} = \theta_\gamma = 3k\Theta_{\gamma 1}$, and $\Theta_{\gamma l} = 0$ for $l \geq 2$. We can combine the second of Eqs. (5.15) with the second of Eqs. (5.17) to eliminate the interaction term. In the remaing equation, we use $\theta_{\rm B} = 3k\Theta_{\gamma 1}$, $\Theta_{\gamma 2} = 0$, and we eliminate $\Theta_{\gamma 1}$ using the first of Eqs. (5.15). Finally, we can replace $\frac{a'}{a}R$ by R', and $3(1+R)$ by $c_{\rm s}^{-2}$. We are left with the second-order differential equation

$$\Theta_{\gamma_0}{}'' + \frac{R'}{1+R}\Theta_{\gamma 0}{}' + k^2 c_{\rm s}^2 \Theta_{\gamma 0} = -\frac{k^2}{3}\psi + \frac{R'}{1+R}\phi' + \phi'', \qquad (5.38)$$

where we can clearly identify a baryon-induced damping term $\frac{R'}{1+R}\Theta_{\gamma 0}{}'$, a pressure term with time-dependent effective mass $k^2 c_{\rm s}^2 \Theta_{\gamma 0}$, and a gravitational driving term on the r.h.s.

Diffusion damping

On top of these effects, we must take into account the fact that close to recombination, the tight-coupling approximation breaks down. Random scattering processes tend to erase perturbations below the photon diffusion length. In a first-order approximation, this length can be found by treating photon diffusion as a random walk, in which photons would pick up a completely random direction at each new interaction with an electron. In this limit, the comoving distance travelled by a

photon between the early universe and some time η would follow

$$r_d^2(\eta) \sim \int_{\eta_{\rm in}}^{\eta} d\eta\, \Gamma_\gamma\, r_\gamma^2, \tag{5.39}$$

where Γ_γ stands for the interaction rate computed with respect to conformal time, and r_γ for the photon mean free path in comoving space. In our case, we know that $\Gamma_\gamma = a n_e \sigma_{\rm T}$. The comoving mean free path (always in natural units) is then given by $r_\gamma = \delta x = \delta\eta = 1/\Gamma_\gamma = (a n_e \sigma_{\rm T})^{-1}$. Finally, we get the expression

$$r_d^2(\eta) \sim \int_{\eta_{\rm in}}^{\eta} \frac{d\eta}{a n_e \sigma_{\rm T}}, \tag{5.40}$$

which does not depend on $\eta_{\rm in}$, provided that $\eta \gg \eta_{\rm in}$. A better approximation to r_d can be found for instance in Hu, 1995, but the preceding result is by far sufficient for understanding the effect of diffusion damping on the CMB spectrum. Photon diffusion will erase perturbations with a wavelength smaller than $\lambda_d \equiv a\, r_d$, i.e., with a wavenumber greater than $k_d \equiv 2\pi/r_d$.

All these driving and damping effects lead to an interesting phenomenology for acoustic oscillations, that we will summarize below. This discussion is essential for understanding the impact of cosmological parameters (and later of neutrinos) on the CMB spectrum. We will distinguish two stages: radiation domination, and the epoch between radiation/matter equality and decoupling.

Radiation domination: Constant acoustic oscillations

During radiation domination, approximate analytic solutions are easy to obtain. One can work in the limit where $R = 0$, $c_{\rm s} = 1/\sqrt{3}$, baryons or cold dark matter density perturbations are negligible with respect to the photons' perturbations and the photon–baryon fluid is tightly coupled. A combination of the $0-0$ and $i-i$ components of the Einstein equation then leads to a simple second-order differential equation. Its two solutions correspond to the growing and decaying adiabatic modes. Indeed, as long as we neglect all fluids but one (the photons), we cannot find entropy modes. The growing solution, involving the Bessel function $J_{3/2}(k c_{\rm s}\eta)$, has the following asymptotic behaviour:

- At wavelengths larger than the sound horizon, all transfer functions are constant over time,

$$4\Theta_{\gamma 0}(\eta, k) = \delta_\gamma(\eta, k) = \frac{4}{3}\delta_{\rm B}(\eta, k) = -2\phi(\eta, k) = -2\psi(\eta, k) = -\frac{4}{3} \tag{5.41}$$

  (given our definition of transfer functions in Section 5.1.4, this means that the photon perturbations are related to the initial curvature perturbation through

$\Theta_{\gamma 0}(\eta, \vec{k}) = -\frac{1}{3}\mathcal{R}(\eta, \vec{k})$). In this regime, acoustic waves propagation is negligible because the comoving sound horizon $r_s \simeq \eta/\sqrt{3}$ is very small with respect to the comoving wavelength $\frac{2\pi}{k}$, and the modes are still frozen to their initial value.

- Inside the sound horizon,

$$4\Theta_{\gamma 0}(\eta, k) = \delta_\gamma = \frac{4}{3}\delta_B(\eta, k) = 4\cos[kr_s(\eta)] \tag{5.42}$$

$$-2\phi(\eta, k) = -2\psi(\eta, k) = -\frac{6}{(k\eta)^2}\cos[kr_s(\eta)]\,. \tag{5.43}$$

Thus, after entering the sound horizon, the modes of photon density oscillate with a constant amplitude, whereas metric fluctuations decay with time. Gravitational forces and time dilation effects then become negligible with respect to pressure forces. Indeed, by inserting these solutions into Eq. (5.38), we clearly see that for $(k\eta) \gg 1$, the driving term on the r.h.s. can be neglected with respect to the term $k^2 c_s^2 \delta_\gamma$ induced by photon pressure. In this limit, Eq. (5.38) reduces to a simple harmonic oscillator equation $\delta_\gamma'' + \frac{k^2}{3}\delta_\gamma = 0$. One can also check that the Poisson equation (5.21) combined with the Friedmann equation gives the correct relation between the asymptotic solutions (5.42) and (5.43).

From equality to decoupling: Damped acoustic oscillations

Several phenomena make the evolution more complicated from the time of matter/radiation equality until that of decoupling:

- The growth of the baryon fraction R and the decrease of the sound speed c_s affect the amplitude of the acoustic oscillations.
- The growth of R also implies that the photon–baryon fluid couples more and more to gravity for the same amount of pressure, shifting the zero point of oscillations in such a way as to increase the fluid density in gravitational potential wells. We can check this from Eq. (5.38). Neglecting the time variation of ϕ, the zero point of temperature oscillations corresponds to $k^2 c_s^2 \Theta_{\gamma 0} = -\frac{k^2}{3}\psi$, i.e., to $\Theta_{\gamma 0} = -(1+R)\psi$. Taking the real space counterpart of this relation, we see that for a gravitational potential well ($\psi < 0$), the value of the overdensity $\delta_\gamma = 4\Theta_{\gamma 0} > 0$ that corresponds to this equilibrium increases with R.
- The metric perturbations are now also influenced by the nonrelativistic matter components (baryons and potentially cold dark matter). So inside the Hubble radius, ϕ and ψ do not decay as quickly as during radiation domination. Thus the gravitational driving term in Eq. (5.38) affects the temperature evolution in a different way than during radiation domination.

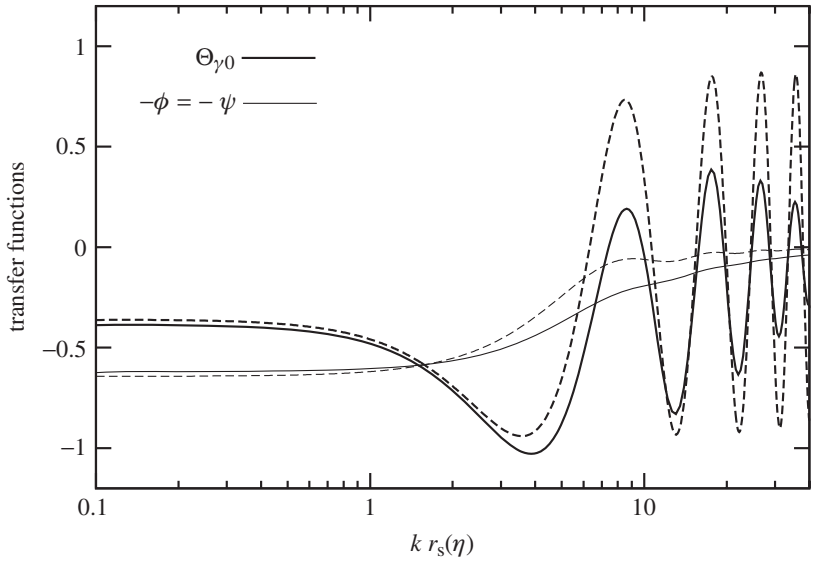

Figure 5.1 A snapshot of the transfer functions $\Theta_{\gamma 0}(\eta, k)$ (thick) and $-\phi(\eta, k) = -\psi(\eta, k)$ (thin) at the time of equality (dashed) and decoupling (solid), in a neutrinoless ΛCDM universe. The wavenumber axis has been rescaled in each case by the exact value of $r_s(\eta)$, to show that the phase of the oscillations is determined by the sound horizon. The negative signs of $\Theta_{\gamma 0}$ and $-\psi$ in the long-wavelength limit comes from the fact that transfer functions have all been normalized with respect to the curvature perturbation $\mathcal{R}$. A positive curvature perturbation corresponds to a gravitational potential hill ($\psi > 0$) and to an underdense region ($\delta_\gamma < 0$) with lower temperature ($\Theta_{\gamma 0} < 0$), and vice versa.

- The baryons and photons cannot be modeled as a single tightly coupled fluid at wavelengths below the diffusion length of the photon λ_d. In Fourier space, scattering processes introduce an exponential cutoff in $\Theta_{\gamma 0}(\eta, k)$ shaped like $\exp[-(k/k_d)^2]$.

To keep our discussion reasonably brief, we do not treat each individual effect here, but refer the reader to, e.g., Hu, 1995 for more details. The leading effects are, however, easy to understand. They are illustrated in Fig. 5.1, which shows the transfer functions $\Theta_{\gamma 0}(\eta, k)$ and $-\psi(\eta, k)$ at the times of equality (dashed curves) and of decoupling (solid curves). We recall that $\phi(\eta, k)$ is equal to $\psi(\eta, k)$ as long as there is no anisotropic stress contribution to the Einstein equations, which is the case in a neutrinoless universe before photon decoupling (because $\Theta_{\gamma 2} \simeq 0$). These transfer functions have been solved numerically with the CMB Boltzmann code CLASS (Blas *et al.*, 2011). The difference between the dashed and solid curves corresponds precisely to the few effects described earlier.

At equality, we see that the numerical results agree with the asymptotic solutions (5.41, 5.42, 5.43), with temperature oscillations roughly symmetric around $\Theta_{\gamma 0} = -\psi$ inside the sound horizon, and of constant amplitude in the large-k limit, in which metric fluctuations are negligible.

At decoupling, the amplitude of photon oscillations has been reduced on all subhorizon scales. The zero point of oscillations has been shifted down with respect to $\Theta_{\gamma 0} = -\psi$, leading to an enhancement of the absolute value of the first/third/fifth/... extremum in $\Theta_{\gamma 0}(\eta, k)$ with respect to the second/fourth/sixth/... extremum. Finally, we can see the exponential damping of oscillations in the large-k limit. These three crucial effects are controlled respectively by the duration of the transition stage between equality and decoupling, by the baryon fraction at decoupling and by the value of the diffusion wavenumber k_d.

A last feature can be noticed in Figure 5.1: even in the super-Hubble limit $k \to 0$, one can see a small evolution in the photon and metric transfer functions between equality and decoupling. The reason is that, although the curvature perturbation $\mathcal{R}$ is a conserved quantity on super-Hubble scales in a universe with adiabatic initial conditions, density contrasts and metric perturbations are not. At the time of equality, the equation of state of the universe changes, and all perturbations readjust to another set of constant values, slightly different from those during radiation domination. Using Einstein equations, one can show that for super-Hubble scales and during matter domination the transfer functions are subject to

$$4\Theta_{\gamma 0}(\eta, k) = \delta_\gamma(\eta, k) = \frac{4}{3}\delta_{\rm B}(\eta, k) = -\frac{8}{3}\phi(\eta, k) = -\frac{8}{3}\psi(\eta, k) = -\frac{8}{5}. \quad (5.44)$$

The coefficients of the last three terms differ slightly from those in Eq. (5.41), valid during radiation domination. In Fig. 5.1, the value of each transfer function at equality and for $k \to 0$ is halfway between Eq. (5.41) and Eq. (5.44), whereas at decoupling it follows Eq. (5.44). This technical detail was worth mentioning in order to understand numerical factors in the Sachs–Wolfe formula that will be introduced in Section 5.1.6.

From decoupling to the current epoch: Gravitational clustering

The evolution of perturbations after decoupling will be discussed in detail in Chapter 6. To anticipate, we simply mention here that in the ideal case of a purely matter-dominated universe, $\phi = \psi$ is constant over time on all scales (super-Hubble and sub-Hubble). In the real universe, this is not true:

- Close to radiation domination, because we know that during radiation domination metric fluctuations quickly decay inside the sound horizon. So, at decoupling, there is still a residual decay of ϕ and ψ.

- During a cosmological constant or dark energy (DE)-dominated stage, which also leads to a decay of the potentials.
- On small scales if there are neutrinos, as we shall see in Chapter 6.

During these stages, nonrelativistic matter components are self-gravitating and their density contrast grows, leading to structure formation.

5.1.6 Temperature anisotropies

Temperature power spectrum

Temperature anisotropies on the last scattering surface can be expanded in spherical harmonics as

$$\frac{\delta T}{T}(\hat{n}) = \sum_{lm} a_{lm} Y_{lm}(\hat{n}). \tag{5.45}$$

The temperature anisotropy seen in a direction $\hat{n}$ is a property of photons traveling along the direction $-\hat{n}$. Hence $\frac{\delta T}{T}(\hat{n})$ coincides with the function $\Theta_\gamma(\eta, \vec{x}, -\hat{n})$ studied in Section 5.1.2, computed today ($\eta = \eta_0$) and at the position of the observer, which we can choose to be the origin for simplicity ($\vec{x} = \vec{o}$). Each a_{lm} can be extracted from the sky map,

$$a_{lm} = (-1)^l \int d\hat{n}\, Y^*_{lm}(\hat{n}) \Theta_\gamma(\eta_0, \vec{o}, \hat{n}), \tag{5.46}$$

where we performed a change of variable $\hat{n} \to -\hat{n}$ inside the integral and used $Y_{lm}(-\hat{n}) = (-1)^l Y_{lm}(\hat{n})$. The function $\Theta_\gamma(\eta, \vec{x}, \hat{n})$ can be expanded in Fourier space and in Legendre multipoles, as in Section 5.1.2. After some simple algebra, the expression for the a_{lm}'s reduces to

$$a_{lm} = (-i)^l \int \frac{d^3k}{2\pi^2} Y_{lm}(\hat{k}) \Theta_{\gamma l}(\eta_0, \vec{k}). \tag{5.47}$$

Given that there is a linear relation between multipoles a_{lm} and Fourier modes $\Theta_{\gamma l}(\eta_0, \vec{k})$, it is clear that

- as long as we assume that first-order cosmological perturbations are gaussian, the a_{lm}'s are also gaussian distributed, and their statistics is fully described by two-point correlation functions $\langle a_{lm} a^*_{l'm'} \rangle$;
- because different Fourier modes of a gaussian random field are uncorrelated, $\langle \Theta_{\gamma l}(\eta, \vec{k}) \Theta_{\gamma l}(\eta, \vec{k}')^* \rangle \propto \delta^{(3)}(\vec{k} - \vec{k}')$, different multipoles are also uncorrelated, $\langle a_{lm} a^*_{l'm'} \rangle \propto \delta_{ll'} \delta_{mm'}$;
- the isotropy of the universe, implying an isotropic power spectrum in Fourier space (depending on k but not on $\hat{k}$), also implies an isotropic harmonic spectrum

(depending on l but not m), denoted as

$$C_l = \langle a_{lm} a_{lm}^* \rangle, \qquad \forall m. \tag{5.48}$$

The harmonic power spectrum C_l is precisely the quantity that we want to compute for a given cosmological model and to compare with observations. As a matter of principle, the true harmonic power spectrum in our universe cannot be extracted from observations, because we observe only one realization of the underlying theory describing its evolution, in a finite fraction of our past light cone. However, using an assumption of ergodicity, we can build an estimator of the true power spectrum, taking advantage of the fact that all multipoles with a given l should have the same variance C_l. For an ideal all-sky experiment providing multipoles $a_{lm}^{\rm obs}$, the best estimator reads

$$C_l^{\rm obs} = \frac{1}{2l+1} \sum_{-l \leq m \leq l} \left| a_{lm}^{\rm obs} \right|^2 . \tag{5.49}$$

Note that for a realistic experiment affected by partial sky coverage, anisotropic foregrounds and instrumental noise, building optimal estimators becomes a non-trivial task.

This estimator is expected to deviate randomly from the unknown underlying spectrum. The average deviation for a given l can easily be computed for an ideal full-sky experiment. The estimator $C_l^{\rm obs}$ is obtained by averaging over $(2l+1)$ independent gaussian numbers centered at zero, each with variance C_l. Hence, it obeys a χ^2 distribution with $(2l+1)$ degrees of freedom, a mean equal to C_l and a variance $\sqrt{2/(2l+1)}C_l$ (note that this distribution is asymmetric around its peak, especially at low l). As expected, the variance decreases with increasing l, because for high multipoles we can average over more independent realizations of the same stochastic process. This random deviation, playing the role of a theoretical error, is called *cosmic variance*.

Brute-force calculation of the temperature anisotropy spectrum

A brute-force approach to computing the temperature anisotropy spectrum up to some multipole $l_{\rm max}$ consists of integrating all equations with at least $l_{\rm max}$ multipoles in the photon equations Eq. (5.15), between some initial time (at which all wavenumbers of interest are on super-Hubble scales) and today. Using Eq. (5.48), (5.47), (5.33) and the relation of orthogonality of spherical harmonics, we find that the temperature spectrum is given as a function of the photon transfer function (evaluated today) and of the curvature primordial spectrum by

$$C_l = \frac{1}{2\pi^2} \int \frac{dk}{k} [\Theta_{\gamma l}(\eta_0, k)]^2 \mathcal{P}_{\mathcal{R}}(k). \tag{5.50}$$

A technical issue comes from the fact that the hierarchy of coupled photon equations is infinite. Any given numerical algorithm can only integrate over a finite number of multipoles, and the truncation in l-space may cause a reflection of power down to lower multipoles. Let us briefly discuss how to avoid such problems.

As discussed in Sections 5.1.2 and 5.1.3, before photon decoupling, only the first two photon multipoles are important. After that time, higher and higher multipoles are populated. An approximate free-streaming solution (neglecting the gravitational coupling of photons, i.e., neglecting the sourcing of photon perturbations by metric perturbations) reads $\Theta_{\gamma l}(\eta, k) \propto j_l(k\eta)$, where $j_l(x)$ denote spherical Bessel functions. These functions peak near $x = l + \frac{1}{2}$, and feature damped oscillations for $x > l$. This gives a rough idea of the shape of the actual solution. In particular, it shows that at a given time η and as a function of l, $\Theta_{\gamma l}(\eta, k)$ peaks around $l \sim k\eta$, whereas multipoles with $l \gg k\eta$ are vanishingly small. This can be understood geometrically: at time η, the observer sees photons emitted on his own last scattering surface, at a comoving radius $r = (\eta - \eta_{\rm LS})$ away from him (assuming no spatial curvature). As soon as $\eta \gg \eta_{\rm LS}$, we can approximate r by η. Fourier modes of comoving wavelength $2\pi/k$ on this surface are seen by the observer under an angle $\theta = 2\pi/(kr)$ in the small-angle approximation. This means that the angular separation between a maximum and a minimum is $\theta = \pi/(kr)$, and that in multipole space the contribution peaks near $l \sim \pi/\theta \sim kr \sim k\eta$. Hence, for a brute-force calculation of the anisotropy spectrum today and until multipole $l_{\rm max}$, one should choose a maximum value of k on the order of $k_{\rm max} \sim l_{\rm max}/\eta_0$. A typical choice in numerical codes is $k_{\rm max} = 2l_{\rm max}/\eta_0$. This ensures that even today and for the largest wavenumbers, the transfer function $\Theta_{\gamma l}(\eta, k)$ has vanishingly small multipoles for $l > l_{\rm max}$, so that a truncation at $l_{\rm max}$ is harmless.

This brute-force approach is extremely time-consuming, because it relies on the integration of thousands of coupled equations for each wavenumber. In addition, it does not shed much light on the underlying physics. In the next section, we will introduce the alternative line-of-sight approach. This method provides a much more intuitive expression for the various contributions to each C_l, and speeds up Boltzmann codes in a spectacular way.

Line-of-sight integral

Let us consider photons travelling along a given geodesic, between one point on the last scattering surface and a CMB detector. This geodesic is not a straight line, because of gravitational lensing effects caused by intervening matter fluctuations. However, changes in the direction of propagation of photons are only important for second-order perturbation theory. Because in this chapter we limit ourselves to first-order perturbations, we can approximate each photon geodesic as a straight line. This means that a bunch of photons reaching us today from a direction $-\hat{n}$

has been traveling since decoupling in a constant direction $\hat{n}$. Their comoving coordinate at time η was $\vec{x} = -r\hat{n} = -(\eta_0 - \eta)\hat{n}$, because relativistic particles travel toward us with an evolution of the radial coordinate r given by $dr = -d\eta$ in natural units. Any function $\mathcal{F}(\eta, \vec{x}, \hat{n})$ evolves along such a trajectory according to the total derivative

$$\frac{d\mathcal{F}}{d\eta} = \mathcal{F}' + \frac{d\vec{x}}{d\eta} \cdot \vec{\nabla}\mathcal{F} = \mathcal{F}' + \hat{n} \cdot \vec{\nabla}\mathcal{F}, \tag{5.51}$$

where we used the straight-line approximation $d\hat{n}/d\eta = 0$. We wish to integrate the Boltzmann equation over the photon trajectory and relate the temperature fluctuation observed today to the one on the last scattering surface. For this purpose, it is necessary to consider the function $\mathcal{F}(\eta, \vec{x}, \hat{n}) \equiv \Theta_\gamma(\eta, \vec{x}, \hat{n}) + \psi(\eta, \vec{x})$, where Θ_γ is the photon temperature perturbation and ψ one of the two metric perturbations (both introduced in Section 5.1.2). The total derivative of this sum is

$$\frac{d}{d\eta}(\Theta_\gamma + \psi) = {\Theta_\gamma}' + \psi' + \hat{n} \cdot \vec{\nabla}(\Theta_\gamma + \psi). \tag{5.52}$$

We can use the Boltzmann equation (5.13) and write the r.h.s. as

$$\frac{d}{d\eta}(\Theta_\gamma + \psi) = a n_e \sigma_T (\Theta_{\gamma 0} - \Theta_\gamma + \hat{n} \cdot \vec{v}_\mathrm{B}) + \psi' + \phi'. \tag{5.53}$$

We want to put all the terms involving $\Theta_\gamma(\eta, \vec{x}, \hat{n})$ inside a total derivative, in order to integrate it along the line of sight. This is possible after introducing the integral of the scattering rate along the line of sight,

$$\tau(\eta) \equiv \int_\eta^{\eta_0} d\eta\, a n_e \sigma_\mathrm{T}, \tag{5.54}$$

called the optical depth. The visibility function $g(\eta) \equiv -\tau(\eta)' e^{-\tau(\eta)}$ can be interpreted as the probability of a photon reaching us today having experienced its last scattering at time η. The decoupling time η_LS can actually be defined as the maximum of this function. Note that n_e scales like a^{-3} between electron–positron annihilation and recombination, and remains very small after that time. As a consequence, $\tau(\eta)$ is huge for $\eta \ll \eta_\mathrm{rec}$ and tiny for $\eta \gg \eta_\mathrm{rec}$, expressing the transition from an opaque to a transparent universe taking place around recombination. We can now take Eq. (5.53), replace $a n_e \sigma_\mathrm{T} = -\tau'$, multiply both sides by $e^{-\tau}$, and rearrange the terms as

$$\frac{d}{d\eta}\left[e^{-\tau}(\Theta_\gamma + \psi)\right] = g\left(\Theta_{\gamma 0} + \psi + \hat{n} \cdot \vec{v}_\mathrm{B}\right) + e^{-\tau}(\phi' + \psi'). \tag{5.55}$$

We finally integrate this relation along the line of sight, beween some arbitrary initial time η_in chosen well before photon decoupling, and the present time η_0. We can use the fact that in the limit $\eta_\mathrm{in} \ll \eta_\mathrm{LS}$, the exponential $e^{-\tau(\eta_\mathrm{in})}$ is vanishingly

small, whereas $e^{-\tau(\eta_0)}$ equals one by definition. We obtain

$$\Theta_\gamma(\eta_0, \vec{o}, \hat{n}) = -\psi(\eta_0, \vec{o}) + \int_{\eta_{\rm in}}^{\eta_0} d\eta \left\{ g \left(\Theta_{\gamma 0} + \psi + \hat{n} \cdot \vec{v}_{\rm B} \right) + e^{-\tau} (\phi' + \psi') \right\}. \tag{5.56}$$

The quantity on the l.h.s. is the temperature fluctuation for photons crossing the origin today in a direction $\hat{n}$. Hence, it represents the temperature anisotropy seen by the observer in the direction $-\hat{n}$. The first term on the right is the metric fluctuation today at the observer's location, causing a local blueshifting of incoming photons if we live in a potential well. Because this term is isotropic, a CMB experiment could not distinguish between this contribution and a shift in the average photon temperature, typically of the order of $[\psi(\eta_0, \vec{o}) \times \overline{T}] \sim 10^{-5} \overline{T}$. This effect is tiny, so from now on we will neglect the term $\psi(\eta_0, \vec{o})$ in Eq. (5.56). The remaining terms in the integral show that in a given direction and for a given recombination history, the observed temperature anisotropy depends entirely on two quantities, namely

- the sum $(\Theta_{\gamma 0} + \psi + \hat{n} \cdot \vec{v}_{\rm B})$ along the portion of the line-of-sight where the visibility function is not negligible, i.e., around the time of decoupling (and also close to us, if the universe gets reionized at low redshift);
- the sum $(\phi' + \psi')$ along the portion of the line of sight where $e^{-\tau}$ is not negligible, i.e., between decoupling and today.

Because for $\eta \ll \eta_{\rm LS}$, the two functions $g(\eta)$ and $e^{-\tau(\eta)}$ are negligible, the result of the integral in Eq. (5.56) does not depend on the value of $\eta_{\rm in}$. This equation is therefore often written in the limit $\eta_{\rm in} = 0$.

Equation (5.56) proves that the knowledge of all photon multipoles $\Theta_{\gamma l}(\eta, \vec{x}, \hat{n})$ with $l > 1$ is not directly needed for computing CMB anisotropies. This suggests that the whole CMB anisotropy spectrum could be obtained with a much more economical method than the brute–force approach described previously. Indeed, the approach that we summarized here in real space can be transposed into Fourier space, as pointed out by Zaldarriaga and Harari, 1995. Starting from the Fourier-expanded version of the Boltzmann equation (5.13), we can put all terms involving $\Theta_\gamma(\eta, \vec{k}, \mu)$ inside a total time derivative, integrate along the line of sight, perform an integration by parts in order to put all the μ-dependence in a factor $e^{ik\mu(\eta - \eta_0)}$, expand this factor in Legendre space using spherical Bessel functions, and obtain the following exact expression for the photon transfer function:

$$\Theta_{\gamma l}(\eta_0, k) = \int_{\eta_{\rm in}}^{\eta_0} d\eta \left\{ g \left(\Theta_{\gamma 0} + \psi \right) + \left(g k^{-2} \theta_{\rm B} \right)' + e^{-\tau} (\phi' + \psi') \right\} j_l[k\,(\eta_0 - \eta)], \tag{5.57}$$

where we omit the argument (η, k) of the four transfer functions $(\phi, \psi, \Theta_{\gamma 0}, \theta_b)$ standing on the r.h.s. The quantity between curly brackets is called the temperature source function, usually denoted by $S^{\rm T}(\eta, k)$. The temperature anisotropy spectrum then follows from Eq. (5.50).

Equations (5.57) and (5.50) show that to compute the temperature spectrum up to some arbitrary multipole $l_{\rm max}$, a Boltzmann code needs only to find the evolution of the four quantities $(\phi, \psi, \Theta_{\gamma 0}, \theta_{\rm B})$. Of course, to use Einstein equations, it is necessary to include a few more variables, namely the density, velocity and shear perturbation of each species. Including higher-temperature multipoles $\Theta_{\gamma\, l}$ with $l > 2$ in the differential equations remains necessary to avoid some artificial reflection of power caused by the truncation in l-space. But the truncation scheme should be designed only for accurately computing the first few multipoles. A nice scheme was proposed by Ma and Bertschinger, 1995 in the context of brute-force calculations. Because free-streaming photons approximately follow $\Theta_{\gamma l}(\eta, k) \propto j_l(k\eta)$ in the limit of negligible gravitational interactions, the recurrence relation statisfied by spherical Bessel functions can be used to extrapolate the behaviour of a multipole $\Theta_{\gamma(l+1)}$ given that of multipoles $\Theta_{\gamma l}$ and $\Theta_{\gamma(l-1)}$. This offers a way to smoothly truncate the hierarchy at a given l, limiting the reflection of power with respect to setting $\Theta_{\gamma(l+1)}$ brutally to zero. With such a scheme, a truncation of the Boltzmann hierarchy at an $l_{\max\gamma}$ of a few tens will introduce a very small error into the solution for multipoles $l = 0, 1, 2$. The power of the line-of-sight approach is summarized by the fact that a truncation at $l_{\max\gamma} = O(10)$ is sufficient for computing the C_l's up to $l_{\rm max} = O(10^3)$.

However, the value of $l_{\rm max}$ still determines the maximum wavenumber $k_{\rm max} \sim l_{\rm max}/\eta_0$ at which the source function needs to be evaluated, because this wavenumber carries information about perturbations on the last scattering surface seen today under an angle $\theta \sim \pi/l_{\rm max}$. The reduction of the number of differential equations takes place in multipole space, not in wavenumber space. But the factor $[l_{\max\gamma}/l_{\rm max}]$ makes it possible to gain a few orders of magnitude in computation time over the brute-force approach.

The line-of-sight approach was implemented for the first time in the Boltzmann code CMBFAST by Seljak and Zaldarriaga, 1996, and is used by all other modern codes.

Sachs–Wolfe, Doppler and integrated Sachs–Wolfe contributions

One can understand physically the few terms contributing to the observed CMB anisotropies in Eq. (5.56):

1. As first shown by Sachs and Wolfe, 1967, the most obvious contribution to the observed temperature fluctuation in one direction is given by the intrinsic

temperature fluctuation on the last scattering surface in the same direction, corrected by a gravitational shift (photons coming from a gravitational potential well [resp. hill] on the last scattering surface are redshifted [resp. blueshifted] when they leave this surface, and are seen with a lower [resp. higher] temperature). The *Sachs–Wolfe contribution* (SW) can be defined as the part of temperature anisotropies sourced by the term $g(\Theta_{\gamma 0} + \psi)$ in Eq. (5.56). The last scattering surface can really be thought of as a surface rather than a thick shell in the instantaneous decoupling limit, i.e., in the ideal situation in which the mean free path of photons would go from zero to infinity at $\eta = \eta_{\rm LS}$. In this limit, one can replace the visibility function $g(\eta)$ with the Dirac delta function $\delta(\eta - \eta_{\rm LS})$, which has the correct normalization. Indeed, one can easily check from the definition of g that $\int d\eta\, g(\eta) = 1$. One can then integrate the Sachs–Wolfe term in Eq. (5.56) and find a contribution

$$\Theta_\gamma^{\rm SW}(\eta_0, \vec{o}, \hat{n}) \simeq \Theta_{\gamma 0}(\eta_{\rm LS}, \vec{x}_{\rm LS}, \hat{n}) + \psi(\eta_{\rm LS}, \vec{x}_{\rm LS}), \tag{5.58}$$

where $\vec{x}_{\rm LS} \equiv (\eta_{\rm LS} - \eta_0)\hat{n}$ is the comoving coordinate at the time of decoupling of a photon hitting us today from the direction $-\hat{n}$. We know from Eq. (5.44) that for small values of k (corresponding to super-Hubble scales) and during matter domination, there is a relation $\Theta_{\gamma 0} = -2/3\,\psi$. This means that in a CMB map smeared over small-scale fluctuations, the SW contribution to the temperature anisotropy in one direction is given by

$$\Theta_\gamma^{\rm SW,smoothed}(\eta_0, \vec{o}, \hat{n}) \simeq \frac{1}{3}\psi(\eta_{\rm LS}, \vec{x}_{\rm LS}) \simeq -\frac{1}{2}\Theta_{\gamma 0}(\eta_{\rm LS}, \vec{x}_{\rm LS}, \hat{n}), \tag{5.59}$$

i.e., that hot regions in the observed anisotropy map correspond to cold regions on the last scattering surface, and vice versa. The reason is that photons leaving a hot, overdense region lose a lot of energy when climbing out of the gravitational potential well. Stated differently, the gravitational redshift effect wins against the intrinsic temperature contribution.

2. Photons are emitted from a tightly coupled baryon–electron fluid, with a different peculiar velocity at each point on the last scattering surface. This velocity, projected along the line of sight, induces a Doppler shift in the photon wavelenght. The *Doppler contribution* is the one sourced by the term $g\hat{n}\cdot\vec{v}_{\rm B}$ in Eq. (5.56). In the instantaneous decoupling limit, this term simply gives the familiar Doppler formula

$$\Theta_\gamma^{\rm Doppler}(\eta_0, \vec{o}, \hat{n}) \simeq \hat{n} \cdot \vec{v}_{\rm B}(\eta_{\rm LS}, \vec{x}_{\rm LS}). \tag{5.60}$$

3. Along the line of sight, photons are continuously redshifted or blueshifted by metric fluctuations. The Boltzmann equation itself shows that the temperature changes because of gradients in the gravitational potential ψ, and because of

time variations in the metric fluctuation ϕ. Physically, the first effect accounts for the gain or loss of energy of photons feeling gravitational forces, and the second effect represents a local correction to the average time dilation, responsible for cosmological redshift in an expanding universe. If the gravitational potential were static, the first effect would be conservative; i.e., the integral of the gradient over the line of sight would give the difference between ψ at the point of last scattering and at the observer's location. We already discussed this contribution: the value of ψ at last scattering is included in the Sachs–Wolfe term, and the value at the observer's location appears in Eq. (5.56) and has been shown to be negligible. However, for a time-varying gravitational potential, the gradient does not coincide any more with the total derivative along the line of sight, and photons pick up a cumulative temperature shift accounted for by the integral of ψ' along the line of sight. Similarly, the cumulative effect of local time dilation is accounted for by the integral of ϕ'. These two effects form the so-called *integrated Sachs–Wolfe contribution* (ISW), encoded in the term $e^{-\tau}(\phi' + \psi')$ in Eq. (5.56). In the instantaneous decoupling limit, we can replace $e^{-\tau}$ by the Heaviside function $H(\eta - \eta_{\rm LS})$ and obtain

$$\Theta_\gamma^{\rm ISW}(\eta_0, \vec{o}, \hat{n}) \simeq \int_{\eta_{\rm LS}}^{\eta_0} d\eta (\phi' + \psi'). \tag{5.61}$$

The features of the cosmic microwave background spectrum: Sachs–Wolfe plateau, acoustic peaks and damping tail

We discussed the various terms appearing in Eq. (5.56), which give the contribution to the temperature anisotropy observed in a given direction. We should now use this decomposition to understand the shape of the temperature power spectrum C_l in multipole space.

The temperature spectrum is given by Eqs. (5.57) and (5.50), i.e., by the line-of-sight integral of the source function $S^{\rm T}(\eta, k)$, followed by a convolution with the primordial power spectrum. The source function contains the three generic terms identified in the previous subsection: a Sachs–Wolfe contribution $g(\Theta_{\gamma 0} + \psi)$, a Doppler contribution $(gk^{-2}\theta_{\rm B})'$, and an integrated Sachs–Wolfe contribution $e^{-\tau}(\phi' + \psi')$. Figure 5.2 shows the contribution of each of these three terms to the full temperature spectrum.

Using the facts that the visibility function is very peaked around recombination, that the spherical Bessel function $j_l(x)$ is peaked near $x \sim l$ and that the primordial spectrum $\mathcal{P}_\mathcal{R}$ is nearly scale-independent, it is easy to derive mathematically a result that can easily be understood geometrically, namely that the SW contribution to the temperature spectrum C_l multiplied by l^2 is qualitatively similar to the square

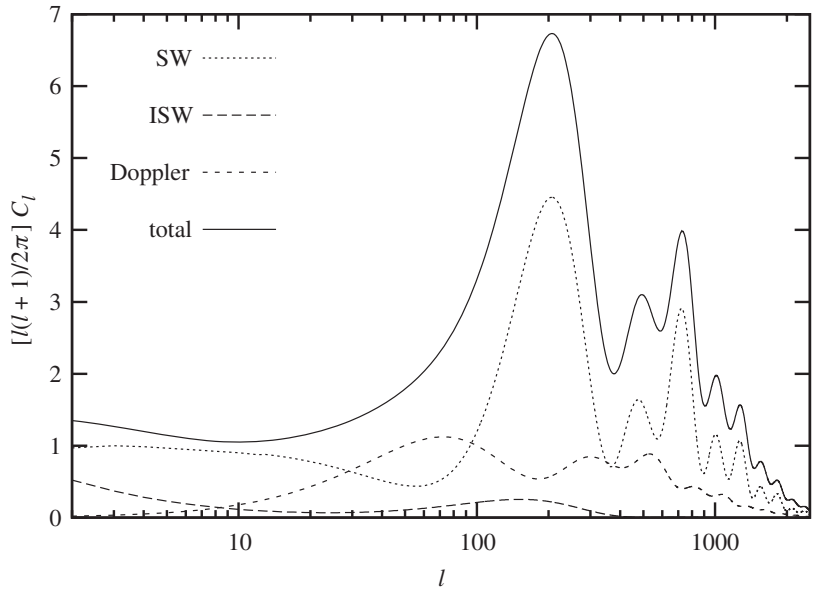

Figure 5.2 For a ΛCDM neutrinoless universe, the spectrum of CMB temperature anisotropies obtained numerically from the full temperature source function, or from individual contributions explained in the text: Sachs–Wolfe term (SW), integrated Sachs–Wolfe term (ISW) and Doppler term. Note that the full spectrum is not exactly given by the sum of the other three because of correlations between the terms.

of the SW transfer function in Fourier space,

$$l^2 C_l \propto \left[\Theta_\gamma(\eta_{\rm LS}, k) + \psi(\eta_{\rm LS}, k)\right]^2_{k=l/(\eta_0-\eta_{\rm LS})}, \tag{5.62}$$

where in the relation between k and l, we assume a flat universe for simplicity. The reason is that anisotropy multipoles at a given l are created mainly by Fourier modes of wavelength $\lambda \sim 2\pi a(\eta_{\rm LS})/k$ on the last scattering surface seen today under an angle $\theta = \lambda/d_{\rm A}(\eta_{\rm LS}) \sim 2\pi/l$ (note the factor of 2: for a given multipole, π/l gives the angle between a maximum and a minimum, corresponding to half a wavelength of the perturbation on the surface). In a spatially flat universe, we have $d_{\rm A}(\eta_{\rm LS}) = a(\eta_{\rm LS})(\eta_0 - \eta_{\rm LS})$, whereas in a spatially nonflat universe, this expression should be changed accordingly, using (2.83). This gives $2\pi/l \sim 2\pi/[k(\eta_0 - \eta_{\rm LS})]$.

This is only an approximate result, because in reality a given wavenumber contributes to an ensemble of multipoles, with the maximum contribution corresponding to the preceding relation. However, this picture gives a rather good understanding of the shape of the SW contribution in Fig. 5.2, which is indeed very similar to the square of the sum of $\Theta_\gamma(\eta_{\rm LS}, k)$ and $\psi(\eta_{\rm LS}, k)$ plotted in Figure 5.1. On small l's, the flat asymptote of the SW spectrum, called the Sachs–Wolfe plateau,

corresponds to large wavelengths still above the sound horizon at decoupling, which are frozen. On larger l's, we recognize the acoustic peaks already discussed in Section 5.1.5. The first is given by the correlation length on the last scattering surface, corresponding to the sound horizon at decoupling. Secondary peaks represent harmonics of the same feature, and are modulated by all the effects due to baryons, gravitational effects and diffusion damping mentioned in Section 5.1.5. We see clearly in Figure 5.2 the enhancement of odd peaks with respect to even peaks, which one would also see by taking the square of $[\Theta_{\gamma 0} + \psi]$ in Fig. 5.1, explained by the shift in the zero point of oscillations given by $\Theta_{\gamma 0} = -(1 + R)\psi$. Finally, we see how diffusion damping affects secondary peaks: the suppression, accounted for by a factor of $\exp[-(k/k_{\rm D})^2]$ in Fourier space, is well represented by a factor $\exp[-(l/l_{\rm D})^2]$ in multipole space, with $l_d \sim k_d(\eta_0 - \eta_{\rm LS})$. Diffusion damping of CMB fluctuations is often called Silk damping, although the famous work of Silk (1968) refers primarily to the damping of baryon density perturbations, occurring roughly at the same epoch.

We can carry on a similar discussion for the Doppler term, despite its slightly more complicated geometrical structure, because this term comes from the projection of a gradient along the line of sight. This explains the derivative in the Doppler source function $(g\theta_{\rm B})'/k^2$. Still, this term is sourced by $\theta_{\rm B}$ and $\theta'_{\rm B}$ mutiplied by functions very peaked near $\eta = \eta_{\rm LS}$, and the contribution of the Doppler term to the C_l's is set by the value of the transfer function $\theta_{\rm B}(\eta, k)$ and its time derivative at the time of decoupling. This contribution is negligible on the scale of the Sachs–Wolfe plateau, because outside the sound horizon perturbations are frozen, and the photon–baryon fluid velocity remains very low. Inside the sound horizon, $\theta_{\rm B}$ and $\theta'_{\rm B}$ exhibit the same oscillatory patterns as $\Theta_{\gamma 0}$, but with a phase shifted by respectively $\pi/2$ and π, as for any oscillator. This explains the shape of the Doppler contribution in Fig. 5.2.

Finally, the ISW contribution would vanish if between decoupling and today, the universe was a perfect matter-dominated universe. In this case, as mentioned in Section 5.1.5 and to be proved in Section 6.1.1, the metric perturbations would be static everywhere and at any time, $\phi' = \psi'$. The ISW contribution picks up nonzero contributions:

- First, because at the time of decoupling, the universe is still near the beginning of matter domination, and metric fluctuations, which were quickly decaying inside the Hubble radius during radiation domination, did not completely freeze out. The residual time variation of ϕ and ψ generates an early integrated Sachs–Wolfe effect (EISW).
- Second, because at late times, when the cosmological constant Λ (or more generally dark energy) changes the universe's expansion-rate behaviour, metric

fluctuations start decaying again. This late integrated Sachs–Wolfe (LISW) effect could be considered a secondary rather than a primary anisotropy, in the sense that it is not related to cosmological perturbations near the last scattering surface, but to gravitational interactions between free-streaming CMB photons and neighbouring galaxy clusters.

These two distinct contributions can easily be identified in the ISW curve of Fig. 5.2. The EISW effect cannot affect modes which are still outside the sound horizon at decoupling, for which no time evolution can occur, so that the EISW is negligible for $l \ll 100$. For modes inside the sound horizon, the EISW contribution to $l^2 C_l$ tends to decrease as a function of l, as a consequence of the factor k^{-2} in the Doppler term of the source function. Therefore, in Fig. 5.2, the EISW contribution is the one peaking around $l \sim 200$, enhancing the first acoustic peak in the total C_l's. The LISW effect is present on all scales, because dark energy domination produces a decay of metric fluctuations at all wavelengths. Because this effect also decreases with l for the same reason, it peaks at $l = 2$, and is only visible in Fig. 5.2 for $l \leq 30$. This term tilts the Sachs–Wolfe plateau in the total spectrum.

Shape and parameter dependence of the temperature spectrum

To conclude this section, it is worthwhile to summarize the dependence of the CMB temperature spectrum on the various effects discussed so far, and to relate them to the free cosmological parameters of a neutrinoless minimal ΛCDM model.

Let us first recall the relevant effects affecting the CMB temperature spectrum for each multipole range:

- For $l \ll 100$, the spectrum receives a SW contribution from modes which are still above the sound horizon at decoupling, leading to a Sachs–Wolfe plateau that depends on the primordial spectrum amplitude and tilt n_s. It also depends upon a LISW contribution which is related to the duration of Λ or dark energy domination and tends to tilt the Sachs–Wolfe plateau.
- For $l \geq 100$, the spectrum exhibits a series of acoustic peaks corrected by subdominant Doppler peaks, corresponding to the fundamental mode and harmonic decomposition of the correlation length $d_s(\eta_{\rm LS})$ on the last scattering surface. These peaks are modulated by various effects: their amplitude is globally suppressed during the transition era between equality and decoupling; odd peaks are enhanced with respect to even peaks when the baryon content of the universe increases; the first peak is further enhanced by the EISW effect; finally, diffusion damping causes an exponential suppression at high l.

There is one last effect to be taken into account in the minimal ΛCDM model, which we did not discuss previously because it is caused by astrophysical phenomena after

photon decoupling. When the first stars form (typically around redshift 10), the universe is believed to be partially reionized by starlight. A small fraction of CMB photons can then be rescattered by free electrons. This effect is negligible for modes entering into the Hubble scale very recently (at $z \ll 10$), but for all other modes it results in a scale-independent suppression of the CMB spectrum, accounted for by a factor $\exp[-\tau_{\rm reion}]$, where $\tau_{\rm reion}$ is the optical depth of reionization, measured to be on the order of ~ 0.1. Hence, reionization produces a steplike supression in the C_l's, with a step location around $l_{\rm step} \sim 40$ (corresponding to modes crossing the Hubble radius near $z \sim 10$). For $l \gg l_{\rm step}$, the effect of reionization is completely parameterized by $\tau_{\rm reion}$, whereas around $l_{\rm step}$ the shape of the step could depend on the details of the reionization history, which is poorly constrained by current data.

We can now relate these effects more explicitly to the free parameters of a neutrinoless minimal ΛCDM model, whereas neutrino effects will be introduced later in Section 5.3. This model has six free parameters:

- The primordial spectrum amplitude A_s and tilt $n_{\rm s}$.
- The baryon density $\omega_{\rm B} = \Omega_{\rm B} h^2$.
- The total nonrelativistic matter density $\omega_{\rm M} = (\Omega_{\rm B} + \Omega_{\rm C})h^2$.
- Either the cosmological constant density fraction Ω_Λ or the Hubble parameter today, $H_0 = 100\,h$ km s^{-1}Mpc^{-1}. Because we are assuming the universe to be spatially flat, for fixed $\omega_{\rm M}$, there is a one-to-one correspondence between values of Ω_Λ and of $h = \sqrt{\omega_{\rm M}/(1-\Omega_\Lambda)}$.
- The optical depth to reionization $\tau_{\rm reion}$.

We consider $\omega_\gamma = \Omega_\gamma h^2$ as a fixed parameter, because the CMB temperature today is accurately measured. In this model, the redshift of equality between radiation and matter is set by $\omega_{\rm M}$, because the radiation density $\omega_{\rm R} = \Omega_{\rm R} h^2$ is fixed by the measurement of the CMB temperature today. The redshift of equality between matter and Λ depends only on Ω_Λ.

The degrees of freedom controlling the shape of the CMB temperature spectrum are as follows:

(C1) The peak location, which depends on the angle $\theta = d_{\rm s}(\eta_{\rm LS})/d_{\rm A}(\eta_{\rm LS})$. The sound horizon at decoupling, $d_{\rm s}(\eta_{\rm LS})$, depends on the expansion history and sound speed in the photon–baryon fluid until decoupling. It is affected by changes in $\omega_{\rm B}$ (setting the baryon-to-photon ratio in the sound speed expression) and $\omega_{\rm M}$ (setting the redshift of equality between matter and radiation). The angular diameter distance at decoupling, $d_{\rm A}(\eta_{\rm LS})$, depends on the expansion history after decoupling, i.e., on Ω_Λ or h (controlling the time of equality between matter and Λ and the critical density today).

(C2) The contrast between odd and even peaks depends on $(\omega_{\rm B}/\omega_\gamma)$ (with ω_γ fixed by the CMB temperature today), i.e., on the balance between gravity and pressure in the tightly coupled photon–baryon fluid before decoupling.

(C3) The amplitude of all peaks further depends on the amount of expansion between equality and decoupling. Because the redshift of decoupling is almost fixed by the thermodynamics, this amount mainly depends on the redshift of equality, i.e., on $(\omega_{\rm M}/\omega_{\rm R})$. A larger $\omega_{\rm M}$ means that equality took place earlier. All peaks are then smaller, because the amplitude of acoustic oscillations decreased during a longer stage. The first peak is additionally supressed by a smaller EISW effect: at decoupling, metric fluctuations were closer to their constant asymptotic value. Conversely, a smaller $\omega_{\rm M}$ leads to higher peaks, especially the first one.

(C4) The envelope of the secondary peaks in the large-l limit depends on the angle $\theta = \pi/l_d = \lambda_d(\eta_{\rm LS})/d_{\rm A}(\eta_{\rm LS})$. The diffusion length λ_d is controlled by the expansion history and recombination history before decoupling. Because the integrand in Eq. (5.40) is increasing very rapidly with time before recombination (when n_e drops to nearly zero), λ_d depends essentially on the free electron density n_e at decoupling, which is fixed by $\omega_{\rm B}$ in the minimal ΛCDM model, and on the conformal time at decoupling $\eta_{\rm LS}$: the integral in Eq. (5.40) has a negligible dependence on the expansion and electron fraction at the time of equality and before. Therefore, λ_d depends essentially on $\omega_{\rm B}$ and $\omega_{\rm M}$, whereas we know that $d_{\rm A}(\eta_{\rm LS})$ depends on $\omega_{\rm M}$ and Ω_Λ or h.

(C5) The global amplitude of the C_l's is proportional to the amplitude $A_{\rm s}$ of the primordial spectrum, as can be checked from Eq. (5.50).

(C6) The global tilt of the C_l's depends trivially on the tilt $n_{\rm s}$ of the primordial spectrum, through the convolution in Eq. (5.50) (in the approximation of Eq. (5.62) in which a given k contributes essentially to a given l, this is even more obvious).

(C7) The slope of the Sachs–Wolfe plateau is controlled not only by the tilt $n_{\rm s}$, but also by the LISW effect, which enhances the first few multipoles. The amplitude of the LISW depends on the duration of the Λ-dominated stage, i.e., on the time of equality between matter and Λ, fixed by the ratio $(\Omega_\Lambda/\Omega_{\rm M})$ (in terms of the parameter basis discussed above, this ratio is given by $\Omega_\Lambda/(1-\Omega_\Lambda)$). A larger Ω_Λ implies a longer Λ domination and an enhanced LISW effect.

(C8) The global amplitude of the spectrum at $l \gg 40$ relative to the one at $l < 40$ depends on $\tau_{\rm reion}$. This effect is not degenerate with that of the time of equality, which also suppresses the peaks, but starting from a higher l and not in a constant way; it is not degenerate either with the effect of $A_{\rm s}$, provided that the spectrum is observed also for $l \leq 40$.

For simplicity, we have been assuming that the recombination redshift was fixed. In fact, the free electron density $n_e(z)$ and the redshift of recombination $z_{\rm LS}$ have a small dependence at least on the baryon density and on the primordial helium fraction Y_p. Hence these parameters can slightly affect the sound horizon at decoupling, the duration of the transition era and the photon diffusion length, with some additional impact on the CMB through the effects (C1), (C3) and (C4). However, the CMB is much more sensitive to $\omega_{\rm B}$ through the relative amplitude of the peaks than through its small impact on $z_{\rm LS}$, and the effect of Y_p is negligible when this parameter is varied within the range indicated by measurements of primordial element abundances or by standard BBN. Therefore, for most purposes, the recombination history and redshift of decoupling can indeed be considered as fixed.

This enumeration shows eight distinct ways to alter the shape of the temperature spectrum, controlled by only six parameters. So in principle, the measurement of the CMB temperature spectrum alone should give independent constraints on each parameter of the minimal ΛCDM model. To some extent, this is already the case with WMAP temperature results (Komatsu *et al.*, 2011). In practice, however, cosmic variance and instrumental noise lead to large error bars on the C_l's for the smallest and largest multipole values, leading to partial parameter degeneracies and to a degradation of some of the constraints. For instance, in the minimal ΛCDM case, Ω_Λ and $\tau_{\rm reion}$ are poorly constrained by the CMB temperature alone, because effects (C7) and (C8) can be constrained only through measurements at low l, plagued by cosmic variance. Degeneracies can be reduced by combining CMB temperature data with polarization information, or with other types of cosmological observations, or by performing more accurate measurements: this is the goal of the Planck satellite, which will make very accurate observations up to scales where primary anisotropies are anyway suppressed by diffusion damping ($l \sim 2500$).

5.1.7 Polarization anisotropies

The cross section of Thomson scattering depends on photon polarization: more precisely, on the orientation of the polarization vector relative to the scattering plane. However, in the tight-coupling regime, the photon polarization remains isotropically distributed at any point. Indeed, in the frame comoving with the tightly coupled photon–baryon(–electron) fluid, all quantities can only be isotropic because of the high interaction rate.

Around the time of recombination, such an isotropy disappears. The photons experience their last interactions in regions of space where anisotropies are growing. The quadrupolar component $\Theta_{\gamma^2}(\eta, \vec{x})$ of these anisotropies is responsible for a net polarization of scattered photons. Hence, polarization patterns appear on the last scattering surface and are strongly correlated with temperature patterns.

The observable polarization map is a vector field on a sphere, rather than a scalar field like temperature. Hence, it can be decomposed into two modes: a gradient field and a curl field, or by analogy with electromagnetism, an E-polarization and a B-polarization component. It is possible to define the harmonic power spectrum of the E and B modes, as well as three cross-correlation spectra for the products TE, TB and EB. Parity invariance implies that only the first cross-correlation term is nonzero after last scattering. The TB and EB cross-correlation spectra can be generated only at the level of secondary anisotropies, in particular, through the weak lensing of the last scattering surface. Moreover, as long as the total stress–energy tensor in the universe contains only scalar perturbations (following the definition of Section 5.1.2), no B modes can be excited.

The calculation of the spectra $C_l^{\rm EE}$ and $C_l^{\rm TE}$ in a universe containing only scalar perturbations can be carried on along the same line as for temperature anisotropies. The photon polarization is described by a new degree of freedom, whose evolution is described by the Boltzmann equation. In the previous section, we neglected polarization in the scattering term and obtained a simplified equation governing the evolution of temperature anisotropies $\Theta_\gamma(\eta, \hat{n}, \vec{x})$. The full Boltzmann equation leads to two hierarchies of equations for temperature and polarization multipoles. The two sets of equations are coupled, but the impact of polarization terms in the evolution of temperature anisotropies is rather small, so that our previous discussion of temperature anisotropies remains valid to a very good approximation. As for temperature, one can define a source function for E-mode polarization and express the polarization anisotropy as the integral of this source along the line of sight.

For brevity, we do not provide explicit expressions for polarization anisotropies here, because the neutrino effect on polarization is not qualitatively different from that on temperature (discussed in Section 5.3). Measuring the CMB polarization spectrum and TE cross spectrum helps in removing parameter degeneracies in the ΛCDM model, because some physical effects have intrinsically different consequences in the polarization sector. For instance, reionization imprints a distinct effect on $C_l^{\rm EE}$. Because the neutrino effect is qualitatively similar for temperature and polarization, and because current CMB experiments measure the temperature spectrum with much higher accuracy, we will not make any other references to polarization anisotropies in the rest of this book.

5.1.8 Tensor perturbations

As mentioned in Section 5.1.2, Bardeen (1980) classified metric and stress–energy tensor perturbations according to their behaviour under spatial rotations: scalar, vector and tensor modes. At first order in perturbation theory, these sectors are decoupled and can be studied independently.

Until this point our discussion has addressed only scalar perturbations. Vector perturbations accounting for vorticity tend to decay after their possible excitation by nonlinear phenomena such as phase transitions or topological defects. In standard cosmology, they do not make any sizable contribution to CMB anisotropies. Tensor perturbations are fundamentally different from scalars and vectors, because they describe two propagating degrees of freedom (called the polarization states of the graviton in the context of quantum gravity, or the polarization states of gravitational waves at the classical level). For scalar and vector modes, metric perturbations are responding only to excitations in the stress–energy tensor of matter, whereas for tensor modes, the two polarization states can be excited by quantum effects during inflation. Starobinsky (1979) found that very generically, after a stage of inflation, primordial gravitational waves are generated with a nearly scale-invariant power spectrum, whose amplitude depends on the square of the Hubble parameter when observable wavelengths cross the Hubble scale during inflation.

Gravitational waves are coupled to all species having non-negligible tensor degrees of freedom in their perturbed stress–energy tensor $\delta T_{\mu\nu}$. These degrees of freedom are contained in the nondiagonal part of the spatial stress tensor δT_{ij}. They vanish to a very good approximation for cold dark matter because of its very small velocity dispersion, as well as for baryons and tightly coupled photons, because interactions enforce a diagonal stress tensor accounting for isotropic pressure. Hence, the only species efficiently coupled with gravitational waves are photons after decoupling and collisionless species before their nonrelativistic transition (namely, in the minimal ΛCDM scenario, neutrinos).

Extra gravitational waves can be generated after inflation by nonlinear phenomena such as phase transitions and topological defects. In the minimal cosmological scenario, it is assumed that the former can impact only small scales, comparable to the Hubble radius during the transition and cannot affect CMB anisotropies, whereas topological defects (if any) do not contribute significantly to total large-scale perturbations. Hence we only need to consider primordial gravitational waves from inflation, which are known to contribute to temperature anisotropies on large angular scales (typically $l < 150$) and to E-type and B-type polarization anisotropies on all scales.

The influence of neutrinos on tensor CMB anisotropies was studied analytically by Weinberg, 2004 and implemented by Lewis in the Boltzmann code CAMB.[2] We will see in Section 5.3 that the influence of neutrinos on scalar CMB anisotropies can only be significant for modes crossing the horizon during radiation domination or at the beginning of matter domination, i.e., on small scales. This is also true for their influence on tensor anisotropies.

[2] See `http://cosmologist.info/notes/CAMB.pdf`, Section XVI.

Even if we assume that inflation took place at high energy and produced a detectable amount of primordial gravitational waves, small-scale temperature and E-polarization anisotropies are largely dominated by scalar contributions. For B-polarization, there is no scalar contamination to primordial anisotropies, but on small scales gravitational lensing effects generate a leak from E-type to B-type polarization, in such a way that the contribution of tensor perturbations to the spectrum $C_l^{\rm BB}$ is also subdominant.

Hence tensor modes could only be detected in the CMB on large scales, on which the impact of neutrinos must be negligible. For this reason, we choose not to discuss tensor perturbations in the following.

5.2 Neutrino perturbations

Having presented in Section 5.1 the basics of linear cosmological perturbation theory in the absence of neutrinos, we now focus on the specific evolution of neutrino perturbations.

5.2.1 Perturbation equations

In this book, we are mainly interested in the description of the three standard active neutrinos. We present here the formalism describing the cosmological perturbations of such neutrinos in the massless limit, as well as in the more realistic massive case. Massless neutrino equations can safely be employed for collisionless particles which are still relativistic today, i.e., in the case of ordinary neutrinos, when their mass m_ν is smaller than $T_{\nu,0} \simeq 1.68 \times 10^{-4}$ eV, which might be the case for only one neutrino mass state given experimental results on flavour oscillations (see Chapter 1). We will also occasionally consider more exotic cases such as neutrinos with high chemical potentials, large nonthermal distortions, light or heavy sterile neutrinos. We will see that all these cases can still be described by one of the two sets of equations introduced hereafter. Only neutrinos with nonstandard interactions require a different set of equations, which would depend very much on the type of interactions. This exotic assumption will only be mentioned briefly at the end of this chapter.

Massless neutrinos and other relativistic relics

When studying the impact of massless neutrinos on the CMB, we need only to consider fully decoupled neutrinos. Indeed, the details of neutrino decoupling would only impact cosmological perturbations which are already inside the Hubble length when $T \sim$ MeV. Such scales are not observable. In the CMB spectrum, they have been suppressed by diffusion damping and are masked anyway by foreground

contamination in real data sets. In the large-scale structure spectrum, a strong nonlinear evolution has erased all memory of the early linear evolution on such small scales.

We have seen in Sections 2.4.2 and 4.1 that standard active neutrinos have a frozen background distribution function $f_{\nu 0}(y)$ of the Fermi–Dirac type (with negligible mass and chemical potential),

$$f_{\nu 0}(y) = \left(e^{\frac{y}{a\overline{T}_\nu}} + 1\right)^{-1}, \tag{5.63}$$

with a constant product $a\,\overline{T}_\nu$ after neutrino decoupling. Nonthermal distortions of this distribution due to entropy release at the $e^\pm$ annihilation stage are very small, on the level of a few percent at most, and can be completely neglected in our discussion because all present (and forthcoming) data are completely blind to such a small effect. This means that the neutrino equation of evolution can be derived following the same steps as for photons, with just a sign difference in f accounting for Fermi–Dirac statistics (but this makes no difference in the final equations), and of course assuming no interaction. Hence, we could write an equation of evolution for the neutrino temperature perturbation Θ_ν which would be strictly identical to Eqs. (5.13) or (5.15) for Θ_γ in the collisionless limit $\sigma_{\rm T} = 0$.

We can remain at a more general level and assume that we simply deal with any kind of decoupled relativistic particles, with an arbitrary background distribution function $f_{\nu 0}(y)$. The absence of an explicit time dependence in this distribution is appropriate if the species is indeed decoupled. This covers the case of massless neutrinos with chemical potentials or a nonthermal distribution, as well as any other decoupled relativistic relic. The way to simplify the Boltzmann equation in this case is not to parameterize f_ν explicitly in terms of temperature fluctuations, as in Eq. (5.11), but to introduce the momentum average of the perturbation of the distribution function relative to the background value

$$F_\nu(\vec{x}, \hat{n}, \eta) = \frac{\int y^2 dy\; y[f_\nu(\vec{x}, y, \hat{n}, \eta) - f_{\nu 0}(y)]}{\int y^2 dy\; y f_{\nu 0}(y)}. \tag{5.64}$$

By plugging into the above formula the phase space distribution of thermal relics with a negligible chemical potential, one can easily show that this quantity exactly coincides with the temperature perturbation Θ_ν multiplied by four. If we take the Boltzmann equation (2.92) in the collisionless limit (sometimes called the Vlasov equation), integrate the Liouville operator over momentum and simplify it using the same steps as for photons in Section 5.1.2 (always at order one in perturbations), we obtain an equation of motion for F_ν,

$$F_\nu' + \hat{n} \cdot \vec{\nabla} F_\nu - 4\phi' + 4\hat{n} \cdot \vec{\nabla}\psi = 0. \tag{5.65}$$

We can expand this equation in Fourier space, and as for photons, notice that the isotropy of the background implies that the equation is axially symmetric around $\hat{n}$. Moreover, F_ν follows the same symmetry at initial time. In fact, before neutrino decoupling, neutrino perturbations can only depend on direction through a Doppler-induced dipole along the axis defined by $\hat{n}$, and after decoupling, this remains true for all modes above the Hubble radius, for causality reasons. So the symmetry is preserved throughout the evolution, and the Fourier transform of $F_\nu(\vec{x}, \hat{n}, \eta)$ depends only on the arguments $F_\nu(\vec{k}, \mu, \eta)$, with $\mu = \hat{k} \cdot \hat{n}$. This function follows

$$F_\nu' + ik\mu F_\nu - 4\phi' - ik\mu 4\psi = 0. \tag{5.66}$$

Expanding this equation in Legendre polynomials,

$$F_\nu(\vec{k}, \mu, \eta) = \sum_l (-i)^l (2l+1) F_{\nu l}(\vec{k}, \eta) P_l(\mu), \tag{5.67}$$

we get an infinite hierarchy of equations:

$$\begin{aligned} {F_{\nu 0}}' &= -kF_{\nu 1} + 4\phi' \\ {F_{\nu 1}}' &= \frac{k}{3}(F_{\nu 0} - 2F_{\nu 2} + 4\psi) \\ {F_{\nu l}}' &= \frac{k}{(2l+1)}\left[lF_{\nu(l-1)} - (l+1)F_{\nu(l+1)}\right], \qquad \forall\, l \geq 2. \end{aligned} \tag{5.68}$$

The relation between the first multipoles of F_ν and the perturbations $\delta_\nu, \theta_\nu, \sigma_\nu$ can be derived from Eq. (5.10):

$$\delta_\nu = F_{\nu 0}, \qquad \theta_\nu = \frac{3}{4} k F_{\nu 1}, \qquad \sigma_\nu = \frac{1}{2} F_{\nu 2}. \tag{5.69}$$

One can check that the first two equations in (5.68) coincide with the general continuity and Euler equations for a species with equation of state $\overline{P}/\overline{\rho} = 1/3$, a sound speed $c_s^2 = \delta P/\delta\rho = 1/3$, and some unspecified anisotropic pressure.

Massive neutrinos

Massive neutrinos should be described by a set of equations interpolating from CDM equations in the large mass limit to massless neutrino equations in the small mass limit. We can assume that at the time at which we impose initial conditions, neutrinos are already decoupled but still relativistic, with a given background distribution $f_{\nu 0}(y)$. We know that for standard active neutrinos $f_{\nu 0}(y)$ is given by Eq. (5.63), but because we are also interested in sterile neutrinos and nonstandard active neutrinos, we keep the discussion at a more general level and assume only that $f_{\nu 0}(y)$ has no explicit time dependence after neutrino decoupling.

The difference between massive and massless neutrinos appears when the terms $d\vec{x}/d\eta$ and $dy/d\eta$ are replaced in the Liouville operator. For nonrelativistic particles, these terms are given respectively by $y\hat{n}/\epsilon$ and by Eq. (5.4), and depend explicitly on the mass through the energy ϵ. In that case, the collisionless Boltzmann equation cannot be simplified by integrating over momentum. The physical explanation is that for nonrelativistic particles, gravitational interactions induce a relative momentum shift depending on the momentum itself, i.e., some nonthermal distortions of the perturbed phase-space distribution. The Boltzmann equation can still be simplified to some extent by introducing the relative fluctuation of the phase-space distribution,

$$\Psi_\nu(\eta, \vec{x}, y, \hat{n}) = \frac{f_\nu(\eta, \vec{x}, y, \hat{n})}{f_{\nu 0}(\eta, y)} - 1, \tag{5.70}$$

expressed at first order in perturbations.

As long as neutrinos remain relativistic, the quantity $\Psi_\nu(\eta, \vec{x}, y, \hat{n})$ can be related to the variables introduced previously for massless neutrinos. In the case of standard neutrinos with a Fermi–Dirac distribution, we can write the perturbed distribution in the particular form $f_\nu(\eta, \vec{x}, y, \hat{n}) = f_{\nu 0}(y/[a\overline{T}_\nu\{1 + \Theta_\nu(\eta, \vec{x}, \hat{n})\}])$ with constant $a\overline{T}_\nu$ and make a Taylor expansion at first order in Θ_ν to find

$$\Psi_\nu(\eta, \vec{x}, y, \hat{n}) = -\Theta_\nu(\eta, \vec{x}, \hat{n}) \frac{d \ln f_{\nu 0}(y)}{d \ln y}. \tag{5.71}$$

In the general case, Ψ_ν can be identified in the relativistic limit with

$$\Psi_\nu(\eta, \vec{x}, y, \hat{n}) = -\frac{1}{4} F_\nu(\eta, \vec{x}, \hat{n}) \frac{d \ln f_{\nu 0}(y)}{d \ln y}. \tag{5.72}$$

Equations (5.71) and (5.72) are no longer valid when the particles become nonrelativistic and gravitational interactions introduce nonthermal distortions.

If we take the Boltzmann equation (2.92) in the collisionless limit, replace $f_\nu(\eta, \vec{x}, y, \hat{n})$ as a function of $\Psi_\nu(\eta, \vec{x}, y, \hat{n})$ and simplify the Liouville operator using the same steps as for photons and massless neutrinos (always at order one in perturbations), we obtain an equation of motion for Ψ_ν:

$$\Psi_\nu' + \frac{y}{\epsilon} \hat{n} \cdot \vec{\nabla} \Psi_\nu + \frac{d \ln f_{\nu 0}}{d \ln y} \left[\phi' - \frac{\epsilon}{y} \hat{n} \cdot \vec{\nabla} \psi \right] = 0. \tag{5.73}$$

In the relativistic limit, the ratio (y/ϵ) is equal to unity, and using Eq. (5.72), we immediately recover the massless neutrino Boltzmann equation. As for photons and massless neutrinos, one can transform Eq. (5.73) to Fourier space, make use of the axial symmetry around $\hat{n}$, expand Ψ_ν in Legendre polynomials and obtain

an infinite hierarchy of equations:

$$\begin{aligned}
\Psi_{\nu 0}{}' &= -\frac{yk}{\epsilon}\Psi_{\nu 1} - \phi' \frac{d\ln f_{\nu 0}}{d\ln y} \\
\Psi_{\nu 1}{}' &= \frac{yk}{3\epsilon}\left(\Psi_{\nu 0} - 2\Psi_{\nu 2}\right) - \frac{\epsilon k}{3y}\psi \frac{d\ln f_{\nu 0}}{d\ln y} \\
\Psi_{\nu l}{}' &= \frac{yk}{(2l+1)\epsilon}\left[l\Psi_{\nu(l-1)} - (l+1)\Psi_{\nu(l+1)}\right], \qquad \forall\, l \geq 2.
\end{aligned} \tag{5.74}$$

Finally, using Eq. (5.10), one can show that the usual four scalar degrees of freedom of the perturbed stress–energy tensor can be obtained by integrating $\Psi_{\nu\, l=0,1,2}$ over momentum:

$$\delta\rho_\nu = \overline{\rho}_\nu \delta_\nu = 4\pi a^{-4} \int y^2 dy\, \epsilon\, f_{\nu 0}(y)\Psi_0 \tag{5.75}$$

$$\delta P_\nu = \frac{4\pi}{3} a^{-4} \int y^2 dy\, \frac{y^2}{\epsilon}\, f_{\nu 0}(y)\Psi_0 \tag{5.76}$$

$$(\overline{\rho}_\nu + \overline{P}_\nu)\theta_\nu = 4\pi a^{-4} \int y^2 dy\, \epsilon\, f_{\nu 0}(y)\Psi_1 \tag{5.77}$$

$$(\overline{\rho}_\nu + \overline{P}_\nu)\sigma_\nu = 4\pi a^{-4} \int y^2 dy\, \frac{y^2}{\epsilon}\, f_{\nu 0}(y)\Psi_2. \tag{5.78}$$

By integrating the first two equations (5.74) over momentum y, one can recover the general continuity and Euler equations, this time with no exact analytic expression for $\overline{P_\nu}/\overline{\rho_\nu}$, and no exact relation between $\delta\rho_\nu$, δP_ν and σ_ν. For details on this procedure, see Shoji and Komatsu, 2010; Lesgourgues and Tram, 2011.

Deep in the nonrelativistic limit, the ratio (y/ϵ) goes asymptotically to zero. In that case, the integrand of δP_ν is suppressed by a factor of $(y/\epsilon)^2$ with respect to that of $\delta\rho_\nu$; i.e., $\delta P_\nu/\delta\rho_\nu$ is of order $(\overline{T}_\nu/m_\nu)^2$ and pressure perturbations can be neglected. The same is true for the ratios $\overline{P}_\nu/\overline{\rho}_\nu$ and σ_ν/δ_ν. Thus, the continuity and Euler equations for nonrelativistic neutrinos become identical to those for cold dark matter.

5.2.2 Neutrino isocurvature modes

The number of independent initial conditions for the whole system of cosmological perturbations is equal to the number of first-order equations describing their evolution of super-Hubble wavelengths. We know that there are two first-order equations for baryons, two for CDM, and also two for photons, despite the infinite hierarchy of Legendre momenta in the Boltzmann equation for photons. As explained in Section 5.1.3, the reason is that as long as photons are tightly coupled,

all multipoles above $l = 0$ (the monopole acounting for local density fluctuations) and $l = 1$ (the dipole due to the relative motion between the tightly coupled fluid and the coordinate frame) are negligible, as clearly seen from the interaction terms in Eq. (5.15), in the limit of an infinite interaction rate.

A similar simplification holds for each distinct neutrino species at leading order in the long-wavelength approximation. As long as neutrinos are in thermal equilibrium, they have vanishing multipoles for $l > 1$, for the same reasons as for photons. After decoupling occurs, these multipoles remain suppressed by a factor $(k\eta)^l$ on super-Hubble wavelengths, as can be checked from Eq. (5.68). Because $F'_{\nu l}$ is sourced by $kF_{\nu(l-1)}$, higher multipoles are suppressed by increasing powers of $(k\eta)$. Physically, this is a simple consequence of causality. It takes some amount of time for high multipoles to grow from zero to a significant value. For a given wavelength, this happens after Hubble crossing, i.e., after entering the causal horizon (computed starting from some initial time after the end of inflation).

Thus, as long as we neglect multipoles $l > 1$ when fixing initial conditions on super-Hubble scales, we can say that all perturbations in a universe with N species can be described by $2N$ equations, leading to $2N$ independent solutions: one growing adiabatic mode, $(N - 1)$ isocurvature growing modes and N decaying modes. Moreover, if we choose this initial time so that all neutrino species are relativistic, they can all be described by the same pair of equations (the first two of Eqs. (5.74) in the limit $F_{\nu 2} = 0$), and they count as only one species. We see that in the minimal ΛCDM model, including the usual three neutrino species, one has $N = 4$, because the counting runs over photons, baryons, CDM and generic relativistic neutrinos.

This picture has been refined by the analysis of Bucher *et al.*, 2000, who pointed out that if we search for the solutions of a system with one more equation (that for the evolution of the neutrino anisotropic stress $\sigma_\nu = F_{\nu 2}/2$), then there is one more isocurvature growing mode, corresponding to an initial excitation of the neutrino flux divergence θ_ν, compensated for by an opposite excitation of θ_γ in order to keep a diagonal stress–energy tensor in the limit $(k\eta) \to 0$. In other words, if we allow an initial excitation of θ_ν, then all multipoles $F_{\nu l}$ with $l \geq 1$ are larger by one power of $(k\eta)$, and one should keep the $l = 2$ equation in order to derive a consistent solution at leading order. This new solution has been called the *neutrino isocurvature velocity* mode (NIV). The previously found neutrino isocurvature mode was then renamed the *neutrino isocurvature density* mode (NID). However, no plausible mechanism leading to an excitation of the NIV mode has been proposed so far.

This logic cannot be pushed to higher order. The next step would consist of searching for a solution with an initial excitation of the neutrino anisotropic stress, compensated for by an opposite excitation of the photon anisotropic stress.

However, σ_γ must remain very small due to Thomson scattering, as well as σ_ν until neutrino decoupling.

We already mentioned that even if some isocurvature modes are excited in the primoridal universe, thermal equilibrium forces species to share the same local fluctuations in number density, and erases any entropy perturbation. Hence, isocurvature modes should be taken into account only if they are attached to an ever-decoupled species, whereas neutrinos are coupled until $T \sim 1$ MeV. This argument could in principle be avoided in two cases: if the universe reheats at very low temperature and neutrinos never reach thermal equilibrium, or if they are thermal relics with high chemical potentials, corresponding to a large lepton asymmetry. The chemical potentials $\mu_{\nu_i}(t, \vec{x})$ could in principle fluctuate spatially in such a way as to violate the adiabaticity condition. One can show that under such assumptions, the NID mode can be excited (Malik and Wands, 2009).

In summary, the NIV mode sounds very unlikely to be produced in the early universe, and the NID mode would require a complicated mechanism implying large lepton asymmetries. Moreover, none of these modes is favoured by current data (Castro *et al.*, 2009). For these reasons, we will not consider isocurvature modes in the following.

5.2.3 Adiabatic mode in the presence of neutrinos

We explained in Section 5.1.3 that adiabatic initial conditions have a simple meaning on super-Hubble scales. They correspond to a perturbed universe described at each point by the background evolution, with a local time-shift function $t \longmapsto t + \delta t(\vec{x})$ (or the same using conformal time η). We showed that this leads to a universal relation (5.24) giving for the neutrino density transfer function

$$\delta_\nu(\eta, k) = \delta_\gamma(\eta, k). \tag{5.79}$$

On super-Hubble scales, the Einstein 0–0 equation (5.20) relates ψ to the total density perturbation in the universe, coming from photons and neutrinos during radiation domination. Because photons and neutrinos share the same density contrast, the relation $\delta_\gamma = -2\psi$ found in the neutrinoless case is still valid in the presence of neutrinos. Hence the curvature perturbation $\mathcal{R}$, given by Eq. (5.29), is also related to δ_γ in the same way. All these quantities are still constant over time for adiabatic initial conditions. Higher neutrino momenta θ_ν/k and σ_ν vanish in the $\eta \to 0$ limit, because they contribute to the nondiagonal part of the stress–energy tensor, whereas the background stress–energy tensor is diagonal. The leading contribution to θ_ν/k (resp. σ_ν) in the Newtonian gauge is of order one (resp. two) in a $(k\eta)$ expansion (Ma and Bertschinger, 1995). The coefficients of these terms and

of higher-order terms can be computed analytically by solving the full system of equations in the super-Hubble limit. Higher-order terms are generally included in the initial condition equations implemented in Boltzmann codes.

However, the relation $\phi = \psi$ is not valid any more. One can check from Eq. (5.22) (using the Friedmann equation) that a total anisotropic stress proportional to η^2 implies a constant offset between the two metric perturbations. The growing adiabatic solution of the full system of equations is such that

$$\phi - \psi = \frac{2}{5} R_\nu \psi \tag{5.80}$$

with

$$R_\nu \equiv \frac{\overline{\rho}_\nu}{\overline{\rho}_\gamma + \overline{\rho}_\nu} = \frac{\frac{7}{8}\left(\frac{4}{11}\right)^{4/3} N_{\rm eff}}{1 + \frac{7}{8}\left(\frac{4}{11}\right)^{4/3} N_{\rm eff}} = \frac{0.2271\, N_{\rm eff}}{1 + 0.2271\, N_{\rm eff}}, \tag{5.81}$$

where we use the definition of the effective neutrino number in (2.198). In summary, in the presence of neutrinos, the relation (5.41) between density and metric perturbations during radiation domination and on super-Hubble scales becomes

$$\begin{aligned} 4\Theta_{\gamma 0}(\eta, k) = \delta_\gamma(\eta, k) = \delta_\nu(\eta, k) &= \frac{4}{3}\delta_{\rm B}(\eta, k) \\ &= -2\left(1 + \frac{2}{5} R_\nu\right)\phi(\eta, k) = -2\psi(\eta, k) = -\frac{4}{3}. \end{aligned} \tag{5.82}$$

The presence of the factor R_ν in this relation gives the confusing impression that the leading-order solution for density perturbations on super-Hubble scales is affected by the neutrino anisotropic stress, responsible for the constant offset between ϕ and ψ. This would contradict the general interpretation of the adiabatic mode: if adiabatic perturbations are equivalent to a local time-shift of background quantities, the neutrino anisotropic stress should be irrelevant on super-Hubble scales, because it contributes only to the vanishing nondiagonal part of the stress–energy tensor. In fact, there is no contradiction, because the shift of ϕ by a constant amount $\frac{2}{5} R_\nu \psi$ has no observable consequences. All equations of evolution depend on the metric through the time-dilation term ϕ' and the gravitational force $k^2\psi$. The derivative ϕ' is not affected by the offset, and its leading contribution is of order $(k\eta)$. We conclude that the neutrino anisotropic stress (and more generally the presence of neutrinos) changes the evolution of all densities only at next-to-leading order in a $(k\eta)$ expansion. The fact that metric perturbations themselves are affected at leading order is a kind of gauge artifact. In other gauges, it is clear that R_ν plays no role in metric perturbations at leading order.

This technical discussion will become important when the effect of neutrinos on the CMB and large-scale structure power spectra is discussed: we will use the

fact that the presence of neutrinos has no impact on other species on super-Hubble scales. This result was illustrated here during radiation domination, but it remains true during matter domination.

5.2.4 Free-streaming length

After their decoupling, neutrinos free-stream, or in other words, evolve like freely falling particles. Because the universe is expanding, free-streaming is not relevant on all scales at a given time. We can introduce two quantities describing the scale above which neutrino free-streaming can be ignored:

1. a dynamical quantity, the *free-streaming scale* $\lambda_{\rm fs}$ (or $k_{\rm fs}$ in comoving Fourier space), showing on which scales free-streaming can be neglected in the equations of evolution at any given time;
2. an integrated quantity, the *free-streaming horizon* $d_{\rm fs}$ (or $r_{\rm fs}$ in comoving space), giving the average distance travelled by neutrinos between the early universe and a given time, and hence showing which scales could be affected at all by neutrino free-streaming at this time.

The first quantity could be defined as the product of the average neutrino velocity c_ν by the Hubble time $t_{\rm H} \equiv 1/H$, but most authors prefer to define the free-streaming length by analogy with the Jeans length:

$$\lambda_{\rm fs}(\eta) = a(\eta)\frac{2\pi}{k_{\rm fs}} \equiv 2\pi\sqrt{\frac{2}{3}}\frac{c_\nu(\eta)}{H(\eta)}. \tag{5.83}$$

In the Jeans case, the quantity c_ν should be replaced by the sound speed $c_{\rm s}$ of a given fluid. The justification of the prefactor $2\pi\sqrt{2/3}$ for the Jeans length is that for a fluid i with constant sound speed dominating the expansion of the universe, the continuity, Euler, Friedmann and Poisson equations can be combined into the following equation of evolution on sub-Hubble scales:

$$\delta_i'' + \frac{a'}{a}\delta_i' + \left(k^2 - \frac{3a^2H^2}{2c_{\rm s}^2}\right)c_{\rm s}^2\delta_i = 0. \tag{5.84}$$

The effective mass $(k^2 - k_{\rm J}^2)c_{\rm s}^2$ changes sign when k is equal to the Jeans wavenumber. Hence the Jeans length represents the scale below which pressure forbids gravitational collapse in the fluid. By analogy, the free-streaming length is the scale below which collisionless particles cannot remain confined in gravitational potential wells, because of their velocity dispersion.

The second quantity is defined like any other comoving horizon scale:

$$d_{\rm fs}(\eta) = a(\eta)\, r_{\rm fs}(\eta) \equiv a(\eta)\int_{\eta_{\rm in}}^{\eta} c_\nu(\eta)\, d\eta. \tag{5.85}$$

We recall that neutrinos travel along geodesics with on average $dx = c_\nu\, dt/a = c_\nu\, d\eta$, and provided that $\eta_{\rm in}$ is chosen after the end of inflation (which makes perfect sense, because neutrinos were produced by reheating after that time), $d_{\rm fs}(\eta)$ is independent of $\eta_{\rm in}$ as long as $\eta_{\rm in} \ll \eta$.

Relativistic neutrinos

If neutrinos are still relativistic today, their velocity is given at all times by $c_\nu = c = 1$, and we find

$$\lambda_{\rm fs} = 2\pi\sqrt{\frac{2}{3}}H^{-1}, \qquad d_{\rm fs} = a\eta; \tag{5.86}$$

i.e., the free-streaming scale is given by the Hubble radius times a numerical factor, and the free-streaming horizon is equal to the particle horizon. Both quantities are very close to each other. During radiation domination $a\eta = H^{-1}$, and during matter domination $a\eta = 2H^{-1}$.

Neutrinos becoming nonrelativistic during matter domination

Neutrinos become nonrelativistic when their average momentum $\langle p\rangle$ falls below their mass m_ν. For a relativistic Fermi–Dirac distribution with negligible chemical potential, the average momentum is given as a function of the temperature by $\langle p\rangle = 3.15\, T_\nu$. We will denote the temperature of ordinary active neutrinos in the instantaneous decoupling limit as

$$T_\nu^{\rm a} \equiv (4/11)^{1/3} T. \tag{5.87}$$

The active neutrino temperature today, $T_{\nu\,0}^{\rm a}$, can easily be inferred from the known value of the CMB temperature, T_0. Ordinary neutrinos with $T_\nu \simeq T_\nu^{\rm a}$ become nonrelativistic during matter or Λ domination if their mass is in the range from

$$3.15\,(4/11)^{1/3} T_0 = 5.28 \times 10^{-4}\ {\rm eV} \tag{5.88}$$

to approximately

$$(1 + z_{\rm eq})\, 5.28 \times 10^{-4}\ {\rm eV} \simeq 1.5\ {\rm eV} \tag{5.89}$$

(because current observations indicate that the redshift of equality is close to $z_{\rm eq} = 2900$). More generally, the redshift of the transition is given by

$$z_{\rm nr} = \left(\frac{m_\nu}{5.28 \times 10^{-4}\ {\rm eV}}\right)\left(\frac{T_\nu^{\rm a}}{T_\nu}\right) - 1. \tag{5.90}$$

After the nonrelativistic transition, the velocity dispersion (also called thermal velocity)

$$c_\nu = \frac{\langle p \rangle}{m_\nu} = 3.15\,\frac{T_\nu}{m_\nu} = 158\,(1+z)\left(\frac{T_\nu^{\rm a}}{T_\nu}\right)\left(\frac{1\ {\rm eV}}{m_\nu}\right){\rm km\,s^{-1}} \tag{5.91}$$

scales like $c_\nu \propto a^{-1} \propto \eta^{-2}$. Hence, during matter domination, the free-streaming length of nonrelativistic neutrinos increases like η while the comoving free-streaming length decreases like η^{-1}. The free-streaming length and wavenumber are given by

$$\lambda_{\rm fs} = 8.10\,(1+z)\frac{H_0}{H(z)}\left(\frac{T_\nu}{T_\nu^{\rm a}}\right)\left(\frac{1\ {\rm eV}}{m_\nu}\right)h^{-1}{\rm Mpc} \tag{5.92}$$

$$k_{\rm fs} = 0.776\,(1+z)^{-2}\frac{H(z)}{H_0}\left(\frac{T_\nu}{T_\nu^{\rm a}}\right)\left(\frac{m_\nu}{1\ {\rm eV}}\right)h\,{\rm Mpc}^{-1} \tag{5.93}$$

with $H(z)^2 = H_0^2[\Omega_\Lambda + \Omega_k(1+z)^2 + \Omega_{\rm M}(1+z)^3]$ during matter and Λ domination; see (2.61). In the second equation and in the rest of this section we also assume that the scale factor today is fixed to one.

At the time of the transition, the free-streaming wavenumber passes through a minimum usually denoted $k_{\rm nr}$. An approximation to $k_{\rm nr}$ is found by simply plugging Eq. (5.90) into Eq. (5.93),

$$k_{\rm nr} \equiv k_{\rm fs}(\eta_{\rm nr}) \simeq 0.0178\,\Omega_{\rm M}^{1/2}\left(\frac{T_\nu^{\rm a}}{T_\nu}\right)^{1/2}\left(\frac{m_\nu}{1\ {\rm eV}}\right)^{1/2}h\,{\rm Mpc}^{-1}, \tag{5.94}$$

assuming that the transition takes place during matter domination, when $H(z)/H_0 \simeq \Omega_{\rm M}^{1/2}(1+z)^{3/2}$. Note that sometimes $k_{\rm nr}$ is simply defined as the wavenumber such that $k_{\rm nr} = aH$ at the time of the nonrelativistic transition. With respect to the definition adopted previously, there is only a factor $\sqrt{3/2}$ of difference.

The comoving free-streaming horizon is equal to η in the relativistic regime. After that time, in the approximation in which c_ν would switch from 1 to $(\eta_{\rm nr}/\eta)^2$ at $\eta = \eta_{\rm nr}$, it is given by

$$r_{\rm fs}(\eta > \eta_{\rm nr}) \simeq \eta_{\rm nr}\,(2 - \eta_{\rm nr}/\eta) \simeq \sqrt{\frac{3}{2}}\frac{4}{k_{\rm nr}}\left(1 - \frac{1}{2}\left[\frac{1+z}{1+z_{\rm nr}}\right]^{1/2}\right), \tag{5.95}$$

where we used the expression $\eta = 2/(aH) \propto a^{1/2}$ valid during matter domination. Taking a recent Λ or curvature-dominated stage into account would change the result by a very small amount at late times. For $z \ll z_{\rm nr}$, the comoving free-streaming horizon $r_{\rm fs}$ remains very close to the minimum comoving free-streaming scale $(2\pi/k_{\rm nr})$ (they differ at most by 28%). Strictly speaking, the comoving

free-streaming horizon is the right quantity to be computed if one wishes to know above which comoving scale free-streaming can be neglected. However, in most of the literature this role is attributed to $(2\pi/k_{\rm nr})$, which makes no difference in practice, at least for particles becoming nonrelativistic after the time of equality between matter and radiation.

Neutrinos becoming nonrelativistic during radiation domination

Most of this book is focused on ordinary active neutrinos with sub-eV mass. Occasionally we will refer to heavy sterile neutrinos with mass in the keV range. In this case the redshift of the nonrelativistic transition, still given by Eq. (5.90) in the case of a thermal momentum distribution, falls within the radiation-dominated era. After that time, the neutrino velocity c_ν (still subject to Eq. (5.91)) evolves like $c_\nu \propto a^{-1} \propto \eta^{-1}$. At the same time $H = 1/a\eta \propto \eta^{-2}$. Hence, during radiation domination, the free-streaming length of nonrelativistic neutrinos increases like $\lambda_{\rm fs} \propto \eta$, while the comoving free-streaming length remains constant. After the time of equality between radiation and matter, we have just seen that the free-streaming length decreases. Hence, it reaches its maximum between $\eta_{\rm nr}$ and $\eta_{\rm eq}$. The free-streaming length and wavenumber are still given by (5.92) and (5.93) with now $H(z)^2 = H_0^2[\Omega_\Lambda + \Omega_k(1+z)^2 + \Omega_{\rm M}(1+z)^3 + \Omega_{\rm R}(1+z)^4]$. Hence the minimum value of $k_{\rm fs}$ is given by

$$k_{\rm nr} \equiv k_{\rm fs}(\eta_{\rm nr}) \simeq 0.776\,\Omega_{\rm R}^{1/2} \left(\frac{T_\nu^{\rm a}}{T_\nu}\right) \left(\frac{m_\nu}{1\ {\rm eV}}\right) h\ {\rm Mpc}^{-1} \tag{5.96}$$

and differs from its counterpart (5.94) for neutrinos with sub-eV mass.

In the approximation in which c_ν would switch from 1 to $(\eta_{\rm nr}/\eta)$ at $\eta = \eta_{\rm nr}$, and to $(\eta_{\rm nr}\eta_{\rm eq}/\eta^2)$ at $\eta = \eta_{\rm eq}$, the comoving free-streaming horizon reads

$$\begin{aligned} r_{\rm fs}(\eta > \eta_{\rm eq}) &\simeq \eta_{\rm nr}\left(2 + \ln(\eta_{\rm eq}/\eta_{\rm nr}) - \eta_{\rm eq}/\eta\right) \\ &\simeq \sqrt{\frac{3}{2}}\frac{2}{k_{\rm nr}}\left(1 + \frac{1}{2}\log\left(\frac{1+z_{\rm nr}}{1+z_{\rm eq}}\right) - \frac{1}{2}\left(\frac{1+z}{1+z_{\rm eq}}\right)^2\right), \end{aligned} \tag{5.97}$$

where we used the expression $\eta = 1/(aH) \propto a$ during radiation domination and $\eta = 2/(aH) \propto a^{1/2}$ during matter domination (taking a recent Λ or curvature-dominated stage into account would change the result by a very small amount at late times). The last term is usually negligible, but the second term, with the logarithm, can be important for heavy particles becoming nonrelativistic at high redshift. In this case, $r_{\rm fs}$ can be significantly larger than $(2\pi/k_{\rm nr})$, and the latter does not give a good approximation of the scale below which free-streaming can be neglected. We see that the difference between the two comes from the stage between $\eta_{\rm nr}$ and $\eta_{\rm eq}$, during which the comoving free-streaming scale is constant

while the comoving free-streaming horizon grows logarithmically (Boyarsky *et al.*, 2009d).

5.2.5 Linear evolution of neutrino perturbations

Relativistic regime

If relativistic neutrinos were not coupled gravitationally, the equation of motion for perturbations in Fourier space (5.66) would be solved by simple plane waves, $F_\nu(\eta, k, \mu) \propto \exp(-ik\mu\eta)$. Because the Legendre coefficients of plane waves are spherical Bessel functions, the solution in multipole space would read $F_{\nu l}(\eta, k) \propto j_l(k\eta)$. This explains why the last of Eqs. (5.68) coincides exactly with the recurrence relation of spherical Bessel functions. In the super-Hubble limit, we see that $F_{\nu 0} = \delta_\nu$ would be constant whereas other multipoles would grow like $(k\eta)^l$: this is indeed the correct behaviour expected for the growing adiabatic mode in the Newtonian gauge.

In the actual equation of evolution, the first few multipoles $F_{\nu l}$ are sourced by metric perturbations. More precisely, in the Newtonian gauge, the evolution of the monopole is sourced by a time-dilation term involving ϕ', whereas the evolution of the dipole is driven by the gradient of the gravitational potential ψ. The full solution is found to be qualitatively similar to that of the homogenous equation, although the amplitude and phase of the multipoles are slightly modified by the coupling with metric perturbations.

Spherical Bessel functions $j_l(x)$ grow as a function of x until $x \simeq l + \frac{1}{2}$, and then feature damped oscillations. For neutrinos, this means that as time evolves, power is transferred from small to large multipoles. In the super-Hubble limit, all the power is in $F_{\nu 0} = \delta_\nu$. At Hubble crossing, it is transferred to $l = 1$, then to $l = 2$, etc. A given multipole reaches its maximum close to $\eta \sim l/k$. This can be understood geometrically. At time η, the observer sees neutrinos emitted on his own neutrino last scattering surface, i.e., on a sphere centered on him and of comoving radius $r = (\eta - \eta_{\nu \mathrm{LS}})$, where $\eta_{\nu \mathrm{LS}}$ is the neutrino decoupling time. At typical times of interest (close to photon decoupling), $\eta \gg \eta_{\nu \mathrm{LS}}$ and the radius of the sphere can be approximated as $r = \eta$. Fourier modes of comoving wavelength $2\pi/k$ on the sphere are seen by the observer under an angle $\theta = 2\pi/(kr)$ in the small-angle approximation. This means that in multipole space the contribution of a given wavenumber peaks near $l \sim 2\pi/\theta \sim kr \sim k\eta$.

Nonrelativistic regime

When neutrinos become nonrelativistic, the stress part of their stress–energy tensor becomes negligible. We saw explicitly in Eq. (2.47) that in the limit $\langle E \rangle \sim m \gg$

$\langle p \rangle$, the pressure P becomes much smaller than the energy density ρ. As shown at the end of Section 5.2.1, the ratios $\delta p_\nu / \delta \rho_\nu$ and $\sigma_\nu / \delta \rho_\nu$ become tiny for the same reasons. Massive neutrinos can then be followed by exploiting the first two of Eqs. (5.74) only. By integrating these equations over momentum in the limit $y \ll \epsilon$, one could show that they are *asymptotically* equivalent to the CDM equations of evolution (5.19).

5.2.6 Practical implementation and approximations

As for photons, a technical issue comes from the fact that the hierarchy of coupled neutrino equations is infinite. A given numerical code can integrate only a finite number of equations, but a truncation of the hierarchy at some multipole $l_{\mathrm{max}\,\nu}$ may cause a reflection of power from $l_{\mathrm{max}\,\nu}$ down to lower multipoles. Let us briefly discuss how to avoid such problems.

Brute-force integration

Because at a given time and for a given wavenumber, massless neutrino perturbations are populated until $l \sim k\eta$, the most secure way to avoid any reflection of power for a given mode k would be to truncate the neutrino equations well above $l = k\eta_0$, where η_0 is the conformal age of the universe. For instance, a sharp truncation at $l_{\mathrm{max}\,\nu} = 2k\eta_0$ gives accurate results. In the case of massive neutrinos, all multipoles with $l \geq 2$ decay after η_{nr}, so the truncation only needs to be performed at $l_{\mathrm{max}\,\nu} > k\eta_{\mathrm{nr}}$.

These schemes are accurate but heavy. We have seen in Section 5.1.6 that for computing the CMB spectrum until l_{max}, we must compute the evolution of perturbations up to a wavenumber $k_{\mathrm{max}} \sim l_{\mathrm{max}}/\eta_0$, even when using the line-of-sight approach. So, for massless neutrinos, the truncation should be implemented at $l_{\mathrm{max}\,\nu} \sim 2l_{\mathrm{max}}$ at least for the largest wavenumbers. This implies that thousands of equations must be integrated for many wavenumbers. For massive neutrinos, the number of multipoles can be reduced by a factor of $(\eta_{\mathrm{nr}}/\eta_0)$, but on the other hand the Boltzmann equation Eq. (5.74) must be integrated for a discrete set of momenta y. In both cases the computation time is prohibitive.

Usual truncation scheme

In reality, we need to get accurate solutions for only the first three multipoles $l = 0, 1, 2$, i.e., for $(\delta_\nu, \theta_\nu, \sigma_\nu)$, because these are the only quantities appearing in the linearized Einstein equations. So the goal of a given truncation scheme is to avoid the reflection of power at $l_{\mathrm{max}\,\nu}$ contaminating the multipoles $l = 0, 1, 2$ significantly. Hence the situation for neutrinos is identical to that for photons in the line-of-sight approach.

The truncation formula proposed by (Ma and Bertschinger, 1995) for photons and mentioned in Section 5.1.6 can be applied to neutrinos too, because it only assumes that high multipoles satisfy the same recurrence relation as the spherical Bessel function $j_l(k\eta)$. For massless neutrinos this gives

$$F_{\nu\,[l_{\max\nu}+1]} = \frac{(2l_{\max\nu}+1)}{k\eta}\,F_{\nu\,l_{\max\nu}} - F_{\nu\,[l_{\max\nu}-1]}, \tag{5.98}$$

whereas for massive neutrinos

$$\Psi_{\nu\,[l_{\max\nu}+1]} = \frac{(2l_{\max\nu}+1)\epsilon}{yk\eta}\,\Psi_{\nu\,l_{\max\nu}} - \Psi_{\nu\,[l_{\max\nu}-1]}. \tag{5.99}$$

With such a scheme and for both massless and massive neutrinos, $l_{\max\nu}$ can be reduced typically to 20 or less, depending on the required precision. This approach is the one most commonly implemented in Boltzmann codes and leads to a reasonable computational time. Even with such a gain, neutrinos are still the species described by the largest number of equations in a Boltzmann code. For this reason, several approximation schemes have been devised.

Implicit solutions

The truncation formula of Ma and Bertschinger, 1995 would be exact if gravitational source terms in the Boltzmann equation could be neglected. By applying Green's method, it is possible to derive an exact implicit solution for Eq. (5.66) including these terms (Shoji and Komatsu, 2010; Blas *et al.*, 2011). For massless neutrinos, the solution for the transfer function $F_\nu(k,\mu,\eta)$ is

$$F_\nu(k,\mu,\eta) = F_\nu(k,\mu,\eta_{\rm in})e^{-ik\mu\eta} + \int_{\eta_{\rm in}}^{\eta} e^{-ik\mu(\eta-\tilde\eta)}4[\phi'(k,\tilde\eta) + ik\mu\,\psi(k,\tilde\eta)]d\tilde\eta. \tag{5.100}$$

For adiabatic modes, the initial condition is given by $F_\nu(k,\mu,\eta_{\rm in}) = \delta_\nu(k,\eta_{\rm in}) = \delta_\gamma(k,\eta_{\rm in})$, plus higher-order terms in $(k\eta)$. To write this solution in Legendre space, it is necessary to integrate the term $[ik\mu\,\psi]$ by parts so that the integral depends on μ only through the factor $e^{-ik\mu(\eta-\tilde\eta)}$, and then to expand the exponential in spherical Bessel functions (see Blas *et al.*, 2011 for a synchronous gauge version of this calculation). The same steps are described by Shoji and Komatsu, 2010 for the massive neutrino equation.

These formal solutions are not immediately useful, because metric fluctuations cannot be considered an external source term. In other words, their evolution depends on the neutrino fluctuation evolution and cannot be computed in advance before integrating Eq. (5.100). However, these solutions can be useful for deriving or justifying several approximation schemes.

Imperfect fluid approximations

Usually, imperfect fluid equations describe weakly coupled species, such that the mean free path of particles exceeds the typical scale on which macroscopic quantities (defined by coarse grain) experience spatial fluctuations. One might think that the case of decoupled neutrinos is very different, because they are collisionless and cannot be considered a fluid at all. However, in a cosmological context, an imperfect fluid approach could be applied to neutrino perturbations expanded in Fourier space. Indeed, for wavelengths larger than the Hubble radius (or more precisely than the free-streaming scale), the propagation of neutrinos can be neglected. In this limit, the neutrino perturbation equations are equivalent to perfect fluid equations. We have already seen that with adiabatic initial conditions, neutrino density fluctuations are identical to photon density fluctuations on super-Hubble scales, although neutrinos are collisionless and photons are tightly coupled at high redshift. Around the time of Hubble crossing, the mean free path (which can be identified with the free-streaming horizon) is still not much bigger than the characteristic length in the Friedmann universe, namely the Hubble radius: thus, an imperfect fluid approximation may in principle give good results. Later, for modes well inside the horizon, it is obvious that the free-streaming horizon cannot be considered small anymore, and so there is no reason for an imperfect fluid approximation to work. However, in this limit, the gravitational back-reaction of neutrinos on photons, baryons and CDM is very small (as we shall see in Sections 5.3.3 and 6.1.4). So we do not need neutrino perturbation approximations to be very precise, unless we want to understand the clustering properties of the neutrinos themselves.

In general, a theory of imperfect fluids involves equations for shear viscosity, bulk viscosity, heat conduction, entropy flux, etc. These possibilities have not all been investigated in detail in the context of neutrino cosmology, but several people have proposed an approximate evolution equation for shear viscosity, i.e., for the anisotropic stress σ_ν, on top of the continuity and Euler equations. In other words, the Boltzmann hierarchy (5.68) or (5.74) could be closed at $l = 2$ (and integrated over momentum in the case of massive neutrinos), using some particular approximation. This can be very efficient because it reduces the number of neutrino equations to three for each wavenumber.

An imperfect fluid approximation could be used at any time or could be substituted into the full equations only inside the Hubble radius, when $k\eta$ exceeds some threshold value $[k\eta]_{\rm fluid}$ (Blas *et al.*, 2011; Lesgourgues and Tram, 2011). The advantage of the second case is that an error in the neutrino sector would have a moderate impact on other quantities, because the gravitational coupling between neutrinos and other species is relevant mainly around Hubble crossing. This approach is also efficient because at the time when the approximation is switched, only modes up to $l \sim [k\eta]_{\rm fluid}$ are populated. So before using the

approximation, we can truncate the hierarchy with Eq. (5.98) or (5.99) at a lower $l_{\max\nu} \sim [k\eta]_{\rm fluid}$.

The first concrete fluid approximation was proposed by Hu, 1998. The idea is to use a shear equation of the form

$$\sigma_\nu' = -3\frac{a'}{a}\frac{c_{\rm eff}^2}{w}\sigma_\nu + \frac{8}{3}\frac{c_{\rm vis}^2}{1+w}\theta_\nu \tag{5.101}$$

with two given coefficients $c_{\rm eff}$ (the effective sound speed) and $c_{\rm vis}$ (the effective viscosity speed). Hu proposes to replace the first coefficient with the adiabatic sound speed ($c_{\rm eff}^2 = \bar{P}'/\bar{\rho}'$), and $c_{\rm vis}^2$ with the equation of state parameter $w = \bar{P}/\bar{\rho}$. For relativistic neutrinos, these different factors reduce to $c_{\rm eff}^2 = c_{\rm vis}^2 = w = 1/3$. Also, during radiation domination, a'/a can be replaced with $1/\eta$. In these two limits, the above equation becomes equivalent to the shear equation in Eq. (5.68) when the usual truncation scheme is applied at $l_{\max\nu} = 2$ (so F_3 is replaced as a function of σ_ν and θ_ν using Eq. (5.98)).

More accurate alternatives have been discussed in the literature. Shoji and Komatsu (2010) start from the implicit exact solution for massive neutrinos, and assume a sharp truncation at $l = 3$ ($\Psi_3 = 0$). Blas *et al.* (2011) start from the implicit exact solution for massless neutrinos, and infer a shear evolution equation by keeping only the leading terms inside the Hubble radius, when $(k\eta) \gg 1$. Lesgourgues and Tram (2011) generalize the latter approach to massive neutrinos. The merits of these different schemes are discussed in these works. It appears that the accuracy of imperfect fluid approximations can be largely sufficient for fitting the CMB and LSS spectrum in future experiments.

Other approximations

The most computationally expensive part in a Boltzmann code is usually the integration of massive neutrino equations, because the Legendre momenta Ψ_l of the perturbed phase space distribution must be followed for several discrete values of momentum y (and even if the number of momenta can be kept small thanks to a quadrature approach; see Lesgourgues and Tram, 2011). We have seen in Eq. (5.72) that as long as neutrinos are relativistic, the y dependence of Ψ_l is known and given by $[d\ln f_{\nu 0}(y)/d\ln y]$. Deviations from this form can be captured by a Taylor expansion in the parameter

$$\frac{\sqrt{\epsilon^2 - y^2}}{y} = \frac{am}{y}, \tag{5.102}$$

which grows from zero to one in the relativistic regime, and from one to infinity in the nonrelativistic one. Then the transfer function $\Psi_l(\eta, k, y)$ can be written in the

form

$$\Psi_l(\eta, k, y) = -\frac{1}{4}\frac{d\ln f_{\nu 0}(y)}{d\ln y}\left[\sum_i \left(\frac{am}{y}\right)^i \tilde{\Psi}_l(\eta, k)^{(i)}\right]. \qquad (5.103)$$

Howlett *et al.* (2012) used the exact equation of motion for Ψ_l to show that

- $\tilde{\Psi}_l^{(0)}$ reduces to F_ν, as expected from the relativistic limit of Eq. (5.72);
- $\tilde{\Psi}_l^{(1)}$ vanishes;
- $\tilde{\Psi}_l^{(2)}$ is subject to a hierarchy of equations, like that for F_ν but with different coefficients;
- higher-order terms can be neglected for the purpose of computing CMB anisotropies, even if good precision is required.

In this scheme, the full massive neutrino equations are replaced with those for massless neutrinos, plus a duplicate set of equations for $\tilde{\Psi}_l^{(2)}$. This approach is not as fast as fluid approximations, but it is simpler, robust, and easy to generalize to higher order.

5.3 Effects of neutrinos on primary cosmic microwave background anisotropies

5.3.1 How can decoupled species affect the cosmic microwave background?

It is always difficult to discuss the impact of a given species (neutrinos, CDM, early dark energy, etc.) on the CMB, because several effects mix with each other, and it is sometimes impossible to separate them clearly. However, we can make a general classification of these effects, which will help us to understand the effect of massless or massive neutrinos in the next subsections.

Species coupled only gravitationally with the photon–baryon(–electron) fluid can only impact the CMB through the Friedmann equation, or through the recombination history, or finally, through the linearized Einstein equations via metric perturbations. Hence, it is useful to adopt a classification in terms of background and perturbation effects.

(a) *Background effects* are encoded in a modified evolution of the scale factor $a(\eta)$, or possibly of the free electron fraction $X_e(\eta)$. We can notice already that neutrinos have no impact on the recombination history, and only affect $a(\eta)$ (during radiation domination in the case of massless neutrinos, and also slightly during matter and Λ domination in the case of massive neutrinos). In Section 5.1, we showed that the spectrum of CMB anisotropies in the minimal ΛCDM model depends on a small number of effects or "degrees of freedom", each of them being related to characteristic scales (sound

horizon, diffusion length, angular diameter distance), to characteristic times (equality between radiation and matter, equality between matter and Λ), to the primordial spectrum and to density ratios (e.g., the balance between pressure and gravity in the tightly coupled photon–baryon fluid relates to $\omega_{\rm B}$, or more precisely to $\omega_{\rm B}/\omega_\gamma$, with ω_γ fixed by the measurement of the CMB temperature today). The list of these effects is presented at the end of Section 5.1.6 with labels (C1)–(C8). In the following sections, we will relate the impact of neutrinos to variations of these characteristic scales, times and ratios. We will also see that the background effects of a given species depend on which particular set of other parameters is kept fixed when the density of this species is increased; sometimes these background effects can be completely absorbed by tuning other parameters at the same time. For this reason, background effects can be thought to be "indirect" and difficult (or sometimes even impossible) to probe with observations. We will provide a detailed discussion of these issues in the next subsections.

(b) *Perturbation effects* can instead be considered as "direct". The presence of a decoupled species can modify the evolution of metric fluctuations, and back-reacts on the perturbations of the photon–baryon fluid. In the next subsections, we will do our best to cancel the background effect of neutrinos (by tuning other parameters) in order to single out their direct perturbation effect. Let us discuss separately perturbation effects occuring before and after photon decoupling:

(b.1) *Before decoupling*, a key observation is that the impact of a species coupled only gravitationally to photons and baryons can only be important around the time of sound horizon crossing for that species. Indeed, on super-Hubble scales, the growing adiabatic mode is subject to universal relations between δ_γ, $\delta_{\rm B}$ and the curvature perturbation $\mathcal{R}$, not affected by the presence of other species: we checked this explicitly for neutrinos in Section 5.2.3. In the opposite limit, well inside the sound horizon, we have seen in Section 5.1.5 that metric fluctuations have decayed. Once $|\phi|$ and $|\psi|$ are much smaller than $|\Theta_\gamma|$, there can be no gravitational feedback on photon fluctuations in Eq. (5.38), and neutrinos or other decoupled species cannot be relevant. Hence, the only region in which the effect of neutrinos on primary CMB anisotropies should be discussed is that of sound horizon crossing before photon decoupling.

(b.2) *Soon after decoupling*, a given species can impact the CMB via the early ISW effect. We mentioned earlier that the EISW is negligible on small scales, and peaks for wavenumbers crossing the Hubble scale roughly around the time of decoupling. In the space (k, η), this region is close to the one described in (b.1) and extends it to higher η and slightly smaller k. The EISW depends on

the time variation of $(\phi + \psi)$ at a given wavenumber after decoupling. As briefly mentioned at the very end of Section 5.1.5 and shown in Chapter 6, this variation would vanish in a fully matter-dominated universe. Changing the neutrino abundance or mass implies that we play with the fraction of total matter which does not cluster like CDM (because neither relativistic neutrinos nor nonrelativistic neutrinos cluster below their free-streaming scale). Hence, neutrinos can play a crucial role in the determination of the time needed for $(\phi + \psi)$ to reach a nearly constant asymptotic value after decoupling, and of the amplitude of the EISW. This effect is distinct from the global enhancement of the EISW caused by a delay in the time of equality between radiation and matter, which we would classify as a background effect.

(b.3) *At low redshift*, massless neutrinos cannot play a role in the late ISW effect, because their density is completely negligible, but massive neutrinos can, because below their free-streaming scale they do not cluster like CDM and introduce a very small but nonzero derivative $(\phi' + \psi')$. This effect is distinct from that of a change in the time of equality between matter and Λ, which would be classified as a background effect. Because it is related to secondary anisotropies imprinted in the recent universe, we will discuss it in Section 6.3.1 of the next chapter (and find that it is almost negligible).

5.3.2 Effects of massless neutrinos

A single free parameter, the effective neutrino number

We know that all relativistic collisionless species are described by the same equations (5.68) integrated over momentum, including all neutrinos and relics such that $m \ll \langle p \rangle$ (at least until today), with or without chemical potentials and/or non-thermal distortions. All these cases are encoded in one single parameter, the total density of such species today (which can be scaled back to the past, because for relativistic species $\rho_{\rm R} \propto a^{-4}$). This density can be specified, e.g., by giving the total radiation density $\omega_{\rm R}$ (including photons and extra relics), or the fractional radiation density $\Omega_{\rm R}$, or the effective neutrino number $N_{\rm eff}$ defined in (2.198). In this section we choose to use $N_{\rm eff}$ as a free parameter. The neutrinoless ΛCDM model discussed in section 5.1 corresponds to $N_{\rm eff} = 0$, whereas the actual minimal ΛCDM model including the usual three families of active neutrinos (with masses assumed to be negligible) assumes $N_{\rm eff} = 3.046$, as explained in Section 4.1. Here, $N_{\rm eff}$ will be considered as a seventh free parameter on top of the six ΛCDM parameters ($A_{\rm s}$, $n_{\rm s}$, $\omega_{\rm B}$, $\omega_{\rm M}$, Ω_Λ or $h = \sqrt{\omega_{\rm M}/(1-\Omega_\Lambda)}$, $\tau_{\rm reion}$) defined in Section 5.1.6.

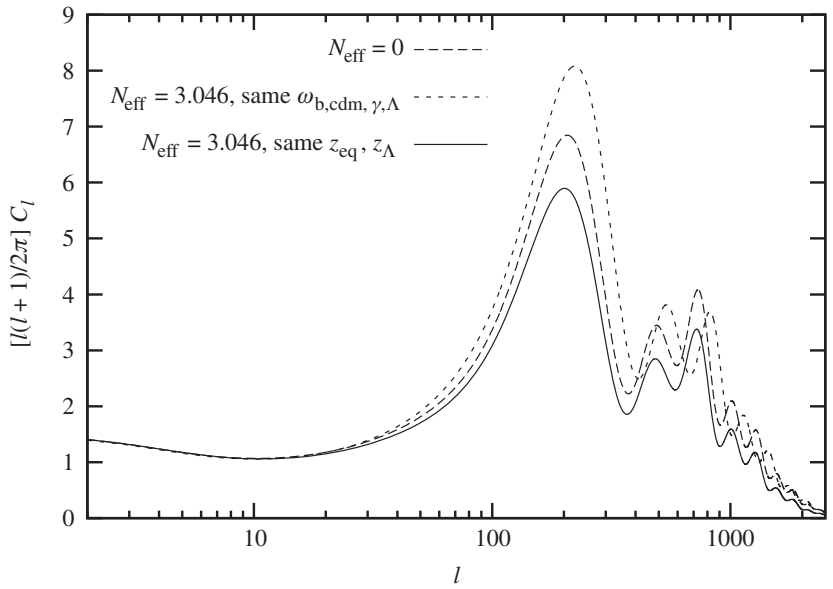

Figure 5.3 Spectrum of CMB temperature anisotropies for a neutrinoless model (middle curve) a model with $N_{\rm eff} = 3.046$ and identical parameters $(A_{\rm s}, n_{\rm s}, \omega_{\rm B}, \omega_{\rm M}, \Omega_\Lambda, \tau_{\rm reion})$ (top curve) and a model with $N_{\rm eff} = 3.046$ and the same redshift of equality between radiation and matter and between matter and Λ (lower curve; see the text for details). The difference between the middle and lower curves can be attributed entirely to neutrino perturbation effects, plus a shift in the diffusion damping scale.

Background effects

We start by comparing two models with $N_{\rm eff} = 0$ and $N_{\rm eff} = 3.046$, sharing identical values of $(A_{\rm s}, n_{\rm s}, \omega_{\rm B}, \omega_{\rm M}, \Omega_\Lambda, \tau_{\rm reion})$. We will see later that the choice to keep these parameters fixed is not very illuminating, and we will take a second approach in the next paragraphs.

The middle and top curves in Fig. 5.3 show the temperature spectrum of these two models. The difference can be explained by the sum of some perturbation effects (that we will described later separately), plus the following background effects:

1. A different redshift of equality (described as effect (C3) at the end of Section 5.1.6). Indeed, in the presence of relativistic relics, this redshift is given by

$$z_{\rm eq} = \frac{\omega_{\rm M}}{\omega_\gamma \left[1 + \frac{7}{8}\left(\frac{4}{11}\right)^{4/3} N_{\rm eff}\right]} = \frac{\omega_{\rm M}}{\omega_\gamma \left[1 + 0.2271 N_{\rm eff}\right]}. \qquad (5.104)$$

Because ω_γ is fixed by the measurement of the CMB temperature today, known up to four digits, this formula has two free parameters, $\omega_{\rm M}$ and $N_{\rm eff}$. Increasing $N_{\rm eff}$ with $\omega_{\rm M}$ fixed implies a shorter stage between equality and decoupling, leading to higher peaks (especially the first one), as explained in Section 5.1.6.

2. A different peak scale (effect (C1), related to the ratio $d_{\rm s}(\eta_{\rm LS})/d_{\rm A}(\eta_{\rm LS})$ or $r_{\rm s}(\eta_{\rm LS})/r_{\rm A}(\eta_{\rm LS})$). The comoving sound horizon at decoupling depends on the expansion history before $\eta_{\rm LS}$, and in particular on the time of equality. A later equality implies a smaller sound horizon at decoupling, so all peaks are shifted to higher l's. The comoving angular diameter distance $r_{\rm A}(\eta_{\rm LS})$, depending only on the expansion history after $\eta_{\rm LS}$, is the same in these two models.
3. A tiny change in the diffusion scale (effect (C4), related to the ratio $d_{\rm d}(\eta_{\rm LS})/d_{\rm A}(\eta_{\rm LS})$ or $r_{\rm d}(\eta_{\rm LS})/r_A(\eta_{\rm LS})$). Both $r_s(\eta_{\rm LS})$ and $r_{\rm d}(\eta_{\rm LS})$ are given by integrals running from $\eta = 0$ to $\eta_{\rm LS}$, respectively Eq. (5.37) and Eq. (5.40). However, the integrand of Eq. (5.40) increases more quickly with time, roughly as a^2. Hence $r_{\rm D}(\eta_{\rm LS})$ depends only on the expansion and thermal history immediately before decoupling and is affected by a change in $z_{\rm eq}$ only by a negligible amount. This explains why in Figure 5.3, the secondary peaks of the middle and upper curves share roughly the same envelope $\exp[-(l/l_{\rm D})^2]$. However, the third and higher peaks of the model with $N_{\rm eff} = 3.046$ moved to larger l in such a way as to fall inside the diffusion damping region: hence their amplitude is suppressed, even if effect (C3) alone would have the opposite effect.

Other effects (C2), (C5), (C6), (C7), (C8) are controlled by the parameters $(A_{\rm s}, n_{\rm s}, \omega_{\rm B}, \Omega_\Lambda, \tau_{\rm reion})$ and are the same in the two models.

In the previous comparison, the direct perturbation effect of neutrinos was masked by the large impact of the change in the time of equality. To make a more useful comparison, we should vary $N_{\rm eff}$ not with other cosmological parameters fixed, but with the quantities governing the effects (C1)–(C8) unchanged, if this is possible. This approach was taken previously by (Bashinsky and Seljak, 2004) and summarized by (Hou *et al.*, 2011).

In increasing the effective neutrino number from zero to $N_{\rm eff}$, we enhance the radiation density by a factor

$$\alpha \equiv (1 + 0.2271\, N_{\rm eff}). \tag{5.105}$$

If we simultaneously increase the matter density $\omega_{\rm M}$ by the same amount, the redshift of equality between radiation and matter will not vary, and effect (C3) will be the same for the two models. If this is done by enhancing the CDM density with fixed $\omega_{\rm B}$, effect (C2) will also remain constant. We should keep Ω_Λ fixed in order to maintain the same redshift of equality between matter and Λ, and leave effect (C7) unaffected. Finally, $A_{\rm s}$, $n_{\rm s}$, $\tau_{\rm reion}$ should also be left invariant, in order

to preserve (C5), (C6), (C8). We must now check if the remaining effects (C1) and (C4) are affected by such a transformation or not. In summary:

- We increase $\omega_{\rm R}$ and $\omega_{\rm M}$ by the same amount α, while keeping Ω_Λ fixed.
- Hence the reduced Hubble parameter $h = \sqrt{\omega_{\rm M}/(1-\Omega_\Lambda)}$ increases by $\sqrt{\alpha}$.
- This implies that ω_Λ also increases by α, so the three densities $\rho_{\rm R}(z)$, $\rho_{\rm M}(z)$ and $\rho_\Lambda(z)$ are rescaled by the same amount. Indeed, the proper way to keep the two redshifts of equality fixed is to multiply all densities by the same factor. The Friedmann equation shows that the Hubble parameter as a function of redshift, $H(z)$, is rescaled by $\sqrt{\alpha}$.
- The functions $\eta(z)$, $r_{\rm s}(z)$, $r_{\rm A}(z)$, obtained by integrating over $d\eta$ (or equivalently, after a change of variable, over dz/H), are all rescaled by $\alpha^{-1/2}$.
- The square of the function $r_{\rm D}(z)$ is obtained by integrating over $(d\eta/an_e)$, or equivalently over (zdz/n_eH). Because the reionization history controlled by the parameter $X_e(z)$ is unaffected by the transformation, $r_{\rm D}(z)^2$ is also rescaled by $\alpha^{-1/2}$.

We conclude that effect (C1) is unaffected by this transformation: both $r_{\rm s}(\eta_{\rm LS})$ and $r_{\rm A}(\eta_{\rm LS})$ have been rescaled by the same factor, with a constant ratio.[3] Instead, effect (C4) has been changed, because $r_{\rm D}$ decreases by $\alpha^{-1/4}$, whereas the ratio $r_{\rm D}(\eta_{\rm LS})/r_{\rm A}(\eta_{\rm LS})$ increases by $\alpha^{1/4}$. So in the second model, diffusion damping occurs at larger angles, i.e., at smaller l's.

We conclude that the difference between the original model and the rescaled model should only be attributed to diffusion damping and to neutrino perturbation effects. This is illustrated in Fig. 5.3. The lower curve has been obtained by rescaling all densities as described. The peaks of the $N_{\rm eff} = 0$ and $N_{\rm eff} = 3.046$ models now have roughly the same location and shape, with, however, an overall amplitude suppression (resulting from neutrino free-streaming, as developed in the next subsection) and a smaller damping tail.

Our goal was to increase $N_{\rm eff}$ without affecting effects (C1)–(C8), in order to eliminate background effects and to isolate the direct gravitational effect of neutrinos. This was not fully achieved by the previous transformation, because effect (C8) varied. However, in the framework of the minimal ΛCDM model with free $N_{\rm eff}$, (C1) and (C8) cannot be kept fixed simultaneously. Because $\omega_{\rm M}$ is determined by the redshift of equality and $\omega_{\rm B}$ by the baryon-to-photon ratio, we

[3] One could go further and show that in the equation of evolution for the tightly coupled photon–baryon fluid, a rescaling of $H(z)$ with fixed $R(z)$ can be completely eliminated. At the same time as $H(z)$ is rescaled by $\sqrt{\alpha}$, all wavenumbers should be rescaled by the same factor. But because $d_{\rm A}$ is rescaled by the inverse of $\sqrt{\alpha}$, after a projection in harmonic space, the spectrum C_l is left invariant. Hence, as long as tight coupling holds, the transformation discussed here leaves the CMB invariant. Differences can show up only beyond the tight-coupling approximation, i.e., at the level of diffusion damping, or through the gravitational back-reaction of other species mediated by metric fluctuations.

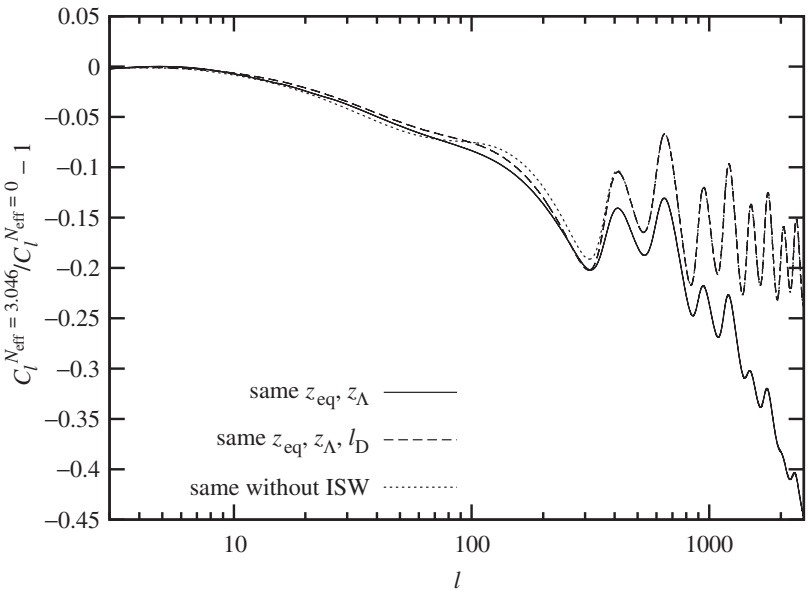

Figure 5.4 CMB temperature spectrum for models with $N_{\rm eff} = 3.046$ divided by the spectrum of a model with $N_{\rm eff} = 0$. The lower curve corresponds to the case in which the two models share the same redshift of equality between radiation and matter and between matter and Λ (so it is the ratio of the lower and middle curves in Figure 5.3). The upper curve is obtained by additional tuning of the primordial helium fraction Y_p, in such a way as to keep the diffusion damping scale $r_{\rm d}/r_{\rm A}$ constant. Hence the upper curve illustrates the effect of neutrinos at the level of perturbations only.

can adjust effects (C1) and (C8) only by playing with h. But $r_{\rm s}$ is proportional to h^{-1} whereas $r_{\rm d}$ is proportional to $h^{-1/2}$, so both effects cannot be compensated for at the same time. However, we could try to change the recombination history. As noticed by Bashinsky and Seljak, 2004, this is a useful way to gain further insight into the effect of relativistic neutrinos.

In Fig. 5.4, the lower curve shows the spectrum of the previous model with $N_{\rm eff} = 3.046$ divided by that of the neutrinoless model. This ratio can be described as a steplike suppression with superimposed oscillations, plus a rapid decrease for $l > 700$. We suspect that this rapid decrease is due to diffusion damping, i.e., to the shifting of the envelope $\exp[-(l/l_{\rm D})^2]$ to a smaller $l_{\rm D}$ in the $N_{\rm eff} = 3.046$ model. This can be checked by decreasing the primordial helium fraction Y_p defined in (2.157) in the model with neutrinos. Indeed, changing this parameter leads to a rescaling of n_e at the redshifts of interest, leaving all other characteristic times and scales fixed, apart from a very small change in the decoupling time $\eta_{\rm LS}$ which turns out to be negligible. In order to increase $r_{\rm D}$ and keep the same ratio $r_{\rm d}(\eta_{\rm LS})/r_{\rm A}(\eta_{\rm LS})$

as in the neutrinoless model, we need to decrease Y_p to unrealistically small values, around $Y_p = 0.02$. In a real data analysis, the primordial helium fraction is given either by the prediction of standard Big Bang nucleosynthesis (to about 0.25, with a weak dependence on $\omega_{\rm B}$), or by direct measurements of primordial element abundances. Values significantly smaller than 0.24 would conflict with both BBN predictions and direct observations, but the exercise performed here should be regarded as purely formal. The spectrum of the model with $N_{\rm eff} = 3.046$ and low helium fraction, divided by that of the original neutrinoless model, is shown in Fig. 5.4 (upper curve). As expected, the exponential suppression at $l > 700$ has now been removed. The remaining features can be attributed to the direct effect of neutrinos at the level of perturbations.

Perturbation effects

As discussed at the beginning of Section 5.3, the direct effect of neutrino perturbations on the CMB can be important when a given mode crosses the sound horizon, and acoustic oscillations are driven by metric fluctuations (i.e., by the term on the r.h.s. of Eq. (5.38)). Metric fluctuations quickly decay inside the sound horizon, and their time variation tends to boost temperature fluctuations until ϕ and ψ become negligible with respect to Θ_γ (more details on the effect of the driving term can be found, e.g., in Hu, 1995). After that stage, we have seen that oscillations go on with a constant amplitude during the radiation-dominated stage, or with a decreasing amplitude after the time of equality, caused by the increasing baryon fraction and by diffusion damping on small scales.

In the presence of free-streaming neutrinos, we expect metric fluctuations to be smaller for wavelengths inside the free-streaming scale (which coincides with the Hubble radius for relativistic neutrinos), because neutrinos cannot cluster on those scales. During radiation domination, neutrinos account for a large fraction of total matter, so they can reduce metric fluctuations by a significant amount. Hence, neutrinos reduce the boosting of temperature fluctuations during the driven oscillation stage. At the end, we observe smaller CMB anisotropies for all scales entering the sound horizon before decoupling, and especially during radiation domination.

An analytic approximation of the impact of neutrinos on the driving term was derived by Hu and Sugiyama, 1996, leading to the conclusion that the oscillation amplitude inside the sound horizon is reduced by $(1 + 4/15 R_\nu)^{-1}$ with respect to a neutrinoless model. So we expect the CMB peaks to be reduced by

$$\frac{\Delta C_l}{C_l} = \left(1 + \frac{4}{15} R_\nu\right)^{-2} = \left(1 + \frac{4}{15} \times \left[\frac{0.2271 N_{\rm eff}}{1 + 0.2271 N_{\rm eff}}\right]\right)^{-2}. \qquad (5.106)$$

For the two models that we compared in Figs. 5.3 and 5.4, this formula predicts 19% suppression between $N_{\rm eff} = 0$ and $N_{\rm eff} = 3.046$, in rather good agreement with the average value of the upper curve in 5.4 for the largest values of l. Notice that for intermediate values corresponding to the first two peaks, the effect is only partial because the modes entered the sound horizon at the beginning of matter domination. For a small variation of $N_{\rm eff}$ around three, Eq. (5.106) corresponds to a variation of the C_l's in the region of acoustic oscillations given by

$$\frac{\Delta C_l}{C_l} = -0.072\ \Delta N_{\rm eff}. \tag{5.107}$$

A more detailed analysis was presented later by (Bashinsky and Seljak, 2004). This work concludes with a reduction of the amplitude with respect to the neutrinoless case by

$$\frac{\Delta C_l}{C_l} = \left(1 - 0.2683 R_\nu + O(R_\nu^2)\right)^2, \tag{5.108}$$

found to be in very good agreement with Eq. (5.106). The same reference also shows that in real space, neutrinos (traveling at the speed of light) tend to pull temperature perturbations (propagating at a lower velocity $c_{\rm s} \sim c/\sqrt{3}$) out of gravitational potential wells. In Fourier space, this "neutrino drag" effect tends to shift the phase of oscillations in such a way that acoustic peaks are seen on larger scales, i.e., for smaller values of l. The analytic approximation of Bashinsky and Seljak, 2004 predicts a shift with respect to the neutrinoless case by

$$\Delta l_{\rm peak} = -\frac{r_{\rm A}(\eta_{\rm LS})}{r_{\rm s}(\eta_{\rm LS})} \left(0.1912\pi\, R_\nu + O(R_\nu^2)\right). \tag{5.109}$$

This approximation does not work as well as that for the amplitude of the peaks. For instance, it would correspond to a shift $\Delta l_{\rm peak} \simeq 20$ between the middle and lower curves of Fig 5.3, whereas the actual shift is closer to 10. The phase shift also explains the oscillatory pattern of the curves in Fig. 5.4.

Note that in the two models that we are comparing, $\omega_{\rm C}$ is different. Like neutrinos, CDM couples gravitationally with the photon–baryon fluid. So one could argue that the effects observed here are a superposition of gravitational effects due to both neutrinos and CDM. However, during radiation domination, the CDM density is negligible. So the perturbation effects of an enhanced CDM component are subleading for modes entering the sound horizon during radiation domination. This explains why the analytic prediction for the neutrino effect in Eq. (5.106) is a very good approximation to the full numerical result shown in Fig. 5.4.

So far, we have discussed only effects occuring before decoupling, through the driving term in the photon–baryon oscillator equation. As mentioned in the previous

subsection, neutrinos can also induce a difference in the EISW effect. However, this effect is subleading, as shown by the dashed curve in Fig. 5.4, in which we removed the whole ISW contribution to each spectrum before taking the ratio. For the sake of brevity, we will not discuss the details of this tiny correction.

5.3.3 Effects of massive neutrinos

A mode-dependent situation

Whereas a single parameter $N_{\rm eff}$ catches all possible effects of massless neutrinos (or more generally collisionless ultrarelativistic relics), massive neutrino effects are described by more parameters, especially if one goes beyond the minimal picture. The two parameters $N_{\rm eff}$ (describing the neutrino abundance in the early universe, when they are still ultrarelativistic) and ω_ν (the total density of neutrinos today, dominated by the contribution of at least two nonrelativistic mass eigenstates) are certainly playing a key role. However, in the perturbation equation for neutrinos, it is not possible to integrate quantities in momentum space in order to obtain reduced equations as for massless neutrinos, and it is not possible to factor out the total neutrino mass. In principle, individual masses could play a role, as well as any modification of the phase-space distribution function due, for instance, to chemical potentials or nonthermal distortions. In the following, we will assume for simplicity that all neutrinos have the same mass (as in the degenerate limit of the normal and inverted hierarchy scenarios) and share the same Fermi–Dirac distribution function (which is almost true in the minimal scenario, because nonthermal distortions imprinted around the time of electron–positron annihilation are extremely small, as discussed in Section 4.2.3). At the end of this section we will briefly discuss the effect of different individual masses and see that for standard active neutrinos, only the total mass M_ν is detectable in practice.

We saw in Section 5.2.4 that active neutrinos with a mass $m_\nu < 1.5$ eV become nonrelativistic after the time of equality between matter and radiation. We can safely restrict our discussion to this case. We will see later that heavier active neutrinos would strongly contradict current cosmological bounds.

Background effects

We have seen in Section 5.3.2 that the most relevant way to study the impact of a given parameter on the CMB spectra is to vary it while keeping fixed at the same time all characteristic times, scales and density ratios, which control the physical effects (C1)–(C8) described at the end of Section 5.1.6. A particularly important quantity is the redshift of equality between matter and radiation. Because we assumed that $m_\nu < 1.5$ eV, we should count neutrinos as radiation at that time, so

$z_{\rm eq}$ is given by

$$z_{\rm eq} = \frac{\omega_{\rm B} + \omega_{\rm C}}{\omega_\gamma \left[1 + 0.2271 N_{\rm eff}\right]}, \tag{5.110}$$

where the neutrinos are counted in the $N_{\rm eff}$ factor. The comparison between different masses should be performed at fixed $(\omega_{\rm B} + \omega_{\rm C})$, or better at fixed $\omega_{\rm B}$ and $\omega_{\rm C}$ in order to keep a fixed ratio $(\omega_{\rm B}/\omega_\gamma)$ (and not affect (C2) or (C3)). This means that the total nonrelativistic matter density today, $\omega_{\rm M} = \omega_{\rm B} + \omega_{\rm C} + \omega_\nu$, should be increased at the same time as the neutrino mass.

Two models with different neutrino masses but sharing the same values of $(A_{\rm s}, n_{\rm s}, \omega_{\rm B}, \omega_{\rm C}, \tau_{\rm reion})$ are strictly equivalent until the time of the nonrelativistic transition at redshift $z_{\rm nr} \propto m_\nu$. After that time, neutrinos dilute like $\rho_\nu \propto a^{-3}$ instead of a^{-4} and play the role of extra nonrelativistic matter. Therefore, the mass has an impact on the expansion history $H(z)$ at $z < z_{\rm nr}$, on the comoving angular diameter distance to recombination $r_{\rm A}(\eta_{\rm LS})$, and on the redshift of equality between matter and the cosmological constant z_Λ. Only if neutrinos are nonrelativistic at decoupling, i.e., roughly for $m_\nu \geq 0.6$ eV (see Eq. (5.90)) does their mass also impact the comoving sound horizon $r_{\rm s}(\eta_{\rm LS})$ and the damping scale $r_{\rm D}(\eta_{\rm LS})$ at decoupling.

By tuning h and Λ, still related through $h = \sqrt{\omega_{\rm M}/(1 - \Omega_\Lambda)}$, we have the possibility of keeping constant one of the two quantities $d_{\rm A}(\eta_{\rm LS})$ or z_Λ, but not both simultaneously. Because the scales of the peak and of the damping tail (controlled by $r_{\rm A}(\eta_{\rm LS})$ through effects (C1) and (C7)) are much better constrained by the data than the slope of the Sachs–Wolfe plateau (controlled by z_Λ through (C7)), the most interesting comparison is achieved by keeping $d_{\rm A}(\eta_{\rm LS})$ fixed. For masses much smaller than 0.6 eV, this will lead to the same peak scale and damping tail. For masses close to 0.6 eV or higher, $r_{\rm s}(\eta_{\rm LS})$ and $r_d(\eta_{\rm LS})$ are also affected, but we can always tune h to keep the same peak scale, at the expense of a small change in the diffusion damping scale.

In summary, we can increase m_ν with a constant redshift of equality and peak scale. The effects (C1)–(C8) then remain unaffected with the exception of

1. the LISW effect (C7), due to a shift in z_Λ;
2. eventually the diffusion damping effect (C4), but only for neutrinos already nonrelativistic at decoupling, i.e., with $m_\nu \geq 0.6$ eV.

Differences in the CMB spectra beyond those two effects should be attributed to the direct gravitational impact of massive neutrinos at the perturbation level.

We compare in Fig. 5.5 three spectra obtained with the same values of $(A_{\rm s}, n_{\rm s}, \omega_{\rm B}, \omega_{\rm C}, \tau_{\rm reion})$ and three active neutrinos with a common mass $m_\nu = M_\nu/3$, with either $M_\nu = 0$ eV, 3×0.3 eV or 3×0.6 eV. The two massive models

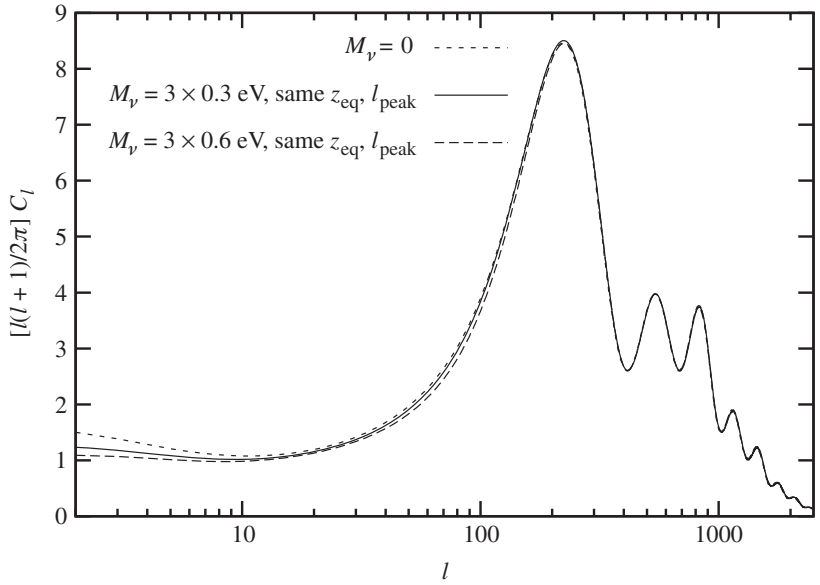

Figure 5.5 Spectrum of CMB temperature anisotropies for a massless neutrino model (highest curve for $l \leq 100$), a model with three degenerate neutrinos of total mass $M_\nu = 3 \times 0.3$ eV (middle curve for $l \leq 100$), and one with $M_\nu = 3 \times 0.6$ eV (lowest curve for $l \leq 100$). In all cases the redshift of equality between radiation and matter and the scale of the peaks has been kept constant.

correspond to a nonrelativistic transition at respectively $z_{nr} = 570$ or $z_{nr} = 1100$. When increasing the mass, we decrease h in order to keep the same peak scale. The ratios of the two massive cases divided by the massless case are shown in Fig. 5.6.

The difference due to the LISW is the most obvious one, leading to different slopes for $l < 20$ in Fig. 5.5, and to the sharp decrease for the same multipoles in Fig. 5.6. Models with a higher mass have a smaller h, a smaller Ω_Λ, and hence a smaller LISW effect. The small shift in the damping scale is seen better in Fig. 5.6 in the form of a rise at $l > 500$, especially for the model with nonrelativistic neutrinos at decoupling, as expected. Remaining differences in the range $20 < l < 500$ should be attributed to direct perturbation effects induced by neutrino masses.

Perturbation effects

We expect perturbation effects to be caused either by the gravitational driving of the photon–baryon oscillator equation before decoupling (effect described as (b.1)) at the beginning of Section 5.3), or by the neutrino mass impact on the evolution of $(\phi + \psi)$ after decoupling, i.e., by the EISW effect (described as (b.2)). To separate these two effects, we show in Fig. 5.6 the difference between the ratios obtained

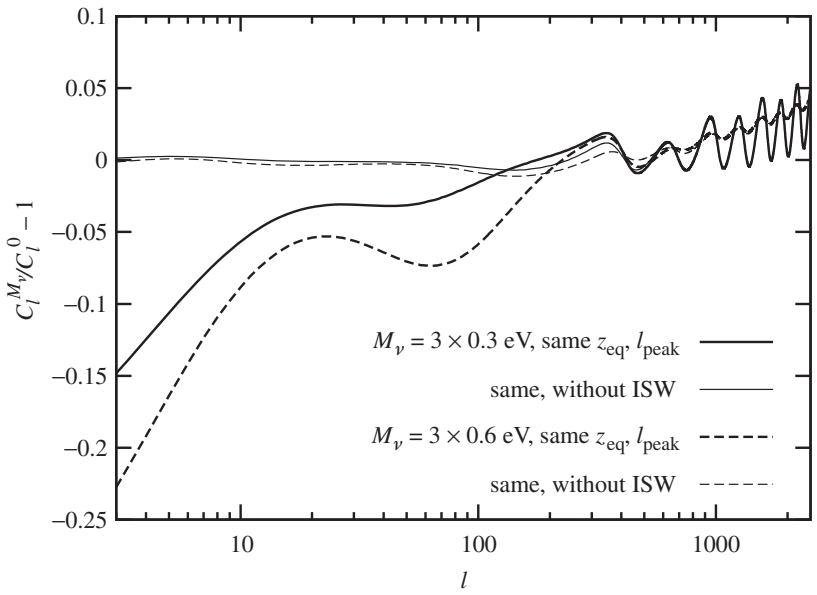

Figure 5.6 CMB temperature spectrum for models with either $M_\nu = 3 \times 0.3$ eV or $M_\nu = 3 \times 0.6$ eV divided by the spectrum of a model with three massless neutrinos sharing the same (standard) temperature. From left to right, the differences can be attributed to the LISW effect, EISW effect, gravitationally driven oscillations effect and diffusion damping, as explained in the text. To separate better the impact of the LISW plus EISW effect, the thin lines show the result of the comparison when the full ISW contribution is removed from each spectrum.

with the full temperature spectra (solid curves) and with the spectra without the ISW contribution (dashed curves).

The largest effect in the range $20 < l < 500$ is caused by the EISW: it leads to a depletion of the spectrum for $20 < l < 200$. This depletion is also visible in Fig. 5.5. Its amplitude is roughly given by

$$\frac{\Delta C_l}{C_l} \simeq \left(\frac{m_\nu}{10\ \mathrm{eV}}\right), \tag{5.111}$$

i.e., 3% for $m_\nu = M_\nu/3 = 0.3$ eV. Its location is also related to the neutrino mass, because this effect is caused by the fact that for wavenumbers $k < k_{\rm nr}$ neutrinos behave as a clustering component, whereas in the absence of neutrino mass they would behave as a free-streaming component like photons. Hence $(\phi + \psi)$ experiences less decay for these modes: we are closer to the limit of a fully matter-dominated universe for which $(\phi + \psi)$ would remain constant at horizon crossing. This implies a smaller EISW effect for $k < k_{\rm nr}$, visible in the CMB spectra above a given angle. The magnitude of this effect scales with the ratio $(\overline{\rho}_{\rm R}/\overline{\rho}_{\rm M})$ at the time when $k = k_{\rm nr}$ crosses the horizon, so it decreases with the neutrino mass.

A smaller effect related to the evolution prior to recombination is visible in the curves without ISW in the range $30 < l < 500$. For the model with relativistic neutrinos at decoupling, $M_\nu = 3 \times 0.3$ eV, this effect remains below the percent level. For the model with $M_\nu = 3 \times 0.6$ eV, we see a 3% depletion of the spectrum around $l \sim 100$, caused by the fact that the last wavenumbers approaching the sound horizon just before decoupling do not see free-streaming neutrinos, and do not experience the full boosting effect already mentioned in the case of massless neutrinos.

Effect of mass splitting

In principle, the depletion in the CMB power spectrum caused by the EISW effect depends on the time at which neutrinos become nonrelativistic, i.e., on individual masses. However, in practice, the mass-splitting effect is too small to be detectable. The difference between the temperature spectrum for the minimal-inverted-hierarchy scenario and for a normal-hierarchy scenario with the same mass (see Section 1.4.1) remains below the level of one per mill for all multipoles, i.e., beyond the sensitivity level of Planck and even of a next generation of CMB satellite. We will see in Section 6.1.4 that the effect of mass splitting on large-scale structure is significantly greater, but still very difficult to observe.

5.3.4 Effects of interacting neutrinos

If neutrinos are not collisionless at temperature $T \ll 1$ MeV because of some kind of nonstandard interaction, all the "direct perturbation effects" described earlier can be modified. For any given interaction between neutrino and other species, or any self-interaction term, the CMB spectrum can be computed with a modified Boltzmann code featuring a coupling term in the hierarchy of Boltzmann equations for neutrinos. This has been studied, for instance, in the case of neutrino interactions with putative extra light degrees of freedom or with dark matter or in the mass-varying neutrino (MaVaN) scenario, in which neutrinos are assumed to be coupled with a scalar field accounting for dark energy. This case will be reported in Section 6.5.3 of the next chapter, because this scenario affects LSS observables but not the CMB (such neutrinos would still be relativistic and have negligible interactions at the epoch of decoupling).

In another simple limiting case, neutrinos would reduce to a perfect or imperfect fluid because of a nonstandard self-interaction term. In this situation, they could be subject to fluid equations with some unknown sound speed c_s relating pressure to density perturbations, and eventually (in the case of an imperfect fluid with shear viscosity) with some unknown viscosity parameter $c_{\rm vis}$ relating the neutrino anisotropic stress σ_ν to the bulk velocity θ_ν. In such models, neutrinos would not

free-stream inside the Hubble radius, and their perturbation evolution would be radically different. The picture presented in Section 5.3.2 and Fig. 5.4 would not hold any more: such neutrinos would not reduce and shift the CMB peaks like ordinary neutrinos. We will not discuss this case in further detail because recent analyses (De Bernardis *et al.*, 2008 or Archidiacono *et al.*, 2011) show that ordinary collisionless neutrinos provide a better fit to the data than such a self-interacting neutrino fluid. More detail on this type of analysis is also presented in Section 6.5.3.

5.4 Bounds on neutrinos from primary cosmic-microwave-background anisotropies

5.4.1 Cosmic microwave background and homogeneous cosmology data sets

The best current constraints on the CMB temperature spectrum for $l \leq 1000$ come from the seven years of observations with the Wilkinson Microwave Anisotropy Probe satellite (WMAP7, Dunkley *et al.*, 2009). Other experiments probe smaller angular scales, with the most recent constraints provided by the 2008 observation campaign of the Atacama Cosmology Telescope (ACT-2008, Dunkley *et al.*, 2011) and by the South Pole Telescope (SPT, Keisler *et al.*, 2011).

The accuracy of parameter extraction from CMB data is usually bounded by instrumental errors at high l's, and by cosmic variance at low l's. These limitations lead to a poor determination of parameter combinations along directions of degeneracies. For instance, we have seen in Section 5.1.6 that the effect (C7), namely the late ISW effect, is difficult to measure accurately because of cosmic variance. Hence, the value of the cosmological constant of the minimal ΛCDM model can only be probed through other effects such as (C1) and (C4) for which Ω_Λ impacts the data in combination with other parameters such as ω_M. In the parameter basis $(\omega_\mathrm{M}, \omega_\mathrm{B}, h, \tau_\mathrm{reion}, A_\mathrm{s}, n_\mathrm{s})$ with $\Omega_\Lambda = 1 - \omega_\mathrm{M}/h^2$, this leads to a degeneracy in the space of reconstructed (ω_M, h) values, and to a poor determination of these two parameters from CMB data alone.

Therefore, it is useful to combine CMB data with an external data set. We leave the discussion of large scale structure observations for the next chapter. We will only discuss in this section the combination of CMB data with probes of homogeneous cosmology, i.e., of the expansion history and geometry of the universe. Currently, the most stringent constraints are derived from

- Direct measurements of the Hubble parameter today, which can be obtained from various techniques. One of them is based on measuring the slope of the luminosity distance–redshift relation of nearby Type Ia supernovae (SNIa) at $z < 0.1$. This technique is identical to the one used to probe the universe's acceleration, but

applied here to objects at smaller redshift. Indeed, the luminosity distance–redshift relation of nearby supernovae depends mainly on H_0, whereas at high redshift it probes also the spatial curvature and acceleration of the universe, as we discussed in Chapter 2. For some of these supernovae, the relation between the absolute magnitude and the time of extinction can be accurately calibrated by resolving cepheids in the same galaxy and measuring the distance independently. Using this method, Riess *et al.* (2009) obtain $H_0 = 74.2 \pm 3.6\,\mathrm{km\,s^{-1}Mpc^{-1}}$ (68% confidence level). This measurement will be referred to hereafter as "H_0".

- Measurements of the angular scale of baryon acoustic oscillations. The origin of baryonic oscillations in the matter power spectrum will be explained in the next chapter, in Section 6.1.2. By measuring only the characteristic angular scale of these oscillations, and comparing them to the scale of acoustic peaks in the CMB, one essentially probes the angular diameter–redshift relation in the redshift range where the matter power spectrum is measured (and not the clustering of matter on large scales, which would fall in the category of LSS data). We will refer to recent constraints on the angular diameter distance at redshifts $z = 0.2$ and $z = 0.35$ by Percival *et al.* (2010) as "BAO". These measurements are useful for constraining the late-time cosmology and resolving degeneracies, e.g., between H_0 and $\omega_{\rm M}$ (they are also sensitive to curvature in non-spatially flat models).
- Measurements of the luminosity distance-redshift relation with distant SNIa, probing simultaneously the Hubble radius and the parameters ruling the expansion law at small redshifts, such as $\Omega_{\rm M} = 1 - \Omega_\Lambda$ in a flat universe, or the cosmological constant and curvature in a more general case. Recent data analyses include Hicken *et al.*, 2009; Kessler, 2009; Conley *et al.*, 2011.

The level of systematic errors in SNIa data sets is still under investigation, although considerable progress is being made in this area. At the moment of writing, CMB+SNIa constraints are very interesting but still treated with care, whereas H_0 and BAO constraints are considered very robust. We will report below several constraints based on the combination of CMB with BAO and H_0 data.

Other techniques are making fast progress. For instance, Moresco *et al.* (2012a) recently used a determination of the Hubble parameter $H(z)$ as a function of redhsift in the range $0.09 < z < 1.75$, based on the observation of the evolution of early-type galaxies, treated as "cosmic chronometers" (Moresco *et al.*, 2012b). We will refer to this data set as "OHD" (standing for Observational Hubble Parameter).

5.4.2 Neutrino abundance

We explained in Section 5.3.2 how the abundance of relativistic relics, given in terms of the effective neutrino number $N_{\rm eff}$, impacts the CMB temperature spectrum. We

saw that varying $N_{\rm eff}$ with fixed $\omega_{\rm M}$ shifts the time of equality between radiation and matter, but because this time is very well constrained by the CMB data through effect (C3) of Section 5.1.6, it is more relevant to study the impact of $N_{\rm eff}$ with fixed $z_{\rm eq}$ rather than fixed $\omega_{\rm M}$. We showed that $N_{\rm eff}$ can be varied together with $\omega_{\rm M}$ and h in such a way as to keep a constant redshift of equality between radiation and matter, and between matter and Λ. This transformation results in a small variation of the CMB for $l \leq 1000$, due to direct perturbation effects, and in a more radical variation for $l > 1000$, due to a change in the diffusion damping scale. This discussion was illustrated by Fig. 5.4, which presents a rather extreme comparison between two models with $N_{\rm eff} = 0$ and $N_{\rm eff} = 3.046$. Small changes on the order of $\Delta N_{\rm eff} \sim 1$ around the standard value $N_{\rm eff} \simeq 3$ lead to much smaller variations than on this figure.

Because the small variation of the temperature spectrum for $l \leq 1000$ can easily be mimicked by a change in the primordial spectrum tilt and amplitude, a CMB experiment precise only in the range $2 < l < 900$ such as WMAP cannot measure $N_{\rm eff}$ accurately alone. Dunkley *et al.* (2009) reported a bound[4] $N_{\rm eff} > 2.7$ at the 95% confidence level (C.L.) using WMAP 5-year data. Interestingly, WMAP alone brings indirect evidence for the existence of the cosmological neutrino background: a model with $N_{\rm eff} = 0$ degrades the effective χ^2 of the data by 8.2 with respect to a model with $N_{\rm eff} = 3$. Of course, it is still possible that the neutrino background predicted by the standard cosmological model is not present, whereas other relativistic relics would account for this nonzero $N_{\rm eff}$. The only way to disprove this assumption would be through a direct measurement of cosmological neutrinos, which is far beyond current technology, as explained in Chapter 7. However, this eventuality appears as unlikely as unnecessarily complicated.

Because varying $N_{\rm eff}$ with a constant $z_{\rm eq}$ affects the diffusion damping scale and the high-l tail of the CMB temperature spectrum, we expect that the inclusion of more CMB data on small angular scales could resolve the degeneracy and tighten bounds on $N_{\rm eff}$. This has been confirmed by data from the ACT and SPT experiments: WMAP7+ ACT-2008 give $N_{\rm eff} = 5.3 \pm 1.3$ (68% C.L.) (Dunkley *et al.*, 2011; Hamann, 2011), whereas WMAP7+SPT give $N_{\rm eff} = 3.85 \pm 0.62$ (68% C.L.) (Keisler *et al.*, 2011). The standard value $N_{\rm eff} = 3.046$ is well inside the 95% C.L. interval.

[4] All the bounds reported in this book are Bayesian credible intervals. They stand for the preferred interval for a given parameter, at a given confidence level, within a given model, with given priors on model parameters (unless otherwise stated, flat priors), after marginalization over all other parameters. Some different bounds inspired by the frequentist approach to data fitting are sometimes discussed in the literature. As a rule of thumb, one should keep in mind that all different definitions of parameter bounds tend to match each other when a parameter is really measured by a given data set, whereas they may differ significantly for parameters that are not *required* by the data and can only be bounded from above or below by the data. In that case the bounds are only valid under some precise assumptions and should be regarded as indicative only.

Because $N_{\rm eff}$ participates in parameter degeneracy together with $\omega_{\rm M}$ and h (along which $z_{\rm eq}$ remains constant, as explained in Section 5.3.2), any external data set bringing information on these other two parameters makes it possible to tighten the bounds on $N_{\rm eff}$. Komatsu *et al.* (2011) found that the combination of WMAP7+BAO+H_0 leads to $N_{\rm eff} = 4.34^{+0.86}_{-0.88}$ (68% C.L.), a result well compatible with the standard value.

Finally, the combination of WMAP7+ACT-2008+BAO+H_0 gives $N_{\rm eff} = 4.56 \pm 0.75$ (68% C.L.), that of WMAP7+SPT+BAO+H_0 gives $N_{\rm eff} = 3.86 \pm 0.42$ (68% C.L.), and WMAP7+SPT+H_0+OHD gives $N_{\rm eff} = 3.5 \pm 0.3$ (68% C.L.). Currently, these are the most stringent bounds on $N_{\rm eff}$ not involving LSS data (and we shall see in Section 6.5.2 that current LSS data do not bring significant improvements for the determination of this particular parameter). They show a marginal preference for extra relativistic degrees of freedom, because the standard value 3.046 sits roughly at the lower end of the 95% C.L. credible interval. However, no robust conclusion can be drawn at the moment. Indeed, this marginal preference for $N_{\rm eff} > 3$ could be due to

- Yet unknown systematic errors in the high-l CMB data sets.
- Underestimated systematic errors in the BAO+H_0 data sets, shifting the results along the valley of degeneracy in $(N_{\rm eff}, \omega_{\rm M}, h)$ space. For instance, if future determinations of H_0 prefer lower values than today (closer to $70\,{\rm km\,s^{-1}Mpc^{-1}}$ or slightly below), the marginal evidence for an excess of radiation will disappear.
- The fact that we are not fitting the correct model to the data, and we are missing the impact of extra physics and parameters. For instance, when the primordial helium fraction is left as a free parameter, there is a degeneracy between $N_{\rm eff}$ and Y_p such that the WMAP7+SPT bound enlarges to $N_{\rm eff} = 3.4 \pm 1.0$ (68% C.L.) (Keisler *et al.*, 2011). However, if the WMAP7+SPT data are not affected by systematics, lowering $N_{\rm eff}$ to 3.046 requires a high helium fraction in slight tension with direct measurement of the helium abundance (Nollett and Holder, 2011), or in strong tension with standard BBN predictions for Y_p, given the allowed range for $\omega_{\rm B}$ indicated by CMB data. Bounds on $N_{\rm eff}$ also become weaker when other degrees of freedom are introduced into the fitted model, such as free neutrino masses, a dark energy component with an arbitrary equation of state instead of a cosmological constant, a spatial curvature, or a significant amount of primordial gravitational waves.

In conclusion, CMB data combined with homogeneous cosmology data are able to establish the existence of a relativistic relic background, with a density compatible to standard predictions for the neutrino background at the 95% C.L. Despite some marginal evidence, there is no reason at the moment to claim an

excess which, if confirmed, could be explained in several different ways, related to neutrino physics (light sterile neutrinos, leptonic asymmetry, nonthermal distorsions due to new particles decaying into neutrinos) or not (other light or massless relics, early dark energy, energy density of a gravitational wave background, modifications to the Friedmann equation due to extensions of Einstein gravity, etc.).

Future CMB experiments will allow a more accurate determination of $N_{\rm eff}$. Using data from the Planck satellite alone (Perotto *et al.*, 2006), the 1σ error bar (equivalent to half of the 68% C.L. allowed range) is expected to shrink down to $\sigma(N_{\rm eff}) \sim 0.46$, without using CMB lensing extraction techniques mentioned in the next chapter. Major progress will be achieved by combining future CMB data with other probes of large-scale structure, as we shall see in Section 6.5.2.

5.4.3 Neutrino masses

We have seen in Section 5.3.3 that CMB experiments can hardly resolve the splitting of the total neutrino mass $M_\nu = \sum_i m_{\nu_i}$ between different families. Most constraints discussed so far in the literature refer to three degenerate neutrinos with mass $m_\nu = M_\nu/3$. The corresponding bounds on M_ν apply in fact to all scenarios with three light neutrinos. We will discuss the case of extra light species separately, together with LSS bounds, in Section 6.5.2. We do not address in this chapter bounds on heavy sterile neutrinos, with masses in the keV range, falling into the category of warm dark matter (WDM). Such relics have no impact on CMB physics, and can only be probed with LSS experiments, as explained in Chapter 6.

For three light degenerate neutrinos, we explained in Section 5.3.3 that if the neutrino mass is increased while $(\omega_{\rm B}, \omega_{\rm C})$ are kept fixed and h is decreased to keep the peak scale constant, then the CMB temperature spectrum varies by a very small amount, with the most pronounced effects being on angular scales $l < 20$ (LISW effect) and $20 < l < 500$ (EISW effect). This discussion was illustrated by Fig. 5.6.

WMAP data alone can constrain the total neutrino mass, with an upper bound $M_\nu < 1.3$ eV (95% C.L.) for the minimal ΛCDM model with massive neutrinos (seven free parameters). Because the leading effects appear for $l < 500$, adding small-scale CMB data from ACT-2008 or SPT does not bring about significant improvements.

However, this transformation (corresponding to a direction of degeneracy in parameter space) requires h to decrease when M_ν increases, in order to keep a constant peak scale. Any additional constraint on h does help reduce this degeneracy. Indeed, the bound from WMAP7+BAO+H_0 is significantly stronger: $M_\nu < 0.58$ eV

(95% C.L.), whereas the combination WMAP7+OHD+H_0 gives[5] $M_\nu < 0.48$ eV (95% C.L.).

These mass bounds appear to be very robust from the point of view of the data being used. However, as usual, they can be relaxed by introducing other physical ingredients and free parameters into the model. One parameter known to be slightly degenerate with M_ν is the number of light/massless species $N_{\rm eff}$. Hence mass bounds must be investigated separately when allowing for the presence of extra massless or light relics. The same is true with other ingredients such as an arbitrary dark energy equation of state, a spatial curvature, or a significant amount of primordial gravitational waves. All these cases have been considered, but in combination with LSS data, so we will report the corresponding mass bounds in Chapter 6.

The expected sensitivity of the Planck satellite alone to neutrino masses is $\sigma(M_\nu) \sim 0.2$ eV for a minimal model with seven parameters, not using CMB lensing extraction techniques mentioned in the next chapter. Much better bounds can be obtained using CMB lensing extraction and other LSS observations, as we shall see in Section 6.5.1.

[5] Here we assume that for this particular data set, the 95% C.L. bound is equal to twice the 68% C.L. bound, which seems to be the case, judging from Fig. 8 of Moresco *et al.*, 2012a.

6

Recent times: neutrinos and structure formation

There are several ways to observe the large-scale structure of our universe on different scales and redshifts. This structure is even more sensitive to the neutrino abundance, mass spectrum and properties than CMB anisotropies, and offers several opportunities to measure neutrino parameters. If the universe can be described by general relativity and does not feature significant dark energy perturbations, all observables related to large-scale structure can be inferred from the matter power spectrum $P(\eta, k)$ defined through

$$\langle \delta_{\rm M}(\eta, \vec{k}) \delta^*_{\rm M}(\eta, \vec{k}') \rangle = P(\eta, k)\, \delta^{(3)}(\vec{k} - \vec{k}'). \tag{6.1}$$

Here $\delta_{\rm M}$ is the relative density perturbation of nonrelativistic matter components. In a ΛCDM universe with CDM, baryons and nonrelativistic neutrinos, $\delta_{\rm M}$ can be decomposed as

$$\delta_{\rm M} = \delta\rho_{\rm M}/\bar{\rho}_{\rm M} = \left(\sum_{i={\rm B,C},\nu} \bar{\rho}_i \delta_i \right) \Big/ \left(\sum_{i={\rm B,C},\nu} \bar{\rho}_i \right). \tag{6.2}$$

In this chapter, for simplicity, we will often use the same letter to denote a function of conformal time η, or of the corresponding redshift z, or finally of the corresponding scale factor a. For instance, we will write indifferently $P(\eta, k)$, $P(z, k)$ or $P(a, k)$.

As we shall see in Section 6.4, galaxy or cluster redshift surveys probe $P(\eta, k)$ modulo a light-to-mass bias factor (or function). Instead, observations of weak lensing and of the late integrated Sachs–Wolfe contribution to the CMB probe the power spectrum of metric fluctuations, on scales smaller than the Hubble radius. The latter can be related to $P(\eta, k)$ using the Poisson equation

$$k^2\phi = k^2\psi = -4\pi G a^2 \bar{\rho}_{\rm M} \delta_{\rm M} \tag{6.3}$$

(during matter and Λ domination, we can ignore the photon and neutrino anisotropic stresses, implying $\phi = \psi$, and in the gravitational source term $\sum_i \bar{\rho}_i \delta_i$ we can

ignore the subdominant contribution of relativistic species). Finally, Lyman-α observations probe the one-dimensional matter power spectrum, related to the three-dimensional one by a simple convolution.

Because the matter power spectrum is so crucial, we will devote the first two sections of this chapter to the computation and parameter dependence of $P(\eta, k)$. Fluctuations on a sufficiently large scale and/or at sufficiently large redshift can be described by linear theory. Observations of $P(\eta, k)$ in the linear regime store a maximum amount of information concerning cosmological parameters, and are less affected by theoretical errors, bias and non-gaussianity issues. Section 6.1 will be entirely devoted to the properties of the linear matter power spectrum, and in particular to the impact of neutrinos on this quantity. However, it is also important to compute neutrino effects on the nonlinear power spectrum, either because some observational methods probe only the mildly nonlinear regime, or in order to increase the amount of information extracted from a given data set covering both linear and nonlinear scales, or finally because some specific neutrino effects show up only in the nonlinear region (for instance, for heavy sterile neutrinos). We will review nonlinear issues in Section 6.2. Then we will come back to CMB fluctuations, and explain in Section 6.3 how secondary anisotropies are influenced by neutrino properties at small redshift. We will give a brief summary of current and future techniques for measuring the matter power spectrum in Section 6.4. Finally, we will present observational constraints on neutrino parameters in Section 6.5.

6.1 Linear matter power spectrum

The computation of the linear matter power spectrum is as subtle as that of the CMB temperature spectrum. In this section, we will review this topic in a simple and qualitative way, insisting on the physical issues that are important for understanding the possible impact of neutrinos on $P(\eta, k)$.

Because the matter power spectrum of a ΛCDM model (with eventually relativistic or nonrelativistic neutrinos) depends on the evolution of the three density fluctuations $\delta_{\rm C}$, $\delta_{\rm B}$, δ_ν, the relative abundances of the underlying components are important. They can be parameterized by the CDM, baryon and neutrino fractions

$$f_{\rm C} \equiv \frac{\bar\rho_{\rm C}}{\bar\rho_{\rm C}+\bar\rho_{\rm B}+\bar\rho_\nu}, \quad f_{\rm B} \equiv \frac{\bar\rho_{\rm B}}{\bar\rho_{\rm C}+\bar\rho_{\rm B}+\bar\rho_\nu}, \quad f_\nu \equiv \frac{\bar\rho_\nu}{\bar\rho_{\rm C}+\bar\rho_{\rm B}+\bar\rho_\nu} \tag{6.4}$$

subject to $f_{\rm C}+f_{\rm B}+f_\nu = 1$. Because CDM and baryons are nonrelativistic during the CMB and structure formation epochs, $f_{\rm B}/f_{\rm C}$ can always be regarded as constant. The neutrino fraction f_ν becomes asymptotically constant after the nonrelativistic

transition of neutrino species. If one neutrino species is much heavier than the others, f_ν becomes roughly constant as soon as this species becomes nonrelativistic, because lighter species represent a negligible fraction of f_ν. If several species have masses of the same order of magnitude, f_ν can have a nontrivial evolution with various steps before reaching its constant asymptote.

To introduce technical difficulties one after another, we will first summarize in Section 6.1.1 the properties of the matter power spectrum in a universe containing no neutrinos ($f_\nu = 0$) and a negligible baryon fraction ($f_\mathrm{B} \ll 1$). In this limit, CDM does not experience gravitational feedback from baryons and neutrinos, and simple solutions can be derived. We will then discuss the impact of baryons in Section 6.1.2, of relativistic relics such as massless neutrinos in Section 6.1.3, of hot dark matter such as light neutrinos in Section 6.1.4, and of warm dark matter such as heavy sterile neutrinos in Section 6.1.5.

6.1.1 Neutrinoless universe with cold dark matter

Equation of evolution for cold dark matter

Baryons always play a crucial role in the dynamics of the tightly coupled photon–baryon fluid, but if $f_\mathrm{B} \ll f_\mathrm{C}$, they play a negligible role with respect to CDM for linear structure formation. In a neutrinoless universe, the only significant contribution to the matter power spectrum then comes from CDM perturbations, so we only need to follow the evolution of $\delta_\mathrm{C}(\eta, k)$. On super-Hubble scales and for adiabatic initial conditions, we know from Eqs. (5.24), (5.41) and (5.44) that δ_C is constant and related to metric fluctuations through

$$\delta_\mathrm{C}(\eta, k) = -\frac{3}{2}\phi(\eta, k) = -\frac{3}{2}\psi(\eta, k) = -1 \quad (\eta < \eta_\mathrm{eq}) \tag{6.5}$$

$$\delta_\mathrm{C}(\eta, k) = -2\phi(\eta, k) = -2\psi(\eta, k) = -\frac{6}{5} \quad (\eta > \eta_\mathrm{eq}) \tag{6.6}$$

(these relations apply to transfer functions normalized to $\mathcal{R}(\eta_\mathrm{ini}, \vec{k}) = 1$, as explained in Section 5.1.4). On sub-Hubble scales, we expect δ_C to grow because of gravitational collapse. The growth rate could potentially depend on

- The expansion rate: faster expansion implies less efficient gravitational interactions, because all physical distances between two bodies increase with the scale factor. In typical equations of evolution, this effect is accounted by a "Hubble friction" term.
- Gravitational interactions with other species (in the present case, only with photons, because we assumed baryons to be negligible in terms of density and gravitational back-reaction, and neutrinos to be absent).

The equation of evolution for $\delta_{\rm C}$ is obtained by combining the continuity and Euler equations (5.19) into

$$\delta_{\rm C}{}'' + \frac{a'}{a}\delta_{\rm C}{}' = -k^2\psi + 3\phi'' + 3\frac{a'}{a}\phi'. \tag{6.7}$$

The second term on the left-hand side accounts for Hubble friction. The first term on the right-hand side represents the gravitational attraction force (generated by CDM itself and all other species if relevant), whereas the next two terms are related to dilation, i.e., to local variations of the expansion rate.

Modes crossing the Hubble scale during matter domination

Equation (6.7) is easy to solve after the time of equality between matter and radiation. First, we notice that only collisionless relativistic particles (only decoupled photons in a neutrinoless universe) can contribute to the total anisotropic stress σ. Because the density of photons is subdominant after radiation-to-matter equality, anisotropic stress can be neglected, and the Einstein equation (5.22) implies $\phi = \psi$. Next, because cold dark matter is a pressureless self-gravitating fluid in this regime, it will not experience acoustic oscillations, and both $\delta_{\rm C}$ and ϕ must be smooth over a Hubble time scale, rather than oscillating with a pulsation of order k. So the time derivatives of ϕ on the right-hand side should be negligible with respect to $k^2\psi = k^2\phi$. The latter quantity is given inside the Hubble radius by the Poisson equation (5.21)

$$k^2\phi = k^2\psi = -4\pi G a^2 \bar{\rho}_{\rm C}\delta_{\rm C}. \tag{6.8}$$

Finally, the equation of evolution for CDM inside the Hubble radius and after equality can be approximated as

$$\delta_{\rm C}{}'' + \frac{a'}{a}\delta_{\rm C}{}' - 4\pi G a^2 \bar{\rho}_{\rm C}\delta_{\rm C} = 0. \tag{6.9}$$

During matter domination, the scale factor evolves like $a \propto \eta^2$ and the Friedmann equation gives

$$4\pi G a^2 \bar{\rho}_{\rm C} \simeq 4\pi G a^2 \bar{\rho}_{\rm tot} = \frac{3}{2}\left(\frac{a'}{a}\right)^2. \tag{6.10}$$

Then equation (6.9) becomes

$$\delta_{\rm C}{}'' + \frac{2}{\eta}\delta_{\rm C}{}' - \frac{6}{\eta^2}\delta_{\rm C} = 0 \tag{6.11}$$

and has two trivial solutions. The growing mode, $\delta_{\rm C} \propto \eta^2 \propto a$, gives the famous growth rate of structures during matter domination in the linear regime. During Λ domination, one should replace (a'/a) using the Friedmann law in the presence of

both $\bar{\rho}_{\rm C}$ and $\bar{\rho}_\Lambda$. The solution is a hypergeometric function and is the same for each k modulo an arbitrary constant of integration, because the equation of evolution is k-independent. We will not write this solution explicitly but will incorporate it into a function $g(a;\Omega_{\rm M})$ defined as

$$g(a;\Omega_{\rm M}) = \frac{a_{\rm M}\,\delta_{\rm C}(a,k)}{a\,\delta_{\rm C}(a_{\rm M},k)}, \tag{6.12}$$

where $a_{\rm M}$ is the scale factor at some arbitrary time deep inside the matter-dominated regime, when $\delta_{\rm C} \propto a$. This definition is convenient because it allows us to write the growing mode for $\delta_{\rm C}$ as

$$\delta_{\rm C}(a,k) \propto a\,g(a;\Omega_{\rm M}) \tag{6.13}$$

during both matter and Λ domination, with $g(a;\Omega_{\rm M}) = 1$ deep inside the matter-dominated regime. Hence g stands for the correction to the linear growth factor of $\delta_{\rm C}$ induced by the cosmological constant. By enhancing the universe's expansion and the Hubble friction term, Λ tends to slow down structure formation; hence g decreases monotonically from one to zero. A simple approximation for g today (Kofman *et al.*, 1993) reads

$$g(a_0;\Omega_{\rm M}) \simeq (\Omega_{\rm M})^{0.2}/\left[1 + 0.003(\Omega_\Lambda/\Omega_{\rm M})^{4/3}\right] \tag{6.14}$$

with $\Omega_\Lambda = 1 - \Omega_{\rm M}$, because we restrict the discussion to a spatially flat universe.

For modes crossing the Hubble scale during matter domination, it is easy to match the super-Hubble solution of Eq. (6.6) to this sub-Hubble solution. This can be done either by solving Eqs. (5.20) and (6.7) simultaneously during matter domination, or even more simply by using the Einstein equation $\delta G^i_i = \delta T^i_i$:

$$\left(2\frac{a''}{a} - \left(\frac{a'}{a}\right)^2\right)\psi + \frac{k^2}{3}(\phi - \psi) + \phi'' + \frac{a'}{a}(\psi' + 2\phi') = 4\pi G a^2\,\delta p. \tag{6.15}$$

Deep inside the matter-dominated era, this equation simplifies considerably, because

- With a negligible contribution of relativistic species and of Λ to the Friedmann equation, the scale factor evolves as $a \propto \eta^2$, and the factor in front of ψ vanishes.
- Because the density of photons is subdominant, anisotropic stress can be neglected during matter domination, and the Einstein equation (5.22) implies $\phi = \psi$. Hence the second term in Eq. (6.15) can be neglected.
- Similarly, the total pressure term on the right-hand side of Eq. (6.15) receives only contributions from relativistic particles (photons in a neutrinoless universe), which are subdominant during the matter era: at leading order we can neglect this term also.

Hence, to a first approximation, the equation governing the evolution of $\phi = \psi$ during the matter era is

$$\phi'' + \frac{6}{\eta}\phi' = 0. \tag{6.16}$$

The solutions are combinations of a constant mode and of a decaying mode $\phi \propto \eta^{-5}$. After equality, the decaying mode quickly becomes negligible, and metric fluctuations are constant in time on all scales. It is always surprising to see that when structures form, the gravitational potential is constant even inside the Hubble radius. This results from a cancellation between the effects of gravitational clustering and of cosmological expansion during matter domination.

We can now come back to Eq. (6.7) with a constant source term on the right-hand side, and write the most general solution,

$$\delta_{\rm C} = D_{\rm C}^g + \frac{D_{\rm C}^d}{\eta} - \frac{k^2\eta^2}{6}\psi, \tag{6.17}$$

where $D_{\rm C}^g$ and $D_{\rm C}^d$ are two constants of integration depending on $\vec{k}$. These constants can be found explicitly by matching with the super-Hubble limit given in Eq. (6.6). Neglecting the decaying mode proportional to $D_{\rm C}^d$, we find that the result for the transfer function of CDM perturbations reads

$$\delta_{\rm C}(\eta, k) = -\frac{6}{5} - \frac{k^2\eta^2}{10}. \tag{6.18}$$

If we want an expression depending on a rather than η, we can use the two relations

$$k^2\eta^2 = \frac{4k^2}{a^2H^2} \quad \text{and} \quad \frac{H^2}{H_0^2} = \Omega_{\rm M}\left(\frac{a}{a_0}\right)^{-3}, \tag{6.19}$$

both valid during matter domination, even if they involve $\Omega_{\rm M}$, the fractional matter density today, and H_0, the Hubble rate today. In combination with Eq. (6.18), these relations give

$$\delta_{\rm C}(a, k) = -\frac{6}{5} - \frac{2}{5}\,\Omega_{\rm M}^{-1}\frac{k^2}{a_0^2H_0^2}\cdot\frac{a}{a_0} \tag{6.20}$$

during matter domination. Finally, a matching with the solution $a\,g(a;\Omega_{\rm M})$ valid during both matter and Λ domination shows that the CDM transfer function reads

$$\delta_{\rm C}(a, k) = -\frac{6}{5} - \frac{2}{5}\,\Omega_{\rm M}^{-1}\frac{k^2}{a_0^2H_0^2}\cdot\frac{a\,g(a;\Omega_{\rm M})}{a_0} \tag{6.21}$$

at any time between equality and today, and for any wavenumber k crossing the Hubble scale during matter domination. The square of this transfer function multiplied by the primordial spectrum (defined in Section 5.1.4) gives the matter power spectrum for all modes $k < k_{\rm eq}$ with

$$k_{\rm eq} \equiv a_{\rm eq} H_{\rm eq}. \tag{6.22}$$

Moreover, we can only measure the matter power spectrum on scales that are sub-Hubble today, so we can assume $k \gg a_0 H_0$ and neglect the constant term in Eq. (6.21). Finally, the large-wavelength branch of the power spectrum is

$$\begin{aligned} P(a,k) &= \delta_{\rm C}(a,k)^2 P_{\mathcal{R}}(k) \qquad (6.23)\\ &= \frac{2\pi^2}{k^3}\left(\frac{2}{5}\,\Omega_{\rm M}^{-1}\frac{k^2}{a_0^2 H_0^2}\cdot\frac{a\,g(a;\Omega_{\rm M})}{a_0}\right)^2 \mathcal{P}_{\mathcal{R}}(k)\,, \qquad (a_0 H_0 < k < k_{\rm eq}). \end{aligned}$$

Modes crossing the Hubble scale during radiation domination

We have achieved only half of the task of this section: we have not yet discussed the evolution of scales crossing the Hubble radius during radiation domination. This involves subtle issues related to the way to treat Eq. (6.7) for $\eta \leq \eta_{\rm eq}$. One could assume naively that because CDM does not dominate the expansion during radiation domination, the Poisson equation

$$k^2\psi = -4\pi G a^2\left(\bar\rho_\gamma\delta_\gamma + \bar\rho_{\rm C}\delta_{\rm C}\right) \tag{6.24}$$

can be simplified by neglecting the CDM contribution. In that case, ψ could be inferred from the oscillatory evolution of the self-gravitating photon fluid, and could be plugged into the right-hand side of Eq. (6.7) as an external source term. This approach is, however, incorrect. CDM fluctuations can be neglected in the Poisson equation only as long as

$$\left|\frac{\delta_{\rm C}}{\delta_\gamma}\right| < \frac{\bar\rho_\gamma}{\bar\rho_{\rm C}} = \frac{a_{\rm eq}}{a}. \tag{6.25}$$

The term on the right-hand side of this inequality is greater than one during radiation domination but decreases with expansion. The term on the left-hand side starts from (3/4) on super-Hubble scales (see Eq. (5.24)), and grows on sub-Hubble scales, because CDM is pressureless and experiences gravitational clustering (we will see later at what rate this growth takes place). Hence, inevitably, the CDM contribution to the Poisson equation becomes dominant well inside the Hubble radius. In this regime, it is the CDM component rather than the relativistic one that behaves like a self-gravitating fluid. Tightly coupled photons actually decouple from gravity in this limit: we have already seen in Section 5.1.5 that pressure forces take over from gravitational forces in the photon equation of evolution (5.38). Hence, deep inside

the Hubble scale and during radiation domination, CDM is already governed by the same equation as during matter domination, namely Eq. (6.9).

The most subtle issue consists of solving the CDM equation of motion just after Hubble crossing, when both photons and CDM are contributing to the Poisson equation. The literature offers various analytic approaches for studying this regime. It is possible to solve the coupled equations of motion simultaneously for tightly coupled photons and CDM perturbations. After a few approximations, one is led to analytic solutions of a rather complicated form (involving the cosine integral). A much simpler approach has been used since the work of Mészáros (1974), although Weinberg (2002) was the first to establish it on firm mathematical ground. Weinberg pointed out that the solution of the full system describing the evolution of $(\delta_\gamma, \delta_{\rm C}, \phi, \psi)$ can be decomposed into fast modes (oscillating with a pulsation on the order of k or $kc_{\rm s}$) and slow modes (only evolving over a Hubble time scale). Power counting arguments show that for fast modes, $\delta_{\rm C}$ is always subdominant in the Poisson equation, whereas for slow modes, it is δ_γ that is subdominant.[1] This nontrivial result implies that fast modes can be inferred from the photon equation of motion and Einstein equations with $\delta_{\rm C}$ set to zero, and vice-versa for slow modes. In other words, the gravitational back reaction of one species on the other species can be neglected. At the end of the calculation, the full solution for metric fluctuations is given by the sum of all modes, i.e., by the superposition of damped acoustic oscillations with zero mean value (for fast modes) and a smooth function shifting the zero-point of the oscillations (for slow modes), accounting for CDM gravitational clustering.

As long as we are interested in the CDM evolution, we need to bother only about slow modes, and we can employ the very same equation as in other regimes, namely Eq. (6.9). This equation can be combined with the Friedmann equation sourced by the sum of $\bar\rho_{\rm R} = \bar\rho_\gamma$ and $\bar\rho_{\rm M} = \bar\rho_{\rm C}$,

$$\left(\frac{a'}{a}\right)^2 = \frac{8\pi G}{3} a^2(\bar\rho_{\rm M} + \bar\rho_{\rm R}). \tag{6.26}$$

After introducing the parameterization

$$\bar\rho_{\rm M} = \bar\rho_{\rm eq}(a/a_{\rm eq})^{-3}, \qquad \bar\rho_{\rm R} = \bar\rho_{\rm eq}(a/a_{\rm eq})^{-4}, \qquad y \equiv a/a_{\rm eq} \tag{6.27}$$

and changing variables from η to y, one obtains a simple second-order equation for $\delta_{\rm C}$ involving only y, called the Mészáros equation,

$$y(1+y)\frac{d^2\delta_{\rm C}}{dy^2} + \left(1 + \frac{3y}{2}\right)\frac{d\delta_{\rm C}}{dy} - \frac{3}{2}\delta_{\rm C} = 0, \tag{6.28}$$

[1] The proof presented in Weinberg (2002) applies to equations in the synchronous gauge, but on sub-Hubble scales the synchronous and Newtonian gauges lead to the same equations and solutions.

with two exact analytical solutions first derived by (Mészáros, 1974; Groth and Peebles, 1975; see also Weinberg, 2008), which we do not write here for conciseness. It is sufficient for the rest of the discussion to admit that the fastest-growing solution is proportional to $\ln(y)$ deep inside radiation domination, and to y deep inside matter domination. During radiation domination, the transfer function $\delta_{\rm C}(a,k)$ properly normalized to adiabatic initial conditions has a sub-Hubble limit

$$\delta_{\rm C}(a,k) \longrightarrow \alpha + \beta \ln\left(\frac{k}{aH}\right) \qquad (\eta \ll \eta_{\rm eq}, k \gg aH), \tag{6.29}$$

where α and β are two numerical coefficients independent of k. We see that CDM clusters much more slowly during radiation domination than during matter domination (because $\delta_{\rm C}$ grows logarithmically rather than linearly with the scale factor), as a consequence of the different expansion law. This is a key result for understanding structure formation. In total, for a qualitative understanding of the matter power spectrum, it is sufficient to approximate the growth of CDM perturbations during radiation domination with Eq. (6.29) evaluated at the time of equality, i.e., when $aH = a_{\rm eq}H_{\rm eq} \equiv k_{\rm eq}$, and to perform a crude matching with the sub-Hubble solution during matter and Λ domination, i.e., with the second term in Eq. (6.21). This means that during the matter- and Λ-dominated stages, the CDM transfer function is

$$\delta_{\rm C}(a,k) = \big(\alpha + \beta \ln(k/k_{\rm eq})\big)\, \frac{a\, g(a;\Omega_{\rm M})}{a_{\rm eq}}. \tag{6.30}$$

To homogenize this result with its counterpart of Eq. (6.23) for modes $k < k_{\rm eq}$, we notice that at equality

$$\frac{H_{\rm eq}^2}{H_0^2} = \Omega_{\rm R}(a_0/a_{\rm eq})^4 + \Omega_{\rm M}(a_0/a_{\rm eq})^3 = 2\Omega_{\rm M}(a_0/a_{\rm eq})^3, \tag{6.31}$$

from which we infer

$$\frac{a}{a_{\rm eq}} = \frac{a\, a_{\rm eq}^2 H_{\rm eq}^2}{2\Omega_{\rm M} a_0^3 H_0^2} = \frac{a\, k_{\rm eq}^2}{2\Omega_{\rm M} a_0^3 H_0^2}. \tag{6.32}$$

Finally, following the same steps as in Eq. (6.23), the matter power spectrum of modes crossing the Hubble scale during radiation domination is

$$P(a,k) = \frac{2\pi^2}{k^3}\left(\frac{1}{2}\Omega_{\rm M}^{-1}\frac{k_{\rm eq}^2}{a_0^2 H_0^2}\cdot\frac{a\, g(a;\Omega_{\rm M})}{a_0}\left[\alpha + \beta\ln\left(\frac{k}{k_{\rm eq}}\right)\right]\right)^2 \mathcal{P}_{\mathcal{R}}(k). \tag{6.33}$$

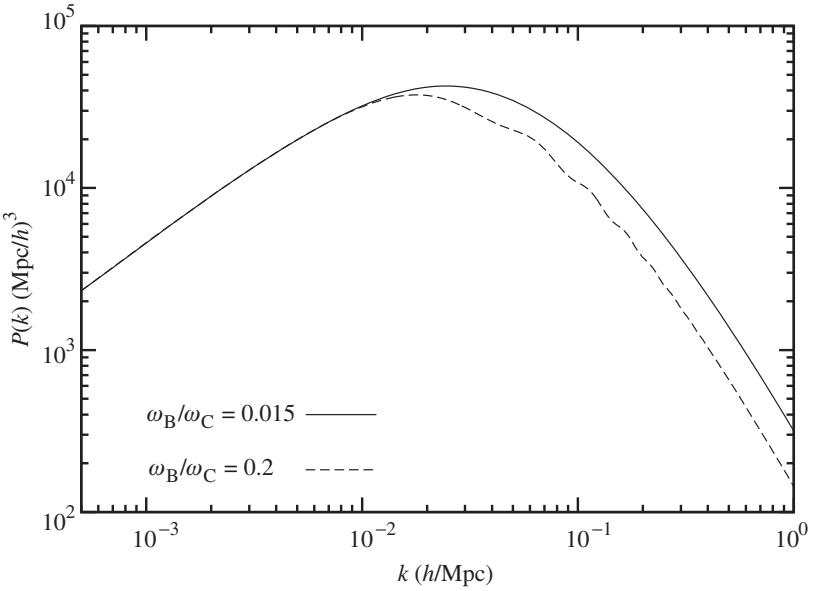

Figure 6.1 Matter power spectrum for two neutrinoless ΛCDM models with the same primordial spectrum and Ω_M, but different baryon-to-CDM ratios ω_B/ω_C. The difference between the two curves clearly shows the baryon effects described in the text (suppression of power for $k \geq k_{eq}$ and imprint of small acoustic oscillations).

Matter power spectrum in practical units

In summary, the two asymptotes of the matter power spectrum (6.23, 6.33) read

$$P(a,k) = \left(\frac{a\, g(a;\Omega_M)}{a_0}\right)^2 \frac{k\,\mathcal{P}_\mathcal{R}(k)}{\left(\Omega_M a_0^2 H_0^2\right)^2} \times \begin{cases} \frac{8\pi^2}{25} & (a_0 H_0 < k < k_{eq}) \\ \frac{k_{eq}^4}{2k^4}\left(\alpha + \beta \ln\left(\frac{k}{k_{eq}}\right)\right)^2 & (k > k_{eq}). \end{cases} \tag{6.34}$$

For a scale-invariant power spectrum (a constant $\mathcal{P}_\mathcal{R}$), the matter power spectrum scales like k on large scales, and like $k^{-3}\ln(k)^2$ on small scales. This behavior is indeed well reproduced by numerical results (see for instance Fig. 6.1, where the upper curve corresponds to a neutrinoless ΛCDM model with negligible baryon fraction). An analytic approximation to the matter power spectrum in the intermediate range $k \sim k_{eq}$ can be obtained from the full solution of the Mészáros equation (see, e.g., Weinberg, 2008). Accurate fits to the numerical results have also been derived by Eisenstein and Hu, 1998. The fact that the spectrum of a ΛCDM model with negligible baryon fraction is smooth instead of keeping track of acoustic oscillations is counterintuitive; it is a consequence of the absence of efficient

gravitational back reaction of photons over CDM during radiation domination, as already explained after Eq. (6.25).

The matter power spectrum is usually expressed as a function of k in units of h/Mpc. It is worth coming back on this choice. Although comoving wavenumbers do not represent physical quantities, the ratio a_0/k is a physical distance that can be expressed in units of megaparsecs (because $2\pi a_0/k$ is the current wavelength of the comoving Fourier mode k). However, the evolution of cosmological perturbations inside the Hubble radius depends primarily on how far inside the Hubble radius is a given Fourier mode, i.e., on the dimensionless ratio $k/(aH)$. Hence it is useful to plot the power spectrum as a function of the dimensionless number $k/(a_0H_0)$. A different choice for the value of H_0 will then leave the overall shape of the power spectrum $P(a, k/(a_0H_0))$ invariant (if all other relevant characteristic times or scales do not change simultaneously). However, by definition of the reduced Hubble parameter and in units such that $c = 1$, we have $H_0 = h/3000$ Mpc^{-1}. Hence

$$\frac{k}{a_0H_0} = 3000 \left[\frac{k/a_0}{1\,h\,\mathrm{Mpc}^{-1}}\right]. \tag{6.35}$$

Thus it is equivalent to plot the spectrum as a function of $k/(a_0H_0)$ or of

$$\tilde{k} \equiv \left[\frac{k/a_0}{1\,h\,\mathrm{Mpc}^{-1}}\right]. \tag{6.36}$$

Because astrophysicists often use the implicit assumption that $a_0 = 1$ in plots involving comoving wavenumbers, the matter power spectrum is usually displayed as a function of k in units of h/Mpc along the horizontal axis, i.e., as a function of $\tilde{k}$. We must reexpress our results for P as a function of $\tilde{k}$ if we want to comply with standard conventions and remove a trivial dependency on H_0.

The same discussion holds for the units of the power spectrum itself. In Eq. (6.34), the quantities k^{-1} and (a_0H_0) are comoving scales. Other quantities such as Ω_M, (a/a_0), $g(a;\Omega_\mathrm{M})$ or $\mathcal{P}_\mathcal{R}$ are dimensionless. So P represents a cube comoving scale, and a_0^3P has the dimension of the cube of physical length. The quantity left invariant by a change of H_0 is then the ratio of a_0^3P to the cube of the Hubble radius today, i.e., the dimensionless number $a_0^3H_0^3P$. Because

$$a_0^3H_0^3P = 3000^{-3}\left[\frac{a_0^3P}{1\,h^{-3}\mathrm{Mpc}^3}\right], \tag{6.37}$$

plotting $a_0^3H_0^3P$ is equivalent to plotting

$$\tilde{P} \equiv \left[\frac{a_0^3P}{1\,h^{-3}\mathrm{Mpc}^3}\right]. \tag{6.38}$$

This explains why plots usually show P in units of $h^{-3}\mathrm{Mpc}^3$, with an implicit assumption that $a_0 = 1$. The expression for $\tilde{P}$ as a function of $\tilde{k}$ can easily be obtained from Eq. (6.34):

$$\tilde{P}(a,\tilde{k}) = \mathcal{N}\left(\frac{a\,g(a;\Omega_\mathrm{M})}{a_0\,\Omega_\mathrm{M}}\right)^2 \tilde{k}\,\mathcal{P}_\mathcal{R}(\tilde{k}) \times \begin{cases} \frac{8\pi^2}{25} & (\tilde{k} < \tilde{k}_\mathrm{eq}) \\ \frac{\tilde{k}_\mathrm{eq}^4}{2\tilde{k}^4}\left(\alpha + \beta \ln\left(\frac{\tilde{k}}{\tilde{k}_\mathrm{eq}}\right)\right)^2 & (\tilde{k} > \tilde{k}_\mathrm{eq}) \end{cases} \tag{6.39}$$

with

$$\mathcal{N} \equiv \left(\frac{1\,h\,\mathrm{Mpc}^{-1}}{H_0}\right)^4 = 3000^4. \tag{6.40}$$

As expected, the rescaled power spectrum does not depend explicitly on the value of H_0. Apart from the primordial power spectrum, it actually depends on only two free parameters: Ω_M and $\tilde{k}_\mathrm{eq}$ (we recall that α and β are uniquely fixed by the solution of the Mészáros equation with adiabatic initial conditions). Indeed, Ω_M (equal to $(1 - \Omega_\Lambda)$) governs the time of equality between matter and Λ, and the amount of perturbation damping during Λ domination, encoded in $g(a;\Omega_\mathrm{M})$, whereas $\tilde{k}_\mathrm{eq}$ defines the scale of the transition between the two asymptotes, or in other words the scale of the peak in the matter power spectrum. The Ω_M factor in the denominator just comes from the fact that we expressed the power spectrum as a function of a/a_0 rather than conformal time, and the coefficient of proportionality between a/a_0 and η^2 during matter domination depends on the matter density in the universe, i.e., on $\Omega_\mathrm{M} H_0^2$ (as can be checked from Eq. (6.19)).

6.1.2 Neutrinoless universe with cold dark matter and baryons

Because current observations favour a value of the baryon fraction close to $f_\mathrm{B} \sim 0.2$, the results of the previous section do not provide a realistic description of linear structures in the universe. Let us follow the same steps as in Section 6.1.1 and identify the changes brought about by the presence of baryons.

Baryon drag epoch

An important characteristic time for structure formation is that of baryon decoupling, which does not coincide exactly with that of photon decoupling. In Section 5.1.6, we defined the photon decoupling time η_LS as the maximum of the photon visibility function, i.e., the most likely time for the last scattering of photons. To understand structure formation, we should compute the time at which baryons are effectively released by the photons and start to cluster like free-falling

nonrelativistic particles. The baryon interaction term on the r.h.s. of Eq. (5.17) (often called the baryon drag term, because it describes how baryons tend to drag photons towards gravitational potential wells) corresponds to an interaction rate $R^{-1}an_e\sigma_{\rm T}$, from which we can define the drag depth (see, e.g., Hu and Sugiyama, 1996),

$$\tau_{\rm dr}(\eta) \equiv \int_{\eta}^{\eta_0} d\eta\, R^{-1}an_e\sigma_{\rm T}. \tag{6.41}$$

The drag depth is similar to the photon optical depth of Eq. (5.54) with an additional R^{-1} factor. It goes from infinity in the tightly coupled limit to zero in the decoupled limit. The characteristic time $\eta_{\rm dr}$ at which baryon drag stops being efficient, defined through $\tau_{\rm dr}(\eta_{\rm dr}) = 1$, is usually called the baryon drag time (a slightly misleading terminology, because it marks the end of drag effects). Because in realistic models recombination takes place at the beginning of matter domination with $R = 3\bar{\rho}_{\rm B}/4\bar{\rho}_\gamma < 1$, the release of baryons takes place soon after photon decoupling (in terms of redshifts, $z_{\rm dr} < z_{\rm LS}$). We mentioned in Section 5.1.6 that the value $z_{\rm LS}$, fixed by the recombination history, has a very mild dependence on the few parameters affecting the free electron fraction evolution $n_e(z)$, such as $\omega_{\rm B}$, the primordial helium fraction $Y_{\rm P}$, and eventually $N_{\rm eff}$. For realistic parameter values, $z_{\rm LS}$ varies by such small amounts that it can usually be considered a fixed number. Instead $z_{\rm dr}$ has a strong dependence on $\omega_{\rm B}$ due to the factor R appearing in the definition of $\tau_{\rm dr}$. Baryons are released earlier if the baryon density is increased.

We have seen in Section 5.1.5 that in the tight-coupling regime $\eta \ll \eta_{\rm dr}$, baryons track photons with $\delta_{\rm B} = \frac{3}{4}\delta_\gamma$. At recombination and until $\eta_{\rm dr}$, baryon fluctuations on scales smaller than the photon and baryon mean free paths are erased by diffusion effects. This mechanism is called Silk damping (Silk, 1968). After the baryon drag epoch, baryon fluctuations evolve according to the same equation as any other colisionless species, identical to Eq. (6.7) for CDM:

$$\delta_{\rm B}{}'' + \frac{a'}{a}\delta_{\rm B}{}' = -k^2\psi + 3\phi'' + 3\frac{a'}{a}\phi'. \tag{6.42}$$

Modes crossing the Hubble scale after the baryon drag epoch

As in Section 6.1.1, we first discuss the evolution of perturbations on large scales – more precisely, on comoving scales crossing the Hubble radius after the baryon drag epoch. For such modes, the CDM and baryon density perturbations are equal to each other at any time, because they start from the same initial conditions (5.41), (5.44) and they are subject to the same equation of evolution (6.7), (6.42) during and after Hubble crossing. The total matter perturbation is then equal to

$$\delta_{\rm M} = (1 - f_{\rm B})\delta_{\rm C} + f_{\rm B}\delta_{\rm B} = \delta_{\rm C} = \delta_{\rm B}. \tag{6.43}$$

The three quantitites $\delta_{\rm C}$, $\delta_{\rm B}$ and $\delta_{\rm M}$ evolve exactly like $\delta_{\rm C}$ in a universe with $f_{\rm B} \ll 1$, and the power spectrum is still given by the large-scale asymptote of Eq. (6.39), independent of $f_{\rm B}$.

Modes crossing the Hubble scale before the baryon drag epoch

Before the baryon drag time, the behavior of baryon fluctuations $\delta_{\rm B} = \frac{3}{4}\delta_\gamma = 3\Theta_{\gamma 0}$ can be inferred from that of photon fluctuations, already studied in Section 5.1.5. Baryons experience acoustic oscillations, with a boost after horizon crossing due to gravitational driving forces, a constant amplitude during radiation domination deep inside the Hubble length, a decreasing amplitude with a shift of the zero point of oscillations at the beginning of matter domination, and finally, an exponential suppression on small scales during recombination due to Silk damping.

To understand the evolution of CDM, the arguments of Weinberg, 2002 concerning fast and slow modes can still be applied. Soon after Hubble crossing and for slow modes, $\delta_{\rm B}$ and δ_γ are negligible with respect to $\delta_{\rm C}$. For fast modes, the contrary is true. Hence, the evolution of $\delta_{\rm C}$ is still given by Eq. (6.9). Because $\bar\rho_{\rm C} = \bar\rho_{\rm M} - \bar\rho_{\rm B}$, this equation can be written as

$$\delta_{\rm C}{}'' + \frac{a'}{a}\delta_{\rm C}{}' - 4\pi G\bar\rho_{\rm M}(1 - f_{\rm B})\delta_{\rm C} = 0 \tag{6.44}$$

and can be put in the Mészáros form following the same steps as in (6.26) and (6.27), but with now an extra factor $(1 - f_{\rm B})$,

$$y(1+y)\frac{d^2\delta_{\rm C}}{dy^2} + \left(1 + \frac{3y}{2}\right)\frac{d\delta_{\rm C}}{dy} - \frac{3}{2}(1 - f_{\rm B})\delta_{\rm C} = 0. \tag{6.45}$$

We see that the impact of baryons consists of reducing the gravitational force term, for a fixed Hubble friction term. By shifting the balance between gravitational attraction and background expansion, baryons reduce the growth rate of CDM. This is confirmed by the solution of the equation, during both radiation and matter domination. For instance, using the Friedmann equation, it is easy to show that deep inside matter domination, the fastest-growing solution of Eq. (6.45) is

$$\delta_{\rm C} \propto a^{1-\frac{3}{5}f_{\rm B}}. \tag{6.46}$$

In summary, CDM perturbations reach the baryon drag epoch with a reduced amplitude with respect to the $f_{\rm B} = 0$ limit. Modes entering earlier in the Hubble radius are subject to a reduced growth rate for a longer time, so $\delta_{\rm C}(\eta_{\rm dr}, k)$ is negatively tilted with respect to the $f_{\rm B} = 0$ limit, with less and less power at large k. The suppression of $\delta_{\rm C}(\eta_{\rm dr}, k)$ tends to saturate in the large k limit, because in the early radiation-dominated regime, the impact of baryons is very small.

At the baryon drag time, it is obvious that $|\delta_{\rm B}| \ll |\delta_{\rm C}|$ for wavenumbers well inside the Hubble radius. Indeed, baryon fluctuations have been oscillating together with photons and have been further suppressed by Silk damping. Meanwhile, CDM fluctuations have been growing because of gravitational clustering.

The evolution of baryons after the drag time is governed by Eq. (6.42), which has a simple solution during matter domination in the limit of constant metric fluctuations,

$$\delta_{\rm B} = D_{\rm B}^{g} + \frac{D_{\rm B}^{d}}{\eta} - \frac{k^2\eta^2}{6}\psi. \tag{6.47}$$

We see that baryon perturbations reach asymptotically the same value as those of CDM, given by $-(k^2\eta^2\psi)/6$. This is not surprising, because both species are nonrelativistic and fall into the same potential wells. Because they start from a much smaller value, the matching of this solution with that for $\eta \leq \eta_{\rm dr}$ leads to coefficients $D_{\rm B}^{g}$ and $D_{\rm B}^{d}$ such that $D_{\rm B}^{g} + D_{\rm B}^{d}/\eta_{\rm dr}$ is negative. The time needed for baryon fluctuations to reach the same value as CDM fluctuations is greater for smaller scales, because in the large-k limit the ratio $|\delta_{\rm B}/\delta_{\rm C}|$ is smaller at $\eta_{\rm dr}$. However, on all cosmological scales of interest in this book (i.e., scales which are still in the linear or midly nonlinear regime today), baryon and CDM fluctuations become equal to each other at a redshift varying between $z_{\rm dr} \sim 1000$ for large scales and $z \sim 100$ for small scales. After that time, we can follow a single variable $\delta_{\rm M} = f_{\rm B}\delta_{\rm B} + (1 - f_{\rm B})\delta_{\rm C}$, whose evolution follows

$$\delta_{\rm M}{}'' + \frac{a'}{a}\delta_{\rm M}{}' - 4\pi G\bar{\rho}_{\rm M}\delta_{\rm M} = 0. \tag{6.48}$$

This equation is again identical to the one governing the CDM evolution in a universe with $f_{\rm B} \simeq 0$. In fact, it describes the exact evolution of $\delta_{\rm M}$ at any time after baryon drag, even when $|\delta_{\rm B}| < |\delta_{\rm C}|$ (as can be shown using Eqs. (5.21), (6.7) and (6.42)). Therefore, instead of following separately $\delta_{\rm B}$ and $\delta_{\rm C}$ between baryon drag and the time at which $\delta_{\rm B} = \delta_{\rm C}$, it is sufficient to perform a matching at $\eta = \eta_{\rm dr}$ between the solutions $\delta_{\rm B}(\eta, k)$, $\delta_{\rm C}(\eta, k)$ for $\eta \leq \eta_{\rm dr}$ and the solution of the above equation for $\eta \geq \eta_{\rm dr}$. A priori, the matching process should give the coefficient of the growing mode of $\delta_{\rm M}$ (growing linearly with a during matter domination) as a linear combination of the four numbers $\delta_{\rm C}(\eta_{\rm dr}, k)$, $\delta_{\rm C}(\eta_{\rm dr}, k)'$, $\delta_{\rm B}(\eta_{\rm dr}, k)'$ and $\delta_{\rm B}(\eta_{\rm dr}, k)'$.

This matching has been studied in detail by Hu and Sugiyama, 1996 and Eisenstein and Hu, 1998. The leading term turns out to be the first one, and also the last one if $f_{\rm B}$ is not too small. The fact that the contribution of $\delta_{\rm C}(\eta_{\rm dr}, k)'$ is negligible comes from the fact that $\delta_{\rm C}(\eta, k)$ is slowly varying before the matching. Instead, baryon fluctuations are quickly evolving before the baryon drag time, and their

time derivative at $\eta_{\rm dr}$ plays a crucial role in the subsequent evolution of baryon fluctuations.

We know that the transfer function $\delta_{\rm C}(\eta_{\rm dr}, k)$ is smoothly increasing with k (see Eq. (6.30)), whereas $\delta_{\rm B}(\eta_{\rm dr}, k)$ is oscillating and quickly decreasing with k (because of combined effects of acoustic oscillations and Silk damping). The derivative $\delta_{\rm B}(\eta_{\rm dr}, k)'$ is also oscillating and decreasing with k, with a phase shifted by $\pi/2$. Hence in the large k limit, the contribution of baryons to the growing mode of $\delta_{\rm M}$ is negligible, and the result of the matching is as simple as

$$\delta_{\rm M}(\eta_{\rm dr}, k) \simeq \left[\frac{\bar\rho_{\rm C}}{\bar\rho_{\rm C} + \bar\rho_{\rm B}}\right] \delta_{\rm C}(\eta_{\rm dr}, k). \tag{6.49}$$

The factor between brackets is simply equal to $f_{\rm C} = 1 - f_{\rm B}$ in the present case, but more generally, if other species such as massive neutrinos were present, it would be given by $(1 + \omega_{\rm B}/\omega_{\rm C})^{-1}$.

In the large-k limit, baryon fluctuations do not contribute directly to the final matter power spectrum, but the amplitude of total matter fluctuations is suppressed by a factor $f_{\rm C}$ with respect to that of CDM fluctuations at $\eta = \eta_{\rm dr}$. This accounts for the reduced growth rate of $\delta_{\rm C}$ (see Eq. (6.46)) between baryon drag and the time at which $\delta_{\rm B} = \delta_{\rm C}$.

In the limit $f_{\rm B} \ll 1$, the CDM transfer function during matter and Λ domination (for modes crossing the Hubble radius during radiation domination) was given by Eq. (6.30). The previous discussion suggests that baryon effects can be accounted for by modifying this result in the following way:

$$\delta_{\rm C}(a, k) = \left[\alpha\left(\tfrac{\omega_{\rm B}}{\omega_{\rm C}}\right) + \beta\left(\tfrac{\omega_{\rm B}}{\omega_{\rm C}}\right) \ln\left(\frac{k}{k_{\rm eq}}\right) + \gamma(k)\sin[k r_{\rm s}(\eta_{\rm dr})]\right] \frac{a\, g(a;\Omega_{\rm M})}{a_{\rm eq}}. \tag{6.50}$$

The coefficients α and β are now functions of the baryon-to-CDM fraction, where this dependence accounts for the reduced growth of CDM perturbations during radiation and matter domination, until the time at which $\delta_{\rm B} = \delta_{\rm C}$. The extra contribution from baryon perturbations, significant only on intermediate scales crossing the Hubble radius at the end of radiation domination, oscillates like $\sin[k r_{\rm s}(\eta_{\rm dr})]$ because it comes from the derivative of $\delta_{\rm B}$ or $\Theta_{\gamma,0}$, which oscillate like $\cos[k r_{\rm s}(\eta_{\rm dr})]$. The envelope of these oscillations is given by a function $\gamma(k)$ decreasing with k. We did not write explicitly the dependence of γ on parameters such as the baryon density and the Silk damping scale.

In summary, the presence of a significant baryon fraction affects the shape of the matter power spectrum on small scales. The expression (6.39) for $\tilde P(a, \tilde k)$ should

be replaced in the $\tilde{k} \gg \tilde{k}_{\rm eq}$ limit by

$$\tilde{P}(a,\tilde{k}) = \mathcal{N}\left(\frac{a\, g(a;\Omega_{\rm M})}{a_0 \Omega_{\rm M}^0}\right)^2 \tilde{k}\, \mathcal{P}_{\mathcal{R}}(\tilde{k}) \times \frac{\tilde{k}_{\rm eq}^4}{4\tilde{k}^4}\left(\alpha\left(\frac{\omega_{\rm B}}{\omega_{\rm C}}\right) + \beta\left(\frac{\omega_{\rm B}}{\omega_{\rm C}}\right) \ln\left(\frac{k}{k_{\rm eq}}\right) + \gamma(k)\sin[k r_{\rm s}(\eta_{\rm dr})]\right)^2 . \tag{6.51}$$

The baryon impact is illustrated in Fig. 6.1.

Spectrum shape and evolution as a function of cosmological parameters

We can now review the effect of cosmological parameters on the matter power spectrum in a neutrinoless ΛCDM universe, in the same way as in Section 5.1.6 for the CMB temperature spectrum. We introduced in Eq. (6.38) the quantity $\tilde{P}(a,\tilde{k})$ referring to the matter power spectrum expressed in units of $h^{-3}{\rm Mpc}^3$, as a function of the scale factor and of Fourier wavenumbers expressed in units of $h{\rm Mpc}^{-1}$. When evaluated today, $\tilde{P}(a_0,\tilde{k})$ depends on

(P1) The scale $\tilde{k}_{\rm eq}$, which determines the location of the maximum in the matter power spectrum. Following equations (6.35, 6.36), this scale is given by the dimensionless ratio $[a_{\rm eq}H_{\rm eq}]/[a_0 H_0]$ divided by a factor of 3000. Using Eq. (6.31), is easy to show that this ratio is equal to $[2\Omega_{\rm M}(1+z_{\rm eq})]^{1/2}$.

(P2) The baryon-to-CDM fraction $(\omega_{\rm B}/\omega_{\rm C})$, which alters the shape of the large-scale asymptote. When this fraction increases, the spectrum is suppressed for $\tilde{k} \geq \tilde{k}_{\rm eq}$, accounting for a reduction in the growth rate of CDM perturbations as long as $|\delta_{\rm B}| \ll |\delta_{\rm C}|$, but on intermediate scales some small baryon acoustic oscillations (BAO's) inherited from the baryon density fluctuations prior to the baryon drag epoch are imprinted.

(P3) The phase of the BAO's depends on the sound horizon at the drag epoch $r_{\rm s}(\eta_{\rm dr})$, and the decrease of the oscillation amplitude with k (more difficult to observe precisely) depends on the Silk damping scale $r_{\rm d}(\eta_{\rm dr})$. Both parameters depend strongly on $\omega_{\rm B}$. Note that the scale of BAO oscillations differs from that of CMB oscillations not only due to the difference between $r_{\rm s}(\eta_{\rm LS})$ and $r_{\rm s}(\eta_{\rm dr})$, but also due to a phase shift by $\pi/2$.

(P4) The overall amplitude of the matter spectrum depends on both $\Omega_{\rm M}$ (given by $(1-\Omega_\Lambda)$, because we are dealing with spatially flat ΛCDM models) and on the primordial spectrum amplitude $A_{\rm s}$ (defined in Eq. (5.34)).

(P5) The overall tilt of the matter spectrum depends on that of the primodial spectrum $n_{\rm s}$ (also defined in Eq. (5.34)).

As a function of time, the matter power spectrum of a neutrinoless universe has a fixed shape (as long as we do not reach such high redshifts that on small scales

$\delta_{\rm B} \neq \delta_{\rm C}$). It evolves with the scale factor like $[a\, g(a;\Omega_{\rm M})]^2$, or as a function of redshift like

$$\tilde{P}(z,\tilde{k}) = (1+z)^{-2} g(z;\Omega_{\rm M})^{-2}. \tag{6.52}$$

Prior to Λ domination, when $g(z;\Omega_{\rm M}) \simeq 1$, the product $(1+z)^2 \tilde{P}(z,\tilde{k})$ is independent of redshift.

6.1.3 Impact of massless neutrinos

We have seen in Section 5.3.2 that the impact of massless neutrinos or any relativistic relics on the evolution of linear cosmological perturbations can be parameterized by a single degree of freedom, the effective neutrino number $N_{\rm eff}$ (defined in Eq. (2.198)), irrespective of the details of the phase-space distribution function. Following the same logic as in Section 5.3.1, we notice that a variation in $N_{\rm eff}$ can potentially affect the matter power spectrum through

(a) *Background effects*: Enhancing the radiation density can change some characteristic times and scales that control the matter power spectrum. According to the results of the previous section, for a fixed primordial spectrum $\mathcal{P}_{\mathcal{R}}(\tilde{k})$, the matter power spectrum is affected by four effects (P1)–(P4) depending mainly on $(\Omega_{\rm M}, z_{\rm eq}, \omega_{\rm B}/\omega_{\rm C}, \omega_{\rm B})$. The variation of these four parameters with $N_{\rm eff}$ depends on which quantities are chosen to be fixed when $N_{\rm eff}$ varies, as we shall see later.

(b) *Perturbation effects*: Neutrino perturbations can have a direct impact on matter perturbations due to the gravitational coupling between neutrinos, CDM and baryons. As explained in Section 5.3.1, this coupling can only be important during radiation domination and immediately after Hubble crossing; otherwise relativistic neutrino fluctuations are too small to back-react on matter perturbations.[2]

    We can already guess that direct perturbation effects are small. Indeed, we know from Section 5.2.5 that the perturbations $\delta_\nu(\eta,k) = F_{\nu 0}(\eta,k)$ of free-streaming relativistic particles oscillate after Hubble crossing with a pulsation k. Hence, in Weinberg's decomposition of the full solution in fast modes and slow modes (see Section 6.1.1), neutrinos couple only with fast modes. Therefore, before the baryon drag epoch, neutrino perturbations cannot have a significant back-reaction on CDM perturbations, which are described entirely in terms of slow modes. The Mészáros equation (6.28) (or (6.45) if the baryon fraction is not negligible) still applies to scenarios with relativistic relics, with no further modification.

[2] This category of effect was called (b.1) in Section 5.3.1. Effects called (b.2) and (b.3) are specific to photons and are irrelevant for the matter power spectrum calculation.

Fast modes (describing photon and baryon oscillations) are instead affected by the presence of neutrino perturbations. We actually summarized the corresponding effects in Section 5.3.2. The gravitational feedback of free-streaming neutrinos just after horizon crossing reduces the amplitude of acoustic oscillations in the coupled photon–baryon fluid and slightly shifts the oscillation phase (Hu, 1995; Bashinsky and Seljak, 2004). These effects are imprinted in baryon fluctuations $\delta_{\rm B}(\eta, k)$ prior to the baryon drag time, and in BAO features in the total matter power spectrum after that time.

In summary, we expect direct effects of neutrino perturbations to show up only in the amplitude and phase of baryon acoustic oscillations.

To check this with numerical results, we would like to vary $N_{\rm eff}$ and cancel all background effects, in order to isolate direct neutrino perturbation effects. This is impossible, because background effects depend on $(\Omega_{\rm M}, z_{\rm eq}, \omega_{\rm B}/\omega_{\rm C}, \omega_{\rm B})$: if we keep these four quantities fixed, then $N_{\rm eff}$ is also fixed through Eq. (5.104) (assuming of course that ω_γ is also fixed by the measurement of the CMB temperature):

$$z_{\rm eq} = \frac{\omega_{\rm M}}{\omega_\gamma\,[1+0.2271 N_{\rm eff}]} \quad \Longrightarrow \quad [1+0.2271 N_{\rm eff}] = \frac{\omega_{\rm B}(1+\omega_{\rm C}/\omega_{\rm B})}{z_{\rm eq}\,\omega_\gamma}. \tag{6.53}$$

However, if we vary $N_{\rm eff}$ while keeping only $(\Omega_{\rm M}, z_{\rm eq}, \omega_{\rm B}/\omega_{\rm C})$ fixed, we expect the fraction of the matter power spectrum inherited from CDM perturbations (i.e., from slow modes during radiation domination) to be unaffected. In the following subsections, we will see how the spectrum changes if we vary $N_{\rm eff}$ while keeping fixed either $(\Omega_{\rm M}, z_{\rm eq}, \omega_{\rm B}/\omega_{\rm C})$ or $(\Omega_{\rm M}, z_{\rm eq}, \omega_{\rm B})$. The second option is also relevant, because LSS data are usually used in combination with CMB data, which tend to fix accurately $\omega_{\rm B}$ (in fact, the ratio $\omega_{\rm B}/\omega_\gamma$) rather than $\omega_{\rm B}/\omega_{\rm C}$, as explained in Section 5.1.6.

Varying $N_{\rm eff}$ with fixed redshifts of equality and baryon-to-cold dark matter ratio

Fixing $(\Omega_{\rm M}, z_{\rm eq}, \omega_{\rm B}/\omega_{\rm C})$, i.e., the two redshifts of equality (between radiation and matter, and between matter and Λ) and the baryon-to-CDM ratio, can be achieved by multiplying the radiation density, matter density and squared Hubble parameter by the same factor. For instance, to compare a neutrinoless model with a model of given $N_{\rm eff}$, we can perform the transformation

$$(\omega_{\rm C}, \omega_{\rm B}, h) \longrightarrow (\alpha\omega_{\rm C}, \alpha\omega_{\rm B}, \sqrt{\alpha}h) \tag{6.54}$$

with $\alpha = [1+0.2271 N_{\rm eff}]$. This leaves the three quantities $(\Omega_{\rm M}, z_{\rm eq}, \omega_{\rm B}/\omega_{\rm C})$ invariant. We have done a similar transformation in Section 5.3.2 in order to identify

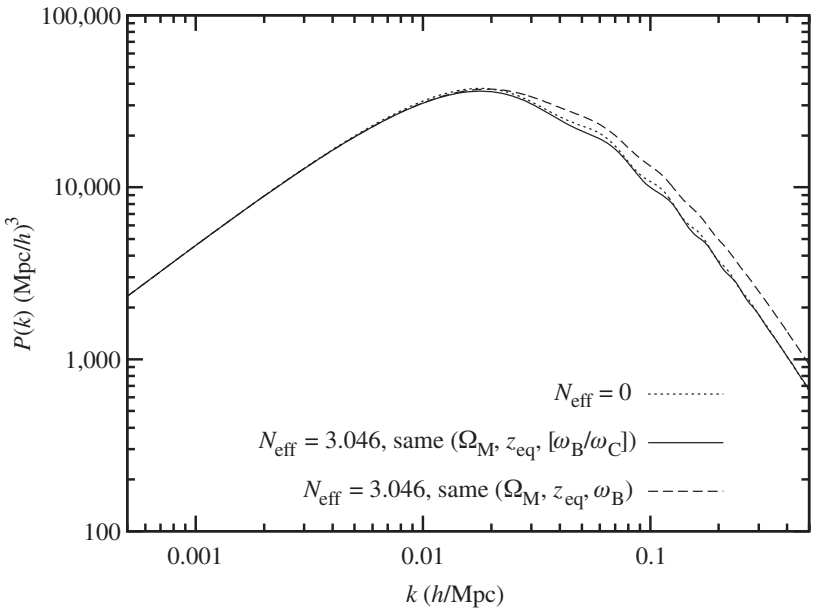

Figure 6.2 Matter power spectrum for a neutrinoless model (dotted line), a model with $N_{\rm eff} = 3.046$ and the same redshifts of equality and baryon-to-CDM ratio (solid line) and a model with $N_{\rm eff} = 3.046$ and the same redshifts of equality and baryon density (dashed line). The difference between the middle and lower curves (a shift in BAO scales and amplitude) is due to a combination of neutrino perturbation effects and a different baryon density $\omega_{\rm B}$, affecting the baryon drag time and hence the sound horizon at that time.

neutrino perturbation effects on the CMB. The difference was that in Section 5.3.2, the matter density $\omega_{\rm M} = \omega_{\rm C} + \omega_{\rm B}$ was increased with a fixed baryon density. In the present case, our goal is to leave effects (P1), (P2), (P4) of Section 6.1.2 unaffected (as well as (P5), because the primordial spectrum is unchanged). The only expected modifications to the matter power spectrum come from (P3), because $\omega_{\rm B}$ has changed, and from direct neutrino perturbation effects. However, these two effects can alter only the phase and amplitude of BAO's. We show in Fig. 6.2 that this is indeed the case. The BAO phase shift is mainly due to the fact that the model with a higher $N_{\rm eff}$ has a high baryon density $\omega_{\rm B}$, so baryons are released earlier with a low value of the sound horizon $r_{\rm s}(\eta_{\rm dr})$. It follows that the BAO peaks are shifted to slightly smaller scales (larger wavenumbers). The phase shift due to neutrino drag is of opposite sign, but of smaller amplitude.

Varying $N_{\rm eff}$ with fixed redshifts of equality and baryon density

Fixing $\omega_{\rm B}/\omega_{\rm C}$ was useful for illustrative purposes, but in practice the CMB tends to fix $\omega_{\rm B}$ with very good precision, and LSS data are used to resolve remaining

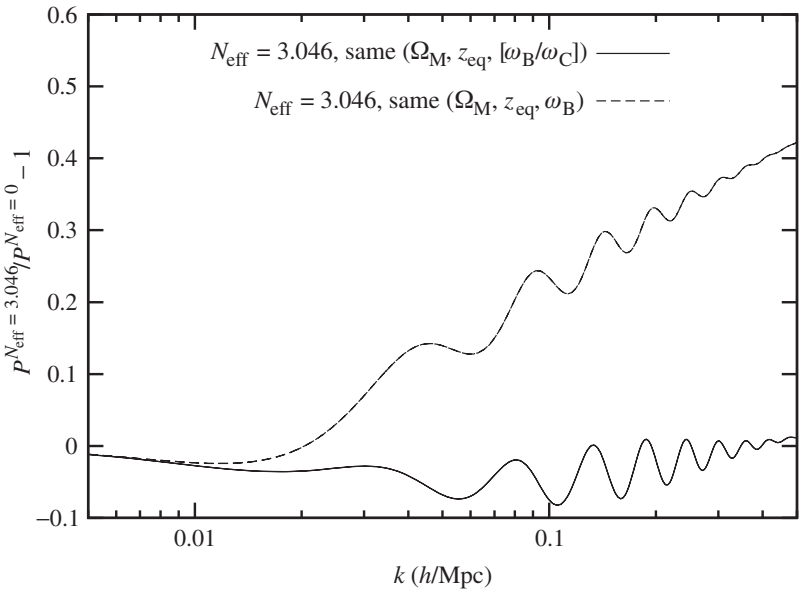

Figure 6.3 Matter power spectrum for models with $N_{\rm eff} = 3.046$ divided by the spectrum of a model with $N_{\rm eff} = 0$. The lower curve corresponds to the case in which the two models share the same redshifts of equality and baryon-to-CDM ratio, whereas in the upper one they have the same redshifts of equality and baryon density.

parameter degeneracies. If we now perform the transformation

$$(\omega_{\rm C}, \omega_{\rm B}, h) \longrightarrow ([\alpha\omega_{\rm C} + (\alpha - 1)\omega_{\rm B}], \omega_{\rm B}, \sqrt{\alpha}h), \tag{6.55}$$

still with $\alpha = [1 + 0.2271 N_{\rm eff}]$, the two redshifts of equality are still left invariant, but the baryon-to-CDM ratio decreases. This is exactly the same transformation as in Section 5.3.2. We now expect the matter power spectrum to be modified by effect (P2) and by small neutrino perturbation effects. This is confirmed by Fig. 6.2: the low baryon-to-CDM ratio results in a high amplitude on small scales; the BAO amplitude is damped both by the smaller baryon fraction and by neutrino perturbation effects; the small phase shift in BAOs due to neutrino drag is hardly visible in Fig. 6.2 but appears in Fig. 6.3 when we take the ratio of the two spectra.

6.1.4 Impact of hot dark matter

We will now scrutinize the effect of neutrino masses on the linear matter power spectrum. As we will see later, cosmological bounds are such that we can restrict the discussion to the case of neutrinos with $m_\nu \leq 1.5$ eV. Hence we assume that

neutrinos become nonrelativistic after the time of equality between radiation and matter (see Eq. (5.90)).

Evolution of neutrino perturbations

The effect of neutrinos on the matter power spectrum presents many similarities to that of baryons (studied in Section 6.1.2), with an analogy between the baryon drag time and the nonrelativistic transition time. Before the nonrelativistic transition, neutrinos free-stream below the wavelength $\lambda_{\rm fs}$ defined in Section 5.2.4, i.e., roughly on all sub-Hubble scales. Their density $\delta_\nu(\eta, k)$ is strongly suppressed with respect to that of nonrelativistic species, because pressure forces are much stronger than gravitational forces and prevent gravitational collapse. After the nonrelativistic transition, we have seen at the end of Section 5.2 that the equation of state $w = \bar{P}_\nu/\bar{\rho}_\nu$, the sound speed $\delta p_\nu/\delta\rho_\nu$ and the anistropic-stress-to-density ratio δ_ν/σ_ν decay proportionally to a^{-2}. Their order of magnitude is given roughly by c_ν^2, i.e., by $(\bar{T}_\nu/m_\nu)^2$; (see Eq. (5.91)).

If all these ratios vanished, neutrinos would be described by the same equation as CDM and decoupled baryons:

$$\delta_\nu{}'' + \frac{a'}{a}\delta_\nu{}' = -k^2\psi + 3\phi'' + 3\frac{a'}{a}\phi'. \tag{6.56}$$

However, pressure perturbations and shear viscosity cannot be completely neglected and continue to play a role in the equation of motion on sub-Hubble scales. Like decoupled baryons, neutrinos fall in the same gravitational potential wells as any other nonrelativistic species, and tend to an equilibrium solution, but because of pressure and shear, this solution differs from that for baryons (Ringwald and Wong, 2004):

$$\delta_\nu \sim (k_{\rm fs}/k)^2\delta_{\rm B} = (k_{\rm fs}/k)^2\delta_{\rm C}. \tag{6.57}$$

However, the growth rate of $\delta_\nu(\eta, k)$ between the nonrelativistic transition and the time at which equilibrium is reached is much lower than for baryons, because of pressure forces and viscosity. A detailed study of this evolution shows that today, $\delta_\nu = \delta_{\rm C}$ holds only for wavenumbers $k \leq k_{\rm nr}$. For larger wavenumbers the ratio $\delta_\nu(\eta_0, k)/\delta_{\rm C}(\eta_0, k)$ decreases slowly as a function of k, as illustrated in Figure 6.4.

Impact on the total matter power spectrum

This has important consequences for the total matter power spectrum:

- For modes $k < k_{\rm nr}$, the matter power spectrum of a ΛCDM model with massive neutrinos is the same as that of a massless model (if the two models share the

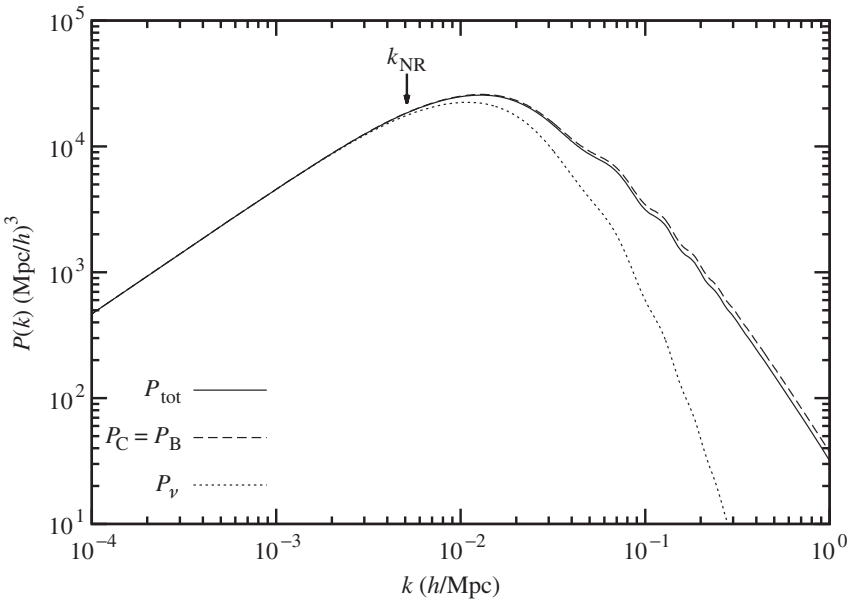

Figure 6.4 Matter power spectrum at redshift zero for a ΛCDM model with three degenerate massive neutrino species ($m_\nu = 0.3$ eV), compared to the individual power spectrum of CDM, baryon and neutrino density perturbations. In this model $k_{\rm nr}$ is equal to $5.1 \times 10^{-3} h$/Mpc (see Eq. (5.94)). For wavenumbers $k > k_{\rm nr}$, neutrino perturbations remain smaller than CDM and baryon perturbations, because of their low growth rate after the nonrelativistic transition.

same $\Omega_{\rm M}$ and primordial power spectrum). Indeed, before the Hubble radius is crossed, all perturbations are subject to the usual universal relations given by Eq. (5.24) for adiabatic initial conditions. After Hubble crossing, if $k < k_{\rm nr}$, neutrino free-streaming can be neglected: massive neutrinos share the same evolution as CDM and fall into the same potential wells, with δ_ν quickly reaching the asymptotic value of Eq. (6.57). Hence all quantitites evolve exactly as described in Section 5.24, with neutrinos being counted as part of the cold dark matter component. Because the matter power spectrum depends only on $\Omega_{\rm M}$ and $\mathcal{P}_\mathcal{R}(k)$ for wavenumbers $k < k_{\rm eq}$, and because $k_{\rm nr} < k_{\rm eq}$, two models with different neutrino masses but the same total matter fraction and primordial spectrum are indistinguishable on those scales.

- for $k \gg k_{\rm nr}$, we can use the fact that at low redshift and for the cosmological scales of interest in this book, $|\delta_\nu| \ll |\delta_{\rm C}| = |\delta_{\rm B}|$. If we expand the total matter fluctuation as

$$\delta_{\rm M} = f_{\rm C}\delta_{\rm C} + f_{\rm B}\delta_{\rm B} + f_\nu\delta_\nu \tag{6.58}$$

(with $f_{\rm C} + f_{\rm B} + f_\nu = 1$), we see that the matter power spectrum is given by

$$P(\eta, k) \simeq (f_{\rm C} + f_{\rm B})^2 P_{\rm C}(\eta, k) = (1 - f_\nu)^2 P_{\rm C}(\eta, k), \tag{6.59}$$

where $P_{\rm C}(\eta, k)$ is the CDM power spectrum

$$\langle \delta_{\rm C}(\eta, \vec{k}) \delta^*_{\rm C}(\eta, \vec{k}') \rangle = P_{\rm C}(\eta, k)\, \delta^{(3)}(\vec{k} - \vec{k}'). \tag{6.60}$$

So we can understand the impact of neutrino masses on those scales by simply studying the evolution of $\delta_{\rm C}$. We know that after Hubble crossing and before the baryon drag epoch, this evolution is described by Eq. (6.9):

$$\delta''_{\rm C} + \frac{a'}{a}\delta'_{\rm C} = 4\pi G \bar{\rho}_{\rm C} \delta_{\rm C}. \tag{6.61}$$

The term on the right-hand side is derived from the Poisson equation. It does not involve photon, relativistic neutrino and baryon perturbations for the reasons developed in Sections 6.1.1, 6.1.2 and 6.1.3: we are dealing with the slow mode part of the solution, whereas other perturbations are either negligible or contributing to fast modes. The right-hand side cannot involve nonrelativistic neutrino perturbations either, because after the nonrelativistic transition $|\delta_\nu| \ll |\delta_{\rm C}|$ for wavenumbers $k \gg k_{\rm nr}$.

After the baryon drag epoch, we have seen in Section 6.1.2 that there is a simple equation of evolution (6.48) for the weighted average between $\delta_{\rm C}$ and $\delta_{\rm B}$. We cannot denote this average $\delta_{\rm M}$ any more because total matter now also includes neutrinos. We should rather denote it as $\delta_{\rm CB} \equiv (f_{\rm C}\delta_{\rm C} + f_{\rm B}\delta_{\rm B})/(f_{\rm C} + f_{\rm B})$, subject to the equation of evolution

$$\delta''_{\rm CB} + \frac{a'}{a}\delta'_{\rm CB} - 4\pi G(\bar{\rho}_{\rm C} + \bar{\rho}_{\rm B})\delta_{\rm CB} = 0. \tag{6.62}$$

Again, neutrino perturbations do not appear in this equation, for the same reasons as in Eq. (6.9). The conclusion is that neutrino masses can affect the evolution of $\delta_{\rm C}$ and $\delta_{\rm CB}$ only through the magnitude of the expansion rate (a'/a) relative to the density of clustering species $\bar{\rho}_{\rm C}$ or $(\bar{\rho}_{\rm C} + \bar{\rho}_{\rm B})$. The background density of massive neutrinos $\bar{\rho}_\nu$ contributes to the expansion rate through the Friedmann equation, but not to the density of clustering species. Hence massive neutrinos enhance the Hubble friction term relative to the self-clustering term in the preceding equations. This leads to a reduction of the growth rate of $\delta_{\rm C}$ and $\delta_{\rm CB}$, which will be discussed below in more detail.

- In the intermediate region (k slightly larger than $k_{\rm nr}$), neutrino perturbations, although smaller than CDM perturbations, are not completely negligible, at least at small redshift. Hence there is a smooth transition between the region where neutrino masses have no effect, and that in which they have a maximal effect.

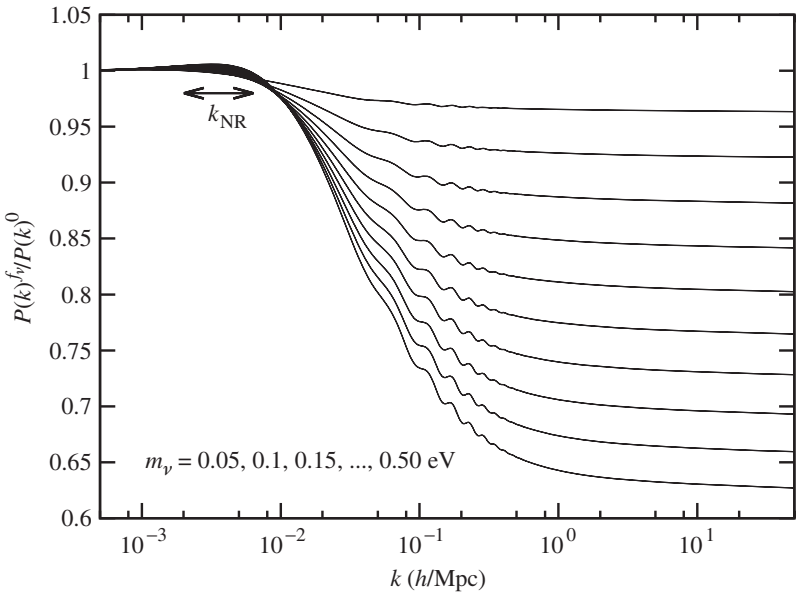

Figure 6.5 Steplike suppression of the matter power spectrum due to neutrino mass. The power spectrum of a ΛCDM model with two massless and one massive species has been divided by that of a massless model, for several values of m_ν between 0.05 eV and 0.50 eV, spaced by 0.05 eV. All spectra have the same primordial power spectrum and the same parameters ($\Omega_{\rm M}$, $\omega_{\rm M}$, $\omega_{\rm B}$).

In summary, neutrino masses produce a smooth steplike suppression of the matter power spectrum on scales $k > k_{\rm nr}$. This step is shown in Fig. 6.5 for various masses. In the next subsection, we show how to estimate the suppression factor analytically as a function of neutrino masses in the small-scale limit.

Suppression factor for $k \gg k_{\rm nr}$

Several approaches to estimating the neutrino mass impact on small scales analytically or semianalytically have been discussed in the literature. A very accurate (but also very technical) discussion has been presented in Hu and Eisenstein, 1998 (see also Holtzman, 1989; Pogosian and Starobinsky, 1995; Ma, 1996; Novosyadlyj *et al.*, 1998). For conciseness, we prefer to follow here the simple approach of Lesgourgues and Pastor, 2006 (although with a more precise and elaborate discussion of matching issues). An even simpler discussion was presented in Tegmark (2005), at a very sketchy level.

Our goal is to estimate the ratio of the matter power spectrum with neutrino masses (with a given neutrino fraction f_ν) to that with massless neutrinos ($f_\nu = 0$), in the large-wavenumber limit $k \gg k_{\rm nr}$. Equation (6.59) shows that this ratio can

be formulated in terms of CDM transfer functions

$$P(\eta, k)^{f_\nu} / P(\eta, k)^0 = (1 - f_\nu)^2 \left[\delta_{\rm C}^{f_\nu}(\eta, k) / \delta_{\rm C}^0(\eta, k) \right]^2 . \tag{6.63}$$

We need to specify which parameters should be kept fixed in the comparison. The two models should of course have the same $\Omega_{\rm M}$ and the same primordial spectrum, in order to have the same large-scale limit. Following the logic of similar discussions in Section 5.3, we would like ideally to cancel any difference in the background evolution of the two models by playing with other parameters than neutrino masses. This is obviously impossible, because the background density of each massive species $\bar\rho_{\nu_i}(a)$ has a nontrivial evolution, switching from $\bar\rho_{\nu_i} \propto a^{-4}$ to $\bar\rho_{\nu_i} \propto a^{-3}$ around $a = a_{\rm nr}(m_{\nu_i})$. However, if we fix $\omega_{\rm M}$ to the same value in the two models, the background evolution $H(a)$ is identical at least for $a \gg a_{\rm nr}$ (more precisely, in the case of neutrinos with nondegenerate masses, after the nonrelativistic transition of the heaviest neutrinos, when the total neutrino density $\bar\rho_\nu$ scales at least approximately like a^{-3}). A fixed $\omega_{\rm M}$ can easily be achieved by compensating for the increase of ω_ν by a decrease of $\omega_{\rm B}$, $\omega_{\rm C}$ or both. We will discuss different choices in the following.

In summary, we wish to compare a reference massless ΛCDM model that we call **R**, with parameters $(\omega_{\rm C}^{\mathbf{R}}, \omega_{\rm B}^{\mathbf{R}}, \omega_{\rm M}^{\mathbf{R}})$ such that

$$\omega_{\rm M}^{\mathbf{R}} = \omega_{\rm C}^{\mathbf{R}} + \omega_{\rm B}^{\mathbf{R}}, \tag{6.64}$$

to a massive ΛCDM model that we call **M**, with parameters $(\omega_{\rm C}^{\mathbf{M}}, \omega_{\rm B}^{\mathbf{M}}, \omega_\nu^{\mathbf{M}}, \omega_{\rm M}^{\mathbf{M}})$ such that

$$\begin{aligned}
\omega_{\rm M}^{\mathbf{M}} &= \omega_{\rm C}^{\mathbf{M}} + \omega_{\rm B}^{\mathbf{M}} + \omega_\nu^{\mathbf{M}} \\
\omega_{\rm M}^{\mathbf{M}} &= \omega_{\rm M}^{\mathbf{R}} \\
\omega_\nu^{\mathbf{M}} &= f_\nu \, \omega_{\rm M}^{\mathbf{R}} \\
\omega_{\rm C}^{\mathbf{M}} + \omega_{\rm B}^{\mathbf{M}} &= (1 - f_\nu) \, \omega_{\rm M}^{\mathbf{R}}.
\end{aligned} \tag{6.65}$$

Our approach consists of approximating the background evolution of the massive model, in order to use known results for the massless case. Figure 6.6 shows an example of background evolution for two models $\mathbf{M}_1$ and $\mathbf{M}_3$ with the same f_ν and two different mass splittings, compared with their common reference model **R** with the same $\omega_{\rm M}$. As a first approximation, we could try to compute the evolution of $\delta_{\rm C}(\eta, k)$ in a given model **M**, assuming the background expansion of model **R**. This background approximation would lead to the correct density in the relativistic and nonrelativistic limits, but it would be very crude and would make the transition much smoother than it is in reality, with an overestimate of the expansion rate close to the transition, as can be seen in Fig. 6.6. Moreover, the error would increase

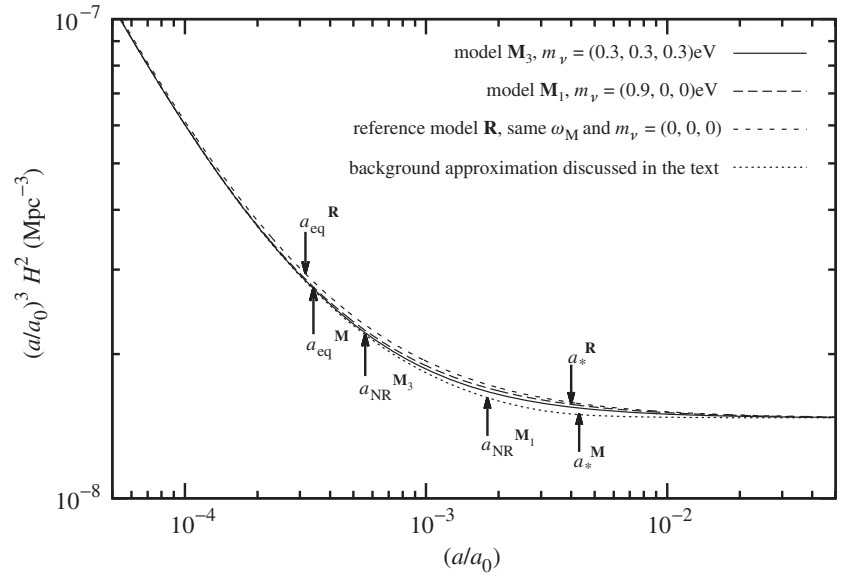

Figure 6.6 Background evolution for two models $\mathbf{M}_1$ and $\mathbf{M}_3$ with the same f_ν and two different mass splittings, compared with their common reference model $\mathbf{R}$ with the same $\omega_{\rm M}$. To see the difference between the various models clearly, we plot the squared expansion rate H^2 multiplied by $(a/a_0)^3$: this ratio is constant deep inside the matter-dominated regime and after the nonrelativistic transition of neutrinos. For each model, we show the scale factor at equality and, if relevant, at the time of the nonrelativistic transition for massive neutrinos. Finally, we show another background evolution discussed in the text and used for deriving an approximate analytic formula for the small-scale suppression factor, as well as the scale factor a_* at which we perform a matching between two classes of solutions in this approximation scheme.

in the small-f_ν limit, which is the most interesting one given current bounds on neutrino masses. Indeed, in this limit, the expansion rate in model $\mathbf{M}$ remains lower than that in model $\mathbf{R}$ for a longer time.

We will discuss a different approximation based on the fact that the neutrinos we are considering become nonrelativistic after the time of equality. Hence, before the nonrelativistic transition, the massive model is practically equivalent to a massless model $\tilde{\mathbf{M}}$ with the same CDM and baryon density parameters ($\omega_{\rm C}^{\mathbf{M}}$, $\omega_{\rm B}^{\mathbf{M}}$). The times of equality in models $\mathbf{R}$ and $\mathbf{M}$ or $\tilde{\mathbf{M}}$ differ by a factor

$$\frac{\omega_{\rm C}^{\mathbf{M}} + \omega_{\rm B}^{\mathbf{M}}}{\omega_{\rm C}^{\mathbf{R}} + \omega_{\rm B}^{\mathbf{R}}} = (1 - f_\nu), \tag{6.66}$$

with equality taking place later in the model $\mathbf{M}$ or $\tilde{\mathbf{M}}$. When approaching the neutrino nonrelativistic transition, the background evolution of $\mathbf{M}$ and $\tilde{\mathbf{M}}$ starts to

differ, but we can choose to go on approximating the massive model with model $\tilde{\mathbf{M}}$ until the total density in $\tilde{\mathbf{M}}$ reaches the true density of $\mathbf{M}$ during matter domination. After that time, we neglect the photon density and consider that the total matter density scales like a^{-3} until Λ domination. In other words, we approximate the true background evolution of $\mathbf{M}$ with that of the massless model $\tilde{\mathbf{M}}$, matched at a given time to a radiationless model with the right matter and Λ densities. Such an approximation tends to underestimate the expansion rate at times close to the nonrelativistic transition, as can be seen from the lower curve in Fig. 6.6. However, the decisive advantage of this scheme is that it becomes exact in the small-f_ν limit. Also, we will see that it leads to simple analytical predictions. The error made on the expansion rate is larger when at least one neutrino species becomes nonrelativistic close to equality, i.e., in the large-f_ν limit, and for a fixed f_ν, when the mass is concentrated in a single species. This can be seen in Fig. 6.6 by comparing the $\mathbf{M}_1$ and $\mathbf{M}_3$ curves with the curve corresponding to our approximation: the $\mathbf{M}_1$ curve is further away from the approximation. In this plot, in order to enhance the difference between the various curves, we choose a large total mass (0.9 eV), already in tension with current data. For smaller masses the approximation becomes very good.

To ensure the continuity of $H(a)$, the matching between perturbations in the $\tilde{\mathbf{M}}$ model and in the radiationless model should be performed at a scale factor $a_*^{\mathbf{M}}$ such that[3]

$$\omega_{\rm M}^{\tilde{\mathbf{M}}} \left(\frac{a_*^{\mathbf{M}}}{a_0}\right)^{-3} + \omega_{\rm R}^{\tilde{\mathbf{M}}} \left(\frac{a_*^{\mathbf{M}}}{a_0}\right)^{-4} = \omega_{\rm M}^{\mathbf{R}} \left(\frac{a_*^{\mathbf{M}}}{a_0}\right)^{-3}, \tag{6.67}$$

i.e., for

$$\frac{a_0}{a_*^{\mathbf{M}}} = \frac{f_\nu\, \omega_{\rm M}^{\mathbf{R}}}{\omega_\gamma\, (1 + 0.2271 N_{\rm eff})}. \tag{6.68}$$

The Mészáros equation (modified in the presence of baryons; see Eq. (6.45)) gives the evolution of $\delta_{\rm C}$ as a function of $y = a/a_{\rm eq}$, and depends only on $\bar{\rho}_{\rm C}/(\bar{\rho}_{\rm C} + \bar{\rho}_{\rm B})$. If the baryon-to-CDM density ratio is the same in models $\tilde{\mathbf{M}}$ and $\mathbf{R}$, i.e., if

$$\omega_{\rm C}^{\mathbf{M}} = (1 - f_\nu)\, \omega_{\rm C}^{\mathbf{R}} \tag{6.69}$$

$$\omega_{\rm B}^{\mathbf{M}} = (1 - f_\nu)\, \omega_{\rm B}^{\mathbf{R}}, \tag{6.70}$$

then all perturbations are identical in the two models $\tilde{\mathbf{M}}$ and $\mathbf{R}$ for $a \leq a_*^{\mathbf{M}}$, modulo a shift in time

$$\delta_{\rm C}^{\tilde{\mathbf{M}}}(a, k) = \delta_{\rm C}^{\mathbf{R}}((1 - f_\nu)a, k)\,. \tag{6.71}$$

[3] The calculation of the suppression factor presented in Lesgourgues and Pastor (2006) is identical to the present one, except for a different (semiempirical) choice for the matching time, $a_*^{\mathbf{M}} = a_{\rm nr}/\sqrt{1 - f_\nu}$, not compatible with a continuous $H(a)$.

After $a = a_*^{\mathbf{M}}$, because we assume that the total background density scales exactly like a^{-3} until Λ domination, the relevant equations of evolution (Eq. (6.9) before baryon drag or (6.62) after baryon drag) can be approximated during the rest of the matter-dominated stage as

$$\delta_{\rm C}'' + \frac{2}{\eta}\delta_{\rm C}' - \frac{6}{\eta^2}(1-f_\nu)\delta_{\rm C} = 0 \quad \text{for } \eta \leq \eta_{\rm dr} \tag{6.72}$$

$$\delta_{\rm CB}'' + \frac{2}{\eta}\delta_{\rm CB}' - \frac{6}{\eta^2}(1-f_\nu)\delta_{\rm CB} = 0 \quad \text{for } \eta \geq \eta_{\rm dr}. \tag{6.73}$$

These equations have two exact solutions proportional to $\eta^{2p_\pm} \propto a^{p_\pm}$ with

$$p_\pm = \frac{-1 + \sqrt{1 + 24(1-f_\nu)}}{4}. \tag{6.74}$$

For $f_\nu \ll 1$, these exponents read

$$p_+ \simeq 1 - (3/5) f_\nu + O(f_\nu^2), \tag{6.75}$$

$$p_- \simeq -(3/2) + (3/5) f_\nu + O(f_\nu^2). \tag{6.76}$$

Current bounds on neutrino masses are such that terms of order f_ν^2 can safely be neglected, so from now on we will use these first-order expressions for $p_\pm$. We see that they have opposite signs and correspond respectively to growing and decaying modes. When the cosmological constant starts to play a role, we know that the coefficient of Eqs. (6.72), (6.73) change, and that in the absence of massive neutrinos the growing mode would be given by $[a\, g(a;\Omega_{\rm M})]$ (with the function g defined in Section 6.1.1). Numerical simulations confirm that in a very good approximation, the solutions with massive neutrinos can be approximated as $[a\, g(a;\Omega_{\rm M})]^{p_\pm}$.

We should now perform a matching between the solution $\delta_{\rm C}^{\tilde{\mathbf{M}}}(a,k)$ for $a \leq a_*^{\mathbf{M}}$ and a linear combination of the two solutions $[a\, g(a;\Omega_{\rm M})]^{p_\pm}$ for $a \geq a_*^{\mathbf{M}}$. We will assume for simplicity that the matching selects a pure growing mode, such that the density perturbation just after the matching reads

$$\delta_{\rm C}^{\mathbf{M}}(a,k) = \left[\frac{a}{a_*^{\mathbf{M}}}\right]^{p_+} \delta_{\rm C}^{\tilde{\mathbf{M}}}\left(a_*^{\mathbf{M}}, k\right). \tag{6.77}$$

At late times, taking into account the effect of baryon drag and of Λ domination, the perturbations read

$$\delta_{\rm CB}^{\mathbf{M}}(a,k) = \delta_{\rm C}^{\mathbf{M}}(a,k) = F(\omega_{\rm B}/\omega_{\rm C}) \left[\frac{a\, g(a;\Omega_{\rm M})}{a_*^{\mathbf{M}}}\right]^{p_+} \delta_{\rm C}^{\tilde{\mathbf{M}}}\left(a_*^{\mathbf{M}}, k\right), \tag{6.78}$$

where the function F is equal to one if the matching at $a_*^{\mathbf{M}}$ takes place after the baryon drag epoch, or to $(1+\omega_{\rm B}/\omega_{\rm C})^{-1}$ in the opposite situation (see Eq. (6.49)).

Using the equivalence between the models $\tilde{\mathbf{M}}$ and $\mathbf{R}$ summarized by Eq. (6.71), we can rewrite this equality as

$$\delta^{\mathbf{M}}_{\rm CB}(a,k) = F(\omega_{\rm B}/\omega_{\rm C}) \left[\frac{a\, g(a;\Omega_{\rm M})}{a^{\mathbf{M}}_*}\right]^{p_+} \delta^{\mathbf{R}}_{\rm C}\left((1-f_\nu)a^{\mathbf{M}}_*, k\right). \qquad (6.79)$$

To find the suppression factor, we should finally relate the CDM density perturbation at $a^{\mathbf{R}}_* \equiv (1-f_\nu)a^{\mathbf{M}}_*$ to the matter density perturbation today in the reference model. We can follow the same steps as in the massive model, i.e., match the solution at $a \leq a^{\mathbf{R}}_*$ with a linear combination of the two solutions $[a\, g(a;\Omega_{\rm M})]^{p_\pm}$ for $a \geq a^{\mathbf{R}}_*$, with now $p_+ = 3/5$ and $p_- = -3/2$ in the massless case. Also, we need to be consistent with previous assumptions concerning the derivative of the solution at the time of matching. By selecting the growing mode in the previous matching, we explicitly assumed that in the model $\tilde{\mathbf{M}}$,

$$\frac{d}{da}\delta^{\tilde{\mathbf{M}}}_{\rm C}(a,k) = [1-(3/5)f_\nu]\,\delta^{\tilde{\mathbf{M}}}_{\rm C}(a,k) \qquad (6.80)$$

at $a = a^{\mathbf{M}}_*$. Then the exact correspondence between models $\tilde{\mathbf{M}}$ and $\mathbf{R}$, summarized by Eq. (6.71), implies that

$$\frac{d}{da}\delta^{\mathbf{R}}_{\rm C}(a,k) = [1-(3/5)f_\nu]\,\delta^{\mathbf{R}}_{\rm C}(a,k) \qquad (6.81)$$

at $a = a^{\mathbf{R}}_*$. A matching with the two solutions $a^{3/5}$, $a^{-3/2}$ in the subsequent matter-dominated stage gives the coefficients of the growing and decaying modes:

$$\delta^{\mathbf{R}}_{\rm C}(a,k) = \left[\left(1-\frac{6}{25}f_\nu\right)\left(\frac{a}{a^{\mathbf{R}}_*}\right) + \frac{6}{25}f_\nu\left(\frac{a}{a^{\mathbf{R}}_*}\right)^{-3/2}\right]\delta^{\mathbf{R}}_{\rm C}\left(a^{\mathbf{R}}_*, k\right). \qquad (6.82)$$

At late times, we should keep only the growing mode and take into account baryon drag and Λ domination,

$$\delta^{\rm R}_{\rm M}(a,k) = F(\omega_{\rm B}/\omega_{\rm C})\left(1-\frac{6}{25}f_\nu\right)\left[\frac{a\, g(a;\Omega_{\rm M})}{a^{\mathbf{R}}_*}\right]\delta^{\mathbf{R}}_{\rm C}\left(a^{\mathbf{R}}_*, k\right), \qquad (6.83)$$

where $F(\omega_{\rm B}/\omega_{\rm C})$ is the same as in Eq. (6.79), because the two models $\mathbf{M}$ and $\mathbf{R}$ share the same baryon-to-CDM fraction. We now take the ratio of Eq. (6.79) and Eq. (6.83) and find the relation

$$\delta^{\mathbf{M}}_{\rm CB}(a,k) = \left(1-\frac{6}{25}f_\nu\right)^{-1}\frac{a^{\mathbf{R}}_*}{a^{\mathbf{M}}_*}\left[\frac{a\, g(a;\Omega_{\rm M})}{a^{\mathbf{M}}_*}\right]^{-(3/5)f_\nu}\delta^{\mathbf{R}}_{\rm M}(a,k). \qquad (6.84)$$

We can use $(a_*^{\mathbf{R}}/a_*^{\mathbf{M}}) = (1 - f_\nu)$ and take the square of this equality to obtain a relation between the matter power spectra of the two models (using Eq. (6.63)),

$$P^{f_\nu}(a,k) = \frac{(1-f_\nu)^4}{(1-(6/25)f_\nu)^2}\left[\frac{a\,g(a;\Omega_{\rm M})}{a_*^{\mathbf{M}}}\right]^{-(6/5)f_\nu} P^0(a,k)\,. \tag{6.85}$$

We can finally replace $a_*^{\mathbf{M}}$ by its explicit expression (6.68) and write our final result as

$$\frac{P(a,k)^{f_\nu}}{P(a,k)^0} = \frac{(1-f_\nu)^4}{(1-(6/25)f_\nu)^2}\left[\frac{a\,g(a;\Omega_{\rm M})}{a_0}\cdot\frac{f_\nu\,\omega_{\rm M}}{\omega_\gamma\,(1+0.2271N_{\rm eff})}\right]^{-(6/5)f_\nu}. \tag{6.86}$$

We recall that in this equation $N_{\rm eff}$ should be summed over all neutrinos (massive and massless). This result could also be expressed as a function of the scale factor at equality, in either the massless or the massive model. For instance, if $a_{\rm eq}^0$ denotes the redshift of equality in the massless model,

$$\frac{P(a,k)^{f_\nu}}{P(a,k)^0} = \frac{(1-f_\nu)^4}{(1-(6/25)f_\nu)^2}\left[\frac{a\,g(a;\Omega_{\rm M})}{a_{\rm eq}^0}f_\nu\right]^{-(6/5)f_\nu}. \tag{6.87}$$

In the derivation of this result, we made four approximations:

- We used $p_+ \simeq 1-(3/5)f_\nu$: this approximation leads to negligible errors for realistic models with $f_\nu \leq 0.1$.
- We assumed that solutions for $\delta_{\rm C}^{\mathbf{M}}(\eta,k)$ during Λ domination are given by $(a\,g(a;\Omega_{\rm M}))^{p_\pm}$ instead of solving the full equation of evolution. However, this approximation is excellent for the growing mode, and the solution for the decaying mode is anyway irrelevant at late times.
- In the massive model, we approximated the background evolution in such a way that (a'/a) near the transition was underestimated, especially when the highest neutrino mass was large and the transition took place close to equality. More expansion implies a slower growth of perturbations in the massive model, i.e., a reduction of the suppression factor.
- In the massive model **M**, we assumed in the matching process that only the growing mode proportional to $a^{1-(3/5)f_\nu}$ was excited. If we assume that a small fraction of $\delta_c^{\mathbf{M}}$ goes to the decaying mode, both $\delta_c^{\mathbf{M}}$ and $\delta_c^{\mathbf{R}}$ are affected, but the total effect is a reduction of the suppression factor.

We see that the first two approximations have a negligible impact, whereas the last two go in the same direction, and we expect Eq. (6.86) to slightly overestimate the suppression factor. It can be shown that the worst approximation is actually the third one; this is important for understanding the difference between the degenerate

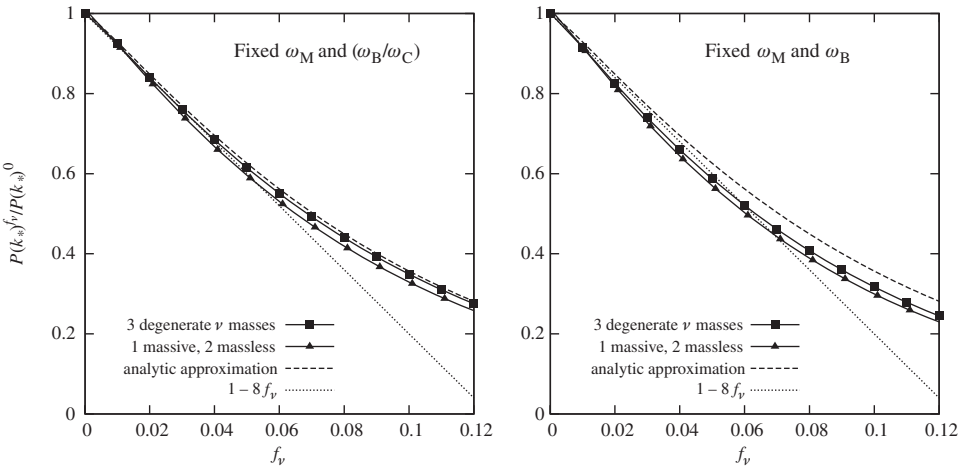

Figure 6.7 Suppression factor $P(\eta,k)^{f_\nu}/P(\eta,k)^0$ computed today for $k = 10\,h$/Mpc, as a function of the total neutrino fraction f_ν. The result depends on the mass splitting but is always contained between the two displayed curves corresponding to a single massive neutrino or three degenerate neutrinos, i.e., to the maximal and minimal values of the heaviest mass that can be involved for each value of f_ν. We show for comparison the analytic approximation of Eq. (6.86) as well as the well-known linear approximation $(1-8f_\nu)$. On the left, the comparison was performed with fixed values of ω_M and (ω_B/ω_C), as explicitly assumed when deriving the analytical formula. On the right, we kept ω_M and ω_B fixed (with the increase in ω_ν compensated for by a decrease in ω_C), and we compare with the same approximations.

and single-mass scenarios, and more generally for the discussion of mass splitting effects in the next subsection.

These expectations are confirmed by Fig. 6.7 (left plot). For the case of degenerate masses, the analytic prediction is accurate by better than 1%, whereas for a single massive species the error can reach 3% (at least for $f_\nu \leq 0.12$, i.e., throughout the range compatible with current data). Indeed, we have seen earlier that our approximation for the background evolution of the massive model gets worse when the time of nonrelativistic transition of at least one species gets closer to the time of equality. So, in the single mass case, the underestimation of the suppression factor is greater.

For a given neutrino fraction f_ν, i.e., a total mass M_ν, there are an infinity of models corresponding to different ways to split M_ν between several species. However, the heaviest individual mass is always inside the range defined by the previous two cases, i.e., between the degenerate case ($m_\nu = M_\nu/N_\nu$) and the single-massive-neutrino case ($m_\nu = M_\nu$). Because it is mainly the heaviest mass that determines the time at which our background approximation becomes not so good

and produces an error, the two models displayed in Fig. 6.7 can be seen as limiting cases, and the discrepancy between the analytic formula and the numerical results cannot be larger than for the single-mass model. We will come back to mass splitting issues in more detail in the next subsection.

In Fig. 6.7 (left plot), we also show the famous linear approximation of (Hu *et al.*, 1998) to the suppression factor,

$$\frac{P(a,k)^{f_\nu}}{P(a,k)^0} \simeq 1 - 8 f_\nu. \tag{6.88}$$

This fit is accurate at the 2% level for $f_\nu \leq 0.05$, but departs significantly from the numerical solution for a larger neutrino fraction.

In Fig. 6.7, the numerical estimate of the suppression factor was done at the scale $k = 10\,h$/Mpc. Of course, on such a small scale, real matter perturbations are strongly nonlinear today. However, on this scale, the ratio $P(a,k)^{f_\nu}/P(a,k)^0$ has reached its asymptotic value up to very good accuracy: we checked that the factor inferred from $k = 100\,h$/Mpc agrees to better than 1% with that computed at $k = 10\,h$/Mpc. This is not the case on larger scales: the factor computed at $k = 1\,h$/Mpc is as much as 2% larger (but, coincidentally, it is in even better agreement with the analytical prediction of Eq. (6.86)).

We performed all this exercise assuming that the baryon-to-CDM fraction is the same in the massive model and in the reference model. In practice, however, it is useful to consider the effect of neutrino masses when the baryon fraction $\omega_{\rm B}$ is fixed, because this parameter is accurately determined by CMB observations. If we go along the same lines of reasoning fixing $\omega_{\rm B}^{\mathbf{R}} = \omega_{\rm B}^{\mathbf{M}}$, then we should assume that the ratio $\omega_{\rm B}/\omega_{\rm C}$ is larger in model **M** than in model **R**. Hence the matter power spectrum of **M** will be suppressed both by neutrino masses as described previously, and (to a smaller extent) by an increase in the baryon fraction, with the consequences described in Section 6.1.2. In this case, the suppression factor is smaller, as can be checked in the right plot of Fig. 6.7. The discrepancy between the analytic prediction of Eq. (6.86) and numerical results increases up to about 6% (for realistic values of $\omega_{\rm B}$ and $\omega_{\rm C}$). In that case, the linear fit of Eq. (6.88) remains very accurate for $f_\nu \leq 0.01$, but in the range $f_\nu \in [0.01\ 0.05]$ the error can reach 3%. A linear fit $(1 - 8.5\,f_\nu)$ would be better in that case.

Mass splitting

The effect of neutrino masses on the matter power spectrum does not depend only on the total mass $M_\nu = \sum_i m_{\nu_i}$ for essentially two reasons:

1. The scale at which a given neutrino mass m_{ν_i} starts to have an impact on the matter power spectrum depends on $k_{\rm nr} \propto m_{\nu_i}^{1/2}$ (see Eq. (5.94)). If there is a single

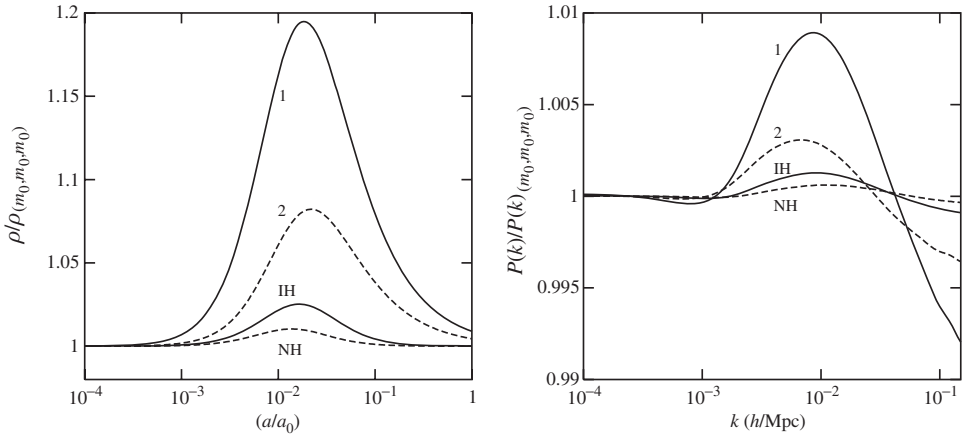

Figure 6.8 (Left) Evolution of the total neutrino energy density as a function of the scale factor for models where the same total mass $M_\nu = 0.12$ eV is distributed among the three species in various ways: only one massive eigenstate (1), two degenerate massive states (2), normal hierarchy (NH), inverted hierarchy (IH). All curves are normalized to the case with three degenerate massive states. (Right) Comparison of the matter power spectrum obtained for the same models, divided each time by that with three degenerate massive states. Differences in the mass splitting affect the position and amplitude of the break in the power spectrum. (Reprinted from Lesgourgues and Pastor, 2006, with permission from Elsevier.)

mass in the problem, as in scenarios with N massive neutrinos and $(N_\nu - N)$ massless ones, the steplike suppression starts at a smaller wavenumber k if the mass is smaller, i.e., if M_ν is distributed equally among all species. If there are several masses, the location and shape of the step are rather model-dependent: we will illustrate this below and compare the most relevant cases, namely the normal hierarchy (NH) and inverted hierarchy (IH) scenarios preferred by neutrino oscillation experiments.

2. We have seen in the previous subsection that the amplitude of the step is controlled mainly by f_ν, i.e., by M_ν, but with an additional dependence on the detailed background evolution close to the nonrelativistic transition(s). The case of degenerate masses is very close to the analytic approximation of the last section, because neutrinos remain relativistic for a maximum amount of time for a given M_ν, because no mass is larger than M_ν/N_ν. For any other mass splitting, the background density is enhanced for a limited amount of time with respect to the degenerate scenario. This was illustrated in Fig. 6.6 for the single-mass scenario, and more examples are given in Fig. 6.8 (left plot). Any temporary enhancement of the background density leads to slower growth of CDM and baryon fluctuations for a little while, and to a stronger steplike suppression.

These differences are of course very small for a fixed total mass. The maximum discrepancy can be observed in the comparison of the degenerate and single-mass scenarios, on small scales where the neutrino mass effect is maximum, and at $z = 0$. We see in Fig. 6.7 that even in this case the effect is only on the order of 3%. The discrepancy between realistic scenarios (NH and IH), on scales close enough to the linear regime to enable precise observations with an ideal instrument (i.e., k not too large and/or z not too small), is much smaller and typically below the percent level. It is therefore unlikely that these effects can be probed at a good significance level in the future, but because the most ambitious forecasts suggest that discrimination is marginally possible (Pritchard and Pierpaoli, 2008; Jimenez *et al.*, 2010), we will describe them in more detail.

In Fig. 6.8, we compare the total neutrino density evolution $\rho_\nu(a)$ and the current matter power spectrum $P(a_0, k)$ of five models with the same total mass $M_\nu = 0.12$ eV: one, two, three degenerate massive species (with two, one, zero massless species); three massive species with normal hierarchy; and three massive species with inverted hierarchy. All curves are normalized to the case of three degenerate species. For the NH and IH scenario, squared mass differences were chosen in the range probed by experimental data, leading to $(m_1, m_2, m_3) = (3.03, 3.15, 5.82) \times 10^{-2}$eV in the NH case, and $(m_1, m_2, m_3) = (5.11, 5.18, 1.71) \times 10^{-2}$eV in the IH case.

The model with a single massive species features the highest mass and the earliest nonrelativistic transition. In this model, the background density is significantly enhanced with respect to the degenerate model when the scale factor is in the range between $a_{\rm nr}(M_\nu)$ and $a_{\rm nr}(M_\nu/N_\nu)$. Hence the step starts at a larger wavenumber $k_{\rm nr}(M_\nu)$, but goes deeper. So the spectra of the two models must cross each other at some point, and their ratio has the bumpy shape seen in Fig. 6.8 (right plot). The same arguments explain the difference between the two-masses scenario and the degenerate case.

The NH and IH scenarios are more similar to the degenerate case, because they feature three masses. The heaviest mass is roughly the same in the two cases, 0.0582 eV versus 0.0518 eV in our example. In the IH scenario, however, two neutrinos become nonrelativistic almost at the same time. There is a short period during which the NH scenario has one nonrelativistic neutrino with $m_\nu = 0.0582$ eV, whereas the IH scenario has two of them with a summed mass of $0.0511 + 0.0518 = 0.1029$ eV. Hence the total density is enhanced for a short amount of time in the IH case, with slower growth of CDM perturbations: this explains why the amplitude of the spectrum on scales $k \gg k_{\rm nr}$ is a bit smaller in the IH scenario. For intermediate wavenumbers crossing the Hubble scale when the universe contains two relativistic species in the NH case, or one relativistic species

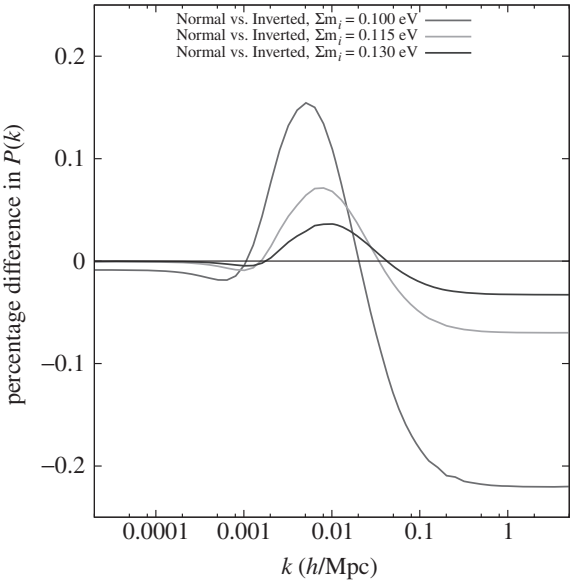

Figure 6.9 Ratio of matter power spectra for pairs of models with three massive neutrinos, subject to either the normal or the inverted hierarchy scenario, but with a common total mass for each pair: from bottom to top on the right, $M_\nu = 0.100$, 0.115 or 0.130 eV. Squared mass differences were fixed to $\delta m^2 = 7.6 \times 10^{-5}$eV and $\Delta m^2 = \pm 2.4 \times 10^{-3}$eV. The first total mass is very close to the minimum allowed value for the inverted hierarchy given these differences, $M_\nu = 0.0994$ eV. (Reprinted from Lesgourgues and Tram, 2011, with permission from IOP.)

in the IH case, however, the IH spectrum is less affected by neutrino free-streaming and appears to be enhanced.

The previous comparison is useful for pedagogical purposes, but in practice it is more useful to look at differences between the NH and IH cases for given values of the total mass. These differences are shown in Fig. 6.9. When the total mass increases, the two models become closer to the degenerate case and more similar to each other. For smaller masses, the effects discussed in the previous paragraph are clearly identified. Also, the IH model with the smallest total mass has its large-scale amplitude reduced by 0.01%. This effect, too small to be observable, is related to the presence of a very light neutrino in this model, just finishing its nonrelativistic transition today. Its nonnegligible pressure slightly affects metric perturbations at large wavelengths.

Because the power spectrum of realistic neutrino mass scenarios depart from the degenerate model by only a fraction of percent for a given f_ν, the analytic formula (6.86) is very accurate for these scenarios (to better than 1%, at least for $f_\nu \leq 0.12$).

Scale-dependent growth factor

We saw in Eq. (6.52) that in the absence of neutrino masses, the power spectrum evolves as a function of redshift (or of the scale factor) as $[g(z;\Omega_{\rm M})/(1+z)]^2$ (or $[a\,g(a;\Omega_{\rm M})]^2$) on all scales. The linear growth factor is defined (up to a normalization factor) as the time-dependent part of the square root of the matter power spectrum. This means that in absence of neutrino masses, the linear growth factor is independent of k and proportional to $[g(z,\Omega_{\rm M})/(1+z)]$.

We know that the power spectrum on large scales $k < k_{\rm nr}$ is unaffected by neutrino masses (as long as $\Omega_{\rm M}$ is kept fixed). On small scales $k \gg k_{\rm nr}$, we must instead take into account a correction factor very well approximated by Eq. (6.86). This approximation is valid at least in the redshift range in which we can observe large-scale structure (in this range, f_ν can be considered as independent of time). Taking this correction into account, the small-scale matter power spectrum grows proportionally to $[g(z;\Omega_{\rm M})/(1+z)]^{2-(6/5)f_\nu}$; i.e., the linear growth factor evolves like

$$[g(z;\Omega_{\rm M})/(1+z)]^{1-(3/5)f_\nu}, \qquad (k \gg k_{\rm nr}). \tag{6.89}$$

On intermediate scales such that k is not much bigger than $k_{\rm nr}$, the linear growth factor interpolates smoothly from $[g(z;\Omega_{\rm M})/(1+z)]$ to Eq. (6.89). An analytic approximation for intermediate scales can be found (e.g., in Hu and Eisenstein, 1998). Hence a crucial effect of neutrino masses is to render the linear growth factor scale-dependent. This can be formulated differently by saying that for a given total neutrino mass M_ν, the steplike suppression of the matter power spectrum is less pronounced at high redshift, as illustrated in Fig. 6.10. This observation is important for the detection of neutrino masses with LSS observations: by comparing the matter power spectrum at different redshifts, it is possible in principle to observe the redshift dependence of neutrino mass effects, on top of their wavenumber dependence.

Impact of the phase-space distribution function

We have seen in Section 4.1 that ordinary active neutrinos are expected to acquire small flavour-dependent nonthermal corrections at decoupling. These are, however, too small to be detectable with cosmological observables. At the level of precision reachable by current and future experiments, the phase-space distribution of ordinary active neutrinos can be approximated as a Fermi–Dirac distribution, with a temperature slightly enhanced with respect to $T_\nu^{\rm a} \equiv (4/11)^{1/3} T_\gamma$ in such way that the three active species lead to an effective neutrino number equal to $N_{\rm eff} = 3.046$ instead of 3 (as can be inferred from Eq. (4.21) and Table 4.1).

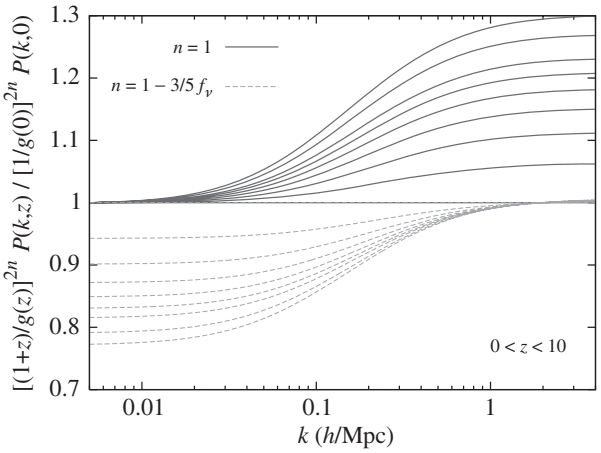

Figure 6.10 Shape distortion of the matter power spectrum $P(k, z)$ at different redshifts. *Upper solid curves:* The power spectra are divided by $[a\, g(a; \Omega_{\rm M})]^2 = [g(z)/(1 + z)]^2$, which accounts for the evolution on large scales. From top to bottom, the curves correspond to $z = 10, 8, 6, 5, 4, 3, 2, 1, 0$. *Lower dashed curves:* The power spectra are divided instead by $[a\, g(a; \Omega_{\rm M})]^{2-6/5\, f_\nu} = [g(z)/(1 + z)]^{2-6/5\, f_\nu}$, which approximates the power spectrum evolution on small scales. From top to bottom, the curves correspond to $z = 0, 1, 2, 3, 4, 5, 6, 8, 10$. All cosmological parameters are kept fixed and the neutrino density fraction is $f_\nu = 0.1$. (Reprinted from Lesgourgues and Pastor, 2006, with permission from Elsevier.)

In some extensions of the minimal cosmological model, it is necessary to compute the matter power spectrum in the presence of hot relics with a different phase-space distribution. First, active neutrinos may feature a large leptonic asymmetry described by chemical potentials, as discussed in Section 4.2.4. Under some even more radical assumptions, active neutrinos could also acquire large nonthermal distortions, e.g., through the decay of an unstable particle into neutrinos after neutrino decoupling (Cuoco *et al.*, 2005); see Section 4.4.3 . It has also been suggested that under very unusual assumptions, neutrinos could follow Bose–Einstein statistics (Dolgov *et al.*, 2005). Additional hot relics could also have a temperature different from that of active neutrinos, a chemical potential, a Bose–Einstein distribution or a nonthermal distribution.

Among all these possibilities, we can distinguish two situations with different consequences for cosmological perturbations. Hot relics may have

(a) A Fermi–Dirac distribution with arbitrary temperature, or a rescaled Fermi–Dirac distribution (e.g., for sterile neutrinos being populated by nonresonant oscillations with active neutrinos). These relics lead to the same signature as ordinary active neutrinos, with simply a different correspondence between the parameters describing the relic properties (mass, temperature, rescaling

factor) and those describing effects in the matter power spectrum ($k_{\rm nr}$ and $f_\nu = \omega_\nu/\omega_{\rm M}$).

(b) Another distribution. In that case they lead to the same signature as ordinary active neutrinos in the small- and large-scale limits, but to a different step shape on intermediate scales (for k slightly larger than $k_{\rm nr}$).

Indeed, for case (a), let us consider some hot relics called "x" with a Fermi–Dirac distribution, possibly rescaled by a number χ, an arbitrary temperature $T_{\rm x}$ and two internal degrees of freedom (as for one pair $(\nu_i, \bar\nu_i)$). After a change of variable from y to $\tilde y = (T_\nu^{\rm a}/T_{\rm x})y$ and $\tilde m_{\rm x} = (T_\nu^{\rm a}/T_{\rm x})m_{\rm x}$, the perturbation equations (5.74–5.78) for x are exactly identical to those of thermal relics with temperature $T_\nu^{\rm a}$, except for a global factor $\chi(T_{\rm x}/T_\nu^{\rm a})^4$ in the expression for density and pressure. Hence a rescaling of the phase-space distribution is mathematically equivalent to a change of temperature. These two effects cannot be distinguished at the level of linear perturbations. Before their nonrelativistic transition, such particles would contribute to the radiation density as

$$\Delta N_{\rm eff} = \chi(T_{\rm x}/T_\nu^{\rm a})^4, \tag{6.90}$$

whereas today their density would be given by

$$\omega_{\rm x} = \chi\left(\frac{T_{\rm x}}{T_\nu^{\rm a}}\right)^3 \frac{m_{\rm x}}{94.1{\rm eV}}. \tag{6.91}$$

Their average velocity would be subject to Eq. (5.91) with $T_\nu = T_{\rm x}$, leading to

$$k_{\rm nr} \equiv k_{\rm fs}(\eta_{\rm nr}) \simeq 0.0178\,\Omega_{\rm M}^{1/2}\left(\frac{T_\nu^{\rm a}}{T_{\rm x}}\right)^{1/2}\left(\frac{m_{\rm x}}{1\ {\rm eV}}\right)^{1/2} h\,{\rm Mpc}^{-1}. \tag{6.92}$$

These particles would affect the matter power spectrum both through a change in the radiation density, parameterized by $\Delta N_{\rm eff}$ and described in Section 6.1.3, and through a steplike suppression, parameterized by $f_{\rm x} = \omega_{\rm x}/\omega_{\rm M}$ and $k_{\rm nr}$ and described previously in this subsection.

For case (b), the effects of chemical potentials, of different statistics or of nonthermal distortions should be studied case by case. In the relativistic regime, any nonthermal distortion is equivalent to a change in $N_{\rm eff}$, as mentioned in Section 5.3.2. But in the nonrelativistic regime, all details in the distribution can be important, because the equation of motion for neutrinos cannot be integrated over momentum. We know that hot relics do not affect the largest scales, and that in the small-scale limit the matter power spectrum depends only on the CDM and baryon evolution, with no impact of the gravitational back reaction of neutrinos even in the radiation-dominated stage (see Section 6.1.3). So the phase-space distribution of hot dark matter is irrelevant in this limit for a given value of the HDM density fraction. But on intermediate scales (k slightly larger than $k_{\rm nr}$), the matter

power spectrum receives contributions from each nonrelativistic component: CDM, baryons and neutrinos. In this range, nontrivial phase-space distributions can leave a distinct signature, through modification of the shape of the neutrino power spectrum. The steplike suppression in the total matter power spectrum can then be sharper or smoother. This is illustrated in Hannestad *et al.*, 2005, for the case of a Bose–Einstein versus Fermi–Dirac statistics, and in Lesgourgues and Pastor, 1999, for active neutrinos with chemical potentials.

Instead of studying each subcase of (b) separately, one could try to constrain the phase-space distribution with a model-independent approach. For instance, an arbitrary distribution can be described by the infinite series of its statistical moments. Observations can be used to provide model-independent constraints at least on the first few moments. The analysis of Cuoco *et al.*, 2005 shows that due to parameter degeneracies (between neutrino and cosmological parameters), it is difficult to constrain more than the mass and the first two moments of a given species, related respectively to their density-to-mass ratio ω_ν/m_ν and their contribution to $N_{\rm eff}$. However, this conclusion is based on the use of linear observables only (CMB and linear matter power spectrum). The nonlinear evolution could potentially enhance the impact of differences in higher momenta.

6.1.5 Impact of warm dark matter

Qualitative behavior of warm dark matter perturbations

If their mass and velocity dispersion fall into an appropriate range, dark matter particles may become nonrelativistic deep inside the radiation-dominated epoch, and preserve the shape of the CDM matter power spectrum down to cluster or galaxy scales, but not further. Such a dark matter component is called warm dark matter (WDM). For example, heavy sterile neutrinos could play the role of WDM. As for hot dark matter, the impact of WDM on the matter spectrum depends on its phase-space distribution function. There is a wide variety of equally plausible scenarios for the production of WDM particles, leading to either thermal or nonthermal distributions. For instance, the case of resonantly or nonresonantly produced sterile neutrinos was already mentioned in Section 4.2.5.

Because WDM particles become nonrelativistic during radiation domination, their free-streaming scale remains almost constant between the time of their nonrelativistic transition and of radiation-to-matter equality, as explained in Section 5.2.4. For wavenumbers much smaller than $k_{\rm nr}$ (defined in Eq. (5.96)), the evolution of cosmological perturbations is unaffected by the warm nature of dark matter particles, and equivalent to that in a scenario with an equivalent amount of CDM. The explanation is the same as for HDM in Section 6.1.4: on large scales, before horizon crossing, nonrelativistic matter perturbations obey a universal solution for

adiabatic initial conditions, whereas after horizon crossing, the WDM sound speed and anisotropic stress can be neglected, and density fluctuations are subject to the same equation (6.9) as CDM.

For smaller scales, during the relativistic regime, the WDM mass is negligible and perturbations are subject to the same equations as ultrarelativistic relics. We know from Section 5.2.5 that in this regime, density fluctuations are strongly suppressed on sub-Hubble scales. After the time of the nonrelativistic transition, they start to grow under the effect of gravitational collapse, but at a rate reduced with respect to CDM, due to the fact that pressure and anisotropic stress decay slowly and still play a role in the equations. Hence the WDM power spectrum is suppressed with respect to that of CDM for all small scales with $k > k_{\rm nr}$. The shape of the WDM power spectrum can be studied semianalytically (Boyanovsky and Wu, 2011) or numerically with Boltzmann codes.

We discussed in Section 5.2.4 the difference between the maximum comoving free-streaming scale $[2\pi/k_{\rm nr}]$ and the comoving free-streaming horizon $r_{\rm fs}$. We showed that for HDM particles becoming nonrelativistic after radiation domination, these two quantitites are very close to each other, whereas for WDM particles becoming relativistic during radiation domination, they represent two distinct scales, given by different combinations of parameters (see Eqs. (5.96) and (5.97)). We saw that the difference comes from the fact that between $\eta_{\rm nr}$ and $\eta_{\rm eq}$: the former remains constant, whereas the latter grows logarithmically. Analytical and numerical approaches confirm that the characteristic scale below which the WDM spectrum differs from the CDM one is given by the free-streaming horizon. This matches physical expectations: the suppression of the WDM spectrum with respect to the CDM one is caused by diffusion damping in a medium of collisionless particles, and the diffusion length of an average WDM particle between the early universe and a given time is indeed given by the free-streaming horizon.

Pure warm dark matter

We first consider the case in which all dark matter in the universe is warm. In particular, the ΛWDM scenario shares the same cosmological parameters and physical ingredients as the ΛCDM scenario, except that cold particles are replaced by warm particles with a nonnegligible velocity dispersion. The power spectrum of this model can be parameterized as

$$P_{\Lambda{\rm WDM}}(\eta, k) = P_{\Lambda{\rm CDM}}(\eta, k) T(\eta, k)^2, \tag{6.93}$$

where $P_{\Lambda{\rm CDM}}$ is the spectrum of a model with an equivalent amount of CDM, and $T(\eta, k)$ is a transfer function accounting for the effect of WDM velocities. The previous discussion suggests that $T(\eta, k) = 1$ for $k r_{\rm fs}(\eta) < 1$, whereas $T(\eta, k) < 1$ for $k r_{\rm fs}(\eta) > 1$.

The shape of the transfer function depends on the WDM phase-space distribution. The two most studied cases in the literature are those of

- a thermal WDM relic with a Fermi–Dirac distribution and an unknown temperature $T_{\rm x}$,
- or a nonthermal relic with a rescaled Fermi–Dirac distribution, the same temperature $T_{\rm x} = T_\nu$ as active neutrinos, and some unknown rescaling factor χ.

The latter case is motivated by the possibility that WDM consists of sterile neutrinos, populated by nonresonant interactions with active neutrinos. This model is often called DW after the work of Dodelson and Widrow (1994). We already discussed such distribution functions for light HDM particles in the previous section. Following the same lines, it is easy to show through a change of variable that a DW model with mass, temperature and rescaling factor $(m_{\rm x}, T_\nu, \chi)$ is described by the same equations as a thermal model with mass and temperature

$$(m_{\rm th}, T_{\rm th}) = (\chi^{1/4} m_{\rm x}, \chi^{1/4} T_\nu). \tag{6.94}$$

Following Eq. (6.91), the common WDM density of these two equivalent models is given by

$$\omega_{\rm x} = \chi \left(\frac{T_\nu}{T_\nu^{\rm a}}\right)^3 \frac{m_{\rm x}}{94.1{\rm eV}} = \left(\frac{T_{\rm th}}{T_\nu^{\rm a}}\right)^3 \frac{m_{\rm th}}{94.1{\rm eV}}. \tag{6.95}$$

The first equality can be used to eliminate χ from Eq. (6.94) and find another useful relation between the equivalent mass of the DW and thermal models:

$$m_{\rm x} = 4.43\ {\rm keV} \left(\frac{T_\nu}{T_\nu^{\rm a}}\right) \left(\frac{0.25(0.7)^2}{\omega_{\rm x}}\right)^{1/3} \left(\frac{m_{\rm th}}{1\ {\rm keV}}\right)^{4/3}. \tag{6.96}$$

The numerical study of these two degenerate cases by Bode *et al.*, 2001 (updated by Viel *et al.*, 2005) shows that the transfer function $T(k, \eta)$ is nearly independent of time within the redshift range where the matter power spectrum can be observed, and decays asymptotically like $T(k) \propto k^{-10}$ in the large-k limit. The transition between the two asymptotes is well accounted for by the expression

$$T(k) = \left[1 + (k/k_{\rm break})^p\right]^{-10/p} \tag{6.97}$$

with $p = 2.24$. The value of $k_{\rm break}$ was obtained as a function of the WDM mass-to-temperature ratio and of other cosmological parameters by fitting Eq. (6.97) to numerical results in a range of plausible parameter values:

$$k_{\rm break} = \frac{1}{0.24} X^{0.83} \left(\frac{\omega_{\rm x}}{0.25.(0.7)^2}\right)^{0.16} {\rm Mpc}^{-1} \quad \text{with } X \equiv \frac{m_{\rm x}/T_{\rm x}}{1\ {\rm keV}/T_\nu^{\rm a}}. \tag{6.98}$$

This relation can be applied indifferently to DW and thermal WDM models, because two equivalent models share the same ratio $m_{\rm th}/T_{\rm th} = m_{\rm x}/T_\nu$. Physically, this ratio represents the WDM velocity dispersion up to a numerical factor (we are dealing here with Fermi–Dirac-shaped distributions, with $c_{\rm x} = 3.15\ T_{\rm x}/m_{\rm x}$, as in Eq. (5.91)). The reason for which $k_{\rm break}$ depends on both the velocity dispersion and the warm dark matter density is precisely that this scale is determined by the free-streaming horizon, rather than the maximum free-streaming scale. Equation (5.97) only gives a crude analytic approximation for $r_{\rm fs}$, based on a simplification of the expansion law $a(t)$ and of the velocity evolution $c_{\rm x}(a)$. Still, this approximation is sufficient to explain the parametric dependence of Eq. (6.98). Indeed, if we combine Eq. (5.97) (with the last term neglected for $z \ll z_{\rm eq}$) with Eq. (5.96), and replace $(1 + z_{\rm eq})$ with $(\omega_{\rm x} + \omega_{\rm B})/\omega_{\rm R}$, we get

$$r_{\rm fs} = \frac{3.16 \times 10^{-3}}{\omega_{\rm R}\, X} \left[1 + \frac{1}{2} \ln \left(\frac{\omega_{\rm R}\, X}{5.28 \times 10^{-7} (\omega_{\rm x} + \omega_{\rm B})} \right) \right] \text{Mpc}. \tag{6.99}$$

Replacing $\omega_{\rm R}$ with its fixed value and $\omega_{\rm B}$ with its observed value, one can check that this expression is well fitted by

$$r_{\rm fs} \propto X^{-1} (X/\omega_{\rm x})^{0.16} = X^{0.84} \omega_{\rm x}^{-0.16}, \tag{6.100}$$

at least within the range of phenomenologically interesting values of X. This explains the parametric dependence of the fitting formula (6.98) for $k_{\rm break}$. The WDM transfer function can in fact be written as

$$T(k) = \left[1 + \beta (k r_{\rm fs})^p \right]^{-10/p}, \tag{6.101}$$

where β is a numerical factor. An analytic study of the WDM perturbation evolution by Boyanovsky and Wu, 2011 leads to an approximate expression for $T(k)$ very close to the fitting formula (6.97).

For other nonthermal distributions, results can be derived case by case. By computing the velocity dispersion $c_{\rm x}$ and the density $\omega_{\rm x}$ of a nonthermal WDM species and applying the previous formulas blindly, one may obtain totally inaccurate predictions. For instance, typical WDM distributions for resonantly produced sterile neutrinos (Shi and Fuller, 1999; Laine and Shaposhnikov, 2008) lead to a very different power spectrum than in the thermal or DW case. The reason is that a significant fraction of such WDM particles have a very low velocity and fall into the CDM category. Hence the impact of such a model on the matter power spectrum is closer to that of a mixture of CDM and thermal WDM, briefly reviewed in the next subsection, as illustrated in Boyarsky *et al.*, 2009c. Other examples are discussed by Boyanovsky and Wu, 2011.

Mixture of warm dark matter and cold dark matter

Mixed cold plus warm dark matter models are relevant not only to scenarios where two different particles with very different mass and velocity dispersion contribute to the matter density in the universe but also as an approximation to the case of a unique dark matter particle with a nonthermal distribution (enhanced in the small momentum limit with respect to a thermal distribution), as mentioned in the previous paragraph.

This case is qualitatively similar to the mixed hot plus cold dark matter one, i.e., to a ΛCDM model with massive neutrinos. For scales such that $kr_{\rm fs} \leq 1$, the warm nature of some of the dark matter particles does not play a role, and the model is equivalent to a ΛCDM model with the same total dark matter density. For smaller scales, WDM density perturbations are suppressed with respect to $\delta_{\rm C}$ for the reasons explained at the beginning of Section 6.1.5. One can show that for $kr_{\rm fs} > 1$ one still has $|\delta_{\rm w}| < |\delta_{\rm C}|$ today (as is the case for the density perturbation of massive neutrinos for $k > k_{\rm nr}$). In the small-wavelength limit, the matter power spectrum of a mixed model with a warm fraction $f_{\rm w} \equiv \omega_{\rm w}/\omega_{\rm M}$ is suppressed for two reasons:

- the total matter power spectrum comes from the CDM component only and is reduced by a factor of $(1 - f_{\rm w})^2$, in the same way as with HDM (see Eq. (6.59));
- CDM perturbations $\delta_{\rm C}$ grow at a lower rate because in the usual equation of evolution (6.7), WDM contributes to the Hubble friction term, again as is the case with HDM.

Hence the mixed ΛCWDM power spectrum is steplike suppressed with respect to the ΛCDM one, with just a different scale, shape and amplitude than for light massive neutrinos. The suppression factor in the small-scale limit can be estimated as a function of $f_{\rm w}$ following the same lines as in Section 6.1.4. The only difference is that WDM particles are already nonrelativistic at the approach of radiation-to-matter equality. Boyarsky *et al.* (2009d) provide an approximation for this factor,

$$\frac{P_{\Lambda{\rm WDM}}(\eta_0, k)}{P_{\Lambda{\rm CDM}}(\eta_0, k)} \longrightarrow (1 - f_{\rm w})^2 \left(\frac{a_0\, g(a_0)}{a_{\rm eq}}\right)^{-\frac{3}{2} f_{\rm w}} \simeq 1 - 14 f_{\rm w} + O(f_{\rm w}^2), \quad (6.102)$$

which is clearly different from its counterpart for mixed ΛCHDM models in Eqs. (6.87) and (6.88). The full numerical ΛCWDM power spectrum is presented in the same reference.

We do not discuss here the case of mixed ΛWHDM or ΛCWHDM models, which are similar to the previously discussed cases but with an additional steplike suppression because of the hot relics.

6.2 Nonlinear matter power spectrum

The theory of linear cosmological perturbations presented in Sections 5.1, 5.2 and 6.1 cannot describe matter fluctuations in our universe at small redshift and on small scales. A given comoving Fourier mode k enters into the nonlinear regime when the variance of matter fluctuations integrated in spheres of comoving radius $2\pi/k$ becomes of the same order as the average matter density. The power spectrum of the ΛCDM model leads to hierarchical structure formation, with smaller scales entering earlier into the nonlinear regime.

Thanks to galaxy, cluster and weak lensing surveys, we can observe matter fluctuations on scales significantly larger than the nonlinear scale, but we can compare only observed power spectra with linear predictions up to that scale. The amount of information extracted from a given data set would increase if the comparison could be pushed to smaller scales, under the condition that theoretical errors remain smaller than instrumental errors. This provides a strong motivation for computing power spectra on mildly or even strongly nonlinear scales.

For instance, in measurements of the three-dimensional matter power spectrum $P(k)$, the number of independent modes in the survey scales as the cube of $k_{\rm max}$, the maximum wavenumber at which we trust theoretical predictions and that we decide to include in theoretical fits of the data. Naively, this seems to imply that the error bar on cosmological parameters decreases as $k_{\rm max}^{3/2}$. In fact, the amount of information contained in the matter power spectrum tends to saturate at large $k_{\rm max}$, because deep inside the nonlinear regime, the nonlinear spectrum $P_{\rm nl}(z,k)$ loses sensitivity to early linear perturbations and to the underlying cosmology. However, it remains true that modelling the nonlinear spectrum is a key ingredient for improving the sensitivity of LSS observations to neutrino parameters.

6.2.1 N-body simulations

Nonlinear structure formation can be simulated with N-body codes. In this approach, cold dark matter (as well as eventually baryons and other dark matter species) is represented as a set of N-body particles, with typical mass on the order of a million solar masses or more, not to be confused with fundamental particles. These particles are initially distributed inside a box in such a way that the power spectrum of the smoothed distribution coincides with the linear power spectrum $P(z_{\rm ini},k)$ of a given cosmological model. After this step, they need to be evolved only under gravitational interactions. In current N-body codes, the expansion of the universe is taken into account through a Hubble friction term in the particle equation of motion, but gravitational interactions are computed in the nonrelativistic limit, using the Poisson equation. Indeed, during matter and Λ

domination, simulated particles are nonrelativistic, implying metric fluctuations much smaller than one (because $\phi \sim (v/c)^2$). N-body simulations are performed in boxes in comoving space with periodic boundary conditions. Their comoving spatial resolution scales like the volume of the box divided by the number of particles N.

N-body algorithms

Because gravity is a long-range interaction, the motion of one particle depends on the force exercised by all other particles. A brute-force calculation would imply the computation of $N(N-1)$ forces between pairs of particles, which becomes impossible for millions of particles. Various clever approximations have been discussed and tested in N-body codes.

First, the so-called tree method consists of replacing the force exercised by many particles located in a given region with the force exercised by a unique particle, located at the center of this region and of equivalent mass. Such an approximation does not introduce significant errors provided that this region is far enough from the point at which we want to evaluate the force, and not too dense. The simulation box is divided into large cells, each of them split into smaller subcells, and so on. When evaluating the force on a given particle, a sophisticated algorithm chooses the most appropriate cell size to be used in different regions, with larger cells in remote underdense regions, and smaller cells in nearby overdense regions. Instead of evaluating $(N-1)$ forces from all other particles, the code typically needs to evaluate $\log N$ forces from variable-size cells. Hence, with the tree method, the simulation time scales like $N \log N$.

The particle-mesh (PM) method consists of replacing the true particle distribution at each new time step with a collection of other pointlike particles located at the nodes of a regular grid. The value of the mass placed at each node is obtained by interpolating the underlying particle distribution, in such a way that the two distributions smoothed over a distance larger than the grid size are identical. The new particle distribution can be represented as a mass distribution function $\rho(\vec{x}_i)$ in discrete space, which is easy to expand in Fourier space. The gravitational potential $\psi(\vec{k})$ is then trivially inferred from the Poisson equation and transformed back to real space. Its gradient gives the gravitational force at each point and is used to evolve the set of true particles over one time step. This approach is very fast even with respect to the tree method, but it mistreats gravitational interactions on scales comparable to the grid size or smaller.

The TreePM method is a hybrid approach in which long-range forces are calculated with the PM method, and short-range forces with the tree method. The two approaches are matched smoothly around a scale corresponding to a few PM grid cells. Some state-of-the-art codes such as GADGET (Springel, 2005) are based on

the TreePM approach. There are other powerful methods and codes on the market, but we do not mention them here, because the following discussion of neutrino implementations in N-body codes refers mainly to TreePM methods.

Hot dark matter particles

The first difference between cold and hot particles in an N-body simulation appears at the level of the initial spatial distribution, because these species are subject to different linear power spectra featuring either a cutoff or a steplike suppression on small scales. When two different species coexist, distinct sets of N-body particles must be used for each component, and the initial spatial distribution of each species must reflect its own linear power spectrum. For instance, when simulating a ΛCDM model with massive neutrinos, it is necessary to introduce cold particles with a steplike suppressed spectrum and hot particles with a spectrum with a different slope on small scales, as illustrated in Fig. 6.4. Moreover, it is crucial to compute the linear power spectrum at the correct initial redshift with a linear Boltzmann code, because for mixed models the linear spectra have a nontrivial redshift dependence (and a scale-dependent growth factor). For instance, we have seen in Section 6.1.4 that for fixed neutrino masses, the steplike suppression in the CDM power spectrum is smaller at high redshift than today. Note that the distributions of the two species must be statistically correlated: in a universe with adiabatic initial conditions, overdensities in one species coincide with overdensities in another species, even if the power spectra are different.

This first step raises no particular difficulties. There exist various algorithms for drawing initial particle distributions under the constraint of a given arbitrary power spectrum. These codes are based either on the Zel'dovich approximation (ZA), consistent with first-order perturbation theory, or on second-order Lagrangian perturbation theory (2LPT) for more precise settings. They are not difficult to generalize to the case of several correlated species with distinct spectra.

Second, the initial velocity distribution of N-body particles should reflect the phase-space distribution of fundamental particles in a given HDM model. For cold particles, previously mentioned algorithms (ZA or 2LPT) assign initially to each particle a peculiar velocity consistent with the local gravitational flow, whose divergence is related to the scalar degree of freedom $\theta_{\rm C}$ of linear perturbation theory. This peculiar velocity is often called the Zel'dovich velocity. For hot particles, after assigning Zel'dovich velocities (corresponding to the bulk motion inside the gravitational potential), it is necessary to add random velocities reflecting the phase-space distribution $f_0(y)$. Because N-body codes rely on Newtonian gravity, the starting redshift should be chosen in such way that particles are initially nonrelativistic, so the momentum appearing in the phase-space distribution can be replaced by $p = mv$ (or $y = amv$). Hence, for particles with a thermal distribution, typical

velocities are of the order of $v \sim [\langle p \rangle / m] \sim [T/m]$. Even in the nonrelativistic regime, typical thermal velocities can be significantly higher than Zel'dovich velocities at the initial time. Later, they decrease as the inverse of the scale factor because of the universe's expansion, which is consistently taken into account by the simulation.

The presence of large thermal velocities raises computational difficulties for two reasons. A priori, the integration time step should scale like the inverse of typical velocities in order to resolve particle trajectories with good accuracy. If thermal velocities are higher than Zel'dovich velocities by one or two orders of magnitude, the simulation will be slowed down in the same proportions with respect to a CDM simulation. Second, HDM particles should fill a large volume in phase space. The phase-space volume of cold particles is null, because they are not given any velocity dispersion: initially, they have a unique possible velocity at each point, corresponding to the Zel'dovich velocity. Instead, in the ideal case, hot particles with a thermal velocity higher than the Zel'dovich velocity should have a nearly isotropic velocity distribution in each point, like the true distribution of underlying fundamental particles. In practice, one needs to introduce more hot particles than cold particles in the simulation to obtain consistent results down to a given resolution scale; otherwise the sampling of phase space is not sufficient, and shot noise quickly dominates the evolution, leading to incorrect predictions for the nonlinear power spectrum.

Despite the large CPU time and memory cost of such simulations, consistent results have been obtained by various groups for mixed ΛCHDM models (Brandbyge *et al.*, 2008; Viel *et al.*, 2010; Bird *et al.*, 2012). These works show that because neutrinos experience less clustering than CDM on small scales, their short-range gravitational interactions can be neglected. Hence, in the TreePM code GADGET, the tree part can be evaluated only for CDM particles, whereas the mesh part includes both species. It has also been shown that to follow CDM clustering correctly, it is sufficient to set the integration time step to the same value as in a pure CDM simulation. The main limitation of these simulations comes from memory requirements, in that many neutrino particles are needed to keep shot noise at an acceptable level. Because shot noise is directly related to the phase-space volume of the particles, i.e., to the magnitude of thermal velocities (compared to Zel'dovich velocities), simulations become more difficult for faster particles, i.e., lighter neutrinos. The starting redshift $z_{\rm ini}$ should decrease with the neutrino mass, in order to have low enough thermal velocities when initial conditions are set. But for small masses, $z_{\rm ini}$ may have to be pushed to values at which CDM particles are already in the nonlinear regime, so their initial conditions cannot be set correctly. This problem can be alleviated by making use of the 2LPT algorithm. So far, simulations with cold plus hot particles have been carried successfully with three degenerate neutrino species

of total mass $M_\nu = 3m_\nu \geq 0.15$ eV. These simulations converge to a maximum wavenumber on the order of $k \sim 10\,h$/Mpc.

Alternative approaches for hot dark matter

To study the small-scale nonlinear clustering of a given HDM species, it is unavoidable to model this species with N-body particles, and run heavy simulations. However, to study the nonlinear clustering of CDM and compute the total nonlinear matter power spectrum in mixed ΛCHDM models, it is possible to use several types of approximation. Mistreating neutrinos on small scales is not necessarily an issue, because we expect $\delta_\nu \ll \delta_{\rm C}$ on those scales. For instance, instead of introducing hot particles from the beginning, one can describe neutrinos as a fluid discretized on a grid, following linear equations solved by an external Boltzmann code (Brandbyge and Hannestad, 2009), until some late time at which they are converted into particles, when their thermal velocities are sufficiently small (Brandbyge and Hannestad, 2010). Alternatively, one can postulate some approximate fluid equations for the neutrino component (similar in spirit to those discussed in Section 5.2.5) and treat neutrinos with the same numerical machinery as the baryonic component, i.e., with a smoothed-particle hydrodynamics (SPH) approach, less time-consuming than a pure N-body approach (Hannestad *et al.*, 2012b). The accuracy of these approximate methods is still being discussed and investigated (Bird *et al.*, 2012).

Results for ΛCDM models with massive neutrinos

A consistent picture is emerging from all recent ΛCHDM simulations. We know from Section 6.1.4 that at the linear level, the massive-to-massless power spectrum ratio $P^{f_\nu}(z,k)/P^0(z,k)$ has the shape of a smooth step, departing from one above the wavenumber $k_{\rm nr}$, and reaching a plateau roughly between $k = 1\,h$/Mpc and $10\,h$/Mpc, depending on neutrino masses. The amplitude of the step for fixed $(\Omega_{\rm M}, \omega_{\rm M}, \omega_{\rm B}/\omega_{\rm C})$ is well approximated by Eq. (6.86) or Eq. (6.87), and remains close to $(1 - 8f_\nu)$ for $f_\nu \leq 0.05$ and at $z = 0$.

The same ratio computed from the nonlinear results of N-body simulations has the shape of a spoon (Brandbyge *et al.*, 2008; Viel *et al.*, 2010; Bird *et al.*, 2012; Hannestad *et al.*, 2012b). The results of Bird *et al.*, 2012 for three massive species of total mass $M_\nu = 0.6$ eV are shown in Fig. 6.11. At $z = 0$, the ratio reproduces linear results up to a scale on the order of $k \sim 0.1\,h$/Mpc; then it keeps decreasing until reaching a dip, and finally it goes up at least to the scale at which simulation errors blow up. At redshift zero, the scale of the dip is on the order of $k = 1\,h$/Mpc, and the maximal suppression at this scale is close to $(1 - 10f_\nu)$. At redshift $z > 0$, the same features are observed, but shifted to smaller scales.

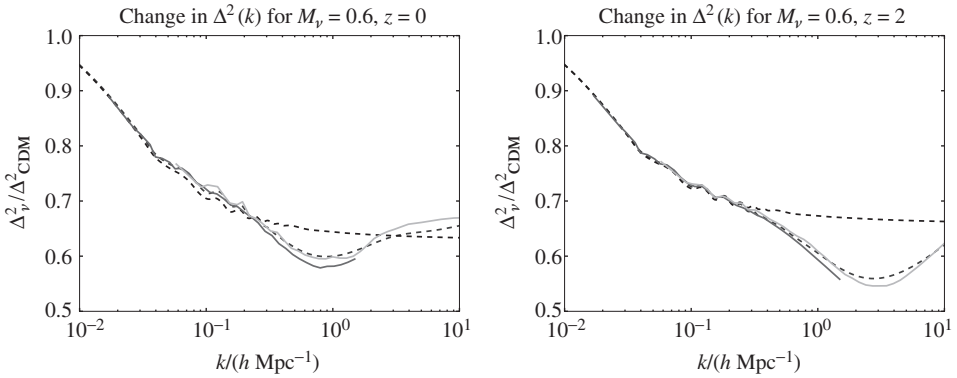

Figure 6.11 Spoon-shaped suppression of the matter power spectrum due to neutrino masses. The solid lines show the power spectrum of a ΛCDM model with three massive species of total mass $M_\nu = 0.6$ eV, divided by that of a massless model with the same parameters ($\Omega_{\rm M}$, $\omega_{\rm M}$). Baryons have been neglected in these simulations. In each plot, the two solid lines correspond to two different N-body simulations with different resolution scales. The step-shaped dashed line shows the linear predictions, studied in Section 6.1.4, whereas the spoon-shaped dashed curve shows the outcome of the fitting formula HALOFIT, recalibrated in order to incorporate massive neutrino effects. (Reprinted from Bird *et al.*, 2012, with permission from Elsevier.)

The spoon shape is easy to understand qualitatively. In the presence of massive neutrinos and for a fixed total matter density $\omega_{\rm M}$, CDM perturbations grow more slowly on scales $k \gg k_{\rm nr}$, at least in the linear theory. Hence, they enter a bit later into the nonlinear regime. The enhancement of the linear power spectrum due to nonlinear clustering is then a bit smaller in the massive case, and this effect adds up to the suppression already observed at the linear level. This explains why the ratio falls to $(1 - 10\,f_\nu)$ instead of $(1 - 8\,f_\nu)$ at redshift zero. On smaller scales, another effect takes over. It is well known that deep inside the nonlinear regime, the matter power spectrum gradually loses memory of initial conditions and becomes insensitive, e.g., to the details of the growth rate of CDM perturbations in the linear regime. So, in the large k limit, the ratio between the power spectrum of a massive and a massless model should reach one asymptotically. At redshift $z > 0$, the same features can be identified at larger wavenumbers, because the scale of nonlinearity is smaller.

Bird *et al.* (2012) have used the results of N-body simulations to re-calibrate the nonlinear power spectrum fitting formula HALOFIT (Smith *et al.*, 2003) in the case of ΛCHDM models with three degenerate neutrinos of arbitrary mass. Brandbyge *et al.* (2010) focused on the impact of massive neutrinos on smaller scales and computed the neutrino density profile in galactic halos, as well as the halo mass

function (number of halos as a function of their mass) in the presence of massive neutrinos.

Warm dark matter particles

In principle, all previous remarks concerning the implementation of HDM particles in N-body simulations may apply to WDM particles. However, the latter case is simpler, because for phenomenologically interesting WDM masses and phase-space distributions, the velocity dispersion of particles at the beginning of a typical N-body simulation (i.e., for $10 < z < 100$) are lower than the Zel'dovitch velocities (Boyarsky *et al.*, 2009d). This means that thermal velocities can be safely neglected in most cases, and that WDM particles are equivalent to CDM particles with an initially different power spectrum, featuring a cutoff for $kr_{\rm fs} > 1$, as explained in Section 6.1.5. However, to resolve the same scales, it is necessary to introduce a larger number of particles in the WDM case (see, e.g., Wang and White, 2007; Lovell *et al.*, 2012). Also, simulations of mixed ΛCWDM models can be carried out with a single type of particles, initially following the linear power spectrum of the cold plus warm components.

Several recent simulations of ΛWDM and ΛCWDM have been carried out in different contexts, for instance, on mildly nonlinear scales, in order to fit data from Lyman-α absorption in quasar spectra, or on strongly nonlinear scales for studying galaxy halo profiles and galaxy satellite abundances. See, e.g., Macciò and Fontanot, 2009; Dunstan *et al.*, 2011; Polisensky and Ricotti, 2011; Schneider *et al.*, 2011; Lovell *et al.*, 2012; Macciò *et al.*, 2012a,b; Viel *et al.*, 2012.

6.2.2 Analytic approaches

Several analytic approaches have been proposed to deal with the computation of the nonlinear power spectrum on mildly nonlinear scales, with the goal of avoiding tedious numerical simulations. Many (but not all) of these methods try to solve the nonlinear continuity and Euler equations of dust (i.e., of cold particles),

$$\begin{aligned} &\delta' + \vec{\nabla}\cdot\left[(1+\delta)\vec{v}\right] = 0 \\ &\vec{v}' + \mathcal{H}\,\vec{v} + (\vec{v}\cdot\vec{\nabla})\vec{v} = -\vec{\nabla}\phi, \end{aligned} \tag{6.103}$$

where the gravitational potential ϕ is given by the Poisson equation. These equations are valid in the single-flow approximation: they neglect shell crossing between various flows of CDM particles, which inevitably appear when modes enter in the deeply nonlinear regime. Such techniques include one-loop calculations, renormalized perturbation theory, and renormalization group methods. Some of these methods have been extended in order to account for a neutrino component: Wong

(2008) and Saito *et al.* (2009) studied one-loop perturbation theory, whereas Lesgourgues *et al.* (2009) used the time renormalization group method. These works treat neutrinos as a linearly evolving species, coupled gravitationally to CDM and baryons, that are subject to the preceding nonlinear equations. The results correctly reproduce the departure from linear theory, although in a very limited range of scales (roughly until $k \simeq 0.2\,h$/Mpc for $z > 2$, or until $k \simeq 0.15\,h$/Mpc at $z = 1$). In the future, new approaches may lead to significant progress in this field.

6.3 Impact of neutrinos on secondary cosmic microwave background anisotropies

We have studied in Chapter 5 the impact of neutrinos on primary CMB anisotropy, defined as the contribution to CMB maps of physical phenomena taking place until the epoch of recombination. Secondary anisotropy, caused by the rescattering or the deflection of CMB photons in the recent universe, can also be sensitive to neutrinos – interestingly, when those are already nonrelativistic. In Chapter 5, we mentioned two sources of secondary anisotropy: the late integrated Sachs–Wolfe (LISW) effect, and the reionization of the universe due to star formation. Without giving a list of all sources of secondary anisotropy, we will briefly review in this section the two secondary effects currently identified as the most relevant for constraining neutrinos: the LISW effect, and CMB weak lensing.

6.3.1 Late integrated Sachs–Wolfe effect

We have seen in Section 5.1.6 that CMB temperature anisotropies pick up an integrated Sachs–Wolfe (ISW) contribution,

$$\frac{\delta T}{T}(\hat{n}) = \int_{\eta_{\rm LS}}^{\eta_0} d\eta\,(\phi' + \psi'), \tag{6.104}$$

where the integral runs along each line of sight. We know from Section 6.1.1 that in the minimal ΛCDM model (without massive neutrinos) and deep inside the matter-dominated regime, the two Newtonian gauge metric fluctuations ϕ and ψ are equal to each other and independent of time. Hence the ISW contribution can be separated into an early and a late term. The second one reads

$$\left.\frac{\delta T}{T}(\hat{n})\right|_{\rm LISW} = 2\int_{\eta_{\rm M}}^{\eta_0} d\eta\,\phi', \tag{6.105}$$

where $\eta_{\rm M}$ is some arbitrary time deep inside the matter-dominated regime. Inside the Hubble radius, the metric fluctuation ϕ can be related to the total density

fluctuation using the Friedmann and Poisson equations:

$$\phi(\eta, k) = -\frac{3}{2}\frac{a^2H^2}{k^2}\delta_{\rm M}(\eta, k). \tag{6.106}$$

Under the matter-dominated regime, the product $[a^2H^2]$ evolves like η^{-2}, whereas matter perturbation grows linearly with the scale factor, i.e., like η^2. We see that indeed ϕ is constant, at least in a first approximation. When we approach Λ domination, $\bar{\rho}_\Lambda$ starts to play a role in the Friedmann equation, and both $[a^2H^2]$ and $\delta_{\rm M}$ start to evolve differently. Then a net integrated Sachs–Wolfe effect accumulates along each line of sight.

In the presence of massive neutrinos, we have seen that the solution for $\delta_{\rm M}(\eta, k)$ and hence for $\phi'(\eta, k)$ is not affected at large scales such that $k \ll k_{\rm nr}$. At smaller scales, $\delta_{\rm M}(\eta, k)$ grows at a lower rate, as $(a\, g(a; \Omega_{\rm M}))^{1-(3/5)f_\nu}$ instead of $a\, g(a; \Omega_{\rm M})$ (see Eq. (6.76)). Hence, ϕ experiences some extra damping during all stages: it decays like $a^{-(3/5)f_\nu}$ during matter domination, and like a more complicated function during Λ domination. For realistic neutrino masses, f_ν is much smaller than one, and this extra damping is very small, but because this effect accumulates over a long duration, it can be important at small redshift.

A subtle point is that neutrino mass has two opposite effects on the LISW contribution. On one hand, in presence of neutrino mass, metric fluctuations are slightly erased on small scales, because of neutrino free-streaming, and the LISW effect tends to be suppressed. On the other hand, ϕ decreases a bit more quickly because of neutrino masses, so in absolute value ϕ' is enhanced. The competition between these two effects has been described with numerical solutions and analytic approximations by Lesgourgues *et al.*, 2008.

The LISW contribution is difficult to observe, because CMB maps mix primary and secondary anisotropy. A change in the LISW contribution to the first few multipoles $l \leq 10$ can affect the slope of the plateau in the CMB spectrum significantly, but these are the scales on which cosmic variance is very large. For higher multipoles the LISW signal is overseeded by primary anisotropies. As explained earlier, the neutrino mass effect is expected to be maximal on small scales. Hence, in practice, the CMB temperature spectrum is insensitive to LISW-induced neutrino mass effects.

However, the LISW contribution can be disentangled from the primary anisotropies by cross-correlating CMB and large-scale structure maps. Various techniques offer the possibility of reconstructing the matter distribution in shells centered on us. For instance, by observing galaxies in all directions and in a given redshift bin (centered on a value z_i), one can infer the map of matter fluctuations in a shell of radius $r_i(z_i)$, modulo a bias factor. With such a map $\delta_{{\rm G}_i}(\hat{n})$, one can compute a harmonic power spectrum $C_l^{{\rm G}_i{\rm G}_i}$, using the same expansion and definitions as

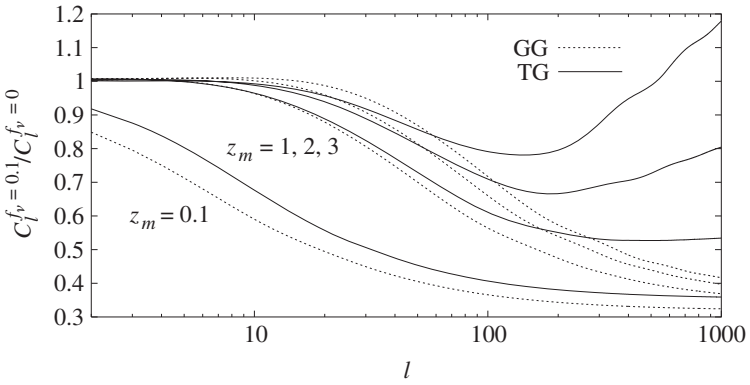

Figure 6.12 Matter autocorrelation spectrum $C_l^{\mathrm{G}_i\mathrm{G}_i}$ and matter–temperature cross-correlation spectrum $C_l^{\mathrm{TG}_i}$ for a model with massive neutrinos, divided by the same quantitites for a model with massless neutrinos. Matter fluctuations have been evaluated in four shells centered on redshift $z_i \in \{0.1, 1, 2, 3\}$. The massive model has a HDM density fraction $f_\nu = 0.1$ due to three degenerate neutrino species with mass $m_\nu = 0.41$ eV each. As in Fig. 6.5, the massless and massive models share the same values of $(\Omega_{\mathrm{M}}, \omega_{\mathrm{M}}, \omega_{\mathrm{B}})$. (Reprinted with permission from Lesgourgues *et al.*, 2008. Copyright 2008 by the American Physical Society.)

for CMB maps (see Section 5.1.6). If the redshift bin is narrow, the map represents matter fluctuations in a thin shell, and the spectrum $C_l^{\mathrm{G}_i\mathrm{G}_i}$ is directly related to the matter power spectrum $P(z_i, k)$ with a one-to-one correspondence

$$k = \frac{a(\eta_i)\, l}{d_{\mathrm{A}}(\eta_i)} \tag{6.107}$$

in the small-angle limit.

The cross-correlation spectrum $C_l^{\mathrm{TG}_i}$ of the temperature and density maps would vanish in the absence of secondary anisotropy; however, the LISW contribution depends on the same structures and gravitational potential distribution as the density map. Therefore, the cross correlation makes it possible to extract the LISW signal in a given redshift bin, given by Eq. (6.105), with the integral running only inside the bin. Because the LISW part depends on ϕ', which can be related to δ'_{M} through the Poisson equation, the cross-correlation spectrum $C_l^{\mathrm{TG}_i}$ depends on both $P(z_i, k)$ and its derivative with respect to time or redshift.

Figure 6.12 illustrates the impact of neutrino masses on the autocorrelation and cross-correlation spectra $C_l^{\mathrm{G}_i\mathrm{G}_i}$ and $C_l^{\mathrm{TG}_i}$ in four redshift bins centered on $z_i \in \{0.1, 1, 2, 3\}$. The autocorrelation spectrum is suppressed by neutrino masses at small angles (large l's) in the same way as the matter power spectrum. The scale of the step is constant in Fourier space (we know that it is given by k_{nr}). But in

angular or harmonic space, this scale is seen under a larger angle (smaller l) at smaller redshift.

Because of these two opposite effects, the effect of neutrino masses on the cross-correlation spectrum is not so trivial. For $z_i = 0.1$, the cross-correlation spectrum follows almost the same steplike suppression as the autocorrelation spectrum. The step is, however, slightly balanced by the fact that in the massive case, time derivatives of metric fluctuations decrease faster. This second effect actually takes over on small angular scales and at high redshift. In this limit, the LISW effect is negligible with massless neutrinos (because metric fluctuations are static) but not with massive neutrinos (because metric fluctuations decay like $\phi \propto a^{-(3/5)f_\nu}$): neutrino masses enhance the cross-correlation spectrum. Lesgourgues *et al.* (2008) showed that for realistic experiments, these effects could be detectable in the future, but with such error bars that this method does not offer such a sensitive probe of neutrino masses as, e.g., galaxy or CMB weak lensing.

6.3.2 Cosmic microwave background lensing

Another source of secondary anisotropies comes from the weak gravitational lensing of the last scattering surface caused by large-scale structure (reviewed by Lewis and Challinor, 2006). The trajectories of CMB photons are slightly deflected by matter fluctuations localized at redshifts $z \leq 3$. At leading order in perturbations, CMB lensing can be described entirely in terms of a two-dimensional deflection field $\hat{d}(\hat{n})$. The deflection field represents the difference between the direction $\hat{n}$ in which photons have been emitted from the last scattering surface, and the direction $\hat{n} + \hat{d}(\hat{n})$ in which they are actually observed. It is given by the gradient of a lensing potential φ, related to the Newtonian metric perturbations ϕ and ψ through a convolution along the line of sight

$$\varphi(\hat{n}) = -\int_{\eta_{\rm LS}}^{\eta_0} d\eta\, \frac{\chi(\eta_{\rm LS}) - \chi(\eta)}{\chi(\eta)\chi(\eta_{\rm LS})}\, (\phi + \psi)_{(\eta, \vec{x}=r(\eta)\hat{n})}, \tag{6.108}$$

where $\chi(\eta)$ is the comoving distance defined in Eq. (2.67) (in a flat universe $\chi(\eta) = r(\eta) = (\eta_0 - \eta)$). During matter domination, we can relate $\phi = \psi$ to matter density fluctuations through the Friedmann and Poisson equation (6.106). Therefore, the harmonic power spectrum $C_l^{\varphi\varphi}$ of a given map $\varphi(\hat{n})$ can be inferred from the matter power spectrum $P(z, k)$, convolved in redhsift space with a given kernel. As expected, in the presence of neutrino masses, the lensing spectrum features steplike suppression on small scales, illustrated in Fig. 6.13.

It is not obvious how to infer the lensing power spectrum from observations, because we can observe CMB anisotropies only after lensing effects take place. The deflection field can, however, be extracted statistically, by studying the

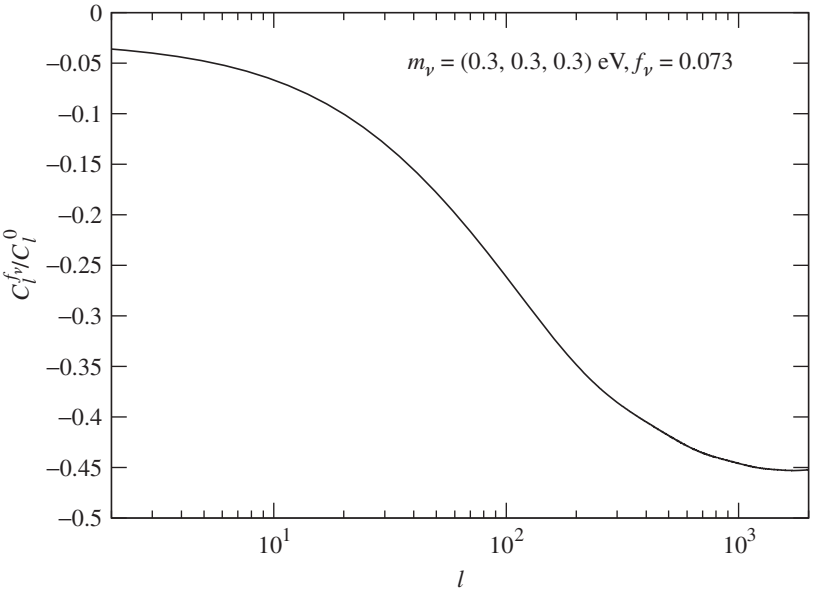

Figure 6.13 CMB lensing spectrum $C_l^{\varphi\varphi}$ for a model with massive neutrinos, divided by the same quantity for a model with massless neutrinos. The massive model has a hot dark matter density fraction $f_\nu = 0.073$ due to three degenerate neutrino species with mass $m_\nu = 0.3$ eV each. As in Fig. 6.5, the massless and massive models share the same values of $(\Omega_{\rm M}, \omega_{\rm M}, \omega_{\rm B})$.

nongaussianity and nontrivial correlations induced by weak lensing in temperature and polarization maps. Okamoto and Hu (2003) and Hirata and Seljak (2003) have discussed various estimators of the lensing power spectrum, which can be seen as nonlinear transformations of CMB maps that make it possible to estimate $C_l^{\varphi\varphi}$ with an error bar given by the spectrum of primary anisotropy and of instrumental noise. Other estimators can be used to reconstruct the lensing deflection map $\varphi(\hat{n})$ or the delensed CMB anisotropy maps. Current and future CMB experiments are able to detect the lensing power spectrum with a good signal-to-noise ratio. Thanks to this technique, the CMB offers an opportunity to probe the effect of neutrino masses on the growth of structure at small redshift $z \leq 3$, with a better sensitivity than through the previously discussed LISW effect.

6.4 Observing the large-scale structure

The matter power spectrum can be probed with various techniques on different scales and at different redshifts. In this section, we give a very brief summary of the methods used (or expected to be used in the future) for constraining neutrino parameters, without entering into any technical detail.

6.4.1 Galaxy and cluster power spectrum

Galaxy maps (or, similarly, cluster maps) can be smoothed over small scales and Fourier transformed in order to provide a power spectrum. Relating such a spectrum to the total matter power spectrum discussed in Sections 6.1 and 6.2 is a tricky exercise for several reasons:

- Galaxies are not perfect tracers of the total dark matter: there is no reason for the relative density perturbation in observed galaxies $\delta_{\rm G}(\eta, \vec{x})$ to be equal to the total matter density perturbation $\delta_{\rm M}(\eta, \vec{x})$. In Fourier space, the relation between galaxy clustering and total matter clustering can be parameterized with a light-to-mass bias function $b(\eta, k) \equiv \delta_{\rm G}(\eta, k)/\delta_{\rm M}(\eta, k)$. Fortunately, several arguments based on numerical simulations, analytical modeling of galaxy formation or comparisons between various data sets show that on linear scales, the bias is independent of k, so that we can relate the power spectrum of galaxies to that of total matter:

$$P_{\rm G}(\eta, k) = b^2(\eta) P(\eta, k). \tag{6.109}$$

  However, the numerical value of the bias factor depends both on time and on the type of galaxies selected in a given data set, because this parameter is related to the way in which galaxies form inside gravitational potential wells. Different galaxy surveys may select different types of galaxies, with different median redshifts, corresponding to specific average bias values. When theoretical predictions are fitted to a given galaxy power spectrum $P_{\rm G}(\eta, k)$, it is customary to leave the bias as a free parameter and to marginalize the posterior parameter probability over it. Hence, data on the galaxy power spectrum probe the shape of the matter power spectrum, but not its overall amplitude. Eventually, some prior on the bias can be inferred from higher-order statistics or from simulations.
- For each object, a given survey measures the sky coordinates (i.e., two angles (θ, ϕ)) and the redshift. Hence, actual galaxy maps are obtained in redshift space (θ, ϕ, z), rather than in spherical comoving coordinates (θ, ϕ, r). To measure the three-dimensional Fourier spectrum $P(k)$, it is necessary to convert redshifts into comoving distances. Assuming a fiducial cosmology, one can perform such a conversion using Eqs. (2.8), (2.67). These relations take into account the average Hubble flow, but not the peculiar velocities of individual objects, induced by coherent motions of galaxies inside potential wells, that affect each redshift through the Doppler effect. Hence, this operation introduces an error on the power spectrum (or in other words, a k-dependent bias) known as the redshift-space distortion. This distortion remains negligible for scales in the linear regime,

corresponding to sufficiently small Fourier modes of the velocity field, and becomes important on nonlinear scales.

- We have seen in Section 6.2 that on small scales, it is not a trivial exercise to model nonlinear corrections to the linear power spectrum with sufficient accuracy.

In summary, fitting a theoretical linear power spectrum to some real data set is not too difficult on large (linear) scales provided that the linear bias is marginalized over, whereas on small (nonlinear) scales it is necessary to model nonlinear biasing, redshift-space distortions and nonlinear corrections. Moreover, on small scales, the nonlinear evolution alters the (a priori gaussian) statistics of primordial perturbations. In principle, this should also be taken into account in the expression for the data likelihood.

These complications can be avoided by limiting theoretical fits to very large scales, but then a lot of information contained in the data is not used. It is a major challenge to push the comparison to smaller scales without introducing systematic errors larger than the statistical errors of the data set. Swanson *et al.* (2010) illustrate how uncertainties in the modeling of nonlinear corrections, nonlinear biasing and redshift space distortions affect the sensitivity of galaxy surveys to neutrino mass measurements.

In the following, we will show bounds on the shape of $P(z, k)$ derived from three recent data sets: the halo power spectrum of the Large Red Galaxy (denoted later as Gal-LRG), measured by Reid *et al.*, 2010a, the spectrum of the MegaZ catalogue (Gal-MegaZ), used by Thomas *et al.*, 2010 and the WiggleZ Dark Energy Survey (Gal-WiggleZ), used by Riemer-Sørensen *et al.*, 2012. The first two data sets are actually extracted from the same big survey, the Sloan Digital Sky Survey (SDSS). Technical details on the different methods and underlying assumptions can be found in these references.

For sufficiently deep galaxy surveys, it is possible to separate galaxies into redshift bins and compute different correlation functions at different redshifts. This technique, called tomography, can be very useful for constraining the scale-dependent growth factor induced by neutrino masses. In that case, the data can be reduced to a set of two-dimension power spectra in different shells, instead of a three-dimensional power spectrum with a given median redshift. For a given shell, corresponding to a given redshift bin, the density in each direction $\delta_{\rm G}(\hat{n})$ can be expanded in spherical harmonics. It is then possible to estimate the harmonic power spectrum $C_l^{\rm GG}$ in each redshift bin, using the same definition as for the CMB power spectrum (see Section 5.1.6). We already saw such a quantity in Section 6.3.1. Recently, such a tomographic analysis was used by Xia *et al.*, 2012 for constraining neutrinos, using galaxies from the Canada–France–Hawaii-Telescope Legacy Survey (CFHTLS), split into three redshift bins covering the ranges

$0.5 < z < 0.6$, $0.6 < z < 0.8$ and $0.8 < z < 1.0$ (this data set will be denoted as Gal-CFHTLS).

Several galaxy surveys with better sensitivity and larger volume are about to release data or have been planned over the next decades, including the Baryon Oscillation Spectroscopic Survey[4] (BOSS), the Dark Energy Survey[5] (DES), the Large Synoptic Survey Telescope[6] (LSST) and the Euclid satellite.[7] Also, Wang *et al.*, 2005 pointed out that in the future, accurate measurements could be inferred from cluster surveys. Because clusters are more luminous than galaxies, they can be mapped up to higher redshift. One advantage of gathering high-redshift data is that they can be used to probe the same comoving scale at a time when perturbations are closer to the linear regime.

6.4.2 Cluster mass function

Instead of probing the matter power spectrum $P(z, k)$ directly from the spatial distribution of objects, it is possible to constrain integrated quantities of the type $\int dk\, P(k)W(k)$, where $W(k)$ stands for a given window function. One such quantity is related to the histogram of cluster masses. If the mass of a significant number of galaxy clusters within a given redshift bin is known, this histogram gives an estimate of the so-called *cluster mass function*, $dn(M, z)/dM$, with dn being the number of clusters of redshift approximately equal to z, and with a mass in the range $[M, M + dM]$. This function is related to $\sigma^2(M, z)$, the variance of the density in spheres enclosing a mass M, itself derived from the convolution of the power spectrum $P(z, k)$ with an appropriate window function. Although one should in principle compute $dn(M, z)/dM$ for each theoretical model and compare it to the raw data, it is customary to reduce observational constraints to a single bound on a combination of the two cosmological parameters to which this method is mostly sensitive. The first parameter, called σ_8, is related to the amplitude of the linear power spectrum today on typical cluster scales. Its square gives the variance of the density in spheres of radius $R = 8\,h^{-1}$Mpc. This parameter is obtained by convolving $P(z, k)$ with a given window function at $z = 0$. The second parameter is $\Omega_{\rm M}$: it specifies both the fraction of the total energy density in the universe in the form of clustering matter, and the linear growth factor $g(z; \Omega_{\rm M})$ (neglecting massive neutrino effects). Approximate constraints from cluster abundances take the form of a measurement of $\sigma_8\Omega_{\rm M}^{\alpha}$, where α is an exponent depending on the details of the catalogue and of the method (in particular, on how the clusters have been selected).

[4] cosmology.lbl.gov/BOSS/. [5] www.darkenergysurvey.org/.
[6] www.lsst.org/. [7] sci.esa.int/euclid.

In the following we will refer to bounds derived from cluster abundances probed by X-ray observations from the ROSAT survey, presented by Mantz *et al.*, 2010 (denoted later as Clus-ROSAT), and by optical observations from the MaxBCG catalogue, presented by Reid *et al.*, 2010b (denoted later as Clus-MaxBCG). Cluster abundances are also probed by weak lensing observations, but current bounds on the total neutrino mass from this method do not compete with the ones mentioned (Kristiansen *et al.*, 2007).

6.4.3 Galaxy weak lensing

The images of observed galaxies are distorted by gravitational lensing effects, caused by density fluctuations along the line of sight. One of these effects is called cosmic shear. It corresponds to the squeezing of an image in one direction in the sky, and its stretching in the orthogonal direction. Because such distortions are coherent over the angular size of the lensing potential wells responsible for lensing, they tend to align the apparent major axis of galaxies slightly in a given patch of the sky. Hence the average cosmic shear in a given direction can be estimated statistically by averaging over major axis orientations.

Let us consider a catalogue of galaxy images, and assume that the number density of galaxies per redshift $g(z)$ is roughly isotropic. Assuming a fiducial cosmology, one can infer from $g(z)$ the density of galaxies with respect to comoving radius, $g(r)$. The galaxy catalogue can be divided into small solid angles or pixels. Because the intrinsic orientation of apparent galaxy major axes is randomly distributed (at least to a good approximation), the average orientation in each pixel gives an estimate of the average cosmic shear in the direction of the pixel, up to a shot noise term which decreases when the number of galaxies per pixel increases.

The distortion of a source galaxy sitting at coordinates $(\theta, \phi, r_{\rm s})$, corresponding to the direction of observation $\hat{n} = (\theta, \phi)$, is related to the metric fluctuations ϕ and ψ integrated along the line of sight and weighted by a given kernel,

$$\varphi(\hat{n}; r_{\rm s}) = -\int_{\eta_s}^{\eta_0} d\eta \, \frac{\chi(\eta_{\rm s}) - \chi(\eta)}{\chi(\eta)\chi(\eta_{\rm s})} \, (\phi + \psi)_{(\eta, \vec{x} = r(\eta)\hat{n})}, \tag{6.110}$$

where $\chi(\eta)$ and $r(\eta)$ are respectively the comoving distance and radial coordinate of an object seen at time η. This expression for the lensing potential φ is identical to the one presented in Section 6.3.2 for CMB lensing, although the source is now located at an arbitrary point rather than on the last scattering surface. Because observations probe the metric fluctuations at sub-Hubble distances, we can identify ϕ and ψ with the gravitational potential. For an ensemble of galaxies distributed according to the selection function $g(r_s)$, the average observed cosmic shear is

given by the average lensing potential

$$\varphi(\hat{n}; g) = \frac{\int_0^{r_s^{\max}} dr_s\, g(r_s)\, \phi(\hat{n}; r_s)}{\int_0^{r_s^{\max}} dr_s\, g(r_s)}. \tag{6.111}$$

The analysis of a catalogue of images leads to a map of the lensing potential $\varphi(\hat{n}; g)$, which can be expanded in spherical harmonics. It is then possible to measure the harmonic lensing power spectrum $C_l^{\varphi\varphi}$, using the same definition as for the CMB power spectrum (see Section 5.1.6), and to compare it with theoretical predictions. After equation (6.110) is expanded in spherical harmonics, it is easy to show that the theoretical lensing spectrum $C_l^{\varphi\varphi}$ is given by the convolution of $P(z, k)$ with an appropriate kernel. Typically, $C_l^{\varphi\varphi}$ depends on the average matter power spectrum $P(z, k)$ over a redshift range $0 \leq z \leq z_e$, where z_e is the redshift of an object located at half the distance to the source (i.e., at the Einstein radius), and over a wavenumber range corresponding to the size of objects located at the same redshifts and seen under an angle $\theta = \pi/l$. Hence, the small-scale suppression of $P(z, k)$ as a function of k due to neutrino masses is visible in the lensing spectrum $C_l^{\varphi\varphi}$ in the large l limit. However, the step in $P(k)$ (or the spoon shape of Fig. 6.11, if we take into account nonlinear corrections) is smoothed by the various integrals leading to $C_l^{\varphi\varphi}$. Still, the advantage of cosmic shear observations is that they are directly related to the density power spectrum $P(k)$: they make it possible to measure cosmological parameters without any assumption on the light-to-mass bias function $b(k)$.

If the number of source galaxies is sufficient, it is possible to split the catalogue in several redshift bins i, described by selection functions $g_i(r)$ such that $g(r) = \sum_i g_i(r)$, and to measure the lensing spectrum $C_l^{\varphi_i\varphi_i}$ in each redshift bin. Because sources in each bin are sensitive to the gravitational potential integrated up to a different comoving radius r and a different conformal times $\eta = \eta_0 - r$, this tomographic approach makes possible a three-dimensional reconstruction of the gravitational potential in our past-line cone and is sensitive to the variation of the power spectrum with redshift. As for galaxy redshift surveys, cosmic shear tomography is particularly useful for measuring neutrino masses, because it can probe the scale-dependent growth factor induced by neutrino masses, over an extended range of redshifts.

Current cosmic shear surveys make it possible to put bounds on neutrino parameters: we will refer later to results from the CFHTLS presented by Tereno *et al.*, 2009 and denoted as WL-CFHTLS. Spectacular improvements are expected from future cosmic shear surveys like Pan-STARRS,[8] or the DES, LSST and the Euclid surveys already mentioned in Section 6.4.1.

[8] pan-starrs.ifa.hawaii.edu/.

6.4.4 Cosmic microwave background lensing

We have already described CMB lensing in Section 5.1.6. This technique leads to another lensing spectrum $C_l^{\varphi\varphi}$ which is complementary to the one inferred from tomographic weak lensing surveys. This spectrum can be seen as coming from an ultimate redshift bin corresponding to sources with a radial coordinate $r_s = r_{LS}$, lensed mainly by structures up to $z \sim 3$. The CMB lensing spectrum in a small region of the sky has been estimated by the South Pole Telescope[9] (SPT), but with too large error bars to give interesting constraints on neutrinos. In the next section, we will mention the expected sensitivity of CMB lensing observations by Planck[10] and several ground-based instruments.

6.4.5 Lyman alpha forests

The most luminous and distant compact objects that we can observe are quasars. Some of the photons emitted by quasars interact along the line of sight. In particular, a fraction of photons are absorbed at the Lyman alpha wavelength by hydrogen atoms located in the interstellar galactic medium (IGM). The absorbed fraction in a given point of the photon trajectory is proportional to the local density of neutral hydrogen. Because photons are continuously redshifted, absorption at a given point is seen by the observer as a depletion of the spectrum at a given frequency. Hence, inside a limited range called the *Lyman alpha forest*, the frequency dependence of quasar spectra is a tracer of the spatial fluctuations of the hydrogen density along the line of sight. Lyman alpha forests in quasar spectra offer an opportunity to reconstruct the hydrogen density fluctuation along several lines of sight in a given redshift range. After Fourier expanding each spectrum and averaging over many spectra, one gets an estimate of the so-called flux power spectrum $P_F(z, k)$.

If this spectrum were probing only linear scales, we could assume that hydrogen fluctuations are equal to total baryon fluctuations, which in turn are equal to total matter fluctuations after the baryon drag epoch. In that case, the flux power spectrum would be directly related to the linear one-dimensional matter power spectrum $P_{1D}(k)$, which is related to the usual three-dimensional $P(k)$ through a simple integral. Unfortunately, the flux power spectrum does not probe linear scales, but mildly nonlinear scales. In order to relate $P_F(z, k)$ to $P(k)$, it is necessary to perform N-body simulations with a hydrodynamic treatment of baryons, accounting for the complicated thermodynamic evolution of the IGM (which depends on star formation). Also, a limitation of this technique comes from the fact that the emitted quasar spectra already have a nontrivial frequency dependence, and that photons

[9] pole.uchicago.edu/. [10] www.rssd.esa.int/planck/.

are affected by several other effects than Lyman alpha absorption along the line of sight. Nevertheless, a careful modeling of all relevant effects makes it possible to obtain interesting constraints. The fact that Lyman alpha forests probe mildly nonlinear scales rather than strongly nonlinear ones is of course crucial for keeping systematic errors under control. Lyman alpha observations typically constrain the matter power spectrum in the wavenumber range $0.3 < k < 3\,h$/Mpc and in the redshift range $2 < z < 5$.

In the next section we will mention neutrino bounds inferred from quasar spectra obtained by the SDSS and presented in Viel *et al.*, 2010, denoted as Lyα-SDSS.

6.4.6 21-cm surveys

Instead of mapping the distribution of hydrogen atoms through the absorption rate of photons traveling from quasars, it should be possible to observe directly the photons emitted by these atoms at a wavelength $\lambda = 21$ cm, when they flip from one hyperfine level to the other. While travelling towards the observer, these photons are redshifted, and they are seen with a wavelength indicating the position of the emitting atoms in redshift space.

Recent theoretical progress in this field shows that using this technique, future dedicated experiments should be able to map hydrogen and hence baryonic fluctuations at very high redshift (typically $6 < z < 12$) and to probe the matter power spectrum deep inside the matter-dominated regime on linear scales (Pritchard and Loeb, 2011). This field is still in its infancy, and the forecasts presented in the next section have to be taken with care, because of the difficulty of making a realistic estimate of systematic errors in future data sets.

6.5 Large-scale structure bounds on neutrino properties

6.5.1 Active neutrino masses

Current bounds

Using LSS observations in combination with CMB data offers an opportunity to observe (or to bound) the steplike suppression of the matter power spectrum in the presence of neutrino masses, explained in Section 6.1.4 and illustrated in Fig. 6.5. The use of CMB data is crucial to constrain parameters such as the baryon density, the primordial spectrum amplitude, the tilt and a combination of $\omega_{\rm M}$ and h. Without such constraints, there would be too much freedom in the matter power spectrum fitted to LSS data for identification of a smooth steplike suppression.

Current data sets are far from reaching the sensitivity required to probe the mass splitting of the total mass $M_\nu = \sum_i m_{\nu_i}$ between different species, whose effect is

Table 6.1 *95% CL upper bounds on the total neutrino mass M_ν in eV, for various combinations of CMB, homogeneous cosmology and LSS data sets*

Data	Reference	$w=-1$	$w\neq -1$
WMAP7+Gal-LRG+H_0	(Komatsu *et al.*, 2011)	0.44	0.76
WMAP5+Gal-MegaZ+BAO+SNIa	(Thomas *et al.*, 2010)	0.325	0.491
WMAP5+Gal-MegaZ+BAO+SNIa+H_0	(Thomas *et al.*, 2010)	0.281	0.471
WMAP7+Gal-WiggleZ	(Riemer-Sørensen *et al.*, 2012)	0.60	–
WMAP7+Gal-WiggleZ+BAO+H_0	(Riemer-Sørensen *et al.*, 2012)	0.29	–
WMAP7+Gal-CFHTLS	(Xia *et al.*, 2012)	0.64(0.44)	–
WMAP7+Gal-CFHTLS+H_0	(Xia *et al.*, 2012)	0.41(0.29)	–
WMAP5+BAO+SNIa+Clus-ROSAT	(Mantz *et al.*, 2010)	0.33	0.43
WMAP5+H_0+Clus-MaxBCG	(Reid *et al.*, 2010b)	0.40	0.47
WMAP5+BAO+SNIa+WL-CFHTLS	(Tereno *et al.*, 2009)	0.53	–

Note: The first seven lines refer to galaxy power spectrum measurements, the next two lines to cluster mass function measurements and the last line to a weak lensing survey. The acronyms of CMB and homogeneous cosmology data are introduced in Section 5.4.1, those of LSS data in Sections 6.4.1, 6.4.2 and 6.4.3. Bounds in the first column assume a minimal ΛCDM model with massive neutrinos (seven parameters). In the last column, the cosmological constant was replaced with a dark energy component with arbitrary equation-of-state parameter w (eight parameters).

described in Section 6.1.4. The constraints mentioned in the following have been derived in the case of three degenerate neutrinos with mass $m_\nu = M_\nu/3$, but they roughly apply to the total mass of any scenario. Also, the bounds shown in the first column of Table 6.1 have been obtained under the assumption of a minimal ΛCDM model with massive neutrinos, featuring seven free parameters. More conservative bounds are sometimes derived for basic extensions of this model, with one or two more parameters. The constraints do not change significantly on assuming, for instance, a primordial spectrum with a running of the tilt $[d\ln n_{\rm s}/d\ln k]$ or a significant contribution to the CMB from primordial gravitationnal waves (Reid *et al.*, 2010b). Parameters known to be slightly degenerate with neutrino masses and leading to weaker bounds are w, the equation-of-state parameter of a dark energy component (substituting the cosmological constant), and $N_{\rm eff}$. The degeneracy with w, explained in Hannestad, 2005a, is illustrated by the last column in Table 6.1. The degeneracy with $N_{\rm eff}$, explained in Hannestad and Raffelt, 2004 or Crotty *et al.*, 2004, will be discussed in Subsection 6.5.2.

We summarize in Table 6.1 the main constraints on M_ν at the time of writing, obtained from combinations of CMB plus homogeneous cosmology data (see Section 5.4.1), galaxy power spectrum data (see Section 6.4.1) and cluster abundance data (see Section 6.4.2). In the case of the Gal-WiggleZ, Gal-CFHTLS and WL-CFHTLS data, bounds were presented for only the seven-parameter model. For the

Gal-CFHTLS case, the first bounds correspond to a conservative analysis limited to scales for which nonlinear corrections are small and well under control, whereas the bounds in parentheses rely on including slightly smaller scales.

Including Lyman alpha data is a delicate issue. It requires extensive *N*-body simulations with a hydrodynamic treatment of baryons and of the thermodynamics of the IGM (see Section 6.2), as well as extra HDM particles (see Section 6.4.5). On has to keep under control systematic errors coming both from uncertainties on the flux power spectrum, and from the fact that simulations can be performed for only a limited number of models and must be extrapolated to other models following some particular scheme. A few bounds in the literature were derived without including HDM particles in simulations, or with data sets probably affected by large systematic errors (because these data indicated a global power spectrum amplitude significantly larger than the one derived from CMB data). A conservative analysis based on Ly-α-SDSS data was presented by Viel *et al.*, 2010. In this case, neutrinos were included as HDM particles in *N*-body simulations, and the data were marginalized over a global normalization factor. This analysis gives a bound $M_\nu < 0.9$ eV (95% CL) from Ly-α-SDSS data alone.

In conclusion, the combination of available data sets to date indicates that the total neutrino mass is below 0.3 eV at the 95%CL (0.5 eV if we allow for dark energy with arbitrary w). This means that the degenerate scenario in which all neutrinos share roughly the same mass is almost excluded. The data are about to probe the region in which masses are different from each other, and are ranked according to the NH or IH scenario (see Section 1.4.1). Other recent summaries of existing bounds have recently been presented (González-García *et al.*, 2010; Hannestad, 2010; Reid *et al.*, 2010b; Abazajian *et al.*, 2011; Komatsu *et al.*, 2011; Wong, 2011).

Future bounds

In the very near future, significant improvements in the neutrino mass bounds will be triggered by the Planck CMB satellite and the Baryon Oscillation Spectroscopic Survey (BOSS). The forecasts presented in Perotto *et al.*, 2006 predict a neutrino mass sensitivity of $\sigma(M_\nu) \sim 0.1$ eV from Planck alone, using the lensing extraction technique of Okamoto and Hu, 2003. This would be twice as good as without lensing extraction. Sekiguchi *et al.* (2010) find that the combination of Planck (with lensing extraction) with BAO-scale information from BOSS could lower the error to $\sigma(M_\nu) \sim 0.06$ eV. Gratton *et al.* (2008) find that adding Lyman alpha data from BOSS should lead to comparable sensitivities, and even better results might be expected from the addition of galaxy power spectrum data from the same survey.

With better tomographic data (for either galaxy clustering or cosmic shear), it will become possible to probe the scale dependence of the growth factor induced by neutrino masses (or in other words, the fact that the steplike suppression has an amplitude increasing with time, as illustrated in Fig. 6.10) and to reach spectacular sensitivites. We present below the typical sensitivity expected for a collection of planned surveys (not all approved). These numbers should be taken with care, because forecasts are based on an idealization of each experiment, as well as on several assumptions such as the underlying cosmological model, or even the fiducial value of the neutrino mass itself.

Lahav *et al.* (2009) find that the measurement of the galactic harmonic power spectrum in seven redshift bins by the Dark Energy Survey (DES) should lead to a sensitivity of $\sigma(M_\nu) \sim 0.06$ eV when combined with Planck data (without lensing extraction). Similar bounds were found by Namikawa *et al.*, 2010 for another combination of comparable experiments. This shows that at the horizon of 2014 or 2015, a total neutrino mass close to $M_\nu \simeq 0.1$ eV could be marginally detected at the 2σ level by cosmological observations. Because this value coincides with the lowest possible total mass in the inverted hierarchy scenario, the latter could start to be marginally ruled out in case the data still prefer $M_\nu = 0$.

Kitching *et al.* (2008) find that the sensitivity of cosmic shear data from a satellite experiment comparable to Euclid would shrink to $\sigma(M_\nu) \sim 0.03$ eV in combination with Planck (without lensing extraction). The forecast of Carbone *et al.*, 2011, based on galaxy clustering data also from Euclid (completed at small redhsift by similar data from BOSS), gives comparable numbers. Constraints based on the ground-based Large Synoptic Survey Telescope should be slightly weaker (Hannestad *et al.*, 2006). Hence, in the early 2020s, we expect that a combination of cosmological data sets could detect the total neutrino mass of the normal hierachy scenario, $M_\nu \simeq 0.05$ eV, at the 2σ level. If the total mass is instead close to $M_\nu \simeq 0.1$ eV, it will be detected at the 4σ level. However, in that case, available experiments will not have enough sensitivity to make the difference between an inverted and a normal hierarchy scenario with the same M_ν: the mass-splitting effects illustrated in Figure 6.9 are too small to be detected by such surveys (Lesgourgues *et al.*, 2004).

Even more progress could be provided by 21-cm surveys (see Section 6.4.6). It is difficult to make reliable predictions for this technique, given the number of unanswered questions needing to be addressed first. Pritchard and Pierpaoli (2008) find a sensitivity of $\sigma(M_\nu) \sim 0.075$ eV for the combination of Planck with the Square Kilometer Array (SKA) project, or $\sigma(M_\nu) \sim 0.0075$ eV with the Fast Fourier Transform Telescope (FFTT). However, they show that such impressive experiments would still fail in discriminating between the NH and IH scenarios

(of course, such a question would still be around only if the detected total mass is not smaller than 0.1 eV).

An eventual post-Planck CMB satellite or post-Euclid survey would also have a great potential. Lesgourgues *et al.* (2006) find that a CMB satellite of the next generation could get $\sigma(M_\nu) \sim 0.03$ eV alone, thanks to a very precise reconstruction of the CMB lensing potential. Wang *et al.* (2005) discuss the potential of cluster surveys. Finally, Jimenez *et al.* (2010) show how far the characteristics of a hypothetical galaxy or cosmic shear survey should be pushed to discriminate between two allowed NH and IH scenarios with the same total mass.

6.5.2 Neutrino abundance and light sterile neutrinos

The relevance of LSS observations for measuring the effective neutrino number $N_{\rm eff}$ was stressed in Section 6.1.3. Let us recall that the matter power spectrum has a very small dependence on $N_{\rm eff}$ when this parameter is varied while ($\Omega_{\rm M}$, $z_{\rm eq}$, $\omega_{\rm B}/\omega_{\rm C}$) are kept fixed: only the scale of BAOs is affected by such a transformation (see Fig. 6.2, solid versus dashed curve). However, both CMB and BAO data fix $\omega_{\rm B}/\omega_\gamma$, not $\omega_{\rm B}/\omega_{\rm C}$. The matter power spectrum amplitude and slope do change on small scales when $N_{\rm eff}$ is varied while ($\Omega_{\rm M}$, $z_{\rm eq}$, $\omega_{\rm B}$) are kept fixed (see Fig. 6.2, solid versus dotted curve). Hence, a measurement of the matter power spectrum with a good resolution of the BAO scale and/or in combination with CMB data is sensitive to $N_{\rm eff}$.

Bounds on $N_{\rm eff}$ for negligible neutrino masses

Let us first discuss the bounds on $N_{\rm eff}$ obtained under the assumption that all neutrinos (or other possible light relics) have negligible masses with respect to the sensitivity of current experiments (i.e., with respect to 0.1 eV). In that case, the minimal model to be fitted to the data has seven free parameters. For such a model, Reid *et al.* (2010b) find $N_{\rm eff} = 4.16^{+0.76}_{-0.77}$ (68% CL) for WMAP7+H_0+Gal-LRG, and $N_{\rm eff} = 3.77^{+0.67}_{-0.76}$ (68% CL) for WMAP5+H_0+Clus-MaxBCG (for the meaning of these acronyms, see Sections 5.4.1, 6.4.1 and 6.4.2). Using the most recent galaxy power spectrum data, Xia *et al.* (2012) find $N_{\rm eff} = 3.98^{+1.04}_{-0.51}$ (68% CL) for WMAP7+H_0+Gal-CFHTLS.

By comparing these numbers with those presented in Section 5.4.2 for various combinations of CMB and homogeneous cosmology data sets, we see that current LSS experiments do not play an important role in bounding $N_{\rm eff}$. The best complementary data sets to WMAP are still small-scale CMB data (from SPT and ACT), Hubble parameter data (referred as H_0 or OHD in Section 5.4.2), or BAO-scale data. Hence we refer the reader to Section 5.4.2 for a detailed discussion of current

bounds on $N_{\rm eff}$, on how much they depend on the underlying model, and on their possible implications.

In the future, the sensitivity of LSS experiments to $N_{\rm eff}$ will increase significantly. Perotto *et al.* (2006) find that using lensing extraction, Planck can lower the error bar from $\sigma(N_{\rm eff}) \sim 0.5$ to $\sigma(N_{\rm eff}) \sim 0.3$. Kitching *et al.* (2008) find that the combination of cosmic shear data from a satellite experiment comparable to Euclid would give $\sigma(N_{\rm eff}) \sim 0.1$ when combined with Planck. The forecast of Carbone *et al.* (2011) based on galaxy clustering data also from Euclid (completed at small redshift with similar data from BOSS and combined again with Planck) gives $\sigma(N_{\rm eff}) \sim 0.09$. Such a sensitivity would still not be sufficient to test the details of neutrino decoupling in the standard scenario, leading to $N_{\rm eff} = 3.046$, but it could exclude at high significance the assumption of extra light relics, unless their density is very much suppressed with respect to that of active neutrinos.

Bounds on $N_{\rm eff}$ in the presence of active/sterile neutrino masses

If we allow simultaneously for extra light degrees of freedom and small masses (for active neutrinos and/or for these extra relics), observational bounds become rather model-dependent. Indeed, the effect of the corresponding parameters can be degenerate, to a limited extent (Crotty *et al.*, 2004; Hannestad and Raffelt, 2004). Furthermore, mass-splitting issues can become relevant in this case. We saw in Section 6.5 that in a minimal scenario with $N_{\rm eff} \simeq 3$ and a given total mass $M_\nu \geq 0.1$ eV, the difference between NH and IH is almost impossible to detect. However, in a scenario with $N_\nu > 3$, there are a priori no oscillation data constraining the difference between active and sterile neutrino masses, so we could equally well assume that the total mass resides mainly in one sterile species, or is split equally between all species. With high enough values of $N_{\rm eff}$ and M_ν, these two assumptions lead to significant differences in the matter power spectrum (qualitatively similar to those illustrated in Fig. 6.8), and each of them should be studied separately.

For instance, Hamann *et al.* (2010) investigated several cases, including that of three massless active neutrinos plus $N_{\rm s}$ degenerate neutrinos of mass $m_{\rm s}$ each. For the data combination WMAP7 + ACBAR + BICEP + QuAD + H_0 + Gal-LRG, they find

$$3.046 < N_{\rm eff} < 6.15, \qquad m_{\rm s} < 0.66\,{\rm eV} \quad (95\%{\rm C.L.}). \tag{6.112}$$

When they assume instead three degenerate active neutrinos of mass m_ν each, plus $N_{\rm s}$ massless sterile neutrinos, they find for the same data

$$3.10 < N_{\rm eff} < 6.80, \qquad m_\nu < 0.42\,{\rm eV} \quad (95\%{\rm C.L.}). \tag{6.113}$$

Finally, Giusarma *et al.* (2011) assumed a third scenario with three degenerate active neutrinos, each with mass m_ν, plus N_s degenerate neutrinos of mass m_s each. For the data combination WMAP7+H_0+Gal-LRG they quote the bound

$$3.26 < N_\mathrm{eff} < 7.66, \quad m_\nu < 0.36\,\mathrm{eV}, \quad m_\mathrm{s} < 0.70\,\mathrm{eV} \quad (95\%\mathrm{C.L.}). \qquad (6.114)$$

The bounds for sterile neutrinos are larger because m_s can correspond to fewer than three species, whereas m_ν is always shared among three species. These bounds are already outdated (especially by SPT), but they illustrate the difference between various cases. For each of these cases, the correlations between N_eff and masses (illustrated by contour plots which can be found in these references) show that bounds on N_eff and on masses are both relaxed with respect to simpler models with either the masses fixed to zero, or N_eff fixed to 3.046. The weakening of the joint bounds can reach a factor of 2 in some cases.

Giusarma *et al.* (2012) showed that the bounds on such models are rather robust, even when more general cosmological models with extra parameters are assumed. Hamann *et al.* (2011) presented an update and a more detailed discussion of some of these cases.

Concerning future joint bounds on N_eff and M_ν, the combination of Euclid lensing data and Planck data would give $\sigma(M_\nu) \sim 0.14$ eV and $\sigma(N_\mathrm{eff}) \sim 0.12$, assuming that all species are degenerate in mass (Debono *et al.*, 2010). Giusarma *et al.* (2011) present similar forecasts in a few other cases.

Properties of possible extra relativistic relics

In all these studies, extra relics are assumed to share the same Fermi–Dirac distribution and the same temperature as active neutrinos. In the case of sterile neutrinos, this is motivated by the assumption of a large mixing angle between active and sterile neutrinos. With such assumptions, the difference $N_\mathrm{eff} - 3.046$ can be directly interpreted as the number of extra species. Note that the main motivation for light sterile neutrinos comes from anomalies in LSND, MiniBoone and nuclear reactor data (see Section 1.4.1). These anomalies provide very marginal evidence for sterile neutrinos with a mass of order eV. The cases $N_\mathrm{eff} \simeq 4$ or 5 and $M_\nu \sim 1$ eV are already excluded by the bounds we have just reported (see Hamann *et al.*, 2011 for more details), not even speaking of BBN bounds discussed in Section 4.4.1. Therefore, possible eV-mass sterile neutrinos should have a suppressed nonthermal distribution (and/or a lower temperature than active neutrinos). However, this is unlikely, because they are expected at the same time to have a large mixing angle.

If extra relics are assumed to have a different temperature or to be nonthermally distributed, bounds on $(N_\mathrm{eff} - 3.046)$ cannot be immediately interpreted as the number of extra species. We discussed different phase-space distributions in

Section 6.1.4, and considered two cases (a) and (b). In case (a), i.e., relics with a rescaled Fermi–Dirac distribution or just a different temperature, the previous upper bounds can be translated into bounds on the rescaling factor χ or on the temperature T_s. This can be done by equating ($\Delta N_{\rm eff}$, ω_s, $k_{\rm nr}$) in the thermal and nonthermal cases, because these are the three quantities really probed by observations. This situation is discussed in the analysis of (Acero and Lesgourgues, 2009). In case (b), i.e., for any other phase-space distribution function, a specific analysis is needed for each particular model.

Finally, the previous bounds assume that extra massless or light relics are collisionless, and free-stream on small scales like ordinary neutrinos. Some nonstandard interaction may change the clustering properties of these relics without affecting their background evolution. Archidiacono *et al.* (2011) address this issue by introducing more freedom in the perturbation equations of massless relics. They promote two coefficients in Eq. (5.68) to the rank of free parameters. One of these coefficients is simply the sound speed $c_{\rm eff}$ relating pressure perturbations to density perturbations. The other relates the shear σ to the bulk velocity θ and is called the viscosity speed. Ordinary collisionless species are described by setting $(c^2_{\rm eff}, c^2_{\rm vis}) = (1/3, 1/3)$, whereas self-interacting particles could be described by lower values. The case $(c^2_{\rm eff}, c^2_{\rm vis}) = (1/3, 0)$ is that of a relativistic perfect fluid. In this limit the Boltzmann hierarchy reduces to a simple pair of equations, the continuity and Euler equations.[11] Archidiacono *et al.* (2011) fit such a model to the data combination WMAP7+ACT-2008+SPT+H_0+Gal-LRG and find that observations prefer a standard value of the sound speed, but leave the viscosity speed unconstrained. In other words, if extra ultrarelativistic relics are present, we do not know whether they are collisionless or not.

6.5.3 Nonstandard properties of active neutrinos

Let us now assume that the universe contains the three ordinary neutrino species, possibly with nonstandard properties, and no other massless or light relics.

The simplest deviation from the standard picture would consist of a large leptonic asymmetry leading to significant chemical potentials in the Fermi–Dirac distribution of each species. If neutrino masses are considered negligible given the sensitivity of the data, the effect of chemical potentials is entirely described by an enhancement of $N_{\rm eff}$, which can be computed following Eq. (4.51). The previous

[11] Other works have addressed this problem with different parameterizations. Some of them are problematic because the standard case of collisionless species is not one particular point in the space of free model parameters. In particular, this happens when the Boltzmann hierarchy is truncated at $l = 2$ with a given value of $c_{\rm vis}$, as in the imperfect fluid approximation (Hu, 1998). In that case, taking $c^2_{\rm vis} = 1/3$ only provides a crude approximation to the actual behavior of collisionless species.

bounds on $N_{\rm eff}$ can be then translated into bounds on the chemical potentials, with no information on the splitting of the leptonic asymmetry between different species. If neutrino masses are taken into account, a specific analysis is required, as in Lesgourgues and Pastor, 1999, with in principle two free parameters per species (mass and chemical potential). Extra distortions are introduced by neutrino oscillations until the BBN epoch, as explained in Section 4.4.2. We do not report results for this case, because leptonic asymmetries are still constrained more strongly by a combination of BBN and oscillation data than by CMB and LSS observations, as discussed by Castorina *et al.*, 2012. Current constraints on these asymmetries are summarized by the results of Mangano *et al.*, 2012 described in Section 4.4.2. In the future, the increasing sensitivity of CMB and LSS data to neutrino masses and abundances will provide even better limits on the leptonic asymetry.

Besides, the phase-space distribution of active neutrinos could be distorted, e.g., by the decay of a particle into neutrinos after neutrino decoupling (Cuoco *et al.*, 2005). It could also depart from Fermi–Dirac statistics under very unusual assumptions (Dolgov *et al.*, 2005). As long as neutrino masses can be neglected, these scenarios can be probed through their impact on $N_{\rm eff}$. If masses are assumed to be significant, such cases also require specific studies. The range of possible nonstandard assumptions is so wide that we do not present explicit observational bounds in this book. Particular examples of such analyses can be found, e.g., in Cuoco *et al.*, 2005 or Hannestad *et al.*, 2005.

Neutrinos could also be coupled with other species. Many nonstandard particle physics models leading to neutrino interactions have been presented in the literature (see Section 4.4.3). Cosmological bounds on these models can be obtained case by case, or through some more or less generic parameterization. Hereafter we briefly summarize some of the approaches that have been followed so far.

One can simply assume that neutrinos experience self-interactions preventing them from streaming freely. In the massless neutrino limit, this assumption would simply lead to a reduction of the neutrino anisotropic stress. Trotta and Melchiorri (2005) and De Bernardis *et al.* (2008) proposed to parameterize this effect through a viscosity speed $c_{\rm vis}$ accounting for the relation between the neutrino anisotropic stress σ_ν and the bulk velocity θ_ν. The limit $c_{\rm vis} = 0$ is that of strongly self-interacting massless neutrinos, behaving as a perfect relativistic fluid. The case $c^2_{\rm vis} = 1/3$ corresponds to an imperfect fluid whose evolution closely mimicks (but not perfectly) that of ordinary collisionless neutrinos, as shown in Hu, 1998. Fitting such a model to data shows that the case of a perfect relativistic fluid is strongly disfavoured with respect to ordinary free-streaming neutrinos. However, this conclusion is mainly driven by CMB data. So it is not excluded that neutrinos free-stream normally until recombination, and experience later some self-interactions driving their effective viscosity speed to zero (Basbøll *et al.*, 2009).

Several authors studied the case in which some (or all) of the neutrinos are tightly coupled to a new scalar particle. In that case the perturbations of the whole neutrino–scalar fluid can be described with one continuity and one Euler equation, just like the photon–baryon fluid in the tightly coupled limit. This would be equivalent to the previous approach in the limit $c^2_{\rm vis} = 0$ if the neutrino and scalar particles were ultrarelativistic. These models have a richer phenomenology when scalar and neutrino masses are taken into account. For instance, most neutrinos could decay into bosons in the early universe, so that no effects from neutrino masses could ever be observed in LSS data (Beacom *et al.*, 2004). Less extreme cases have been investigated by Hannestad, 2005b; Bell *et al.*, 2006. Current constraints on these models are still very weak, and dominated by the fact that CMB observations confirm the presence of ultrarelativistic free-streaming neutrinos around the time of photon decoupling. A positive detection of neutrino mass effects in LSS data would prove that neutrinos free-stream until today and rule out most of these models. Models where neutrinos are coupled to dark matter with mass in the MeV range have been studied in Mangano *et al.*, 2006b; Serra *et al.*, 2010. In this case, too, the bounds on the typical parameter of these scenario, the interaction cross section, are quite loose.

Finally let us mention the mass-varying neutrino (MaVaN) scenarios. In these, neutrinos are coupled to a scalar field with a dynamical vacuum expectation value, in such a way that the effective neutrino mass would depend on the field value. In this case, the neutrino evolution remains standard until the time of the nonrelativistic transition. After that time, the coupling term becomes important and triggers a nontrivial evolution both in the scalar field and in the neutrino sector, so that the average neutrino mass varies with time. The effective mass can either increase or decrease in the recent universe, depending on the model. The linear perturbation equations of neutrinos and of the scalar field can be integrated using a dedicated Boltzmann code, which yields the corresponding CMB and LSS power spectra. If the coupling is not very small (i.e., if the neutrino mass variation is significant), perturbations grow very quickly on large scales, signalling an instability in the model. Assuming that this instability is incompatible with the data, França *et al.* (2009) derived some strong bounds from current CMB and LSS observations. Instead, Mota *et al.* (2008) pointed out that unstable perturbations might back-react on the background evolution without conflicting observations. This possibility is currently being investigated with nonlinear simulations (Ayaita *et al.*, 2012).

6.5.4 Heavy sterile neutrinos (warm dark matter)

We have seen in Section 6.1.5 that WDM particles becoming nonrelativistic during radiation domination are indistinguishable from CDM particles on large scales.

Both CMB observations and LSS data limited to linear scales are perfectly compatible with a ΛCDM model. They show no evidence for a depletion of the matter power spectrum on small scales that would be imprinted below the free-streaming horizon in the presence of WDM.

So any possible evidence for WDM must be searched for in LSS data on small scales. Although small-scale galaxy clustering or weak lensing data are in principle sensitive to WDM masses, they are available today at small redshifts for which the scale of nonlinearity is relatively large. This raises several difficulties. First, we know that nonlinear corrections, redshift space distortions and nonlinear biasing are difficult to compute on nonlinear scales. Second, the nonlinear evolution tends to mask the effect of WDM. Indeed, a transfer of power from larger to smaller scales tends to move the break in the matter power spectrum to smaller scales, and to make it smoother. In other words, if we go deeper inside the nonlinear regime, we must search for WDM signatures at even smaller scales. For these reasons, given the sensitivity of current data and the status of nonlinear simulations, the most stringent cosmological bounds on WDM are those derived from Lyman alpha forest data. Indeed, this technique probes mildly nonlinear scales at very high redshift ($2 < z < 4$). On Lyman alpha scales and at $z = 3$, the WDM-induced break could be clearly visible, whereas on the same scale and at $z \simeq 1$ it could have been essentially erased. Still, Lyman alpha data must be used in combination with CMB and eventually other LSS data sets to measure all of the parameters of the ΛWDM model. To fit theoretical WDM models to Lyman alpha data, performing specific hydrodynamical simulations with WDM particles is unavoidable. Implementing WDM particles in simulations is much simpler than for HDM particles, as explained in Section 6.2.1.

We presented an explicit form for the break in the matter power spectrum in Eq. (6.97). This formula corresponds either to a thermal WDM distribution or to a rescaled Fermi–Dirac distribution. We know that the latter case is a good approximation to scenarios in which heavy sterile neutrinos are populated by nonresonant oscillations with active neutrinos, the Dodelson–Widrow scenario. A fit to Lyman alpha and other cosmological data gives a lower bound on the parameter $k_{\rm break}$ of Eq. (6.97), i.e., on the ratio $m_{\rm x}/T_{\rm x}$. This bound can be formulated as a lower limit for the mass of DW sterile neutrinos $m_{\rm DW}$ by assuming $T_{\rm x} \simeq T_\nu^{\rm a}$ and $m_{\rm x} = m_{\rm DW}$. It can also be translated into a bound on the mass of a thermal WDM particle (see Eq. (6.94) and the following relations). Using a combination of WMAP5, extra small-scale CMB data, SNIa, H_0, Gal-LRG and Ly-α-SDSS data sets,[12] Boyarsky *et al.* (2009d) obtained a bound $m_{\rm DW} > 12$ keV (95%CL).

[12] For the meaning of these acronyms, see Sections 5.4.1 and 6.4.

ΛCWDM models in which WDM particles (either thermal or DW) would coexist with CDM particles in the universe can be described with two parameters on top of the usual six ΛCDM parameters: the WDM fraction $f_{\rm w} = \omega_{\rm w}/(\omega_{\rm C} + \omega_{\rm w})$ and the velocity dispersion parameter $m_{\rm x}/T_{\rm x}$ (or directly the mass $m_{\rm DW}$ if $T_{\rm x} \simeq T_\nu^{\rm a}$ is assumed). As mentioned in Section 6.1.5, the power spectrum of such models is steplike suppressed (at the level of linear theory). The step amplitude and location are controlled by the two WDM parameters. The possible existence of a step is much less constrained by the data than that of a break. For the same combination of data sets, Boyarsky *et al.* (2009d) derived some joint bound in $(f_{\rm w}, m_{\rm DW})$ parameter space. For $f_{\rm w} < 0.35$, it appears that any mass is compatible with the data. For larger fractions, the bound increases gradually and reaches the previous value when $f_{\rm w} = 1$.

We mentioned in Section 6.1.5 that the DW model and thermal model are just two out of many possibilities for the WDM phase-space distribution. For instance, for sterile neutrinos populated by resonant oscillations, the phase-space distribution leads roughly to the same cosmological signature as in a mixed warm plus cold model. Using this similarity, Boyarsky *et al.* (2009c) showed that for resonantly produced sterile neutrinos the bound is much weaker than in the DW model, so that a mass of 2 keV is still well compatible with the data.

Lyman alpha bounds on sterile neutrino masses are complementary to various astrophysical bounds. First, the WDM characteristics can be probed by the small-scale structure of the universe: halo profiles, number of satellite galaxies, morphology of the galactic center, etc. These indications are, however, subject to huge uncertainties, and although several arguments tend to favour WDM (see, e.g., Lovell *et al.*, 2012), they must be taken with care. Second, if sterile neutrinos are too heavy, or if their mixing angle with active neutrinos is too large, a neutrino decay line should be clearly visible in galaxy halos using X-ray observations. More precisely, it is possible for a sterile neutrino to decay into a photon and an active neutrino via a 1-loop process, with branching ratio $27\alpha/(8\pi) \approx 1/128$. The radiative decay width (Pal and Wolfenstein, 1982) is

$$\Gamma(\nu_s \to \gamma\,\nu_a) = \frac{9\alpha}{2048\pi^4} G_{\rm F}^2 \sin^2 2\theta\, m_{\rm s}^5 \simeq \frac{1}{1.5\times 10^{32}\ {\rm s}} \frac{\sin^2 2\theta}{10^{-10}} \left[\frac{m_{\rm s}}{\rm keV}\right]^5 \quad (6.115)$$

in the case of Dirac neutrinos (for Majorana neutrinos the rate gets an extra factor of two). Even if sterile neutrinos are required to be cosmologically stable, a very small fraction of them will decay following this channel. Because the radiative decay is a two-body process, the signal is a monochromatic flux of X-rays with energy $E_\gamma \simeq m_{\rm s}/2$. Emitted photons may be observed by X-ray instruments such as the XMM-Newton, Chandra X-ray, and Suzaku observatories, especially in the direction of dark matter halos (Abazajian *et al.*, 2001; Dolgov and Hansen, 2002;

Feng, 2010; Boyarsky *et al.*, 2006). Null results exclude the upper right region of Fig. 4.7. Future X-ray observations may extend sensitivities to the entire range of parameters plotted in Fig. 4.7 (Abazajian, 2009; den Herder *et al.*, 2009).

Hence X-ray bounds on the sterile neutrino mass depend on the mixing angle. The relic density $\omega_{\rm DW}$ of DW sterile neutrinos can also be inferred from the mass and mixing angle. Joint constraints from cosmological and X-ray data in $(m_{\rm DW}, \omega_{\rm DW})$ parameter space are incompatible with each other: the DW scenario is now excluded with a good confidence level (see, e.g., Boyarsky *et al.*, 2008). In the case of resonant production, cosmological bounds are much weaker, and a large allowed window remains open (Boyarsky *et al.*, 2009c), as illustrated in Fig. 4.7.

3.2 Role of a large leptonic asymmetry, PRD 60, 103521 (1999)

Cosmological implications of a Relic Neutrino Asymmetry

Julien Lesgourgues * and Sergio Pastor †
SISSA–ISAS and INFN, Sezione di Trieste
Via Beirut 2-4,I-34013 Trieste, ITALY

We consider some consequences of the presence of a cosmological lepton asymmetry in the form of neutrinos. A relic neutrino degeneracy enhances the contribution of massive neutrinos to the present energy density of the Universe, and modifies the power spectrum of radiation and matter. Comparing with current observations of cosmic microwave background anisotropies and large scale structure, we derive some constraints on the neutrino degeneracy and on the spectral index in the case of a flat Universe with a cosmological constant.

I. INTRODUCTION

It is generally assumed that our Universe contains an approximately equal amount of leptons and antileptons. The lepton asymmetry would be of the same order as the baryon asymmetry, which is very small as required by Big Bang Nucleosynthesis (BBN) considerations. The existence of a large lepton asymmetry is restricted to be in the form of neutrinos from the requirement of universal electric neutrality, and the possibility of a large neutrino asymmetry is still open. From a particle physics point of view, a lepton asymmetry can be generated by an Affleck-Dine mechanism [1] without producing a large baryon asymmetry (see ref. [2] for a recent model), or even by active-sterile neutrino oscillations after the electroweak phase transition (but in this last case, it might not be of order unity) [3]. This lepton asymmetry can postpone symmetry restoration in non-supersymmetric or supersymmetric models [4] (note that this is also true for other charges [5]).

In this paper we study some cosmological implications of relic degenerate neutrinos[1]. We do not consider any specific model for generating such an asymmetry, and just assume that it was created well before neutrinos decouple from the rest of the plasma. An asymmetry of order one or larger can have crucial effects on the global evolution of the Universe. Among other effects, it changes the decoupling temperature of neutrinos, the primordial production of light elements at BBN, the time of equality between radiation and matter, or the contribution of relic neutrinos to the present energy density of the Universe. The latter changes affect the evolution of perturbations in the Universe. We focus on the anisotropies of the Cosmic Microwave Background (CMB), and on the distribution of Large Scale Structure (LSS). We calculate the power spectrum of both quantities, in the case of massless degenerate neutrinos, and also for neutrinos with a mass of 0.07 eV, as suggested to explain the experimental evidence of atmospheric neutrino oscillations at Super-Kamiokande [6]. The cosmological implications of neutrinos with such a small mass are known to be very small, but we will see that this conclusion is modified if a large neutrino degeneracy exists. We also include in our analysis the possibility that the dominant contribution to the present energy density in the Universe is due to a cosmological constant: $\Omega_\Lambda \sim 0.6 - 0.7$, keeping the Universe flat ($\Omega_0 + \Omega_\Lambda = 1$), as suggested by recent observations (see [7] and references therein).

The effect of neutrino degeneracy on the LSS power spectrum was studied in ref. [8], as a way of improving the agreement with observations of mixed dark matter models with eV neutrinos, in the case of high values of the Hubble parameter. Also, Adams & Sarkar [9] calculated the CMB anisotropies and the matter power spectrum, and compared them with observations in the $\Omega_\Lambda = 0$ case for massless degenerate neutrinos. More recently, Kinney & Riotto [10] also calculated the CMB anisotropies for massless degenerate neutrinos in the $\Omega_\Lambda = 0.7$ case.

This paper is organized as follows. In section II, we calculate the contribution of massive degenerate neutrinos to the present energy density of the Universe. In section III, we explain how to calculate the power spectra, with the help of the code `cmbfast` [11]. In section IV, we discuss the effect of the degeneracy on CMB anisotropies and the matter power spectrum, both for massless neutrinos and $m_\nu = 0.07$ eV. Finally, in section V, we derive some

*E-mail: lesgour@sissa.it
†E-mail: pastor@sissa.it

[1] Here, by degeneracy, we mean that there exists a large neutrino-antineutrino asymmetry, or vice versa, and not a degeneracy in the mass sense.

constraints on the neutrino degeneracy from CMB and LSS data, in the particular case of a flat Universe with an arbitrary cosmological constant and for standard values of other cosmological parameters.

II. ENERGY DENSITY OF MASSIVE DEGENERATE NEUTRINOS

The energy density of one species of massive degenerate neutrinos and antineutrinos, described by the distribution functions f_ν and $f_{\bar\nu}$, is (here and throughout the paper we use $\hbar = c = k_B = 1$ units)

$$\rho_\nu + \rho_{\bar\nu} = \int \frac{d^3\vec{p}}{(2\pi)^3}\, E_\nu (f_\nu(p) + f_{\bar\nu}(p)) = \frac{1}{2\pi^2}\int_0^\infty dp\; p^2 \sqrt{p^2 + m_\nu^2}(f_\nu(p) + f_{\bar\nu}(p)) \;, \tag{1}$$

valid at any moment. Here p is the magnitude of the 3-momentum and m_ν is the neutrino mass.

When the early Universe was hot enough, the neutrinos were in equilibrium with the rest of the plasma via the weak interactions. In that case the distribution functions f_ν and $f_{\bar\nu}$ changed with the Universe expansion, keeping the form of a Fermi-Dirac distribution,

$$f_\nu(p) = \frac{1}{\exp\left(\dfrac{p}{T_\nu} - \dfrac{\mu}{T_\nu}\right) + 1} \qquad f_{\bar\nu}(p) = \frac{1}{\exp\left(\dfrac{p}{T_\nu} + \dfrac{\mu}{T_\nu}\right) + 1} \tag{2}$$

Here μ is the neutrino chemical potential, which is nonzero if a neutrino-antineutrino asymmetry has been previously produced. Later the neutrinos decoupled when they were still relativistic[2], and from that moment the neutrino momenta just changed according to the cosmological redshift. If a is the expansion factor of the Universe, the neutrino momentum decreases keeping ap constant. At the same time the neutrino degeneracy parameter $\xi \equiv \mu/T_\nu$ is conserved, with a value equal to that at the moment of decoupling. Therefore one can still calculate the energy density of neutrinos now from eq. (1) and eq. (2), replacing μ/T_ν by ξ and p/T_ν by $p/(y_\nu T_0)$, where $T_0 \simeq 2.726$ K and y_ν is the present ratio of neutrino and photon temperatures, which is not unity because once decoupled the neutrinos did not share the entropy transfer to photons from the successive particle annihilations that occurred in the early Universe. In the standard case, the massless non-degenerate neutrinos decoupled just before the electron-positron pairs annihilated to photons, from which one gets the standard factor $y_\nu = (4/11)^{1/3}$.

In the presence of a significant neutrino degeneracy ξ the decoupling temperature $T(\xi)$ is higher than in the standard case [12,13]. The reaction rate Γ of the weak processes, that keep the neutrinos in equilibrium with the other species, is reduced because some of the initial or final neutrino states will be occupied. The authors of ref. [13] used the Boltzmann equation to calculate Γ for the process $\nu_d + \bar\nu_d \leftrightarrow e^+ + e^-$ (here ν_d denotes degenerate neutrinos), including the corresponding Fermi blocking factors. It was found that the neutrino decoupling temperature is $T_{dec}(\xi) \approx 0.2\xi^{2/3}\exp(\xi/3)$ MeV (for ν_μ or ν_τ). Therefore if ξ is large enough, the degenerate neutrinos decouple before the temperature of the Universe drops below the different mass thresholds, and are not heated by the particle-antiparticle annihilations. The ratio of neutrino and photon temperatures is thus reduced accordingly.

The present contribution of these degenerate neutrinos to the energy density of the Universe can be parametrized as $\rho_\nu = 10^4 h^2 \Omega_\nu$ eV cm^{-3}, where Ω_ν is the neutrino energy density in units of the critical density $\rho_c = 3H^2 M_P^2/8\pi$, $M_P = 1.22 \times 10^{19}$ GeV is the Planck mass and $H = 100h$ Km s^{-1} Mpc^{-1} is the Hubble parameter. The value of ρ_ν can be calculated as a function of the neutrino mass and the neutrino degeneracy ξ, or equivalently the present neutrino asymmetry L_ν defined as the following ratio of number densities

$$L_\nu \equiv \frac{n_\nu - n_{\bar\nu}}{n_\gamma} = \frac{1}{12\zeta(3)} y_\nu^3 [\xi^3 + \pi^2 \xi] \tag{3}$$

We show[3] in figures 1 and 2 the contours in the (m_ν, L_ν) and (m_ν, ξ) planes that correspond to some particular values of $h^2\Omega_\nu$. One can see from the figures that there are two limits: massive non-degenerate neutrinos and massless degenerate neutrinos. The first case corresponds to the vertical lines, when one recovers the well-known bound on the neutrino mass $m_\nu \lesssim 46$ eV for $h^2\Omega_\nu = 0.5$. On the other hand, for very light neutrinos, the horizontal lines set a maximum value on the neutrino degeneracy, that would correspond to a present neutrino chemical potential

[2] Unless the neutrino mass is comparable to the decoupling temperature, $\mathcal{O}(m_\nu) \sim$ MeV.

[3] Here we assume $\xi > 0$, but the results are also valid for $\xi < 0$ provided that ξ and L_ν are understood as moduli.

$\mu_0 \lesssim 7.4 \times 10^{-3}$ eV, also for $h^2\Omega_\nu = 0.5$. In the intermediate region of the figures the neutrino energy density is $\rho_\nu \simeq m_\nu n_\nu(\xi)$ and the contours follow roughly the relations

$$L_\nu \left(\frac{m_\nu}{\mathrm{eV}}\right) \simeq 24.2 h^2 \Omega_\nu$$

$$(\pi^2 \xi + \xi^3) \left(\frac{m_\nu}{\mathrm{eV}}\right) \simeq \frac{350}{y_\nu^3} h^2 \Omega_\nu \tag{4}$$

A similar calculation has been recently performed in reference [14]. However the difference between neutrino and photon temperatures was not properly taken into account for large ξ. It was argued that, since the number density of highly degenerate neutrinos is larger than in the non-degenerate case, the neutrinos would have been longer in thermal contact with e^+e^-, therefore sharing with photons the entropy release. However this is not the case [13] as we discussed before.

The presence of a neutrino degeneracy can modify the outcome of Big Bang Nucleosynthesis (for a review see [15]). First a larger neutrino energy density increases the expansion rate of the Universe, thus enhancing the primordial abundance of ^{4}He. This is valid for a nonzero ξ of any neutrino flavor. In addition if the degenerate neutrinos are of electron type, they have a direct influence over the weak processes that interconvert neutrons and protons. This last effect depends on the sign of ξ_{ν_e}. Both effects may be simultaneously important and it could be possible in principle to explain the observed primordial abundances with a large baryon density, $\Omega_B h^2 \approx 1$ [12,13]. However this possibility is ruled out by the fact that in that case our Universe would have been radiation dominated during a longer period and the observed large-scale structure would be difficult to explain. From BBN one gets the following constraint [13]

$$-0.06 \lesssim \xi_{\nu_e} \lesssim 1.1 \tag{5}$$

while a sufficiently long matter dominated epoch requires

$$|\xi_{\nu_\mu, \nu_\tau}| \lesssim 6.9 \tag{6}$$

This estimate from [13] agrees with our analysis in section V. Assuming that the degenerate neutrinos are ν_μ or ν_τ, this places a limit on the degeneracy as shown by the horizontal line in figures 1 and 2.

III. POWER SPECTRA CALCULATION

We compute the power spectra of CMB anisotropies and large-scale structure using the Boltzmann code `cmbfast` by Seljak & Zaldarriaga [11], adapted to the case of one family of degenerate neutrinos (ν, $\bar{\nu}$), with mass m_ν and degeneracy parameter ξ. Let us first review the required modifications. We use the notations of Ma & Bertschinger [16], and for all issues not specific to our case, we refer the reader to this review.

Background quantities can be rewritten in terms of two dimensionless parameters (M, Q)

$$M = \frac{m_\nu}{T_{\nu 0}} = \frac{m_\nu(\mathrm{eV})}{8.6170 \times 10^{-5} \times (4/11)^{1/3}\ T_0(\mathrm{K})}, \qquad Q = \frac{a\ p}{T_{\nu 0}} \tag{7}$$

(we are assuming $y_\nu = (4/11)^{1/3}$, and therefore $\xi \leq 12$ [13]; the scale factor is defined so that $a = 1$ today). For Super-Kamiokande neutrinos with $m_\nu = 0.07$ eV, $M \simeq 417$. We then get for the mean density, pressure and phase-space distributions

$$\begin{aligned}
\bar{\rho}_\nu + \bar{\rho}_{\bar{\nu}} &= \frac{T_\nu^4}{2\pi^2} \int Q^2 dQ \sqrt{Q^2 + a^2 M^2}\, (f_\nu(Q) + f_{\bar{\nu}}(Q))\,, \\
\bar{P}_\nu + \bar{P}_{\bar{\nu}} &= \frac{T_\nu^4}{6\pi^2} \int Q^2 dQ \frac{Q^2}{\sqrt{Q^2 + a^2 M^2}}\, (f_\nu(Q) + f_{\bar{\nu}}(Q))\,, \\
f_\nu(Q) &= \frac{1}{e^{Q-\xi} + 1}, \qquad f_{\bar{\nu}}(Q) = \frac{1}{e^{Q+\xi} + 1}.
\end{aligned} \tag{8}$$

In the case of massive degenerate neutrinos, these integrals must be calculated for each value of the scale factor, and also at the beginning of the code in order to find Ω_ν today. On the other hand, for massless neutrinos, there is an exact analytic solution

$$\bar{\rho}_\nu + \bar{\rho}_{\bar{\nu}} = 3(\bar{P}_\nu + \bar{P}_{\bar{\nu}}) = \frac{7}{8}\frac{\pi^2}{15}T_\nu^4 \left[1 + \frac{30}{7}\left(\frac{\xi}{\pi}\right)^2 + \frac{15}{7}\left(\frac{\xi}{\pi}\right)^4\right]. \tag{9}$$

So, if we define an effective number of massless neutrino families $N_{eff} \equiv 3 + 30/7(\xi/\pi)^2 + 15/7(\xi/\pi)^4$, the mean density and pressure for all neutrinos will be given by these ones for one massless non-degenerate family, multiplied by N_{eff}.

Let us now consider perturbed quantities. We define Ψ_ν and $\Psi_{\bar{\nu}}$, the perturbations of the phase space distribution for ν and $\bar{\nu}$, through

$$\begin{aligned} \delta f_\nu(\vec{x}, Q, \hat{n}, \tau) &= f_\nu(Q)\Psi_\nu(\vec{x}, Q, \hat{n}, \tau)\ , \\ \delta f_{\bar{\nu}}(\vec{x}, Q, \hat{n}, \tau) &= f_{\bar{\nu}}(Q)\Psi_{\bar{\nu}}(\vec{x}, Q, \hat{n}, \tau) \end{aligned} \tag{10}$$

($\hat{n}$ is the momentum direction: $\vec{p} \equiv p\hat{n}$). For our purpose, which is to integrate the linearized Einstein equations, it can be shown that only the following linear combination is relevant

$$\Psi \equiv \frac{f_\nu \Psi_\nu + f_{\bar{\nu}}\Psi_{\bar{\nu}}}{f_\nu + f_{\bar{\nu}}}. \tag{11}$$

Using the Boltzmann equations for Ψ_ν and $\Psi_{\bar{\nu}}$, it is straightforward to show that the evolution of Ψ (in Fourier space and in the synchronous gauge, see [16], eq. (40)) obeys

$$\frac{\partial \Psi}{\partial \tau} + i\frac{Q}{\sqrt{Q^2 + a^2M^2}}(\vec{k}.\hat{n})\Psi + \frac{d\ln(f_\nu + f_{\bar{\nu}})}{d\ln Q}\left[\dot{\eta} - \frac{\dot{h} + 6\dot{\eta}}{2}(\hat{k}.\hat{n})^2\right] = 0\ . \tag{12}$$

This equation depends on ξ only through the last term, which is the gravitational source term.

In the case $\xi = 0$, the quantity $(d\ln(f_\nu)/d\ln Q)$ has a simple interpretation: it is the Q-dependence of a planckian perturbation of the phase space distribution. In other words, a shift of the blackbody temperature $\Delta T/T(\vec{x}, \hat{n}, \tau)$ corresponds to a perturbation

$$\Psi(\vec{x}, Q, \hat{n}, \tau) = -\frac{\Delta T}{T}(\vec{x}, \hat{n}, \tau)\frac{d\ln(f_\nu)}{d\ln Q}. \tag{13}$$

Since the gravitational source term in the Boltzmann equation is proportional to this quantity, the planckian shape is unaltered for massless neutrinos, and also for massive neutrinos when they are still relativistic (indeed, when $Q^2 \gg a^2M^2$, the Q-dependence of the Boltzmann equation (12) vanishes in the second term, and remains only in the third term). When $\xi \neq 0$, the source term in eq. (12) is proportional to

$$\frac{d\ln(f_\nu + f_{\bar{\nu}})}{d\ln Q} = -\frac{Q(1 + \mathrm{ch}\xi\ \mathrm{ch}Q)}{(\mathrm{ch}\xi + \mathrm{e}^{-Q})(\mathrm{ch}\xi + \mathrm{ch}Q)}. \tag{14}$$

When neutrinos are still relativistic, Ψ is proportional to this quantity, even if it cannot be simply interpreted in terms of blackbody temperature perturbations.

We can now specify all the changes required in `cmbfast`, first in the case of massive degenerate neutrinos. As usual, Ψ can be expanded in a Legendre series: $\Psi = \sum_{l=0}^{\infty}(-i)^l(2l+1)\Psi_l P_l$. It is easy to show that for each multipole Ψ_l, the evolution equation and the initial condition are both identical to those of the non-degenerate case, provided that we replace $(d\ln(f_\nu)/d\ln Q)$ by eq. (14). So, in summary, one only needs to modify the homogeneous phase-space distribution, its logarithmic derivative with respect to Q, and the initial calculation of Ω_ν. Also, in order to obtain a good precision in the CMB anisotropy spectra, one must set $l = 5$ for the number of multipoles Ψ_l to be time-integrated. For transfer functions, the value $l = 25$ proposed by the code is sufficient.

In the case of massless degenerate neutrinos, the situation is even simpler. The Q-dependence of the Boltzmann equation can be integrated away, just like in the non-degenerate case. For this purpose, we must introduce the Q-independent variable F_ν

$$F_\nu(\vec{k}, \hat{n}, \tau) \equiv \frac{\int Q^3 dQ(f_\nu + f_{\bar{\nu}})\Psi}{\int Q^3 dQ(f_\nu + f_{\bar{\nu}})} \equiv \sum_{l=0}^{\infty}(-i)^l(2l+1)F_{\nu l}P_l, \tag{15}$$

and integrate by part the last term in equation (12). The multipoles $F_{\nu l}$ are exactly identical for degenerate and non-degenerate massless neutrinos, because they share the same evolution equations and initial conditions. So, the effect of ξ arises only through the background quantities in eq. (8) and is completely described by introducing an effective number of massless neutrinos.

IV. RESULTS

First, as a consistency check, we compute CMB anisotropies and transfer functions for different values of ξ, choosing a very small mass $m_\nu \leq 0.001$ eV. We check that the results match exactly those obtained with the unmodified version of `cmbfast`, when the appropriate effective neutrino number N_{eff} is specified.

The effect of ξ and m_ν on the CMB anisotropy spectrum can be seen in figure 3. We choose a set of cosmological parameters ($h = 0.65$, $\Omega_b = 0.05$, $\Omega_\Lambda = 0.70$, $\Omega_{CDM} = 1 - \Omega_b - \Omega_\nu - \Omega_\Lambda$, $Q_{rms-ps} = 18$ μK, flat primordial spectrum, no reionization, no tensor contribution), and we vary ξ from 0 to 5, both in the case of massless degenerate neutrinos (solid lines) and degenerate neutrinos with $m_\nu = 0.07$ eV (dashed lines). Let us first comment the massless case. The main effect of ξ is to boost the amplitude of the first peak[4]. Indeed, increasing the energy density of radiation delays matter-radiation equality, which is known to boost the acoustic peaks [17] (the same explanation holds for the effect of Ω_Λ in flat models). For the same reason, all peaks are shifted to higher multipoles, by a factor $((1+a_{eq}/a_*)^{1/2} - (a_{eq}/a_*)^{1/2})^{-1}$ [17] (a_{eq} is the scale factor at equality, and increases with ξ, while the recombination scale factor a_* is almost independent of the radiation energy density). Secondary peaks are then more affected by diffusion damping at large l, and their amplitude can decrease with ξ.

In the case of degenerate neutrinos with $m_\nu = 0.07$ eV, the results are quite similar in first approximation. Indeed, the effects described previously depend on the energy density of neutrinos at equality. At that time, they are still relativistic, and identical to massless neutrinos with equal degeneracy parameter. However, with a large degeneracy, Ω_ν today becomes significant: for $\xi = 5$, one has $\Omega_\nu = 0.028$, i.e. the same order of magnitude as Ω_b. Since we are studying flat models, $\Omega_\nu = 0.028$ must be compensated by less baryons, cold dark matter (CDM) or Ω_Λ. In our example, Ω_b and Ω_Λ are fixed, while Ω_{CDM} slightly decreases. This explains the small enhancement of the first peak compared to the massless case. Even if this effect is indirect, it is nevertheless detectable in principle (even if one does not impose the flatness condition, the effect of Ω_ν will be visible through a modification of the curvature). In figure 3, for $\xi = 0$, the first peak maximum is enhanced by only 0.37%, while for $\xi = 5$, there is an increase of 3.4%, detectable by the future satellite missions *MAP* and *Planck*, unless there are large parameter degeneracies. It is well-known that such degeneracies are generally removed when CMB and LSS data are combined for parameter extraction [18].

We plot in figure 4 the power spectrum $P(k)$ for the same models as in figure 3, normalized on large scales to COBE. The effect of both parameters ξ and m_ν is now to suppress the power on small scales. Indeed, increasing ξ postpones matter-radiation equality, allowing less growth for fluctuations crossing the Hubble radius during radiation domination. Adding a small mass affects the recent evolution of fluctuations, and has now a direct effect: when the degenerate neutrinos become non-relativistic, their free-streaming suppresses growth of fluctuations for scales within the Hubble radius. For non-degenerate neutrinos, this effect is known to reduce power on those scales by a relative amount $\Delta P/P \sim 8\Omega_\nu/\Omega_0$ [19] (we introduced $\Omega_0 = 1 - \Omega_\Lambda$). So, even with $m_\nu = 0.07$ eV and $\xi = 0$, it is significant, especially at low Ω_0. In the models of figure 4, $P(k)$ decreases by ~ 5 %, in agreement with the theoretical prediction ($\Omega_\nu = 1.8 \times 10^{-3}$, $\Omega_0 = 0.3$). However, at $\xi = 5$ (i.e. $\Omega_\nu = 0.028$), this effect is even larger: $P(k)$ decreases by a factor 2.2, instead of an expected 1.7. This effect is likely related to the phase-space distribution of neutrinos with a chemical potential: their average momentum is shifted to larger values, making the free-streaming suppression mechanism even more efficient.

Let us compare our results with those of previous works. The effect of ξ on the CMB for massless neutrinos and $\Omega_\Lambda = 0$ is the same as that one found in [9]. We also agree with the revised results in [10].

V. COMPARISON WITH OBSERVATIONS

Since the degeneracy increases dramatically the amplitude of the first CMB peak, we expect large ξ values to be disfavored in the case of cosmological models known to predict a fairly high peak. On the other hand, a high ξ is likely to be allowed (or even favored) for models that predict systematically a low peak, unless a large scalar spectral index $n \geq 1.2$ (*blue tilt*) is invoked. For instance, the degeneracy is likely to be favored by: (i) a large contribution of tensor perturbations; (ii) a significant effect from reionization; (iii) a low baryon density; (iv) a large h ($h \geq 0.7$); (v) flat models with $\Omega_\Lambda \leq 0.6$; etc. For such models, the peak amplitude can be boosted by ξ, keeping n close to one, which is more natural from the point of view of inflation. However, a careful case-by-case analysis is required,

[4] In fact, this is not true for very large values of ξ. In such cases, recombination can take place still at the end of radiation domination, and anisotropies are suppressed. For our choice of cosmological parameters, this happens for $\xi \gtrsim 7$, but in such a case the location of the first peak is $l \gtrsim 450$, and the matter power spectrum is strongly suppressed.

since the effects of ξ and n on CMB and LSS spectra are far from being equivalent. Our goal here is not to explore systematically all possibilities, but to briefly illustrate how ξ can be constrained by current observations for flat models with different values of Ω_Λ. Recent results from supernovae [20], combined with CMB constraints, favor flat models with $\Omega_\Lambda \sim 0.6 - 0.7$ [7].

We choose a flat model with $h = 0.65$, $\Omega_b = 0.05$, $Q_{rms-ps} = 18$ μK, no reionization and no tensor contribution, and look for the allowed region in the space of free parameters (Ω_Λ, ξ, n). The allowed region will not be defined using a maximum likelihood analysis, but with the more conservative technique called "concordance" by Wang et al. [21], which consists in taking the intersection of regions allowed by each experiment.

For simplicity, we take into account only a few constraints on the matter power spectrum, known to be representative of the large amount of available data: the value of σ_8 (the variance of mass fluctuations in a sphere of radius $R = 8h^{-1}$Mpc) given for flat models in [22], at 95 % confidence level (CL)[5]; a χ^2 comparison with the STROMLO-APM redshift survey [24], at scales well within the linear regime, also with 95 % CL[6]; and finally, the constraint on bulk velocity at $R = 50h^{-1}$ Mpc [25], taking into account the cosmic variance. Except for the updated σ_8 constraint, we use exactly the same experimental tests as in [26], and refer the reader to this paper for details. For CMB data, we perform a χ^2 analysis based on 19 experimental points and window functions, taking into account the Saskatoon calibration uncertainty, in the way suggested by [27]. The list of data that we use is given in [26], and again allowed regions correspond to 95 % CL[7]. We do not take into account the most recent experiments, for which window functions are still unpublished; they are anyway in good agreement with the data considered here.

We plot in figure 5 the LSS and CMB allowed regions in (ξ, n) parameter space, corresponding to $\Omega_\Lambda = 0, 0.5, 0.6, 0.7$. For $\Omega_\Lambda = 0.5 - 0.7$, the LSS window just comes out of σ_8 limits. For $\Omega_\Lambda = 0$, the lower LSS constraint is from σ_8, and the upper one from APM data. In the case of degenerate neutrinos with $m_\nu = 0.07$ eV, the windows are slightly shifted at large ξ, since, as we saw, the effect of ξ is enhanced (dotted lines on the figure). The CMB allowed regions do not show this distinction, given the smallness of the effect and the imprecision of the data. One can immediately see that LSS and CMB constraints on n are shifted in opposite direction with ξ: indeed, the effects of ξ and n both produce a higher CMB peak, while to a certain extent they compensate each other in $P(k)$. So, for $\Omega_\Lambda = 0.7$, a case in which a power spectrum normalized to both COBE and σ_8 yields a too high peak[8], a neutrino degeneracy can only make things worst. On the other hand, for $\Omega_\Lambda = 0.5 - 0.6$, a good agreement is found up to $\xi \simeq 3$.

Let us finally consider the $\Omega_\Lambda = 0$ case in which, after COBE normalization of the power spectrum, there is a well known discrepancy between the amplitude required by σ_8 and the shape probed by redshift surveys: these two constraints favor different values of n. We find that the neutrino degeneracy can solve this problem with $\xi \gtrsim 3.5$; however, the allowed window is cut at $\xi \simeq 6$ by CMB data, and we are left with an interesting region in which $\Omega_0 = 1$ models are viable. This result is consistent with [9]. However, current evidences for a low Ω_0 Universe [20,28] are independent of the constraints used here, so there are not many motivations at the moment to consider this window seriously.

VI. CONCLUSIONS

We have considered some cosmological implications of a large relic neutrino degeneracy. We have shown that this degeneracy enhances the contribution of massive neutrinos to the present energy density of the Universe. For instance, neutrinos with a small mass $m_\nu \sim 10^{-2}$ eV can contribute significantly to Ω_0, provided that there is a large neutrino-antineutrino asymmetry.

Our main result is the computation of the power spectra of CMB anisotropies and matter density in presence of a neutrino degeneracy. We found, in agreement with [9], that it boosts the amplitude of the first CMB peak, shifts the peaks to larger multipoles, and supresses small scale matter fluctuations. These effects follow the increase of neutrino energy density, that delays matter-radiation equality.

We extended the calculation to the case of massive degenerate neutrinos, and showed the results for a mass of 0.07 eV, as suggested by the Super-Kamiokande experiment. This mass has a small effect on CMB anisotropies. Indeed,

[5]The Viana & Liddle result [22] is in very good agreement with an independent derivation by Girardi et al. [23].

[6]This confidence level stands for the goodness-of-fit of the model: when χ^2 is greater than some value, the probability that we find the observed dataset, assuming the model to be valid, is smaller than 5 %. For the APM data, we have $9 - 3$ degrees of freedom, and the limiting value is found in numerical tables to be $\chi^2 = 12.5$.

[7]Here we have $19 - 3$ d.o.f.; the 95 % CL is given by $\chi^2 = 26$.

[8]At least, for the values of the other cosmological parameters considered here. This situation can be easily improved, for instance, with $h = 0.7$.

such light neutrinos are still relativistic at recombination, but in presence of a degeneracy, they can account for a substantial part of the density today, of order $\Omega_\nu \sim 10^{-2}$. Also, we showed that small scale matter fluctuations are much more suppressed when the degenerate neutrinos are massive, because free-streaming of non-relativistic neutrinos is more efficient when their average momentum is boosted by the chemical potential.

We compared our results with observations, in the restricted case of a flat universe with arbitrary (Ω_Λ, ξ, n) and fixed values of other cosmological parameters. We found that for $\Omega_\Lambda \simeq 0.5 - 0.6$, a large degeneracy is allowed, up to $\xi \simeq 3$. However, this upper bound is smaller than the value $\xi \simeq 4.6$ needed to explain the generation of ultra-high energy cosmic rays by the annihilation of high-energetic neutrinos on relic neutrinos with mass $m_\nu = 0.07$ eV [29]. We also tried smaller values of Ω_Λ, even if they are not favored by combined CMB and supernovae data. It turns out that a large degeneracy can account for both CMB and LSS constraints even with $\Omega_0 = 1$, provided that $3.5 \leq \xi \leq 6$. This analysis could be extended to other cosmological models. For instance, the degeneracy is likely to be compatible with a large contribution of tensor perturbations to large scale CMB anisotropies.

Finally, it turns out that the degeneracy parameter and the mass of degenerate neutrinos have effects within the level of detectability of future CMB observations and redshift surveys, even with $m_\nu \sim 0.07$ eV. However, a careful analysis should be performed in order to detect possible parameter degeneracy between ξ, m_ν and other cosmological parameters.

ACKNOWLEDGEMENTS

We thank S. Borgani, A. Masiero and A.Yu. Smirnov for useful discussions, as well as W. Kinney and A. Riotto for correspondence. This work has been supported by INFN and by the TMR network grant ERBFMRXCT960090.

---

[1] I. Affleck and M. Dine, Nucl. Phys. **B249**, 361 (1985)
[2] A. Casas, W.Y. Cheng and G. Gelmini, Nucl. Phys. **B538**, 297 (1999)
[3] R. Foot, M.J. Thomson and R.R. Volkas, Phys. Rev. **D53**, 5349 (1996)
[4] A.D. Linde, Phys. Rev. **D14**, 3345 (1976); J. Liu and G. Segre, Phys. Lett. **B338**, 259 (1994); B. Bajc, A. Riotto and G. Senjanović, Phys. Rev. Lett. **81**, 1355 (1998)
[5] H.E. Haber and H.A. Weldon, Phys. Rev. **D25**, 502 (1982); A. Riotto and G. Senjanović, Phys. Rev. Lett. **79**, 349 (1997)
[6] Y. Fukuda *et al.* [Super-Kamiokande Collaboration], Phys. Rev. Lett. **81**, 1562 (1998)
[7] C.H. Lineweaver, Astrophys. J. **505**, L69 (1998)
[8] G.B. Larsen and J. Madsen, Phys. Rev. **D52**, 4282 (1995)
[9] J.A. Adams and S. Sarkar, preprint OUTP-98-70P and talk presented at the workshop on *The Physics of Relic Neutrinos*, Trieste, September 1998
[10] W.H. Kinney and A. Riotto, preprint hep-ph/9903459
[11] U. Seljak and M. Zaldarriaga, Astrophys. J. **469**, 437 (1996)
[12] K. Freese, E.W. Kolb and M.S. Turner, Phys. Rev. **D27**, 1689 (1983)
[13] H. Kang and G. Steigman, Nucl. Phys. **B372**, 494 (1992)
[14] P.B. Pal and K. Kar, Phys. Lett. **B451**, 136 (1999)
[15] S. Sarkar, Rept. Prog. Phys. **59**, 1493 (1996) and references therein
[16] C. Ma and E. Bertschinger, Astrophys. J. **455**, 7 (1995)
[17] W.T. Hu, Ph.D. Thesis (1995), preprint astro-ph/9508126
[18] D.J. Eisenstein, W. Hu and M. Tegmark, Astrophys. J. **518**, 2 (1999)
[19] W. Hu, D.J. Eisenstein and M. Tegmark, Phys. Rev. Lett. **80**, 5255 (1998)
[20] S. Perlmutter *et al.*, Nature **391**, 51 (1998); P.M. Garnavich *et al.*, Astrophys. J. **493**, L53 (1998); A.G. Riess *et al.*, Astron. J. **116**, 1009 (1998)
[21] L. Wang, R.R. Caldwell, J.P. Ostriker, and P.J. Steinhardt, preprint astro-ph/9901388
[22] P. Viana and A.R. Liddle, MNRAS **303**, 535 (1999)
[23] M. Girardi, S. Borgani, G. Giuricin, F. Mardirossian and M. Mezzetti, Astrophys. J. **506**, 45 (1998)
[24] J. Loveday, G. Efstathiou, B.A. Peterson, and S.J. Maddox, Astrophys. J. **400**, L43 (1992)
[25] T. Kolatt and A. Dekel, Astrophys. J. **479**, 592 (1997)
[26] J. Lesgourgues, D. Polarski and A.A. Starobinsky, MNRAS **308**, 281 (1999)
[27] C.H. Lineweaver and D. Barbosa, Astron. & Astroph. **329**, 799 (1998); Astrophys. J. **496**, 624 (1998)

[28] N.A. Bahcall, X. Fan, and R. Cen, Astrophys. J. **485**, L53 (1997); X. Fan, N.A. Bahcall, and R. Cen, Astrophys. J. **490**, L123 (1997); V.R. Eke, S. Cole, C.S. Frenk, and J.P. Henry, MNRAS **298**, 1145 (1998)
[29] G. Gelmini and A. Kusenko, Phys. Rev. Lett. **82**, 5202 (1999)

FIG. 1. Present energy density of massive degenerate neutrinos as a function of the degeneracy ξ. The curves correspond to different values of $h^2\Omega_\nu$ and the horizontal line is the upper bound from eq. (6).

FIG. 2. Same as figure 1 for the neutrino asymmetry L_ν.

FIG. 3. CMB anisotropy spectrum for different models with one family of degenerate neutrinos. Solid lines account for the case of massless degenerate neutrinos, and correspond, from bottom to top, to $\xi = 0, 3, 5$. Dashed lines correspond to degenerate neutrinos with mass $m_\nu = 0.07$ eV. Other parameters are fixed to $h = 0.65$, $\Omega_b = 0.05$, $\Omega_\Lambda = 0.70$, $\Omega_{CDM} = 1 - \Omega_b - \Omega_\nu - \Omega_\Lambda$, $Q_{rms-ps} = 18$ μK, $n = 1$. We neglect reionization and tensor contribution.

FIG. 4. Present power spectrum of matter density, for the same parameters as in the previous figure. From top to bottom, to $\xi = 0, 3, 5$.

FIG. 5. LSS and CMB constraints in (ξ, n) space, for different choices of Ω_Λ: from top left to bottom right, $\Omega_\Lambda = 0, 0.5, 0.6, 0.7$. The underlying cosmological model is flat, with $h = 0.65$, $\Omega_b = 0.05$, $Q_{rms-ps} = 18$ μK, no reionization, no tensor contribution. The allowed regions are those where the labels are. For LSS constraints, we can distinguish between degenerate neutrinos with $m_\nu = 0$ (solid lines) and $m_\nu = 0.07$ eV (dotted lines).

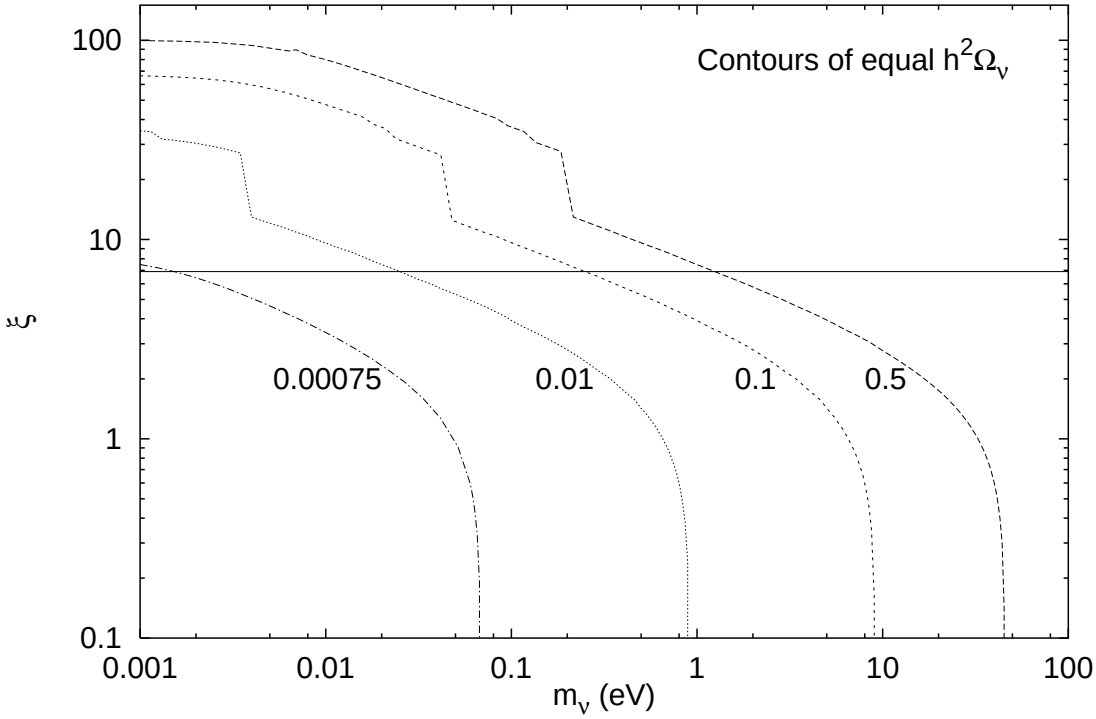
Contours of equal $h^2\Omega_\nu$
100
10
1
0.1
ξ
0.00075
0.01
0.1
0.5
0.001
0.01
0.1
1
10
100
m_ν (eV)

Figure 1

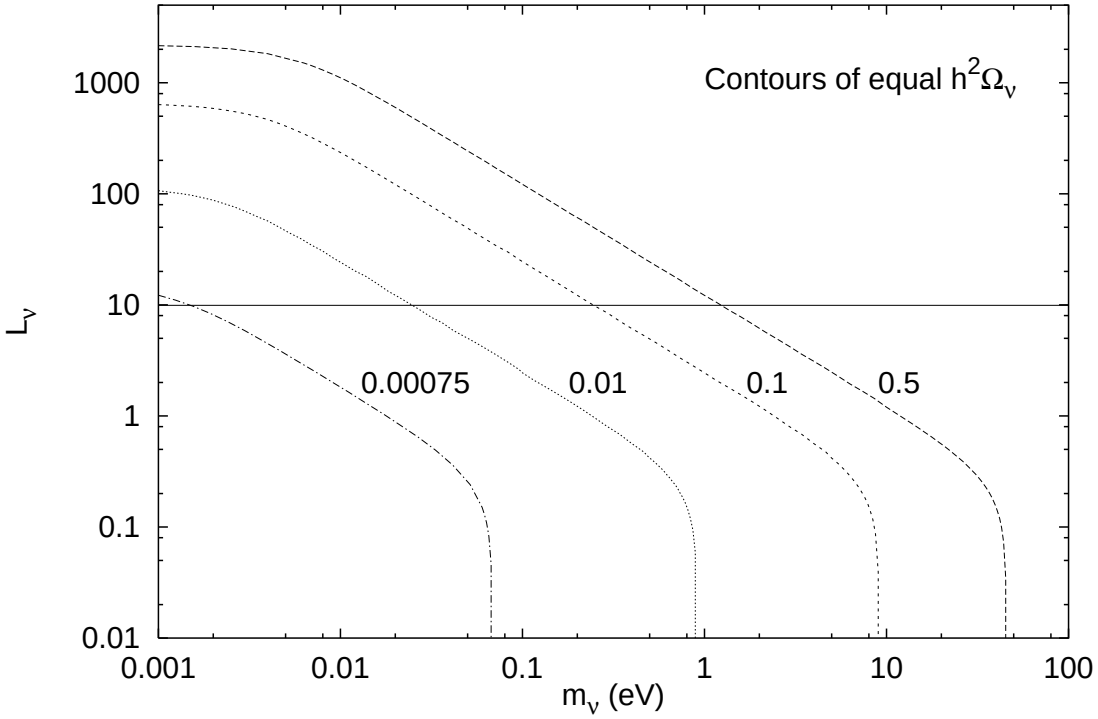
Contours of equal $h^2\Omega_\nu$
0.00075
0.01
0.1
0.5
L_ν
m_ν (eV)
1000
100
10
1
0.1
0.01
0.001
0.01
0.1
1
10
100

Figure 2

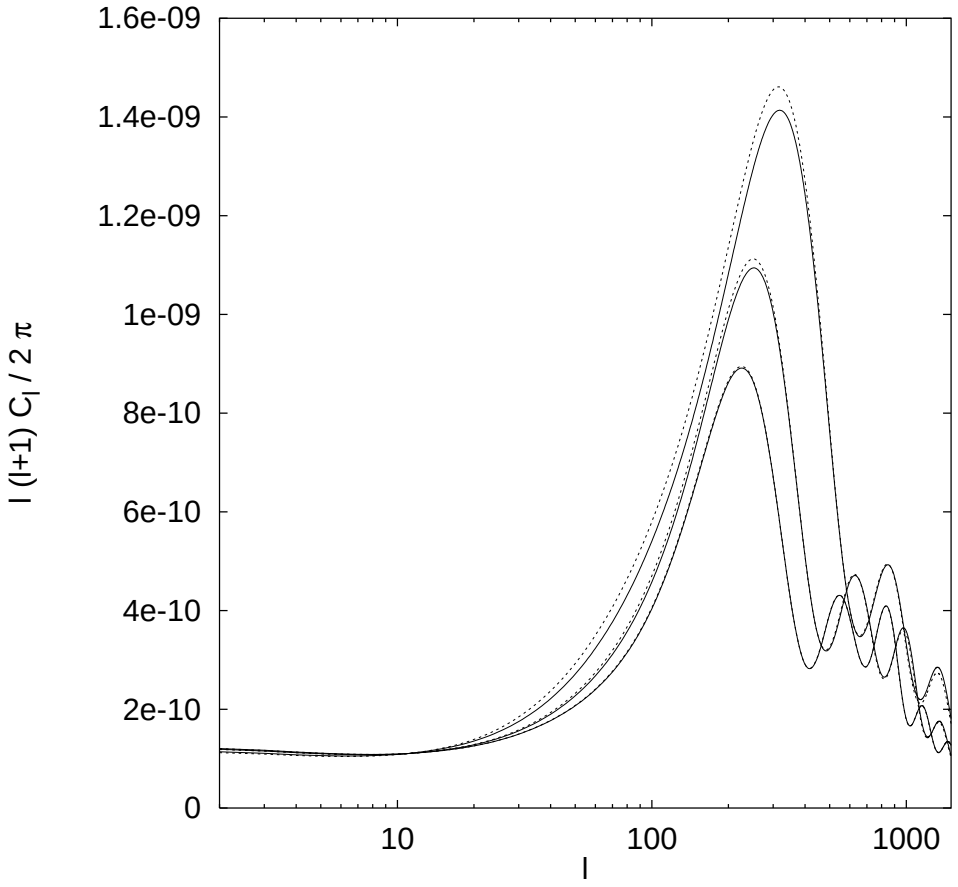
1.6e-09
1.4e-09
1.2e-09
1e-09
8e-10
6e-10
4e-10
2e-10
0
10
100
1000
l
l (l+1) C_l / 2 π

Figure 3

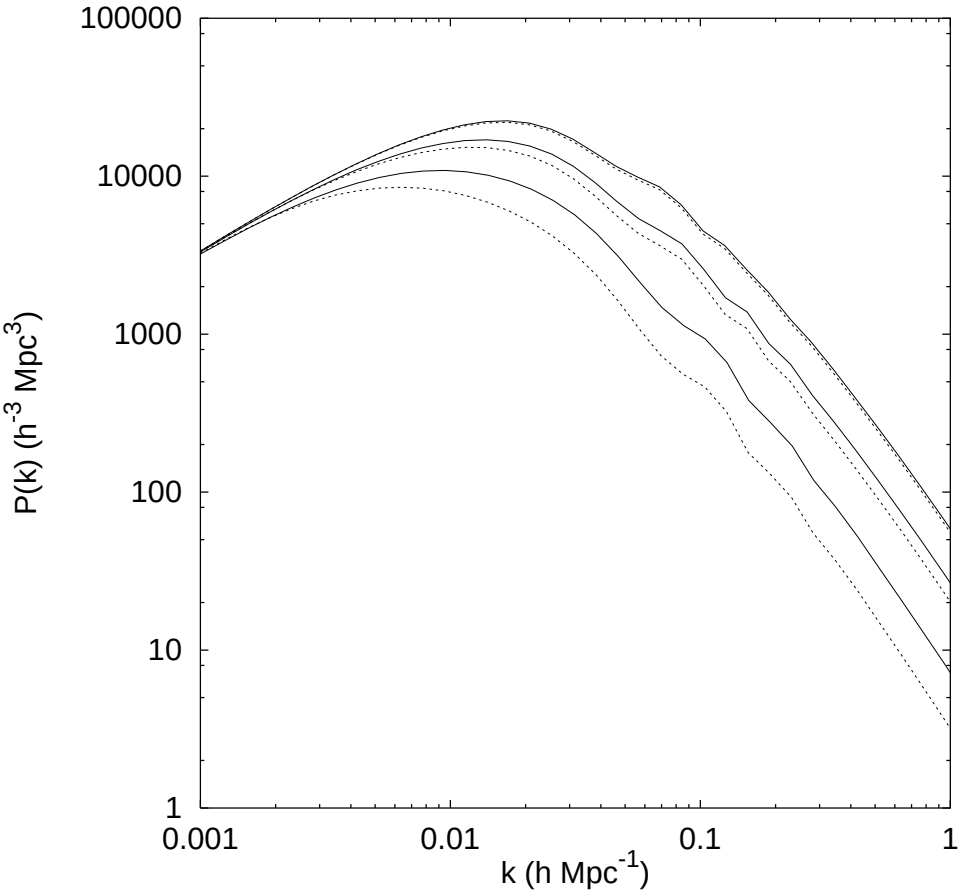

Figure 4

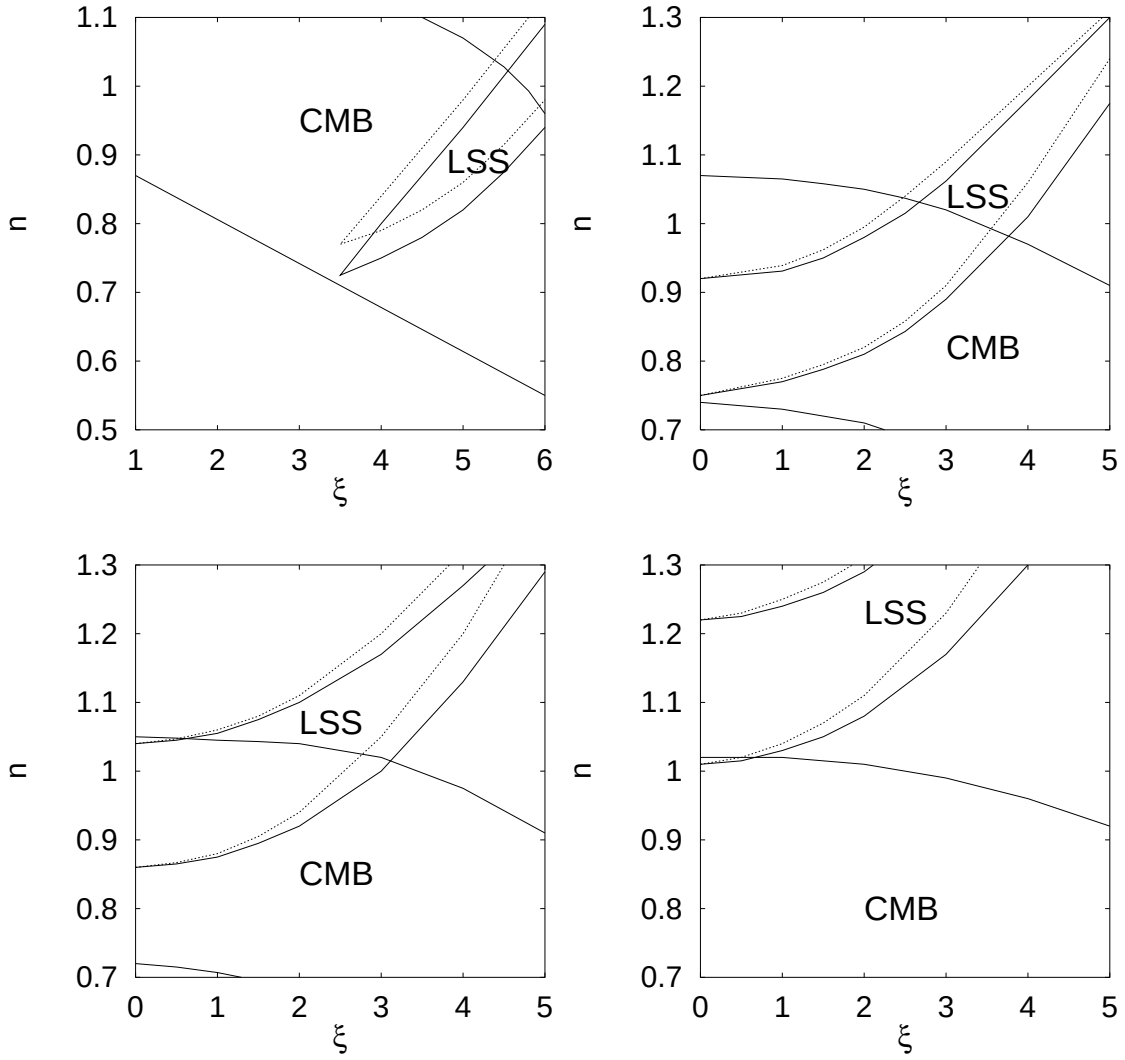

Figure 5

3.3 Implementation of neutrinos in Boltzmann codes, JCAP 1109, 032 (2011)

Preprint typeset in JHEP style. - HYPER VERSION CERN-PH-TH/2011-084, LAPTH-012/11

The Cosmic Linear Anisotropy Solving System (CLASS) IV: Efficient implementation of non-cold relics

Julien Lesgourgues[a,b,c], **Thomas Tram**[d,b]

[a] *Institut de Théorie des Phénomènes Physiques, École Polytechnique Fédérale de Lausanne, CH-1015, Lausanne, Switzerland.*

[b] *CERN, Theory Division, CH-1211 Geneva 23, Switzerland.*

[c] *LAPTh (CNRS - Université de Savoie), BP 110, F-74941 Annecy-le-Vieux Cedex, France.*

[d] *Department of Physics and Astronomy, University of Aarhus, DK-8000 Aarhus C, Denmark.*

Abstract: We present a new flexible, fast and accurate way to implement massive neutrinos, warm dark matter and any other non-cold dark matter relics in Boltzmann codes. For whatever analytical or numerical form of the phase-space distribution function, the optimal sampling in momentum space compatible with a given level of accuracy is automatically found by comparing quadrature methods. The perturbation integration is made even faster by switching to an approximate viscous fluid description inside the Hubble radius, which differs from previous approximations discussed in the literature. When adding one massive neutrino to the minimal cosmological model, `CLASS` becomes just 1.5 times slower, instead of about 5 times in other codes (for fixed accuracy requirements). We illustrate the flexibility of our approach by considering a few examples of standard or non-standard neutrinos, as well as warm dark matter models.

Contents

1. Introduction

The inclusion of massive, non-cold relics in a Boltzmann code is complicated by the fact that it is necessary to evolve the perturbation of the distribution function on a momentum grid. A grid size of N points together with L terms in the expansion of the perturbation leads to $N \cdot L$ added equations to the system. In public Boltzmann codes like `CMBFAST` [1], `CAMB` [2] and `CMBEASY` [3], distributions are sampled evenly with fixed step size and maximum momentum, adapted to the case of a Fermi-Dirac shaped distribution function $f(p)$.

Moreover, the analytic expression for $f(p)$ is hard-coded in many places in those codes, and implicitly assumed e.g. in the mass to density relation, so that exploring other models like neutrinos with chemical potentials and flavour oscillations, neutrinos with non-thermal corrections, extra sterile neutrinos or any kind of warm dark matter candidate requires non-trivial changes to these codes.

We present here the way in which generic Non-Cold Dark Matter (NCDM) relics are implemented in the new Boltzmann code `CLASS`[1] (Cosmic Linear Anisotropy Solving System), already presented in a series of companion papers [4, 5, 6]. In order to ensure a complete flexibility, `CLASS` assumes an arbitrary number of NCDM species, each with an arbitrary distribution function $f_i(p)$. For each species, this function can be passed by the user under some (arbitrarily complicated) analytic form in a unique place in the code, or in a file in the case of non-trivial scenarios that requires a numerical simulation of the freeze-out process. All other steps (finding a mass-density relation, optimising the momentum sampling and computing the derivative of $f_i(p)$) are done automatically in order to ensure maximum flexibility.

In Sec. 2, we present an automatic quadrature method comparison scheme which allows `CLASS` to find an optimal momentum sampling, given $f_i(p)$ and some accuracy requirement, and in Sec. 3, we devise a new approximation scheme allowing us to drastically reduce the computational time for wavelengths inside the Hubble radius. Finally, in Sec. 4 and 5, we illustrate these methods with several examples based on standard and non-standard massive neutrinos, and different types of warm dark matter candidates.

2. Optimal momentum sampling

The formalism describing the evolution of any NCDM species is given by the massive neutrino equations of Ma & Bertschinger [7]. We will follow the notations from this paper closely, with the exceptions

$$q \equiv \frac{q_{\texttt{MB}}}{T_{\texttt{ncdm},0}} \,, \qquad \epsilon \equiv \frac{\epsilon_{\texttt{MB}}}{T_{\texttt{ncdm},0}} = \left(q^2 + a^2 \frac{m^2}{T^2_{\texttt{ncdm},0}} \right)^{\frac{1}{2}} \,, \tag{2.1}$$

where $T_{\texttt{ncdm},0}$ is the temperature of the non-cold relic today, in the case of a thermal relic. If the relic is non-thermal, $T_{\texttt{ncdm},0}$ is just a scale of the typical physical momentum of the particles today. Note that the perturbation equations Eq. (2.4) are still the same as in [7], since they depend only on the ratio q/ϵ which is not affected by this rescaling.

2.1 Perturbations on a grid

We are not interested in the individual momentum components of the perturbation, Ψ_l, but only in the perturbed energy density, pressure, energy flux and shear stress of each

[1] available at `http://class-code.net`. This paper is based on version `v1.1` of the code.

NCDM species, which are integrals over Ψ_l [7]:

$$\delta\rho_{\mathtt{ncdm}} = 4\pi \left(\frac{T_{\mathtt{ncdm},0}}{a}\right)^4 \int_0^\infty f_0(q)\mathrm{d}q q^2 \epsilon \Psi_0, \tag{2.2a}$$

$$\delta p_{\mathtt{ncdm}} = \frac{4\pi}{3} \left(\frac{T_{\mathtt{ncdm},0}}{a}\right)^4 \int_0^\infty f_0(q)\mathrm{d}q \frac{q^4}{\epsilon} \Psi_0, \tag{2.2b}$$

$$(\bar{\rho}_{\mathtt{ncdm}} + \bar{p}_{\mathtt{ncdm}})\, \theta_{\mathtt{ncdm}} = 4\pi k \left(\frac{T_{\mathtt{ncdm},0}}{a}\right)^4 \int_0^\infty f_0(q)\mathrm{d}q q^3 \Psi_1, \tag{2.2c}$$

$$(\bar{\rho}_{\mathtt{ncdm}} + \bar{p}_{\mathtt{ncdm}})\, \sigma_{\mathtt{ncdm}} = \frac{8\pi}{3} \left(\frac{T_{\mathtt{ncdm},0}}{a}\right)^4 \int_0^\infty f_0(q)\mathrm{d}q \frac{q^4}{\epsilon} \Psi_2. \tag{2.2d}$$

In the rest of the article, we will omit all `ncdm` subscripts, and dots will denote derivatives with respect to conformal time, τ.

Note that Ψ_0 and Ψ_1 are gauge-dependent quantities, while higher momenta are not. The gauge transformation can be derived from the corresponding gauge transformation of the integrated quantities. The relation between Ψ_1 in the conformal Newtonian gauge and in the synchronous one reads:

$$\Psi_{1,\mathrm{Con.}} = \Psi_{1,\mathrm{Syn.}} + \alpha k \left[\frac{\epsilon}{q} + \frac{1}{3}\frac{q}{\epsilon}\right] \ , \tag{2.3}$$

with $\alpha \equiv (\dot{h} + 6\dot{\eta})/(2k^2)$, where h and η are the usual scalar metric perturbations in the synchronous gauge. In the rest of this paper, we will work exclusively in the synchronous gauge. The evolution of the Ψ_l's are governed by the Boltzmann equation as described in [7], and leads to the following system of equations:

$$\dot{\Psi}_0 = -\frac{qk}{\epsilon}\Psi_1 + \frac{\dot{h}}{6}\frac{\mathrm{d}\ln f_0}{\mathrm{d}\ln q}, \tag{2.4a}$$

$$\dot{\Psi}_1 = \frac{qk}{3\epsilon}\left(\Psi_0 - 2\Psi_2\right), \tag{2.4b}$$

$$\dot{\Psi}_2 = \frac{qk}{5\epsilon}\left(2\Psi_1 - 3\Psi_3\right) - \left(\frac{\dot{h}}{15} + \frac{2\dot{\eta}}{5}\right)\frac{\mathrm{d}\ln f_0}{\mathrm{d}\ln q}, \tag{2.4c}$$

$$\dot{\Psi}_{l\geq 3} = \frac{qk}{(2l+1)\,\epsilon}\left(l\Psi_{l-1} - (l+1)\,\Psi_{l+1}\right). \tag{2.4d}$$

We can write the homogeneous part of this set of equations as

$$\dot{\mathbf{\Psi}} = \frac{qk}{\epsilon} A \mathbf{\Psi} \equiv \alpha\left(\tau\right) A \mathbf{\Psi}, \tag{2.5}$$

where A is given by

$$A = \begin{bmatrix} -1 & & & & & \\ \frac{1}{3} & & -\frac{2}{3} & & & \\ & \ddots & & \ddots & & \\ & & \frac{l}{2l+1} & & -\frac{l+1}{2l+1} & \\ & & & \ddots & & \ddots \\ & & & & \ddots & \end{bmatrix} \tag{2.6}$$

The solution can be written in terms of the matrix exponential,

$$\mathbf{\Psi}(\tau) = e^{\int_{\tau_i}^{\tau} \mathrm{d}\tau' \alpha(\tau') A} \mathbf{\Psi}(\tau_i) \tag{2.7}$$

$$= U e^{\int_{\tau_i}^{\tau} \mathrm{d}\tau' \alpha(\tau') D} U^{-1} \mathbf{\Psi}(\tau_i), \tag{2.8}$$

where A has been diagonalised such that $A = UDU^{-1}$ and D is a diagonal matrix of eigenvalues of A. The largest eigenvalue of A (using the complex norm) goes toward $\pm i$ for $l_{\max} \to \infty$, so the largest frequency oscillation in the system is

$$\omega_{\max} \simeq k \int_{\tau_i}^{\tau} \mathrm{d}\tau' \left(1 + \frac{M^2}{q^2} a\left(\tau'\right)^2\right)^{-\frac{1}{2}}. \tag{2.9}$$

2.2 Quadrature strategy

There is no coupling between the momentum bins, so our only concern is to perform the indefinite integrals numerically with sufficient accuracy while using the fewest possible points. We are interested in the integrals in Eq. (2.2), which are all on the form

$$\mathcal{I} = \int_0^{\infty} \mathrm{d}q f_0(q)\, g(q), \tag{2.10}$$

where $f_0(q)$ is the phase space distribution and $g(q)$ is some function of q. We will assume that $g(q)$ is reasonably well described by a polynomial in q, which we checked explicitly for the functions in Eq. (2.2). Under this assumption, we can determine the accuracy of any quadrature rule on $\mathcal{I}$ by performing the integral

$$\mathcal{J} = \int_0^{\infty} \mathrm{d}q f_0(q)\, t(q), \tag{2.11}$$

where $t(q)$ is a test function. Given a set of different quadrature rules for performing the integral $\mathcal{I}$, the idea is to choose the rule which can compute $\mathcal{J}$ to the required accuracy `tol_ncdm` using the fewest possible points.

We define a quadrature rule on $\mathcal{I}$ to be a set of weights W_i and a set of nodes q_i, such that

$$\mathcal{I} \simeq \sum_{i=1}^{n} W_i g(q_i). \tag{2.12}$$

Note that the distribution function itself has been absorbed into the weights. The optimal quadrature rule will depend on both the distribution $f_0(q)$ and the accuracy requirement `tol_ncdm`, but the specific method used for obtaining the rule is decoupled from the rest of the code; the output is just two lists of n points, $\{q_i\}$ and $\{W_i\}$. `CLASS` tries up to three different methods for obtaining the most optimal quadrature rule, each with its own strength and weaknesses. These are Gauss-Laguerre quadrature, adaptive Gauss-Kronrod quadrature and a combined scheme. We will now discuss each of them.

2.3 Gauss-Laguerre quadrature

Most of the time, the distribution function will be close to a Fermi-Dirac distribution, and the integrand is exponentially decaying with q. The Gauss-Laguerre quadrature formula is well suited for exponentially decaying integrands on the interval $(0;\infty)$, so this is an obvious choice. The rule is

$$\int_0^\infty \mathrm{d}q e^{-q} h\left(q\right) \simeq \sum_{i=1}^{n} w_i h\left(q_i\right), \tag{2.13}$$

where the nodes q_i are the roots of L_n, the Laguerre polynomial of degree n and the weights can be calculated from the formula

$$w_i = \frac{q_i}{\left(n+1\right)^2 \left[L_{n+1}\left(q_i\right)\right]^2}. \tag{2.14}$$

If we put $h(q) = e^q f_0(q) g(q)$ we obtain the rule

$$W_i = w_i e^{q_i} f_0\left(q_i\right). \tag{2.15}$$

This rule will be very effective when the ratio f_0/e^{-q} is well described by a polynomial, but it will converge very slowly if this is not the case.

2.4 Adaptive sampling

When an integrand has structure on scales smaller than the integration interval, an adaptive integration scheme is often the best choice, since it will subdivide the interval until it resolves the structure and reach the required accuracy. We will use the 15 point Gauss-Kronrod quadrature formula as a basis for our adaptive integrator; 7 of the 15 points can be used to obtain a Gauss quadrature estimate of the integral, and the error estimate on the 15 point formula is then $\mathrm{err}_{\mathrm{est.}} = 200|G7 - K15|^{1.5}$.

The Gauss-Kronrod formula is defined on the open interval $(-1,1)$, but it can be rescaled to work on an arbitrary open interval (a,b). We transform the indefinite integral into a definite integral by the substitution $x = (q+1)^{-1}$:

$$\int_0^\infty \mathrm{d}q f\left(q\right) = -\int_0^1 \mathrm{d}x \frac{\mathrm{d}q}{\mathrm{d}x} f\left(q\left(x\right)\right) = \int_0^1 \mathrm{d}x x^{-2} f\left(q\left(x\right)\right). \tag{2.16}$$

This integral can then be solved by the adaptive integrator. If the tolerance requirement is not met using the first 15 points, the interval is divided in two and the quadrature method is called recursively on each subinterval.

This method is very efficient when the integrand is smooth. For practical purposes, this will be the case unless the phase-space distribution is read from a file with sparse sampling: in this case, the code must interpolate or extrapolate the file values in order to cover the whole momentum range, and the next method may be more efficient.

2.5 Integration over tabulated distributions

If some distribution function is not known analytically, but only on a finitely sampled grid on $(q_{\rm min}, q_{\rm max})$, we have to interpolate the distribution function within the interval, and we have to extrapolate the behaviour outside the interval. Inside the interval we use a spline interpolation, while we assume $f(q < q_{\rm min}) \equiv f(q_{\rm min})$ close to zero. For the tail, we assume the form $f(q) = \alpha e^{-\beta q}$. Requiring the function and its first derivative to be continuous at the point $q = q_{\rm max}$ leads to the following equations for α and β:

$$\alpha = f(q_{\rm max}) e^{\beta q_{\rm max}}, \tag{2.17}$$

$$\beta = -f(q_{\rm max})^{-1} \left.\frac{{\rm d}f}{{\rm d}q}\right|_{q=q_{\rm max}} . \tag{2.18}$$

In the combined scheme we use the 4 point Gauss-Legendre method on the interval $(0, q_{\rm min})$, adaptive Gauss-Kronrod quadrature on $(q_{\rm min}, q_{\rm max})$ and the 6 point Gauss-Laguerre rule on the tail $(q_{\rm max}, \infty)$[2]. This scheme works well when the integrand is interpolated from tabulated points.

2.6 Implementation in CLASS

When `CLASS` initialises the background structure, it will find optimal momentum samplings for each of the species. More specifically, we start by computing the integral of the distribution function multiplied by the test function at high accuracy, which gives a reference value which can be used for comparison. It also creates a binary tree of refinements, from which we can extract integrals at various levels, where level 1 is the best estimate. We choose the highest possible level which results in an error which is less than the input tolerance, and we extract the nodes and weights from that level.

The code will now search for the lowest number of nodes required for computing the integral with the desired accuracy using Gauss-Laguerre quadrature. The most efficient method, the method using the lowest number of points, is then chosen. For a distribution not departing too much from a Fermi-Dirac one, this will usually be Gauss-Laguerre quadrature.

The scheme suggested here has the benefit, that there is just one tolerance parameter directly related to how well the integral is approximated, *independently* of the distribution function. However, for this to be exactly true, we require the test function to be a sufficiently realistic representation of $q^n \Psi_l$ for $n = 2, 3, 4$ and $l = 0, 1, 2$ for the perturbations. We have checked this using different test functions, but in the end we found the polynomial $f(q) = a_2 q^2 + a_3 q^3 + a_4 q^4$ to be adequate. The coefficients were chosen such that

$$a_n \int_0^\infty {\rm d}q \frac{q^n}{e^q + 1} = 1. \tag{2.19}$$

When the phase-space distribution function is passed in the form of a file with tabulated (q_j, f_j) values, the code compares the three previous methods (still with a common tolerance

[2]This version of the rule is obtained by a simple substitution.

parameter) and keeps the best one, which is usually the third one in the case of a poor sampling of the function, or one of the other two in the opposite case.

Note that higher accuracy is needed for integrating background quantities (density, pressure, etc.) than perturbed quantities (the Ψ_l's). On the other hand, the code spends a negligible time in the computation of the former, while reducing the number of sampling points for perturbations is crucial for reducing the total computing time. Hence, `CLASS` calls the quadrature optimisation algorithm twice for each NCDM species, with two different accuracy parameters. The background tolerance is set to a smaller value leading to a finer sampling.

We conclude this section by noticing that this whole process sounds very sophisticated, but requires a negligible computing time in `CLASS`. What really matters is to reduce the number of discrete momenta in the perturbation equations, and this is indeed accomplished thanks to the previous steps (as we shall see in Sec. 5).

3. Sub-Hubble Approximation

3.1 Fluid approximation

Various kinds of approximations for massive neutrino perturbations have been discussed in the past [8, 9, 10]. The approximation discussed here is different and consists in an extension of the Ultra-relativistic Fluid Approximation presented in [5], applying only to the regime in which a given mode has entered the Hubble radius. The idea is that after Hubble crossing, there is an effective decoupling between high multipoles (for which power transfers from smaller l's to higher l's, according to the free-streaming limit) and low multipoles (just sourced by metric perturbation). Hence, when $k\tau$ exceeds some threshold, we can reduce the maximum number of multipoles from some high $l_{\rm max}$ down to $l_{\rm max} = 2$. We showed in [5] that this Ultra-relativistic Fluid Approximation (UFA) allows simultaneously to save computing time (by reducing the number of equations) and to increase precision (by avoiding artificial reflection of power at some large cut-off value $l_{\rm max}$).

In the case of massive neutrinos, we expect the same arguments to hold in the relativistic regime, while in the non-relativistic limit all multipoles with $l > 1$ decay and the species behave more and more like a pressureless fluid. Hence, some kind of fluid approximation is expected to give good results in all cases.

We write the continuity equation and the Euler equation in the usual way. In the synchronous gauge we have

$$\dot{\delta} = -(1+w)\left(\theta + \frac{\dot{h}}{2}\right) - 3\frac{\dot{a}}{a}\left(c^2_{\rm Syn.} - w\right)\delta, \tag{3.1a}$$

$$\dot{\theta} = -\frac{\dot{a}}{a}\left(1 - 3c_g^2\right)\theta + \frac{c^2_{\rm Syn.}}{1+w}k^2\delta - k^2\sigma. \tag{3.1b}$$

Here, c_g^2 is the adiabatic sound speed, and $c^2_{\rm Syn.} \equiv \frac{\delta p}{\delta \rho}$ is the effective sound speed squared in the synchronous gauge. The latter can be related to the physical sound speed defined

in the gauge comoving with the fluid, that we denote $c_{\rm eff}$. The above equations can then be written as:

$$\dot{\delta} = -(1+w)\left(\theta + \frac{\dot{h}}{2}\right) - 3\frac{\dot{a}}{a}\left(c_{\rm eff}^2 - w\right)\delta + 9\left(\frac{\dot{a}}{a}\right)^2(1+w)\left(c_{\rm eff}^2 - c_g^2\right)\frac{\theta}{k^2}, \tag{3.2a}$$

$$\dot{\theta} = -\frac{\dot{a}}{a}\left(1 - 3c_{\rm eff}^2\right)\theta + \frac{c_{\rm eff}^2}{1+w}k^2\delta - k^2\sigma. \tag{3.2b}$$

Later on, we will close the system by an evolution equation for the shear σ, but first we will discuss how to calculate the adiabatic sound speed and how to approximate the effective sound speed $c_{\rm eff}^2$.

3.2 Sound speeds

The adiabatic sound speed can be expressed as

$$\begin{aligned} c_g^2 = \frac{\dot{p}}{\dot{\rho}} = w\frac{\dot{p}}{p}\left(\frac{\dot{\rho}}{\rho}\right)^{-1} &= -w\frac{\dot{p}}{p}\left(\frac{\dot{a}}{a}\right)^{-1}\frac{1}{3(1+w)} \\ &= \frac{w}{3(1+w)}\left(5 - \frac{\mathfrak{p}}{p}\right), \end{aligned} \tag{3.3}$$

where the quantity $\mathfrak{p}$ (called the pseudo-pressure inside `CLASS`) is a higher moment pressure defined by

$$\mathfrak{p} \equiv \frac{4\pi}{3}a^{-4}\int_0^\infty f_0(q)\mathrm{d}q\frac{q^6}{\epsilon^3}. \tag{3.4}$$

With this formulation, we can compute the adiabatic sound speed in a stable and accurate way, without needing to evaluate the time-derivative of the background pressure $\dot{p}$. When the `ncdm` species is no longer relativistic, its pressure perturbation δp defined in Eq. (2.2b) is an independent quantity. Since we do not have an evolution equation for δp, we approximate $c_{\rm eff}^2$ by c_g^2. This approximation is sometimes as much as a factor 2 wrong as shown on Fig. 1.

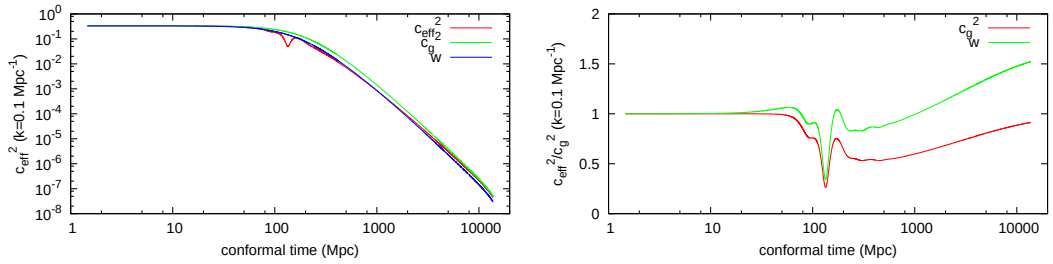

Figure 1: Effective sound speed squared $c_{\rm eff}^2$ for a mass of $m = 2.0$ eV. *Left panel:* The effective sound speed plotted together with the adiabatic sound speed squared c_g^2 and the equation of state parameter w. In the relativistic and the non-relativistic limit we have $c_{\rm eff}^2 = c_g^2$ as expected, but the behaviour of $c_{\rm eff}^2$ in between the two limits are non-trivial. *Right panel:* The ratios $c_{\rm eff}^2/c_g^2$ and $c_{\rm eff}^2/w$. One can see that c_g^2 is a better approximation to $c_{\rm eff}^2$ than w, but neither catches the full evolution.

3.3 Evolution equation for the shear

Given an ansatz for Ψ_3, we can derive a formally correct evolution equation for the shear. We follow Ma and Bertschinger, and close the system using their suggested recurrence relation for massive neutrinos[3]. The truncation law presented in Ma and Bertschinger is valid for $l_{\max} > 3$: in this case, all quantities are gauge-invariant. When writing the same ansatz for $l_{\max} = 3$, we have to face the issue of the gauge dependence of Ψ_1. Asssuming that the truncation law holds for gauge-invariant quantities, one obtains in the synchronous gauge:

$$\Psi_3 \approx \frac{5\epsilon}{qk\tau}\Psi_2 - \left(\Psi_1 + \alpha k\left[\frac{\epsilon}{q} + \frac{1}{3}\frac{q}{\epsilon}\right]\right). \tag{3.5}$$

Throughout this subsection and the next one, one can recover Newtonian gauge equations by simply taking $\alpha = 0$. We now differentiate equation (2.2d):

$$\dot{\sigma} + \frac{\dot{a}}{a}\left(1 - 3c_g^2\right)\sigma = \frac{1}{\rho + p}\frac{8\pi}{3}a^{-4}\int_0^\infty f_0(q)\mathrm{d}qq^4\frac{\partial}{\partial\tau}\left(\frac{\Psi_2}{\epsilon}\right) . \tag{3.6}$$

We can compute the right-hand side using Eq. (2.4c) and replace Ψ_3 with its approximate expression from (3.5). After carrying out integrals over momentum, one gets:

$$\dot{\sigma} = -3\left(\tau^{-1} + \frac{\dot{a}}{a}\left[\frac{2}{3} - c_g^2 - \frac{1}{3}\frac{\Sigma}{\sigma}\right]\right)\sigma + \frac{2}{3}\left[\Theta + \alpha k^2\frac{w}{1+w}\left(3 + \frac{\mathfrak{p}}{p}\right)\right], \tag{3.7}$$

where we have borrowed the notation

$$(\rho + p)\,\Theta = 4\pi k a^{-4}\int_0^\infty f_0(q)\mathrm{d}qq^3\frac{q^2}{\epsilon^2}\Psi_1, \tag{3.8}$$

$$(\rho + p)\,\Sigma = \frac{8\pi}{3}a^{-4}\int_0^\infty f_0(q)\mathrm{d}q\frac{q^4}{\epsilon}\frac{q^2}{\epsilon^2}\Psi_2, \tag{3.9}$$

from [10]. From the definition it is clear that $\Theta \to \theta$ and $\Sigma \to \sigma$ in the relativistic limit, and that Θ and Σ become suppressed in the non-relativistic regime compared to θ and σ. Our differential equation for σ differs from its Newtonian gauge counterpart in [10], because we have used the recurrence relation to truncate the hierarchy, while Shoji and Komatsu have used $\Psi_3 = 0$. The evolution equation for the shear can be further simplified by using Eq. (3.3), leading to:

$$\dot{\sigma} = -3\left(\tau^{-1} + \frac{\dot{a}}{a}\left[\frac{2}{3} - c_g^2 - \frac{1}{3}\frac{\Sigma}{\sigma}\right]\right)\sigma + \frac{2}{3}\left[\Theta + \alpha k^2\left(8\frac{w}{1+w} - 3c_g^2\right)\right] . \tag{3.10}$$

3.4 Estimating higher order momenta

One way to close the system governing the fluid approximation is to replace Θ and Σ by the usual quantities θ and σ multiplied by functions depending only on background quantities

[3]The recurrence relation in the massless limit is better motivated theoretically, since $\Psi_l \propto j_l(k\tau)$ when metric perturbations vanish or satisfy a simple constraint (namely, $\dot{\phi} + \dot{\psi} = 0$ in the Newtonian gauge). In the massive case, the formal solution involves more complicated oscillating functions with arguments going from $\sim k\tau$ in the massless limit to $\sim (k\tau)^{-1}$ in the massive limit, as can be checked from eq. (2.9).

(in the same way that we already approximated δp by $c_g^2 \delta\rho$). More explicitly, our aim is to write an approximation of the type $\Sigma = 3 w_\sigma \sigma$, where w_σ could be any function of time going from one third in the relativistic limit to zero in the non-relativistic one. Since θ and Θ are not gauge-independent, we should search for a similar approximation holding on their gauge-independent counterpart. In the synchronous gauge, such an approximation would read

$$\left[\Theta + \alpha k^2 \left(8\frac{w}{1+w} - 3c_g^2\right)\right] = 3 w_\theta \left[\theta + \alpha k^2\right] \ . \tag{3.11}$$

However, we will stick to the notations of [8], who introduced a viscosity speed related to our w_θ through

$$c_{\rm vis}^2 = \frac{3}{4} w_\theta (1+w) \ . \tag{3.12}$$

With such assumptions, the approximate equation for the shear would read

$$\dot\sigma = -3\left(\frac{1}{\tau} + \frac{\dot a}{a}\left[\frac{2}{3} - c_g^2 - w_\sigma\right]\right)\sigma + \frac{4}{3}\frac{c_{\rm vis}^2}{1+w}\left[2\theta + 2\alpha k^2\right] \ . \tag{3.13}$$

Since the suppression factor q^2/ϵ^2 which appears in Eq. (3.8, 3.9) compared to Eq. (2.2c, 2.2d) is also found in the pressure integral compared to the energy density integral, we may guess that the relative behaviour is similar, i.e. related by w. This leads to a guess $w_\sigma = w$ and $w_\theta = w$ which implies $c_{\rm vis}^2 = \frac{3}{4} w\,(1+w)$. However, the same logic would imply $c_{\rm eff}^2 = w$, which we have shown in Fig. 1 is not exactly true.

Let us investigate a bit how to approximate higher momenta quantities like Θ and Σ. If we want to approximate Θ for instance, we may assume some functional form of $\Psi_1(q)$ described by a single (time dependent) parameter. We can make the ansatz $\Psi_1(q/\epsilon) \approx a_{1n}(t)\left(\frac{q}{\epsilon}\right)^n$, and then use θ to determine the parameter $a_{1n}(t)$. We then find

$$\Theta \approx \theta \frac{\int_0^\infty f_0(q) {\rm d}q q^3 \frac{q^2}{\epsilon^2}\left(\frac{q}{\epsilon}\right)^n}{\int_0^\infty f_0(q) {\rm d}q q^3 \left(\frac{q}{\epsilon}\right)^n}. \tag{3.14}$$

The guess $c_{\rm vis}^2 = \frac{3}{4} w\,(1+w)$ can be seen to be a special case of this approach having $n = -1$. The problem is that the value of n best approximating the behavior of Ψ_1 and other momenta is not the same in the relativistic and non-relativistic limit. In fact our testing shows that this guess sources σ too much during the relativistic to non-relativistic transition compared to the exact solution. Instead we got much better results by using $c_{\rm vis}^2 = 3 w c_g^2$, which avoids this excessive sourcing during the transition, while still reducing to 1/3 in the relativistic limit.

For the ratio Σ/σ, the assumption of a q-independent Ψ_2 (i.e. $n = 0$) yields $w_\sigma = \mathfrak{p}/(3p)$, which provides satisfactory results and is adopted in the schemes described below.

We speculate that by pushing these kinds of considerations further, one could find better approximations for $c_{\rm eff}^2$, $c_{\rm vis}^2$ and w_σ. It is also possible that another independent equation could be found, and that it would allow a better determination of $c_{\rm eff}$.

3.5 Implementation in CLASS

For comparison, we have implemented 3 different Non-Cold Dark Matter Fluid Approximations (NCDMFA) in `CLASS` which differ only in their respective equation for the shear. In correspondence with the Ultra-relativistic Fluid Approximation discussed in [5], we have named the approximations `MB`, `Hu` and `CLASS`: in the relativistic limit, they reduce to their relativistic counterpart in [5]. In all three approximations we are using Eq. (3.2a) and (3.2b) as the first two equations with $c_{\rm eff} = c_g$. The respective equations for the shear read

$$\dot{\sigma}_{\texttt{MB}} = -3\left(\frac{1}{\tau} + \frac{\dot{a}}{a}\left[\frac{2}{3} - c_g^2 - \frac{1}{3}\frac{\mathfrak{p}}{p}\right]\right)\sigma + \frac{4}{3}\frac{c_{\rm vis}^2}{1+w}\left[2\theta + \dot{h} + 6\dot{\eta}\right], \quad c_{\rm vis}^2 = 3wc_g^2, \quad (3.15a)$$

$$\dot{\sigma}_{\texttt{Hu}} = -3\frac{\dot{a}}{a}\frac{c_g^2}{w}\sigma + \frac{4}{3}\frac{c_{\rm vis}^2}{1+w}\left[2\theta + \dot{h} + 6\dot{\eta}\right], \qquad c_{\rm vis}^2 = w, \quad (3.15b)$$

$$\dot{\sigma}_{\texttt{CLASS}} = -3\left(\frac{1}{\tau} + \frac{\dot{a}}{a}\left[\frac{2}{3} - c_g^2 - \frac{1}{3}\frac{\mathfrak{p}}{p}\right]\right)\sigma + \frac{4}{3}\frac{c_{\rm vis}^2}{1+w}\left[2\theta + \dot{h}\right], \qquad c_{\rm vis}^2 = 3wc_g^2. \quad (3.15c)$$

The second shear equation, named `Hu`, corresponds exactly to the prescription of Ref. [8] for approximating massive neutrinos. The first shear equation, `MB`, comes directly from (3.13) with the values of w_σ and $c_{\rm vis}$ motivated in the previous subsection. Finally, in [5], we found that removing the $\dot{\eta}$ term leads to slightly better results for the matter power spectrum, and can be justified using an analytic approximation to the exact equations. By analogy, we also define in the massive neutrino case a `CLASS` approximation identical to the `MB` one except for the omission of this term.

In Fig. 2 we have tested these three fluid approximations in a model with no massless neutrinos and 3 degenerate massive neutrinos. The three approximations work very well as long as the neutrinos are light and become non-relativistic after photon decoupling. Like in the massless case, the `CLASS` approximation is slightly better for predicting the matter power spectrum on small scales, and we set it to be the default method in the code. When the mass increases, the fluid approximation alters the CMB spectra on small angular scales ($l \geq 2500$), but the error remains tiny (only 0.02% for $l = 2750$ for three species with $m = 1$eV). The effect on the matter power spectrum is stronger: with three 1 eV neutrinos, the $P(k)$ is wrong by 1 to 3% for $k \in [0.05; 1]h\mathrm{Mpc}^{-1}$. Hence, we recommend to use the fluid approximation for any value of the mass when computing CMB anisotropies, and only below a total mass of one or two eV's when computing the matter power spectrum. However, cosmological bounds on neutrino masses strongly disfavour larger values of the total mass. This means that in most projects, `CLASS` users can safely use the fluid approximation for fitting both CMB and large scale structure data.

4. Standard massive neutrinos

We first illustrate our approach with the simple case of standard massive neutrinos with a Fermi-Dirac distribution. In this case, for each neutrino, the user should provide two numbers in the input file: the mass m, and the relative temperature `T_ncdm` $\equiv T_\nu/T_\gamma$ (the ratio of neutrino to the photon temperature). The `CLASS` input file `explanatory.ini` recommends to use the value `T_ncdm`=0.71599, which is "fudged" in order to provide a

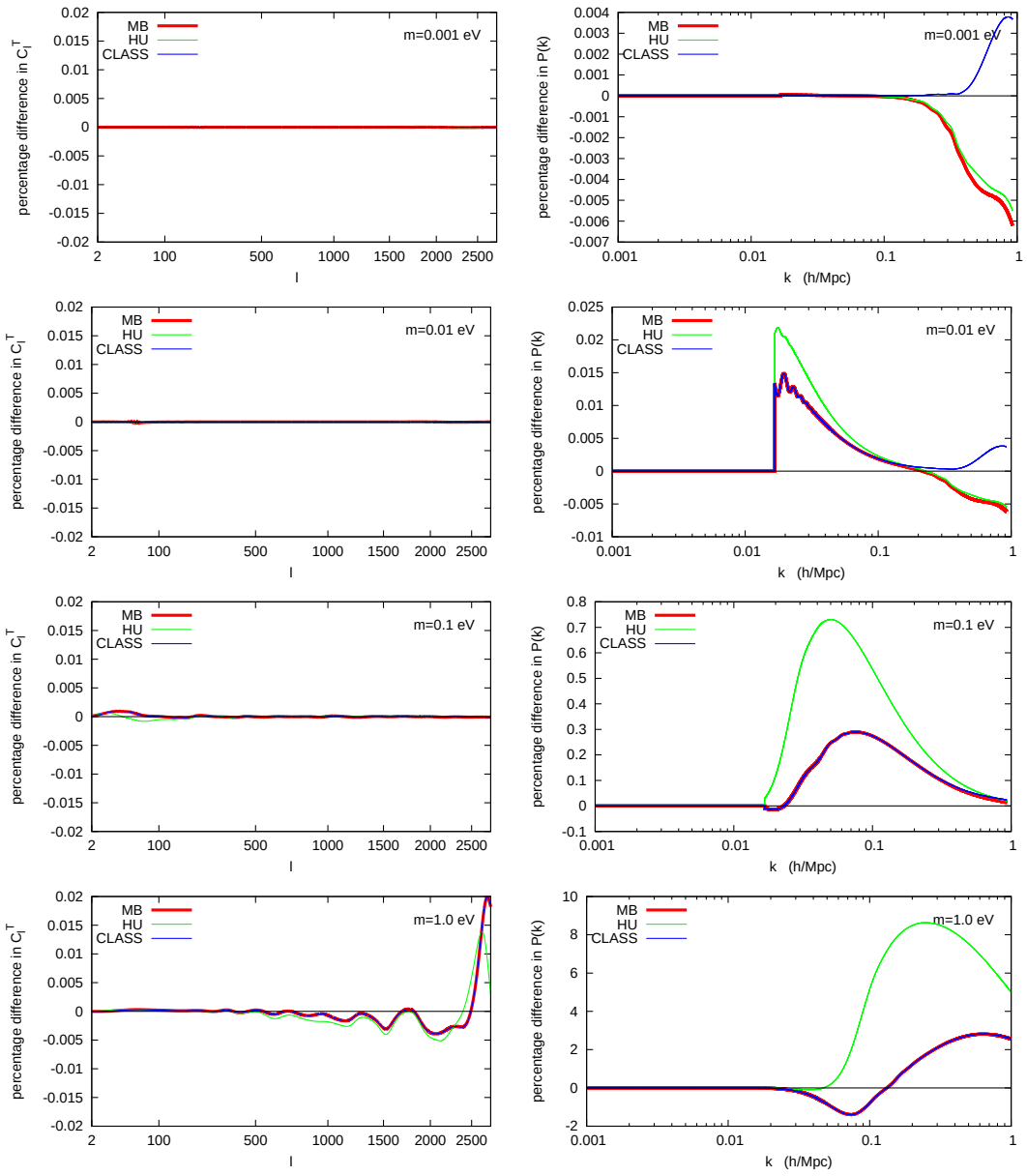

Figure 2: On the left, we have shown the percentage difference in the C_l^T for three degenerate neutrino species with mass $m = 0.001$eV, $m = 0.01$eV, $m = 0.1$eV and $m = 1$eV respectively, in runs with/without the fluid approximation. The fluid approximation works very well as long as the neutrinos are relativistic, so this is what we expect. On the right we have shown the matter power spectrum for the same masses. Here the agreement is not so good as the mass becomes higher.

mass-to-density ratio $m/\omega_\nu = 93.14$ eV in the non-relativistic limit. This number gives a very good approximation to the actual relic density of active neutrinos, resulting from an accurate study of neutrino decoupling [11]. However, when comparing the `CLASS` results

with those from `CAMB`, we take `T_ncdm`=0.7133 in order to recover the mass-to-density ratio assumed in that code. Finally, if no temperature is entered, the code will default to the instantaneous decoupling value of $(4/11)^{1/3}$.

4.1 Agreement with CAMB

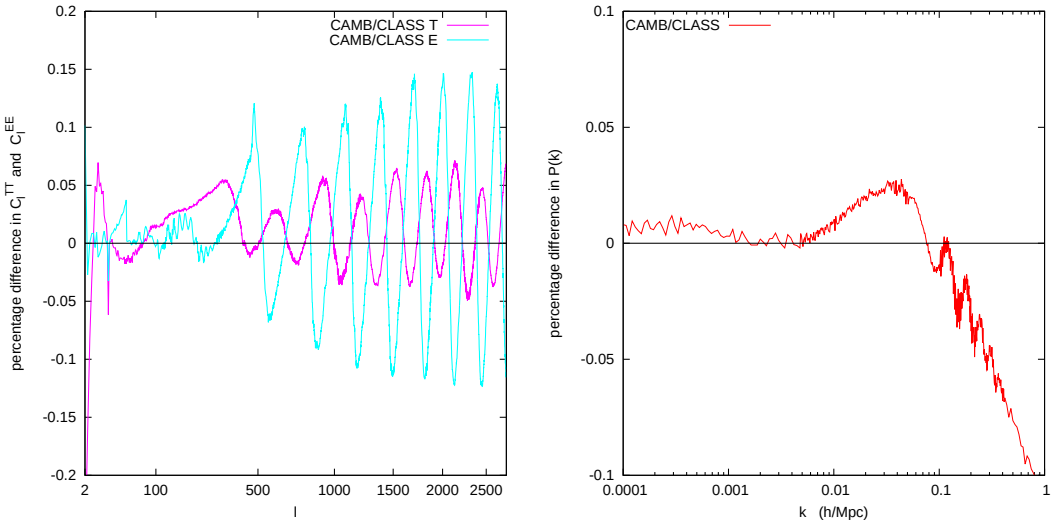

Figure 3: Relative difference between `CAMB` and `CLASS` spectra in a model with $\Omega_\nu = 0.02$, two massless neutrinos, and reference accuracy settings. The two codes agree rather well.

In Fig. 3, we compare the CMB and matter power spectrum from `CAMB` and `CLASS` (without the NCDM fluid approximation) for two massless and one massive neutrino with $\Omega_\nu = 0.02$ (corresponding to a mass $m \simeq 0.923$eV). We used high accuracy settings for `CAMB`, described in [6] under the name *[CAMB:07]*. For `CLASS`, we used the input file `cl_ref.pre`, which corresponds to the setting *[CLASS:01]* in [6] for parameters not related to NCDM; for the latter, `cl_ref.pre` contains the settings described in the first column of Table 1. For such settings and in absence of massive neutrinos, the two temperature spectra would agree at the 0.01% level in the range $l \in [20; 3000]$; at the 0.02% level for polarization in the same range; and at the 0.01% level for the matter power spectrum for $k < 1h\text{Mpc}^{-1}$. With a neutrino mass close to 1 eV, we see in Fig. 3 that the discrepancy is approximately six times larger than in the massless case. However, it remains very small: even with massive neutrinos the two codes agree to better than 0.1% for the CMB and matter power spectra. This is by far sufficient for practical applications.

In a perfect implementation of massless and massive neutrinos in Boltzmann codes, we expect that in the relativistic limit $m \ll T_\nu^0$ (where T_ν^0 is the neutrino temperature today) the spectra would tend towards those obtained with three massless species (provided that we are careful enough to keep the same number of relativistic degrees of freedom $N_{\rm eff}$). We performed this exercise for both codes, and the results are presented in Fig. 4. It appears that with a small enough mass, `CLASS` can get arbitrarily close to the fully relativistic case:

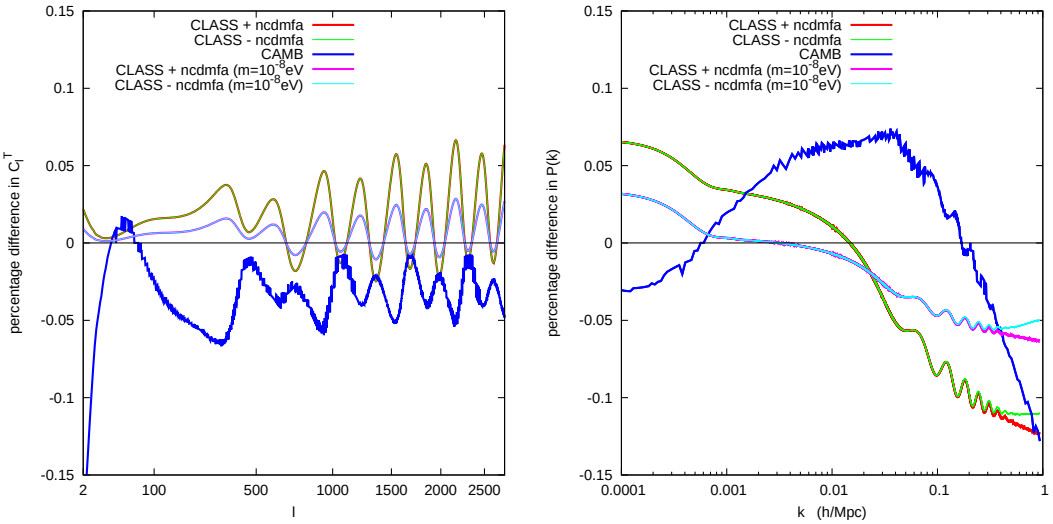

Figure 4: This is a test of how well `CAMB` and `CLASS` recovers the massless limit. We compute a model with $\Omega_\nu = 1.2 \cdot 10^{-4}$ and 3 massive neutrinos with degenerate mass. This setting corresponds to a neutrino mass of $m_i = 2.8 \cdot 10^{-4}$eV, which is not exactly massless, but it is the best we can do since the mass parameter can not be set directly in `CAMB`. Setting the mass parameter in `CLASS` to $m_i = 10^{-8}$eV reveals that we are in part seeing the effect of the neutrino going slightly non-relativistic at late times.

with a mass of 10^{-8}eV, the difference is at most of 0.03% in the C_l's and 0.05% in the $P(k)$. This test is another way to validate the accuracy of our implementation.

4.2 Accuracy settings

We now come to the question of defining degraded accuracy settings for computing the spectra in a fast way, while keeping the accuracy of the results under control. For such an exercise, we need to define a measure a precision. Like in [6], we will use an effective χ^2 which mimics the sensitivity of a CMB experiment like Planck to temperature and E-polarisation anisotropies. Taking the runs with accuracy settings `cl_ref.pre` as a reference, we decrease the precision for each parameter while keeping the $\Delta\chi^2$ roughly below a given limit, chosen to be either 0.1 or 1. This exercise was already performed in [6] for all parameters not related to NCDM, leading to the definition of two precision files `chi2pl0.1.pre` and `chi2pl1.pre` which are available on the `CLASS` web site. Here, we only need to set the NCDM precision parameters in these two files to correct values. Our results are listed in Table 1, in the second and third columns. They take advantage of the fluid approximation, and use an extremely small number of momenta (8 or 5 only). We checked that these settings provide the correct order of magnitude for $\Delta\chi^2$ within a wide range of neutrino masses, at least up to 2 eV. This is shown in Table 2 for the two cases `chi2pl0.1.pre` and `chi2pl1.pre`, as well as for the case `chi2pl1.pre` with the fluid approximation removed. Around $m = 2$ eV, the error induced by the fluid approximation starts increasing significantly: when exploring this region, the user should either turn off

the approximation, or increase the value of the $k\tau$ trigger. Given current limits on active neutrino masses, the interesting mass range to explore is below 2 eV, and in most projects, the `CLASS` users can safely employ the default settings of `chi2pl0.1.pre` and `chi2pl1.pre` including the fluid approximation.

These settings are optimised for fitting the CMB spectra only. For the matter power spectra, the files `chi2pl0.1.pre` and `chi2pl1.pre` produce an error of the order of a few per cents in the range $k \in [0.05; 1]h\text{Mpc}^{-1}$ (for any neutrino mass and with/without the fluid approximation). In order to get accurate matter power spectra, it is better to employ the settings `cl_permille.pre`, `cl_2permille.pre`, `cl_3permille.pre`, which lead to a precision of 1, 2 or 3 per mille for C_l^{TT} in the range $2 < l < 3000$, even in the presence of neutrino masses. In these files, we fixed the fluid approximation trigger to a rather larger value in order to get a precision of one permille for the matter power spectrum for $k < 0.2h\text{Mpc}^{-1}$ and $m < 2$ eV, or a bit worse for mildly non-linear scales $k \in [0.2; 1]h\text{Mpc}^{-1}$. The power spectrum accuracy with such settings is indicated in Table 3 for various values of the mass.

	`cl_ref.pre`	`chi2pl0.1.pre`	`chi2pl1.pre`
`tol_ncdm_bg`	10^{-10}	10^{-5}	10^{-5}
`tol_ncdm`	10^{-10}	10^{-4}	10^{-3}
`l_max_ncdm`	51	16	12
fluid approximation	none	`ncdmfa_class`	`ncdmfa_class`
$k\tau$ trigger	–	30	16
number of q (back.)	28	11	11
number of q (pert.)	28	8	5
number of neutrino equations	1428	136→3	65→3

Table 1: Accuracy parameters related to NCDM in the three precision files `cl_ref.pre`, `chi2pl0.1.pre` and `chi2pl1.pre`. When the fluid approximation is used, the method described in section 3 is employed, and the switching time is set by the above values of $k\tau$. Below these parameters, we indicate the corresponding number of momenta sampled in background quantities and in perturbation quantities, as well as the number of neutrino perturbation equations integrated over time, equal to (`l_max_ncdm`+1) times the number of sampled momenta when the fluid approximation is not used, and to three afterwards.

4.3 Performance

The quadrature method reveals to be extremely useful since even with five values of the momenta, we get accurate results leading to 0.2%-0.3% accuracy on the $C_l's$, 0.1% accuracy on the $P(k)$ and $\Delta\chi^2 \sim 1$. Traditional Boltzmann codes employ 14 momenta in order to achieve a comparable precision. In the presence of massive neutrinos, the total execution time of a Boltzmann code is dominated by the integration of the perturbation equations, which depends on the total number of perturbed variables, itself dominated by the number of massive neutrino equations. By reducing the number of momenta from 14 to 5, the quadrature method speeds up the code by more than a factor two. We find that the use of the fluid approximation leads to an additional 25% speed up for standard accuracy settings

mass (eV)	`chi2pl0.1.pre`	`chi2pl1.pre`	same without approx.
10^{-3}	0.087	0.94	0.90
10^{-2}	0.087	0.93	0.92
0.1	0.092	0.90	0.92
1	0.083	0.96	0.82
2	0.157	1.10	0.93

Table 2: For a CMB instrument with the sensitivity of Planck, χ^2 difference between the spectra obtained with reference accuracy settings and with degraded accuracy settings, for various values of the neutrino mass (all models have two massless and one massive neutrinos). This shows that our accuracy settings `chi2pl0.1.pre` and `chi2pl1.pre` always lead to an accuracy of roughly $\Delta\chi^2 \sim 0.1$ or $\Delta\chi^2 \sim 1$ respectively. The last column correspond to the settings of `chi2pl1.pre`, but without the fluid approximation.

mass (eV)	$k < 0.2h\mathrm{Mpc}^{-1}$	$k \in [0.2;1]h\mathrm{Mpc}^{-1}$
10^{-3}	0.04%	0.12%
10^{-2}	0.04%	0.12%
0.1	0.05%	0.12%
1	0.06%	0.8%
2	0.2%	1.5%

Table 3: Maximum error induced by any of the `cl_permille.pre`, `cl_2permille.pre` or `cl_3permille.pre` precision settings on the linear matter power spectrum $P(k)$, for approximately linear scales $k < 0.2h\mathrm{Mpc}^{-1}$ (first column) or mildly non-linear scales $k \in [0.2;1]h\mathrm{Mpc}^{-1}$ (second column), and for various values of the neutrino mass (all models have two massless and one massive neutrinos). The fluid approximation introduces an error which remains below the per mille level until $k = 0.2h\mathrm{Mpc}^{-1}$ for $m < 2$ eV, and exceeds this level for larger masses.

(like those in the file `chi2pl1.pre`). In total, for a single massive neutrino, our method speeds up the code by a factor 3. This means that instead of being 4.5 times slower in presence of one massive neutrino, `CLASS` only becomes 1.5 times slower. We checked these numbers with various masses and accuracy settings.

4.4 Realistic mass schemes

We have proved in this section that `CLASS` can be employed in any project requiring high-precision computations of cosmological observables in presence of massive neutrinos. It is of course perfectly suited for realistic situations with different neutrino species and masses.

To illustrate this, we display in Figure 5 the ratio of pairs of matter power spectra for models with three massive neutrinos satisfying constraints from atmospheric/solar oscillation experiments [12] ($\Delta m^2_{21} = 7.6 \times 10^{-5}\mathrm{eV}^2$, $\Delta m^2_{32} = \pm 2.4 \times 10^{-3}\mathrm{eV}^2$). Each pair of models corresponds to one normal hierarchy and one inverted hierarchy scenario, with the same total mass M_ν, equal to 0.100 eV, 0.115 eV or 0.130 eV. The first total mass is very close to the minimum allowed value for the inverted hierarchy, $M_\nu \simeq 0.0994$ eV. For each pair or models with a given M_ν:

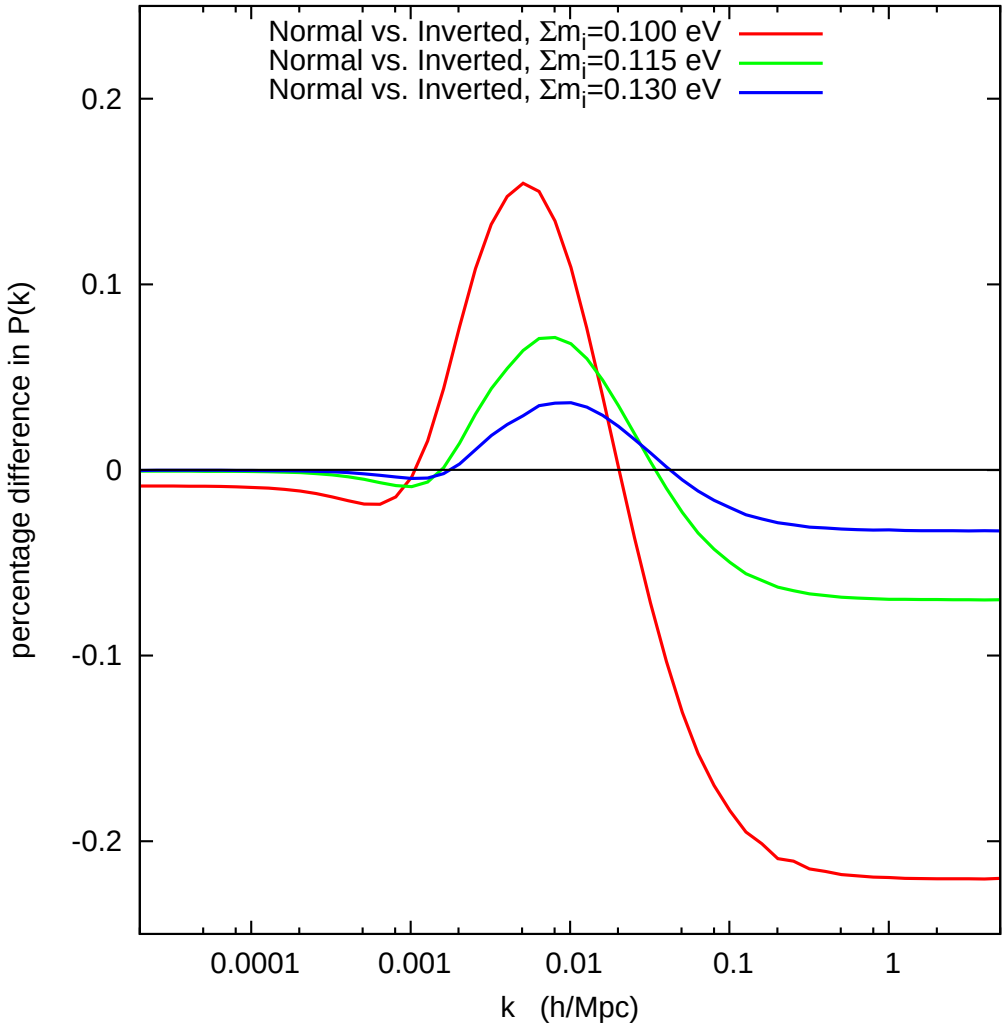

Figure 5: Ratio of matter power spectra for pairs of models with three massive neutrinos, obeying either to the normal or inverted hierarchy scenario, but with a common total mass for each pair: $M_\nu = 0.100$ eV, 0.115 eV or 0.130 eV. The various effects observed here are discussed in the text.

- on intermediate scales, the bump reflects the difference in the three free-streaming scales involved in the two models.

- in the large k limit, the two spectra are offset by 0.03% to 0.22%: it is known that in this limit, the suppression in the power spectrum induced by neutrino free-streaming depends mainly on the total mass (through the famous $-8f_\nu$ approximate formula), but also slightly on the mass splitting (in [13], a more accurate formula gives the suppression as a function of both the total mass and number of degenerate massive neutrinos). When M_ν increases, the two models are less different from each other (they go towards a common limit, namely the degenerate mass scenario), and the discrepancy is less pronounced.

- in the small k limit, the two spectra are nearly identical. The tiny difference, which increases when M_ν decreases, is due to the fact that in the inverted hierarchy model, there is a very light neutrino just finishing to complete its non-relativistic transition today. It therefore has a non-negligible pressure, which slightly affects metric perturbations on large wavelengths.

Observing the difference between these two models would be extremely challenging, although 21 cm surveys could reach enough sensitivity [14].

5. Beyond standard massive neutrinos

In this section we will illustrate the power and flexibility of the non-cold Dark Matter implementation in `CLASS`, by implementing different models which have already been studied elsewhere in the literature.

5.1 Massive neutrinos with large non-thermal corrections

It is plausible that some new physics can introduce non-thermal corrections to an otherwise thermal Fermi-Dirac distribution function. One might think of using CMB and large scale structure data to put bounds on such non-thermal corrections, as was described e.g. in [15]. `CLASS` is ideally suited for playing with such models. As a test case, we take the following distribution from [15]:

$$f(q) = \frac{2}{(2\pi)^3}\left[\frac{1}{e^q+1} + \frac{A\pi^2}{q^2\sqrt{2\pi}\sigma}\exp\left(-\frac{(q-q_c)^2}{2\sigma^2}\right)\right], \tag{5.1}$$

which is the Fermi-Dirac distribution with an added Gaussian peak in the number density. This distribution could presumably be the result of some particle suddenly decaying into neutrinos at a late time.

In practise, we only need to change the expression for $f(q)$ in `CLASS`, which appears in a unique line (in the function `background_ncdm_distribution()`). All the rest, like density-to-mass relation and computation of the logarithmic derivative, is done automatically by the code. In particular, we do not need to change the accuracy parameters `tol_ncdm` and `tol_ncdm_bg`: the momentum sampling algorithm automatically increases the number of momenta by a significant amount, in order to keep the same precision. If this was not the case, the effect of the peak would be underestimated because of under sampling, and the parameter extraction would then likely be biased.

In Fig. 6, we show the CMB and matter power spectra for this model, relative to a standard model with three thermally distributed neutrinos. The two models are chosen to share exactly the same masses and the same initial number of relativistic degrees of freedom $N_{\rm eff}$. Nevertheless, they do not have the same non-relativistic neutrino density and average neutrino momentum; in particular, non-thermal neutrinos in the decay peak become non-relativistic slightly later. This induces a combination of background and perturbation effects affecting CMB and matter power spectra in a significant way.

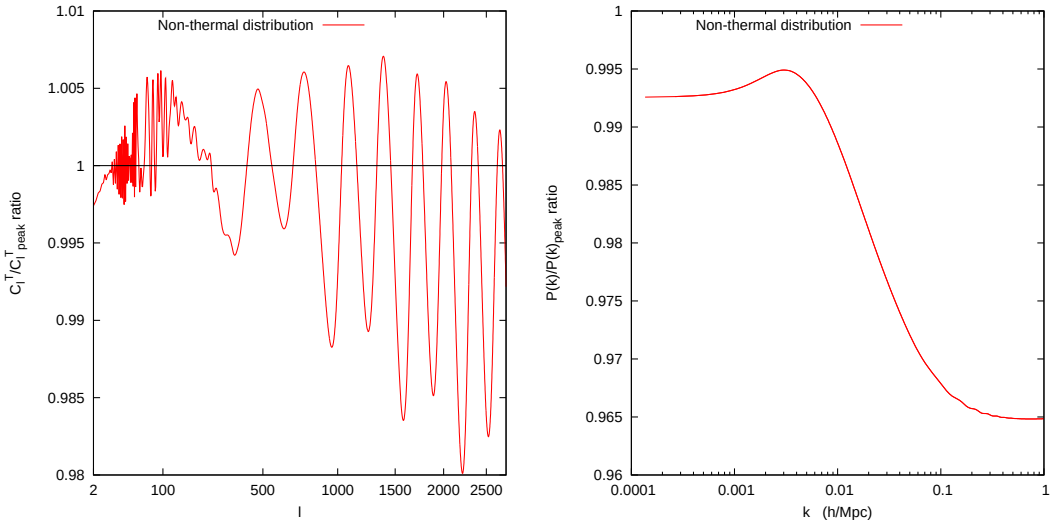

Figure 6: C_l's and $P(k)$'s for a model of 3 degenerate neutrinos with the non-thermal distribution (5.1) using parameters $m = 1.0$ eV, $A = 0.018$, $\sigma = 1.0$ and $q_c = 10.5$. This corresponds to $N_{\rm eff} = 3.98486$. We have compared this model to a model with degenerate thermal neutrinos with the same mass and $N_{\rm eff}$. The signal is due to a combination of background and perturbation effects: although the mass and the relativistic density are the same, the non-relativistic density and the average momentum differ significantly in the two models.

5.2 Warm dark matter with thermal-like distribution

There is an infinity of possible warm dark matter models, since the phase-space distribution of warm dark matter depend on the details of its production mechanism. The most widely studied model is that of non-resonantly produced warm dark matter with a rescaled Fermi-Dirac distribution, having the same temperature as that of active neutrinos. This model is implemented in the default `CLASS` version: when the user enters a temperature, a mass and a density $\Omega_{\rm ncdm}$ (or $\omega_{\rm ncdm}$) for the same species, the code knows that the degeneracy parameter in front of the Fermi-Dirac distribution must be rescaled in order to match these three constraints simultaneously. The code will also ensure that the perturbations begin to be integrated when the non-cold species is still relativistic, in order to properly follow the transition to the non-relativistic regime.

We illustrate this by running a ΛWDM model with a mass of $m = 1$keV or $m = 10$keV and a density $\Omega_{\rm ncdm} = 0.25$, with or without the fluid approximation. We compare the results with those of ΛCDM with $\Omega_{\rm cdm} = 0.25$, in order to show the well-known suppression effect of WDM in the small-scale limit of the matter power spectrum. It appears that the fluid approximation works very well in those cases, unless one wants to resolve the details of the WDM acoustic oscillations on very small scales, first predicted in [16].

5.3 Warm dark matter with non-trivial production mechanism

Non-resonantly produced warm dark matter candidates are severely constrained by Lyman-α bounds, but such bounds do not apply to other warm particles which could have been

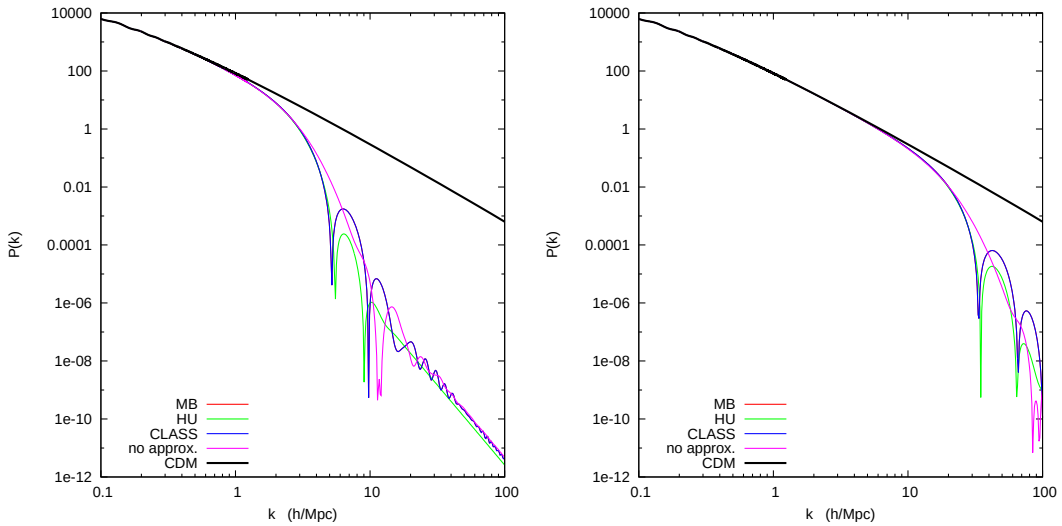

Figure 7: $P(k)$'s for a Warm Dark Matter model with $m = 1$ keV (left) and $m = 10$ keV (right). The fluid approximation can be seen to be a very good approximation in this case, though it does not catch the acoustic oscillations precisely.

produced through more complicated mechanisms (e.g. resonant production), leading to a non-trivial, model-dependent phase-space distribution function [17]. It is not always easy to find a good analytic approximation for such a distribution; this is anyway not an issue for `CLASS`, since the code can read tabulated values of $f(p)$ from an input file.

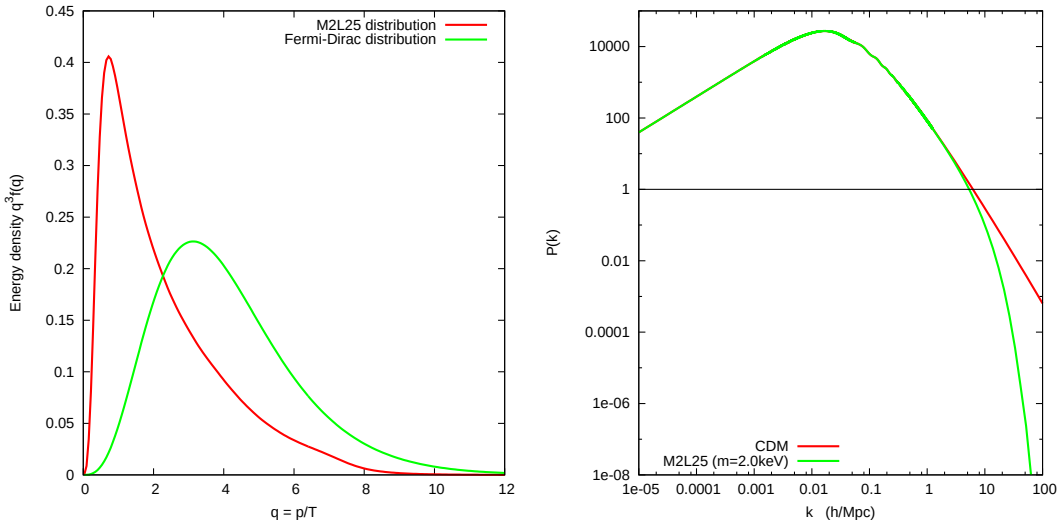

Figure 8: $P(k)$'s for a Warm Dark Matter model with a non-trivial production mechanism for a mass of $m = 2$ keV compared to the same model with Cold Dark Matter. Note that the normalisation of the distribution function is arbitrary; when both `m_ncdm` and one of {`Omega_ncdm`,`omega_ncdm`} is present for some species, `CLASS` will normalise the distribution consistently.

We illustrate this case by taking a particular model for resonantly produced sterile neutrinos, which distribution was computed numerically by [18] (simulating the details of sterile neutrino production and freeze-out), and stored in a file with discrete q_i, f_i values. Again, we only need to specify the name of this file in the `CLASS` input file, to enter a value for the mass and for the density $\Omega_{\rm ncdm}$, and the rest is done automatically by the code (finding the mass-density relation and the correct normalization factor for $f(q)$, defining the new momentum steps, deriving $[d\ln f]/[d\ln q]$ with a good enough accuracy). The assumed $f(q)$ and the resulting matter power spectrum when the mass is set to $m = 2$keV is shown in Fig. 8. By eye, this spectrum seems identical to a thermal-like WDM one, but the cut-off is in fact much smoother due to an excess of low-momentum particles in this model (which behave like a small cold dark matter fraction).

6. Conclusions

A large fraction of the activity in cosmology consists in deriving bounds on particle physics in general, and on the neutrino and dark matter sector in particular. Fitting cosmological data with non-standard neutrinos or other non-cold relics require non-trivial changes in existing public Boltzmann codes. Moreover, running parameter extraction codes including massive neutrinos or more exotic non-cold relics is computationally expensive due to a significant increase in the number of differential equations to be solved numerically for each set of cosmological parameters.

The newly released Cosmic Linear Anisotropy Solving System aims at rendering this task easy and fast. The code provides a very friendly and flexible input file in which users can specify a lot of non-standard properties for the NCDM sector: masses, temperatures, chemical potentials, degeneracy parameters, etc. Moreover, the Fermi-Dirac distribution function is not hard-coded in `CLASS`; it is just a default choice appearing in one line of the code, which can be very easily modified. Even when a non-thermal distribution $f(q)$ does not have a simple analytic expression, the code can be told to read it directly from a file. After reading this function, `CLASS` performs a series of steps in a fully automatic way: finding the mass-density relation, defining an optimal sampling in momentum space with a sophisticated but fast algorithm, and accurately computing the derivative of $f(q)$, needed in the perturbation equations.

In this paper, we presented the main two improvements related to the NCDM sector in `CLASS`: an adaptive quadrature sampling algorithm, which is useful both for the purpose of flexibility (the sampling is always adapted to any new distribution function) and speed (the code sticks to a minimum number of momenta, and hence, of perturbation equations); and a fluid approximation switched on inside the Hubble radius. We showed that the latter approximation works very well for realistic active neutrinos (with a total mass smaller than $1-2$eV), and for warm dark matter candidates becoming non-relativistic during radiation domination. In between these two limits, there is a range in which the accuracy of the fluid approximation is not well established, and in which the user may need to keep the approximation off, at the expense of increasing the execution time. However, the range between a few eV and few keV is usually not relevant in most realistic scenarios.

The adaptive quadrature sampling algorithm and the fluid approximation both contribute to a reduction in the total execution time of the code by a factor of three for ordinary neutrinos. This means that when one massive neutrino species is added to the ΛCDM model, `CLASS` becomes 1.5 times slower instead of 4.5 times slower like other codes. Since the code is already quite fast in the the massless case, we conclude that the global speed up is significant and appreciable when fitting cosmological data.

Acknowledgments

We wish to thank Oleg Ruchayskiy for providing the phase-space distribution of the Warm Dark Matter model, Fig. 8, which gave us an opportunity to test the code in a non-standard scenario. We also wish to thank Emanuele Castorina for many useful discussions on the fluid approximation for neutrinos during his stay at CERN.

References

[1] U. Seljak and M. Zaldarriaga, "A Line of sight integration approach to cosmic microwave background anisotropies," *Astrophys.J.* **469** (1996) 437–444, arXiv:astro-ph/9603033 [astro-ph].

[2] A. Lewis, A. Challinor, and A. Lasenby, "Efficient computation of CMB anisotropies in closed FRW models," *Astrophys.J.* **538** (2000) 473–476, arXiv:astro-ph/9911177 [astro-ph].

[3] M. Doran, "Cmbeasy:: an object oriented code for the cosmic microwave background," *JCAP* **0510** (2005) 011, arXiv:astro-ph/0302138 [astro-ph].

[4] J. Lesgourgues, "The Cosmic Linear Anisotropy Solving System (CLASS) I: Overview," arXiv:1104.2932 [astro-ph.IM].

[5] D. Blas, J. Lesgourgues, and T. Tram, "The Cosmic Linear Anisotropy Solving System (CLASS) II: Approximation schemes," arXiv:1104.2933 [astro-ph.CO].

[6] J. Lesgourgues, "The Cosmic Linear Anisotropy Solving System (CLASS) III: Comparision with CAMB for LambdaCDM," arXiv:1104.2934 [astro-ph.CO].

[7] C.-P. Ma and E. Bertschinger, "Cosmological perturbation theory in the synchronous and conformal Newtonian gauges," *Astrophys.J.* **455** (1995) 7–25, arXiv:astro-ph/9506072 [astro-ph].

[8] W. Hu, "Structure formation with generalized dark matter," *Astrophys.J.* **506** (1998) 485–494, arXiv:astro-ph/9801234 [astro-ph].

[9] A. Lewis and A. Challinor, "Evolution of cosmological dark matter perturbations," *Phys.Rev.* **D66** (2002) 023531, arXiv:astro-ph/0203507 [astro-ph].

[10] M. Shoji and E. Komatsu, "Massive Neutrinos in Cosmology: Analytic Solutions and Fluid Approximation," *Phys.Rev.* **D81** (2010) 123516, arXiv:1003.0942 [astro-ph.CO].

[11] G. Mangano, G. Miele, S. Pastor, T. Pinto, O. Pisanti, *et al.*, "Relic neutrino decoupling including flavor oscillations," *Nucl.Phys.* **B729** (2005) 221–234, arXiv:hep-ph/0506164 [hep-ph].

[12] **Particle Data Group** Collaboration, K. Nakamura *et al.*, "Review of particle physics," *J.Phys.G* **G37** (2010) 075021.

[13] J. Lesgourgues and S. Pastor, "Massive neutrinos and cosmology," *Phys.Rept.* **429** (2006) 307–379, arXiv:astro-ph/0603494 [astro-ph].

[14] J. R. Pritchard and E. Pierpaoli, "Neutrino mass from cosmological 21 cm observations," *Nucl.Phys.Proc.Suppl.* **188** (2009) 31–33.

[15] A. Cuoco, J. Lesgourgues, G. Mangano, and S. Pastor, "Do observations prove that cosmological neutrinos are thermally distributed?," *Phys.Rev.* **D71** (2005) 123501, arXiv:astro-ph/0502465 [astro-ph].

[16] D. Boyanovsky and J. Wu, "Small scale aspects of warm dark matter : power spectra and acoustic oscillations," *Phys.Rev.* **D83** (2011) 043524, arXiv:1008.0992 [astro-ph.CO].

[17] A. Boyarsky, J. Lesgourgues, O. Ruchayskiy, and M. Viel, "Realistic sterile neutrino dark matter with keV mass does not contradict cosmological bounds," *Phys.Rev.Lett.* **102** (2009) 201304, arXiv:0812.3256 [hep-ph].

[18] M. Laine and M. Shaposhnikov, "Sterile neutrino dark matter as a consequence of nuMSM-induced lepton asymmetry," *JCAP* **0806** (2008) 031, arXiv:0804.4543 [hep-ph].

4 Sensitivity forecasts

4.1 Future galaxy redshift surveys, PRD 70, 045016 (2004)

LAPTH-1033/04, IFIC/04-11, PCC-0413

Probing neutrino masses with future galaxy redshift surveys

Julien Lesgourgues
Laboratoire de Physique Théorique LAPTH (CNRS-Université de Savoie), B.P. 110, F-74941 Annecy-le-Vieux Cedex, France

Sergio Pastor
Instituto de Física Corpuscular (CSIC-Universitat de València), Ed. Institutos de Investigación, Apdo. 22085, E-46071 Valencia, Spain

Laurence Perotto
Physique Corpusculaire et Cosmologie (CNRS-IN2P3), 11 place Marcelin Berthelot, 75231 Paris Cedex 05, France
(Dated: February 1, 2008)

We perform a new study of future sensitivities of galaxy redshift surveys to the free-streaming effect caused by neutrino masses, adding the information on cosmological parameters from measurements of primary anisotropies of the cosmic microwave background (CMB). Our reference cosmological scenario has nine parameters and three different neutrino masses, with a hierarchy imposed by oscillation experiments. Within the present decade, the combination of the Sloan Digital Sky Survey (SDSS) and CMB data from the PLANCK experiment will have a 2σ detection threshold on the total neutrino mass close to 0.2 eV. This estimate is robust against the inclusion of extra free parameters in the reference cosmological model. On a longer term, the next generation of experiments may reach values of order $\sum m_\nu = 0.1$ eV at 2σ, or better if a galaxy redshift survey significantly larger than SDSS is completed. We also discuss how the small changes on the free-streaming scales in the normal and inverted hierarchy schemes are translated into the expected errors from future cosmological data.

PACS numbers: 14.60.Pq, 95.35.+d, 98.80.Es

I. INTRODUCTION

Neutrino physics has provided the first clear indication of particle physics beyond the Standard Model, since we have experimental evidences for non-zero neutrino masses. Analyses of data from atmospheric and solar neutrino experiments have shown the allowed regions for the squared mass differences (Δm^2_ν) at two different scales. Such values will be known with better precision in the next years, in particular for the larger atmospheric Δm^2_ν using the results of future long-baseline oscillation experiments.

However, from oscillation experiments no information can be obtained on the absolute values of neutrino masses, since the lightest neutrino mass remains unconstrained. Tritium decay experiments tell us that each neutrino mass cannot be larger than 2.2 eV (95% CL) at present [1], to be improved to ∼0.35 eV with KATRIN [2]. More stringent bounds exist from experiments searching for neutrinoless double beta decay, that will be improved in the near future [3], but unfortunately they depend on the details of the neutrino mixing matrix.

Cosmology offers several advantages: the cosmic neutrino background provides an abundant density of relic neutrinos with an equal momentum distribution for all flavors (up to 1% corrections), which implies that mixing angles have no effect. Although neutrinos cannot be the dominant dark matter component, they can still constitute a small, hot part of the matter density producing an erasure of perturbations at small scales through their free-streaming effect (for a review, see e.g. [4]). A comparison with data from the large scale structure (LSS) of the Universe is thus sensitive to neutrino masses, as emphasized in [5].

At present, cosmological data allow us to bound the total neutrino mass to values of $\sum m_\nu \lesssim 0.6 - 1.0$ eV [6, 7, 8, 9, 10, 11, 12], depending on the data and priors used. These ranges already compromise the 4 neutrino scenarios that could explain the additional large neutrino mass difference required by the LSND results (that also imply a fourth, sterile neutrino), but is not yet capable of reaching the necessary 0.1 eV range in order to test the hierarchical 3 neutrino schemes. But such small masses could be detected in the next future when more precise cosmological data are available, in a parallel effort to those of beta and double beta decay experiments on Earth.

In this paper we analyze the future sensitivities of cosmological data to neutrino masses, extending the pioneering work [5] and in particular the detailed analysis in [13] (see also [14]), that was more recently updated in [15]. In contrast to this last work we consider, in addition to ideal Cosmic Microwave Background (CMB) observations limited only

2

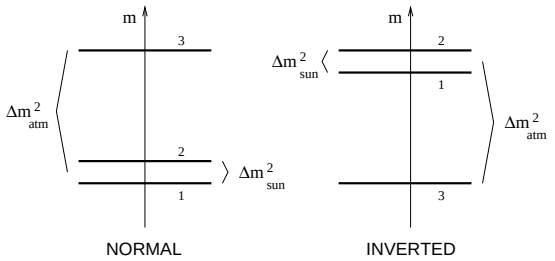

FIG. 1: The two neutrino schemes allowed if $\Delta m^2_{\rm atm} \gg \Delta m^2_{\rm sun}$: normal hierarchy (NH) and inverted hierarchy (IH).

by cosmic variance, the experimental specifications of satellite missions such as PLANCK and the mission concept CMBpol (Inflation Probe), as well as ground-based detectors such as ACT or SPTpol, that will extend the PLANCK data to smaller angular scales. We also increase the number of cosmological parameters of previous analyses, including also the helium fraction, extra relativistic degrees of freedom, spatial curvature, dark energy with constant equation of state, or a primordial spectrum with running tilt. Finally, our work is the first one in which it is assumed that neutrinos have three different masses, in order to compute accurately the free-streaming effect associated to the mass schemes allowed by oscillation experiments.

Note that throughout this work, we will assume that the LSS power spectrum is measured solely with galaxy redshift surveys. For complementary constraints based on gravitational lensing, we refer the reader to Refs. [16, 17].

This paper is organized as follows. In Sec. II we review the expected values of neutrino masses and their impact on Cosmology. We describe future CMB experiments and galaxy surveys in Sec. III and the method to forecast the errors on cosmological parameters in Sec. IV. Finally, we present our results in Sec. V, with a summary and conclusions in Sec. VI.

II. NEUTRINO MASSES

Nowadays we have experimental evidences for neutrino oscillations from solar and atmospheric neutrino detectors, recently also supported from data on neutrinos from artificial sources (Kamland and K2K). Detailed analyses of the experimental data lead to the following values of the mass squared differences (best fit values $\pm$ 3σ ranges)

$$\begin{aligned} \Delta m^2_{\rm atm} = \Delta m^2_{32} &= (2.6^{+1.1}_{-1.2}) \times 10^{-3}\ {\rm eV}^2 \\ \Delta m^2_{\rm sun} = \Delta m^2_{21} &= (6.9^{+2.6}_{-1.5}) \times 10^{-5}\ {\rm eV}^2 \end{aligned} \quad (1)$$

taken from [18]. These ranges are only slightly different in other recent analyses, see e.g. [19, 20], while a lower $\Delta m^2_{\rm atm}$ seems required by new Super-Kamiokande data and 3-dimensional atmospheric fluxes. The errors in the above equation will be significantly reduced with new data from Kamland in the case of Δm^2_{21}, and with data from future long-baseline oscillation experiments such as MINOS, ICARUS and OPERA, which will give the atmospheric Δm^2 with 10% accuracy (reduced to 5% with the superbeam proposal JPARC-SK) [21]. Current data also provide the allowed ranges of the neutrino mixing angles θ_{12} and θ_{23}, and an upper bound on θ_{13}.

Indications for a third, heavier Δm^2_ν exist from the LSND experiment [22], implying a fourth (sterile) neutrino. Such a mass is already being tested by present cosmological data, although not ruled out yet [7, 8, 11, 12], and the LSND results will be checked by the ongoing experiment MiniBoone. Here we choose not to include such a large Δm^2_ν and consider only the values in Eq. 1.

The three neutrino masses that lead to the values in Eq. 1 can be accommodated in two different neutrino schemes, named normal ($m_3 > m_2 > m_1$) and inverted ($m_2 > m_1 > m_3$) hierarchy, as shown in Fig. 1, that we will denote NH and IH. At present we have no indication of which scheme is the correct one. However, it has been suggested that some information could be extracted from future data from Supernova neutrinos, very large baseline oscillation experiments, or neutrinoless double beta decay searches if the effective m_ν is below some threshold (for reviews, see e.g. [23, 24]). In general, determining the type of mass spectrum depends on the precision with which the other mixing parameters would be measured.

Relic neutrinos were created in the Early Universe and decoupled from the rest of the plasma when the temperature dropped below ~ 1 MeV, when they were ultra-relativistic. After decoupling all neutrino flavors kept a Fermi-Dirac spectrum, only distorted at percent level during the process of electron-positron annihilations into photons [25, 26]. It is well-known that massive neutrinos could account for a significant fraction of the total energy density of the

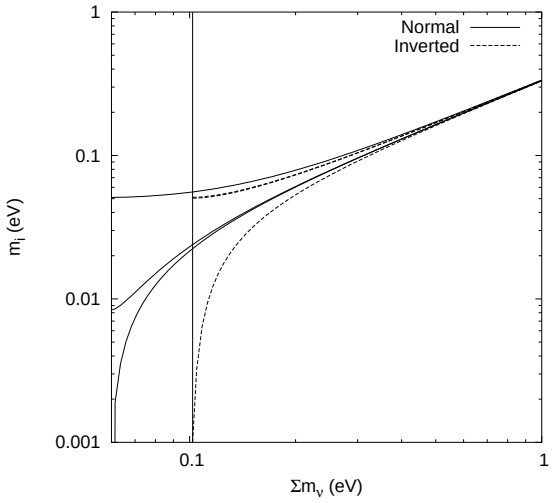

FIG. 2: Neutrino masses as a function of the total mass in the two schemes for the best-fit values of Δm^2 in Eq. 1. The vertical line marks the smallest value of $\sum m_\nu$ in the inverted scenario.

Universe today, being their contribution directly proportional to the number density. For vanishing neutrino chemical potentials, the total neutrino contribution to the critical density is given by

$$\Omega_\nu = \frac{\sum m_\nu}{93.2 \text{ eV}} h^{-2} \ , \tag{2}$$

where h is the Hubble constant in units of 100 km s^{-1} Mpc^{-1} and $\sum m_\nu$ runs over all neutrino mass states. For fixed neutrino masses, Ω_ν would be enhanced if neutrinos decoupled with a significant chemical potential (or equivalently, for large relic neutrino asymmetries), but this possibility is now ruled out [27].

Therefore cosmology is at first order sensitive to the total neutrino mass $\sum m_\nu = m_1 + m_2 + m_3$ (for the 3 neutrino schemes that we consider), but blind to the neutrino mixing angles or possible CP violating phases. This fact differentiates cosmology from terrestrial experiments such as beta decay and neutrinoless double beta decay, which are sensitive to $\sum_i |U_{ei}|^2 m_i^2$ and $|\sum_i U_{ei}^2 m_i|$, respectively, where U is the 3×3 mixing matrix that relates the weak and mass bases.

It is interesting to see how the total mass is distributed among the neutrino states for the two different schemes described above. They are plotted in Fig. 2. For a total mass above $\sim 0.2 - 0.3$ eV the two schemes are similar and correspond to a degenerate scenario where each mass is $\sum m_\nu/3$. However, for smaller masses the number of neutrino states with relevant masses is 2 (1) in the inverted (normal) hierarchy.

The effect of neutrino masses on cosmological observables has been usually considered equivalent for fixed $\sum m_\nu$ (or $\Omega_\nu h^2$). However, many papers noted in the past that this is not the case and could potentially lead to differences, i.e. the neutrino mass spectrum should be incorporated if the sensitivity to neutrino masses is good enough (see, for instance the comments in [15, 16, 28]). As an example, we note that in the mid-1990s it was shown that for CHDM models with the same total neutrino mass (of order some eVs), those with two degenerate massive neutrinos fitted better the data than those with only one (see e.g. [29]).

Fixed the total neutrino mass, a different distribution among the 3 states (m_1, m_2, m_3) causes a slight modification of the transit from a relativistic to a non-relativistic behavior. This can be seen in Fig. 3, where the evolution of the neutrino energy density is plotted for several cases with the same total neutrino mass, equally shared by 1,2 or 3 neutrino states, as well as the realistic NH and IH schemes (taking the best-fit values of Δm^2). Therefore, the evolution of background quantities is not completely independent of the mass splitting. However, the main difference appears at the level of perturbations. Indeed, in the case of non-degenerate massive neutrinos, various free-streaming scales are imprinted in the matter power spectrum $P(k)$. This is illustrated in Fig. 4, where we compare $P(k)$ in the same cases as in Fig. 3. These results were obtained with our modified version of the public code CMBFAST [30] (see section V for details).

We have recently summarized the effects of massive neutrinos on cosmological observables in [12]. Here we simply remind that only neutrinos with masses close to the recombination temperature ($T_{\rm dec} \sim 0.3$ eV) leave an imprint on

4

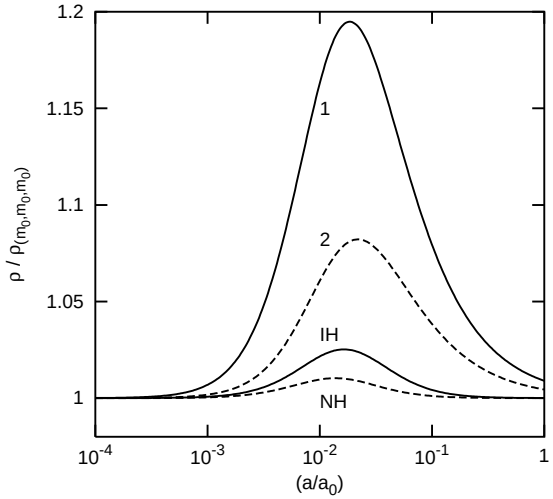

FIG. 3: Evolution of the total neutrino energy density as a function of the scale factor of the Universe for models where the same $\sum m_\nu$ (0.12 eV) is distributed differently. Each line corresponds to the energy density of 4 different cases (only 1 or 2 massive states, Normal and Inverted Hierarchy) normalized to the case with 3 massive states with mass $m_0 = \sum m_\nu/3$.

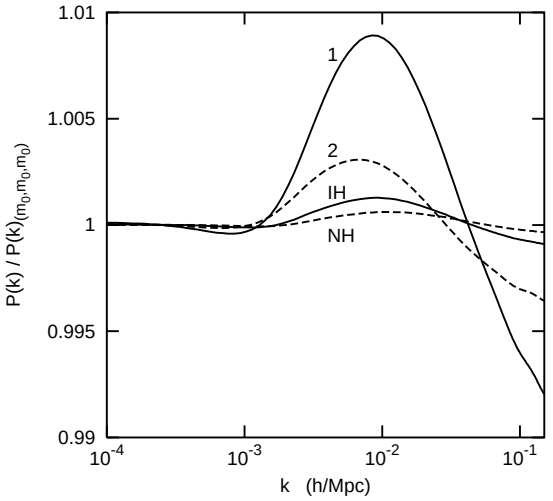

FIG. 4: Comparison of the matter power spectrum obtained for various models where the same $\sum m_\nu$ (0.12 eV) is distributed differently. The four lines correspond to the cases with 1 or 2 massive states, Normal and Inverted Hierarchy, divided each time by that with 3 massive states of equal mass $m_0 = \sum m_\nu/3$. Differences in the various individual masses and free-streaming scales affect the position and amplitude of the break in the power spectrum.

the CMB angular spectra, while neutrinos with smaller masses have almost the same effect as massless neutrinos. On the other hand, the dominant effect is the one induced by free-streaming on the matter power spectrum. Therefore, the usual strategy is to combine CMB and LSS measurements, where the former roughly fix most of the cosmological parameters, while the latter is more sensitive to neutrino masses.

III. FUTURE CMB AND LSS DATA

In this section we briefly describe the experimental projects, planned or in development, that will provide data on the CMB anisotropy spectrum or on the distribution of LSS.

A. CMB experiments

The quality of the first-year data from the Wilkinson Microwave Anisotropy Probe (WMAP) [6], complemented by the results of other experiments at smaller angular scales such as ACBAR, CBI or VSA [31, 32, 33], has shown the importance of CMB data as a probe of cosmological parameters. The CMB experiments measure the temperature fluctuations in the sky that can be expanded in spherical harmonics,

$$\frac{\Delta T}{T}(\theta,\phi) = \sum_{l,m} a_{lm} Y_{lm}(\theta,\phi)\,. \tag{3}$$

If the underlying perturbations are Gaussian, all information is encoded in the angular power spectrum $C_l \equiv \langle |a_{lm}|^2 \rangle$. In addition the CMB experiments can be sensitive to polarization anisotropies, that are expressed in terms of the angular spectra of the E and B modes of polarization, as well as the temperature polarization cross-correlation (TE) spectrum.

After WMAP, the next satellite mission will be PLANCK[1], to be launched in 2007, whose experimental parameters are listed in Table I. After a couple of years, it will provide CMB data more precise than that of WMAP, in particular concerning polarization. We also consider the CMBpol or Inflation Probe mission concept, presented in the framework of NASA's Beyond Einstein Program[2]. This experiment would have better sensitivity than the limit imposed by cosmic variance (up to $l \sim 2300$ for E-polarization, even beyond for temperature).

In parallel to the satellite missions, there will be ground-based experiments that will measure the CMB at smaller angular scales with significantly smaller sky coverage but good sensitivities, such as SPTpol[3] (in construction), ACT[4] (funded in January 2004), or QUaD [34] (in construction). As an example, we consider SPTpol with the characteristics listed in Table I.

The observed power spectrum can be decomposed into primary anisotropies, gravitational lensing distortions, and foreground contamination. The central frequencies of CMB detectors are usually chosen in order to minimize the foreground contribution. In addition, by combining various frequencies, future experiments will have the power to separate efficiently the CMB blackbody from the various foregrounds contributions, even on small angular scales where the latter start to be significant. It is possible to build models for the foregrounds and to predict their impact on parameter extraction [34, 35, 36]; this approach is rather model-dependent, since the level of many foreground signals has not yet been measured experimentally. Here, we will not enter into such details. When dealing with PLANCK, we will employ only three frequency channels from the high frequency instrument (HFI), making the (usual) simplifying assumption that other channels will be used for measuring the various foregrounds, and for cleaning accurately the primary signal. We will do similar assumptions for SPTpol and CMBpol. We will also speculate on the results of an "ideal CMB experiment" limited only by cosmic variance. Then, we will limit ourselves to $l_{\rm max} = 2500$ both for temperature and polarization, which assumes an efficient method for foreground subtraction – in particular of point-like sources and dust – but remains realistic (as indicated by Fig. 7 in [35]). For the two satellite experiments, we assume a sky coverage of $f_{\rm sky} = 0.65$, which represents a conservative estimate of the data fraction that will be included in the analysis in order to avoid galactic foregrounds. For the "ideal CMB experiment", we adopt the more optimistic value $f_{\rm sky} = 1$, assuming that all galactic foregrounds can be subtracted (see e.g. the component separation method described in [37]).

The issue of gravitational lensing distortion is subtle and potentially very interesting. Since lensing is induced by large scale structure, mainly on linear scales, this effect can be accurately predicted for a given matter power spectrum. Therefore, if the gravitational distortion of the CMB maps could be measured directly, there would be an opportunity to extract the matter power spectrum (and the underlying cosmological parameters) independently from redshift surveys. A way of doing this is described in [38, 39, 40], and has been already applied to future neutrino mass extraction by [17]. Here, we do not incorporate this method, and assume that the matter power spectrum is measured only with redshift surveys, leaving a combined analysis for the future. Therefore, throughout the analysis, we will employ the unlensed CMB power spectra[5]. For the T, E and TE modes, lensing distortions are subdominant. In contrast, for the B mode, lensing is expected to dominate over the primary anisotropies at least on small angular scales. The angle above which lensing is subdominant crucially depends on the tensor-to-scalar ratio, an inflationary

---

[1] http://www.rssd.esa.int/index.php?project=PLANCK
[2] http://universe.gsfc.nasa.gov/program/inflation.html
[3] http://astro.uchicago.edu/spt/
[4] http://www.hep.upenn.edu/∼angelica/act/act.html
[5] Note that including lensing corrections is technically easy with CMBFAST. However, this would introduce some correlations among different modes and scales that would artificially lower the predicted errors on each cosmological parameters [17, 38].

Experiment	$f_{\rm sky}$	ν	θ_b	Δ_T	Δ_P
PLANCK	0.65	100	9.5'	6.8	10.9
		143	7.1'	6.0	11.4
		217	5.0'	13.1	26.7
SPTpol	0.1	217	0.9'	12	17
CMBpol	0.65	217	3.0'	1	1.4

TABLE I: Experimental parameters of CMB projects: here θ_b measures the width of the beam, $\Delta_{T,P}$ are the sensitivities per pixel in μK, ν is the center frequency of the channels in GHz and $f_{\rm sky}$ the observed fraction of the sky. For the PLANCK 100 GHz channel, the value of Δ_P takes into account the recent design with eight polarized bolometers.

parameter which order of magnitude is still unknown. So, we follow a conservative approach and not take the B mode into account. This amounts in assuming that the gravitational wave background generated by inflation is small, so that the B mode gives no information on primary anisotropies.

B. Galaxy surveys

The existing data on the distribution of galaxies at large scales come from several galaxy surveys, of which the completed 2dF survey[6] and the ongoing Sloan Digital Sky Survey[7] (SDSS) are the largest. SDSS will complete its measurements in 2005. The matter power spectrum $P(k)$ can be reconstructed from the data, which gives an opportunity to test the free-streaming effect of massive neutrinos. However, the linear power spectrum is found modulo a biasing factor b^2, which reflects the discrepancy between the total matter fluctuations in the Universe, and those actually seen by the instruments. Here we assume that the bias parameter b is independent of the scale k.

An important point concerning LSS data is the non-linear clustering of the smallest scales. The usual approach is to discard any information above an effective cut-off wavenumber $k_{\rm max}$, while considering results at lower k's as a direct estimate of the linear power spectrum. The cut-off value must be chosen with care: if $k_{\rm max}$ is too small, we can lose a lot of information, especially concerning the neutrino free-streaming scale. If $k_{\rm max}$ is too large, we can underestimate the error on cosmological parameters, first by neglecting any theoretical uncertainty in the quasi-linear corrections that could be applied to the spectrum, and second by ignoring the non-gaussianity induced by non-linear evolution [41].

Apart from $k_{\rm max}$, the important parameter characterizing the galaxy survey is its effective volume in k space, defined in [41]. If the number density of objects in the survey $n(\mathbf{r})$ is roughly constant over the survey volume, and if the observed power spectrum $P(k)$ is bigger than $1/n$ over the scales of interest (i.e., from the turn-over scale in $P(k)$ up to $k_{\rm max}$), the effective volume is equal to the actual volume of the survey. This is a reasonable approximation for all the examples that we will consider here. For instance, the SDSS the Bright Red Galaxy (BRG) survey has an effective volume of roughly $V_{\rm eff} \simeq 1$ (Gpc/h)^3 [13] (which comes from a sky coverage $f_{\rm sky} = 0.25$ and a radial length of 1 Gpc h^{-1}).

Beyond SDSS, plans for larger surveys are under discussion. For instance, we can mention the Large Synoptic Survey Telescope[8] (LSST), which in the future could cover the entire sky and at the same time be capable of measuring fainter objects [42]. LSST is designed mainly for weak lensing observations. In order to map the total matter distribution up to half the age of the Universe (i.e., up to a redshift $z \sim 0.8$ or a radial length $l \sim 2.3$ Gpc/h) in a solid angle 30,000 deg^2 ($f_{\rm sky} \sim 0.75$), it could measure 2×10^8 redshifts up to $z = 1.5$. Inspired roughly by these numbers, at the end of this analysis, we will speculate on the possibility to measure the power spectrum in a effective volume as large as $V_{\rm eff} = (4\pi/3) f_{\rm sky} l^3 \sim 40$ (Gpc/h)^3.

The mechanism of structure formation affects larger wavelengths at later times. So, in order to measure the linear power spectrum on small scales, it would be very useful to build high redshift galaxy surveys. This is one of the main goals of the Kilo-Aperture Optical Spectrograph (KAOS) proposal[9]. KAOS could build two catalogs centered around redshifts $z = 1$ and $z = 3$, corresponding roughly to $k_{\rm max} \sim 0.2\ h$ Mpc^{-1} and $k_{\rm max} \sim 0.48\ h$ Mpc^{-1} respectively, instead of $k_{\rm max} \sim 0.1\ h$ Mpc^{-1} today (conservative values). In both catalogs, the number density would be such that

[6] http://www.mso.anu.edu.au/2dFGRS/
[7] http://www.sdss.org
[8] http://www.lsst.org
[9] http://www.noao.edu/kaos

$1/n \sim P(k_{\rm max})$, and the effective volume of the two samples close to $V_{\rm eff} \sim 0.5\,({\rm Gpc}/h)^3$ and $V_{\rm eff} \sim 0.6\,({\rm Gpc}/h)^3$ respectively [10]. This experiment is designed mainly for measuring the scale of baryonic oscillations, in order to constrain dark energy. However, we will see that it would be also appropriate for improving constraints on the neutrino masses.

IV. FORECAST OF FUTURE BOUNDS: FISHER MATRIX ANALYSIS

Since the characteristics of future CMB experiments and galaxy surveys are already known with some precision, it is possible to assume a "fiducial" model, i.e., a cosmological model that would yield the best fit to the future data, and employ the Fisher matrix method to forecast the error with which each parameter will be extracted. This method has been widely used for many cosmological parameters, some of them related to neutrinos. For instance, we can mention that forecast analyses based on the Fisher matrix have shown that with future data there will be a potential sensitivity to an effective number of neutrinos of the order $\Delta N_{\rm eff} \sim 0.2$ [43, 44, 45], a value that is complementary to and will eventually improve the accuracy of primordial nucleosynthesis results (see e.g. [46, 47]).

Starting with a set of parameters x_i describing the fiducial model, one can compute the angular power spectra of CMB temperature and polarization anisotropies C_l^X, where $X = T, E, TE$. Simultaneously, one can derive the linear power spectrum of matter fluctuations $P(k)$, expanded in Fourier space. The error δx_i on each parameter can be calculated from the reduced (dimensionless) Fisher matrix F_{ij}, which has two terms. The first one accounts for the CMB experiment and is computed according to ref. [48]

$$F_{ij}({\rm CMB}) = \sum_{l=2}^{l_{\rm max}} \sum_{X,Y} \frac{\partial C_l^X}{\partial \ln x_i} {\rm Cov}^{-1}(C_l^X, C_l^Y) \frac{\partial C_l^Y}{\partial \ln x_j}\,, \tag{4}$$

where ${\rm Cov}(C_l^X, C_l^Y)$ is the covariance matrix of the estimators of the corresponding CMB spectrum. For instance, the TT element is given by

$${\rm Cov}(C_l^T, C_l^T) = \frac{2}{(2l+1) f_{\rm sky}} \left[C_l^T + (\sum_{\rm ch.} \omega_T B_l^2)^{-1} \right]^2 . \tag{5}$$

Here, the first term arises from cosmic variance, while the second is a function of the experimental parameters summed over the channels: $B_l^2 = \exp(-l(l+1)\theta_b^2/8\ln 2)$ is the beam window function (assumed to be Gaussian), θ_b is the FWHM of the beam and $\omega_T = (\theta_b \Delta_T)^{-2}$ is the inverse square of the detector noise level (Δ_T is the sensitivity per pixel, and the solid angle per pixel can be approximated by θ_b^2). For the experiments that we consider here, all these numbers can be found in Table I. The other terms of the covariance matrix can be found, for instance, in [13].

The second term of the reduced Fisher matrix accounts for the galaxy survey data and is calculated following Tegmark [41],

$$F_{ij}({\rm LSS}) = 2\pi \int_0^{k_{\rm max}} \frac{\partial \ln P_{\rm obs}(k)}{\partial \ln x_i} \frac{\partial \ln P_{\rm obs}(k)}{\partial \ln x_j} w(k)\; d\ln k. \tag{6}$$

Here $w(k) = V_{\rm eff}/(2\pi/k)^3$ is the weight function of the galaxy survey and we have approximated the lower limit of the integral $k_{\rm min} \simeq 0$. We defined $P_{\rm obs}(k) \equiv b^2 P(k)$, and $k_{\rm max}$ is the maximal wave number on which linear predictions are reliable. This expression is only an approximation, since in addition to non-linear clustering it ignores edge effects and redshift space distortions.

Inverting the total Fisher matrix, one obtains an estimate of the 1-σ error on each parameter, assuming that all other parameters are unknown

$$\frac{\delta x_i}{x_i} = (F^{-1})_{ii}^{1/2}. \tag{7}$$

It is also useful to compute the eigenvectors of the reduced Fisher matrix (i.e., the axes of the likelihood ellipsoid in the space of relative errors). The error on each eigenvector is given by the inverse square root of the corresponding eigenvalue. The eigenvectors with large errors indicate directions of parameter degeneracy; those with the smallest errors are the best constrained combinations of parameters.

---

[10] The characteristics of KAOS are taken from the "Purple Book" available on-line at `http://www.noao.edu/kaos`.

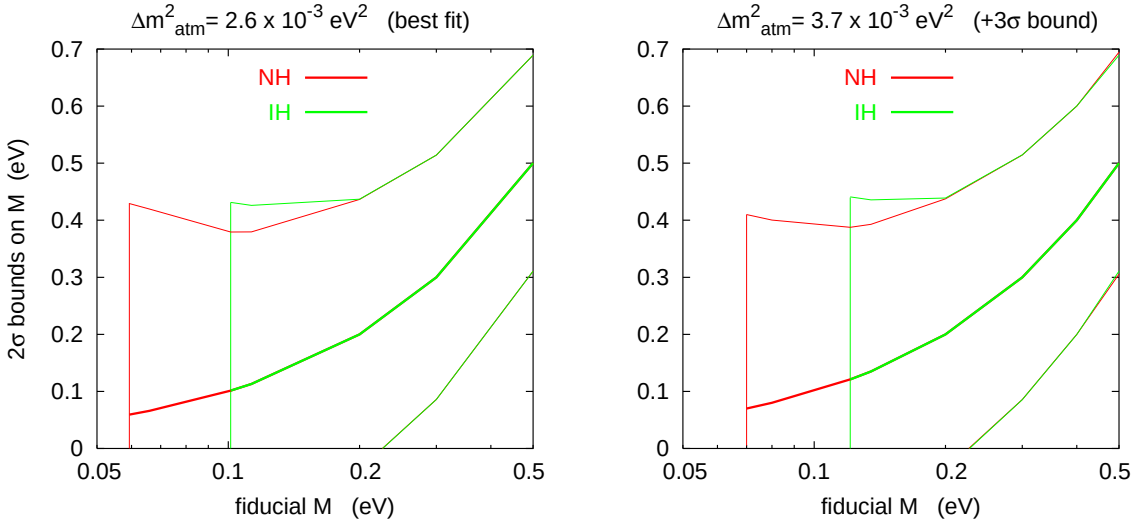

FIG. 5: Predicted 2σ error on the total neutrino mass $M \equiv \sum m_\nu$ as a function of M in the fiducial model, using PLANCK and SDSS (limited to $k_{\rm max} = 0.15\ h\ {\rm Mpc}^{-1}$). The left plot was obtained with the preferred experimental value of $\Delta m^2_{\rm atm}$, and the right plot with the current 3σ upper bound. In each case, we show the results assuming either NH or IH.

V. RESULTS

We have computed the total Fisher matrix from Eqs. 4 and 6, using various experimental specifications. Throughout the analysis, our fiducial model is the concordance "flat ΛCDM" scenario, with parameters close to the current best-fit values and with additional neutrino masses. The nine free parameters with respect to which derivatives are computed are: $\Omega_m h^2$ (matter density, including baryons, cold dark matter and neutrinos), $\Omega_b h^2$ (baryon density), Ω_Λ (cosmological constant), C^T_{200} (amplitude of temperature spectrum at multipole 200), n_s (scalar tilt), τ (optical depth to reionization), y_{He} (fraction of baryonic mass in the form of Helium), $M \equiv \sum m_\nu$ (total neutrino mass) and b (unknown bias of the LSS data). The fiducial value of b is irrelevant by construction, and we will try various values of M, distributed following the NH or IH scheme. Other fiducial values read:

$$(\Omega_m h^2, \Omega_b h^2, \Omega_\Lambda, C^T_{200}, n_s, \tau, y_{He}) = (0.143, 0.023, 0.70, 0.85, 0.96, 0.11, 0.24).$$

All derivatives are computed at zero spatial curvature (by varying h appropriately). Note that we use double-sided derivatives with step 10% for M, 50 % for y_{He}, 5% for all other parameters. We checked carefully that these steps are sufficient in order to avoid possible numerical errors caused by the limited precision of the Boltzmann code – in our case, version 4.5.1 of CMBFAST [30], with option "high precision". We also checked that with twice larger steps, the results change only by a negligible amount. These conditions were not a priori obvious for the smallest neutrino masses studied here, but we increased the precision of the neutrino sector in CMBFAST accordingly. Actually, in order to study three neutrino species with different masses, we performed significant modifications throughout CMBFAST. For each mass eigenstate, we integrate some independent background and perturbation equations, decomposed in 15 momentum values, up to multipole $l = 7$. Finally, we include the small distortions in the neutrino phase-space distributions caused by non-instantaneous decoupling from the electromagnetic plasma (with QED corrections at finite temperature) [26], but these last effects are almost negligible in practice.

A. PLANCK+SDSS

We first derive the precision with which the combined PLANCK and SDSS data will constrain the total neutrino mass in a near future. Experimental specifications for these experiments are given in the previous section, and we choose to limit SDSS data to the scale $k_{\rm max} = 0.15\ h\ {\rm Mpc}^{-1}$ where non-linear effects are still small. Fig. 5 shows the predicted 2σ error on M for various fiducial models, assuming different values of M, the two possible schemes for the mass splitting (either NH or IH), and two different values of $\Delta m^2_{\rm atm}$. The solar mass scale $\Delta m^2_{\rm sun}$ is essentially irrelevant in this analysis, and is kept fixed to the current preferred value of $6.9 \times 10^{-5}\ {\rm eV}^2$. The possible values of

	$\ln C_{200}^T$	n_s	τ	Ω_Λ	$\Omega_m h^2$	$\Omega_b h^2$	**M (eV)**	Y_{He}	$\ln[b^2 P(k_0)]$	X
9 parameters	0.005	0.007	0.005	0.01	0.001	0.0002	**0.11**	0.01	0.007	–
$+ X = N_\nu^{\rm r}$	0.005	0.008	0.005	0.01	0.003	0.0002	**0.12**	0.01	0.007	0.14
$+ X = \Omega_{\rm k}$	0.005	0.008	0.005	0.01	0.002	0.0002	**0.13**	0.01	0.007	0.003
$+ X = w$	0.005	0.008	0.005	0.01	0.002	0.0002	**0.14**	0.01	0.007	0.05
$+ X = \alpha$	0.005	0.010	0.005	0.01	0.001	0.0002	**0.11**	0.02	0.007	0.008

TABLE II: Absolute errors at the 1-σ level for various cosmological models, using PLANCK+SDSS ($k_{\rm max} = 0.15\,h$ Mpc^{-1}). The first line shows our simplest flat ΛCDM model, described by 9 free parameters with fiducial values $C_{200}^T = 0.85$, $n_s = 0.96$, $\tau = 0.11$, $\Omega_\Lambda = 0.70$, $\Omega_m h^2 = 0.143$, $\Omega_b h^2 = 0.023$, $M = 0.3$ eV (normal hierarchy), $Y_{He} = 0.24$. The value chosen for $b^2 P(k_0 = 0.1\,h$ Mpc$^{-1})$ is irrelevant. The next lines have one additional parameter X: an effective number of neutrinos $N_\nu^{\rm r}$ parametrizing the abundance of extra relativistic relics, with fiducial value 0; a free spatial curvature parametrized by $\Omega_{\rm k}$ with fiducial value 0; a free time-independent equation of state for dark energy parametrized by w with fiducial value -1; a free scalar tilt running parametrized by $\alpha = dn_s/d\ln k$ with fiducial value 0.

M are of course bounded from below: the minimal value corresponds to the limit in which the lightest neutrino mass goes to zero, in one of the two NH or IH schemes.

Let us first concentrate on the case in which $\Delta m^2_{\rm atm}$ has its current preferred value of 2.6×10^{-3}eV^2 (left plot). The minimal value of M in the NH (resp. IH) case is approximately 0.06 eV (resp. 0.10 eV). However, the 2σ detection threshold, defined by $M = 2\sigma(M)$, is around 0.21 eV. We conclude that PLANCK+SDSS will probe mainly the region were the three neutrinos are quasi-degenerate in mass, with no possibility to distinguish between the two cases. In absence of clear detection, the 2σ upper bound will be of order 0.2 eV, corresponding to individual masses (0.08, 0.06, 0.06) eV assuming NH, or (0.073, 0.073, 0.053) eV assuming IH. As expected, we find that the 2σ detection threshold is still 0.21 eV when the calculations are performed with a larger value $\Delta m^2_{\rm atm} = 3.7 \times 10^{-3}$ eV^2 (the 3σ upper bound in Eq. 1), as shown in the right plot of Fig. 5.

It is interesting to study whether this precision is limited mainly by a degeneracy between M and some combination of other cosmological parameters, or simply by the experimental sensitivity to the individual effect of M. In the first case, the results could be improved by including priors from other types of experiments on the cosmological parameters; in the second case, one would have to wait for a new generation of CMB and/or LSS experiments. In order to address this point, we computed the eigenvectors and eigenvalues of the reduced Fisher matrix. It turns out that for all our fiducial models, one of the unit eigenvectors points precisely in the direction of M, with coefficient very close to one in this direction (and, of course, the corresponding eigenvalue matches the error previously obtained for M). We conclude that M is not affected by a parameter degeneracy, and that independent measurements of other cosmological parameters would not help very much in constraining neutrino masses. Note that this is not yet the case for current cosmological bounds on neutrino masses, where the addition of priors on parameters such as the Hubble constant or Ω_Λ leads to more stringent bounds (see e.g. [12]).

The absence of large parameter degeneracies applies to our reference model with nine free parameters. It may not necessarily be true in the presence of extra parameters describing deviations from the concordance ΛCDM model. In order to illustrate this point and to test the robustness of our conclusions, we have calculated the error on each parameter for several extended cosmological scenarios, with extra relativistic degrees of freedom, spatial curvature, dark energy with varying density but constant equation of state, or a primordial spectrum with running tilt (see Table II). The neutrino mass bound is found to be quite robust in all these cases, which proves that in none of these models the effect of M can be mimicked by some other parameter combination.

It is also interesting to study the relative impact of CMB temperature, CMB polarization and LSS data on the measurement of M. We show in table III the error on each parameter for SDSS alone, PLANCK alone (with or without polarization), and various combinations of CMB and LSS data, with an explicit dependence on the value of $k_{\rm max}$. The complementarity of PLANCK and SDSS clearly appears. While PLANCK alone would achieve only a 1σ detection of $M = 0.3$ eV and SDSS alone would not detect it at all, the combined data would probe this value at the 3σ level. One can check from Table III that PLANCK data on polarization lowers the error on M by approximately 30%. By diagonalizing the "PLANCK (no pol.)+SDSS" Fisher matrix, we checked that without polarization there would be a significant degeneracy between neutrino mass and optical depth to reionization. Indeed, while reionization lowers the CMB temperature spectrum keeping the matter power spectrum unchanged, the effect of neutrino free-streaming is opposite in first approximation (at least on small scales). So, polarization measurements are indirectly a key ingredient for neutrino mass determination.

	$k_{\rm max}$ (h/Mpc)	$\ln C_{200}^T$	n_s	τ	Ω_Λ	$\Omega_m h^2$	$\Omega_b h^2$	**M (eV)**	Y_{He}	$\ln[b^2 P(k_0)]$
SDSS alone	0.10	–	0.6	–	0.8	0.5	0.1	**7.0**	–	0.3
	0.15	–	0.5	–	0.09	0.4	0.08	**1.5**	–	0.06
	0.20	–	0.1	–	0.05	0.09	0.02	**0.5**	–	0.01
PLANCK (no pol.)	–	0.005	0.02	0.10	0.05	0.006	0.0006	**0.42**	0.03	–
PLANCK (no pol.) + SDSS	0.10	0.005	0.02	0.08	0.02	0.002	0.0004	**0.24**	0.02	0.015
	0.15	0.005	0.02	0.08	0.01	0.001	0.0003	**0.15**	0.02	0.008
	0.20	0.005	0.01	0.07	0.006	0.0009	0.0003	**0.13**	0.02	0.005
PLANCK (all)	–	0.005	0.008	0.005	0.04	0.004	0.0003	**0.30**	0.01	–
PLANCK (all) + SDSS	0.10	0.005	0.007	0.005	0.02	0.002	0.0002	**0.19**	0.01	0.012
	0.15	0.005	0.007	0.005	0.01	0.001	0.0002	**0.11**	0.01	0.007
	0.20	0.004	0.007	0.005	0.006	0.0008	0.0002	**0.08**	0.01	0.005
CMBpol	–	0.003	0.003	0.003	0.006	0.0006	0.00008	**0.07**	0.004	–
CMBpol + SDSS	0.10	0.003	0.003	0.003	0.006	0.0006	0.00008	**0.07**	0.004	0.011
	0.15	0.003	0.003	0.003	0.005	0.0006	0.00007	**0.06**	0.004	0.006
	0.20	0.003	0.003	0.003	0.004	0.0005	0.00007	**0.05**	0.004	0.004

TABLE III: Absolute errors at the 1-σ level, for various experiments and the same ΛCDM model as in table II (with 9 free parameters). In particular, the fiducial value of the total neutrino mass is still $M = 0.3$ eV. When using SDSS, we show the results for three choices of $k_{\rm max}$, the maximal wavenumber on which the data are compared with linear theory predictions: $k_{\rm max} = 0.10\,h$ Mpc^{-1} (conservative), $0.15\,h$ Mpc^{-1} (reasonable), or $0.20\,h$ Mpc^{-1} (optimistic).

	SDSS	SDSS+KAOS	"hypothetical LSS"
PLANCK	0.21	0.16	0.11
CMBpol	0.13	0.10	0.09
"ideal CMB"	0.10	0.09	0.08

TABLE IV: 2-σ detection threshold (in eV) for various combinations of CMB and LSS experiments (assuming the normal hierarchy scenario). The "ideal CMB" experiment is limited only by cosmic variance up to multipole $l = 2500$ and covers 100% of the sky. The "hypothetical LSS" survey has a volume $V_{\rm eff} \simeq 40\,({\rm Gpc}/h)^3$ and probes the linear spectrum up to $k_{\rm max} = 0.15\,h$ Mpc^{-1} (that would be the case of a large galaxy survey covering 75% of the sky up to $z = 0.8$).

B. Post-PLANCK experiments

Here we consider whether future CMB and LSS experiments will reach a better sensitivity on the neutrino mass, in particular at the level of the small values of M expected for the hierarchical normal and inverted schemes. Sensitivities significantly better than 0.1 eV would mean approaching the absolute minimum of M in the NH case or even ruling out the IH scenario.

In the previous section, we mentioned a few CMB missions that have been proposed so far in complement to PLANCK. We will study the impact of a few of them, and of an "ideal CMB experiment" that would be limited only by cosmic variance up to $l = 2500$ (both for temperature and polarization). The main difficulty for reaching this goal would be to subtract accurately small-scale foregrounds, and in particular point-like sources, but even with current technology such an ideal experiment is conceivable. On the other hand, it is difficult to specify the characteristics of an ideal LSS experiment, since it will be limited by technological improvements in instrumentation and data processing. Therefore, we will keep in the analysis a free parameter $V_{\rm eff}$ describing the effective volume of an ideal volume-limited survey.

We show in Fig. 6 the predicted 2σ error in four cases corresponding to SPTpol (upper left), PLANCK (upper right), CMBpol (lower left), and our ideal CMB experiment (lower right). The value of 2σ (in eV) is shown with grey levels, as a function of $k_{\rm max}$ (horizontal axis) and $V_{\rm eff}$ (vertical axis) in units of $V_{\rm eff}({\rm SDSS}) = 1\ ({\rm Gpc}/h)^3$. The total mass has been fixed to $M = 0.11$ eV, distributed according to the NH scheme. We learned from the previous subsection that for higher values of M, the error could be smaller (at most by a factor 2). However, we are now interested in the range $0.05\ {\rm eV} < M < 0.2$ eV, since larger values should be detected by PLANCK+SDSS, and smaller values are excluded by oscillation experiments. In this range, on can safely interpolate the results obtained at $M = 0.11$ eV. In particular, our results for a cosmic-variance limited CMB experiment are in reasonable agreement with those of [15].

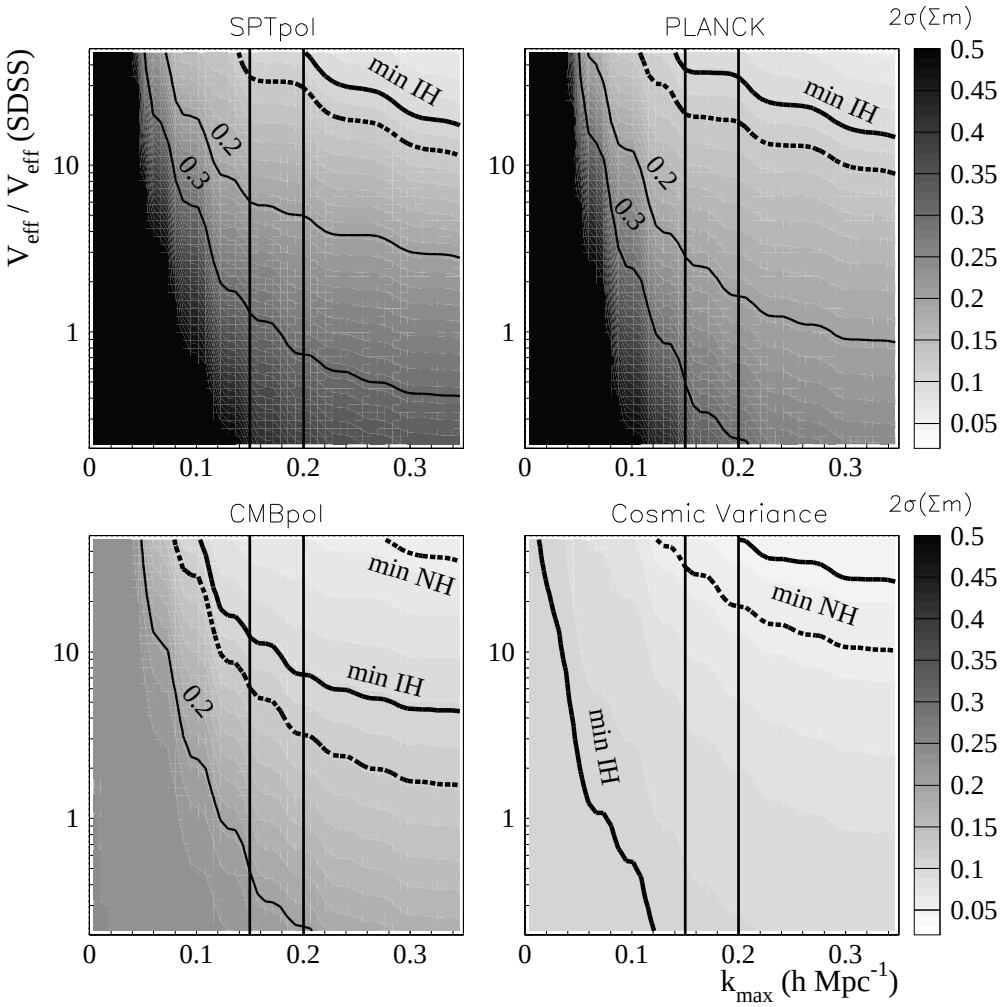

FIG. 6: The grey regions are the 2σ expected errors on $\sum m_\nu$ (eV) for a fiducial value of 0.11 eV, as a function of the parameters of the galaxy survey, where each panel corresponds to a specific CMB experiment. The vertical lines indicate the cut-off wavenumber $k_{\rm max}$ for the linear matter power spectrum at the conservative (optimistic) value $0.15(0.2)\,h$ Mpc^{-1}. The thin contours shown are (from bottom to top) for 0.3 and 0.2 eV, while the thick contours correspond to the minimum values of $\sum m_\nu$ in the IH (lower lines) and NH (upper lines) schemes, assuming the best-fit (solid) or the 3σ upper bound (dashed) value of $\Delta m^2_{\rm atm}$.

For SDSS (or for any survey with $z < 1$) we expect the relevant value of $k_{\rm max}$ to be around $0.15\,h$ Mpc^{-1}. However, depending on the overall amplitude of the matter power spectrum (often parametrized by σ_8, and still poorly constrained) and on future improvements in our understanding of non-linear corrections, this value might appear to be either too optimistic or too pessimistic: this is the reason why it is interesting to leave it as a free parameter.

One can see that replacing PLANCK by CMBpol would lead to a better sensitivity to the neutrino mass, with a 2σ detection threshold at 0.13 eV instead of 0.21 eV. The expected errors for CMBpol, with and without SDSS data, can be found in Table III. Adding to SDSS the two KAOS surveys (centered around $z = 1$ and $z = 3$) would also lead to some improvement. For Planck+SDSS+KAOS we get a 2σ detection threshold of $M \sim 0.16$ eV, while for CMBpol+SDSS+KAOS one could reach $M \sim 0.10$ eV. These results are summarized in Table IV.

There is still room for improvement beyond this set of experiments. In order to make a precise statement on the conclusions that could be drawn on the long term, we keep the "ideal CMB experiment" characteristics and fix $V_{\rm eff}$

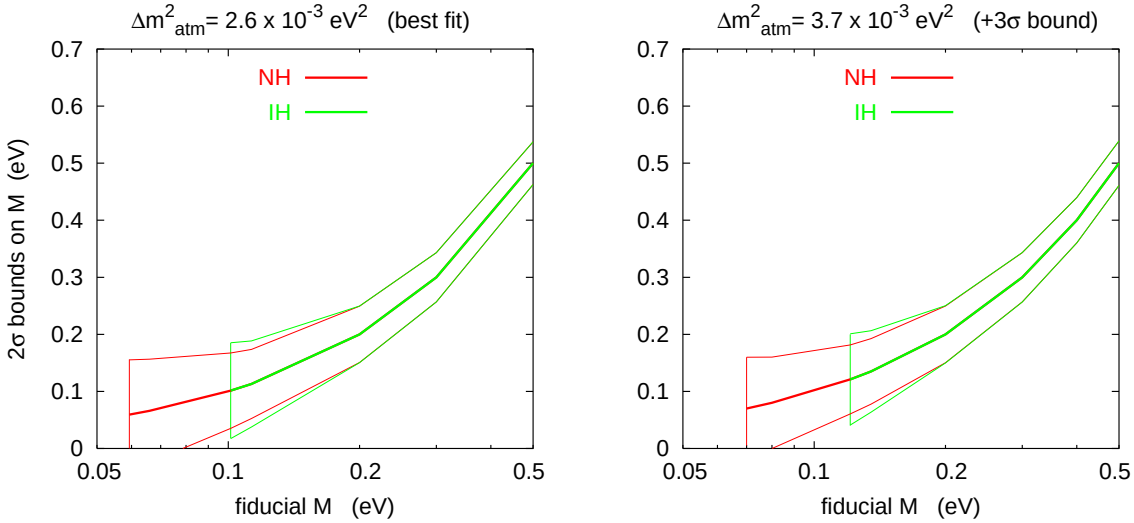

FIG. 7: Predicted 2σ error on $\sum m_\nu$ as a function of $\sum m_\nu$ in the fiducial model, using an ideal CMB experiment (limited only by cosmic variance up to $l = 2500$, both for temperature and polarization) and a redshift survey covering 75% of the sky up to $z \simeq 0.8$ ($V_{\rm eff} = 40\ ({\rm Gpc}/h)^3$), still limited to $k_{\rm max} = 0.15\,h$ Mpc^{-1}. The left plot was obtained with the preferred experimental value of $\Delta m^2_{\rm atm}$, and the right plot with the current 3σ upper bound. In each case, we show the results assuming either NH or IH.

to 40 $({\rm Gpc}/h)^3$ (in section III, we argued that this could hopefully represent the volume of a survey comparable to the LSST project), while keeping $k_{\rm max} = 0.15\,h$ Mpc^{-1}. In Fig. 7, we plot the corresponding results in the same way as we did for PLANCK+SDSS. Assuming the IH scenario, we see that any value of the mass could be detected at the 2σ level. Assuming NH, this is only true at the 1 or 1.5σ level, depending on the value of $\Delta m^2_{\rm atm}$. The 2σ detection threshold is at 0.08 eV.

Our results show, for the first time, that if the available cosmological data are precise enough, the expected errors on the neutrino masses depend not only on the sum of neutrino masses, but also on what is assumed for the mass splitting between the neutrino states. As can be seen from Figs. 5 and 7, the sensitivity on M will be slightly better in the NH case in the mass region close to the minimum value of the IH scheme. These small differences arise from the changes in the free-streaming effect that we have described in section II, and obviously disappear for a total mass in the quasi-degenerate region (above 0.2 eV or so).

In any case, the main contribution of cosmology to the possible discrimination between the neutrino mass schemes will still be the possibility of ruling out the case in which the masses are quasi-degenerate. Even in our most optimistic forecast (Fig. 7), if the preferred value of M turns out to be smaller than 0.1 eV, the error bar will still be too large in order to safely rule out the IH case. We also performed an extended analysis in which, instead of assuming either normal or inverted hierarchy, we introduced a tenth free parameter accounting for a continuous interpolation of the mass spectrum between the two scenarios, for fixed M. By computing the error on this parameter, we obtained a confirmation that the NH and IH scenarios cannot be discriminated directly from the data. However, any analysis of future, very precise cosmological data must take into account the texture of neutrino masses in order to translate the corresponding positive signal (or bound) into M.

VI. CONCLUSIONS

In this paper we have analyzed the sensitivities of future CMB and LSS data to the absolute scale of neutrino masses, taking into account realistic experimental sensitivities and extending the results of previous works [5, 13, 14, 15].

We have considered the values of neutrino masses distributed according to the presently favored three neutrino mass schemes, that follow either a normal or an inverted hierarchy. As discussed in section II, a different distribution of the same total neutrino mass leads to small changes in the cosmological evolution of neutrinos, and in particular in the free-streaming scales (qualitatively discussed, for instance, in [5, 15]). These changes disappear when the total neutrino mass enters the quasi-degenerate region.

We used the Fisher matrix method to forecast the errors on cosmological parameters that can be extracted from

future CMB experiment and redshift survey data, assuming a fiducial 9-dimensional cosmological model close to the currently favored ΛCDM model. Our theoretical CMB and matter power spectra were generated with the standard Boltzmann code CMBFAST, modified in order to include three neutrino states with different masses.

In particular, for the case of PLANCK and SDSS we found good agreement with the results of [13], with a 2σ-error on the total neutrino mass of 0.2 eV that will allow us to probe only the quasi-degenerate neutrino mass region. Better sensitivity will be achieved with the combination CMBpol and SDSS, for which we found 0.12 eV, close to the minimum value of the total neutrino mass in the inverted hierarchy case. These results correspond to a conservative value of $k_{\rm max} = 0.15\,h$ Mpc^{-1}, the maximal wavenumber on which the LSS data are compared with the predictions of linear theory. We also tested how the errors change when including additional cosmological parameters to our fiducial model. In general, we found that the errors on the neutrino masses are not modified in a significant way.

Our results show that the approach where CMB experiments are only limited by cosmic variance (as in [15]) is probably too simplistic. However, if a future CMB experiment is capable of getting close to such an ideal limit, then the combination with data from galaxy redshift surveys larger than SDSS would lead to errors on the total neutrino mass comparable to the minimum values of the hierarchical scenarios. In such a case, we have shown that there exist slight differences in the expected errors between the two hierarchical neutrino schemes for the same total neutrino mass.

In conclusion, we consider that cosmological data can provide valuable information on the absolute scale of neutrino masses, that nicely complements the present and future projects of beta decay and neutrinoless double beta decay experiments. This conclusion is reinforced when one takes into account other cosmological probes of neutrino masses, complementary to the approach of the present paper. We can cite, for instance, studies of the distribution of matter in the Universe through the distortions of CMB maps caused by gravitational lensing (measured from non-gaussianities in the CMB maps) [17] and the weak gravitational lensing of background galaxies by intervening matter [16, 49, 50, 51].

It is interesting to note that any information on the absolute neutrino masses from cosmology will be interesting not only for theoretical neutrino models, but also for connected baryogenesis scenarios which occur through a leptogenesis process (see e.g. [52, 53, 54]).

Acknowledgments

We thank Ilenia Picardi for initial discussions concerning the present work, as well as Martin Hirsch and Simon Prunet for various suggestions, and Bruce Bassett for pointing us to the KAOS proposal. This research was supported by a CICYT-IN2P3 agreement. SP was supported by the Spanish grant BFM2002-00345, the ESF network Neutrino Astrophysics and a Ramón y Cajal contract of MCyT.

[1] J. Bonn et al., Nucl. Phys. Proc. Suppl. **91**, 273 (2001).
[2] A. Osipowicz et al. [KATRIN Coll.], hep-ex/0109033.
[3] S.R. Elliott and P. Vogel, Ann. Rev. Nucl. Part. Sci. **52** 115, (2002) [hep-ph/0202264].
[4] A.D. Dolgov, Phys. Rept. **370**, 333 (2002) [hep-ph/0202122].
[5] W. Hu, D.J. Eisenstein and M. Tegmark, Phys. Rev. Lett. **80**, 5255 (1998) [astro-ph/9712057].
[6] D.N. Spergel et al., Astrophys. J. Suppl. **148**, 175 (2003) [astro-ph/0302209].
[7] S. Hannestad, JCAP **0305**, 004 (2003) [astro-ph/0303076].
[8] Ø. Elgarøy and O. Lahav, JCAP **0304**, 004 (2003) [astro-ph/0303089].
[9] M. Tegmark et al. [SDSS Coll.], Phys. Rev. D, in press [astro-ph/0310723].
[10] V. Barger, D. Marfatia and A. Tregre, hep-ph/0312065.
[11] S. Hannestad and G. Raffelt, hep-ph/0312154.
[12] P. Crotty, J. Lesgourgues and S. Pastor, hep-ph/0402049.
[13] D.J. Eisenstein, W. Hu and M. Tegmark, Astrophys. J. **518**, 2 (1998) [astro-ph/9807130].
[14] J. Lesgourgues, S. Pastor and S. Prunet, Phys. Rev. D **62**, 023001 (2000) [hep-ph/9912363].
[15] S. Hannestad, Phys. Rev. D **67**, 085017 (2003) [astro-ph/0211106].
[16] K.N. Abazajian and S. Dodelson, Phys. Rev. Lett. **91**, 041301 (2003) [astro-ph/0212216].
[17] M. Kaplinghat, L. Knox and Y.S. Song, Phys. Rev. Lett. **91**, 241301 (2003) [astro-ph/0303344].
[18] M. Maltoni, T. Schwetz, M.A. Tórtola and J.W.F. Valle, Phys. Rev. D **68**, 113010 (2003) [hep-ph/0309130].
[19] G.L. Fogli, E. Lisi, A. Marrone and D. Montanino, Phys. Rev. D **67**, 093006 (2003) [hep-ph/0303064].
[20] M.C. González-García and C. Peña-Garay, Phys. Rev. D **68** (2003) 093003 [hep-ph/0306001].
[21] P. Huber, M. Lindner, M. Rolinec, T. Schwetz and W. Winter, hep-ph/0403068.
[22] A. Aguilar et al. [LSND Coll.], Phys. Rev. D **64** (2001) 112007 [hep-ex/0104049].
[23] M.C. González-García and Y. Nir, Rev. Mod. Phys. **75**, 345 (2003) [hep-ph/0202058].

[24] V. Barger, D. Marfatia and K. Whisnant, Int. J. Mod. Phys. E **12**, 569 (2003) [hep-ph/0308123].
[25] A.D. Dolgov, S.H. Hansen and D.V. Semikoz, Nucl. Phys. B **503**, 426 (1997) [hep-ph/9703315].
[26] G. Mangano, G. Miele, S. Pastor and M. Peloso, Phys. Lett. B **534**, 8 (2002) [astro-ph/0111408].
[27] A.D. Dolgov et al., Nucl. Phys. B **632**, 363 (2002) [hep-ph/0201287].
[28] A. Lewis and A. Challinor, Phys. Rev. D **66**, 023531 (2002) [astro-ph/0203507].
[29] J.R. Primack, J. Holtzman, A. Klypin and D.O. Caldwell, Phys. Rev. Lett. **74**, 2160 (1995) [astro-ph/9411020].
[30] U. Seljak and M. Zaldarriaga, Astrophys. J. **469**, 437 (1996) [astro-ph/9603033].
[31] J.H. Goldstein et al., Astrophys. J. **599**, 773 (2003) [astro-ph/0212517].
[32] A.C.S. Readhead et al., astro-ph/0402359.
[33] R. Rebolo et al., astro-ph/0402466.
[34] M. Bowden et al., astro-ph/0309610.
[35] M. Tegmark, D.J. Eisenstein, W. Hu and A. de Oliveira-Costa, Astrophys. J. **530**, 133 (2000) [astro-ph/9905257].
[36] S. Prunet, S.K. Sethi and F.R. Bouchet, Mon. Not. Roy. Astron. Soc. **314**, 358 (2000) [astro-ph/9911243].
[37] G. Patanchon, H. Snoussi, J.F. Cardoso and J. Delabrouille, astro-ph/0302078.
[38] W. Hu, Phys. Rev. D **65**, 023003 (2002) [astro-ph/0108090].
[39] W. Hu and T. Okamoto, Astrophys. J. **574**, 566 (2002) [astro-ph/0111606].
[40] T. Okamoto and W. Hu, Phys. Rev. D **67**, 083002 (2003) [astro-ph/0301031].
[41] M. Tegmark, Phys. Rev. Lett. **79**, 3806 (1997) [astro-ph/9706198].
[42] J.A. Tyson [the LSST Coll.], Proc. SPIE Int. Soc. Opt. Eng. **4836**, 10 (2002) [astro-ph/0302102].
[43] R.E. Lopez, S. Dodelson, A. Heckler and M.S. Turner, Phys. Rev. Lett. **82**, 3952 (1999) [astro-ph/9803095].
[44] R. Bowen et al., Mon. Not. Roy. Astron. Soc. **334**, 760 (2002) [astro-ph/0110636].
[45] S. Bashinsky and U. Seljak, Phys. Rev. D, in press [astro-ph/0310198].
[46] A. Cuoco, F. Iocco, G. Mangano, G. Miele, O. Pisanti and P.D. Serpico, astro-ph/0307213.
[47] R.H. Cyburt, B.D. Fields and K.A. Olive, Phys. Lett. B **567**, 227 (2003) [astro-ph/0302431].
[48] G. Jungman, M. Kamionkowski, A. Kosowsky and D.N. Spergel, Phys. Rev. Lett. **76**, 1007 (1996) [astro-ph/9507080].
[49] Y.S. Song and L. Knox, astro-ph/0312175.
[50] W. Hu, Astrophys. J. **522**, L21 (1999) [astro-ph/9904153].
[51] W. Hu, Phys. Rev. D **66**, 083515 (2002) [astro-ph/0208093].
[52] G.F. Giudice, A. Notari, M. Raidal, A. Riotto and A. Strumia, hep-ph/0310123.
[53] T. Hambye, Y. Lin, A. Notari, M. Papucci and A. Strumia, hep-ph/0312203.
[54] W. Buchmüller, P. Di Bari and M. Plümacher, hep-ph/0401240.

4.2 Sensitivity of CMB lensing extraction, PRD 73, 045021 (2006)

LAPTH-1128/05, IFIC/05-60, APC-05-90

Probing neutrino masses with CMB lensing extraction

Julien Lesgourgues, Laurence Perotto
Laboratoire de Physique Théorique LAPTH (CNRS-Université de Savoie), B.P. 110, F-74941 Annecy-le-Vieux Cedex, France

Sergio Pastor
Instituto de Física Corpuscular (CSIC-Universitat de València), Ed. Institutos de Investigación, Apdo. 22085, E-46071 Valencia, Spain

Michel Piat
Astroparticule et Cosmologie (APC), Collège de France, 11 place Marcelin Berthelot, F-75231 Paris Cedex 05, France

(Dated: February 5, 2008)

We evaluate the ability of future cosmic microwave background (CMB) experiments to measure the power spectrum of large scale structure using quadratic estimators of the weak lensing deflection field. We calculate the sensitivity of upcoming CMB experiments such as BICEP, QUaD, BRAIN, ClOVER and Planck to the non-zero total neutrino mass M_ν indicated by current neutrino oscillation data. We find that these experiments greatly benefit from lensing extraction techniques, improving their one-sigma sensitivity to M_ν by a factor of order four. The combination of data from Planck and the SAMPAN mini-satellite project would lead to $\sigma(M_\nu) \sim 0.1$ eV, while a value as small as $\sigma(M_\nu) \sim 0.035$ eV is within the reach of a space mission based on bolometers with a passively cooled 3-4 m aperture telescope, representative of the most ambitious projects currently under investigation. We show that our results are robust not only considering possible difficulties in subtracting astrophysical foregrounds from the primary CMB signal but also when the minimal cosmological model (Λ Mixed Dark Matter) is generalized in order to include a possible scalar tilt running, a constant equation of state parameter for the dark energy and/or extra relativistic degrees of freedom.

PACS numbers: 14.60.Pq, 95.35.+d, 98.80.Es

I. INTRODUCTION

Nowadays there exist compelling evidences for flavor neutrino oscillations from a variety of experimental data, that includes measurements of solar, atmospheric, reactor and accelerator neutrinos (for recent reviews, see e.g. [1, 2]). The existence of flavor change implies that the three neutrinos mix and have non-zero masses, but oscillation experiments only fix the differences of squared neutrino masses Δm^2_{31} and Δm^2_{21}, which correspond to the values relevant for atmospheric (2.4×10^{-3} eV^2) and solar (8×10^{-5} eV^2) neutrinos, respectively.

Non-zero neutrino masses imply that the Cosmic Neutrino Background (CNB), the sea of relic neutrinos that fill the Universe with a number density comparable to that of photons, influences the cosmological evolution in a more complicated way than that of a pure relativistic component. In particular, the contribution of the CNB to the present energy density of the Universe, measured in units of its critical value, is

$$\Omega_\nu = \frac{\rho_\nu}{\rho_c} = \frac{M_\nu}{93.14\, h^2 \text{ eV}} \qquad (1)$$

where h is the present value of the Hubble parameter in units of 100 km s^{-1} Mpc^{-1} and $M_\nu \equiv m_1 + m_2 + m_3$ is the total neutrino mass. From the experimental values of their mass differences, at least two neutrino mass states are non-relativistic today since both $(\Delta m^2_{31})^{1/2} \sim 0.05$ eV and $(\Delta m^2_{21})^{1/2} \sim 0.009$ eV are larger than the present neutrino temperature $T_\nu \simeq 1.96$ K $\simeq 1.7 \times 10^{-4}$ eV. Since the current upper bound on M_ν from tritium decay experiments [3] is of the order 6 eV (95% CL), we know that the neutrinos account for at least 0.5(1)% and at most 50% of the total dark matter density, where the lower limit corresponds to the minimum of M_ν for masses ordered according to a normal (inverted) hierarchy, characterized by the sign of Δm^2_{31}. Thus, although in the first limit the cosmological effect of neutrino masses would be quite small, the minimal cosmological scenario is in fact a Λ Mixed Dark Matter (ΛMDM) model rather than a plain Λ Cold Dark Matter one.

Considerable efforts are devoted to the determination of the absolute neutrino mass scale, which, combined with oscillation data, would fix the value of the lightest neutrino mass. The future tritium decay experiment KATRIN [4] is expected to reach a discovery potential for $0.3 - 0.35$ eV individual masses, while more stringent bounds exist from experiments searching for neutrinoless

double beta decay[1]. These will be improved in the near future [6], but unfortunately they depend on the details of the neutrino mixing matrix. The quest for M_ν will greatly benefit from cosmological observations, which offer the advantage of being independent of the neutrino mixing parameters since all flavors were equally populated in the early Universe.

Cosmology is sensitive to the neutrino masses through essentially two effects. First, the shape of the two-point correlation function –or power spectrum– of the Cosmic Microwave Background (CMB) temperature and polarization anisotropies on the one hand, and of the Large Scale Structure (LSS) mass density on the other, are both highly sensitive to the abundance of the various cosmological backgrounds: photons, baryons, cold dark matter, etc. The CNB is very specific in the sense that it behaves like a collisionless relativistic medium at the time of acoustic oscillations before photon decoupling (at redshifts $z > 1000$), but like a non-relativistic fluid during most of structure formation (at redshifts $z < 100$, at least for one of the three neutrino mass states). Therefore, the CNB affects at least one of the three following quantities: the redshift of equality between matter and radiation; the redshift of equality between matter and dark energy; or the spatial curvature of the Universe. This effect can be observed in the CMB and LSS power spectra and its amplitude is at most of the order of $(2 f_\nu)$ per cent [7] (f_ν is the current fraction of dark matter density in the form of neutrinos), which corresponds to only 1% in the limit $M_\nu \sim 0.05$ eV.

Fortunately, neutrino masses produce a second effect which is typically four times larger: on small scales neutrinos do not cluster gravitationally because of their large velocities. Even today, the typical neutrino velocity of a non-relativistic eigenstate with mass m_ν is as large as $v \simeq 150\,(1\,\mathrm{eV}/m_\nu)$ km s^{-1}. This simple kinematic effect, called *neutrino free-streaming*, is extremely important for the growth of non-relativistic matter perturbations (CDM and baryons) after photon decoupling. Indeed, the perturbation growth rate is controlled by the balance between gravitational clustering and the Universe expansion. On small scales, free-streaming neutrinos contribute to the total background density $\bar{\rho}$, but not to the total perturbation $\delta\rho$, which shifts the balance in favor of the Universe expansion, leading to a smaller growth rate for CDM and baryon perturbations. This effect is of order $(8 f_\nu)$ per cent in the small-scale matter power spectrum [7, 8, 9].

There are various ways to measure the LSS power spectrum. For instance, the galaxy-galaxy correlation function can be obtained from galaxy redshift surveys, and the density perturbations in hot intergalactic gas clouds at redshift $z \sim 2$ can be inferred from the Lyman-α forest region in the spectrum of distant quasars. At present, a total neutrino mass of $0.4 - 2$ eV is disfavored at 95% CL [10, 11, 12, 13, 14, 15, 16, 17, 18, 19, 20, 21], depending on the used CMB, LSS and other cosmological data.

However, the most promising idea on the long term is to study the weak lensing effects induced by neighboring galaxy clusters. A lensing map can be reconstructed from a statistical analysis, based either on the ellipticity of remote galaxies or on the non-gaussianity of the CMB temperature and polarization anisotropy maps. Weak lensing offers several advantages. Unlike galaxy redshift surveys, it traces directly the total density perturbation and does not involve any light-to-mass bias. Unlike Lyman-α forests data, it probes a large range of scales, which is particularly convenient for observing the step-like suppression of density perturbations induced by neutrino masses. In addition, weak lensing is sensitive to high redshifts, for which non-linear corrections appear only at very small scales. Finally, it enables tomographic reconstruction: by selecting the redshift of the sources, it is possible to obtain independent measurements of the power spectrum at various redshifts, in order to follow the non-trivial evolution of the spectrum amplitude caused by neutrino masses and/or by a possible evolution of the dark energy density. The best lever arm and the highest redshifts are encoded in the lensing of CMB maps, where the source is the photon last scattering surface, located at $z \sim 1100$, and the observed CMB patterns are sensitive to lenses as far as $z \sim 3$ [22, 23, 24]. In addition, CMB lensing observations do not require a devoted experiment: future CMB experiments designed for precision measurements of the primary CMB anisotropies offer for free an opportunity to extract lensing information.

The first paper estimating the sensitivity of future cosmological experiments to small neutrino masses was based on the measurement of the galaxy-galaxy correlation function [9], an analysis that was updated in Refs. [25, 26, 27] and more recently in Ref. [28]. The idea that weak lensing observations (from galaxy ellipticity) were particularly useful for measuring the neutrino mass was initially proposed in Ref. [29]. Then, the first analysis based on CMB lensing extraction was performed in Ref. [30], showing that an extremely small one-sigma error on the total neutrino mass –of the order of $\sigma(M_\nu) \simeq 0.04$ eV– was conceivable for a full-sky experiment with a resolution of 1 arc-minute and a sensitivity per pixel of 1 μK for temperature, 1.4 μK for polarization (these numbers were inspired from preliminary studies for the CMBpol satellite project). Soon after, Ref. [31] studied the neutrino mass sensitivity of future tomographic reconstructions using, on the one hand, galaxy ellipticities in various redshift bins, and on the other CMB lensing, where CMB plays the role of the last redshift bin. The authors found that for sufficiently large cosmic shear surveys, it would not be impossible to reach $\sigma(M_\nu) \simeq 0.02$ eV.

In this paper we want to come back to the prospects coming from CMB lensing alone, and try to improve the

[1] A claim of a positive signal exists [5], which would correspond to an effective neutrino mass of order $0.1 - 0.9$ eV. If confirmed, it would have a profound impact on cosmology.

pioneering analysis in [30, 31] in several directions. First, we analyze the potential of several CMB experiments expected to produce results in the coming years, based on a realistic description of instrumental sensitivities. Second, we discuss the robustness of our results by analyzing (i) the consequences of simplifying assumptions in the construction of the Fisher matrix, (ii) the dependence of the final results on the accuracy of the foreground subtraction process, and (iii) the impact of parameter degeneracies which can appear when non-minimal cosmological scenarios are introduced. Finally, we study the sensitivity of CMB experiments to the way in which the total neutrino mass is split among the three species.

II. BASIC PRINCIPLES OF CMB LENSING EXTRACTION

Weak lensing induces a deflection field $\mathbf{d}$, i.e. a mapping between the direction of a given point on the last scattering surface and the direction in which we observe it. At leading order [32] this deflection field can be written as the gradient of a lensing potential, $\mathbf{d} = \nabla\phi$. The (curl-free) deflection map and the lensing potential map can both be expanded in harmonic space

$$\phi(\hat{n}) \;=\; \sum_{lm} \phi_l^m Y_l^m(\hat{n}) \;, \tag{2}$$

$$(d_\theta \pm i d_\varphi)(\hat{n}) \;=\; \pm i \sum_{lm} d_l^{m\pm1} Y_l^m(\hat{n}) \;, \tag{3}$$

where $\hat{n} = (\theta, \phi)$ is a direction in the sky. There is a simple relation between the deflection and lensing potential multipoles

$$d_l^m = -i\sqrt{l(l+1)}\phi_l^m \;, \tag{4}$$

so that the power spectra $C_l^{dd} \equiv \langle d_l^m d_l^{m*}\rangle$ and $C_l^{\phi\phi} \equiv \langle \phi_l^m \phi_l^{m*}\rangle$ are related through

$$C_l^{dd} = l(l+1)C_l^{\phi\phi} \;. \tag{5}$$

In standard inflationary cosmology, the unlensed anisotropies obey Gaussian statistics in excellent approximation [33], and their two-dimensional Fourier modes are fully described by the power spectra $\tilde{C}_l^{ab}$ where a and b belong to the $\{T, E, B\}$ basis. Weak lensing correlates the lensed multipoles [22, 34] according to

$$\langle a_l^m b_{l'}^{m'}\rangle_{\rm CMB} = (-1)^m \delta_l^{l'}\delta_m^{m'} C_l^{ab} + \sum_{LM} \mathcal{C}(a,b)_{l\;l'\;L}^{m\,m'\,M}\; \phi_L^M \tag{6}$$

where the average holds over different realizations (or different Hubble patches) of a given cosmological model with fixed primordial spectrum and background evolution (i.e. fixed cosmological parameters). In this average, the lensing potential is also kept fixed by convention, which makes sense because the CMB anisotropies and LSS that we observe in our past light-cone are statistically independent, at least as long as we neglect the integrated Sachs-Wolfe effect. In the above equation, C_l^{ab} is the lensed power spectrum (which is nearly equal to the unlensed one, excepted for the B-mode power spectrum which is dominated, at least on small scales, by the conversion of E-patterns into B-patterns caused by lensing). The coefficients $\mathcal{C}(a,b)_{l\;l'\;L}^{m\,m'\,M}$ are complicated linear combinations of the unlensed power spectra $\tilde{C}_l^{ab}$, $\tilde{C}_l^{aa}$ and $\tilde{C}_l^{bb}$, given in [35].

The quadratic estimator method of Hu & Okamoto [35, 36, 37] is a way to extract the deflection field map from the observed temperature and polarization maps. It amounts essentially in inverting Eq. (6). This is not the only way to proceed: Hirata & Seljak proposed an iterative estimator method [32] which was shown to be optimal, but as long as CMB experiments will make noise-dominated measurements of the B-mode, i.e. at least for the next decade, the two methods are known to be equivalent in terms of precision. Even for the most precise experimental project discussed in this work, the quadratic estimator method would remain nearly optimal (the last project listed in Table I corresponds roughly to the hypothetical experiment called "C" in Ref. [32]).

By definition, the quadratic estimator $d(a,b)$ is built from a pair (a,b) of observed temperature or polarization modes, and its multipoles are given by the quadratic form

$$d(a,b)_L^M = \mathcal{N}_L^{ab} \sum_{ll'mm'} \mathcal{W}(a,b)_{l\;l'\;L}^{m\,m'\,M}\; a_l^m b_{l'}^{m'} \;, \tag{7}$$

where the normalization factor $\mathcal{N}_L^{ab}$ is defined in such way that $d(a,b)$ is an unbiased estimator of the deflection field

$$\langle d(a,b)_L^M\rangle_{\rm CMB} = \sqrt{l(l+1)}\phi_L^M \;, \tag{8}$$

and the weighting coefficients $\mathcal{W}(a,b)_{l\;L\;l'}^{m\,m'\,M}$ minimize the variance of $d(a,b)_L^M$ (which inevitably exceeds the power spectrum C_L^{dd} that we want to measure), i.e. minimize the coefficients $a = a'$, $b = b'$ of the covariance matrix

$$\langle d(a,b)_L^M d(a',b')_{L'}^{M'}\rangle_{\rm CMB} = (-1)^M \delta_L^{L'}\delta_M^{M'}[C_L^{dd} + N_L^{aba'b'}] \;. \tag{9}$$

Here the extra term $N_L^{aba'b'}$, which can be considered as noise, derives from the connected and non-connected pieces of the four-point correlation function $\langle aba'b'\rangle$. In Ref. [35], Okamoto & Hu derive a prescription for the weighting coefficients $\mathcal{W}(a,b)_{l\;L\;l'}^{m\,m'\,M}$ such that the contribution of the connected piece is minimal, while that from the non-connected piece is negligible in first approximation [38]. The weighting coefficients are rational functions of the observed power spectra C_l^{ab}, C_l^{aa} and C_l^{bb}, which include contributions from primary anisotropies, lensing and experimental noise. Therefore, if we assume a theoretical model and some instrumental characteristics, we can readily estimate the noise $N_L^{aba'b'}$ expected for a future experiment.

This method works for a given estimator $d(a,b)_L^M$ under the condition that for at least one of the three power

spectra (C_l^{ab}, C_l^{aa}, C_l^{bb}), the lensing contribution is much smaller than the primary anisotropy contribution. This is not the case for the pair $ab = BB$. Therefore, one can only build five estimators, for the remaining pairs $ab \in \{TT, EE, TE, TB, EB\}$. The question of which one is the most precise heavily depends on the experimental characteristics. In addition, it is always possible to build a minimum variance estimator, i.e. an optimal combination of the five estimators weighted according to the five noise terms $N_l^{aba'b'}$ of the experiment under consideration. For the minimum variance estimator, the noise reads

$$N_l^{dd} = \left[\sum_{aba'b'} \left(N_l^{aba'b'} \right)^{-1} \right]^{-1} . \quad (10)$$

III. FORECASTING ERRORS WITH THE FISHER MATRIX

For a future experiment with known specifications, it is possible to assume a cosmological *fiducial model* that will fit best the future data, and then to construct the probability $L(\vec{x}; \vec{\theta})$ of the data $\vec{x}$ given the parameters $\vec{\theta}$ of the theoretical model. The error associated with each parameter θ_i can be derived from the Fisher matrix

$$F_{ij} = - \left\langle \frac{\partial^2 \ln L}{\partial \theta_i \partial \theta_j} \right\rangle , \quad (11)$$

computed in the vicinity of the best-fit model. Indeed, after marginalization over all other free parameters, the one-sigma error (68% confidence limit) on a parameter θ_i would be greater or equal to

$$\sigma(\theta_i) = \sqrt{(F^{-1})_{ii}} . \quad (12)$$

In most cases, the forecasted errors depend only mildly on the exact values of fiducial model parameters; however, they can vary significantly with the number of free parameters to be marginalized out, since complicated fiducial models with many physical ingredients are more affected by parameter degeneracies.

It is usually assumed that for a CMB experiment covering a fraction $f_{\rm sky}$ of the full sky, the probability L of the data $\{a_l^m\}$ is gaussian, with variance $\mathbf{C}_l$. If the experiment observes only one mode, for instance temperature, then $\mathbf{C}_l$ is just a number, equal to the sum of the fiducial model primordial spectrum and of the instrumental noise power spectrum. If instead several modes are observed, for instance temperature, E and B polarization, then $\mathbf{C}_l$ is a matrix. Neglecting the lensing effect, we would get

$$\mathbf{C}_l = \begin{pmatrix} \tilde{C}_l^{TT} + N_l^{TT} & \tilde{C}_l^{TE} & 0 \\ \tilde{C}_l^{TE} & \tilde{C}_l^{EE} + N_l^{EE} & 0 \\ 0 & 0 & \tilde{C}_l^{BB} + N_l^{BB} \end{pmatrix} , \quad (13)$$

where the $\tilde{C}_l^{XX}$'s represent the power spectra of primary anisotropies (we recall that for parity reasons $\tilde{C}_l^{TB} = \tilde{C}_l^{EB} = 0$), and the N_l^{XX}'s are the noise power spectra, which are diagonal because the noise contributing to one mode is statistically independent of that in another mode. It can be shown with some algebra that for any gaussian probability L, the Fisher matrix reads [39]

$$F_{ij} = \frac{1}{2} \sum_l (2l+1) f_{\rm sky} {\rm Trace}[\mathbf{C}^{-1} \frac{\partial \mathbf{C}}{\partial \theta_i} \mathbf{C}^{-1} \frac{\partial \mathbf{C}}{\partial \theta_j}] . \quad (14)$$

In fact, due to the lensing effect, the data is not exactly gaussian. However, the difference between the unlensed and lensed power spectra for (TT, TE, EE) is so small that Eq. (14) remains approximately correct, at least when the B-mode is not included in the covariance matrix of Eq. (13). Beyond this issue, lensing offers the possibility to include an extra piece of information: namely, the map of the lensing potential –or equivalently, of the deflection vector– as obtained from e.g. the quadratic estimators method. Ideally, after lensing extraction, one would obtain four gaussian independent variables: the *delensed* temperature and anisotropy multipoles ($\tilde{T}_l^m$, $\tilde{E}_l^m$, $\tilde{B}_l^m$), and the lensing multipoles d_l^m. In this paper, we will take a fiducial model with no significant amplitude of primordial gravitational waves. In this case, the delensed B-mode is just noise and can be omitted from the Fisher matrix computation. Therefore the data covariance matrix reads

$$\mathbf{C}_l = \begin{pmatrix} \tilde{C}_l^{TT} + N_l^{TT} & \tilde{C}_l^{TE} & C_l^{Td} \\ \tilde{C}_l^{TE} & \tilde{C}_l^{EE} + N_l^{EE} & 0 \\ C_l^{Td} & 0 & C_l^{dd} + N_l^{dd} \end{pmatrix} , \quad (15)$$

where C_l^{dd} is the lensing power spectrum, N_l^{dd} the noise associated to the lensing extraction method (in our case, the minimum variance quadratic estimator), and C_l^{Td} the cross-correlation between the unlensed temperature map and lensing map. This term does not vanish because of the late integrated Sachs-Wolfe effect: the temperature includes some information on the same neighboring cluster distribution as the lensing. Both C_l^{dd} and C_l^{Td} can be computed numerically for a given theoretical model using a public Boltzmann code like CAMB [40], and then N_l^{dd} can be calculated using the procedure of Ref. [35]. This computation can be performed in the full sky: in this work, we will never employ the flat-sky approximation. Note that the B-mode does not appear explicitly in Eq. (15), but actually information from the observed B-mode is employed in the two estimators $d(T, B)$ and $d(E, B)$.

Using Eqs. (14) and (15), it is possible to compute a Fisher matrix and to forecast the error on each cosmological parameter. Let us discuss the robustness of this method. There are obviously two caveats which could lead to underestimating the errors.

First, we assumed in Eq. (15) that the temperature and polarization maps could be delensed in a perfect way. Instead, the delensing process would necessarily leave some residuals, in the form of extra power and correlations in the covariance matrix. However, this is not a relevant

issue, because we are using only the temperature and E-polarization modes, for which the lensing corrections are very small: therefore, considering a small residual or no residual at all makes no difference in practice. We checked this explicitly in a simple way. For a given theoretical model, Boltzmann codes like CAMB [40] are able to compute both the lensed and unlensed power spectra. If the delensing process is totally inefficient, we can say that unlensed temperature and polarization multipoles are recovered with an error of variance

$$E_l^{TT} = |C_l^{TT} - \tilde{C}_l^{TT}| \,, \qquad E_l^{EE} = |C_l^{EE} - \tilde{C}_l^{EE}| \,, \quad (16)$$

that we can treat as additional noise and sum up to the N_l^{TT} and N_l^{EE} terms in the matrix (15). We checked numerically that even with such a pessimistic assumption, the final result does not change significantly, which is not a surprise since $E_l^{aa} \ll \tilde{C}_l^{aa}$. We conclude that the assumption of perfect delensing performed in Eqs. (14) and (15) is not a problem in practice[2].

Second, we assumed a perfect cleaning of all the astrophysical foregrounds which contribute to the raw CMB observations. It is true that CMB experiments are operating in various frequency bands, precisely in order to subtract the foregrounds which frequency dependence is usually non-planckian. However, we still have a poor knowledge of many foregrounds, and some of them could reveal very difficult to remove, introducing extra non-gaussianity and spoiling the lensing extraction process [41, 42]. In particular, the question of foreground subtraction is related to the maximum l at which we should stop the sum in the Fisher matrix expression, i.e. to the smallest angular scale on which we expect to measure primary temperature and polarization anisotropies. If we assume a perfect cleaning, this value should be deduced from instrumental noise. Beyond some multipoles ($l_{\rm max}^T$, $l_{\rm max}^E$), the noise terms (N_l^{TT}, N_l^{EE}) become exponentially large. Thus, in practice, the sum in Eq. (14) can be stopped at any l larger than both $l_{\rm max}^T$ and $l_{\rm max}^E$. However, some foregrounds are expected to be impossible to subtract on very small angular scales (e.g., radio sources, dusty galaxies, or polarized synchrotron radiation and dust emission), so for experiments with a very small instrumental noise, the covariance matrix could be dominated by foreground residuals at smaller l values than those where the instrumental noise explodes.

Since we do not have precise enough data at high galactic latitude and on relevant frequencies, it is difficult at the moment to estimate how problematic foreground contamination will be, but it is clear that one should adopt a very careful attitude when quoting forecasted errors for future experiments with an excellent angular resolution. In the next sections, for each experiment and model, we will derive two results: one optimistic forecast, assuming perfect foreground cleaning up to the scale where the instrumental noise explodes (or in the case of the most precise experiments, up to the limit $l_{\rm max}^T, l_{\rm max}^E < 2750$ beyond which it is obvious that foreground contamination will dominate); and one very conservative forecast, assuming no foreground cleaning at all. In that case, we take the foreground spectra F_l^{TT}, F_l^{EE} and F_l^{TE} of the "mid-model" of Ref. [43], computed with the public code provided by the authors[3]. This model is not completely up-to-date, since it is based on the best data available at the time of publication, and does not include important updates like the level of polarized galactic dust observed by Archeops on large angular scales [44]. Also, for simplicity, it assumes statistically isotropic and Gaussian foregrounds, with no TB or EB correlations. However this approach is expected to provide the correct orders of magnitude, which is sufficient for our purpose. We add these new terms to the covariance matrix of Eq. (15), as if they were extra noise power spectra for the TT, EE and TE pairs. We consistently recompute N_l^{dd}, still using the equations in Ref. [35] but with these extra noise terms included, in order to model the worse possible loss of precision induce by foregrounds in the lensing extraction process. We expect that the true error-bar for each cosmological parameter will be somewhere between our two optimistic and conservative forecasts.

IV. EXPERIMENTAL SENSITIVITIES

We consider seven CMB experiments which are representative of the experimental efforts scheduled for the next decade. The first two, based in the South Pole, are complementary: BICEP[4] (Background Imaging of Cosmic Extragalactic Polarization) [45] is designed for large angular scales, while QUaD[5] (QUest at DASI, the Degree Angular Scale Interferometer) [46] for small angular scales. The second experiment, which is already collecting data, is composed of the QUEST (Q and U Extragalactic Sub-mm Telescope) instrument mounted on the structure of the DASI experiment. A second set of experiments is scheduled in Antarctica at the French-italian Concordia station and in the Atacama plateau in Chile: the BRAIN[6] (B-modes Radiation measurement

[2] Note that replacing $\tilde{C}_l^{TT}$ by C_l^{TT} in (15) would actually be a mistake. Indeed, in this case, the Fisher matrix would include the derivatives of the lensed power spectra with respect to the cosmological parameter. So, the physical effect of each cosmological parameter on lensing distortions would be counted several times, not only in $\partial C_l^{dd}/\partial\theta_i$ but also in $\partial C_l^{ab}/\partial\theta_i$, with $a, b \in \{T, E\}$. This would introduce correlations which would not be taken into account self-consistently, and the forecasted errors would be artificially small, as noticed in [30].

[3] For each experiment, we compute the foreground for each frequency channel, and then compute the minimum variance combination of all components.

[4] http://www.astro.caltech.edu/~lgg/bicep_front.html

[5] http://www.astro.cf.ac.uk/groups/instrumentation/projects/quad/

[6] http://apc-p7.org/APC_CS/Experiences/Brain/index.phtml

from Antarctica with a bolometric INterferometer) [47] instrument for measuring large scales, and the ClOVER[7] (Cl ObserVER) [48] instrument for intermediate scales. BRAIN and ClOVER are designed for unprecedented precision measurements of the B-mode for $l < 1000$. ClOVER was approved for funding by PPARC in late 2004 and could be operational by 2008. At that time, the PLANCK[8] satellite [49] should be collecting data: PLANCK has already been built and should be launched in 2007 by the European Space Agency (ESA). Beyond PLANCK, at least two space projects are under investigation: the mini-satellite SAMPAN (SAtellite to Measure the Polarized ANisotropies) [50] for CNES (Centre National d'Etudes Spatiales), and the more ambitious Inflation Probe project for NASA (National Aeronautics and Space Administration), whose characteristics are not yet settled. The calculations of Ref. [30] were based on numbers inspired from preliminary studies for the CMBpol satellite project: a resolution of 1 arc-minute and a sensitivity per pixel of 1 μK for temperature, 1.4 μK for polarization. Here, the experiment that we will call Inflation Probe is based on one over many possibilities [51]: a bolometer array with a passively cooled 3-4 m aperture telescope, with four years of multifrequency observations and a sensitivity of 2 μK s$^{-1/2}$ per channel.

We list the expected instrumental performances of each experiment in Table I. Each instrument includes many detectors grouped in frequency bands or *channels*. In each channel, the detectors have a given spatial resolution described by the FWHM (Full-Width at Half-Maximum) θ_b of the beam. For a given channel, one can estimate the temperature and polarization sensitivities per pixel of the combined detectors, Δ_T and $\Delta_E = \Delta_B$. The channel noise power spectrum reads

$$N^{aa}_{l,\nu} = (\theta_b \Delta_a)^2 \exp\left[l(l+1)\theta_b^2/8\ln 2\right] \ , \qquad (17)$$

with $a \in \{T, E, B\}$. The noise from individual channels can be combined into the global noise of the experiment

$$N^{aa}_l = \left[\sum_\nu (N^{aa}_{l,\nu})^{-1}\right]^{-1} \ . \qquad (18)$$

Given this input, the computation of the lensing noise N^{dd}_l can be performed numerically following Ref. [35]. In Fig. 1, we show our results for the lensing noise of each experiment, based on each quadratic estimator and on the combined minimum variance estimator. In Fig. 2 we gather information on the noise for the TT, EE and dd power spectra for each experiment. The error-bars ΔC^{aa}_l displayed in Fig. 2 include both cosmic variance and instrumental noise, and assume a multipole binning

Experiment	$f_{\rm sky}$	ν	θ_b	Δ_T	Δ_E
BICEP [45]	0.03	100	60'	0.33	0.47
		150	42'	0.35	0.49
QUaD [52]	0.025	100	6.3'	3.5	5.0
		150	4.2'	4.6	6.6
BRAIN [47]	0.03	100	50'	0.23	0.33
		150	50'	0.27	0.38
		220	50'	0.40	0.56
ClOVER [48]	0.018	100	15'	0.19	0.30
		143	15'	0.25	0.35
		217	15'	0.55	0.76
PLANCK [53]	0.65	30	33'	4.4	6.2
		44	23'	6.5	9.2
		70	14'	9.8	13.9
		100	9.5'	6.8	10.9
		143	7.1'	6.0	11.4
		217	5.0'	13.1	26.7
		353	5.0'	40.1	81.2
		545	5.0'	401	∞
		857	5.0'	18300	∞
SAMPAN [50]	0.65	100	42'	0.13	0.18
		143	30'	0.16	0.22
		217	20'	0.26	0.37
Inflation Probe	0.65	70	6.0'	0.29	0.41
(hypothetical) [51]		100	4.2'	0.42	0.59
		150	2.8'	0.63	0.88
		220	1.9'	0.92	1.30

TABLE I: Sensitivity parameters of the CMB projects considered in this work: $f_{\rm sky}$ is the observed fraction of the sky, ν the center frequency of the channels in GHz, θ_b the FWHM (Full-Width at Half-Maximum) in arc-minutes, Δ_T the temperature sensitivity per pixel in μK and $\Delta_E = \Delta_B$ the polarization sensitivity. For all experiments, we assumed one year of observations, except for the Inflation Probe sensitivity based on four years.

of width $\Delta l = 7$ until $l \sim 70$, and then $\Delta l \sim l/10$

$$\Delta C^{aa}_l = \sqrt{\frac{2}{(2l+1)\,\Delta l\, f_{\rm sky}}}\,(C^{aa}_l + N^{aa}_l) \ . \qquad (19)$$

The top graphs in Figs. 1 & 2 correspond to the BICEP+QUaD and BRAIN+ClOVER combinations. Computing the Fisher matrix for each pair of experiments is not a trivial task, due to the different sky coverages. We follow a method which is certainly not optimal, but has the merit of simplicity. Since in each case, one experiment is optimized for large scales and the other for smaller scales, we assume that below a given value l_c all multipoles are evaluated from BICEP or BRAIN only, while for $l > l_c$ they are taken from QUaD or ClOVER. In Eqs. (14, 15), this amounts in considering $f_{\rm sky}$ as a function of l, and in replacing $f_{\rm sky}(l)$, N^{TT}_l and N^{EE}_l by their BICEP/BRAIN value for $l < l_c$, or by their QUaD/ClOVER value for $l > l_c$. The lensing noise N^{dd}_l is then computed for the combined experiment, following the same prescriptions. For each pair of experiments, we optimized the value of l_c numerically by minimizing the

[7] http://www-astro.physics.ox.ac.uk/∼act/clover.html
[8] http://sci.esa.int/science-e/www/area/index.cfm?fareaid=17 and http://www.planck.fr/

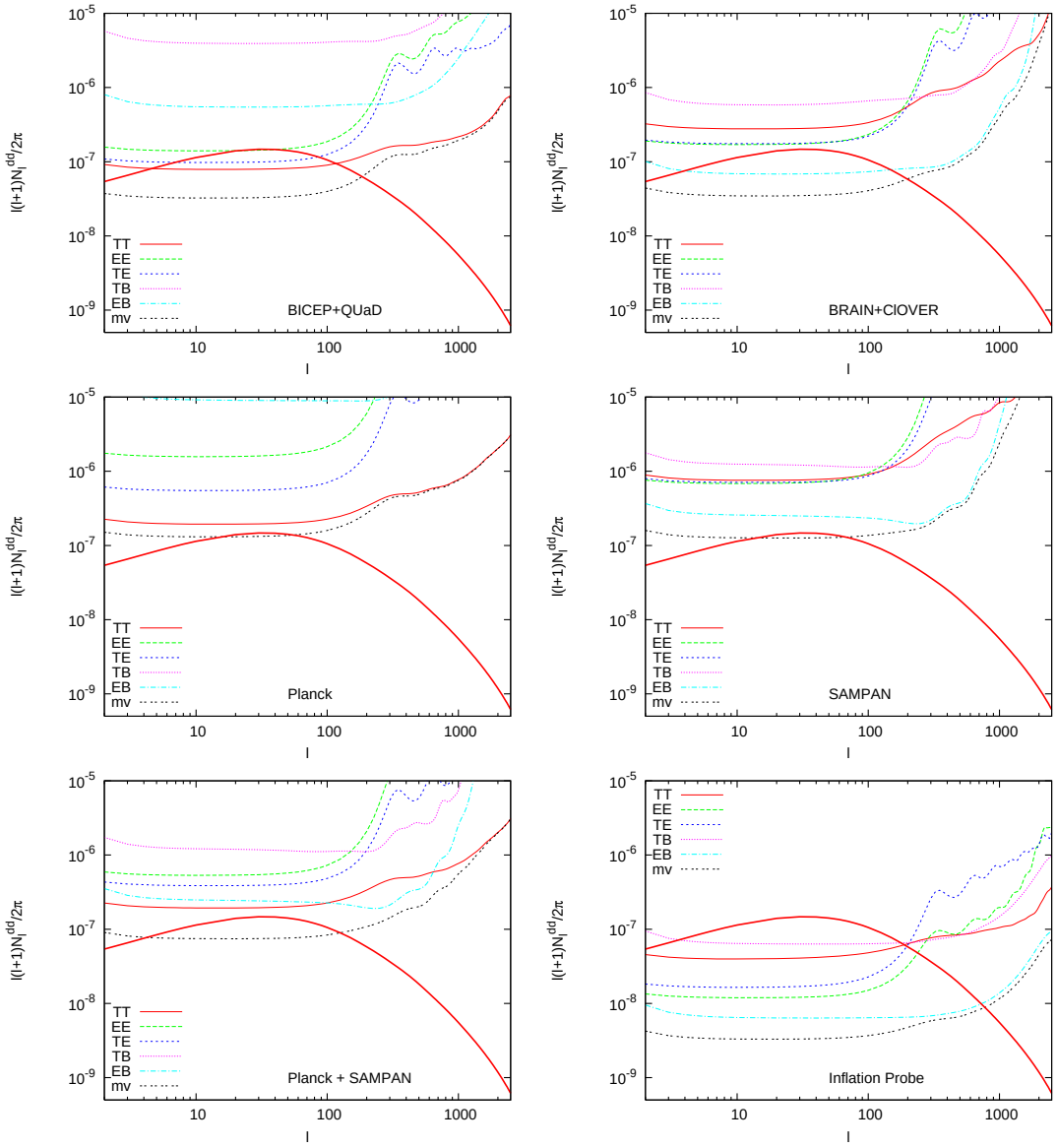

FIG. 1: For six CMB experiments or combinations of experiments, we show the expected noise power spectrum N_l^{dd} for the quadratic estimators $d(a,b)$ built out of pairs $ab \in \{TT, EE, TE, TB, EB\}$, and for the combined minimum variance estimator (mv). The thick line shows for comparison the signal power spectrum $C_l^{dd} = \langle d_l^m d_l^{m*} \rangle$. The sum of the two curves $N_l^{dd} + C_l^{dd}$ represents the expected variance of a single multipole $d(a,b)_l^m$.

forecasted error on the total neutrino mass M_ν. In both cases, we found that $l \sim 300$ was optimal. This method might be less favorable for BRAIN+ClOVER than for BICEP+QUaD, because the first pair of experiments has a large overlap in l-space, for which multipoles could be derived from the two combined datasets.

We find that BICEP+QUaD is able to reconstruct the lensing multipoles d_l^m in the range $2 < l < 200$ with an impressively small noise power spectrum N_l^{dd}. QUaD has both an excellent resolution and a very good sensitivity, and should provide an extremely precise measurement of T and E modes on small angular scales. Therefore, the three quadratic estimators $d(T,T)$, $d(E,E)$ and $d(T,E)$ are particularly efficient.

The main goal of the BRAIN+ClOVER combined experiment is to improve the determination of the B-mode

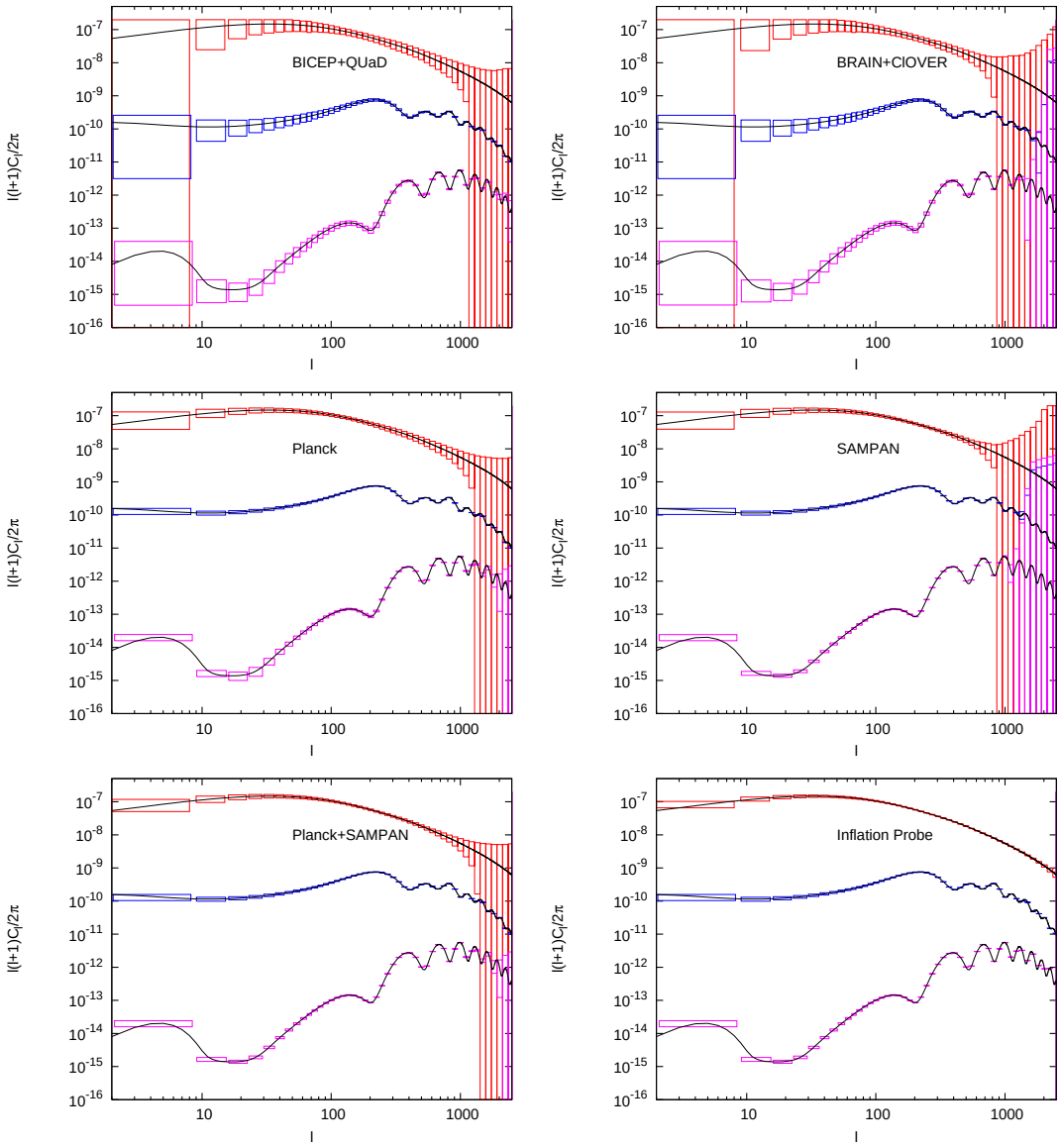

FIG. 2: For the same six CMB experiments or combinations of experiments as in figure 2, we show the expected binned error on the reconstructed power spectra: from top to bottom, C_l^{dd} (using the minimum variance quadratic estimator), C_l^{TT} and C_l^{EE}. The curves represent the power spectra of the fiducial model described in section V.

performed by BICEP+QUaD, especially on large and intermediate scales ($l < 1000$), which are particularly important for detecting gravity waves from inflation. This should be achieved with a sensitivity which is even better than that of BICEP and QUaD, but at the expense of a poorer resolution in the case of ClOVER, leading to large errors for small-scale polarization. In total, this design is roughly equivalent to that of BICEP+QUaD in terms of lensing extraction: BRAIN+ClOVER is also able to reconstruct the lensing multipoles d_l^m in the range $2 < l < 200$. The best estimator is now $d(E, B)$, known to be particularly useful, since E and B are correlated only due to lensing. In this sense, future lensing determinations by BRAIN+ClOVER and by BICEP+QUaD can be seen as complementary, and therefore both particularly interesting.

The Planck satellite has a resolution comparable to QUaD, but a poorer sensitivity than the last four exper-

iments. This explains why the lensing noise shown in Fig. 1 looks a bit disappointing: the signal marginally exceeds the noise only around $l \simeq 40$. However, we should keep in mind that PLANCK will observe the full sky (which leads to $f_{\rm sky} = 0.65$, once the galactic cut has been taken into account), while BICEP+QUaD or BRAIN+CLOVER explore only small regions. Therefore, for a given l, PLANCK makes many more independent measurements of multipoles (T_l^m, E_l^m), and consequently, also of d_l^m. In Fig. 2, one can check that PLANCK still makes a more precise determination of the lensing power spectrum than BICEP+QUaD: both experiments are able to constrain C_l^{dd} up to $l \sim 1100$, but the satellite provides smaller errors.

Since PLANCK is not very sensitive to B-modes, and BRAIN is limited by its small sky coverage, there will be room after these two projects for improving B-mode observations on large angular scales, in view of observing inflationary gravitational waves. This would be the target of the SAMPAN mini-satellite project, which would be a full-sky experiment with excellent sensitivity but poor resolution. We find that for the minimum variance estimator, the noise N_l^{dd} would be at the same level for PLANCK and SAMPAN. However, it is interesting to note that Sampan has a good $d(E,B)$ estimator, while PLANCK is better with $d(T,T)$. Therefore, it sounds particularly appealing to combine the two full-sky experiments, that is technically equivalent to assuming a super-experiment with twelve channels (nine from PLANCK and three from SAMPAN). The results (in the fifth graphs of Figs. 1 & 2) show that with such a combination one could lower the noise N_l^{dd} by a factor two for the minimum variance estimator, in order to constrain C_l^{dd} up to $l \sim 1300$.

Finally, the (hypothetical) version of the Inflation Probe satellite that we consider here has an extremely ambitious resolution and sensitivity, such that the instrumental error would be better than cosmic variance for the B-mode until $l \sim 1500$. For such a precise experiment, assumptions concerning foreground subtraction play a crucial role, since it is very likely that foreground residuals will start dominating the observed power spectrum before instrumental noise. The last graphs in Figs. 1 & 2, which assume perfect foreground cleaning up to $l \sim 2500$, show that lensing multipoles d_l^m could be recovered up to to $l \sim 800$, while C_l^{dd} could be constrained up to at least $l \sim 2500$.

V. FUTURE SENSITIVITIES TO NEUTRINO MASSES

For each experiment, we compute the Fisher matrix following Eqs. (14, 15), for a ΛMDM fiducial model with the parameter values as given below, and considering two possibilities for the number of free parameters that should be marginalized out.

The first possibility is the minimal alternative on the basis of current observations: we marginalize over eight free parameters, standing for the current baryon density $\omega_{\rm b} = \Omega_{\rm b} h^2$, the current total matter density $\omega_{\rm m} = \Omega_{\rm m} h^2$, the current dark energy density Ω_Λ, the total neutrino mass M_ν in eV, the primordial curvature power spectrum amplitude A_s and tilt n_s, the optical depth to reionization τ and the primordial helium fraction $y_{\rm He}$, to which we assign the values $(\omega_{\rm b}, \omega_{\rm m}, \Omega_\Lambda, M_\nu, \ln[10^{10} A_s], n_s, \tau, y_{\rm He}) = (0.023, 0.143, 0.70, 0.1, 3.2, 0.96, 0.11, 0.24)$. We assume no spatial curvature and tensor contribution. Note that the reduced Hubble parameter derives from $h = \sqrt{\omega_{\rm m}/(1-\Omega_\Lambda)}$.

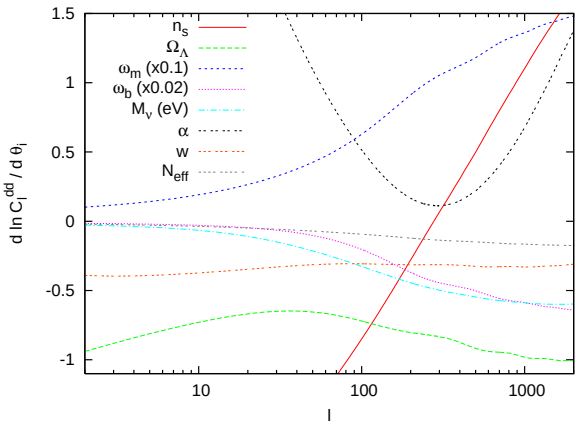

FIG. 3: Logarithmic derivatives of the lensing power spectrum C_l^{dd} with respect to each cosmological parameter. The derivatives with respect to $\omega_{\rm b}$ and $\omega_{\rm m}$ have been rescaled in order to fit inside the figure.

The second possibility, describing non-minimal physical assumptions, is to marginalize over three extra parameters: the scalar tilt running α, which can be non-negligible in some inflationary models with extreme assumptions; the dark energy equation-of-state parameter w; and finally, extra relativistic degrees of freedom which would enhance the total radiation density, parametrized by the effective number of neutrino species $N_{\rm eff}$ (for instance, $N_{\rm eff} = 4$ means that the Universe contains a background of extra relativistic particles with the same density as one extra massless neutrino species). In the fiducial model, these parameters take the values $(\alpha, w, N_{\rm eff}) = (0, -1, 3)$. Our purpose is to find out whether such extra free parameters open up degeneracy directions in parameter space, that would worsen the sensitivity to neutrino masses. It has been shown in recent analyses that these parameter degeneracies indeed appear with current CMB and LSS data (see [14, 15] for $N_{\rm eff}$ and [54, 55] for w).

The derivative of the lensing power spectrum C_l^{dd} with respect to each of these eleven parameters are shown in Fig. 3, with the exception of the derivatives with respect to τ and $y_{\rm He}$ which are null, and with respect to A_s which

Free parameters:	8 parameters of minimal ΛMDM				same + $\{\alpha,\ w,\ N_{\rm eff}\}$			
Lensing extraction:	no	no	yes	yes	no	no	yes	yes
Foreground cleaning:	perfect	none	perfect	none	perfect	none	perfect	none
QUaD+BICEP	1.3	1.6	0.31	0.36	1.5	1.9	0.36	0.40
BRAIN+ClOVER	1.5	1.8	0.34	0.43	1.7	2.0	0.42	0.51
Planck	0.45	0.49	0.13	0.14	0.51	0.56	0.15	0.15
SAMPAN	0.34	0.40	0.10	0.17	0.37	0.44	0.12	0.18
Planck+SAMPAN	0.32	0.36	0.08	0.10	0.34	0.40	0.10	0.12
Inflation Probe	0.14	0.16	0.032	0.036	0.25	0.26	0.035	0.039

TABLE II: Expected 1-σ error on the total neutrino mass M_ν in eV for various CMB experiments or combinations of them. The first (last) four columns correspond to a ΛMDM model with eight (eleven) free parameters. For each of the two models, the four columns show the cases with or without lensing extraction, and with two extreme assumptions concerning the foreground treatment: perfect subtraction or no subtraction at all.

is trivial. All derivatives were computed using the public Boltzmann code camb [40], enabling the highest accuracy options and increasing the `accuracy_boost` parameter to five. Whenever possible, we evaluated double-sided derivatives, and searched for optimal step sizes such that the results were not affected by numerical errors (from the limited precision of the code) nor by contributions from higher-order derivatives.

We quote the results for the total neutrino mass M_ν in Table II, assuming either eight or eleven free parameters. For each of the two cases, we compare the forecasted errors with and without lensing extraction, i.e. using either a 2×2 or a 3×3 data covariance matrix, in order to evaluate the impact of the extraction technique. Finally, in each of the four sub-cases, we quote the results obtained assuming perfect foreground cleaning or no cleaning at all, in order to be sure to bracket the true error. Should we trust more the results based on the eight or eleven parameter model? This depends on future results from cosmological observations: in absence of strong observational motivation for extra parameters, one will probably prefer to stick to the simplest paradigm; however, the next years might bring some surprises, like for instance the detection of a variation in the dark energy density.

Let us comment the results for each experiment. The combination QUaD+BICEP benefits a lot from lensing extraction, since the error decreases from approximately 1.5 eV to at least 0.4 eV. These results are found to be robust against foreground residuals and extra parameter degeneracies. It is interesting that with QUaD+BICEP it should soon be possible to reach in a near future – using CMB only– the same precision that we have today combining many observations of different types (galaxy-galaxy correlation function, Lyman-α forests) which are affected by various systematics. The situation is almost the same for BRAIN+ClOVER, which should also achieve $\sigma(M_\nu)\sim0.4$ eV using lensing extraction.

Planck should make a decisive improvement, lowering the error to $\sigma(M_\nu)\sim0.15$ eV, in excellent agreement with the results of Ref. [30]. Note that without lensing extraction the error would be multiplied by three (by four in the case with extra free parameters). We do not find a significant difference between the forecasted errors in the eight and eleven parameter models. SAMPAN alone is slightly more efficient than Planck, and the combination Planck+SAMPAN is the first one to reach $\sigma(M_\nu)\sim0.1-0.12$ eV, even in the pessimistic case of large foreground residuals and extra free parameters. Thus these future CMB lensing data could help in breaking the parameter degeneracy between M_ν and w [54], that would still be problematic at the level of precision of Planck (without lensing extraction) combined with the galaxy-galaxy correlation function extracted from the Sloan Digital Sky Survey.

Finally, the version of the Inflation Probe satellite that we consider here is able to reach $\sigma(M_\nu)=0.035$ eV both in the eight and eleven parameter cases. Note that when we take instead the CMBpol specifications of Ref. [30], we exactly reproduce their forecast $\sigma(M_\nu)=0.04$ eV (derived for an intermediate case with ten parameters). It is interesting to see that even with such a precise experiment, the results are robust against foreground contamination, since in absence of any cleaning the forecast error increases only by 15%.

We show in Fig. 4 the correlation between M_ν and each free parameter of the eleven-dimensional model, in the cases of Planck and Inflation Probe, with and without lensing extraction. In the parameter basis used in this work, the neutrino mass appears to be mainly degenerate with ω_m, and the lensing extraction process removes most of this degeneracy.

VI. FUTURE SENSITIVITIES TO THE NEUTRINO MASS SPLITTING

In principle, the LSS power spectrum is not sensitive only to the total mass M_ν, but also to the way in which the mass is distributed among the three neutrino states. The reason is twofold: the amount by which the gravitational collapse of matter perturbation is slowed down by neutrinos on small scales depends on the time of the non-relativistic transition for each eigenstate, i.e. on the individual masses; and the characteristic scales at which

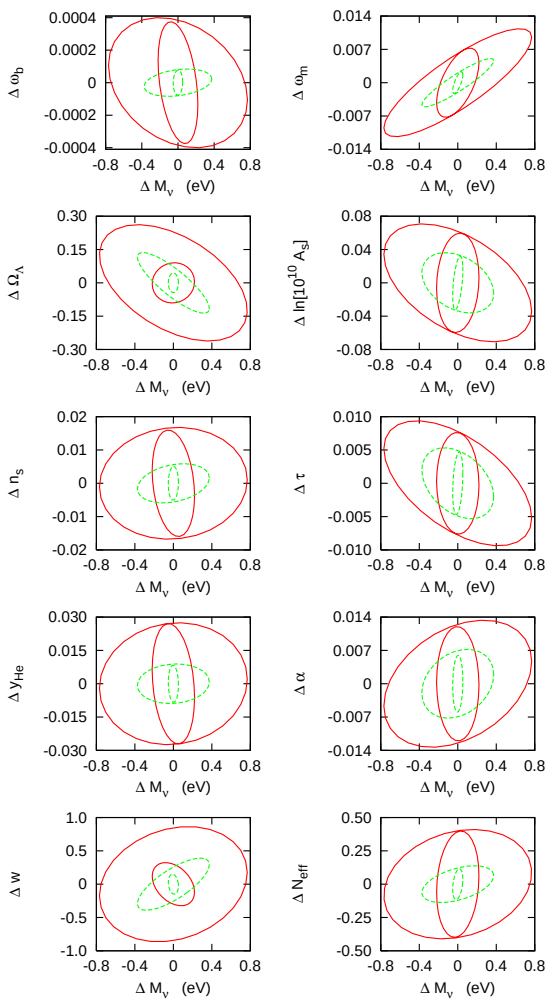

FIG. 4: 1-σ confidence limits on the pairs (M_ν, θ_i), for each parameter θ_i in our eleven-dimensional model. The red solid (green dashed) contours are those expected for Planck (Inflation Probe). For each case, the smaller (larger) ellipse corresponds to the forecasts with (without) lensing extraction.

the free-streaming effect of each neutrino family is imprinted in the power spectrum depends on the value of the wavelengths crossing the Hubble radius at the time of each non-relativistic transition, i.e. again on the individual masses.

The neutrino masses are differently distributed among the three states in the two possible mass schemes, or hierarchies, as shown e.g. in Fig. 1 of [28]. For a total mass M_ν larger than $0.2 - 0.3$ eV all neutrino states approximately share the same mass $m_0 = M_\nu/3$, in the so-called degenerate region. Instead, for smaller M_ν the splitting between the individual masses is more visible, and for the minimum values of M_ν one finds that in the Normal Hierarchy case (NH) there is only one neutrino state with significant mass, or two degenerate states in the Inverted Hierarchy case (IH). In general, for a given M_ν one can calculate the difference between the matter power spectrum in the two cases, as has been computed numerically in Ref. [28].

We would like to study whether the lensing power spectrum derived from a very precise CMB experiment like Inflation Probe would be able to discriminate between the two models. For this purpose, we take the eight parameter model of section V and complete it with a ninth parameter: the number of massive neutrinos $N_\nu^{\rm massive}$, which could be equal to 1, 2 or 3 (the remaining species are assumed to be exactly massless). In a NH scenario with $M_\nu > 0.1$ eV, the mass of the third neutrino is not completely negligible: so, we expect the difference between our simplified scenario with $N_\nu^{\rm massive} = 1$ and that with $N_\nu^{\rm massive} = 2$ to be more pronounced than the difference between realistic NH and IH scenarios (assuming the same total mass M_ν in all models). This statement is confirmed by the numerical results of Ref. [28]. So, if we could show that an experiment like Inflation Probe will be unable to differentiate between the sketchy $N_\nu^{\rm massive} = 1$ and $N_\nu^{\rm massive} = 2$ models, we would conclude that *a fortiori* it will not discriminate between the NH and IH scenarios.

We repeated the computations of section V with a ninth free parameter $N_\nu^{\rm massive}$ with fiducial value $N_\nu^{\rm massive} = 1$. Note that the parameter $N_\nu^{\rm massive}$ should not be confused with the total effective neutrino number $N_{\rm eff}$, which was a free parameter in the last section, and remains fixed to $N_{\rm eff} = 3$ in the present one. We found for Inflation Probe – including lensing extraction and assuming perfect foreground cleaning– a one-sigma error $\sigma\left(N_\nu^{\rm massive}\right) = 2.8$. We conclude that the experiments and techniques discussed in the present paper are far from sufficient for discriminating between the NH and IH scenarios. In any case, as shown in Ref. [28], future results on the total neutrino mass from very precise cosmological data should be interpreted in a slightly different way for the NH and IH cases.

VII. CONCLUSIONS

We have studied the ability of future CMB experiments to measure the power spectrum of large scale structure, using some quadratic estimators of the weak lensing deflection field. We inferred the sensitivity of these experiments to the non-zero neutrino masses indicated by neutrino oscillation data. Our aim was to extend the pioneering paper by Kaplinghat, Knox & Song [30] by further investigating several directions.

First, we based our analysis on the following list of forthcoming CMB experiments (either operational, approved or still in project): BICEP, QUaD, BRAIN, CLOVER and PLANCK, SAMPAN and Inflation Probe, taking into account their detailed characteristics. We found that even before PLANCK, ground-based experi-

ments should succeed in extracting the lensing map with good precision, and could then significantly improve the bounds on neutrino masses. We also found that the SAMPAN mini-satellite project would be able to reduce the Planck error $\sigma(M_\nu)$ from approximately 0.15 eV to 0.10 eV. Finally, the hypothetical version of Inflation Probe that we considered would reach a spectacular sensitivity of $\sigma(M_\nu) \sim 0.035$ eV.

We also tried to discuss two questions raised by the analysis of Ref. [30]: first, is it really accurate to base the Fisher matrix computation on perfectly delensed maps on the one hand, and on the reconstructed lensing map on the other? Second, is it realistic to estimate the noise variance of the lensing quadratic estimators without taking into account any residual foreground contamination? Our answer to these two questions is positive: we did not provide an exact treatment of these very technical issues, but we tried to systematically bracket the results between two over-optimistic and over-pessimistic assumptions, and concluded that the error forecast method of Ref. [30] is robust.

Finally, we investigated the issue of parameter degeneracies involving the neutrino mass, by comparing the results in a simpler model than that of Ref. [30] with those in a more complicated one. Our extended cosmological model allows for a scalar tilt running, a dark energy equation of state parameter $w \neq -1$, and extra degrees of freedom parametrized by the effective number of massless neutrinos $N_{\rm eff}$. These extra parameters were not chosen randomly. The tilt running was shown to be slightly degenerate with the neutrino mass in an analysis involving current CMB and LSS data [17]. The same holds for the equation of state of dark energy [54] and for the effective number of massless neutrinos [14, 15]. However, our results indicate that future CMB experiments will be able to resolve these degeneracies, since we do not find significant discrepancies between the neutrino mass errors obtained for our two cosmological models.

Fortunately, CMB lensing extraction should be regarded as only one of the most promising tools for measuring the absolute neutrino mass with cosmology. It could be combined with future data from tomographic galaxy cosmic shear surveys, which will be very sensitive to neutrino masses [31]. The cross-correlation of LSS information with CMB temperature anisotropies could also reveal very useful for the purpose of measuring M_ν [55]. In the method employed in the present paper, the correlation between temperature and lensing (the Td term) is already taken into account, but it affects the final results only marginally. More interesting should be the cross-correlation of future data from large cosmic shear surveys with that from CMB anisotropies.

In conclusion, our results show that there are good perspectives to detect non-zero neutrino masses using future CMB lensing data, since even in the less favorable case of the smallest $M_\nu \simeq 0.05$ eV in the NH mass scheme the Inflation Probe experiment alone could make a marginal detection (between the one and two sigma levels). Obviously the sensitivity is enhanced for larger values of M_ν, in particular for the mass degenerate and quasi-degenerate regions but also for the minimum of $M_\nu \simeq 0.1$ eV in the IH case. The information on M_ν from analyses of cosmological data will be complementary (and vice versa) to the efforts in terrestrial projects such as tritium beta decay and neutrinoless double beta decay experiments. Of course any positive result on the absolute neutrino mass scale will be a very important input for theoretical models of particle physics beyond the Standard Model.

Acknowledgments

We would like to thank Karim Benabed, Simon Prunet and Jonathan Rocher for extremely useful discussions. This work was supported by a MEC-IN2P3 agreement. SP was supported by the Spanish grants BFM2002-00345 and GV/05/017 of Generalitat Valenciana, as well as by a Ramón y Cajal contract of MEC.

[1] M. Maltoni, T. Schwetz, M.A. Tórtola and J.W.F. Valle, New J. Phys. **6**, 122 (2004) [hep-ph/0405172].
[2] G.L. Fogli, E. Lisi, A. Marrone and A. Palazzo, Prog. Part. Nucl. Phys., in press [hep-ph/0506083].
[3] K. Eitel, Nucl. Phys. Proc. Suppl. **143**, 197 (2005).
[4] A. Osipowicz et al. [KATRIN Coll.], hep-ex/0109033.
[5] H.V. Klapdor-Kleingrothaus et al, Phys. Lett. B **586**, 198 (2004) [hep-ph/0404088].
[6] S.R. Elliott and P. Vogel, Ann. Rev. Nucl. Part. Sci. **52**, 115 (2002) [hep-ph/0202264].
[7] J. Lesgourgues and S. Pastor, in preparation.
[8] J.R. Bond, G. Efstathiou and J. Silk, Phys. Rev. Lett. **45**, 1980 (1980).
[9] W. Hu, D.J. Eisenstein and M. Tegmark, Phys. Rev. Lett. **80**, 5255 (1998) [astro-ph/9712057].
[10] D.N. Spergel et al [WMAP Coll.], Astrophys. J. Suppl. **148**, 175 (2003) [astro-ph/0302209].
[11] S. Hannestad, JCAP **0305**, 004 (2003) [astro-ph/0303076].
[12] M. Tegmark et al, Phys. Rev. D **69**, 103501 (2004) [astro-ph/0310723].
[13] V. Barger, D. Marfatia and A. Tregre, Phys. Lett. B **595**, 55 (2004) [hep-ph/0312065].
[14] S. Hannestad and G. Raffelt, JCAP **0404**, 008 (2004) [hep-ph/0312154].
[15] P. Crotty, J. Lesgourgues and S. Pastor, Phys. Rev. D **69**, 123007 (2004) [hep-ph/0402049].
[16] R. Rebolo et al, Mon. Not. Roy. Astron. Soc. **353**, 747 (2004) [astro-ph/0402466].
[17] U. Seljak et al, Phys. Rev. D **71**, 103515 (2005) [astro-ph/0407372].
[18] G.L. Fogli et al, Phys. Rev. D **70**, 113003 (2004)

[hep-ph/0408045].
[19] K. Ichikawa, M. Fukugita and M. Kawasaki, Phys. Rev. D **71**, 043001 (2005) [astro-ph/0409768].
[20] C.J. MacTavish et al, astro-ph/0507503.
[21] A.G. Sánchez et al, Mon. Not. Roy. Astron. Soc. **366**, 189 (2006) [astro-ph/0507583]
[22] F. Bernardeau, Astron. Astrophys. **324**, 15 (1997) [astro-ph/9611012].
[23] M. Zaldarriaga and U. Seljak, Phys. Rev. D **58**, 023003 (1998) [astro-ph/9803150].
[24] U. Seljak and M. Zaldarriaga, Phys. Rev. Lett. **82**, 2636 (1999) [astro-ph/9810092].
[25] D.J. Eisenstein, W. Hu and M. Tegmark, Astrophys. J. **518**, 2 (1998) [astro-ph/9807130].
[26] J. Lesgourgues, S. Pastor and S. Prunet, Phys. Rev. D **62**, 023001 (2000) [hep-ph/9912363].
[27] S. Hannestad, Phys. Rev. D **67**, 085017 (2003) [astro-ph/0211106].
[28] J. Lesgourgues, S. Pastor and L. Perotto, Phys. Rev. D **70**, 045016 (2004) [hep-ph/0403296].
[29] A.R. Cooray, Astron. Astrophys. **348**, 31 (1999) [astro-ph/9904246].
[30] M. Kaplinghat, L. Knox and Y.S. Song, Phys. Rev. Lett. **91**, 241301 (2003) [astro-ph/0303344].
[31] Y.S. Song and L. Knox, Phys. Rev. D **70**, 063510 (2004) [astro-ph/0312175].
[32] C.M. Hirata and U. Seljak, Phys. Rev. D **68**, 083002 (2003) [astro-ph/0306354].
[33] N. Bartolo, E. Komatsu, S. Matarrese and A. Riotto, Phys. Rep. **402**, 103 (2004) [astro-ph/0406398].
[34] U. Seljak, Astrophys. J. **463**, 1 (1996) [astro-ph/9505109].
[35] T. Okamoto and W. Hu, Phys. Rev. D **67**, 083002 (2003) [astro-ph/0301031].
[36] W. Hu, Astrophys. J. **557**, L79 (2001) [astro-ph/0105424].
[37] W. Hu and T. Okamoto, Astrophys. J. **574**, 566 (2002) [astro-ph/0111606].
[38] A. Cooray and M. Kesden, New Astron. **8**, 231 (2003) [astro-ph/0204068].
[39] M. Tegmark, A. Taylor and A. Heavens, Astrophys. J. **480**, 22 (1997) [astro-ph/9603021].
[40] A. Lewis, A. Challinor and A. Lasenby, Astrophys. J. **538**, 473 (2000) [astro-ph/9911177].
[41] A. Amblard, C. Vale and M.J. White, New Astron. **9**, 687 (2004) [astro-ph/0403075].
[42] A. Cooray, M. Kamionkowski and R.R. Caldwell, Phys. Rev. D **71**, 123527 (2005) [astro-ph/0503002].
[43] M. Tegmark, D.J. Eisenstein, W. Hu and A. de Oliveira-Costa, Astrophys. J. **530**, 133 (2000) [astro-ph/9905257].
[44] N. Ponthieu et al, Astron. Astrophys. **444**, 327 (2005) [astro-ph/0501427].
[45] B.G. Keating et al, in Polarimetry in Astronomy, ed. by S. Fineschi, Proceedings of the SPIE **4843**, 284 (2003).
[46] S. Church et al [QUaD Coll.], New Astron. Rev. **47**, 1083 (2003).
[47] M. Piat et al [BRAIN-CLOVER Coll.], SF2A 2004 proceedings (2004) [astro-ph/0412590].
[48] B. Maffei et al. [BRAIN-ClOVER Coll.], EAS Publications Series **14**, 251 (2005).
[49] J.A. Tauber, Adv. Space Res. **34**, 491 (2004).
[50] F.R. Bouchet et al, SF2A 2005 proceedings (2005) [astro-ph/0510423].
[51] J. Bock, private communication.
[52] M. Bowden et al, Mon. Not. Roy. Astron. Soc. **349**, 321 (2004) [astro-ph/0309610].
[53] The Planck Consortia, "The Scientific Programme of Planck 2004 (Blue Book)", ESA Publication Division (2005).
[54] S. Hannestad, Phys. Rev. Lett. **95**, 221301 (2005) [astro-ph/0505551].
[55] K. Ichikawa and T. Takahashi, astro-ph/0510849.

4.3 Cross-correlation between CMB and LSS, PRD 77, 063505 (2008)

LAPTH-1213/07

Constraining neutrino masses with the ISW-galaxy correlation function

Julien Lesgourgues* and Wessel Valkenburg†
LAPTH, Université de Savoie & CNRS, BP110, F-64941 Annecy-le-vieux Cedex, France

Enrique Gaztañaga‡
Institut de Ciències de l'Espai, CSIC/IEEC, Campus UAB, F. de Ciències, Torre C5 par-2, Barcelona 08193, Spain
(Dated: March 5, 2008)

Temperature anisotropies in the Cosmic Microwave Background (CMB) are affected by the late Integrated Sachs-Wolfe (lISW) effect caused by any time-variation of the gravitational potential on linear scales. Dark energy is not the only source of lISW, since massive neutrinos induce a small decay of the potential on small scales during both matter and dark energy domination. In this work, we study the prospect of using the cross-correlation between CMB and galaxy density maps as a tool for constraining the neutrino mass. On the one hand massive neutrinos reduce the cross-correlation spectrum because free-streaming slows down structure formation; on the other hand, they enhance it through their change in the effective linear growth. We show that in the observable range of scales and redshifts, the first effect dominates, but the second one is not negligible. We carry out an error forecast analysis by fitting some mock data inspired by the Planck satellite, Dark Energy Survey (DES) and Large Synoptic Survey Telescope (LSST). The inclusion of the cross-correlation data from Planck and LSST increases the sensitivity to the neutrino mass m_ν by 38% (and to the dark energy equation of state w by 83%) with respect to Planck alone. The correlation between Planck and DES brings a far less significant improvement. This method is not potentially as good for detecting m_ν as the measurement of galaxy, cluster or cosmic shear power spectra, but since it is independent and affected by different systematics, it remains potentially interesting if the total neutrino mass is of the order of 0.2 eV; if instead it is close to the lower bound from atmospheric oscillations, $m_\nu \sim 0.05$ eV, we do not expect the ISW-galaxy correlation to be ever sensitive to m_ν.

PACS numbers: 98.80.Cq

I. INTRODUCTION

As photons pass through a changing gravitational potential well, they experience a redshift or a blueshift, depending on whether the well grows or decays respectively. Cosmic microwave background (CMB) photons can experience such variations between the time of last scattering and their detection now. This effect was first described by Sachs and Wolfe in 1967 [1], and hence is dubbed the integrated Sachs-Wolfe effect (ISW). During a Cold Dark Matter (CDM) and/or baryon dominated era, the gravitational potential distribution remains frozen, and the ISW effect has no net effect on the blackbody temperature of CMB photons. This property is crucially related to the fact that non-relativistic matter (like CDM and baryons) has a vanishing sound speed, and experiences gravitational clustering on all sub-Hubble scales after photon decoupling, as described by the Poisson equation. In such a situation, the universal expansion and the gravitational contraction compensate each other in such a way as to maintain a static gravitational potential. However, when the expansion rate is affected by any type of matter with a non-vanishing sound speed, e.g. during Dark Energy (DE) domination, the gravitational perturbations decay and the cosmic photon fluid experiences a blue shift, acquiring extra temperature perturbations related to the intervening pattern of matter perturbations. It was first proposed by Crittenden and Turok in 1995 [2] to cross correlate maps of temperature perturbations in the CMB with those of matter overdensities in large scale structures (LSS), in order to measure a possible acceleration of the universe's expansion. However, the CMB and LSS data available at that time were not good enough for such an ambitious goal, and the first strong indication of a positive acceleration came in 1998 from the side of type-Ia supernovae [3, 4]. Analyses of the first (2003) and second (2006) data releases of the Wilkinson Microwave Anisotropy Probe (WMAP) [5, 6] were the first to indicate the existence of Dark Energy independent of acceleration, by means of the location of the second peak in the CMB power spectrum. Simultaneously, a number of interesting papers presented the first detections of the ISW effect by cross-correlating WMAP anisotropy maps with various LSS data sets [7, 8, 9, 10, 11, 12, 13, 14, 15], now able to give an independent measure for the acceleration of the expansion of the universe.

The domination of Dark Energy is not the only source of gravitational potential evolution and of a net ISW effect. On small cosmological scales, as soon as matter perturbations exceed the linear regime, gravitational perturbations start to grow and to redshift CMB photons. This effect, called the Rees-Sciama effect, has

*Electronic address: julien.lesgourgues@lapp.in2p3.fr
†Electronic address: wessel.valkenburg@lapp.in2p3.fr
‡Electronic address: gazta@ieec.uab.es

not been significantly detected until now [16]. CMB photons can also be scattered by gravitational lensing [17] and by the Sunyaev-Zeldovich (SZ) effect [18] (see [9, 10, 19] for detections in CMB-LSS cross-correlation analysis). An other party expected to affect the evolution of gravitational perturbations –at least by a small amount– is the background of massive neutrinos. Over thirty years ago massive neutrinos were proposed as a Hot Dark Matter (HDM) candidate, and later ruled out as the dominant dark component, since HDM tends to wash out small scale overdensities during structure formation [20]. Observed neutrino oscillations however constrain neutrinos to have a mass [21, 22]. In addition, the presence of a Cosmic Neutrino Background (CNB) is strongly suggested on the one hand by the abundance of light elements produced during primordial nucleosynthesis [23, 24, 25], and on the other hand by CMB anisotropies [26, 27, 28, 29, 30, 31, 32, 32, 33, 34]. Therefore, a small fraction of HDM is expected to coexist with the dominant CDM component. On small cosmological scales (for instance, cluster scale), the free-streaming of massive neutrinos should induce a slow decay of gravitational and matter perturbations [35], acting during both matter and Dark Energy domination. This effect depends on the total neutrino mass summed over all neutrino families, $m_\nu = \sum_i m_i$, unlike laboratory experiments based on tritium decay or neutrinoless double-beta decay, which probe different combinations: hence, a cosmological determination of the total neutrino mass would bring complementary information to the scheduled particle physics experiments [37, 38]. The free streaming of massive neutrinos has not yet been detected [36], but there are good prospects to do so in the future, since the smallest total neutrino mass allowed by data on atmospheric neutrino oscillations ($m_\nu \geq \sqrt{\Delta m^2_{\rm atm}} \sim 0.05$ eV) implies at least a 5% suppression in the matter/gravitational small-scale power spectrum [37, 38]. A positive detection –even in the case of minimal mass– could follow from the analysis of future galaxy/cluster redshift surveys [39, 40, 41], weak lensing surveys [42, 43], Lyman-α forest analysis, cluster counts [40], etc. The goal of measuring the neutrino mass from cosmology is very ambitious since each of these methods suffers from its own source of systematics (bias issues, modeling of non-linear clustering, ...). Therefore, a robust detection could only be achieved by comparing the results from various types of experiments.

The goal of this work is to describe a possible cosmological determination of the absolute neutrino mass scale through the ISW effect induced by neutrino free-streaming on CMB temperature maps, using as an observable the cross-correlation function of galaxy-temperature maps. This possibility was investigated previously by Ichikawa and Takahashi [44] (and suggested again recently in [45]). As neutrinos slow down the growth of structure, we expect the blueshift caused by an accelerated expansion to be more pronounced if neutrinos have a larger mass. On the other hand, the distribution of matter inducing the late ISW effect is smoother in case of free-streaming by massive neutrinos. These two antagonist effects should in principle induce some mass-dependent variations in the galaxy-temperature cross-correlation function.

In section II of this paper we give an outline of the theory of the ISW-effect in the presence of a neutrino mass. In section III, we use some mock data with properties inspired from the Planck satellite, Dark Energy Survey (DES) and Large Synoptic Survey Telescope (LSST) in order to show the potential impact of this method in the future.

II. THE GALAXY-ISW CORRELATION IN THE PRESENCE OF NEUTRINO MASS

A. Definitions

The observed galaxy overdensity δ_G in a given direction $\hat{n}$ is defined as

$$\delta_G(\hat{n}) = \int dz\, b(z)\phi_G(z)\delta_m(\hat{n}, z), \tag{1}$$

where z denotes redshift, $b(z)$ is the redshift dependent bias function relating the observed galaxy overdensity to the total matter overdensity, and $\phi_G(z)$ is the galaxy selection function which can be chosen such that only galaxies within a certain range of redshift are considered.

The observed CMB temperature map

$$\Delta_T(\hat{n}) \equiv \frac{T(\hat{n}) - T_0}{T_0} \tag{2}$$

results from various contributions, classified as primary or secondary anisotropies. By definition, secondary anisotropies are induced after photon decoupling and can be correlated to some extent with the surrounding large scale structure. The ISW component is one of these terms, and can be obtained by integrating the scalar metric perturbations (or just the Newtonian gravitational potential on sub-Hubble scales) along each line-of-sight between the last scattering surface and the observer. If the gravitational potential is written as a function of direction $\hat{n}$ and redshift z, the ISW term reads

$$\Delta_T^{ISW}(\hat{n}) = -2\int_0^{z_{\rm dec}} dz\, \frac{d\Phi}{dz}(\hat{n}, z). \tag{3}$$

where $z_{\rm dec}$ is the redshift at decouplig. Immediately after decoupling and before full matter domination, the gravitational potential does vary with time: this is known as the early ISW (eISW) effect, in contrast with the late ISW (lISW) in which we are presently interested. The two maps Δ_T^{eISW}, Δ_T^{lISW} can be computed separately by cutting the above integral in two pieces at some intermediate redshift z_* chosen during full matter domination, when the gravitational potential is static. Note that in presence of massive neutrinos, the potential is never really static on small scales, so the quantity Δ_T^{lISW} might not be uniquely defined. Anyway,

this question is not relevant in practice. The observable quantity is not the late ISW auto-correlation function $\langle\Delta_T^{lISW}(\hat{n})\Delta_T^{lISW}(\hat{n}')\rangle$, but only its cross-correlation with a given survey $\langle\Delta_T^{lISW}(\hat{n})\delta_G(\hat{n}')\rangle$. Then, the redshift distribution $\phi_G(z)$ selects the range in which the ISW effect is being probed, and the choice of z_* becomes irrelevant provided that z_* remains larger than the redshift of all objects in the survey: $\phi_G(z_*) \simeq 0$.

Assuming that the galaxy-temperature cross-correlation function arises solely from the late ISW effect (i.e., assuming that other secondary anisotropies potentially correlated with LSS can be separated or have a negligible amplitude, which is a good assumption on the scales considered hereafter), we can relate the galaxy-temperature correlation multipoles to the real-space correlation function $\langle\Delta_T^{lISW}(\hat{n})\delta_G(\hat{n}')\rangle$. In the Limber approximation (see Appendix), one gets

$$C_l^{TG} = \frac{3\Omega_m H_0^2}{(l+1/2)^2} \times \int_0^{z_*} dz\, b(z)\phi_G(z)H(z)a(z)\left[\partial_z \frac{P(k,z)}{a(z)^2}\right]_{k=\frac{l+1/2}{r(z)}}, \quad (4)$$

where $r(z)$ is the conformal distance up to redshift z, $H_0 = 100h$ km/s/Mpc is the Hubble parameter today, and the matter power spectrum is defined as $\langle\delta_m(\vec{k},z)\delta_m(\vec{k}',z)\rangle \equiv P(k,z)\,\delta^3(\vec{k}-\vec{k}')$. Note that we used the Poisson equation in flat space in order to relate the gravitational potential Φ to the matter overdensity δ_m, and assumed $a(0) = 1$ by convention. Finally, the multipoles C_l^{TG} define the angular correlation function in a Legendre polynomial basis (p_l),

$$w^{TG}(\theta) = \sum_l \frac{2l+1}{4\pi} p_l(\cos\theta) C_l^{TG}. \quad (5)$$

Eq.(4) is often written in a form which assumes that the matter power spectrum is a separable function of wavenumber and redshift. This applies to the case of a (flat) ΛCDM universe, for which one can write

$$P(k,z) = D(\Lambda;z)^2 a(z)^2 P(k,0) \quad (6)$$

with $\partial_z D = 0$ during full matter domination and $\partial_z D > 0$ during Λ domination. Figure 1 (left) shows the evolution of D as a function of z for $\Omega_\Lambda = 1 - \Omega_m = 0.69$. In the case of time-varying Dark Energy, the situation is qualitatively similar, and D just depends on more free parameters than Λ. In the rest of this paper, we will just write this function as $D(z)$ for concision.

B. Effect of neutrino masses

In models with massive neutrinos, the spectrum is not a separable function anymore (in other words, the linear growth factor is scale-dependent), and Eq.(4) cannot be further simplified. However, in order to make analytical estimates of the impact of neutrino masses on C_l^{TG}, it is possible to use some approximate solutions valid only on the largest and smallest wavelength (see [38] and [45] for more details). First, for wavelengths larger than the maximum value of the neutrino free-streaming scale, reached at the time of the transition to the non-relativistic regime, the power spectrum P^{f_ν} is completely unaffected by neutrino masses, and identical to that in a massless neutrino model with the same cosmological parameters (in particular, the same Ω_m and h) noted as P^0:

$$\forall k < k_{\rm nr}, \quad P^{f_\nu}(k,z) = [D(z)a(z)]^2 P^{f_\nu}(k,0) \quad \text{with} \quad P^{f_\nu}(k,0) = P^0(k,0)\ . \quad (7)$$

On the other hand, for wavelengths smaller than the the free-streaming scale today, both the linear growth factor and the amplitude today are affected by neutrino masses, approximately like:

$$\forall k > k_{\rm fs}, \quad P^{f_\nu}(k,z) \simeq [D(z)a(z)]^{2-\frac{6}{5}f_\nu} P^{f_\nu}(k,0) \quad \text{with} \quad P^{f_\nu}(k,0) \simeq [1-8f_\nu]P^0(k,0)\ , \quad (8)$$

where $f_\nu = \Omega_\nu/\Omega_m$ stands for the neutrino density today relative to the *total* matter density (so Ω_m includes baryons, hot and cold dark matter). Here $D(z)$ is always the same function, computed either for $f_\nu \neq 0$ on large scales, or for $f_\nu = 0$ on any scale, with a common value of Ω_Λ (or of Dark Energy parameters). The first approximation in Eqs. (8) is very accurate, as shown in Fig. 1 (left) where we compare the precise linear growth factor obtained numerically with the above solution. The second approximation is poorer, but more accurate ones can be found e.g. in Refs. [38, 45].

Assuming that the galaxy selection function is very peaked around a median redshift z_m, the multipole C_l^{GT} probes mainly fluctuations around the scale $k \sim l/r(z_m)$. If l is larger than $k_{\rm fs}\, r(z_m)$, C_l^{GT} is affected by neutrino masses through the term between brackets in Eq. (4). Using Eqs. (8), this term varies with f_ν like:

$$\partial_z \frac{P^{f_\nu}(k,z)}{a(z)^2} \simeq [(1+C(z)f_\nu)(1-8f_\nu)]\,\partial_z \frac{P^0(k,z)}{a(z)^2}\ , \quad (9)$$
$$\text{with} \quad C(z) = \frac{3}{5}\left(\frac{1}{1+z}\frac{D}{D'} - 1\right)\ .$$

For a typical Dark Energy model, the density fraction $\Omega_{\rm DE}$ becomes negligible for $z > 2$ [55], and hence the ratio D'/D is tiny. So, at hight redshift, the net effect of the neutrino mass is to increase the integrand in C_l^{TG} like:

$$\partial_z \frac{P^{f_\nu}(k,z)}{a(z)^2} \simeq \left[\frac{3}{5}\frac{f_\nu(1-8f_\nu)}{1+z}\frac{D}{D'}\right]\ \partial_z \frac{P^0(k,z)}{a(z)^2}\ . \quad (10)$$

This just reflects the fact that at high redshift, the ISW effect would be null on all scales for $f_\nu = 0$, while for $f_\nu > 0$ it is still active on small scales. However, for $z < 2$, D'/D becomes larger, and for typical values of

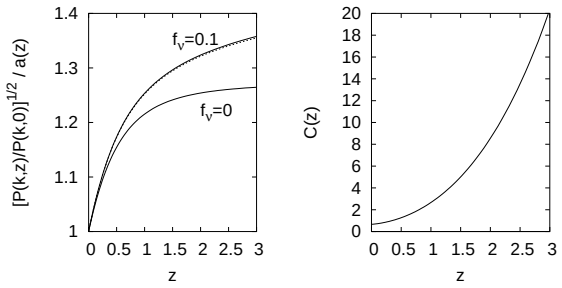

FIG. 1: *(Left)* Redshift evolution of the small-scale linear growth factor, defined here as $[P(k,z)/P(k,0)]^{1/2}/a(z)$ for $k \sim 10\,h\mathrm{Mpc}^{-1}$, and obtained numerically with CAMB for $\Omega_\Lambda = 0.69$. The lower curve corresponds to $f_\nu = 0$ and is exactly equal to the quantity $D(z)$ defined in Eq.(6). The upper, solid curve corresponds to $f_\nu = 0.1$, and is well approximated by the dotted curve, which corresponds to the first of Eqs.(8). *(Right)* The function $C(z)$, defined in Eqs.(9), computed here for $\Omega_\Lambda = 0.69$. Roughly speaking, the effect of neutrino masses on C_l^{TG} changes of sign when this function crosses eighth.

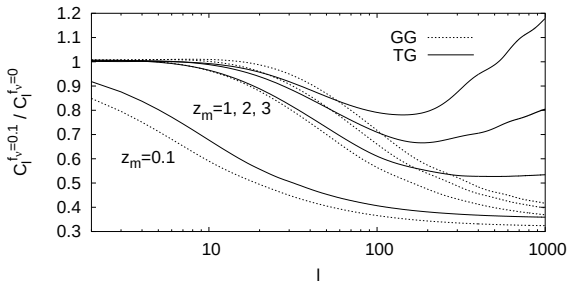

FIG. 2: Ratio of the cross-correlation multipoles C_l^{TG} and auto-correlation multipoles C_l^{GG} obtained for two cosmological models with neutrino density fractions equal to $f_\nu = 0.1$ or 0, and the same value of other cosmological parameters (see the text for details).

$\Omega_{\rm DE} \sim 0.7$ there is always a redshift below which $C(z)$ is smaller than eight. Then, the term between brackets in Eq. (9) is smaller than one, and the net effect of neutrino masses is to decrease $\partial_z[P/a^2]$. In Fig. 1 (right), we plot the function $C(z)$ in the case of a cosmological constant with $\Omega_\Lambda = 0.69$. We see that $C \sim 8$ for $z \sim 2$; so, around this redshift and for $l > k_{\rm fs}\, r(z_m)$, the net effect of neutrino masses on C_l^{GT} changes of sign.

In summary, if z_m is small, the expected effect of neutrino masses on the cross-correlation multipoles C_l^{GT} consists in a step-like suppression at large l's, qualitatively similar to that observed in the galaxy auto-correlation multipoles C_l^{GG}. However the suppression factor is smaller, since the lack of power in the matter power spectrum caused by neutrino free-streaming is balanced by the excess of ISW effect due to the behavior of the linear growth factor in presence of massive neutrinos. When z_m increases, the boost related to the ISW effect is seen more clearly, and ultimately, when z_m is chosen before dark energy domination, the net effect of neutrino masses is to increase C_l^{GT} at large l.

In order to check and quantify these effects, we computed the cross-correlation multipoles C_l^{TG} (and also for comparison the auto-correlation multipoles C_l^{GG}) for two different cosmological models, sharing the same parameters $\Omega_b = 0.053$, $\Omega_m = 0.31$, $\Omega_\Lambda = 0.69$, $h = 0.65$, $A \equiv \ln[10^{10} k^3 \mathcal{R}^2]_{k=0.01/\mathrm{Mpc}} = 3.16$, $n_s = 0.95$, but with two different values of the neutrino density fraction $f_\nu = \Omega_\nu/\Omega_m$, equal to 0 or 0.1 (corresponding to three neutrino species sharing the same mass $m_\nu = 0$ or $m_\nu \simeq 0.41$ eV). We adopted a galaxy selection function of the form

$$\phi_G(z) = \frac{3}{2}\frac{z^2}{z_0^3} \exp\left[-\left(\frac{z}{z_0}\right)^{\frac{3}{2}}\right] , \qquad (11)$$

peaking near the median redshift $z_m \equiv 1.4 z_0$. For illustrative purposes, we choose the four values $z_m = 0.1, 1, 2, 3$, although in practice it would be very challenging to map $\delta_G(\hat{n})$ for $z \geq 2$: presently, available data with a reasonable signal-to-noise ratio range only from $z \sim 0.1$ to $z \sim 1.5$.

In Fig. 2 we plot the ratio of the multipoles C_l^{TG} in the two models, compared with the same ratio for C_l^{GG}. The free-streaming of massive neutrinos is responsible for the step-like suppression of C_l^{GG}, like in the power spectrum $P(k)$. The value of z_m controls the angle under which the free-streaming scale is seen in the map $\delta_G(\hat{n})$, and hence the scale at which the suppression occurs in multipole space. As expected from the previous discussion, the neutrino mass effect on C_l^{TG} is similar to that on C_l^{GG} for small $z_m < 1$, although the suppression factor is slightly smaller, due to the excess of ISW effect in presence of massive neutrinos. For $z_m \geq 1$, the amplification effect due to this excess has a clear and distinct signature at $l \geq 100$, and for $z_m \sim 2$ the ratio displayed in Fig. (2) has a dip around $l \sim 150$. Unfortunatly, we will see in Sec. II C that for $l \geq 100$ this effect is masked by primary CMB anisotropies, which play the role of white noise for the present purpose.

In Fig. 3, we plot directly the mutipoles C_l^{TG} for the same two models. The effect of neutrino masses is clearly visible for all $l > 2$ at $z_m = 0.1$, while for $z_m \geq 1$ it is necessary to reach $l \geq 20$ in order to see a difference (since the maximum free-streaming scale is seen under a smaller angle at higher redshift). Remembering that the effect of neutrino masses on large l's can be split in two contributions, a matter power suppression and an excess of ISW, it is clear from the previous discussion that the latter effect contributes at all redshifts, but its most obvious manifestation is the fact that C_l^{TG} increases with

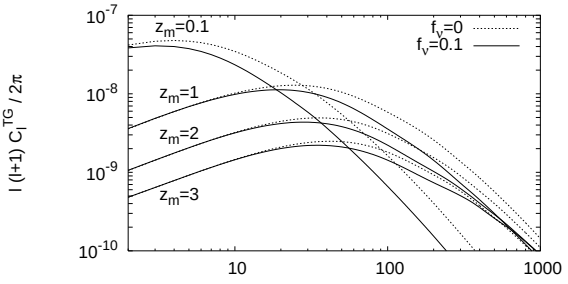

FIG. 3: Dimensionless cross-correlation spectrum in multipole space, $l(l+1)C_l^{TG}/2\pi$, for the same cosmological models as in Fig. 2 (i.e., with three neutrino species sharing the same mass $m_\nu = 0$ or $m_\nu \simeq 0.41$ eV).

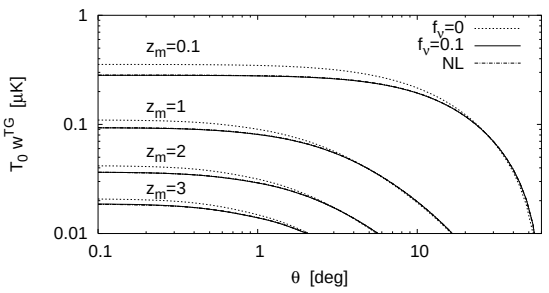

FIG. 4: Angular cross-correlation function, multiplied by the average CMB temperature and displayed in units of micro-Kelvins, for the same cosmological models as in Figs. 2,3. We also plot the same functions including non-linear (NL) corrections to the matter power spectrum: they are indistinguishable from the linear ones.

f_ν for large l's. However, we will see in Sec. II C that only the region with $l \leq 100$ can be probed by observations: then, the neutrino-induced ISW effect is significant, but smaller that the opposite suppression effect.

In Fig. 4, we plot the corresponding angular correlation functions $w^{TG}(\theta)$. In this representation, the fine-structure of the high-l multipole spectrum is by construction averaged out, and it is not possible to see an amplification at high z_m and small θ. The suppression caused by neutrino masses is visible for $z_m = 0.1$ at $\theta \leq 15^o$, and for $z_m \geq 1$ at $\theta \leq 2^o$.

In all these plots, we used only the linear perturbation theory. Doing so, the angular cross-correlation functions depend on the matter power spectrum inside the linear regime. To prove it, we compute again $w^{TG}(\theta)$ from the non-linear power spectrum obtained by applying HALOFIT corrections [46] to the linear one. The result, superimposed in Fig. 4, is indistinguishable from that of linear theory. This shows that non-linear effects on the evolution of matter perturbations has much less impact than that of adding a neutrino mass. This is also true for the multipoles C_l^{TG}, excepted for the smallest redshifts and highest l's (for $z_m = 0.1$, non-linear effects become important for $l > 100$).

C. Detectability

For a set of full-sky CMB and LSS experiments measuring the temperature multipoles a_{lm}^T (resp. galaxy-density multipoles a_{lm}^G) with a noise spectrum N_l^T (resp. N_l^G), the cross-correlation spectrum C_l^{TG} can be reconstructed from the estimator

$$\tilde{C}_l^{TG} = \frac{\sum_{m=-l}^{l} a_{lm}^{T*} a_{lm}^G}{2l+1} \tag{12}$$

with a variance σ_l^{TG} given by

$$(\sigma_l^{TG})^2 = \frac{(C_l^{TG})^2 + (C_l^{TT} + N_l^{TT})(C_l^{GG} + N_l^{GG})}{2l+1} \, . \tag{13}$$

Note that the estimator is not Gaussian, especially for small l's: so, σ_l^{TG} is only an estimate of the true (asymmetric) error bar on the reconstructed power spectrum. If the cross-correlation map can be reconstructed only inside a fraction $f_{\rm sky}$ of the full sky, in first approximation σ_l^{TG} should be multiplied by $f_{\rm sky}^{-1/2}$. The variance is further reduced by $\sqrt{\Delta l}$ in case of data binning with bin width (Δl). Note that in this case the covariance matrix is no longer diagonal, but nevertheless using a diagonal matrix under these approximations has been shown to work well, compared to the exact treatment, if we choose an adequately large binning [47]. In practice, for the multipole range in which we are interested, the CMB noise spectrum N_l^{TT} is much smaller than C_l^{TT} for experiments like WMAP and beyond, and can be safely neglected in the above expression. For a LSS survey consisting in a catalogue of discrete objects (galaxies, clusters, etc.), the noise spectrum is usually dominated by the shot noise contribution $N_l^{GG} \simeq 1/\bar{N}$, where $\bar{N}$ represents the mean number of objects per steradian. The largest ongoing/future surveys (e.g. SDSS) should reach typically the order of 10^8 or even 10^9.

In Fig. 5, we show the typical errorbar that could be expected from a cross-correlation map with coverage $f_{\rm sky} = 0.65$ (corresponding to the usual galactic cut in CMB maps), using an ambitious LSS survey with surface density $\bar{N} = 10^9 {\rm st}^{-1}$ in each redshift bin. We assumed $b(z) \sim 1$ for simplicity. These assumptions correspond essentially to the best measurement that could ever be done, since for such a high surface density the variance of the estimator of a single multipole product $a_{lm}^{T*} a_{lm}^G$ is not affected by instrumental noise, and reduces to

$$\sigma_{lm}^{TG} = C_l^{TG} \sqrt{1 + \frac{C_l^{TT} C_l^{GG}}{(C_l^{TG})^2}} \, . \tag{14}$$

This expression can be interpreted as the product of the cosmic variance term C_l^{TG} times an enhancement factor depending on the correlation coefficient

$(C_l^{TG})^2/(C_l^{TT}C_l^{GG})$. At large l's, the late ISW contribution to the total temperature anisotropy becomes vanishingly small, and the primary anisotropy plays the role of a large noise term, which cannot be removed. In this limit, the correlation coefficient is much smaller than one, and the variance σ_{lm}^{TG} gets correspondingly enhanced. Fig. 5 shows that the spectrum C_l^{TG} can be reconstructed to some extent only in the range $l \leq 100$; beyond, one could only derive upper bounds. Note that the errorbar for each bin is roughly of the same order of magnitude as the effect of neutrino masses when f_ν varies from 0 to 0.1. In Fig. 5, we also show the error degradation when $f_{\rm sky}$ is reduced to 0.25 and $\bar{N}$ to $7\times10^8{\rm st}^{-1}$ in each redshift bin. Finally, in Fig. 6, we plot the corresponding error bars for $w^{TG}(\theta)$. Note that the synthetic error bars for $w^{TG}(\theta)$ are correlated with each other, unlike those for C_l^{TG}. On small angular scales $\theta \leq 1$ (where the effect of neutrino masses is maximal) the 1σ error on $w^{TG}(\theta)$ is of the order of 25%.

We conclude from these estimates that the temperature-galaxy correlation power spectrum C_l^{TG} is potentially sensitive to the neutrino mass in the observable range $10 < l < 100$, as well as the angular correlation function $w^{TG}(\theta)$ for $\theta < 5^o$ at $z = 0.5$ or $\theta < 3^o$ at $z = 1$. Unfortunately, the enhancement of the ISW effect due to the impact of massive neutrinos on the linear growth factor is not directly visible: it would require precise data at high l and high redshift, for which the late ISW effect is masked by primordial anisotropies. The net effect of massive neutrinos on the observable part of C_l^{TG} and on $w^{TG}(\theta)$ is a suppression, caused by the usual free-streaming effect. However this effect is non-trivial in the sense that C_l^{GG} and C_l^{TG} depend on f_ν through different relations, due to the fact that the ISW term involves a time-derivative of the gravitational potential while the galaxy overdensity does not. Hence, the galaxy-temperature correlation spectrum can bring some information on neutrino masses which is not already contained in the sole galaxy auto-correlation spectrum. In the next section, we will quantify this statement by performing a parameter extraction from mock data accounting for future experiments.

III. AN MCMC ANALYSIS OF MOCK DATA

For a given data set consisting in various maps (i.e. multipoles a_{lm}^X) covering a fraction $f_{\rm sky}$ of the full sky and assumed to obey Gaussian statistics, the likelihood function $\mathcal{L}$ is often approximated as

$$\mathcal{L} \propto \Pi_l \left\{ (\det C_l^{\rm th})^{-1/2} \exp\left[-\frac{1}{2} {\rm Trace}\, C_l^{\rm obs} {C_l^{\rm th}}^{-1} \right] \right\}^{(2l+1)f_{\rm sky}} \quad (15)$$

where $C_l^{\rm obs}$ is the data covariance matrix defined by $[C_l^{\rm obs}]_{XY} = \langle a_{lm}^X a_{lm}^Y \rangle$, and $C_l^{\rm th}$ the assumed theoretical covariance matrix for a given fit, which contains the sum of each theoretical power spectrum $C_l^{XY\,\rm th}$ and of the instrumental noise power spectra N_l^{XY}, estimated by modeling the experiment. Of course, the data covariance matrix reconstructed from the observed maps is also composed of signal and noise contributions. Simulating a future experimental data set amounts in computing the noise spectra N_l^{XY}, given some instrumental specifications, and generating randomly some observed spectra $C_l^{XY\rm obs}$, given the theoretical spectra $C_l^{XY\rm fid}$ of the assumed fiducial model and the noise spectra N_l^{XY}. However, for the purpose of error forecast, it is sufficient to replace simply $C_l^{XY\rm obs}$ by the sum $C_l^{XY\rm fid} + N_l^{XY}$: this just amounts in averaging over many possible mock data sets for the same model, and does not change the reconstructed error on model parameters [48].

For instance, if one wants to estimate future errors for a CMB experiment, the maps to consider are temperature and E-polarization: $X \in \{T, E\}$ (here, for simplicity, we consider models with no gravitational waves and discard B-polarization). The covariance matrices then read

$$C_l^{\rm obs} = \begin{pmatrix} C_l^{TT\rm fid} + N_l^{TT} & C_l^{TE\rm fid} \\ C_l^{TE\rm fid} & C_l^{EE\rm fid} + N_l^{EE} \end{pmatrix}, \quad (16)$$

$$C_l^{\rm th} = \begin{pmatrix} C_l^{TT\rm th} + N_l^{TT} & C_l^{TE\rm th} \\ C_l^{TE\rm th} & C_l^{EE\rm th} + N_l^{EE} \end{pmatrix}. \quad (17)$$

Should one consider the combination of CMB data with a future galaxy redshift survey decomposed in N maps associated to N redshift bins, the matrices would become $2+N$ dimensional, with an extra block

$$[C_l]_{2+i,2+j} = C_l^{G_iG_j} + \delta_{ij} N_l^{G_iG_i}, \quad i = 1, ..., N, \quad (18)$$

as well as non-diagonal coefficients $[C_l]_{1,2+i} = C_l^{TG_i}$ accounting for the late ISW effect. Note that all non-diagonal coefficients have no noise term, since the noise contributions in two different maps are expected to be statistically uncorrelated at least at first order.

Finally, the option which is most interesting in our context, is to assume that the galaxy density auto-correlation maps are not known (or just not considered, because they could be plagued by some systematic effects), and that CMB data are only combined with the cross-correlation data, i.e. with N observed power spectra spectra $C_l^{TG_i\rm obs}$. This is exactly what is being done in the current literature, in which authors try to get some new independent bounds on Ω_Λ from CMB plus CMB-LSS cross-correlation data, without employing LSS auto-correlation maps. In the approximation of Gaussian-distributed $C_l^{TG_i}$ with central value $C_l^{TG_i\rm th}$ and covariance given by

$$[{\rm Cov}_l]_{ij} \equiv \left\langle \left(C_l^{TG_i} - \langle C_l^{TG_i} \rangle \right) \left(C_l^{TG_j} - \langle C_l^{TG_j} \rangle \right) \right\rangle$$
$$= \frac{C_l^{TG_i\rm th} C_l^{TG_j\rm th} + (C_l^{TT\rm th} + N_l^{TT})(C_l^{G_iG_j\rm th} + \delta_{ij} N_l^{G_iG_i})}{(2l+1) f_{\rm sky}}, \quad (19)$$

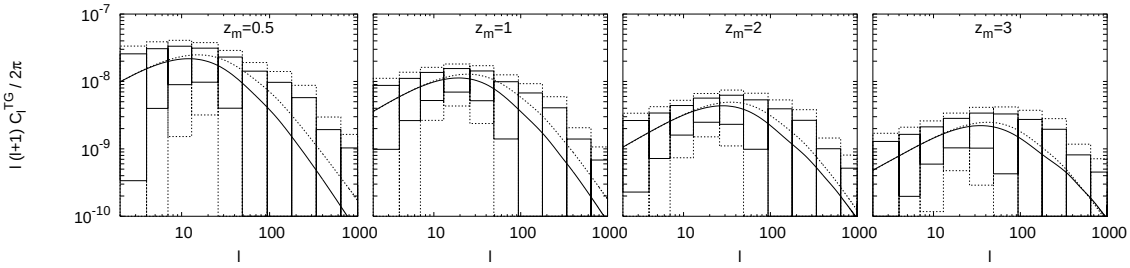

FIG. 5: 68% error forecast on the power spectrum C_l^{TG}, which is displayed for the same two cosmological models as in Figures 2, 3 (with $f_\nu = 0$ or 0.1). The smallest error boxes assumes a LSS survey with sky coverage $f_{\rm sky} = 0.65$ and surface density $\bar{N} = 10^9 {\rm st}^{-1}$ in each redshift bin. The binning in multipole space can be read from the width of each box. The largest error boxes correspond to $f_{\rm sky} 0.25$ and $\bar{N} = 7 \times 10^8 {\rm st}^{-1}$.

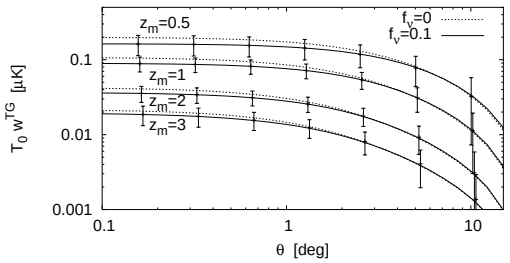

FIG. 6: 68% error forecast on the angular correlation function w^{TG}, which is displayed for the same two cosmological models as in Figures 2, 3 (with $f_\nu = 0$ or 0.1). The error bars assume a LSS survey with sky coverage $f_{\rm sky} = 0.65$ and surface density $\bar{N} = 10^9 {\rm st}^{-1}$ in each redshift bin. The spacing between each error bar reflects the binning width chosen in angular space.

the likelihood of the cross-correlation data reads

$$\mathcal{L} \propto \Pi_l \left(\det {\rm Cov}_l\right)^{-1/2} \exp\left[-\frac{1}{2}\sum_{ij} \Delta_l^i \left[{\rm Cov}_l\right]_{ij}^{-1} \Delta_l^j\right] \tag{20}$$

with $\Delta_l^i \equiv C_l^{TG_i {\rm obs}} - C_l^{TG_i {\rm th}}$. The total likelihood is then the product of the CMB and cross-correlation likelihoods.

In this section, we will focus on three ambitious future experiments: the Planck satellite, to be launched in 2008, which is expected to make the ultimate measurement of CMB temperature anisotropies, dominated by cosmic variance rather than noise up to very high l; the Dark Energy Survey (DES); and the Large Synoptic Survey Telescope (LSST), designed primarily for a tomographic study of cosmic shear, which would provide as a byproduct a very deep and wide galaxy redshift survey (close to ideal for the purpose of measuring the CMB-LSS cross-correlation since $N_l^{G_iG_i} < C_l^{G_iG_i}$ at least for multipoles $l < 100$). For Planck, we computed the noise-noise spectra, N_l^{TT} and N_l^{EE}, like in Ref. [49], with nine frequency channels. For the DES-like survey, we followed Ref. [50] and assumed a total number of galaxies of 250 million in a 5000 square degree area on the sky (or $f_{\rm sky} = 0.13$), with an approximate 1-σ error of 0.1 in photometric redshifts, divided in four redhsift bins with mean redshifts $z_i \in \{0.3, 0.6, 1, 1.3\}$, with the same selection functions as in Ref. [50]. For LSST, we used the same modeling as in [51], with a net galaxy angular number density of 80 per square arcminute and a coverage of $f_{\rm sky} = 0.65$. The galaxies are divided into six redshift bins with mean redshifts $z_i \in \{0.49, 1.14, 1.93, 2.74, 3.54, 4.35\}$. For each bin the selection function, estimated bias b_i and galaxy density n_i are provided in [51] (Fig. 2, Eq. (16) and Table I). The noise spectra $N_l^{G_iG_i}$ are then simply given by $1/n_i$.

We used the public code COSMOMC [52] to do a Monte-Carlo Markov Chain (MCMC) analysis, fitting the theoretical galaxy-temperature correlation to the mock data. For this purpose, we have written a module which computes the correlation multipoles following Eq. (4) and the likelihood of the mock data given each model as described above.

We then ran our modified version of CosmoMC for a model with eight parameters: the usual six of minimal ΛCDM (baryon density $\Omega_b h^2$, dark matter density $\Omega_{dm} h^2$, angular diameter of the sound horizon at last scattering θ, optical depth to reionization τ, primordial spectral index n_s, primordial amplitude $\log[10^{10} A_s]$) plus the total neutrino mass m_ν and the equation-of-state parameter w. Our fiducial model was close to the WMAP best-fitting model with $m_\nu = 0$ and $w = -1$. We considered three possible combinations of data: Planck alone, Planck plus its cross-correlation with DES or LSST (but no information on galaxy auto-correlations), and finally Planck plus LSST, using all information and including the correlation. The probability of each parameter is displayed in Fig. 7 for each of these four cases called respectively CMB (Planck), CMB+GT (Planck+DES or Planck+LSST) and CMB+GT+GG (Planck+LSST).

Obviously the combination CMB+GT+GG does a much better job than CMB+GT for constraining all parameters (and most spectacularly w and m_ν). This is

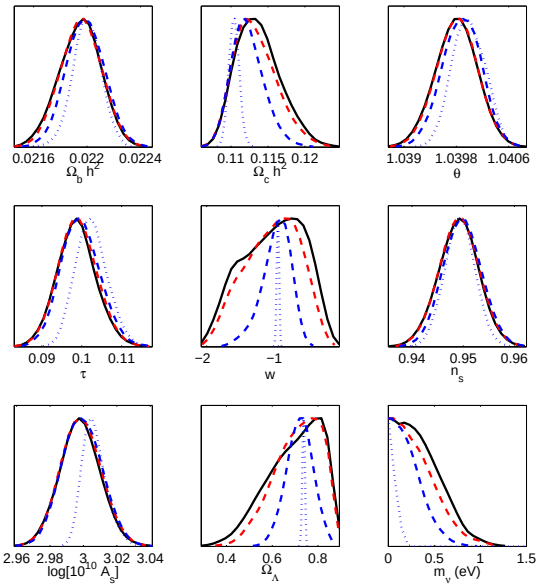

FIG. 7: Marginalized probability of cosmological parameters obtained by fitting some mock data mimicking the properties of Planck, DES and LSST. The solid black curves accounts for CMB only, the red dashed for CMB+GT with Planck+DES, the blue dashed for CMB+GT with Planck+LSST, and the dotted blue for CMB+GT+GG with Planck+LSST (these combinations are precisely defined in the text). In each of these cases the cosmological model consists in ΛCDM (six parameter) plus an arbitrary total neutrino mass m_ν and equation-of-state parameter w. So, only eight of the above nine parameters are independent (as a consequence the prior for Ω_Λ is non-flat). The mock data is based on a fiducial model with $m_\nu = 0$ and $w = -1$.

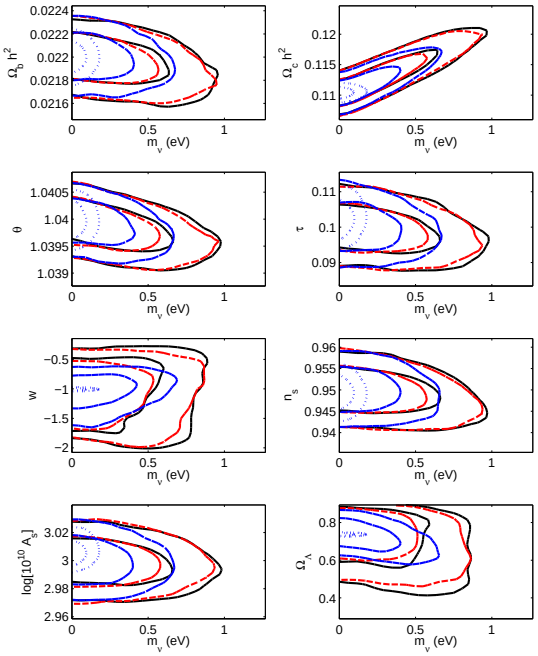

FIG. 8: Two-dimensional marginalized likelihood contours involving m_ν obtained by fitting some mock data mimicking the properties of Planck, DES and LSST. The solid black curves accounts for CMB only, the red dashed for CMB+GT with Planck+DES, the blue dashed for CMB+GT with Planck+LSST, and the dotted blue for CMB+GT+GG with Planck+LSST (these combinations are precisely defined in the text). For each case, the two lines represent the 68% and 95% confidence levels.

mainly due to the fact that the GT cross-correlation is partly screened by primary temperature anisotropies, while the GG signal does not have such an intrinsic noise contribution. We even try to repeat the CMB+GT+GG analysis with all $C_l^{GT_i}$ correlations set to zero, and found no noticeable difference, showing that most sensitivity comes from GG rather than GT terms. However, the comparison between CMB alone and CMB+GT is still interesting *per se*. In fact, we are dealing here with an idealized situation, but in the future the GG auto-correlation signal could appear to be plagued by various systematic effects. In this case, independent information coming from the cross-correlation signal alone might be a useful piece of evidence in favor of the preferred model. Also, if the galaxy bias turns out to be very difficult to estimate with high enough accuracy, one may adopt the point of view of using the GG signal to measure bias, and the CMB+GT signal to estimate the best-fit parameters in some iterative scheme.

In this prospective, it is interesting to note that the CMB+GT combination from Planck and LSST increases significantly the sensitivity of Planck alone mainly for $\Omega_{dm}h^2$ (by 30%), w (by 83%) and m_ν (by 38%). As a consequence, the sensitivity to the related parameter Ω_Λ increases by 76%. For our fiducial model with $m_\nu = 0$, the 95% confidence level upper bound on the total neutrino mass shrinks from 0.77 eV to 0.54 eV (for another fiducial model with $m_\nu > 0$ the sensitivity can only be larger than that, see e.g. [39]). At this level of sensitivity, the parameter m_ν is not correlated with Ω_Λ or w, as can be checked by looking at two-dimensional marginalized likelihood contours in Figure 8. We conclude that the cross-correlation signal derived from Planck and LSST would have some useful sensitivity to both neutrino masses and dark energy parameters. Instead, the correlation between Planck and DES does not bring significant new information with respect to Planck alone.

Ichikawa and Takahashi [44] performed a similar forecast for Planck and LSST (with slightly different specifications), using a Fisher matrix analysis rather than MCMC approach. They find a smaller sensitivity of the cross-correlation data to neutrino mass than we do, possibly because of the various approximations entering into the Fisher matrix approach.

IV. CONCLUSIONS

We have studied here the possibility to use the cross-correlation between CMB and galaxy density maps as a tool for constraining the neutrino mass. On one hand massive neutrinos reduce the cross-correlation spectrum because their free-streaming slows down structure formation; on the other hand, they enhance it because of the behavior of the linear growth in presence of massive neutrinos. Using both analytic approximations and numerical computations, we showed that in the observable range of scales and redshifts, the first effect dominates, but the second one is not negligible. Hence the cross-correlation between CMB and LSS maps could bring some independent information on neutrino masses. We performed an error forecast analysis by fitting some mock data inspired from the Planck satellite, Dark Energy Survey (DES) and Large Synoptic Survey Telescope (LSST). For Planck and LSST, the inclusion of the cross-correlation data increases the sensitivity to m_ν by 38%, w by 83% and $\Omega_{dm}h^2$ by 30% with respect to the CMB data alone. With the fiducial model employed in this analysis (based on eight free parameters) the standard deviation for the neutrino mass is equal to 0.38 eV for Planck alone and 0.27 eV for Planck plus cross-correlation data. This is far from being as spectacular as the sensitivity expected from the measurement of the auto-correlation power spectrum of future galaxy/cluster redshift surveys or cosmic shear experiments, for which the predicted standard deviation is closer to the level of 0.02 eV, leading to a 2σ detection even in the case of the minimal mass scenario allowed by current data on neutrino oscillations (see [38] for a review). However, the method proposed here is independent and affected by different systematics. So, it remains potentially interesting, but only if the neutrino mass is not much smaller than $m_\nu \sim 0.2$ eV.

Acknowledgements

This work was initiated during a very nice and fruitful stay at the Galileo Galilei Institute for Theoretical Physics, supported by INFN. JL would like to thank Ofer Lohav for useful exchanges. The project was completed thanks to the support of the EU 6th Framework Marie Curie Research and Training network "UniverseNet" (MRTN-CT-2006-035863). Numerical simulations were performed on the MUST cluster at LAPP Annecy (IN2P3/CNRS and Université de Savoie). EG acknowledges the support from Spanish Ministerio de Ciencia y Tecnologia (MEC), project AYA2006-06341 with EC-FEDER funding and research project 2005SGR00728 from Generalitat de Catalunya.

Appendix: the Limber approximation

Let us consider some maps $X(\hat{n})$ expanded in spherical harmonics

$$X\left(\hat{n}\right) = \sum_{l=0}^{\infty} \sum_{-l}^{l} a_{lm}^{X} Y_{lm}(\hat{n}) \tag{21}$$

with

$$a_{lm}^{X} = \int d^2n\, Y_{lm}^{*}(\hat{n}) X(\hat{n}). \tag{22}$$

The two-point correlation function of any two statistically isotropic quantities X and Y can be expressed in terms of the power spectrum in multipole space

$$C_l^{XY} = \left\langle a_{lm}^{X} a_{lm}^{Y*} \right\rangle, \tag{23}$$

or in therms of the angular correlation function in a Legendre polynomial basis (p_l)

$$w^{XY}(\theta) = \sum_l \frac{2l+1}{4\pi} p_l(\cos\theta) C_l^{XY}. \tag{24}$$

In the frame of observations, a direction dependent quantity $X(\hat{n})$ is usually a quantity integrated over the line of sight, $X(\hat{n}) = \int dr\, X(\vec{x})$. The expression for a_{lm}^X, (22), can then easily be transformed to Fourier space. Subsequently expanding the plain wave in spherical harmonics and applying the completeness relation for spherical harmonics, one arrives at

$$a_{lm}^{X} = (-i)^l \int dr\, \frac{d^3k}{2\pi^2} X(\vec{k}) j_l(kr) Y_{lm}^{*}(\hat{k}), \tag{25}$$

where $X(\vec{k})$ is the Fourier transform of $X(\vec{x})$, $j_l(r)$ is the spherical Bessel function, and $k = |\vec{k}|$. This expression can be simplified using Limbers approximation, $\int dx\, f(x) j_l(x) \simeq \sqrt{\frac{\pi}{2l+1}} \int dx\, f(x) \delta(l + \frac{1}{2} - x)$, leading to

$$a_{lm}^{X} \simeq (-i)^l \sqrt{\frac{\pi}{2l+1}} \int \frac{dr}{r} \frac{k^2 d\Omega_k}{2\pi^2} X\left(\hat{k}, k\right) Y_{lm}^{*}(\hat{k}), \tag{26}$$

separating the $\vec{k}$ dependence of X in $\hat{k}$ and $k = \frac{l+\frac{1}{2}}{r}$.

[1] R. K. Sachs and A. M. Wolfe, Astrophys. J. **147**, 73 (1967).
[2] R. G. Crittenden and N. Turok, Phys. Rev. Lett. **76**, 575 (1996), astro-ph/9510072.
[3] S. Perlmutter et al. (Supernova Cosmology Project), Astrophys. J. **517**, 565 (1999), astro-ph/9812133.
[4] A. G. Riess et al. (Supernova Search Team), Astron. J. **116**, 1009 (1998), astro-ph/9805201.
[5] D. N. Spergel et al. (WMAP), Astrophys. J. Suppl. **148**, 175 (2003), astro-ph/0302209.

[6] D. N. Spergel et al. (WMAP) (2006), astro-ph/0603449.
[7] P. Fosalba, E. Gaztanaga, and F. Castander, ApJ **350**, L37 (2003), astro-ph/0305468.
[8] S. Boughn and R. Crittenden, Nature **427**, 45 (2004), astro-ph/0305001.
[9] P. Fosalba and E. Gaztanaga, Mon. Not. Roy. Astron. Soc. **350**, L37 (2004), astro-ph/0305468.
[10] N. Afshordi, Y.-S. Loh, and M. A. Strauss, Phys. Rev. **D69**, 083524 (2004), astro-ph/0308260.
[11] N. Padmanabhan, C. M. Hirata, U. Seljak, D. J. Schlegel, J. Brinkmann, and D. P. Schneider, Phys. Rev. D **72**, 043525 (2005), arXiv:astro-ph/0410360.
[12] A. Cabre, E. Gaztanaga, M. Manera, P. Fosalba, and F. Castander, Mon. Not. Roy. Astron. Soc. Lett. **372**, L23 (2006), astro-ph/0603690.
[13] A. Cabre, E. Gaztanaga, M. Manera, P. Fosalba, and F. Castander (2006), astro-ph/0611046.
[14] T. Giannantonio et al., Phys. Rev. **D74**, 063520 (2006), astro-ph/0607572.
[15] J. D. McEwen, P. Vielva, M. P. Hobson, E. Martínez-González, and A. N. Lasenby, Mon. Not. Roy. Astron. Soc. Lett. **376**, 1211 (2007), arXiv:astro-ph/0602398.
[16] N. Puchades, M. J. Fullana, J. V. Arnau, and D. Saez, Mon. Not. Roy. Astron. Soc. **370**, 1849 (2006), astro-ph/0605704.
[17] U. Seljak and M. Zaldarriaga, Astrophys. J. **538**, 57 (2000), arXiv:astro-ph/9907254.
[18] R. A. Sunyaev and Y. B. Zeldovich, Nature (London) **223**, 721 (1969).
[19] N. Afshordi, Y.-T. Lin, D. Nagai, and A. J. R. Sanderson, Mon. Not. Roy. Astron. Soc. **378**, 293 (2007), arXiv:astro-ph/0612700.
[20] J. R. Primack, SLAC Beam Line **31N3**, 50 (2001), astro-ph/0112336.
[21] M. Maltoni, T. Schwetz, M. A. Tortola, and J. W. F. Valle, New J. Phys. **6**, 122 (2004), hep-ph/0405172.
[22] G. L. Fogli, E. Lisi, A. Marrone, and A. Palazzo, Prog. Part. Nucl. Phys. **57**, 742 (2006), hep-ph/0506083.
[23] A. Cuoco et al., Int. J. Mod. Phys. **A19**, 4431 (2004), astro-ph/0307213.
[24] G. Steigman, Int. J. Mod. Phys. **E15**, 1 (2006), astro-ph/0511534.
[25] G. Mangano, A. Melchiorri, O. Mena, G. Miele, and A. Slosar, JCAP **0703**, 006 (2007), astro-ph/0612150.
[26] P. Crotty, J. Lesgourgues, and S. Pastor, Phys. Rev. **D67**, 123005 (2003), astro-ph/0302337.
[27] E. Pierpaoli, Mon. Not. Roy. Astron. Soc. **342**, L63 (2003), astro-ph/0302465.
[28] V. Barger, J. P. Kneller, H.-S. Lee, D. Marfatia, and G. Steigman, Phys. Lett. **B566**, 8 (2003), hep-ph/0305075.
[29] R. Trotta and A. Melchiorri, Phys. Rev. Lett. **95**, 011305 (2005), astro-ph/0412066.
[30] S. Hannestad, JCAP **0601**, 001 (2006), astro-ph/0510582.
[31] S. Hannestad and G. G. Raffelt, JCAP **0611**, 016 (2006), astro-ph/0607101.
[32] K. Ichikawa, M. Kawasaki, and F. Takahashi, JCAP **0705**, 007 (2007), astro-ph/0611784.
[33] F. de Bernardis, A. Melchiorri, L. Verde, and R. Jimenez (2007), arXiv:0707.4170 [astro-ph].
[34] J. Hamann, S. Hannestad, G. G. Raffelt, and Y. Y. Y. Wong, JCAP **0708**, 021 (2007), arXiv:0705.0440 [astro-ph].
[35] J. R. Bond, G. Efstathiou, and J. Silk, Phys. Rev. Lett. **45**, 1980 (1980).
[36] S. Hannestad (2007), arXiv:0710.1952 [hep-ph].
[37] S. Hannestad, Ann. Rev. Nucl. Part. Sci. **56**, 137 (2006), hep-ph/0602058.
[38] J. Lesgourgues and S. Pastor, Phys. Rept. **429**, 307 (2006), astro-ph/0603494.
[39] J. Lesgourgues, S. Pastor, and L. Perotto, Phys. Rev. **D70**, 045016 (2004), hep-ph/0403296.
[40] S. Wang, Z. Haiman, W. Hu, J. Khoury, and M. May, Phys. Rev. Lett. **95**, 011302 (2005), astro-ph/0505390.
[41] S. Hannestad and Y. Y. Y. Wong, JCAP **0707**, 004 (2007), astro-ph/0703031.
[42] Y.-S. Song and L. Knox (2003), astro-ph/0312175.
[43] S. Hannestad, H. Tu, and Y. Y. Y. Wong, JCAP **0606**, 025 (2006), astro-ph/0603019.
[44] K. Ichikawa and T. Takahashi (2005), astro-ph/0510849.
[45] A. Kiakotou, O. Elgaroy, and O. Lahav (2007), arXiv:0709.0253 [astro-ph].
[46] R. E. Smith et al. (The Virgo Consortium), Mon. Not. Roy. Astron. Soc. **341**, 1311 (2003), astro-ph/0207664.
[47] A. Cabre, P. Fosalba, E. Gaztanaga, and M. Manera, ArXiv Astrophysics e-prints (2007), astro-ph/0701393.
[48] L. Perotto, J. Lesgourgues, S. Hannestad, H. Tu, and Y. Y. Y. Wong, JCAP **0610**, 013 (2006), astro-ph/0606227.
[49] J. Lesgourgues, L. Perotto, S. Pastor, and M. Piat, Phys. Rev. **D73**, 045021 (2006), astro-ph/0511735.
[50] L. Pogosian, P. S. Corasaniti, C. Stephan-Otto, R. Crittenden, and R. Nichol, Phys. Rev. **D72**, 103519 (2005), astro-ph/0506396.
[51] M. LoVerde, L. Hui, and E. Gaztanaga, Phys. Rev. **D75**, 043519 (2007), astro-ph/0611539.
[52] A. Lewis and S. Bridle, Phys. Rev. **D66**, 103511 (2002), astro-ph/0205436.
[53] M. Doran and G. Robbers, JCAP **0606**, 026 (2006), astro-ph/0601544.
[54] M. Doran, G. Robbers, and C. Wetterich, Phys. Rev. **D75**, 023003 (2007), astro-ph/0609814.
[55] in the case of "early Dark Energy" models, this statement can only be marginally true (see e.g. in [53, 54])

4.4 Euclid satellite and non-linear corrections, JCAP 1301, 026 (2013)

Preprint typeset in JHEP style - HYPER VERSION CERN-PH-TH/2012-261, LAPTH-046/12

Neutrino masses and cosmological parameters from a Euclid-like survey: Markov Chain Monte Carlo forecasts including theoretical errors

Benjamin Audren[a], **Julien Lesgourgues**[a,b,c], **Simeon Bird**[d], **Martin G. Haehnelt**[e], **Matteo Viel**[f,g]

[a] *Institut de Théorie des Phénomènes Physiques, École PolytechniqueFédérale de Lausanne, CH-1015, Lausanne,Switzerland.*

[b] *CERN, Theory Division, CH-1211 Geneva 23, Switzerland.*

[c] *LAPTh (CNRS - Université de Savoie), BP 110, F-74941 Annecy-le-Vieux Cedex, France.*

[d] *Institute for Advanced Study, 1 Einstein Drive, Princeton, NJ, 08540, USA.*

[e] *Kavli Institute for Cosmology and Institute of Astronomy, Madingley Road, Cambridge, CB3 0HA, UK.*

[f] *INAF/Osservatorio Astronomico di Trieste, Via Tiepolo 11, 34143, Trieste, Italy.*

[g] *INFN-National Institute for Nuclear Physics Via Valerio 2, 34127, Trieste, Italy.*

Abstract: We present forecasts for the accuracy of determining the parameters of a minimal cosmological model and the total neutrino mass based on combined mock data for a future *Euclid*-like galaxy survey and *Planck*. We consider two different galaxy surveys: a spectroscopic redshift survey and a cosmic shear survey. We make use of the Monte Carlo Markov Chains (MCMC) technique and assume two sets of theoretical errors. The first error is meant to account for uncertainties in the modelling of the effect of neutrinos on the non-linear galaxy power spectrum and we assume this error to be fully correlated in Fourier space. The second error is meant to parametrize the overall residual uncertainties in modelling the non-linear galaxy power spectrum at small scales, and is conservatively assumed to be uncorrelated and to increase with the ratio of a given scale to the scale of non-linearity. It hence increases with wavenumber and decreases with redshift. With these two assumptions for the errors and assuming further conservatively that the uncorrelated error rises above 2% at $k = 0.4\,h/\mathrm{Mpc}$ and $z = 0.5$, we find that a future *Euclid*-like cosmic shear/galaxy survey achieves a 1-σ error on M_ν close to 32 meV/25 meV, sufficient for detecting the total neutrino mass with good significance. If the residual uncorrelated errors indeed rises rapidly towards smaller scales in the non-linear regime as we have assumed here then the data on non-linear scales does not increase the sensitivity to the total neutrino mass. Assuming instead a ten times smaller theoretical error with the same scale dependence, the error on the total neutrino mass decreases moderately from $\sigma(M_\nu) = 18$ meV to 14 meV when mildly non-linear scales with $0.1\,h/\mathrm{Mpc} < k < 0.6\,h/\mathrm{Mpc}$ are included in the analysis of the galaxy survey data.

Contents

1. Motivations

Several ambitious ground-based and space-based galaxy surveys have been planned for the next decade (e.g. SKA[1], LSST[2]), or are about to take place (e.g. DES[3]). One of the most ambitious approved missions, the *Euclid*[4] satellite [1], is expected to be launched by ESA in 2019. It will combine a galaxy redshift survey with weak lensing observations, measuring the matter power spectrum and the growth of structure with unprecedented accuracy. This will offer a unique opportunity to improve measurements of cosmological parameters, including the neutrino mass, known to slow down structure formation on intermediate and small scales[2], as well as constraints on dark energy and modified gravity models.

Recent constraints on the total neutrino mass appear to have converged on an upper limit of about 0.3 eV at the 95% confidence level (e.g. [3, 4, 5, 6, 7, 8, 9]), with the

[1] http://www.skatelescope.org/
[2] http://www.lsst.org/lsst/
[3] http://www.darkenergysurvey.org/
[4] http://www.euclid-ec.org

notable exception of Lyman$-\alpha$ forest data, which gives an even lower bound of 0.17eV [10]. These constraints rely on a combination of data from Cosmic Microwave Background (CMB) experiments such as WMAP, Baryonic Acoustic Oscillations (BAOs), SuperNovae (SN) distance moduli, galaxy clustering and cosmic shear (especially from the SDSS[5] and CFHTLS[6] surveys). Data sets provided by Large Scale Structure (LSS) are particularly important, since they are able to probe scales and redshifts affected by neutrino free streaming both in the linear and non-linear regimes. Neutrino oscillation experiments provide a lower bound of 0.05eV on the total neutrino mass, meaning that the allowed range is now significantly squeezed by cosmological data, and well within reach of future planned surveys.

Several forecasts have already been published on the sensitivity of *Euclid* to cosmological parameters, with a focus on dark energy, modified gravity, the neutrino mass, or other extensions of the minimal ΛCDM model (see e.g. [11, 12, 13, 14, 15, 16, 17, 18, 19]). However reliable forecasts are difficult to obtain; interpreting *Euclid* data on small (non-linear) scales will require a more accurate modeling of systematic effects than is currently achievable. This is true for both non-linear corrections to the matter power spectrum, and for effects specific to each survey. In the case of the galaxy redshift survey, for instance, redshift space distortions and scale-dependent bias. In the case of the cosmic shear survey, noise bias in shape measurements [20]. Some authors have pointed out that without considerable progress in modeling these effects, the sensitivity to cosmological parameters might degrade considerably (see e.g. [18]).

Current forecasts tend either to incorporate only linear scales and neglect these systematics, or to include a small range of mildly non-linear scales and model systematics by including nuisance parameters which are then marginalized over. Introducing such nuisance parameters (for instance, in order to describe redshift-space distortions) still assumes that we can predict the shape of these effects, and reduce them to a simple family of curves. Hence, this approach is not the most conservative.

On top of this, many forecasts are affected by a methodology issue: apart from two recent works [19, 21], they are based on a Fisher matrix technique, whose results depend on the step chosen in the calculation of numerical derivatives of the spectrum with respect to the parameters (see e.g. [21, 22]).

The present forecast has three objectives:

- First, we wish to use a reliable forecast method for the sensitivity of a *Euclid*-like survey to ΛCDM parameters and to the total neutrino mass, based not on Fisher matrices, but on a parameter extraction from mock data with Markov Chain Monte Carlo (MCMC). This goal has also been achieved very recently by [19], although with a different approach for modeling the galaxy redshift survey. To our knowledge, the present analysis is the first MCMC forecast of a *Euclid*-like galaxy redshift survey using as an observable the power spectrum $P(k)$ in wavenumber space.

[5] http://www.sdss.org/

[6] http://www.cfht.hawaii.edu/Science/CFHLS/

- Second, we wish to incorporate non-linear corrections using the most accurate available fitting formula accounting for neutrino mass effects, namely the version of HALOFIT [23] presented in Ref. [24]. This formula has been obtained by fitting to a suite of N-body simulations which incorporate neutrinos as free-streaming dark matter particles, using the code first presented in Ref. [25]. The error in this formula specific to the neutrino mass was estimated by Ref. [24] to be Gaussian, with squared variance

$$\alpha(k,z) \equiv \frac{\Delta P(k,z)}{P(k,z)} = \frac{\ln[1+k/k_\sigma(z)]}{1+\ln[1+k/k_\sigma(z)]}\, f_\nu \ , \tag{1.1}$$

  where $f_\nu = \omega_\nu/\omega_m$ and $k_\sigma(z)$ is the non-linear wavenumber as defined and computed in HALOFIT. We include this in the likelihood as a fully correlated error, as described in detail in Appendix A, associated to a unique nuisance parameter.

- In order to obtain conservative results while keeping the analysis simple, we will combine this correlated error with a second uncorrelated error. This second uncorrelated error is assumed to account for extra uncertainties in our approximate modeling of non-linear corrections, redshift space distortions, scale-dependent bias and other systematic effects. By assuming an uncorrelated error on each data point, we remain more conservative than if we marginalized over a small set of nuisance parameters representing several types of fully correlated errors. Throughout this work, we assumed for convenience that the relative theoretical error on the power spectrum was given by Eq. (1.1), with f_ν replaced by a constant factor, by default 0.05. This error grows smoothly from zero on linear scales up to 5% on deeply non-linear scales. For a concordance cosmology and at redshift $z = 0.5$, it reaches 1% near $k = 0.1\,h\mathrm{Mpc}^{-1}$ and 2.3% around $k = 0.6\,h\mathrm{Mpc}^{-1}$. We assume that ten years from now, this will provide a reasonable description of the total uncertainty coming from all systematic effects in each of the two surveys. Occasionally, we will consider the effect of dividing the magnitude of the error by two or ten, to evaluate the effect of better control of non-linear systematics. We emphasise that the exact form of the uncorrelated error is obviously just an educated guess and that a different k-dependence will *e.g.* influence the assessment of how useful pushing to smaller scales will be. Of course, introducing a fully uncorrelated error (or alternatively, form filling functions as in [26]) is very conservative in that it assumes that no modeling of systematics is accurate enough. In several years from now, it might become realistic to model most systematics with several types of correlated errors, and to reduce the residual uncorrelated theoretical error to a smaller level than assumed in this work.

2. Galaxy redshift survey

Throughout this paper, our fiducial model is chosen to be a flat ΛCDM model with three degenerate massive neutrino species. The fiducial parameter values are taken to be $\omega_b = 0.02258$, $\omega_c = 0.1109$, $A_s = 2.43 \times 10^{-9}$ (pivot scale $k_* = 0.05\,h\mathrm{Mpc}^{-1}$), $n_s = 0.963$, $h = 0.710$, $z_{\mathrm{reio}} = 10.3$, $m_\nu = 0.07$ eV (so $M_\nu = 0.21$ eV). For the power spectrum of the mock data, we could take directly the fiducial power spectrum, or generate a random

spectrum realization corresponding to the same model. As illustrated in [22], the two options lead to the same forecast errors, so for simplicity we assume an observed power spectrum equal to the theoretical power spectrum of the fiducial model.

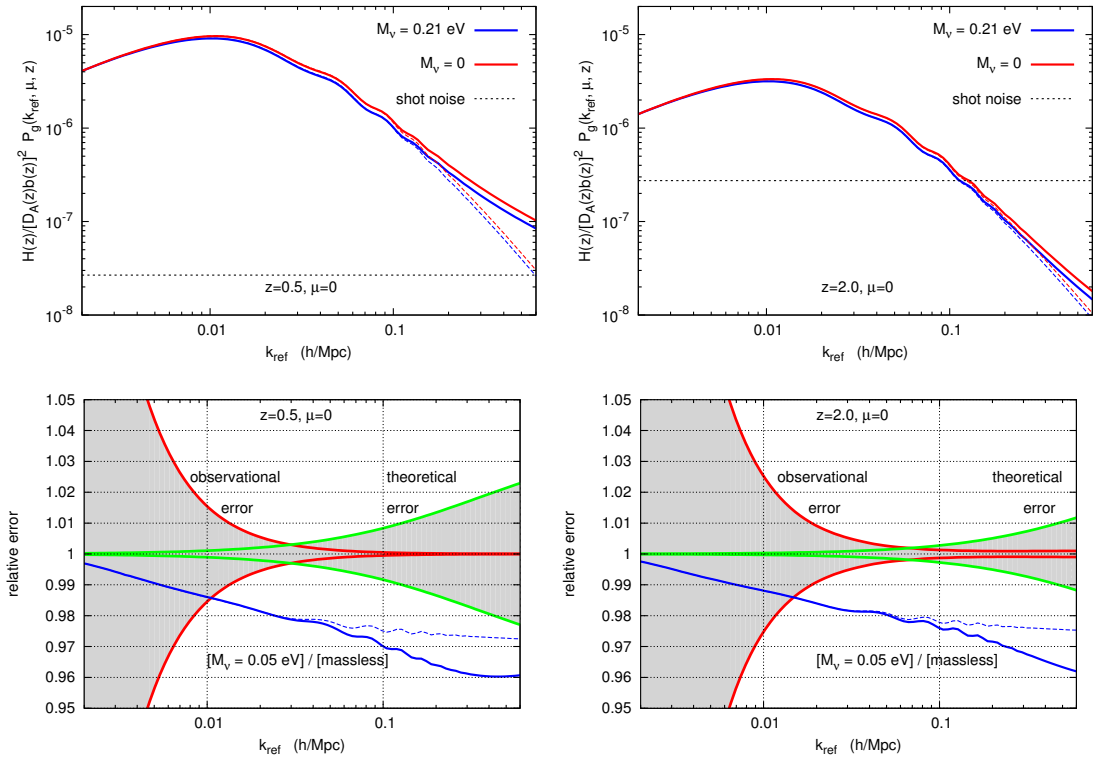

Figure 1: Observable spectrum (top) and relative error on this spectrum (bottom), for the first redshift bin (left) and last redshift bin (right) of a *Euclid*-like galaxy redshift survey. The quantity displayed in the top is the galaxy power spectrum $P_g(k_{\rm ref}, \mu, z)$ as a function of the fiducial wavenumber $k_{\rm ref}$, for fixed redshift and perpendicularly to the line of sight ($\mu = 0$), rescaled by the inverse squared bias $b(z)^{-2}$ and by a factor $H(z)/D_A(z)^2$: it is therefore a dimensionless quantity. The upper plots show a comparison between a model with massless neutrinos and our fiducial model ($M_\nu = 3m_\nu = 0.21$ eV). Solid lines are derived from the non-linear matter power spectrum using the updated HALOFIT version of ref. [24], while dashed lines are derived from the linear power spectrum. The lower plots show the part of the relative error coming from observational or theoretical errors only (cosmic variance is included in the observational error). In these plots, the individual 1-σ error on each data point has been rescaled by the square root of the number of points, in such a way that the edges of the error bands correspond to a shift between theory and observation leading to $\Delta\chi^2 = 1$, when only the observational or theoretical error is incorporated in the likelihood expression. In these lower plots, we also show for comparison the ratio between a massless model and a model with the minimum total mass allowed by neutrino experiments, $M_\nu = 0.05$ eV.

We fit the mock and *Euclid*-like spectra using the MCMC code MONTEPYTHON [27]. MONTEPYTHON uses the Metropolis-Hastings algorithm like COSMOMC [28], but is interfaced with CLASS [29, 30] instead of CAMB [31], is written in `python`, and has extra functionality; it will soon be released publicly, including the *Euclid*-like likelihood codes

used in this work.

Technical details of the assumed likelihood and our analysis are presented in Appendix A. Let us summarize here the essential points. As in most of the recent Fisher-matrix-based forecasts, we assume that the reduced data is described by a set of observable power spectra $P^{\rm obs}(k_{\rm ref}, \mu, z)$, related to the familiar non-linear matter power spectrum $P_{NL}(k, z)$ in a non-trivial way in order to take into account redshift space distortions, linear light-to-mass bias, spectroscopic redshift errors and the Alcock-Paczynsky effect (see A.1). Of course, this modeling is imperfect: for this reason we introduce a theoretical error. For instance, we do not take into account galactic feedback [32], assuming that this contamination can be predicted by simulations up to the level of our residual theoretical error function. The arguments $k_{\rm ref}$ and μ of the observable power spectrum stand respectively for the observed wavenumber assuming the fiducial cosmology, and the cosine of the angle between the observed wavevector and the line of sight. We assume sixteen redshift bins with mean redshift ranging from 0.5 to 2, and bin widths of $\Delta z = 0.1$. For a fixed theoretical model, each observed value of $P^{\rm obs}$ in a bin centered on the point $(k_{\rm ref}, \mu, z)$ follows, to a good approximation, a Gaussian distribution with variance

$$\left(\Delta P^{\rm obs}\right)^2 = \frac{2(2\pi)^2}{k_{\rm ref}^3 V_{\rm survey} d\mu [dk_{\rm ref}/k_{\rm ref}]} \left(P^{\rm th} + 1/n_g\right)^2 , \tag{2.1}$$

where $d\mu$ is the size of the bins in μ space, and $[dk_{\rm ref}/k_{\rm ref}]$ the size of the logarithmic bins in wavenumber space (see A.2). The characteristics of the survey are encoded in $V_{\rm survey}$, the survey volume, and n_g, the comoving number density of galaxies accounting for shot noise (see A.3). Hence, if for *every* observed data point the theory and the observation differed by this amount, the effective χ^2 would increase with respect to its minimum value by the number of data points, namely

$$N = B \frac{2}{d\mu} \frac{\ln(k_{\rm max}/k_{\rm min})}{[dk_{\rm ref}/k_{\rm ref}]} , \tag{2.2}$$

where B is the number of redshift bins.

To illustrate this error, in figure 1, we show the relative error bar on the observed spectrum in the first and last redshift bin, assuming no additional theoretical error. For the purpose of comparing with the theoretical error introduced below, we do not show as usual the error corresponding to a one-sigma deviation for each given data point; we divided each error by $\sqrt{N}$, in such a way that the edge of the error band corresponds to a deviation between the observed and theoretical spectrum leading to $\Delta\chi^2 = 1$. Note that the displayed quantity $\pm\Delta P^{\rm obs}/(P^{\rm obs}\sqrt{N})$ does not depend on the width of the bins in ($k_{\rm ref}$, μ, z) space, but only on $P^{\rm th}$, $V_{\rm survey}$ and n_g.

We incorporate the theoretical error in the likelihood in the way described in section A.4. In few words, this error is normalized in such a way that a shift between theory and observations by a relative amount α (the quantity defined in eq. (1.1)) leads to an increase of the χ^2 by one. This is achieved simply by adding a term $N(\alpha P^{\rm th})^2$ to the total error variance. Figure 1 shows the relative theoretical error on the observed spectrum, normalized in such a way that the edge of the error band corresponds to a deviation

between the observed and theoretical spectrum leading to $\Delta\chi^2 = 1$ when the observational error is switched off. These edges are directly given by $\pm\alpha$.

We see in this figure that our assumption for α leads to an error of 1% at $k = 0.1h\mathrm{Mpc}^{-1}$ and 2.5% at $k = 0.6h\mathrm{Mpc}^{-1}$ for the first redshift bin centered on $z = 0.5$. For the last redshift bin in the galaxy survey, centered on $z = 2$, non-linear corrections appear on smaller scales, and the error is only 1% at $k = 0.6h\mathrm{Mpc}^{-1}$.

$k_{\max}$ (h/Mpc)	un. err.	co. err.	$10^4\omega_b$	$10^4\omega_c$	$10^3 n_s$	$10^{11}A_s$	$10^3 h$	z_{reio}	$3m_\nu = M_\nu$ (meV)
0.1	–	–	1.2	6.2	2.8	3.0	4.1	0.38	18
0.1	1/10	–	1.2	6.9	2.8	3.1	4.5	0.39	18
0.1	1/2	–	1.3	9.5	3.2	3.5	6.1	0.39	23
0.1	•	–	1.3	11	3.4	3.6	6.7	0.40	25
0.1	•	•	1.3	11	3.4	3.6	6.7	0.40	25
0.6	–	–	0.86	2.1	0.37	1.2	0.40	0.23	5.9
0.6	1/10	–	1.1	4.8	2.5	2.7	3.0	0.37	14
0.6	1/2	–	1.2	8.6	3.2	3.4	5.7	0.39	22
0.6	•	–	1.3	10	3.4	3.6	6.7	0.39	25
0.6	•	•	1.3	10	3.4	3.6	6.7	0.39	25

Table 1: Marginalized 1-σ error for each model parameter, in a fit of *Planck* + *Euclid*-like galaxy survey data. The different lines correspond to different choices of $k_{\max}$, to the inclusion or not of the global uncorrelated theoretical error (un. err.), divided by ten (1/10), by two (1/2), or full (•), to that of the specific neutrino-related correlated error (co. err.), and to the use of the non-linear or linear power spectrum. The models with correlated error have one more nuisance parameter e_ν not shown here, with unit 1-σ error.

We performed several forecasts for a combination of *Planck* data and a *Euclid*-like galaxy redshift survey data. It should be stressed that the characteristics of *Euclid* are not yet finalized. Our choice for V_{survey} and $n_g(\bar{z})$, detailed in A.3, should be taken as indicative only. For *Planck*, we follow the method presented in [22] and do not include lensing extraction. For the experimental *Planck* sensitivity, we use the numbers presented in the *Planck* Bluebook[7]. This is a rather conservative model since the sensitivities are based on 14 months of observations instead of 30.

The differences between our forecasts reside in the maximum wavenumber, equal to $k_{\max} = 0.1$ or $0.6\,h\mathrm{Mpc}^{-1}$, and in various prescription for the theoretical error: no error at all, the uncorrelated error described above and in A.4 (divided by ten, by two, or full), or additionally the correlated error accounting for neutrino-mass-related effects (described in A.5). Since we are using an increasing theoretical error on non-linear scales, we expect the amount of information contained in the data to saturate above some value of $k_{\max}$: this is the reason we can consider such a high value as $0.6\,h\mathrm{Mpc}^{-1}$. We did not try even higher values, first because our result would not change, and second because our forecast

[7] http://www.rssd.esa.int/SA/PLANCK/docs/Bluebook-ESA-SCI(2005)1_V2.pdf, page 4, Table 1.1 (using only the best three HFI channels: 100, 143 and 217 GHz).

would become unrealistic: deep in the non-linear regime, the Gaussian assumption for the likelihood breaks down.

Our results are presented in Table 1. Parameters like ω_b and $z_{\rm reio}$ are well determined by CMB data, and their forecast error depends very mildly on our different assumptions. For other parameters, the redshift survey plays a crucial role in removing parameter degeneracies. In that case, even with $k_{\rm max} = 0.1\,h{\rm Mpc}^{-1}$, including the uncorrelated theoretical error makes a difference: the parameter sensitivity degrades by up to 70% for h. The 68% neutrino mass error bar degrades by 40%, from $\sigma(M_\nu) = 0.018$ eV to $\sigma(M_\nu) = 0.025$ eV.

Assuming only this uncorrelated error, the cases $k_{\rm max}$=0.1 $h{\rm Mpc}^{-1}$ and $k_{\rm max}$=0.6 $h{\rm Mpc}^{-1}$ give almost the same results. Hence, our assumption for the theoretical error magnitude is such that most of the information is contained on linear scales. Thanks to realistic (or at least conservative) assumptions for the theoretical error, the results of our forecast are nearly independent of the cut-off $k_{\rm max}$. Without a theoretical error, increasing $k_{\rm max}$ to $0.6\,h{\rm Mpc}^{-1}$ would lead to a spectacular (but totally unrealistic) decrease of the error bars, with $\sigma(M_\nu) = 0.0059$ eV.

If we are more optimistic and half the uncorrelated error, the error bars decrease marginally, as can be seen in the Table (lines starting with "1/2"). The error on the neutrino mass only decrease by $\sim 10\%$. Assuming no error at all implies that the spectrum can be predicted up to the 0.1% level or better on small scales. In comparison, assuming a precision of one percent is not very different from assuming two percent. With the halved error, the sensitivity to the neutrino mass increases from $\sigma(M_\nu) = 0.023$eV to $\sigma(M_\nu) = 0.022$eV when including data in the range from 0.1 to $0.6\,h{\rm Mpc}^{-1}$.

Finally, in a very optimistic forecast with an error ten times smaller, we start to see how extra information can be extracted from non-linear scales; the error decreases from $\sigma(M_\nu) = 0.018$ eV to $\sigma(M_\nu) = 0.014$ eV when pushing $k_{\rm max}$ from 0.1 to $0.6\,h{\rm Mpc}^{-1}$.

The inclusion of an additional correlated error accounting for neutrino-mass-related systematics has a negligible impact on our results. In our forecast, the uncorrelated and correlated part of the error have similar amplitudes and the same shape; however the uncorrelated error allows much more freedom and thus leads significantly more conservative results: this explains why the correlated error has a comparatively small effect. It should be stressed that our results depend not only on the assumed error amplitude at a given scale and redshift, but also on the wavenumber dependence of the error function α. Different assumptions, with a steeper or smoother step in the error function around the scale of non-linearity, would lead to different forecasts. In particular, as already mentioned the actual benefit from pushing to smaller, non-linear scales depends on the assumed k-dependence of the residual uncorrelated theoretical error.

For the case with $k_{\rm max} = 0.6\,h{\rm Mpc}^{-1}$ and no neutrino-related correlated error, we show the one and two-dimensional posterior probability on cosmological parameters in figure 2. We see several pronounced parameter degeneracies. For instance, the neutrino mass is very correlated with ω_c and h. This suggests that further progress could be made by including extra data sets, such as direct measurements of the Hubble parameter, the cluster mass function, supernovae luminosity, 21-cm anisotropies, and so on.

Our results are consistent with those of [14, 17], although a direct comparison is

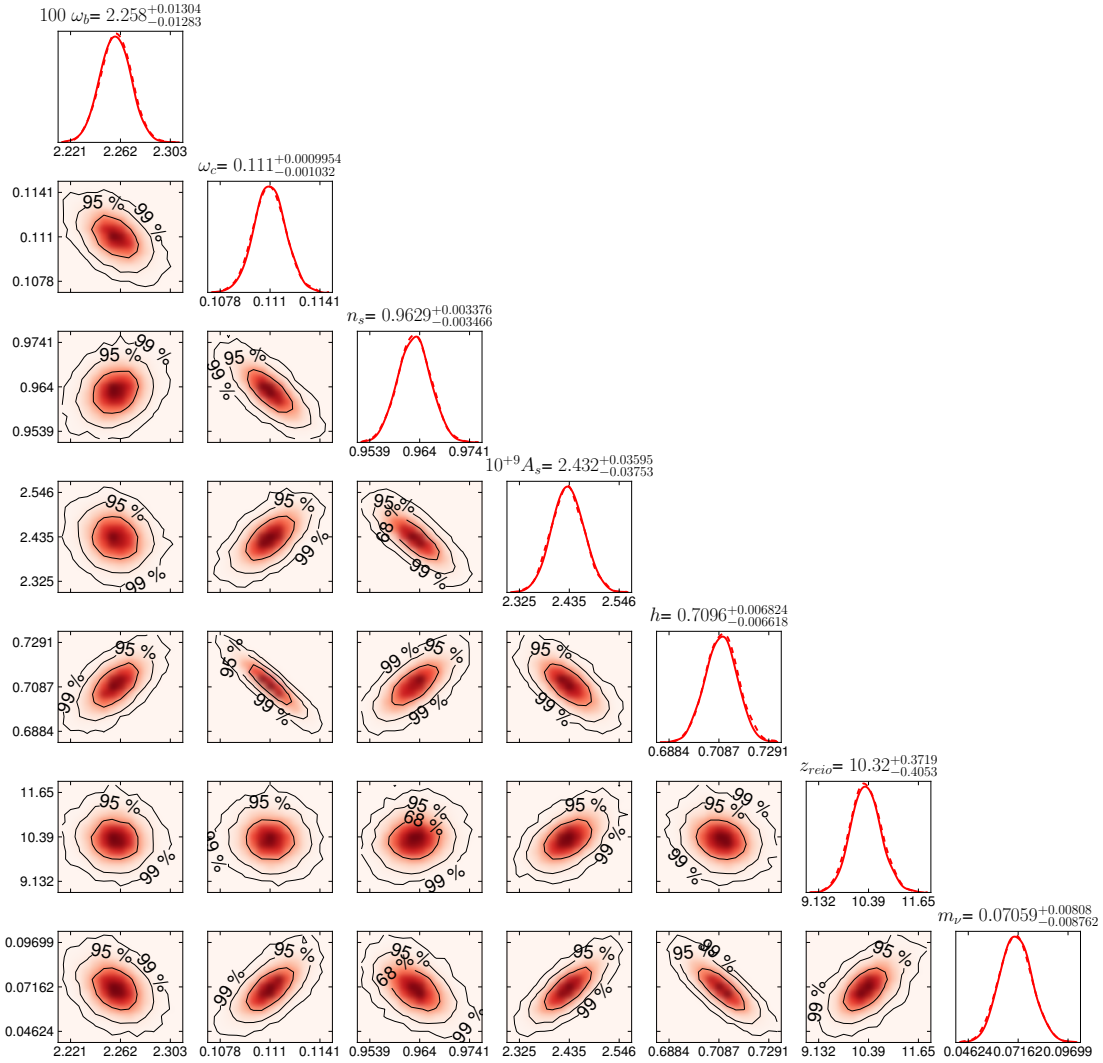

Figure 2: Marginalized posteriors and two-dimensional probability contours in a fit of *Planck* plus a *Euclid*-like galaxy survey mock data, with $k_{\rm max} = 0.6\,h{\rm Mpc}^{-1}$ and a global uncorrelated theoretical error (second line starting from the bottom in Table 1).

difficult, since those authors include two extra parameters, w_0 and w_a, in their forecast. The results in Table 2.1 of [33], based on the same cosmological model, match our prediction in the case with no non-linear scales and no theoretical error included. A similar sensitivity was found by [19] for a Euclid-like photometric redshift survey, referred to as "cg" in their Table 2. However, this reference presents other results based on even more conservative assumptions than ours. We assumed that the bias function for each redshift bin could be determined in advance (up to corrections on non-linear scales contained in our global theoretical error). This assumption has also been made in most recent forecasts, since both

N-body simulations and higher-order statistics in the real data allow the prediction of the redshift-dependent bias of a given population of galaxies, at least on linear scales. Were this approach found to be unreliable, it would be necessary to marginalize over the linear bias in each redshift bin, $b(z_i)$. Ref. [19] did such a marginalization in the runs called "cgb" and "cgbl", with no prior at all on each $b(z_i)$. They found roughly the same error bar on ω_c and h than in our forecast with theoretical error, but a much larger error on the neutrino mass. However, it seems unlikely that at the time when *Euclid* data will be analyzed, no information at all will be available on the linear bias of the observed population of galaxies.

3. Cosmic shear survey

For the case of a *Euclid*-like cosmic shear survey, we stick to the same fiducial model and methodology as in the previous section. The likelihood is now a function of the observed lensing power spectrum $C_l^{\mathrm{obs}\,ij}$ in harmonic space and for each pair ij of redshift bins, taking into account photometric redshift errors and shot noise (for details, see B.1 and B.2). We assume experimental sensitivities summarized in B.3, and cut the observations in five redshift bins covering the range $0 < z < 3.5$ (although a negligible amount of galaxies contribute between 3 and 3.5). We do not take into account intrinsic alignment, assuming that this contamination can be removed up to the level of our residual theoretical error function [34, 35].

As explained in detail in B.4, there is a small technical difference between the likelihood of the galaxy survey and the shear survey in the way we incorporate the uncorrelated theoretical error. For the galaxy survey, the theoretical error was encoded as an extra contribution to the total error variance. This can be justified mathematically by marginalizing over one nuisance parameter for each data point. The shape of the galaxy survey likelihood allows for an analytical minimization over each nuisance parameter, in such a way that nuisance parameters do not appear explicitly in the final likelihood. We found that no such scheme is accurate enough in the case of the (chi-square type) shear likelihood. Hence our likelihood routine performs an explicit minimization over one nuisance parameter per data point. For simplicity, we assume that the error is uncorrelated between different values of l, but not between different bins for a given l: this assumption could be relaxed, at the expense of increasing the computing time.

We fixed $l_{\mathrm{max}} = 2000$, since beyond this value both the shot noise term and the theoretical error are large, as shown in figure 3. This figure also shows the relative error on the observed spectrum in the first and last redshift bins, coming either from observational errors (including cosmic variance) or from the theoretical error, and using exactly the same conventions as in the previous section: the edges of each of the two error bands correspond to a shift between the theory and the observation leading to $\Delta\chi^2 = 1$ when either the observational or the theoretical error are included in the likelihood. The lowest redshift bin incorporates small non-linear scales: this explains why at $l = 2000$, the theoretical error reaches 3.5%.

Our results are presented in Table 2 for three cases: no theoretical error, uncorrelated error only (described in B.4), or additional neutrino-related correlated error (described in

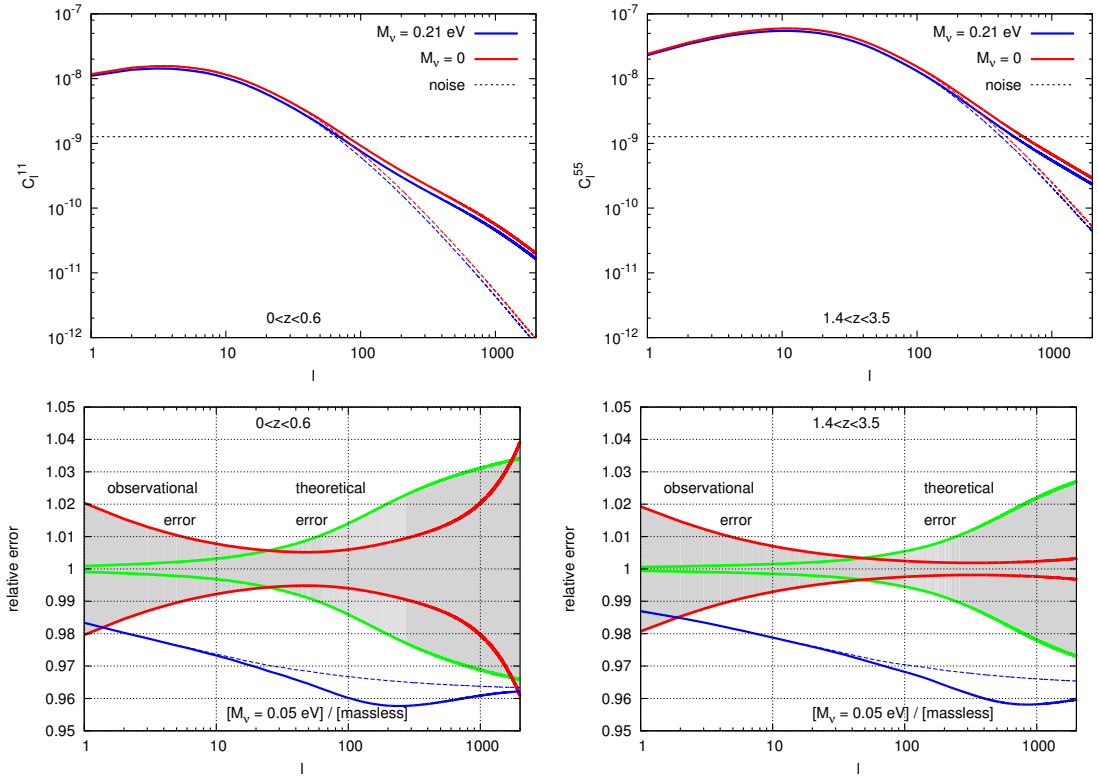

Figure 3: Observable cosmic shear power spectrum (top) and its relative error (bottom) for the first redshift bin (left) and last redshift bin (right) of a *Euclid*-like shear survey. The quantity displayed above is the lensing auto-correlation spectrum C_l^{ii} (dimensionless). The upper plots show the comparison of a model with massless neutrinos to our fiducial model ($M_\nu = 3m_\nu = 0.21$ eV). Solid lines are derived from the non-linear matter power spectrum using the recent update of HALOFIT [24], while dotted lines are derived from the linear power spectrum. The lower plots show the part of the relative error coming from observational or theoretical errors only (cosmic variance is included in the observational error). In these plots, the individual 1-σ error on each data point has been rescaled by the square root of the number of points, in such a way that the edges of the error bands correspond to a shift between theory and observation leading to $\Delta\chi^2 = 1$, when only the observational or theoretical error is incorporated in the likelihood expression. In these lower plots, we also show for comparison the ratio between a massless model and a model with the minimum total mass allowed by neutrino experiments, $M_\nu = 0.05$ eV.

B.5). The impact of the uncorrelated error is again important, but not as pronounced as in the galaxy power spectrum case, because on small scales the precision of the shear survey is limited by a significant shot noise contribution. The neutrino mass error degrades only from $\sigma(M_\nu) = 0.026$ eV to 0.028 eV. For the shear survey we did not perform runs with a twice or ten times smaller error: the result for $\sigma(M_\nu)$ would simply lie between those two numbers. The impact of the neutrino-related error is small but further degrades the sensitivity to $\sigma(M_\nu) = 0.032$ eV. While in the absence of theoretical error the galaxy survey seems more sensitive to the neutrino mass, the performance of the two methods are roughly identical once the same theoretical error ansatz is included.

un. err.	co. err.	$10^4\omega_b$	$10^4\omega_c$	$10^3 n_s$	$10^{11}A_s$	$10^3 h$	$z_{\rm reio}$	$3m_\nu = M_\nu$ (meV)
–	–	1.1	3.9	2.4	2.8	4.0	3.7	26
•	–	1.2	6.3	2.7	2.9	5.2	3.8	28
•	•	1.2	6.6	2.7	3.0	5.3	3.9	32

Table 2: Marginalized 1-σ error for each model parameter, in a fit to *Planck* + *Euclid*-like shear survey data. The different lines correspond to the inclusion or not of the global uncorrelated theoretical error (un. err.), and of the specific neutrino-related correlated error (co. err.). Our preferred prediction is given on the last line, and is very close to that of the second line.

The triangle plot of figure 4 shows that the parameter degeneracies are very similar for the two cases of the galaxy survey and shear survey. Nevertheless, [19] showed that combining the two data sets (with a proper cross-correlation matrix) leads to sensitivity improvements. It would be interesting to test this conclusion in presence of theoretical errors.

Our result are consistent with those of [11], although a direct comparison is difficult, since these authors include several extra parameters (w_0, w_a, r, α_s) in their forecast. The predictions of [19] (case "cs" in their Table 2) lie between our results with and without theoretical errors. This is consistent since on the one hand, these authors use more optimistic survey characteristics (d, $\langle\gamma^2_{rms}\rangle$, $\sigma_{\rm ph}$), and on the other hand, we are including much larger values of l (which is legitimate if our theoretical error is realistic).

4. Conclusions

We have presented forecasts of cosmological parameters by using, in combination with *Planck* data, two *Euclid*-like mock future data sets: a galaxy spectroscopic redshift survey and a cosmic shear survey. We focused our attention on constraints that can be achieved on the total neutrino mass by using the data in the linear and non-linear regimes.

In order to do this conservatively we adopt the following improvements with respect to similar works performed recently in the literature: *i*) we make use of Markov Chain Monte Carlo rather than the Fisher Matrix, which results in more reliable error bars, as well as considering degeneracies between parameters. Ultimately, we found that the posterior probability is very close to a multivariate Gaussian for the model considered. However, a Fisher matrix approach could not have confirmed this, and would not have been explicitly independent of the stepsize in the numerical derivatives. *ii*) we rely on a modification of HALOFIT that accounts for massive neutrinos, and predicts the non-linear matter power spectrum to small scales, based on the results of N-body and hydro simulations. *iii*) we conservatively consider errors both on the non-linear observable power at small scales and on the neutrino induced suppression, and explictly show how to implement these errors in the likelihood calculation.

It is instructive to see that with the shape assumed for the uncorrelated theoretical error, and a conservative assumption on its amplitude (leading to a 2% error at $k_{\rm max} = 0.4\,h/{\rm Mpc}$ and $z = 0.5$), the sensitivity to cosmological parameter is still satisfactory. The

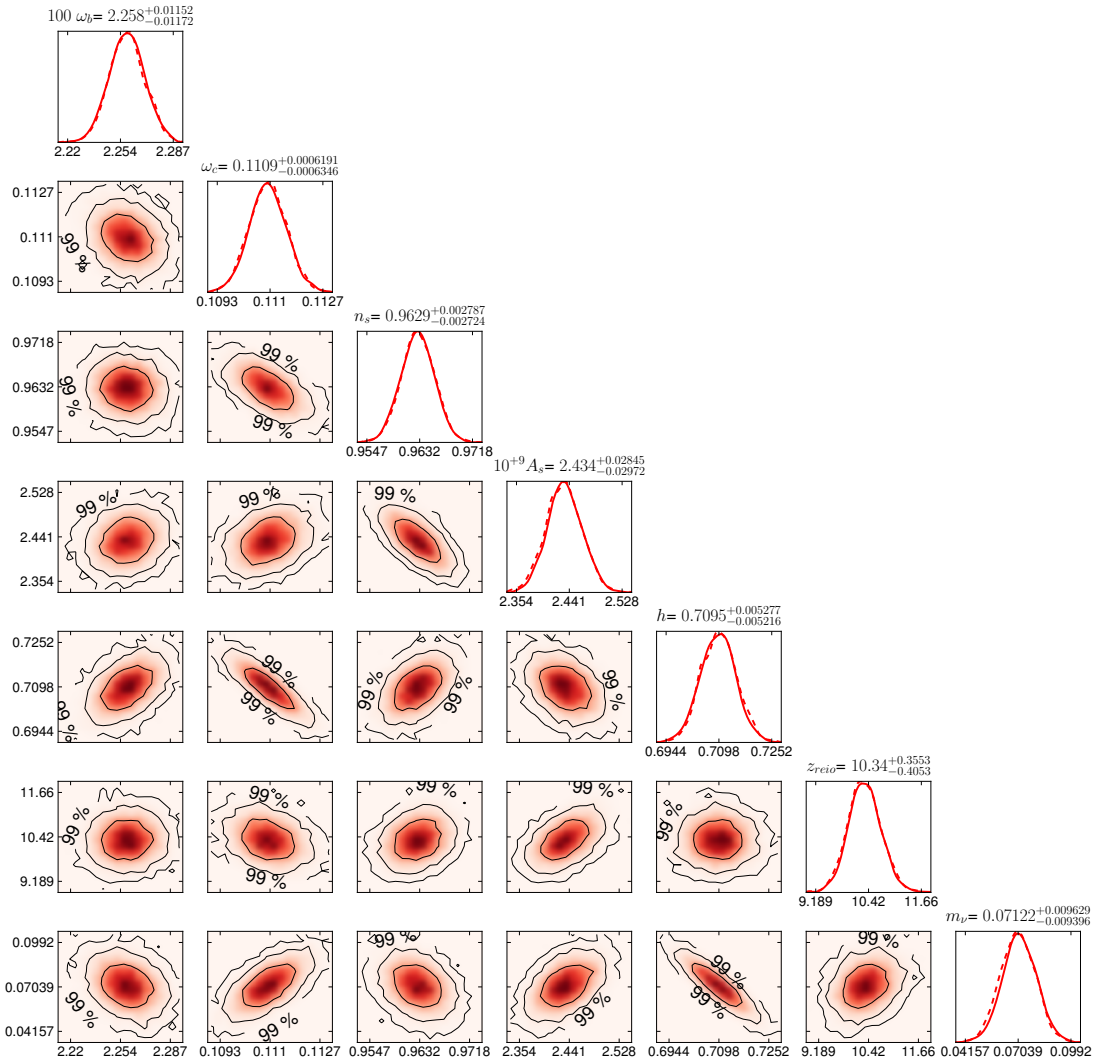

Figure 4: Marginalized posteriors and two-dimensional probability contours in a fit of *Planck* + *Euclid*-like shear survey data, with a global uncorrelated error of 5% on non-linear scales (second model in Table 2).

error bar on the total neutrino mass, of the order of 32 meV (cosmic shear) or 25 meV (redshift survey), would still allow for a two sigma detection of the total neutrino mass in the minimal normal hierarchy scenario. However, with this amplitude and k-dependence of the theoretical error, essentially all the information comes from linear scales. The next interesting question is to check how much the uncorrelated error should be controlled in order to start being sensitive to mildly non-linear scales. Assuming a twice smaller error does not change the parameter sensitivity by a significant amount. Extracting significant information from non-linear scales requires an error ten times smaller, at the level of 0.2%.

Here the error on the neutrino mass decreased from $\sigma(M_\nu) = 18$ meV to 14 meV when adding scales with $0.1 < k < 0.6\,h$/Mpc to the analysis. This shows that it would be extremely useful to be able to predict the observable power spectrum of a given cosmological model up to a residual uncorrelated error of the order of 0.1% (resp. 0.2%) at $k \sim 0.1\,h$/Mpc (resp. $k \sim 0.4\,h$/Mpc) and $z = 0.5$. This will be a major challenge for theoretical and numerical cosmology in the next decade.

Acknowledgements

We would like to thank Henk Hoekstra, Tom Kitching and Valeria Pettorino for their comments on this manuscript. This project is supported by a research grant from the Swiss National Science Foundation. MV acknowledges support from grants: INFN/PD51, ASI/AAE, PRIN MIUR, PRIN INAF 2009 and from the ERC Starting Grant "cosmoIGM". BA and JL acknowledge support from the Swiss National Fundation. SB is supported by NSF grant AST-0907969

A. Galaxy redshift survey implementation

A.1 Observed spectrum

Let $P^{\rm obs}$ be the observed/mock/fiducial power spectrum, and $P^{\rm th}$ the spectrum that one would expect to see given the theoretical model. Each of these quantities relates to the galaxy spectrum P_g and finally to the total non-linear matter spectrum $P_{\rm NL}$ by taking into account redshift distortion effects, spectroscopic redshift errors and light-to-mass bias. A good approximation of such a relation is given by (see e.g. [16, 15]):

$$P^{\rm th/obs}(k_{ref\perp}, k_{ref\parallel}, z) = \frac{D_A(z)^2_{\rm ref} H(z)}{D_A(z)^2 H(z)_{\rm ref}} P_g^{\rm th/obs}(k_{ref\perp}, k_{ref\parallel}, z)\ , \tag{A.1}$$

$$P_g^{\rm th/obs}(k_{ref\perp}, k_{ref\parallel}, z) = b(z)^2 \left[1 + \beta(z,k)\frac{k^2_{ref\parallel}}{k^2_{ref\perp} + k^2_{ref\parallel}}\right]^2 P_{NL}^{\rm th/obs}(k,z) e^{-k^2\mu^2\sigma_r^2}\ , \tag{A.2}$$

with the definitions

$$\beta(k,z) \equiv b(z)^{-1}\frac{d\ln[P_{NL}^{\rm th/obs}(k,z)]^{1/2}}{d\ln a} = \frac{1}{2b(z)}\frac{d\ln P_{\rm NL}^{\rm th/obs}(k,z)}{d\ln a}\ , \tag{A.3}$$

$$k_{{\rm ref}\perp} = k_\perp H(z)_{\rm ref}/H(z), \quad k_{{\rm ref}\parallel} = k_\parallel H(z)_{\rm ref}/H(z), \tag{A.4}$$

$$\mu \equiv \hat{k}_{\rm ref}.\hat{r} = k_{{\rm ref}\parallel}/k_{\rm ref}, \tag{A.5}$$

$$k^2 = \left(\frac{(1-\mu^2)D_A(z)^2_{\rm ref}}{D_A(z)^2} + \frac{\mu^2 H(z)^2}{H(z)^2_{\rm ref}}\right) k^2_{\rm ref}\ . \tag{A.6}$$

Here $b(z)$ is the bias, assumed to be scale-independent in the range of scales of interest, a is the scale factor, $H(z)$ is the Hubble parameter, $D_A(z)$ the angular diameter distance, and $\beta(z,k)$ accounts approximately for redshift space distortions. So we can treat k as a

function of the arguments $(k_{\rm ref}, \mu, z)$ and write

$$P^{\rm th/obs}(k_{\rm ref},\mu,z) = \frac{D_A(z)^2_{\rm ref} H(z)}{D_A(z)^2 H(z)_{\rm ref}} b(z)^2 \left[1+\beta(z,k(k_{\rm ref},\mu,z))\mu^2\right]^2 \times P^{\rm th/obs}_{\rm NL}(k(k_{\rm ref},\mu,z),z) e^{-k(k_{\rm ref},\mu,z)^2\mu^2\sigma_r^2} \tag{A.7}$$

A.2 Likelihood

For a narrow redshift bin b centered on $\bar{z}$, the likelihood reads

$$\mathcal{L}_b = \mathcal{N}_b \exp\left[-\frac{1}{2}\int_{k_{\rm min}<k_{\rm ref}<k_{\rm max}} \frac{d^3\vec{k}_{\rm ref}}{(2\pi)^3} V_{\rm eff}(k_{\rm ref},\mu,\bar{z}) \frac{(P^{\rm obs}(k_{\rm ref},\mu,\bar{z}) - P^{\rm th}(k_{\rm ref},\mu,\bar{z}))^2}{2(P^{\rm th}(k_{\rm ref},\mu,\bar{z}))^2}\right] \tag{A.8}$$

$$= \mathcal{N}_b \exp\left[-\frac{1}{2}\int_{-1}^{1} d\mu \int_{k_{\rm min}}^{k_{\rm max}} \frac{k^2_{\rm ref} dk_{\rm ref}}{(2\pi)^2} V_{\rm eff}(k_{\rm ref},\mu,\bar{z}) \frac{(P^{\rm obs}(k_{\rm ref},\mu,\bar{z}) - P^{\rm th}(k_{\rm ref},\mu,\bar{z}))^2}{2(P^{\rm th}(k_{\rm ref},\mu,\bar{z}))^2}\right], \tag{A.9}$$

with an effective survey volume given by

$$V_{\rm eff}(k_{\rm ref},\mu,\bar{z}) = V_{\rm survey}(\bar{z}) \left[\frac{n_g(\bar{z}) P_g^{\rm th}(k_{\rm ref},\mu,\bar{z})}{1+n_g(\bar{z}) P_g^{\rm th}(k_{\rm ref},\mu,\bar{z})}\right]^2 . \tag{A.10}$$

Later, we will specify the sensitivity of the survey, parameterized by $V_{\rm survey}$, n_g, σ_r, $k_{\rm min}$ and $k_{\rm max}$. We skip here the derivation of the Fisher matrix, obtained by differentiating the above formula twice with respect to the cosmological parameters on which $P^{\rm th}$ depends, and evaluating this derivative at the maximum likelihood point. We checked that this calculation gives exactly the formula commonly used in the literature (see e.g. [16, 15]). For the purpose of the discussion in the next section (and also of the numerical implementation), we wish to write explicitly the discrete limit of the integrals. We discretize μ in a set of equally spaced values μ_i, and $l \equiv \ln k$ in a set of equally spaced values $l_j = \ln k_{{\rm ref}\,j}$. The step sizes are denoted $\Delta\mu$ and Δl respectively. We then expand the integral as a sum, and for simplicity we omit the factors $1/2$ that should weight the boundary terms of each of the two integrals. We introduce the short-cut notations:

$$N_{ij} \equiv \Delta\mu\Delta l \frac{k^3_{{\rm ref}\,j} V_{\rm eff}(k_{{\rm ref}\,j},\mu_i,z)}{(2\pi^2)}, \tag{A.11}$$

$$P^{\rm obs/th}_{ij} \equiv P^{\rm obs/th}(k_{{\rm ref}\,j},\mu_i,z), \tag{A.12}$$

and we get

$$-2\ln\mathcal{L}_b = \sum_{i,j} \frac{\left(P^{\rm obs}_{ij} - P^{\rm th}_{ij}\right)^2}{2(P^{\rm th}_{ij})^2/N_{ij}}. \tag{A.13}$$

This expression is easy to understand from first principles. Let us consider a single variable δ obeying a Gaussian distribution centered on zero and with variance $\langle\delta^2\rangle = P$. If we

observe N independent realization δ_n of the variable δ, we can build an estimator of the variance P of δ,

$$E = \frac{1}{N}\sum_n \delta_n^2. \tag{A.14}$$

The variance of this estimator can be computed by noticing that each δ_n^2 follows a χ^2 distribution of order one, for which the mean is P and the variance $2P^2$. So the sum $\sum_n \delta_n^2$ has a variance $2NP^2$. Finally E has a variance $(2NP^2)/N^2 = 2P^2/N$. Moreover, E is nearly Gaussian if N is large, as a consequence of the central limit theorem. So the probability of the data E given the theory P is a Gaussian of mean P and of variance $2P^2/N$. In other words,

$$-2\ln\mathcal{L}(E|P) = \frac{(E-P)^2}{2P^2/N}\ . \tag{A.15}$$

The previous likelihood follows this form for each discrete term. Indeed each term corresponds to the likelihood of the estimator of the power spectrum in a thin shell in Fourier space. The number of independent measurements, i.e. of independent wavenumbers in each shell, is given by N_{ij}. The role of E and P is played respectively by $P_{ij}^{\rm obs}$ and $P_{ij}^{\rm th}$. Such a likelihood was first derived in pioneering papers like [36, 37].

A.3 Survey specifications

We computed this likelihood for values of $V_{\rm survey}(\bar{z})$, $n_g(\bar{z})$, $\sigma_r(\bar{z})$ inspired from currently plausible *Euclid* specifications, which are likely to change over the next years. We divide the observations into sixteen redshift bins of width $\Delta z = 0.1$, ranging from $\bar{z} = 0.5$ to $\bar{z} = 2.0$. For each bin, we assumed:

- a volume per bin $V_{\rm survey}(\bar{z}) = 4\pi f_{\rm sky}[r(\bar{z})]^2(1+\bar{z})^{-3}\frac{\partial r(z)}{\partial z}\Delta z$, where $r(z)$ is the comoving distance up to a comoving object with redshift z, with the explicit assumption that $a_0 = 1$:

  $$r(z) = \int_0^z \frac{dz'}{H(z')}\ . \tag{A.16}$$

  We assume a sky coverage $f_{\rm sky} = 0.375$.

- a galaxy number density per comoving volume $n_g(\bar{z})$, related to the number of galaxies per square degree $d_g(\bar{z})$ through

  $$n_g(\bar{z}) = \frac{d_g(\bar{z}) \times 41\,253\,{\rm deg}^2}{4\pi[r(\bar{z})]^2\frac{\partial r(z)}{\partial z}\,\Delta z}\ . \tag{A.17}$$

  For $d_g(\bar{z})$, we start from the number presented in Table 2 of [38] for the case of a limiting flux of $3\times10^{-16}{\rm erg\,s^{-1}cm^{-2}}$. Following the recommendation of that paper, we divide these numbers by 1.37 in order to get conservative predictions. Finally, we multiply them by an efficiency factor $\epsilon = 0.25$ (standing for the redshift success rate). For instance, for the first redshift bin, this gives $d_g(\bar{z}) = 9376/1.37\times0.25 = 1710\ {\rm deg}^{-2}$.

- a spectroscopic redshift error $\sigma_r = \frac{\partial r(z)}{\partial z}\sigma_z$ with $\sigma_z = 0.001(1+z)$.

- a scale-independent linear bias $b(\bar{z})$. The choice of $b(\bar{z})$ values affects the final result less crucially than that of $d_g(\bar{z})$. We could adopt the predictions of [39] inferred from N-body simulations, but for simplicity, our forecast is performed under the approximation $b(\bar{z}) = \sqrt{1+\bar{z}}$. So, we assume in this forecast that the linear bias will be accurately measured or predicted for each bin, and that deviations from this prediction (coming from the non-linear evolution) will be known up to the level described by the theoretical error function.

- $k_{\rm min}$ can be chosen arbitrarily close to zero without changing the results.

- we tested two values of $k_{\rm max}$: 0.1 and 0.6 hMpc^{-1}.

A.4 Accounting for a global uncorrelated theoretical error

To present a realistic forecast, one should model all the systematic effects not accounted for by the previous likelihood formula, such as: theoretical errors in the calculation of the linear and non-linear power spectrum, scale-dependence of the bias on small scales, residual shot noise in galaxy counts beyond the contribution already included in the definition of $V_{\rm eff}$, residual errors in the modeling of redshift space distortion beyond the above scheme. On top of these corrections, one may have to take into account the fact that the likelihood is not Gaussian on strongly non-linear scales. In this paper, we limit ourselves to mildly non-linear scales $k \leq k_{\rm max} = 0.6h$Mpc^{-1}, and assume that non-Gaussianity effects are sub-dominant to the previously mentioned systematics. We also neglect to marginalize over residual shot noise in each redshift bin, because Ref. [16, 15] found that this has a negligible impact.

Understanding these various systematics is a major challenge for the future, which should be addressed with better simulations and analytical modeling. Here we want to keep the analysis simple, and model these systematic errors in a simple way, by adding to the spectrum an uncorrelated theoretical error function. By uncorrelated we mean that the errors made at different scales are independent from each other, which is the most conservative possible assumption. In this case, we can introduce an independent Gaussian-distributed nuisance parameter ϵ_{ij} for each data point, and marginalize over it – or rather, to a very good approximation, minimize over it:

$$-2\ln\mathcal{L}_b = \sum_{i,j} \min_{-\infty<\epsilon_{ij}<+\infty} \frac{\left[P_{ij}^{\rm obs} - \left(P_{ij}^{\rm th} + \epsilon_{ij} R_{ij}^{1/2}\right)\right]^2}{2\left(P_{ij}^{\rm th} + \epsilon_{ij} R_{ij}^{1/2}\right)^2 / N_{ij}} + \epsilon_{ij}^2, \tag{A.18}$$

where R_{ij} is the theoretical error variance for a bin in $(\mu, k_{\rm ref})$ space centered on $(\mu_i, k_{{\rm ref}\,j})$. As long as the theoretical error is assumed to be small, it is also a valid approximation to neglect the ϵ_{ij}-dependence of the denominator, in order to find a simple analytic solution for ϵ_{ij}, which, injected back in eq. (A.18), gives

$$-2\ln\mathcal{L}_b = \sum_{i,j} \frac{\left(P_{ij}^{\rm obs} - P_{ij}^{\rm th}\right)^2}{2(P_{ij}^{\rm th})^2/N_{ij} + R_{ij}}. \tag{A.19}$$

In other words, the theoretical error variance simply adds up to the noise variance.

Note that we explicitly checked that it is legitimate to neglect the ϵ_{ij}-dependence of the likelihood denominator when minimizing over ϵ_{ij}. We also coded the full likelihood with explicit minimization over each ϵ_{ij}, and found the same results up to very good accuracy.

We choose a numerical value of R_{ij} motivated mainly by the current level of precision of the HALOFIT algorithm. We assume a relative error on the non-linear power spectrum of the form

$$\alpha(k,z) \equiv \frac{\Delta P_{\rm NL}^{\rm th}(k,z)}{P_{\rm NL}^{\rm th}(k,z)} = \frac{\ln[1+k/k_\sigma(z)]}{1+\ln[1+k/k_\sigma(z)]}\,0.05\ , \tag{A.20}$$

where $k_\sigma(z)$ is the scale of non-linearity computed by HALOFIT. This function increases from zero to 5% around the scale of non-linearity. Using the function $k(k_{\rm ref},\mu,\bar{z})$, this error can easily be propagated to the theoretical observable spectrum

$$\alpha(k_{\rm ref},\mu,\bar{z}) \equiv \alpha(k(k_{\rm ref},\mu,\bar{z}),\bar{z}) = \frac{\Delta P^{\rm th}(k_{\rm ref},\mu,\bar{z})}{P^{\rm th}(k_{\rm ref},\mu,\bar{z})}\ . \tag{A.21}$$

In terms of the discretized observable spectrum, the error reads

$$\alpha_{ij} = \alpha(k_{{\rm ref}\,j},\mu_i,\bar{z})\ . \tag{A.22}$$

The error variance R_{ij} should be proportional to the power spectrum variance $(\alpha_{ij}P_{ij}^{\rm th})^2$. We also assume that the error makes a constant contribution to each logarithmic interval in the space where observations are performed, i.e. is of the form

$$R_{ij} \propto (\alpha_{ij}P_{ij}^{\rm th})^2 \frac{k_{{\rm ref}j}}{d\mu\ dk_{\rm ref}}\ . \tag{A.23}$$

We normalize the error variance R_{ij} in such a way that a one-sigma theoretical error in each data point results in increasing the effective χ^2 by one unit, namely,

$$R_{ij} = \left[2B\left(\ln\frac{k_{\rm max}}{k_{\rm min}}\right)\right](\alpha_{ij}P_{ij}^{\rm th})^2\frac{k_{{\rm ref}j}}{d\mu\ dk_{\rm ref}}\ , \tag{A.24}$$

where B is the number of bins. The role of the normalization factor between squared brackets will become clear below. The likelihood becomes (using eq. (A.19) and going back to the continuous limit)

$$\mathcal{L} = \Pi_b\,\mathcal{N}_b \exp\left[-\frac{1}{2}\int_{-1}^{1}\frac{d\mu}{2}\int_{k_{\rm min}}^{k_{\rm max}}\frac{dk_{\rm ref}}{k_{\rm ref}}\frac{(P^{\rm obs}-P^{\rm th})^2}{(P^{\rm th})^2\left\{\frac{(2\pi)^2}{k_{\rm ref}^3 V_{\rm eff}}+\alpha^2 B\ln\frac{k_{\rm max}}{k_{\rm min}}\right\}}\right]\ , \tag{A.25}$$

where we omitted the argument $(k_{\rm ref},\mu,\bar{z}_b)$ of the functions $P^{\rm th}$, $P^{\rm obs}$, $V_{\rm eff}$ and α. If one assumes that the observed and theoretical spectra differ by $\alpha P^{\rm th}$ for each (k,μ,z), and that in the denominator the theoretical error dominates over the observational one ($V_{\rm eff}=\infty$), then

$$\mathcal{L} = \Pi_b\,\mathcal{N}_b \exp\left[-\frac{1}{2}\int_{-1}^{1}\frac{d\mu}{2}\int_{k_{\rm min}}^{k_{\rm max}}\frac{dk_{\rm ref}}{k_{\rm ref}}\frac{1}{B\ln\frac{k_{\rm max}}{k_{\rm min}}}\right] = (\Pi_b\mathcal{N}_b)\exp\left[-\frac{1}{2}\right]\ , \tag{A.26}$$

which corresponds to a shift by $\Delta\chi^2_{\rm eff} = 1$ with respect to the maximum likelihood $\mathcal{L} = \Pi_b \mathcal{N}_b$.

If we had assumed the error to be fully correlated, instead of increasing the denominator of the likelihood, we would have replaced $P^{\rm th}$ by $P^{\rm th}(1+\epsilon\alpha)$, multiplied the likelihood by $\sqrt{1/2\pi}\exp[-\epsilon^2/2]$, and marginalized/minimized over ϵ. Then, the assumption $P^{\rm obs} = P^{\rm th}(1+\alpha)$ would correspond to an optimal choice $\epsilon = 1$ in the large $V_{\rm eff}$ limit, and would also lead to a shift in $\Delta\chi^2_{\rm eff}$ by one unit with respect to the assumption $P^{\rm obs} = P^{\rm th}$. In our case, we obtain the same shifting while assuming statistically independent errors for each data point.

Finally, the likelihood can be simplified to

$$\mathcal{L} = \Pi_b \mathcal{N}_b \exp\left[-\frac{1}{2}\int_{-1}^{1}\frac{d\mu}{2}\int_{k_{\rm min}}^{k_{\rm max}}\frac{dk_{\rm ref}}{k_{\rm ref}}\frac{\left(\frac{H_{\rm ref}}{D_{A\rm ref}^2}P_g^{\rm obs} - \frac{H}{D_A^2}P_g^{\rm th}\right)^2}{\frac{(2\pi)^2}{k_{\rm ref}^3 V_{\rm survey}}\left(\frac{H}{D_A^2}P_g^{\rm th} + \frac{H}{D_A^2}\frac{1}{n_g}\right)^2 + \left(\alpha\frac{H}{D_A^2}P_g^{\rm th}\right)^2 B\ln\frac{k_{\rm max}}{k_{\rm min}}}\right], \tag{A.27}$$

where we omitted the argument $\bar{z}_b$ in the functions $V_{\rm survey}$, D_A, H and n_g. This is exactly the relation implemented in our code.

A.5 Accounting for an extra neutrino-related error

The impact of massive neutrinos on non-linear corrections to the power spectrum has been investigated in [24]. By comparing with N-body simulations including neutrino particles, the authors of [24] re-calibrated HALOFIT, with a new neutrino mass dependent correction. This fitting procedure is of course not perfect and adds a systematic error growing with the neutrino mass. It was found that the leading error can be described with a correction

$$P_{NL}(k) = P_{NL}^{\rm halofit}(k)(1 + e_\nu \sigma_\nu(k,z)), \qquad \sigma_\nu(k,z) = \frac{\ln[1+k/k_\sigma(z)]}{1+\ln[1+k/k_\sigma(z)]} f_\nu \tag{A.28}$$

with $f_\nu \equiv \omega_\nu/\omega_m$, and e_ν is an unknown correction of unit variance, that we will treat as a Gaussian nuisance parameter. Hence our final definition of the likelihood accounting for both types of error reads

$$\mathcal{L} = \mathcal{N}\exp\left[-\frac{1}{2}\int_{-1}^{1}\frac{d\mu}{2}\int_{k_{\rm min}}^{k_{\rm max}}\frac{dk_{\rm ref}}{k_{\rm ref}}\frac{(P^{\rm obs} - [P^{\rm th}(1+e_\nu\sigma_\nu)])^2}{[P^{\rm th}(1+e_\nu\sigma_\nu)]^2\left[\frac{(2\pi)^2}{k_{\rm ref}^3 V_{\rm eff}} + \alpha^2 B\ln\frac{k_{\rm max}}{k_{\rm min}}\right]}\right] \times \frac{1}{\sqrt{2\pi}}\exp\left[-\frac{1}{2}e_\nu^2\right], \tag{A.29}$$

where we omitted the argument $(k_{\rm ref}, \mu, \bar{z})$ of the functions $P^{\rm obs}$, $P^{\rm th}$, σ_ν, α_ν and $V_{\rm eff}$. Note that the correction proportional to e_ν should not be added to $P^{\rm obs}$ since we are assuming for simplicity that the fiducial value of e_ν in the mock data is zero.

B. Cosmic shear survey implementation

B.1 Observed spectrum

As in e.g. [16, 15], we define the likelihood of the shear auto or cross-correlation power spectrum in bins i and j:

$$C_l^{ij} = H_0^4 \int_0^\infty \frac{dz}{H(z)} W_i(z)\, W_j(z)\, P_{\rm NL}\left(k = \frac{l}{r(z)}, z\right) \ . \tag{B.1}$$

Here, $W_i(z)$ is the window function of the i'th bin. It can be evaluated as a function of the radial distribution of galaxies in each redshift bin, $D_i(z)$, obtained by convolving the full radial distribution $D(z)$ with the photometric redshift uncertainty function $\mathcal{P}(z, z_{\rm ph})$, multiplied the top-hat window function of each bin:

$$W_i(z) = \frac{3}{2}\Omega_m(1+z)F_i(z) \tag{B.2}$$

$$F_i(z) = \int_0^\infty \frac{n_i(z_s)(r(z_s) - r(z))}{r(z_s)} dz_s \tag{B.3}$$

$$n_i(z) = \frac{D_i(z)}{\int_0^\infty D_i(z')dz'} \tag{B.4}$$

$$D_i(z) = \int_{z_i^{\rm min}}^{z_i^{\rm max}} \mathcal{P}(z, z_{\rm ph})\, D(z_{\rm ph})\, dz_{\rm ph} \ . \tag{B.5}$$

The radial distribution $D(z)$ can be arbitrarily normalized, since $n_i(z)$ is anyway normalized to one. We will assume that the photometric redshift uncertainty function is normalized to $\int_0^\infty \mathcal{P}(z, z_{\rm ph})dz_{\rm ph} = 1$, but a different normalization would not impact the final result for the same reason as for $D(z)$. The noise spectrum contaminating the measurement of C_l^{ij} is given by the diagonal matrix in ij space:

$$N_l^{ij} = \delta_{ij}\langle\gamma_{rms}^2\rangle n_i^{-1} \ , \tag{B.6}$$

where $\langle\gamma_{rms}^2\rangle^{1/2}$ is the root mean square intrinsic shear (like in the forecasts of the Euclid Red Book [1], we assume that this quantity is equal to 0.30), and n_i is the number of galaxies per steradian in the i'th bin, given by

$$n_i = 3600\, d\, (180/\pi)^2 \hat{n}_i \ , \tag{B.7}$$

where d is the full number of galaxies per square arcminute in all bins, and $\hat{n}_i$ is the fraction of galaxies in the i'th bin, given by:

$$\hat{n}_i = \frac{\int_{z_i^{min}}^{z_i^{max}} D(z)}{\int_0^\infty D(z)} \ . \tag{B.8}$$

We used the survey specifications for $D(z)$, $\mathcal{P}(z)$, d and f_{sky} detailed in Appendix B.3.

Using $dz/dr = H$, we can write the same integrals in a different way (used in other papers and in our code):

$$C_l^{ij} = \frac{9}{16}\Omega_m^2 H_0^4 \int_0^\infty dr\, r^{-2} g_i(r)\, g_j(r)\, P\left(k = \frac{l}{r}, z(r)\right) \tag{B.9}$$

with

$$g_i(r) = 2r(1+z(r)) \int_0^\infty dr_s \frac{\eta_i(r_s)(r_s - r)}{r_s} \tag{B.10}$$

$$\eta_i(r) = H(r) n_i(z(r)) \tag{B.11}$$

and $n_i(z)$ is the same as before.

B.2 Likelihood

Let's assume some theoretical spectra $C_l^{\mathrm{th\,ij}}$ (here, the spectra of each model that we want to fit to the data, exploring the space of free cosmological parameters), and some observed spectra $\tilde{C}_l^{\mathrm{obs\,ij}}$. The matrix $\tilde{\mathbf{C}}_l^{\mathrm{obs}}$ of element $\tilde{C}_l^{\mathrm{obs\,ij}}$ is called the data covariance matrix. It can be inferred from the observed multipoles $a_{lm}^{\mathrm{obs}\,i}$, which are Gaussian distributed with a variance independent of m in an ideal full-sky experiment, so that

$$\tilde{C}_l^{\mathrm{obs\,ij}} = (2l+1)^{-1} \sum_{m=-l}^{l} [a_{lm}^{\mathrm{obs\,i}*} a_{lm}^{\mathrm{obs\,j}}] \ . \tag{B.12}$$

For a parameter forecast, instead of the covariance matrix of mock data, we can use some fiducial spectra corrected by the noise spectra of the experiment at hand:

$$\tilde{C}_l^{\mathrm{obs\,ij}} = C_l^{\mathrm{fiducial\,ij}} + N_l^{ij} \ . \tag{B.13}$$

This data covariance matrix should be compared with the theoretical covariance matrix defined as

$$\tilde{C}_l^{\mathrm{th\,ij}} = C_l^{\mathrm{th\,ij}} + N_l^{ij} \ . \tag{B.14}$$

We define the determinant of these $N \times N$ symmetric matrices:

$$d_l^{\mathrm{th}} = \det\left(\tilde{C}_l^{\mathrm{th\,ij}}\right) \tag{B.15}$$

$$d_l^{\mathrm{obs}} = \det\left(\tilde{C}_l^{\mathrm{obs\,ij}}\right) \ . \tag{B.16}$$

The determinants are homogeneous polynomials of order N in the spectra, e.g. for $N = 2$:

$$d_l^{\mathrm{th}} = \tilde{C}_l^{\mathrm{th\,11}} \tilde{C}_l^{\mathrm{th\,22}} - (\tilde{C}_l^{\mathrm{th\,12}})^2 \ . \tag{B.17}$$

The quantity d_l^{mix} can be built starting from d_l^{th}, and replacing one after each other the theoretical spectra $\tilde{C}_l^{\mathrm{th}\,ij}$ by the corresponding $\tilde{C}_l^{\mathrm{obs}\,ij}$, e.g. for $N = 2$:

$$d_l^{\mathrm{mix}} = \tilde{C}_l^{\mathrm{obs\,11}} \tilde{C}_l^{\mathrm{th\,22}} + \tilde{C}_l^{\mathrm{th\,11}} \tilde{C}_l^{\mathrm{obs\,22}} - 2\,\tilde{C}_l^{\mathrm{th\,12}} \tilde{C}_l^{\mathrm{obs\,12}} \ . \tag{B.18}$$

So, d_l^{mix} is always linear in the $\tilde{C}_l^{\mathrm{obs}\,ij}$'s. By construction, when $\tilde{C}_l^{\mathrm{th\,ij}} = \tilde{C}_l^{\mathrm{obs\,ij}}$, one has $d_l^{mix} = N d_l^{\mathrm{th}} = N d_l^{\mathrm{obs}}$. Since in an ideal full-sky experiment, the different multipoles are uncorrelated in (l, m) space, the likelihood of the observed spectra given the theoretical spectra is as simple as:

$$\mathcal{L} = \mathcal{N} \Pi_{lm} \left\{ \frac{1}{(d_l^{\mathrm{th}})^{1/2}} \exp\left[-\frac{1}{2} \mathbf{a}_{lm}^{\mathrm{obs}\,\dagger} (\tilde{\mathbf{C}}_l^{\mathrm{th}})^{-1} \mathbf{a}_{lm}^{\mathrm{obs}} \right] \right\} \ , \tag{B.19}$$

where $\mathbf{a}_{lm}^{\rm obs} = \left\{a_{lm}^{\rm obs\,i}\right\}$ is the N-dimensional vector of observed multipoles in each bin, $\tilde{\mathbf{C}}_l^{\rm th}$ is the theoretical covariance matrix of element $C_l^{\rm th\,ij}$ and $\mathcal{N}$ is a normalisation factor. After some simple algebra[8], the likelihood simplifies to

$$\mathcal{L} = \mathcal{N}\,\Pi_l \left\{ \frac{1}{(d_l^{\rm th})^{1/2}} \exp\left[-\frac{(2l+1)}{2} \frac{d_l^{mix}}{d_l^{\rm th}} \right] \right\} \ . \tag{B.20}$$

The effective chi square

$$\chi^2_{\rm eff} \equiv -2\ln\mathcal{L} = -2\ln\mathcal{N} + \sum_l (2l+1)\left(\frac{d_l^{mix}}{d_l^{\rm th}} + \ln d_l^{\rm th} \right) \ , \tag{B.21}$$

reaches its minimum for $\tilde{\mathbf{C}}_l^{obs} = \tilde{\mathbf{C}}_l^{th}$, corresponding to

$$\chi^{2\,\rm min}_{\rm eff} \equiv -2\ln\mathcal{L}_{\rm max} = -2\ln\mathcal{N} + \sum_l (2l+1)\left(N + \ln d_l^{\rm obs} \right) \ . \tag{B.22}$$

The χ^2 relative to the best-fit model is then equal to

$$\Delta\chi^2_{\rm eff} \equiv -2\ln\frac{\mathcal{L}}{\mathcal{L}_{\rm max}} = \sum_l (2l+1)\left(\frac{d_l^{mix}}{d_l^{\rm th}} + \ln\frac{d_l^{\rm th}}{d_l^{\rm obs}} - N \right) \ . \tag{B.23}$$

Finally, a first-order approximation to account for the limited sky coverage of a given experiment, consists of increasing the cosmic variance by a factor $f_{\rm sky}^{-1/2}$, equivalent to postulating:

$$\Delta\chi^2_{\rm eff} \equiv \sum_l (2l+1) f_{\rm sky}\left(\frac{d_l^{mix}}{d_l^{\rm th}} + \ln\frac{d_l^{\rm th}}{d_l^{\rm obs}} - N \right) \ . \tag{B.24}$$

This is precisely the expression used in the code.

B.3 Survey specifications

A given survey is specified by $D(z)$, $\mathcal{P}(z)$, d, and finally by the covered faction of the sky f_{sky}; it can then be decomposed in redshift bins according to some strategy defined by the user. For a *Euclid*-like experiment we use the same characteristics as in the Euclid Red Book [1]:

$$D(z) = z^2 \exp[-(z/z_0)^{1.5}] \quad \text{for} \quad z < z^{max} = 3.5 \tag{B.25}$$
$$\text{with mean redshift} \quad z_{\rm mean} = 1.412 z_0 = 0.9$$
$$\mathcal{P}(z, z_{\rm ph}) = \frac{1}{\sqrt{2\pi\sigma^2_{\rm ph}}} \exp\left[-\frac{1}{2}\left(\frac{z - z_{\rm ph}}{\sigma_{\rm ph}} \right)^2 \right] \tag{B.26}$$
$$\text{with} \quad \sigma_{\rm ph} = 0.05(1+z)$$
$$d = 30\,\text{arcmn}^{-2} \tag{B.27}$$
$$f_{sky} = 0.375 \ . \tag{B.28}$$

We assume five bins, with the first bin starting at $z_1^{min} = 0$, the last one ending at $z_N^{max} = 3.5$, and bin edges $z_i^{min} = z_{i-1}^{max}$ chosen such that each bin contains the same number of galaxies, i.e. $\hat{n}_i = 1/N$.

[8] in particular, using $A^{-1} = \text{adj}(A)/\det(A)$ where $\text{adj}(A)$ is the adjugate matrix of A, i.e. the transpose of the matrix of cofactors of A.

B.4 Accounting for a global uncorrelated theoretical error

Like for the power spectrum likelihood, taking into account an uncorrelated error on each data point is equivalent to minimizing over a number $L \equiv (l_{\rm max} - l_{\rm min} + 1)$ of nuisance parameters ϵ_l:

$$\Delta\chi^2_{\rm eff} \equiv \sum_{l=l_{\rm min}}^{l_{\rm max}} \min_{-\infty<\epsilon<+\infty} \left[(2l+1) f_{\rm sky} \left(\frac{\tilde{d}_l^{mix}(\epsilon_l)}{\tilde{d}_l^{\rm th}(\epsilon_l)} + \ln \frac{\tilde{d}_l^{\rm th}(\epsilon_l)}{d_l^{\rm obs}} - N \right) + \epsilon_l^2 \right] . \tag{B.29}$$

Here, $\tilde{d}_l^{\rm th}(\epsilon_l)$ stands for the determinant of the theory covariance matrix shifted by the theoretical error covariance matrix R_l^{ij}:

$$\tilde{d}_l^{\rm th}(\epsilon_l) = \det(\tilde{C}_l^{\rm th\,ij} + \epsilon_l R_l^{ij}). \tag{B.30}$$

Similarily, $\tilde{d}_l^{\rm mix}(\epsilon_l)$ stands for the sum of N terms, each one being the determinant of a matrix built from $\tilde{C}_l^{\rm th\,ij} + \epsilon_l R_l^{ij}$, where one column has been replaced by the same column in the observed covariance matrix. Hence the quantity $d_l^{\rm mix}$ defined just above eq. (B.18) is identical to $\tilde{d}_l^{\rm mix}(0)$.

Note that for simplicity, we consider here uncorrelated errors for each l, but not for each bin. This approach could easily be generalized to independent bin errors, at the expense of introducing more nuisance parameters.

In the case of the power spectrum likelihood, we could find an analytical approximation of the nuisance parameter value minimizing the effective χ^2. In the present case, we checked that simple approximate solutions are not accurate enough. We perform a numerical minimization over each ϵ_l within the likelihood routine, using Newton's method.

We define our theoretical error covariance matrix R_l^{ij} in a similar way as for the power spectrum likelihood. We start from the power spectrum relative error function $\alpha(k,z)$ defined in eq.(A.20). The power spectrum error can be propagated to a covariance matrix error E_l^{ij}:

$$E_l^{ij} = \frac{9}{16}\Omega_m^2 H_0^4 \int_0^\infty dr\, r^{-2} g_i(r)\, g_j(r)\, \alpha\left(k = \frac{l}{r}, z(r)\right) P^{\rm th}\left(k = \frac{l}{r}, z(r)\right) . \tag{B.31}$$

The theoretical error matrix R_l^{ij} should be proportional to E_l^{ij}. We normalize it to

$$R_l^{ij} = L^{1/2} E_l^{ij}, \tag{B.32}$$

in such a way that enforcing a one-sigma theoretical error for each l results in an increase of the χ^2 by one (as would be the case for a fully correlated theoretical error with the same amplitude). Then, if one assumes that for each l the observed spectra are equal to the theoretical ones shifted by a one-sigma theoretical error ($\tilde{C}_l^{\rm obs} = \tilde{C}_l^{\rm th} + E_l^{ij}$), the minimization gives (up to a very good approximation) $\epsilon_l = L^{-1/2}$, and

$$\Delta\chi^2_{\rm eff} = \sum_l \left[(2l+1) f_{\rm sky} \left(N + 0 - N\right) + L^{-1} \right] = 1. \tag{B.33}$$

B.5 Accounting for an extra neutrino-related error

Finally, we account for the correlated error modelling neutrino-related uncertainties by multiplying the theoretical power spectrum $P^{\rm th}(k,z)$ by a factor $(1+e_\nu\sigma_\nu(k,z))$, as in equation (A.28), as well as adding e_ν^2 to $\Delta\chi^2_{\rm eff}$. The nuisance parameter e_ν is then marginalized over. Note that the factor $(1+e_\nu\sigma_\nu(k,z))$ should not multiply the observed/fiducial spectrum, as long as we assume a fiducial value of e_ν equal to zero.

References

[1] R. Laureijs, J. Amiaux, S. Arduini, J.-L. Augueres, J. Brinchmann, *et al.*, "Euclid Definition Study Report," arXiv:1110.3193 [astro-ph.CO].

[2] J. Lesgourgues and S. Pastor, "Massive neutrinos and cosmology," *Phys.Rept.* **429** (2006) 307–379, arXiv:astro-ph/0603494 [astro-ph].

[3] A. Mantz, S. W. Allen, and D. Rapetti, "The observed growth of massive galaxy clusters - IV. Robust constraints on neutrino properties," *Mon. Not. R. Astron. Soc.* **406** (Aug., 2010) 1805–1814, arXiv:0911.1788 [astro-ph.CO].

[4] B. A. Reid, L. Verde, R. Jimenez, and O. Mena, "Robust neutrino constraints by combining low redshift observations with the CMB," *JCAP* **1** (Jan., 2010) 3, arXiv:0910.0008 [astro-ph.CO].

[5] S. A. Thomas, F. B. Abdalla, and O. Lahav, "Upper Bound of 0.28 eV on Neutrino Masses from the Largest Photometric Redshift Survey," *Physical Review Letters* **105** (July, 2010) 031301, arXiv:0911.5291 [astro-ph.CO].

[6] S. Saito, M. Takada, and A. Taruya, "Neutrino mass constraint from the Sloan Digital Sky Survey power spectrum of luminous red galaxies and perturbation theory," *Physical Review D* **83** (Feb., 2011) 043529, arXiv:1006.4845 [astro-ph.CO].

[7] M. E. C. Swanson, W. J. Percival, and O. Lahav, "Cosmology at the frontier of neutrino physics," in *American Institute of Physics Conference Series*, J. Kouneiher, C. Barbachoux, T. Masson, and D. Vey, eds., vol. 1446 of *American Institute of Physics Conference Series*, pp. 286–297. June, 2012.

[8] S. Riemer-Sorensen, C. Blake, D. Parkinson, T. M. Davis, S. Brough, *et al.*, "The WiggleZ Dark Energy Survey: Cosmological neutrino mass constraint from blue high-redshift galaxies," *Phys.Rev.* **D85** (2012) 081101, arXiv:1112.4940 [astro-ph.CO].

[9] J.-Q. Xia, B. R. Granett, M. Viel, S. Bird, L. Guzzo, *et al.*, "Constraints on Massive Neutrinos from the CFHTLS Angular Power Spectrum," *JCAP* **1206** (2012) 010, arXiv:1203.5105 [astro-ph.CO].

[10] U. Seljak, A. Slosar, and P. McDonald, "Cosmological parameters from combining the Lyman-α forest with CMB, galaxy clustering and SN constraints," *JCAP* **10** (Oct., 2006) 14, arXiv:astro-ph/0604335.

[11] T. Kitching, A. Heavens, L. Verde, P. Serra, and A. Melchiorri, "Finding Evidence for Massive Neutrinos using 3D Weak Lensing," *Phys.Rev.* **D77** (2008) 103008, arXiv:0801.4565 [astro-ph].

[12] I. Debono, A. Rassat, A. Refregier, A. Amara, and T. Kitching, "Weak lensing forecasts for dark energy, neutrinos and initial conditions," arXiv:0911.3448 [astro-ph.CO].

[13] Y. Wang, W. Percival, A. Cimatti, P. Mukherjee, L. Guzzo, *et al.*, "Designing a space-based galaxy redshift survey to probe dark energy," *Mon.Not.Roy.Astron.Soc.* **409** (2010) 737, arXiv:1006.3517 [astro-ph.CO].

[14] C. Carbone, L. Verde, Y. Wang, and A. Cimatti, "Neutrino constraints from future nearly all-sky spectroscopic galaxy surveys," *JCAP* **1103** (2011) 030, arXiv:1012.2868 [astro-ph.CO].

[15] L. Amendola, V. Pettorino, C. Quercellini, and A. Vollmer, "Testing coupled dark energy with next-generation large-scale observations," *Phys.Rev.* **D85** (2012) 103008, arXiv:1111.1404 [astro-ph.CO].

[16] A. B. Belloso, J. Garcia-Bellido, and D. Sapone, "A parametrization of the growth index of matter perturbations in various Dark Energy models and observational prospects using a Euclid-like survey," *JCAP* **1110** (2011) 010, arXiv:1105.4825 [astro-ph.CO].

[17] C. Carbone, C. Fedeli, L. Moscardini, and A. Cimatti, "Measuring the neutrino mass from future wide galaxy cluster catalogues," *JCAP* **1203** (2012) 023, arXiv:1112.4810 [astro-ph.CO].

[18] A. P. Hearin, A. R. Zentner, and Z. Ma, "General Requirements on Matter Power Spectrum Predictions for Cosmology with Weak Lensing Tomography," *JCAP* **1204** (2012) 034, arXiv:1111.0052 [astro-ph.CO].

[19] J. Hamann, S. Hannestad, and Y. Y. Wong, "Measuring neutrino masses with a future galaxy survey," arXiv:1209.1043 [astro-ph.CO].

[20] A. Refregier, T. Kacprzak, A. Amara, S. Bridle, and B. Rowe, "Noise bias in weak lensing shape measurements," arXiv:1203.5050 [astro-ph.CO].

[21] L. Wolz, M. Kilbinger, J. Weller, and T. Giannantonio, "On the Validity of Cosmological Fisher Matrix Forecasts," arXiv:1205.3984 [astro-ph.CO].

[22] L. Perotto, J. Lesgourgues, S. Hannestad, H. Tu, and Y. Y. Wong, "Probing cosmological parameters with the CMB: Forecasts from full Monte Carlo simulations," *JCAP* **0610** (2006) 013, arXiv:astro-ph/0606227 [astro-ph].

[23] **Virgo Consortium** Collaboration, R. Smith *et al.*, "Stable clustering, the halo model and nonlinear cosmological power spectra," *Mon.Not.Roy.Astron.Soc.* **341** (2003) 1311, arXiv:astro-ph/0207664 [astro-ph].

[24] S. Bird, M. Viel, and M. G. Haehnelt, "Massive Neutrinos and the Non-linear Matter Power Spectrum," *Mon.Not.Roy.Astron.Soc.* **420** (2012) 2551–2561, arXiv:1109.4416 [astro-ph.CO].

[25] M. Viel, M. G. Haehnelt, and V. Springel, "The effect of neutrinos on the matter distribution as probed by the intergalactic medium," *JCAP* **6** (June, 2010) 15, arXiv:1003.2422 [astro-ph.CO].

[26] T. Kitching, A. Amara, F. Abdalla, B. Joachimi, and A. Refregier, "Cosmological Systematics Beyond Nuisance Parameters : Form Filling Functions," arXiv:0812.1966 [astro-ph].

[27] B. Audren, K. Benabed, J. Lesgourgues, and S. Prunet *in preparation* .

[28] A. Lewis and S. Bridle, "Cosmological parameters from CMB and other data: A Monte Carlo approach," *Phys.Rev.* **D66** (2002) 103511, arXiv:astro-ph/0205436 [astro-ph].

[29] J. Lesgourgues, "The Cosmic Linear Anisotropy Solving System (CLASS) I: Overview," arXiv:1104.2932 [astro-ph.IM].

[30] D. Blas, J. Lesgourgues, and T. Tram, "The Cosmic Linear Anisotropy Solving System (CLASS) II: Approximation schemes," *JCAP* **1107** (2011) 034, arXiv:1104.2933 [astro-ph.CO].

[31] A. Lewis, A. Challinor, and A. Lasenby, "Efficient computation of CMB anisotropies in closed FRW models," *Astrophys.J.* **538** (2000) 473–476, arXiv:astro-ph/9911177 [astro-ph].

[32] E. Semboloni, H. Hoekstra, J. Schaye, M. P. van Daalen, and I. J. McCarthy, "Quantifying the effect of baryon physics on weak lensing tomography," arXiv:1105.1075 [astro-ph.CO].

[33] **Euclid Theory Working Group** Collaboration, L. Amendola *et al.*, "Cosmology and fundamental physics with the Euclid satellite," arXiv:1206.1225 [astro-ph.CO].

[34] J. Blazek, R. Mandelbaum, U. Seljak, and R. Nakajima, "Separating intrinsic alignment and galaxy-galaxy lensing," *JCAP* **1205** (2012) 041, arXiv:1204.2264 [astro-ph.CO].

[35] D. Kirk, A. Rassat, O. Host, and S. Bridle, "The Cosmological Impact of Intrinsic Alignment Model Choice for Cosmic Shear," arXiv:1112.4752 [astro-ph.CO].

[36] H. A. Feldman, N. Kaiser, and J. A. Peacock, "Power spectrum analysis of three-dimensional redshift surveys," *Astrophys.J.* **426** (1994) 23–37, arXiv:astro-ph/9304022 [astro-ph].

[37] M. Tegmark, "Measuring cosmological parameters with galaxy surveys," *Phys.Rev.Lett.* **79** (1997) 3806–3809, arXiv:astro-ph/9706198 [astro-ph].

[38] J. Geach, A. Cimatti, W. Percival, Y. Wang, L. Guzzo, *et al.*, "Empirical H-alpha emitter count predictions for dark energy surveys," arXiv:0911.0686 [astro-ph.CO].

[39] A. Orsi, C. Baugh, C. Lacey, A. Cimatti, Y. Wang, *et al.*, "Probing dark energy with future redshift surveys: A comparison of emission line and broad band selection in the near infrared," arXiv:0911.0669 [astro-ph.CO].

5 Observational constraints

5.1 Mass and density from first WMAP data, PRD 69, 123007 (2004)

LAPTH-1025/04, IFIC/04-08

Current cosmological bounds on neutrino masses and relativistic relics

Patrick Crotty* and Julien Lesgourgues
Laboratoire de Physique Théorique LAPTH, B.P. 110, F-74941 Annecy-le-Vieux Cedex, France

Sergio Pastor
Instituto de Física Corpuscular (CSIC-Universitat de València), Ed. Institutos de Investigación, Apdo. 22085, E-46071 Valencia, Spain

(Dated: February 4, 2004)

We combine the most recent observations of large-scale structure (2dF and SDSS galaxy surveys) and cosmic microwave anisotropies (WMAP and ACBAR) to put constraints on flat cosmological models where the number of massive neutrinos and of massless relativistic relics are both left arbitrary. We discuss the impact of each dataset and of various priors on our bounds. For the standard case of three thermalized neutrinos, we find $\sum m_\nu < 1.0\,(\text{resp. } 0.6)$ eV (at 2σ), using only CMB and LSS data (resp. including priors from supernovae data and the HST Key Project), a bound that is quite insensitive to the splitting of the total mass between the three species. When the total number of neutrinos or relativistic relics $N_{\rm eff}$ is left free, the upper bound on $\sum m_\nu$ (at 2σ, including all priors) ranges from 1.0 to 1.5 eV depending on the mass splitting. We provide an explanation of the parameter degeneracy that allows larger values of the masses when $N_{\rm eff}$ increases. Finally, we show that the limit on the total neutrino mass is not significantly modified in the presence of primordial gravitational waves, because current data provide a clear distinction between the corresponding effects.

I. INTRODUCTION

Neutrino properties are among the most difficult to be probed experimentally, due to the weakness of their interactions. Data from particle accelerators tell us that there are only three flavor neutrinos, while neutrino oscillation experiments show evidence for non-zero neutrino masses (for a recent review, see e.g. [1]). Recent results strongly constrain the mass differences of the individual neutrino masses (actually masses squared, Δm^2) and mixing angles, but no definite conclusion can be drawn neither on the absolute scale of neutrino masses, nor on the existence of weakly coupled sterile neutrinos. Fortunately, cosmology is quite sensitive to the neutrino sector (see [2] for a review), and can shed light on these questions, as well as other interesting issues regarding the Early Universe, such as the process of neutrino decoupling from the primordial plasma.

Currently, the most popular cosmological model is the flat adiabatic ΛCDM scenario, in which the present density of the Universe is shared between baryons, Cold Dark Matter (CDM) and a cosmological constant Λ. This model makes rather simplistic assumptions concerning the neutrino sector, consisting only of three ultra-relativistic neutrinos. It turns out that with a more refined description of the neutrino sector, one finds that only small corrections to the standard picture are allowed after comparing with current data on Cosmic Microwave Background (CMB) anisotropies and Large Scale Structure (LSS). However, these small corrections carry enough interesting physical implications to justify an active research effort, in particular after the first releases of the WMAP and SDSS data. The results of this effort are not only new cosmological bounds on neutrino properties but also a better understanding of how the errors depend on (i) the experimental CMB and LSS data, (ii) external priors on the cosmological parameters, (iii) intrinsic parameter degeneracies in the theory of cosmological perturbations, (iv) assumptions concerning the underlying cosmological model and parameter space.

We here perform a new analysis using the most recent LSS (2dF, SDSS) and CMB (WMAP, ACBAR) data and an extended cosmological model with an arbitrary number of massive neutrinos and additional relativistic particles, parametrized via an effective number of neutrinos ($N_{\rm eff}$). We extend the recent work of [3] and those that appeared after the release of WMAP data [4]-[13]. In particular, our underlying model is identical to that of ref. [13], but our analysis differs since we include an extended set of data (such as the SDSS results and a more updated version of the 2dF ones), a new prior on the matter density from SN-Ia [14] and non-linear corrections to the LSS power spectrum

*Present address: Department of Neurosurgery, University of Virginia Health System, PO Box 800420, Charlottesville, VA 22908, USA

on scales $0.1\,h$ Mpc$^{-1} < k < 0.2\,h$ Mpc^{-1}. Furthermore, we increase the number of free parameters to ten, in order to analyze the bounds in the presence of primordial tensor perturbations.

The rest of the paper is organized as follows. After a short summary of the effects of neutrino masses and additional relativistic particles in Sec. II, we describe our analysis method and dataset in Sec. III. We discuss our results and compare with previous works in Sec. IV. Finally, we conclude in Sec. V.

II. EFFECTS OF ADDITIONAL RELATIVISTIC PARTICLES AND MASSIVE NEUTRINOS

Non-standard neutrinos and other weakly-interacting light particles leave their imprint on the evolution of the Universe, both at the level of background quantities and spatial perturbations. Here we describe the main effects of additional relativistic particles, massive neutrinos and their simultaneous presence.

A. Enhanced relativistic energy density ($N_{\rm eff}$)

The density of radiation in the Universe is usually assumed to be given by that of photons and of three thermally decoupled neutrinos. These contributions are of the same order and fix the evolution of the Universe in the radiation-dominated epoch (RD). Thus, if the three neutrinos did not decouple thermally, or in the presence of sterile neutrinos, the total density of the Universe during RD (as a function of the photon temperature T_γ) would be significantly affected, producing a change in the time of equality between radiation and matter, and in the sound horizon at the time of decoupling. These changes are known to shift the angular scale of the acoustic peaks in the CMB anisotropy spectrum as well as their amplitude (mainly, through the early integrated Sachs-Wolfe effect). They also have an impact on the matter power spectrum $P(k)$, because a shorter matter-dominated stage implies less growth for perturbations inside the Hubble radius. As a consequence, the wave-length corresponding to the maximum in $P(k)$ will be shifted proportionally to the Hubble scale at the time of equality. Thus, the effect of $N_{\rm eff}$ is mainly to change the background evolution. However, ultra-relativistic particles also have a smaller effect directly at the level of perturbations, explained in detail in Ref. [15].

All these effects can be parametrized by a single quantity: the effective number of relativistic degrees of freedom during RD, defined by the relation

$$\rho_r = \left[1 + \frac{7}{8}\left(\frac{4}{11}\right)^{4/3} N_{\rm eff}\right] \frac{\pi^2}{15} T_\gamma^4 \,. \tag{1}$$

Here, ρ_r stands for the total energy density of radiation and $\rho_\gamma = (\pi^2/15)\, T_\gamma^4$ is the contribution of photons. The parameter $N_{\rm eff}$ is defined in such way that if neutrinos decoupled following the instantaneous decoupling approximation, $N_{\rm eff}$ just gives the number of flavor families. However, $N_{\rm eff}$ could differ from three in the presence of extra relics (sterile neutrinos, light gravitons, gravitinos, majorons, effects from extra dimensions, etc.) or in the case of non-thermal decoupling. Actually, in the standard case a careful study of non-instantaneous neutrino decoupling shows that $N_{\rm eff} = 3.04$ for three flavor families [16, 17]. Note that $N_{\rm eff}$ is constant only when the neutrinos or the other relics are ultra-relativistic.

The value of $N_{\rm eff}$ is constrained by Big Bang Nucleosynthesis (BBN) from the comparison with the measured primordial abundances of light elements. During the BBN epoch the nuclear reactions freeze out at a scale factor that depends on the expansion rate, which in turn is fixed by the total energy density of radiation. A BBN analysis shows that $N_{\rm eff} = 2.5^{+1.1}_{-0.9}$ (2σ) [11] (see also [18]), which is perfectly compatible with the number of flavor neutrinos.

However, it is interesting to measure $N_{\rm eff}$ independently of BBN (e.g. using CMB and LSS data) for at least two reasons. First of all, because the number $N_{\rm eff}$ could change between the two epochs [19, 20]. A second reason is because the standard BBN model might be a good first-order description, but with possible corrections due to spatial inhomogeneities, leptonic asymmetries, etc., that could be evaluated with an independent measurement of $N_{\rm eff}$.

B. Massive neutrinos

Neutrinos that possess masses larger or of the same order than the relevant photon temperature have different effects than a constant $N_{\rm eff}$. For instance, neutrinos heavier than roughly 10^{-3} eV are not relativistic today. Neutrino masses have implications for the evolution of cosmological fluctuations, both at the level of background quantities and directly on the perturbations.

3

It is well-known that massive neutrinos could account for a significant fraction of the total energy density of the Universe today, unlike relativistic thermal relics ($\Omega_r \sim 5.6 \times 10^{-6}$ per neutrino family). For fully non-relativistic flavor neutrinos, the contribution to the present energy density is directly proportional to the number density. For vanishing neutrino chemical potentials, the total neutrino contribution to the critical density is given by

$$\Omega_\nu = \frac{\sum m_\nu}{93.2 \text{ eV}} h^{-2} \ , \tag{2}$$

where h is the Hubble constant in units of 100 km s^{-1} Mpc^{-1} and $\sum m_\nu$ runs over all neutrino mass states. For fixed neutrino masses, Ω_ν would be enhanced if neutrinos decoupled with a significant dimensionless chemical potential $\xi_\nu \equiv \mu_\nu/T$ (or equivalently, for large relic neutrino asymmetries), simply because their number density would increase. In principle there exist some combinations of pairs $(\xi(\nu_e), \xi(\nu_{\mu,\tau}))$ that pass the BBN test and are not yet ruled out by the CMB+LSS limits on $N_{\rm eff}$ [21]. However, it was recently shown that the stringent BBN bounds on ξ_e apply to all flavors, since flavor neutrino oscillations lead to flavor equilibrium before BBN [22, 23, 24]. The contribution of a potential relic neutrino asymmetry is limited to such low values that it can be safely ignored.

When the density of the other fluids (photons, CDM, baryons, dark energy) is kept fixed, the sum over the neutrino masses $\sum m_\nu$ has a direct repercussion on the geometry of the Universe. If instead the spatial curvature is kept fixed, the total mass affects the relative contribution Ω_X of the other fluids. In any case, this background effect has an impact on the observable CMB and LSS power spectra. For masses of the order of 1 eV, this signature is rather small, but can be marginally detectable.

In general, neutrinos tend to stream freely across gravitational potential wells, and to erase density perturbations. Free-streaming is efficient on a characteristic scale called the Jeans length, corresponding roughly to the distance on which neutrinos can travel in a Hubble time. For ultra-relativistic neutrinos, the Jeans length is by definition equal to the Hubble radius c/H, but for non-relativistic ones it grows at a slower rate than c/H (in comoving coordinates, it even decreases with time during matter domination). Neutrinos with masses smaller than approximately $T_{\rm dec} \sim 0.3$ eV are still relativistic at the time of last scattering, and their direct effect on the CMB perturbations is identical to that of massless neutrinos. For bigger masses, the decrease of the free-streaming scale is felt by perturbations which enter inside the Hubble radius before decoupling, which results in a small enhancement of the acoustic peaks with respect to the massless situation.

In the intermediate mass range from 10^{-3} eV to 0.3 eV, the transition to the non-relativistic regime takes place during structure formation, and the matter power spectrum will be directly affected in a mass-dependent way. Wavelengths smaller than the current value of the neutrino Jeans length are suppressed by free-streaming. The largest observable wavelengths, which remain always larger than the neutrino Jeans length, are not affected. Finally, there is a range of intermediate wavelengths which become smaller than the neutrino Jeans length for some time, and then encompass it again: these scales smoothly interpolate between the two regimes. The net signature in the matter power spectrum is a damping of all wavelengths smaller than the Hubble scale at the time of the transition of neutrinos to a non-relativistic regime [25]

$$k > k_{\rm nr} = 0.026 \left(\frac{m_\nu \, \Omega_m}{1 \text{ eV}}\right)^{1/2} h \text{ Mpc}^{-1}. \tag{3}$$

where Ω_m is the contribution of matter to the critical density. The damping is maximal for wavenumbers bigger than the current free-streaming wavenumber $k_{\rm FS}$

$$k > k_{\rm FS} = 0.63 \left(\frac{m_\nu}{1 \text{ eV}}\right) h \text{ Mpc}^{-1}. \tag{4}$$

We have summarized both the background and the direct effects of the neutrino masses on the CMB and LSS perturbations. The total signature is difficult to describe analytically. However, one should remember that for masses of order 1 eV or less, the dominant effect is the one induced by free-streaming on the matter power spectrum. Therefore, the usual strategy is to combine CMB and LSS measurements, where the former roughly fix most of the cosmological parameters, while the latter is sensitive to $k_{\rm FS}$ and provides bounds on the neutrino mass.

C. Combined effects

In a situation with N thermalized massive neutrino species, the cosmological model should include an equal number of parameters, namely $(m_1, \ldots, m_N)$. However, at first order such a model could be described by only two parameters, N and the sum of all individual masses $\sum_{i=1,N} m_i$. This choice not only simplifies the problem, but also provides

the correct contribution of neutrinos to the total energy density both at early times, when all neutrinos are ultra-relativistic and the radiation density depends only on N, and at a late epoch when at least one neutrino mass is large compared with the temperature and the density is given in good approximation by the total mass.

However, for a precise description N and $\sum_{i=1,N} m_i$ are not the only relevant parameters. As an example, let us compare two scenarios with three neutrinos but different mass spectra: a degenerate case with (m_0, m_0, m_0) and a case with $(3m_0, \epsilon, \epsilon)$, where $\epsilon \ll m_0$. In both scenarios the neutrino density is the same for early and late stages of the Universe. But at intermediate temperatures of the order $m_0 \lesssim T_\nu \lesssim 3\, m_0$, the energy densities are different. It is easy to show that the expansion rate is temporarily enhanced in the second scenario, but this will only have a small signature in the CMB spectrum for $m_0 \gtrsim 0.2$ eV. On the other hand, the free-streaming wavenumber $k_{\rm FS}$ of the heaviest neutrino is larger in the second scenario. Thus, in principle we expect more damping and sharper bounds on the mass in the degenerate case.

Nowadays, after many years of experimental effort, we know that neutrinos must be massive in order to explain the evidences for flavor oscillations from measurements of atmospheric and solar neutrinos, independently confirmed by data from the detection of neutrinos from artificial sources at experiments such as K2K and Kamland. These results lead to specific differences between the individual neutrino masses, at two different scales: $\Delta m^2_{\rm atm} \simeq 2.5 \times 10^{-3}$ eV^2 and $\Delta m^2_{\rm sun} \simeq 7 \times 10^{-5}$ eV^2 [1]. But one of the masses remains unconstrained, which reflects the fact that oscillation experiments can not fix the absolute scale of neutrino masses. It is clear that, considering the present cosmological data, in order to have a measurable effect the three neutrinos should have roughly the same mass, following a degenerate scheme (m_0, m_0, m_0), where $m_0 \gtrsim 0.2$ eV.

On the other hand, the positive results from the LSND experiment point to neutrino oscillations with $\Delta m^2 \sim \mathcal{O}(1\ {\rm eV}^2)$. The less disfavored scenario that could explain the LSND data, together with the results of atmospheric and solar neutrino experiments, contains 4 neutrinos following a 3+1 scheme where one of them is much heavier than the others (see for instance [26]) and the fourth neutrino must be sterile. It has been shown [27, 28] that all four neutrino models lead to a full thermalization of the sterile neutrino before BBN, so they are disfavored by BBN. However, current CMB and LSS data can not completely rule out this possibility [7, 13].

The most general scenario is that of a cosmological model with $N^{\rm nr}$ thermally-decoupled massive neutrinos and extra relativistic degrees of freedom, parametrized by $N^{\rm r}$ not necessarily integer. This model is described by a set of $N^{\rm nr}+1$ parameters: $(m_1, \ldots, m_{N^{\rm nr}}, N^{\rm r})$. However, since such a parameter space is too large for a systematic analysis we will consider restricted cases described by only two parameters: the total effective neutrino number $N_{\rm eff} = N^{\rm r} + N^{\rm nr}$ and the total mass M. In order to check the impact of the distribution of the total neutrino mass among the individual states, we will study two cases:

- the model that we call *degenerate* has $N_{\rm eff}$ massive neutrinos with the same mass. Let us emphasize that this is a simplified model where the physical interpretation of non-integer values of $N_{\rm eff}$ is not obvious.
- a second model the we denote *1+r* has only one neutrino with a significant mass, while the other $N_{\rm eff} - 1$ species are ultra-relativistic.

These two models are not chosen arbitrarily. First, the *degenerate* model includes the standard situation with only 3 flavor neutrinos degenerate in mass, while the *1+r* model includes the 3+1 scenario described above. Second, and most importantly, the *degenerate* and *1+r* models appear as limiting situations of the general case once the parameters $N_{\rm eff}$ and M have been fixed. Indeed, the former has the smallest possible value of the free-streaming wavenumber, while the latter has the biggest $k_{\rm FS}$. For any intermediate model (like, for instance, the third case studied in [13], with three effectively massless standard neutrinos and $N_{\rm eff} - 3$ species with equal mass), the observational bounds deduced from the CMB and LSS observations should lay between those that we get in the *degenerate* and *1+r* limits.

III. METHOD AND DATA USED

The WMAP spectrum and many other cosmological data can be accurately fitted with a six-parameter flat ΛCDM model [4, 12], described by the Hubble parameter h, the fractional density of matter $\Omega_m = 1 - \Omega_\Lambda$, the baryon density in dimensionless units $\omega_b = \Omega_b h^2$, the optical depth to reionization τ, and finally, the amplitude and the spectral tilt of primordial perturbations (A_s, n_s). Most of our calculations correspond to a model with eight parameters: the six previous ones plus $N_{\rm eff}$ and M, as previously defined for the *degenerate* and *1+r* models. We will also study the consequences of the presence of a background of primordial gravitational waves, which would contribute to the CMB anisotropy spectrum. For this case, our parameter space will be ten-dimensional, adding the tensor-to-scalar ratio r and the tensor tilt n_t. In all cases, we use the CMBFAST code [29] to calculate the power spectra.

In order to compare the theoretical cosmological models with current observations, we use a Bayesian grid-based method described in some previous works (e.g. [5]), instead of the widely used Monte Carlo Markov Chains (MCMC)

technique employed for instance in [12, 30]. The former has the inconvenient of being considerably slower from the computational point of view, and the advantage of being very robust if the hypersurfaces with the same likelihood in parameter space have very complicated shapes (for instance, an elongated and curved *banana* shape). Also, the MCMC method cannot deal with likelihood distributions with nearly degenerate local minima; mathematically, the existence of local minima cannot be disproved, but in practice, using current data and the wide variety of models discussed in the literature, such a situation never appeared. In order to analyze unusual models with many parameters, it is safe to use at least once a grid-based method, avoiding surprises that could arise from parameter degeneracies. However, our analysis always shows quasi-ellipsoidal likelihood contours for various combinations of parameters. Thus we believe that a MCMC method would give similar results.

For each combination of data set and priors, we plot the Bayesian likelihood of each point in the two-dimensional space of neutrino parameters $(M, N_{\rm eff})$ after marginalization over the other free parameters. Actually, for simplicity we approximate the integration process required for a true marginalization by a maximization of the likelihood over the remaining parameter space. Integration and maximization are known to be equivalent in the case of a multigaussian likelihood distribution and we expect the maximization technique to be reasonably accurate in our case, where we obtained quasi-ellipsoidal contours. We checked this explicitly by computing the marginalized likelihood of each of the six ΛCDM parameters: our results are very close to those of [4, 12], obtained with a MCMC technique and marginalized by integration over the likelihood. Of course, our maximization routine needs to compute the likelihood not only at grid points, but also in between. At a given point in parameter space, this is done by interpolating quadratically each value of the C_l and $P(k)$ from the nearest neighbors of the grid.

Our CMB data include the 1348 correlated points of the Wilkinson Microwave Anisotropy Probe (WMAP), which measure the temperature × temperature (TT) [31] and temperature × E-polarization (TE) [32] correlation functions on the CMB sky. WMAP provides the best available data on multipoles $l \leq 900$. For constraining the TT spectrum on smaller scales, we employ the results of the Arcminute Cosmology Bolometer Array Receiver (ACBAR) experiment [33, 34]. We remove the highest band powers (probing the region $l > 1800$) which could be contaminated by foregrounds. The published ACBAR band powers are decorrelated, so it is self-consistent to use only the first 11 points of data.

Our LSS data set consists of 32 correlated points from the 2 degree Field (2dF) galaxy redshift survey [35], covering the range $0.02\,h\ {\rm Mpc}^{-1} < k < 0.15\,h\ {\rm Mpc}^{-1}$, and of 19 decorrelated points from the Sloan Digital Sky Survey (SDSS) [36] in the range $0.015\,h\ {\rm Mpc}^{-1} < k < 0.20\,h\ {\rm Mpc}^{-1}$. In order to compare the smallest wavelengths with the data, it is necessary to take into account small deviations with respect to the linear power spectrum. Following the analysis in [12], we compute non-linear corrections for each point in parameter space using the numerical procedure described in Appendix C of [37]. Since these corrections rely on N-body simulations of a pure CDM Universe they might not be perfectly optimized for hot plus cold dark matter. However, the models studied here include only a small fraction of non-relativistic neutrino density. Therefore, at first order the fitting formula of [37] should be reasonably accurate in our case (and certainly better than introducing no corrections at all). Each redshift survey is expected to constrain the total matter power spectrum modulo a global normalization factor called the bias b. Unless otherwise stated, all our results were obtained after marginalizing over the 2dF and SDSS bias, treated like two free parameters.

We will also use a prior on the current value of the Hubble parameter, measured by the Hubble Space Telescope (HST) Key project [38]: $h = 0.72 \pm 0.08$ (1σ). Finally, we will impose some constraints on the current density of the cosmological constant deduced from the redshift dependence of type Ia supernovae luminosity. For a flat universe, Perlmutter et al. [39] give a conservative bound $\Omega_m = 0.28 \pm 0.14$ (1σ) that we denote as the SN99 prior. In addition, we will calculate the impact of using the more restrictive result $\Omega_m = 0.28 \pm 0.05$ (1σ) from the recent work by Tonry et al. [14], that we label the SN03 prior.

IV. RESULTS AND COMPARISON WITH PREVIOUS WORKS

A. Degeneracies and priors

In order to understand the impact of each data set and prior on the final results, we will introduce them step by step in the calculation of the likelihood. We will first focus on the *degenerate* model.

We start using only CMB and LSS data without any prior, apart from the top-hat priors defined implicitly by the boundaries of our grid. We look for the two-dimensional probability distribution of the neutrino parameters in the range $0 < M < 2.25\,{\rm eV}$ and $1 < N_{\rm eff} < 9$. We find that most of this parameter space is allowed at 2σ, as shown in panel (a) of Fig. 1. Actually some of the grid boundaries are reached by the allowed models [55], unlike in the rest of our analysis where they have no influence on the 2σ allowed regions.

The physical explanation for such loose constraints is well-known: when the density of relativistic relics is left free,

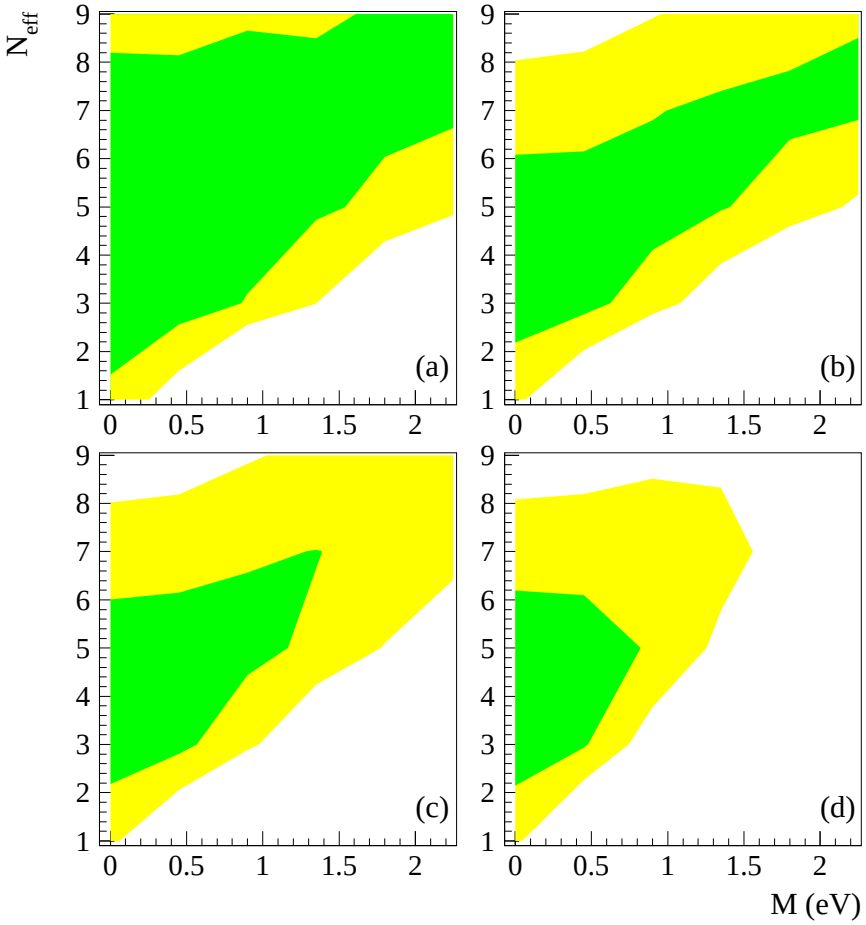

FIG. 1: Two-dimensional likelihood in $(N_{\rm eff}, M)$ space, marginalized over the six remaining parameters of the model. We plot the 1σ (green / dark) and 2σ (yellow / light) allowed regions. Here we used CMB (WMAP & ACBAR) and LSS (2dF & SDSS) data, adding different external priors as defined in section III: (a) no priors, (b) HST, (c) HST+SN99, (d) HST+SN03.

there is a parameter degeneracy between

$$\omega_r \equiv \Omega_r h^2 = 2.47 \times 10^{-5}\, h^2 \left(\frac{T_{\rm CMB}}{2.725\,{\rm K}}\right)^4 \left[1 + \frac{7}{8}\left(\frac{4}{11}\right)^{4/3} N_{\rm eff}\right] \tag{5}$$

and $\omega_m \equiv \Omega_m h^2$. Indeed, one can vary these two quantities in the same proportion while keeping fixed $z_{\rm eq}$, the redshift of equality between matter and radiation. In order to remove this degeneracy, it is necessary to impose some priors on h and Ω_m. Thus we repeat the same analysis, using now the HST prior. In this case, we obtain a band of allowed models shown in panel (b) of Fig. 1. This region stretches up to the maximal values of M and $N_{\rm eff}$ in our grid, so we cannot derive yet limits on these parameters. However, the other grid bounds are now irrelevant, since none of the models allowed at 2σ ever reaches them. The 1σ preferred region includes models with $(M = 0,\ N_{\rm eff} = 3.04)$, showing that there is no evidence for massive neutrinos and/or extra relativistic degrees of freedom. However, it is interesting to see that large departures from the standard ΛCDM model cannot be excluded.

These results show clearly how difficult is to put bounds on the neutrino mass in presence of an excess of relativistic relics during RD, and vice versa. For instance, if we assume $N_{\rm eff} = 3$, we get a 2σ upper bound $M < 0.8$ eV, while for $N_{\rm eff} = 6$ this bound spectacularly increases to $M < 2.2$ eV. This trend was already observed in [7, 8, 13, 40], and can be explained as follows. Suppose that we start from the best-fit standard model with $(M = 0,\ N_{\rm eff} = 3)$, and

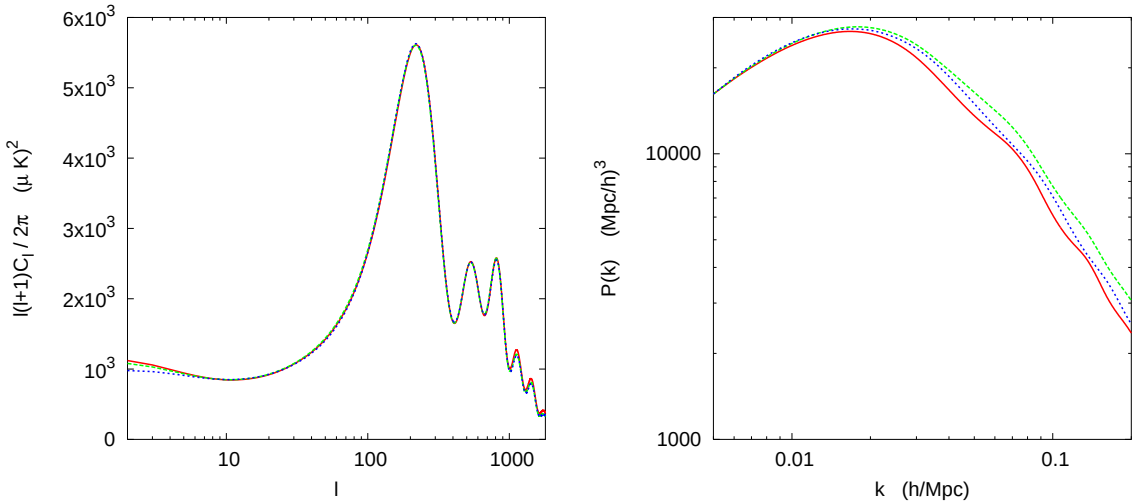

FIG. 2: Illustration of the main parameter degeneracy affecting our results. For three particular models, we plot on the left the CMB temperature spectrum (normalized to WMAP) and on the right the matter power spectrum (two of them have been rescaled by hand for clarity). See the main text for details.

that we increase $N_{\rm eff}$ in such way that the radiation density in the early Universe is multiplied by a factor α. Then, in order to keep the CMB power spectra roughly constant, we should maintain a fixed value both for $z_{\rm eq}$ and Ω_Λ. This would be achieved with a transformation of the type $(\omega_m, h) \longrightarrow (\alpha\,\omega_m, \sqrt{\alpha}\,h)$. However, it is well-known that the shape of the matter power spectrum is given roughly by the parameter $\Gamma = \Omega_m h$, that scales like $\sqrt{\alpha}\,\Gamma$ with the previous transformation, meaning that the spectrum will have more power on small scales relatively to large scales. A neutrino mass can balance this increase through the free-streaming effect. Therefore, models with high values of $N_{\rm eff}$ are compatible with larger neutrino masses.

We illustrate this parameter degeneracy in Fig. 2, where we show the CMB temperature spectrum (normalized to WMAP) and the matter power spectrum for three particular models. The first model (red/solid curves) is the best-fit model for the standard case $(M, N_{\rm eff}) = (0, 3)$. In the second model (green/dashed curves), we have increased the number of degrees of freedom to $N_{\rm eff} = 7$ and performed the transformation on $(\omega_m,\, h)$ as previously discussed, leaving both z_{eq} and Ω_M invariant. We have also increased n_s a little bit. On the CMB figure it is difficult to distinguish the curves because they perfectly overlap, especially for the best measured scales (those of the first acoustic peak), while the difference at $l < 10$ is masked by cosmic variance. But as expected, the shape of the matter power spectrum is modified, with more power on small scales relatively to large scales. This leaves plenty of room for models with a significant neutrino mass and free-streaming effect, like the one featured here (blue/dotted curve) which has $(M, N_{\rm eff}) = (2.25\,{\rm eV}, 7)$.

In order to obtain bounds on the mass, it is necessary to add more restrictive priors. In particular, the supernova priors should help to better constrain Ω_m (around the central value 0.28) and therefore also the shape parameter Γ (around $\Omega_m h = 0.28 \times 0.72 = 0.20$). This value of Γ is in very good agreement with the constraint obtained from LSS data, assuming no neutrino mass: the SDSS power spectrum points to $\Gamma = 0.21 \pm 0.03$ [36]. Therefore, we expect the SN prior to restrict the possibility of a large neutrino free-streaming effect and to improve the upper bound on M. This is what we observe by successively adding the SN99 and SN03 priors in our analysis. The corresponding contours, shown in panels (c) and (d) of Fig. 1, are the main results of this work. With the SN03 prior, our one-dimensional bounds on the effective neutrino number (marginalized over M) read $1.6 < N_{\rm eff} < 7.2$ at 2σ, in very good agreement with our previous results $1.4 < N_{\rm eff} < 6.8$ [5] obtained without SDSS, no SN priors and fixing $M = 0$. The one-dimensional upper bound on the total neutrino mass (marginalized over $N_{\rm eff}$) is $M < 1.1$ eV at 2σ. For comparison, we list the bounds for fixed integer values of $N_{\rm eff}$ are in Table I, for different priors. Since we use more recent 2dF and SDSS data, as well as more restrictive SN priors, we are not surprised to find stronger bounds than Hannestad & Raffelt [13].

	degenerate		1+r	
$N_{\rm eff}$	no priors	HST+SN03	no priors	HST+SN03
3	1.0	0.6	0.8	0.6
4	1.5	0.8	1.2	0.8
5	2.0	1.0	1.6	1.1
6	–	1.1	1.9	1.4
7	–	1.0	–	1.5

TABLE I: The 2σ upper bound on the total neutrino mass M (eV), after marginalization over the six cosmological parameters of the flat ΛCDM model, for particular values of $N_{\rm eff}$. We show the results for two limiting cases of splitting the total mass between the neutrino states: *degenerate* (all neutrinos with the same mass) and *1+r* (one massive neutrino and the other treated as relativistic relics). Here we have used the full CMB and LSS data set, either alone (no priors) or combined with the HST and SN03 priors. For large $N_{\rm eff}$ values and in absence of priors, the upper bound is larger than the maximal value of M in our grid (2.25 eV).

B. Role of LSS data

So far we have used the LSS data as an indication of the shape of the matter power spectrum, but not its overall amplitude. This amplitude is difficult to measure, because of possible differences between the two-point correlation function of luminous galaxies and that of matter, a problem known as the bias uncertainty. The 2dF team has established that the bias b is almost scale-independent, and derived some constraints either on the redshift distortion parameter $\beta = \Omega_m^{0.6}/b$ [41] or directly on b [42]. These two results must be employed with great care since the bias is expected to depend on the mean luminosity and redshift of each particular galaxy sample. In order to use a self-consistent bias prior, we would need to compute some correction factors for each model (see for instance refs. [8, 30, 43]). This technically difficult procedure, that relies on many assumptions, is beyond the goal of the present paper and we prefer to conservatively discard any bias prior, as in [12]. Just for indication, we tried to repeat the previous analysis with a very naive bias prior. Instead of leaving the 2dF bias as a free parameter, we tried to add the constraint $\Omega_m^{0.6}/b_{\rm 2dF} = 0.43 \pm 0.07$ [41] to our full set of data and priors (which includes all the CMB+LSS data, the HST prior, and one of our two supernovae priors). As shown in panel (a) of Fig. 3, our results remain unchanged. This is consistent with the analysis of Elgarøy & Lahav [8], who treat the bias prior in a detailed way and find no impact on the neutrino mass determination.

Since the LSS data plays a crucial role in constraining the neutrino mass, it is worth comparing the impact of the 2dF and SDSS power spectra. We go back to a data set consisting of CMB+LSS+HST+SN99, and remove either the SDSS or 2dF spectrum from the analysis. The results, shown in panels (b) and (c) of Fig. 3, should be compared with the combined analysis previously shown in (c) of Fig. 1. The SDSS power spectrum appears to be much more conservative, in good agreement with previous papers: the WMAP+SDSS constraint on the neutrino mass for $N_{\rm eff} = 3$ is as large as $M < 1.74$ eV [12], while a WMAP+other CMB+2dF analysis gives $M < 0.69$ eV [4]. Consistently, our combined analysis gives intermediate results: for $N_{\rm eff} = 3$ our WMAP+ACBAR+2dF+SDSS bound is $M < 0.9$ eV. Our results seem also consistent with the recent analysis in [3], where the corresponding bound $M < 0.75$ eV was found including data from both galaxy surveys up to $k \lesssim 0.15\, h$ Mpc^{-1}.

Note that in order to employ the SDSS data until $k_{\rm max} \simeq 0.20\, h$ Mpc^{-1}, it is crucial to include the non-linear corrections to the matter power spectrum, in particular for the $N_{\rm eff}$ bounds. The panel (d) of Fig. 1 was obtained with all the CMB and LSS data, plus the HST and SN99 priors, but in absence of non-linear corrections. A comparison with Fig. 1c shows that the constraints on $N_{\rm eff}$ are lifted by one unit. This can be easily understood. Fig. 4 shows a typical power spectrum with and without non-linear corrections. The linear power spectrum has less power on small scales, i.e. a smaller effective shape parameter Γ. As explained earlier in this section, this can be easily compensated by an appropriate increase in $N_{\rm eff}$, ω_m and h, while leaving the CMB spectrum almost invariant.

C. Adding tensors

We have discussed so far the dependence of our results under the choice of data set and priors. However, generally speaking, the bounds on a particular parameter also depend on assumptions concerning the underlying cosmological model, a simple six-parameter flat ΛCDM model in our case. It is clear that by adding extra physical ingredients that would compensate the effect of neutrinos, we would relax the bounds on ($N_{\rm eff}$, M). It is inviable to perform a systematic study of all the ΛCDM variants proposed in the literature, but one of them deserves a particular interest. Indeed, the six-parameter ΛCDM relies on the existence of super-horizon cosmological fluctuations at early times,

9

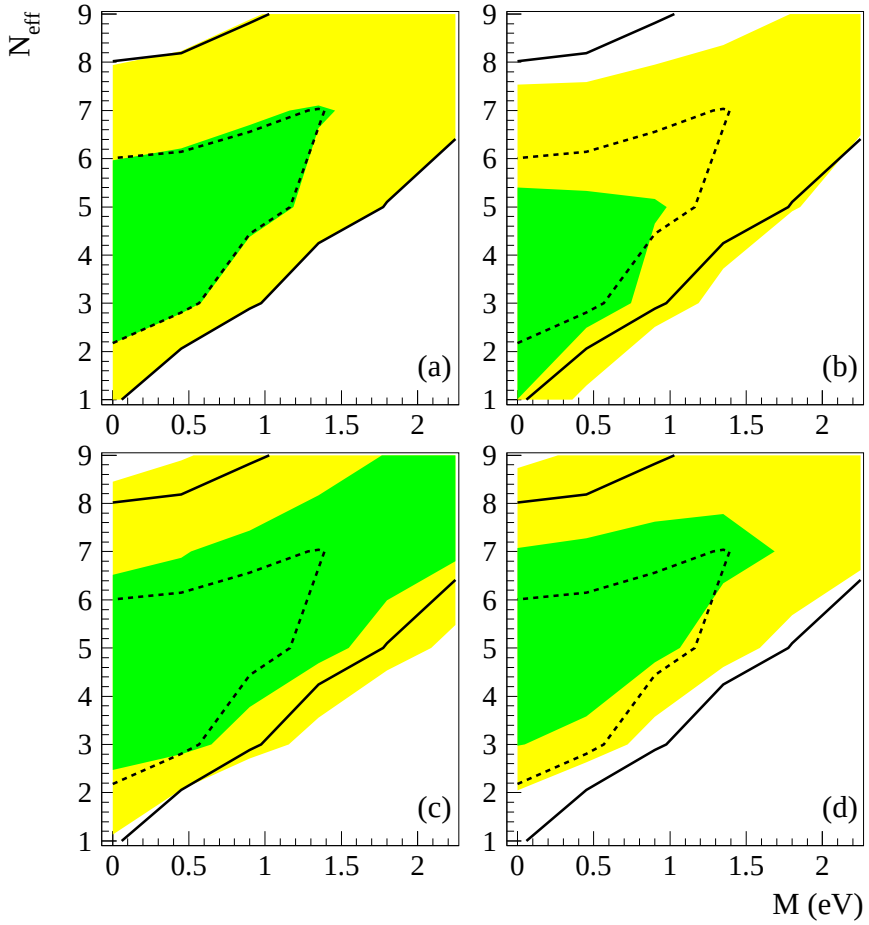

FIG. 3: Impact of various assumptions related to the LSS data set. The default model for which we show 1σ (dashed) and 2σ (solid) contours was obtained with WMAP, ACBAR, 2dF, SDSS, plus the HST and SN99 priors. Each panel shows the 1σ (green / dark) and 2σ (yellow / light) allowed regions (a) when including the 2dF bias prior [41], (b) without the SDSS data, (c) without the 2dF data, (d) without non-linear corrections.

which strongly suggests that perturbations are of inflationary origin. But inflation also predicts a background of primordial tensor perturbations: the question is whether these gravitational waves are large enough to contribute to large-scale CMB anisotropies (fundamentally, this depends on the energy scale of inflation). It is thus important to see how the neutrino parameter bounds evolve in presence of two extra parameters, the relative amplitude and tilt of the primordial tensor spectrum (r, n_t).

Previous analyses [4, 12] showed that for eight-parameter models (flat ΛCDM + tensors) a significant contribution of gravitational waves is disfavored. However, one could expect that in a ten-dimensional model (flat ΛCDM + tensors, with $N_{\rm eff}$ and M), a new parameter degeneracy would show up and relax the various bounds. We performed such an analysis for our full CMB and LSS data set, adding the HST and SN03 priors. The resulting two-dimensional likelihood for ($N_{\rm eff}$, M), marginalized over the other eight parameters, is shown in Fig. 5. It is almost indistinguishable from that with a vanishing contribution of gravitational waves, which shows that the current data is clearly able to distinguish between the respective effects of tensors and neutrinos. Thus the cosmological bound on neutrino masses is robust with respect to tensors. This robustness also holds when including a non-adiabatic, incoherent contribution to the power spectrum such as those predicted by topological defects, as shown in a very recent work [44].

10

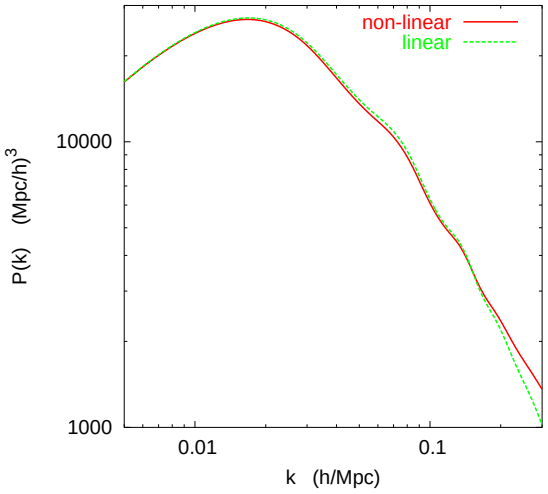

FIG. 4: Matter power spectrum for the best-fit model with $(M, N_{\rm eff}) = (0, 3)$, plotted with and without non-linear corrections. The difference becomes significant in the region $k > 0.15\,h$ Mpc^{-1} probed by the last two points in the SDSS data set.

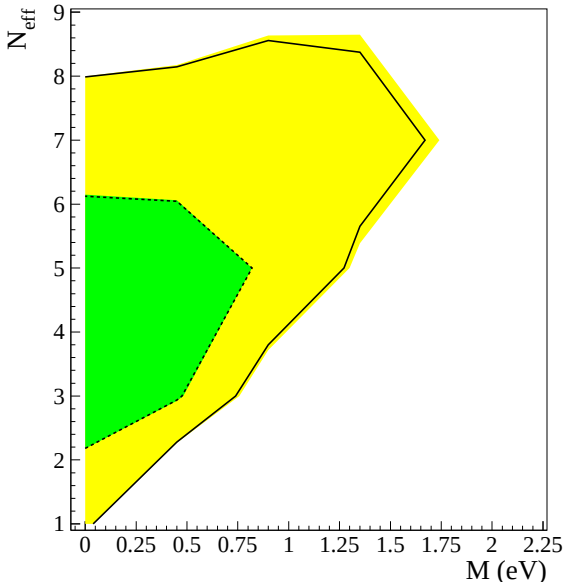

FIG. 5: 1σ (green / dark) and 2σ (yellow / light) allowed regions in (M, $N_{\rm eff}$) space, marginalized over the eight other free parameters of the flat ΛCDM+tensors model. For comparison, we show the contours corresponding to the case with no gravitational waves. The difference is very small, showing the ability of the data to make a clear difference between the effect of neutrinos and gravitational waves.

D. Impact of mass splitting

Our aim is to constrain cosmological models with an arbitrary number of massive neutrinos and with extra relativistic degrees of freedom. However, so far we reduced the analysis to two parameters (M, $N_{\rm eff}$), with the implicit assumption that all neutrinos were degenerate in mass. We have not discussed the fact that for a fixed total number of degrees of freedom $N_{\rm eff}$ and total mass M, the evolution of cosmological perturbations depends on the splitting of the mass between the different species.

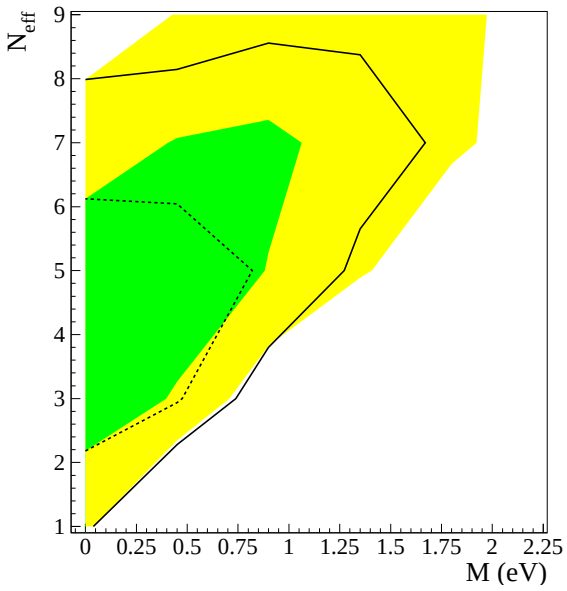

FIG. 6: 1σ (green / dark) and 2σ (yellow / light) allowed regions in (M, $N_{\rm eff}$) space for the *1+r* model, compared with the *degenerate* model (dashed 1σ and solid 2σ contours). Here we have included all CMB and LSS data, plus the HST and SN03 priors.

As explained in section II, for fixed (M, $N_{\rm eff}$), in some sense the opposite case to the *degenerate* model is the *1+r* scenario, for which all the mass corresponds to a single neutrino eigenstate, instead of being equally shared. We built a second grid of *1+r* models and analyzed it with our most restrictive set of data (WMAP+ACBAR+2dF+SDSS) and priors (HST+SN03). We show in Fig. 6 the new allowed regions, compared with the previous ones. In the limit of small mass and small $N_{\rm eff}$, the CMB and LSS power spectra are almost identical in the two cases, because the effect of the mass splitting is second-order with respect to that of the total mass. A priori, this does not guarantee that the (M, $N_{\rm eff}$) iso-likelihood contours are asymptotically equal, because we are doing a Bayesian analysis and the contours are defined with respect to the best-fit model. For instance, in Ref. [13], the best-fit models for the *degenerate* and *1+r* cases correspond to high values of (M, $N_{\rm eff}$) and are different from each other. This explains why the authors find different contours in the two cases even in the massless limit. The same occurs in our analysis when we do not impose any prior. However, when at least the HST prior is taken into account, the best-fit model is very close to $(M, N_{\rm eff}) = (0, 3)$ and the contours only differ at high values of M and $N_{\rm eff}$. As expected from the physical discussion in Sec. II, the model with only one massive neutrino is less constrained: remember that in that case, for a fixed M the free-streaming wavenumber $k_{\rm FS}$ is larger. Therefore, the damping of the matter power spectrum is less efficient. The one-dimensional bounds on the effective number of neutrinos (marginalized over M) now reads $1.6 < N_{\rm eff} < 8.5$ at 2σ, and the limit on the total neutrino mass (marginalized over $N_{\rm eff}$) increases to $M < 1.5$ eV (2σ). The bounds for fixed integer values of $N_{\rm eff}$ are given in the last column of Table I.

V. CONCLUSIONS

We have calculated cosmological bounds on neutrino masses and relativistic relics ($N_{\rm eff}$) using the latest data on CMB (WMAP and ACBAR) and LSS (SDSS and 2dF galaxy surveys) in the framework of an extended flat ΛCDM. In the cases in which a comparison is possible, our results are in good agreement with those of previous analyses [3]-[13]. In the well motivated case of three flavor neutrino with degenerate masses, we found an upper limit on the total masses of $M < 1.0$ (resp. 0.6) eV using only CMB and LSS data and priors (resp. including priors on h and Ω_Λ). The bound for four thermalized neutrinos with only one of them carrying a significant mass is $M < 0.8 - 1.2$ eV, depending on the priors used. Therefore, the 4-neutrino solution to the LSND results is not completely ruled out, but some tension with cosmological data exists, especially if the strong SN03 prior is taken into account.

In the case of arbitrary $N_{\rm eff}$, our results are summarized in Fig. 1 and listed in Table I. They clearly show the

existence of a parameter degeneracy between the total neutrino mass and $N_{\rm eff}$, a trend already observed in previous works [7, 8, 13, 40] that we have explained in Sec. IV. External priors on h and Ω_Λ are found to be of particular importance for constraining respectively $N_{\rm eff}$ and M.

Since the standard ΛCDM model (with its three effectively massless thermal relics) sits within the 1σ preferred region, we find no evidence for exotic physics such as out-of-equilibrium neutrino decoupling, non-standard nucleosynthesis, extra relativistic relics, a significant amount of hot dark matter, etc. However, large deviations from the standard case are still compatible with observations: for instance, a model with one neutrino of mass $M = 1.5$ eV and eight relativistic degrees of freedom is allowed by CMB and LSS data, even when all priors are included (see Fig. 6). In order to exclude this model, it is necessary to take into account the prediction of standard BBN, which gives stronger limits on $N_{\rm eff}$.

The bounds obtained in this paper are based on the observation of cosmological perturbations (CMB and LSS), combined with constraints on the current expansion and acceleration rates of the Universe (HST and SN priors). Therefore they are completely independent from the predictions of primordial nucleosynthesis. It is remarkable that in the space of the two standard BBN free parameters $(\omega_b, N_{\rm eff})$, the preferred regions deduced from cosmological perturbations and from primordial abundances are perfectly compatible with each other, and more or less orthogonal: indeed, our analysis (with the most restrictive priors) gives $0.0215 < \omega_b < 0.0235$ and $1.6 < N_{\rm eff} < 8.5$, while standard BBN favors $0.017 < \omega_b < 0.026$ and $1.6 < N_{\rm eff} < 3.6$ [11] (all these bounds are at the 2σ level).

In order to test their robustness, we have also calculated the bounds on M and $N_{\rm eff}$ in the presence of primordial tensor perturbations. Our results show that the bounds are practically unchanged, because current cosmological data is able to distinguish between the respective effects of tensors and neutrinos.

Finally, we have considered the impact of a different splitting of the total neutrino mass among the individual states, an analysis also recently performed in ref. [13]. We compared the case of complete mass degeneracy (all neutrinos with the same mass) with that where one neutrino state effectively possesses the whole mass. We found that the bounds on the degenerate case are more restrictive due to its more efficient free-streaming, in particular for larger values if $N_{\rm eff}$. However, for three or four neutrinos the differences between the two cases are not significant.

Our bounds are a clear indication that present cosmological data provide interesting bounds on the neutrino sector, complementary to those from terrestrial experiments. These include tritium beta decay experiments, which provide a current upper bound on the total neutrino mass of 6.6 eV at 2σ [45], while the KATRIN experiment [46] is planned to have an accuracy of the order 0.35 eV. Sub-eV sensitivity to neutrino masses is also expected for experiments measuring neutrinoless double beta decays [47], but only for Majorana neutrinos and with a dependence on the details of the mixing matrix.

However, the cosmological bounds should be taken with care, due to their dependence on the data (or priors) used, and also on the assumption of a particular underlying model. Examples are given by the works [10, 48], where non-zero neutrino masses are preferred. This warning should not prevent us to be confident on the power of future cosmological experiments to limit (and eventually detect) neutrino masses and other neutrino properties. For instance, forecast analyses have shown that with future data there will be potential sensitivities to $\Delta N_{\rm eff} \sim 0.2$ [15, 49] (eventually improving BBN results) and neutrino masses of the order $0.1 - 0.2$ eV with Planck and final SDSS data [50, 51, 52], or with galaxy and CMB lensing [53, 54].

Acknowledgments

This research was supported by a CICYT-IN2P3 agreement. SP was supported by the Spanish grant BFM2002-00345, the ESF network Neutrino Astrophysics and a Ramón y Cajal contract of MCyT.

[1] M. Maltoni, talk given at AHEP-2003, Valencia (Spain), Oct 2003 [hep-ph/0401042].
[2] A.D. Dolgov, Phys. Rept. **370**, 333 (2002) [hep-ph/0202122].
[3] V. Barger, D. Marfatia and A. Tregre, hep-ph/0312065.
[4] D.N. Spergel et al., Astrophys. J. Suppl. **148**, 175 (2003) [astro-ph/0302209].
[5] P. Crotty, J. Lesgourgues and S. Pastor, Phys. Rev. D **67**, 123005 (2003) [astro-ph/0302337].
[6] E. Pierpaoli, Mon. Not. Roy. Astron. Soc. **342**, L63 (2003) [astro-ph/0302465].
[7] S. Hannestad, JCAP **0305**, 004 (2003) [astro-ph/0303076].
[8] Ø. Elgarøy and O. Lahav, JCAP **0304**, 004 (2003) [astro-ph/0303089].
[9] V. Barger, J.P. Kneller, H.S. Lee, D. Marfatia and G. Steigman, Phys. Lett. B **566**, 8 (2003) [hep-ph/0305075].
[10] S.W. Allen, R.W. Schmidt and S.L. Bridle, Mon. Not. Roy. Astron. Soc. **346**, 593 (2003) [astro-ph/0306386].
[11] A. Cuoco, F. Iocco, G. Mangano, G. Miele, O. Pisanti and P.D. Serpico, astro-ph/0307213.

[12] M. Tegmark et al. [SDSS Coll.], astro-ph/0310723.
[13] S. Hannestad and G. Raffelt, hep-ph/0312154.
[14] J.L. Tonry et al., Astrophys. J. **594**, 1 (2003) [astro-ph/0305008].
[15] S. Bashinsky and U. Seljak, astro-ph/0310198.
[16] A.D. Dolgov, S.H. Hansen and D.V. Semikoz, Nucl. Phys. B **503**, 426 (1997) [hep-ph/9703315].
[17] G. Mangano, G. Miele, S. Pastor and M. Peloso, Phys. Lett. B **534**, 8 (2002) [astro-ph/0111408].
[18] R.H. Cyburt, B.D. Fields and K.A. Olive, Phys. Lett. B **567**, 227 (2003) [astro-ph/0302431].
[19] M.J. White, G. Gelmini and J. Silk, Phys. Rev. D **51**, 2669 (1995) [astro-ph/9411098].
[20] M. Kaplinghat and M.S. Turner, Phys. Rev. Lett. **86**, 385 (2001) [astro-ph/0007454].
[21] J. Lesgourgues and S. Pastor, Phys. Rev. D **60**, 103521 (1999) [hep-ph/9904411].
[22] A.D. Dolgov et al., Nucl. Phys. B **632**, 363 (2002) [hep-ph/0201287].
[23] Y.Y. Wong, Phys. Rev. D **66**, 025015 (2002) [hep-ph/0203180].
[24] K.N. Abazajian, J.F. Beacom and N.F. Bell, Phys. Rev. D **66**, 013008 (2002) [astro-ph/0203442].
[25] W. Hu, D.J. Eisenstein and M. Tegmark, Phys. Rev. Lett. **80**, 5255 (1998) [astro-ph/9712057].
[26] T. Schwetz, talk given at AHEP-2003, Valencia (Spain), Oct 2003 [hep-ph/0311217].
[27] P. Di Bari, Phys. Rev. D **65**, 043509 (2002). [hep-ph/0108182].
[28] K.N. Abazajian, Astropart. Phys. **19**, 303 (2003) [astro-ph/0205238].
[29] U. Seljak and M. Zaldarriaga, Astrophys. J. **469**, 437 (1996) [astro-ph/9603033].
[30] L. Verde et al., Astrophys. J. Suppl. **148**, 195 (2003) [astro-ph/0302218].
[31] G. Hinshaw et al., Astrophys. J. Suppl. **148**, 135 (2003) [astro-ph/0302217].
[32] A. Kogut et al., Astrophys. J. Suppl. **148**, 161 (2003) [astro-ph/0302213].
[33] C. Kuo et al. [ACBAR Coll.], Astrophys. J. **600**, 32 (2004) [astro-ph/0212289].
[34] J.H. Goldstein et al., Astrophys. J. **599**, 773 (2003) [astro-ph/0212517].
[35] W.J. Percival et al., Mon. Not. Roy. Astron. Soc. **327**, 1297 (2001) [astro-ph/0105252].
[36] M. Tegmark et al. [SDSS Coll.], astro-ph/0310725.
[37] R.E. Smith et al. [The Virgo Consortium Coll.], Mon. Not. Roy. Astron. Soc. **341**, 1311 (2003) [astro-ph/0207664].
[38] W.L. Freedman et al., Astrophys. J. **553**, 47 (2001) [astro-ph/0012376].
[39] S. Perlmutter et al. [Supernova Cosmology Project Coll.], Astrophys. J. **517**, 565 (1999) [astro-ph/9812133].
[40] J. Lesgourgues and A.R. Liddle, Mon. Not. Roy. Astron. Soc. **327**, 1307 (2001) [astro-ph/0105361].
[41] J.A. Peacock et al., Nature **410**, 169 (2001) [astro-ph/0103143].
[42] L. Verde et al., Mon. Not. Roy. Astron. Soc. **335** (2002) 432 [astro-ph/0112161].
[43] O. Lahav et al., astro-ph/0112162.
[44] R.H. Brandenberger, A. Mazumdar and M. Yamaguchi, hep-ph/0401239.
[45] J. Bonn et al., Nucl. Phys. Proc. Suppl. **91**, 273 (2001).
[46] A. Osipowicz et al. [KATRIN Coll.], hep-ex/0109033.
[47] S.R. Elliott and P. Vogel, Ann. Rev. Nucl. Part. Sci. **52**, 115 (2002) [hep-ph/0202264].
[48] A. Blanchard, M. Douspis, M. Rowan-Robinson and S. Sarkar, Astron. Astrophys. **412**, 35 (2003) [astro-ph/0304237].
[49] R. Bowen et al., Mon. Not. Roy. Astron. Soc. **334**, 760 (2002) [astro-ph/0110636].
[50] D.J. Eisenstein, W. Hu and M. Tegmark, Astrophys. J. **518**, 2 (1998) [astro-ph/9807130].
[51] J. Lesgourgues, S. Pastor and S. Prunet, Phys. Rev. D **62**, 023001 (2000) [hep-ph/9912363].
[52] S. Hannestad, Phys. Rev. D **67**, 085017 (2003) [astro-ph/0211106].
[53] M. Kaplinghat, L. Knox and Y.S. Song, astro-ph/0303344.
[54] K.N. Abazajian and S. Dodelson, Phys. Rev. Lett. **91**, 041301 (2003) [astro-ph/0212216].
[55] For fixed $N_{\rm eff} < 2$ or $N_{\rm eff} > 8$, the best-fit models reach the extreme values of $h \in [0.58, 0.90]$ and $\omega_m \in [0.11, 0.25]$. However, the global maximum-likelihood fit has $(M, N_{\rm eff}) = (0, 3)$ and values of the other cosmological parameters well inside the grid boundaries.

5.2 Limits on light sterile neutrinos, PRD 79, 045026 (2009)

CERN-PH-TH/2008-238, LAPTH-1294/08
December 12, 2008

Cosmological constraints on a light non-thermal sterile neutrino

Mario A. Acero[(a,b,c)], Julien Lesgourgues[(d,e)]

(a) *Dipartimento di Fisica Teorica, Università di Torino, Via P. Giuria 1, I–10125 Torino, Italy*

(b) *INFN, Sezione di Torino, Via P. Giuria 1, I–10125 Torino, Italy*

(c) *Laboratoire d'Annecy-le-Vieux de Physique Thórique LAPTH, Université de Savoie, CNRS/IN2P3, 74941 Annecy-le-vieux, France*

(d) *PH-TH, CERN - CH-1211 Geneva 23, Switzerland*

(e) *SB-ITP-LPPC, BSP 312 - EPFL, CH-1015 Lausanne, Switzerland*

Abstract

Although the MiniBooNE experiment has severely restricted the possible existence of light sterile neutrinos, a few anomalies persist in oscillation data, and the possibility of extra light species contributing as a subdominant hot (or warm) component is still interesting. In many models, this species would be in thermal equilibrium in the early universe and share the same temperature as active neutrinos, but this is not necessarily the case. In this work, we fit up-to-date cosmological data with an extended ΛCDM model, including light relics with a mass typically in the range 0.1–10 eV. We provide, first, some nearly model-independent constraints on their current density and velocity dispersion, and second, some constraints on their mass, assuming that they consist either in early decoupled thermal relics, or in non-resonantly produced sterile neutrinos. Our results can be used for constraining most particle-physics-motivated models with three active neutrinos and one extra light species. For instance, we find that at the 3σ confidence level, a sterile neutrino with mass $m_s = 2$ eV can be accommodated with the data provided that it is thermally distributed with $T_s/T_\nu^{\rm id} \lesssim 0.8$, or non-resonantly produced with $\Delta N_{\rm eff} \lesssim 0.5$. The bounds become dramatically tighter when the mass increases. For $m_s \lesssim 0.9$ eV and at the same confidence level, the data is still compatible with a standard thermalized neutrino.

1 Introduction

Neutrino oscillation is a well studied phenomenon, confirmed by strong experimental evidences. Most experimental results are well explained with a three-neutrino oscillation model, involving two independent and well-measured square-mass differences: $\Delta m^2_{sol} = (7.59 \pm 0.21) \times 10^{-5}$ eV^2 [1] and $\Delta m_{atm} = (2.74^{+0.44}_{-0.26}) \times 10^{-3}$ eV^2 [2]. However, some other experiments have shown some anomalies which do not fit in this hypothesis (LSND [3],

Gallium experiments [4], MiniBooNE low energy anomaly [5]). These anomalous results might be due to unknown systematic effects, but all attempts to identify such systematics have failed until now. Otherwise, they could be interpreted as exotic neutrino physics.

In Ref. [6], the MiniBooNE anomaly was explained through a renormalization of the absolute neutrino flux and a simultaneous disappearance of electron neutrinos oscillating into sterile neutrinos (with $P_{\nu_e \to \nu_e} = 0.64^{+0.08}_{-0.07}$). The LSND and Gallium radioactive source experiment [7, 8, 9] anomalies have been studied in Ref. [10], where is it claimed that all these anomalies could be interpreted as an indication of the presence of, at least, one sterile neutrino with rather large mass (few eV's). Ref. [11] also studied the compatibility of the Gallium results with the Bugey [12] and Chooz [13] reactor experimental data, concluding that such a sterile neutrino should have a mass between one and two eV's. Finally, the MiniBooNE collaboration performed global fits of MiniBooNE, LSND, KARMEN2, and Bugey experiments in presence of a fourth sterile neutrino [14] (assuming no renormalization issue for MiniBooNe unlike Ref. [6]). When all four experiments are combined, the compatibility between them is found to be very low (4%); however, when only three of them are included, the compatibility level is usually reasonable (the largest tension being found between LSND and Bugey). In this analysis, the preferred value of the sterile neutrino is usually smaller than 1eV, but still of possible cosmological relevance (for instance, for all four experiments, the best fit corresponds to $\Delta m^2 \sim 0.2 - 0.3$ eV^2).

These various developments suggest that it is important to scrutinize cosmological bounds on scenarios with one light sterile neutrino, which could help ruling them out, given that current bounds on the total neutrino mass assuming just three active neutrinos are as low as $\sum m_\nu < 0.61$eV (using WMAP5, BAO and SN data [15]). This result cannot be readily applied to the models which we consider here. Indeed, scenarios with extra neutrinos require a specific cosmological analysis, for the simple reason that besides affecting the total neutrino mass, additional neutrinos also increase the abundance of relativistic particles in the early universe.

From the point of view of Cosmology, there have been many works constraining simultaneously the sum of neutrino masses and the contribution to the relativistic energy density component of the Universe, parametrized as the effective number of neutrinos, $N_{\rm eff}$ (see for example [16, 17, 18, 19, 20, 21]). Most of these works assume either that the heaviest neutrino (and hence the most relevant one from the point of view of free-streaming) has a thermal distribution, sharing the same value of temperature as active neutrinos, or that all neutrinos are degenerate in mass. However, the results of Refs. [22, 23] can also be applied to the case of very light active neutrinos plus one heavier, non-necessarily thermal sterile neutrino, which is the most interesting case for explaining oscillation anomalies. In terms of physical motivations, it is very likely that the light sterile neutrino required by the LSND anomaly acquires a thermal distribution in the early universe, through oscillations with active neutrinos in presence of a large mixing angle [24]. On the other hand, there are some proposals to avoid these contrains (for a list of some scenarios, see [25]). One of such possibilities is based on a low reheating temperature (T_R) Universe [26, 27, 28, 29], in which, for a sufficiently low T_R, the sterile neutrinos could be non-thermal [30] and its production would be suppressed [28], such that usual cosmological bounds are evaded. In fact, in these models, sterile neutrinos are allowed to have a large mass without entering in conflict with other experimental results, while $T_{\rm dec} \lesssim T_R \lesssim 10$MeV ($T_{\rm dec}$ being the temperature of the cosmic plasma at neutrino decoupling).

In absence of thermalization, cosmological bounds on the sterile neutrino mass become potentially weaker. Hence, it is interesting to study the compatibility of recently proposed scenarios with a light sterile neutrino with the most recent cosmological data, keeping in mind the possibility of a non-thermal distribution. The goal of this paper is hence to study the compatibility of cosmological experimental data (WMAP5 plus small-scale CMB data, SDSS LRG data, SNIa data from SNLS and conservative Lya data from VHS) with the hypothesis of a sterile neutrino with the characteristics sketched above, i.e., with a mass roughly of the order of the electron-Volt, and a contribution to $N_{\rm eff}$ smaller than one.

2 Light sterile neutrino in cosmology: physical effects and parametrization

If a population of free-streaming particles becomes non-relativistic after photon decoupling, its physical effects on the cosmological background and perturbation evolution are mainly described by three quantities:

1. its contribution to the relativistic density before photon decoupling, which affects the redshift of radiation/matter equality, usually parametrized by an effective neutrino number (standing for the relativistic density of the species divided by that of one massless neutrino family in the instantaneous decoupling (id) limit):

$$\Delta N_{\rm eff} \equiv \frac{\rho_s^{\rm rel}}{\rho_\nu} = \left[\frac{1}{\pi^2}\int dp\; p^3 f(p)\right] / \left[\frac{7}{8}\frac{\pi^2}{15} T_\nu^{\rm id\,4}\right] \qquad (1)$$

   with $T_\nu^{\rm id} \equiv (4/11)^{1/3} T_\gamma$,

2. its current energy density, which affects (i) the current energy budget of the Universe (with various consequences for the CMB and LSS spectra, depending on which other parameters are kept fixed), and (ii) the amplitude reduction in the small-scale matter power spectrum due to these extra massive free-streaming particles, parametrized by the dimensionless number ω_s:

$$\omega_s \equiv \Omega_s h^2 = \left[\frac{m}{\pi^2}\int dp\; p^2 f(p)\right] \times \left[\frac{h^2}{\rho_c^0}\right] \qquad (2)$$

   where ρ_c^0 is the critical density today and h the reduced Hubble parameter,

3. the comoving free-streaming length of these particles when they become non-relativistic, which controls the scale at which the suppression of small-scale matter fluctuations occurs. This length can easily be related to the average velocity of the particles today, $\langle v_s \rangle$[1].

[1]The minimum comoving free-streaming wavenumber $k_{\rm fs}$ is controlled by Ω_m and by the ratio $a(t_{\rm nr})/\langle v_s(t_{\rm nr})\rangle$ evaluated when $T = m$, i.e. when $a(t_{\rm nr}) \sim \langle v_s(t_0)\rangle a(t_0)$. Given that $\langle v_s(t_{\rm nr})\rangle \sim \langle v_s(t_0)\rangle a(t_0)/a(t_{\rm nr})$, the minimum comoving free-streaming length just depends on $\langle v_s(t_0)\rangle$ and Ω_m.

However, for whatever assumption concerning the phase-space distribution function $f(p)$, the three numbers $(\Delta N_{\rm eff},\, \omega_s,\, \langle v_s \rangle)$ satisfy a constraint equation. Indeed, the average velocity of the particles today (assumed to be in the non-relativistic regime) is given *exactly* by

$$\langle v_s \rangle \equiv \frac{\int p^2 dp\, \frac{p}{m} f(p)}{\int p^2 dp\, f(p)} = \frac{7}{8}\frac{\pi^2}{15}\left(\frac{4}{11}\right)^{4/3} \frac{T_{\rm CMB}^4 h^2}{\rho_c}\frac{\Delta N_{\rm eff}}{\omega_s} = 5.618\times 10^{-6}\frac{\Delta N_{\rm eff}}{\omega_s} \qquad (3)$$

in units where $c = k_B = \hbar = 1$, and taking $T_{\rm CMB} = 2.726$K. Hence, the three physical effects described above depend on only *two independent parameters*.

Reducing the physical impact of any population of massive free-streaming particles to these three effects (and two independent parameters) is a simplification: two models based on different non-thermal phase-space distributions $f(p)$ can in principle share the same numbers $(\Delta N_{\rm eff},\, \omega_s,\, \langle v_s \rangle)$ and impact the matter power spectrum differently. Indeed, the free-streaming effect depends on the details of $f(p)$ (including high statistical momenta like $\int dp\; p^4 f(p)$, etc.) However, the conclusions of Ref. [18] indicate that for many models with non-thermal distorsions, observable effects can indeed be parametrized by two combinations of $(\Delta N_{\rm eff},\, \omega_s,\, \langle v_s \rangle)$ with good accuracy: other independent parameters would be very difficult to observe[2].

Let us compute the three parameters $(\Delta N_{\rm eff},\, \omega_s,\, \langle v_s \rangle)$ for simple cases. For one species of thermalized free-streaming particles with mass m_s, sharing the same temperature as active neutrinos in the instantaneous decoupling limit, one gets:

$$\Delta N_{\rm eff} = 1, \qquad \omega_s = \frac{m_s}{94.05\ {\rm eV}}, \qquad \langle v_s \rangle = \frac{7\pi^4}{180\zeta(3)}\frac{T_\nu^{\rm id}}{m_s} = \frac{0.5283\ {\rm meV}}{m_s}. \qquad (4)$$

For a light thermal relic with a Fermi-Dirac distribution and a different temperature T_s, these quantities become

$$\Delta N_{\rm eff} = \left(\frac{T_s}{T_\nu^{\rm id}}\right)^4, \qquad \omega_s = \frac{m_s}{94.05{\rm eV}}\left(\frac{T_s}{T_\nu^{\rm id}}\right)^3, \qquad \langle v_s \rangle = \frac{0.5283\ {\rm meV}}{m_s}\left(\frac{T_s}{T_\nu^{\rm id}}\right). \qquad (5)$$

For a non-thermal relic with a free function $f(p)$, there is an infinity of possible models. A popular one is the Dodelson-Widrow scenario [32] (also referred as the "non-resonant production scenario"), motivated by early active-sterile neutrino oscillations in the limit of small mixing angle and zero leptonic asymmetry, which corresponds to the phase-space distribution

$$f(p) = \frac{\chi}{e^{p/T_\nu}+1} \qquad (6)$$

where χ is an arbitrary normalization factor. In this case, in the approximation $T_\nu = T_\nu^{\rm id}$, the three "observable" parameters read

$$\Delta N_{\rm eff} = \chi, \qquad \omega_s = \frac{m_s}{94.05{\rm eV}}\chi, \qquad \langle v_s \rangle = \frac{0.5283\ {\rm meV}}{m_s}. \qquad (7)$$

[2]This conclusion does not apply when the non-thermal distribution $f(p)$ has a sharp peak close to $p = 0$. In this case, particles with very small momentum should be counted within the CDM component, not within the extra massive free-streaming component. Otherwise, one would obtain values of ω_s and $\langle v_s \rangle$ based on an averages between cold and hot/warm particles; then, these parameters would not capture the correct physical effects (see [31])

Hence, a Dodelson-Widrow (DW) model shares that same "observable" parameters ($\Delta N_{\rm eff}$, ω_s, $\langle v_s \rangle$) as a thermal model with $m_s^{\rm thermal} = m_s^{\rm DW} \chi^{1/4}$ and $T_s = \chi^{1/4} T_\nu$. Actually, for these two models, the degeneracy is exact: it can be shown by a change of variable in the background and linear perturbation equations that the two models are strictly equivalent from the point of view of cosmological observables [33, 18]. As mentioned before, in the general case, two models sharing the same ($\Delta N_{\rm eff}$, ω_s, $\langle v_s \rangle$) are not always strictly equivalent, but can be thought to be hardly distinguishable even with future cosmological data. For instance, the low-temperature reheating model analyzed in [27, 28] leads to a distribution of the form

$$f(p) = \frac{\chi p}{e^{p/T_\nu} + 1} \ . \tag{8}$$

This model would in principle deserve a specific analysis, but in good approximation we can expect that by only exploring the parameter space of thermal models (or equivalently, of DW models), we will obtain some very generic results, covering in good approximation most possibilities for the non-thermal distorsions.

3 Analysis

3.1 Data

In the following sections, we will present the results of various runs based on the Boltzmann code CAMB [34] and cosmological parameter extraction code CosmoMC [35]. We modified CAMB in order to implement the proper phase-space distribution $f(p)$ of the thermal or DW model. For simplicity, we assumed in all runs that the three active neutrinos can be described as massless particles. In order to obtain a Bayesian probability distribution for each cosmological parameters, we ran CosmoMC with flat priors on the usual set of six parameters ω_b, $\omega_{\rm dm} = \omega_s + \omega_{\rm cdm}$, θ, τ, A_s, n_s (see e.g. [36]), plus two extra parameters describing the sterile neutrino sector, that will be described in the next sections. We choose the following data set: WMAP5 [37] plus small-scale CMB data (ACBAR [38], CBI [39], Boomerang [40]), the galaxy power spectrum of the SDSS LRG [41] with flat prior on Q [42, 43], SNIa data from SNLS [44] and conservative Lyman-α data from VHS [45]. We do not include more recent Lyman-α data sets, which have much smaller errorbars, but for which the deconvolution of non-linear effects depends on each particular cosmological model, and requires specific hydrodynamical simulations.

3.2 General analysis

Our first goal is to obtain simple results with a wide range of applications. Hence, we should not parametrize the effect of sterile neutrinos with e.g. their mass or temperature: in that case, our results would strongly depend on underlying assumptions for $f(p)$. It is clear from section 2 that nearly "universal" results can be obtained by employing two combinations of the "observable parameters" $\Delta N_{\rm eff}$, ω_s and $\langle v_s \rangle$ (and eventually of other parameters of the ΛCDM model). Here we choose to vary the current dark matter density fraction $f_s = \omega_s/(\omega_s + \omega_{\rm cdm})$ and the current velocity dispersion $\langle v_s \rangle$. As will be clear from our results, these two parameters capture the dominant observable effects, and lead to very clear bounds, since their correlation with other ΛCDM model parameters

is insignificant. Our limits on f_s and $\langle v_s \rangle$ apply exactly to the thermal case and DW case, and approximately to most other cases (modulo the caveat described in the second footnote of section 2).

Our parameter space is represented in Figure 1. We adopt a logarithmic scale for $\langle v_s \rangle$ and display the interesting range

$$1 \text{ km/s} < \langle v_s \rangle < 1000 \text{ km/s} \, . \tag{9}$$

Indeed, with out dataset, particles with smaller velocities would be indistinguishable from cold dark matter; instead, particles with larger velocities would either have $\Delta N_{\rm eff} > 1$ (a case beyond the motivations of this work, and anyway very constrained by the data) or $f_s < 0.02$ (being indistinguishable from extra relativistic degrees of freedom). Assuming a particular value for $\omega_{\rm dm} = \omega_s + \omega_{\rm cdm}$ and for $\Delta N_{\rm eff}$, it is possible to compute the velocity dispersion $\langle v_s \rangle$ as a function of f_s. Since the CMB and LSS data give precise constraints on $\omega_{\rm dm}$, regions of equal $\Delta N_{\rm eff}$ correspond to thin bands in the (f_s, $\langle v_s \rangle$) plane. We show these bands in Figure 1 for $10^{-3} < \Delta N_{\rm eff} < 1$ under the assumption that $\omega_{\rm dm} = 0.11 \pm 0.01$, which corresponds roughly to the 95% confidence limits (C.L.) from all our runs. These iso-$\Delta N_{\rm eff}$ bands are completely model-independent.

Instead, regions of equal mass can only be plotted for a particular model. In Figure 1, we show the bands corresponding to m =1 eV and 10 eV, either in the case of early decoupled thermal relics (blue/dotted lines) or in the DW case (green/dashed lines). For any given mass, these bands intersect each other in a location corresponding to the case of one fourth standard neutrino species with $\Delta N_{\rm eff} = 1$.

We ran CosmoMC with top-hat priors on f_s (in the physical range $[\,0, 1]$) and on $\log_{10}[\langle v_s \rangle / 1\text{km/s}]$ (in the range $[0, 3]$ motivated by the previous discussion). Our results are summarized in Figure 1 (bottom). We see that the upper bound on f_s decreases smoothly as the velocity dispersion increases: when the particles have a larger velocity dispersion, their free-streaming wavelength is larger, so the step-like suppression in the power spectrum (which amplitude depends on f_s) is more constrained. For $\langle v_s \rangle \sim 1$ km/s, we find $f_s \lesssim 0.1$ at the 2σ C.L., while for $\langle v_s \rangle \sim 100$ km/s, we find $f_s \lesssim 0.06$ at the 2σ C.L. When the velocity dispersion becomes larger than 100 km/s, the upper bound on f_s decreases even faster as a function of $\langle v_s \rangle$. This is the case of a HDM component with significant contribution to the number of relativistic d.o.f., for which the observational bounds derive from a combination of the first and second effects described in section 2: in this limit, in addition to being sensitive to the free-streaming effect, the data disfavor a significant increase of the total radiation density corresponding to $\Delta N_{\rm eff}$ of order one or larger.

We should stress that the details of our results depend on the underlying priors. For instance, one could use a flat prior on $\langle v_s \rangle$ instead of its logarithm. Running in the range $0 < \langle v_s \rangle < 1000$ km/s with such a prior would give more focus on the large-$\langle v_s \rangle$ allowed region of Figure 1. However, it would be more interesting to focus on small velocities, in order to understand how our results can be extended without any discontinuity to the case of warmer and heavier dark matter. For this purpose, we ran CosmoMC with a top-hat prior on $0 < \langle v_s \rangle < 1$ km/s, and obtained the results shown in Figure 2. These results are identical to those published in Reference [46] (figure 7). By gluing figure 1 on top of 2, one can obtain a full coverage of the parameter space of ΛCDM models completed by one extra (hot or warm) dark matter species. Figure 2 shows the transition

from the region in which this extra species is indistinguishable from cold dark matter (when $\langle v_s \rangle \leq 0.1$ km/s, the fraction f_s is unconstrained) to the region in which it is warm (for $0.4 \leq \langle v_s \rangle \leq 1$ km/s, there is a nearly constant bound $f_s \lesssim 0.1$ at the 2-σ level). Figure 1 shows instead the transition from warm particles to hot particles (with velocities comparable to those of active neutrinos). The two plots perfectly match each other along the $\langle v_s \rangle = 1$ km/s axis, on which the sterile neutrino fraction is bounded by $f_s \lesssim 0.1$ (2-σ).

3.3 Mass/temperature bounds in the thermal case

We now focus on the particular case of early decoupled thermal relics, with a Fermi-Dirac distribution and a temperature T_s. These models can be parametrized by the mass m_s and the temperature in units of the neutrino temperature, $T_s/T_\nu^{\rm id}$. Our parameter space – and the correspondence with the previous parameters $\Delta N_{\rm eff}$, f_s, $\langle v_s \rangle$ – is shown in Figure 3. In this analysis, we want to focus again on light sterile neutrinos rather than WDM; hence we are not interested in velocities smaller than 1 km/s today. We are not interested either in the case of enhanced particles with $\Delta N_{\rm eff} > 1$. Then, as can be checked in Figure 3, the ensemble of interesting models can be covered by taking a top-hat prior on $\log_{10}(m_s/1\ {\rm eV})$ in the range $[-1, 2]$, and on $T_s/T_\nu^{\rm id}$ in the range $[0, 1]$.

The likelihood contours obtained for this case are shown in Figure 3 (bottom). They are consistent with our previous results: when $\Delta N_{\rm eff} \sim 10^{-2}$ (and hence $T_s/T_\nu^{\rm id} \sim 0.3$), the upper bound on the sterile neutrino fraction is $f_s < 0.1$ at the 2σ C.L.; then this bound decreases smoothly when T_s increases. For a fourth standard neutrino with $T_s = T_\nu^{\rm id}$, the 2σ C.L. (resp. 3σ C.L.) bound is $m_s \lesssim 0.4$ eV (resp. 0.9 eV).

This figure can be conveniently used for model building: for a given value of the mass, it shows what should be the maximal temperature of the thermal relics in order to cope with cosmological observations; knowing this information and assuming a particular extension of the particle physics standard model, one can derive limits on the decoupling time of the particle. For instance, for a mass of $m_s = 0.5$ eV one gets $T_s/T_\nu^{\rm id} \lesssim 0.9$; for $m_s = 1$ eV, $T_s/T_\nu^{\rm id} \lesssim 0.7$; while for $m_s = 5$ eV, $T_s/T_\nu^{\rm id} \lesssim 0.5$. This figure can also be applied to thermally produced axions, like in Refs. [47, 48].

3.4 Mass bounds in the DW case

Finally, for Dodelson-Widrow relics with a distribution function equal to that of standard neutrinos suppressed by a factor χ (which is equal by definition to $\Delta N_{\rm eff}$), we can parametrize the ensemble of models by m_s and χ. Our parameter space – and the correspondence with f_s, $\langle v_s \rangle$ – is shown in Figure 4. Like in the previous section, we are not interested in a current velocity dispersion smaller than 1 km/s today. Then, as can be checked in Figure 4, the ensemble of interesting models can be covered by taking a top-hat prior on $\log_{10}(m_s/1\ {\rm eV})$ in the range $[-1, 2]$; in this range, values of χ smaller than 10^{-2} would correspond to tiny values of f_s, i.e. to particles indistinguishable from massless particles; so, we can take a flat prior on $\log_{10}(\chi)$ in the range $[-2, 0]$.

The likelihood contours obtained for this case are shown in Figure 4 (bottom). We are not surprised to find once more an allowed region corresponding to $f_s \lesssim 0.1$ at the 2σ C.L. when $\Delta N_{\rm eff} = \chi \sim 10^{-2}$ is negligible with respect to one, or less when $\Delta N_{\rm eff}$ grows

closer to one. For a fourth standard neutrino with $T_s = T_\nu^{\rm id}$, the two definitions of the mass (following from the thermal or from the DW cases) are equivalent, and indeed we find $m_s \lesssim 0.4$ eV (2σ C.L.) or $m_s \lesssim 0.9$ eV (3σ C.L.) like in section 3.3.

This figure can also be useful for model building: for a given value of the mass, it shows what should be the maximal value of χ compatible with cosmological observations; in turn, this information can be used to put bounds on the mixing angle between this relic and active neutrinos in non-resonant production models *à la* Dodelson & Widrow. For instance, for a mass of $m_s = 1$ eV, the 2σ C.L. gives $\chi \lesssim 0.5$; for $m_s = 2$ eV, we get $\chi \lesssim 0.2$; while for $m_s = 5$ eV, we get $\chi \lesssim 0.1$.

3.5 Comparison with previous work

The ensemble of cosmological models that we are exploring here is not different from that studied by Dodelson, Melchiorri & Slosar [23] (called later DMS) or by Cirelli & Strumia [22] (called later CS); the difference between these works and the present analysis consists in a different choice of parameters, priors, data set, and also methodology in the case of CS.

For instance, Figure 6a of CS presents constrains in the space ($\log_{10}\Delta N_{\rm eff}$, $\log_{10} m_s$) assuming a DW scenario. Hence, their parameter space is identical to the one we used in section 3.4, excepted for the prior range (which is wider in their case). As far as the data set is concerned, CS use some CMB and galaxy spectrum measurements which are slightly obsolete by now; on the other hand, they employ some additional information derived from BAO experiments, and use SDSS Lyman-α data points that we conservatively excluded from this analysis, since they assume a ΛCDM cosmology. Finally, CS performed a frequentist analysis, and their bounds are obtained by minimizing the χ^2 over extra parameters (while in the present Bayesian analysis, we marginalize over them given the priors).

In order to compare our results with CS, we performed a run with top-hat priors on $\log_{10}\chi = \log_{10}(\Delta N_{\rm eff})$ in the range $[-3, 1]$, and on $\log_{10}(m_s/1\ {\rm eV})$ in the range $[-1, 3]$. In this particular run we compute the 90%, 99% and 99.9% C.L., following CS. Our results are shown in Figure 5, and are consistent with those of our general analysis.

In spite of the different data set and methodology, the 90% and 99% contours are found to be in very good agreement with CS in most of the parameter space. The major difference lies in the small mass region, for which CS get more conservative limits on $\Delta N_{\rm eff}$ than we do, and find a preference for non-zero values of the effective neutrino number $0.5 < \Delta N_{\rm eff} < 4$ (at the 90% C.L.). This qualitative behavior has been nicely explained in Refs. [42, 43]. It is due to the non-linear corrections applied to the theoretical linear power spectrum before comparing it with the observed SDSS and 2dF galaxy power spectra. The approach used in this work (and in the default version of CosmoMC) consists in marginalizing over a nuisance parameter Q (describing the scale-dependence of the bias) with a flat prior. Instead, following Ref. [49], CS impose a gaussian prior on Q. This results in biasing the results towards larger values of $N_{\rm eff}$, and finding marginal evidence for $\Delta N_{\rm eff} > 0$. Of course, this assumption might turn out to be correct; however, it is argued in Refs. [42, 43] that our knowledge on Q (based essentially on N-body simulations for some particular cosmological models) is still too uncertain for getting definite predictions.

The analysis of DMS is Bayesian, like ours. The authors use top-hat priors on the two parameters $-3 < \log_{10}(m_s/1\text{ eV}) < 1$ and $0 < \omega_s < 1$, roughly the same data set as CS, and employ the distribution function of early decoupled thermal relics. Our results based on the same priors (but a different data set) are shown in Figure 6, and are consistent with the previous sections: at the 2σ level, ω_s is such that $f_s \lesssim 0.1$ for $\Delta N_{\rm eff} \sim 10^{-2}$; then, the bound on f_s (and therefore on ω_s) decreases smoothly when m_s decreases (and therefore $\langle v_s \rangle$ increases). These results differ significantly from those of DMS, who find that the upper bound on ω_s peaks near $m \sim 0.25$ eV and then decreases quickly. We do not observe such a behavior: our upper bound on ω_s increases (not so smoothly, but still monotonically) when m_s increases, in agreement with all previous results in this paper. This difference is most likely due to the use made by DMS of more aggressive Lyman-α data from SDSS, of different galaxy power spectrum data, and of a prior on Q, as in CS. This data set puts stronger limits on a possible suppression of the small scale power spectrum. Actually, in absence of sterile neutrinos, the same combination of data is known to produce very strong bounds on neutrino masses, and to prefer $\Delta N_{\rm eff}$ slightly larger than one [49]; in presence of light sterile neutrinos, the results of DMS show that this data also imposes a strong bound $\omega_s < 0.001$ for $1\,\text{eV} < m_s < 10\,\text{eV}$, due to its sensitivity to the sterile neutrino free-streaming effect. Our large scale structure data set (conservative Lyman-α data from VHS, SDSS-LRG and flat prior on Q) is not able to exclude this region.

4 Conclusions

In this work, we studied the compatibility of cosmological experimental data with the hypothesis of a non-thermal sterile neutrino with a mass in the range $0.1 - 10$ eV (or more), and a contribution to $N_{\rm eff}$ smaller than one. We computed Bayesian confidence limits on different sets of parameters, adapted to the case of thermal relics (section 3.3), of non-resonantly produced sterile neutrinos *à la* Dodelson & Widrow (DW, section 3.4), or of generic parameters leading to nearly model-independent results (section 3.2). In each case, we performed a specific parameter extraction from scratch, in order to obtain reliable results assuming flat priors on the displayed parameters. For simplicity, we assumed that the masses of the three active neutrinos are negligible with respect to that of the sterile neutrino.

For a cosmological data set consisting in recent CMB and LSS data, as well as older but very conservative Lyman-α data, we found the conditional probability e.g. on the mass of a thermal relic given its temperature, or on the mass of a DW neutrino given its density suppression factor, etc. These proabilities are such that if the fourth neutrino is a standard one (with $\Delta N_{\rm eff} = 1$), it should have a mass $m_s \lesssim 0.4$ eV (2σ C.L.) or $m_s \lesssim 0.9$ eV (3σ C.L.).

At the 3σ C.L., a mass $m_s = 1$ eV can be accommodated with the data provided that this neutrino is thermally distributed with $T_s/T_\nu^{\rm id} \lesssim 0.97$, or non-resonantly produced with $\Delta N_{\rm eff} \lesssim 0.9$. The bounds become dramatically tighter when the mass increases. At the same confidence level, a mass of just $m_s = 2$ eV requires either $T_s/T_\nu^{\rm id} \lesssim 0.8$ or $\Delta N_{\rm eff} \lesssim 0.5$, while a mass $m_s = 5$ eV requires $T_s/T_\nu^{\rm id} \lesssim 0.6$ or $\Delta N_{\rm eff} \lesssim 0.2$.

Our bounds can hopefully be used for constraining particle-physics-motivated models

with three active and one sterile neutrinos, as those investigated recently in order to explain possible anomalies in neutrino oscillation data. Many of these models can be immediately localized in our figures 3 or 4. For sterile neutrinos or other particles which do not fall in the thermal or DW category, a good approximation consists in computing their velocity dispersion and localizing the model in our figure 5 [3]. Future neutrino oscillation experiments are expected to test the self-consistency of the standard three-neutrino scenario with increasing accuracy. If anomalies and indications for sterile neutrinos tend to persist, it will be particularly useful to perform joint analysis of oscillation and cosmological data, using the lines of this work for the latter part.

Acknowledgments

M.A.A. would like to thank the International Doctorate on AstroParticle Physics (IDAPP) for financial support, as well as LAPTH for hospitality during the realization of most of this work. M.A.A. and J.L. thank INFN for supporting a visit to the Galileo Galilei Institute for Theoretical Physics, in which this project was initiated. J.L. also acknowledges the support of the EU 6th Framework Marie Curie Research and Training network "UniverseNet" (MRTN-CT-2006-035863). Numerical simulations were performed on the MUST cluster at LAPP, Annecy (IN2P3/CNRS and Université de Savoie).

References

[1] S. Abe et al., Phys. Rev. Lett. **100**, 221803 (2008), arXiv:0801.4589.

[2] P. Adamson et al., Phys. Rev. **D77**, 072002 (2008), arXiv:0711.0769.

[3] A. Aguilar et al., Phys. Rev. **D64**, 112007 (2001), arXiv:hep-ex/0104049.

[4] J. N. Abdurashitov et al., Phys. Rev. **C73**, 045805 (2006), arXiv:nucl-ex/0512041.

[5] A. A. Aguilar-Arevalo et al., Phys. Rev. Lett. **98**, 231801 (2007), arXiv:0704.1500.

[6] C. Giunti and M. Laveder, Phys. Rev. **D77**, 093002 (2008), arXiv:0707.4593.

[7] W. Hampel et al., Phys. Lett. **B420**, 114 (1998).

[8] J. N. Abdurashitov et al., Phys. Rev. **C59**, 2246 (1999), arXiv:hep-ph/9803418.

[9] J. N. Abdurashitov et al., Astropart. Phys. **25**, 349 (2006), arXiv:nucl-ex/0509031.

[10] C. Giunti and M. Laveder, Mod. Phys. Lett. **A22**, 2499 (2007), arXiv:hep-ph/0610352.

[11] M. A. Acero, C. Giunti, and M. Laveder, Physical Review D –, (2008), arXiv:0711.4222.

[3] However, this approximation could be not so good when the distribution $p^2 f(p)$ of the non-thermal relic peaks near $p = 0$, as if part of these relics were actually cold, see [31].

[12] Y. Declais et al., Nucl. Phys. **B434**, 503 (1995).

[13] M. Apollonio et al., Eur. Phys. J. **C27**, 331 (2003), arXiv:hep-ex/0301017.

[14] A. A. Aguilar-Arevalo et al., Phys. Rev. **D78**, 012007 (2008), arXiv:0805.1764.

[15] E. Komatsu et al., (2008), arXiv:0803.0547.

[16] A. D. Dolgov, Phys. Rept. **370**, 333 (2002), arXiv:hep-ph/0202122.

[17] P. Crotty, J. Lesgourgues, and S. Pastor, Phys. Rev. **D69**, 123007 (2004), arXiv:hep-ph/0402049.

[18] A. Cuoco, J. Lesgourgues, G. Mangano, and S. Pastor, Phys. Rev. **D71**, 123501 (2005), arXiv:astro-ph/0502465.

[19] J. Lesgourgues and S. Pastor, Phys. Rept. **429**, 307 (2006), arXiv:astro-ph/0603494.

[20] S. Hannestad and G. G. Raffelt, JCAP **0611**, 016 (2006), arXiv:astro-ph/0607101.

[21] N. F. Bell, E. Pierpaoli, and K. Sigurdson, Phys. Rev. **D73**, 063523 (2006), arXiv:astro-ph/0511410.

[22] M. Cirelli and A. Strumia, JCAP **0612**, 013 (2006), arXiv:astro-ph/0607086.

[23] S. Dodelson, A. Melchiorri, and A. Slosar, Phys. Rev. Lett. **97**, 04301 (2006), arXiv:astro-ph/0511500.

[24] P. Di Bari, Phys. Rev. **D65**, 043509 (2002), arXiv:hep-ph/0108182.

[25] K. N. Abazajian, Astropart. Phys. **19**, 303 (2003), arXiv:astro-ph/0205238.

[26] G. F. Giudice, E. W. Kolb, A. Riotto, D. V. Semikoz, and I. I. Tkachev, Phys. Rev. **D64**, 043512 (2001), arXiv:hep-ph/0012317.

[27] G. Gelmini, S. Palomares-Ruiz, and S. Pascoli, Phys. Rev. Lett. **93**, 081302 (2004), arXiv:astro-ph/0403323.

[28] G. Gelmini, E. Osoba, S. Palomares-Ruiz, and S. Pascoli, (2008), arXiv:0803.2735.

[29] C. E. Yaguna, JHEP **06**, 002 (2007), arXiv:0706.0178.

[30] M. Kawasaki, K. Kohri, and N. Sugiyama, Phys. Rev. **D62**, 023506 (2000), arXiv:astro-ph/0002127.

[31] A. Boyarsky, J. Lesgourgues, O. Ruchayskiy, and M. Viel, In preparation.

[32] S. Dodelson and L. M. Widrow, Phys. Rev. Lett. **72**, 17 (1994), arXiv:hep-ph/9303287.

[33] S. Colombi, S. Dodelson, and L. M. Widrow, Astrophys. J. **458**, 1 (1996), arXiv:astro-ph/9505029.

[34] A. Lewis, A. Challinor, and A. Lasenby, Astrophys. J. **538**, 473 (2000), arXiv:astro-ph/9911177.

[35] A. Lewis and S. Bridle, Phys. Rev. **D66**, 103511 (2002), arXiv:astro-ph/0205436.

[36] D. N. Spergel et al., Astrophys. J. Suppl. **170**, 377 (2007), arXiv:astro-ph/0603449.

[37] J. Dunkley et al., (2008), arXiv:0803.0586.

[38] C. L. Reichardt et al., (2008), arXiv:0801.1491.

[39] J. L. Sievers et al., (2005), arXiv:astro-ph/0509203.

[40] C. J. MacTavish et al., Astrophys. J. **647**, 799 (2006), arXiv:astro-ph/0507503.

[41] M. Tegmark et al., Phys. Rev. **D74**, 123507 (2006), arXiv:astro-ph/0608632.

[42] J. Hamann, S. Hannestad, G. G. Raffelt, and Y. Y. Y. Wong, JCAP **0708**, 021 (2007), arXiv:0705.0440.

[43] J. Hamann, S. Hannestad, A. Melchiorri, and Y. Y. Y. Wong, JCAP **0807**, 017 (2008), arXiv:0804.1789.

[44] P. Astier et al., Astron. Astrophys. **447**, 31 (2006), arXiv:astro-ph/0510447.

[45] M. Viel, M. G. Haehnelt, and V. Springel, Mon. Not. Roy. Astron. Soc. **354**, 684 (2004), arXiv:astro-ph/0404600.

[46] A. Boyarsky, J. Lesgourgues, O. Ruchayskiy, and M. Viel, (2008), arXiv:0812.0010.

[47] S. Hannestad, A. Mirizzi, and G. Raffelt, JCAP **0507**, 002 (2005), arXiv:hep-ph/0504059.

[48] S. Hannestad, A. Mirizzi, G. G. Raffelt, and Y. Y. Y. Wong, JCAP **0804**, 019 (2008).

[49] U. Seljak, A. Slosar, and P. McDonald, JCAP **0610**, 014 (2006), astro-ph/0604335.

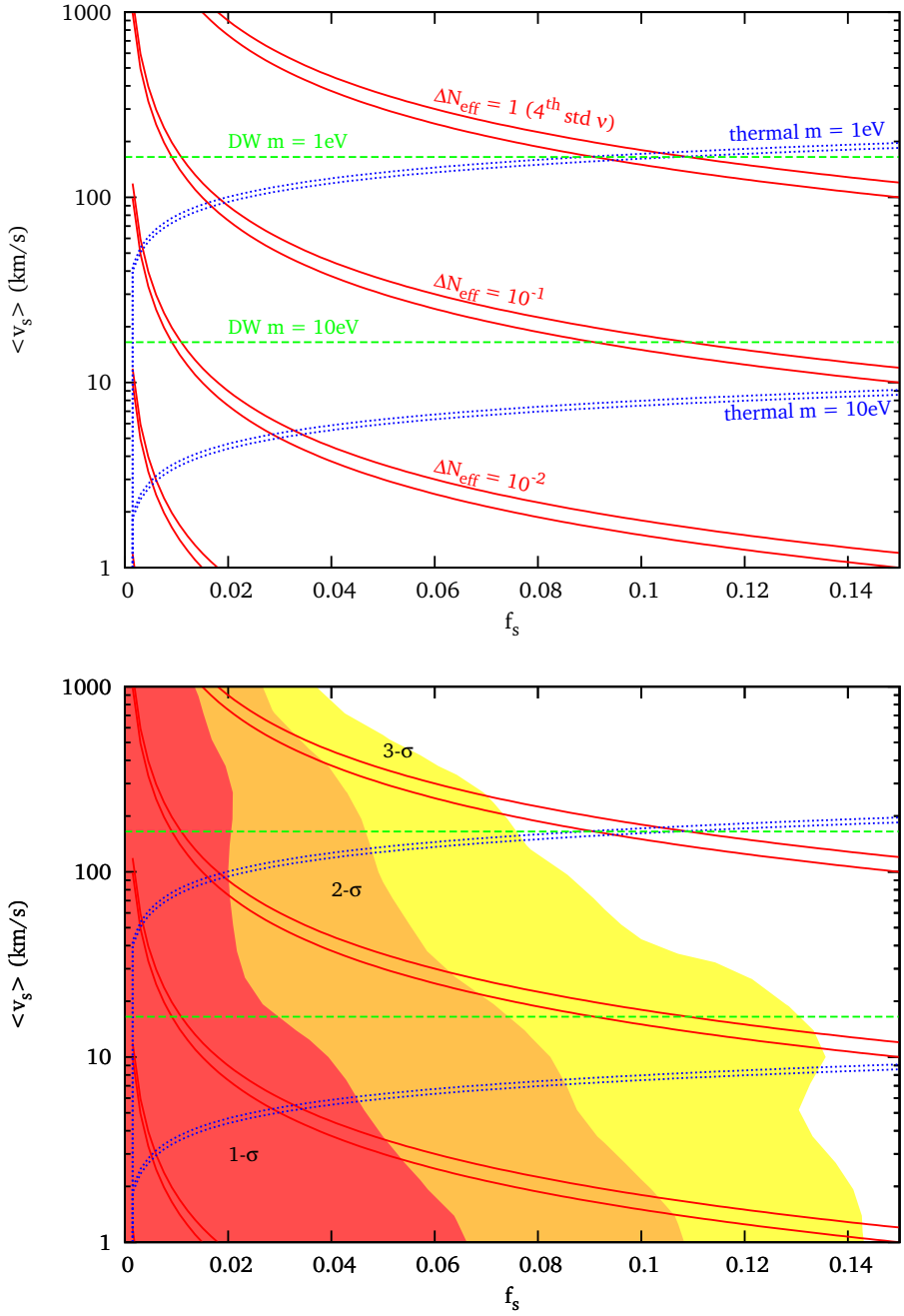

Figure 1: *(Top)* the parameter space $(f_s, \langle v_s \rangle)$ chosen in our general analysis. The thin bands delimited by red/solid lines show regions of equal $\Delta N_{\rm eff}$ (assuming $\omega_{\rm dm} = 0.11 \pm 0.01$); these bands are fully model-independent. We also show the model-dependent regions of equal mass, delimited by blue/dotted lines for the case of early decoupled thermal relics, and consisting in horizontal green/dashed lines for Dodelson-Widrow sterile neutrinos. *(Bottom)* same with, in addition, the regions allowed at the 68.3% (1σ), 95.4% (2σ) and 99.7% (3σ) C.L. by our cosmological data set, in a Bayesian analysis with flat priors on f_s and $\log_{10}\langle v_s \rangle$ within the displayed range.

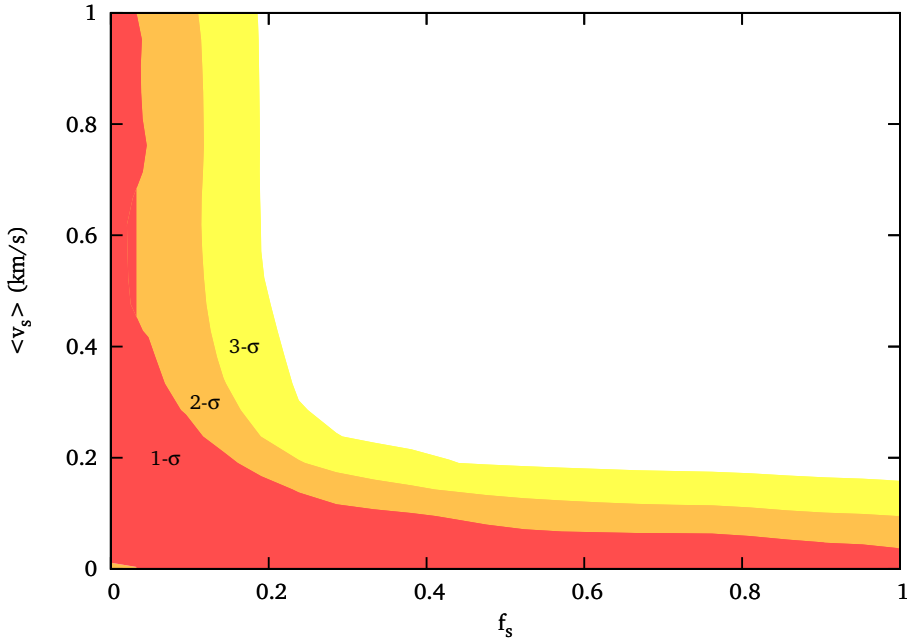

Figure 2: 1σ, 2σ and 3σ contours of the marginalized likelihood for the two parameters $(f_s, \langle v_s \rangle)$, with different priors than in previous figures. As explained in the text, this plot shows the region where the sterile neutrino is heavy and behaves like warm dark matter, in complement to Figure 1, which is based on a different range/prior for $\langle v_s \rangle$ adapted to the case of a light, hot sterile neutrino.

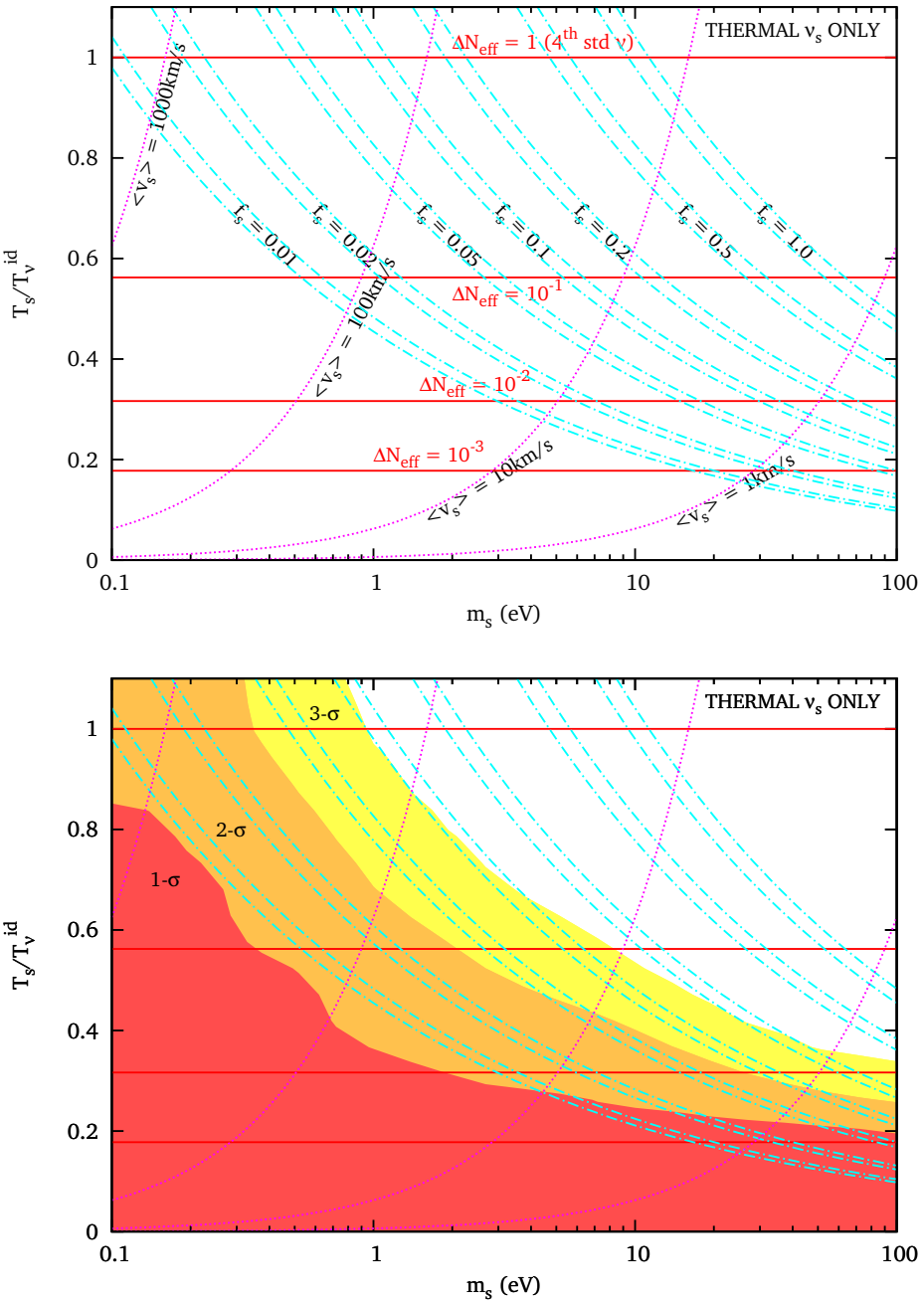

Figure 3: *(Top)* the parameter space (m_s,$T_s/T_\nu^{\rm id}$) used in the particular case of early decoupled thermal relics of temperature T_s (with $T_\nu^{\rm id} \equiv (4/11)^{1/3} T_\gamma$). The thin bands delimited by blue/dot-dashed lines show regions of equal f_s (assuming $\omega_{\rm dm} = 0.11 \pm 0.01$); the magenta/dotted lines correspond to fixed values of the velocity dispersion today; horizontal red/solid lines to fixed $\Delta N_{\rm eff}$. *(Bottom)* same with, in addition, the regions allowed at the 68.3% (1σ), 95.4% (2σ) and 99.7% (3σ) C.L. by our cosmological data set, in a Bayesian analysis with flat priors on $\log_{10}(m_s)$ and $T_s/T_\nu^{\rm id}$ within the displayed range.

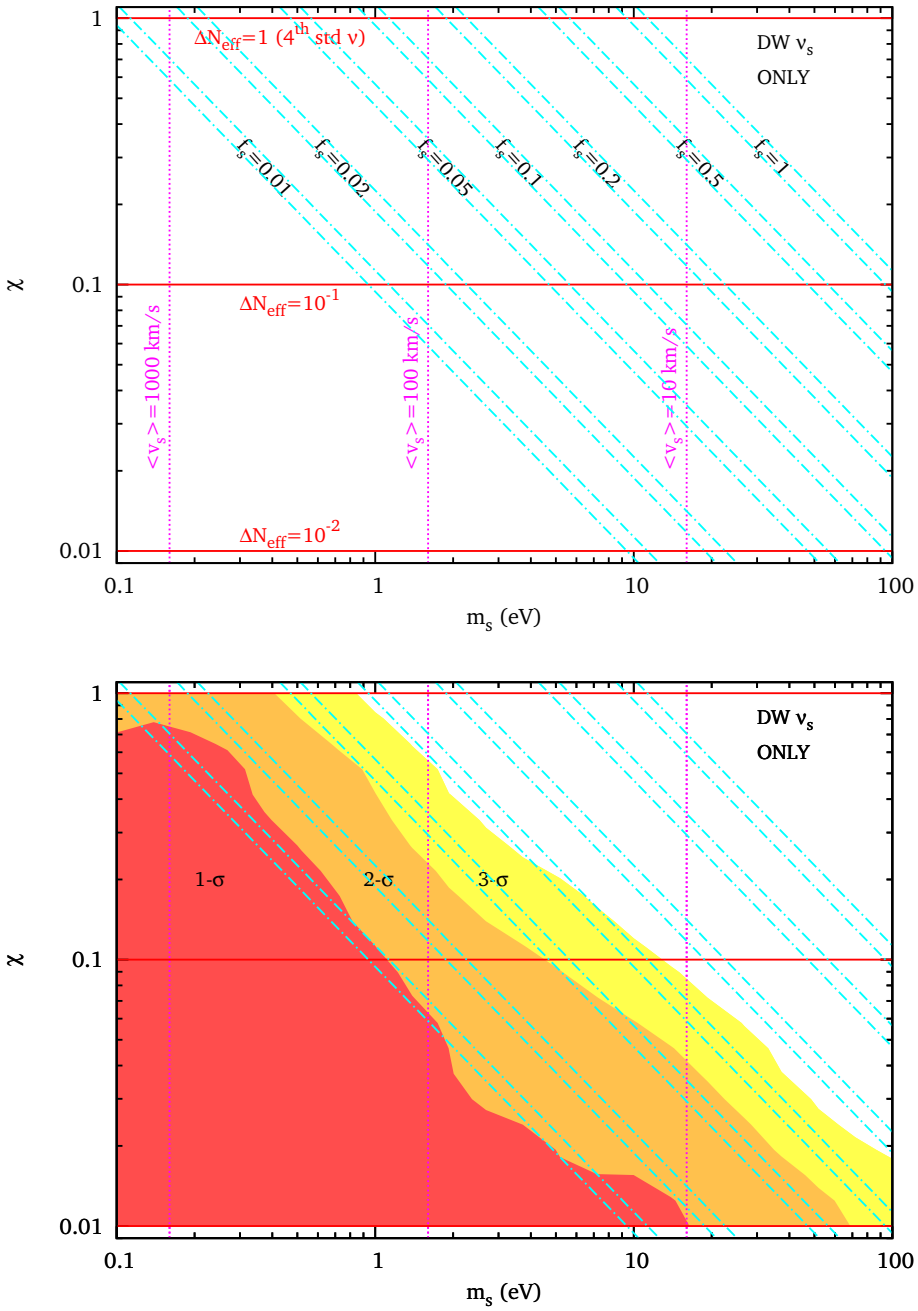

Figure 4: *(Top)* the parameter space (m_s,χ) used in the particular case of DW relics. The thin bands delimited by blue/dot-dashed lines show regions of equal f_s (assuming $\omega_{\rm dm} = 0.11\pm0.01$); the magenta/dotted lines correspond to fixed values of the velocity dispersion today; horizontal red/solid lines to fixed $\Delta N_{\rm eff}$. *(Bottom)* same with, in addition, the regions allowed at the 68.3% (1σ), 95.4% (2σ) and 99.7% (3σ) C.L. by our cosmological data set, in a Bayesian analysis with flat priors on $\log_{10}(m_s)$ and $\log_{10}(\chi)$ within the displayed range.

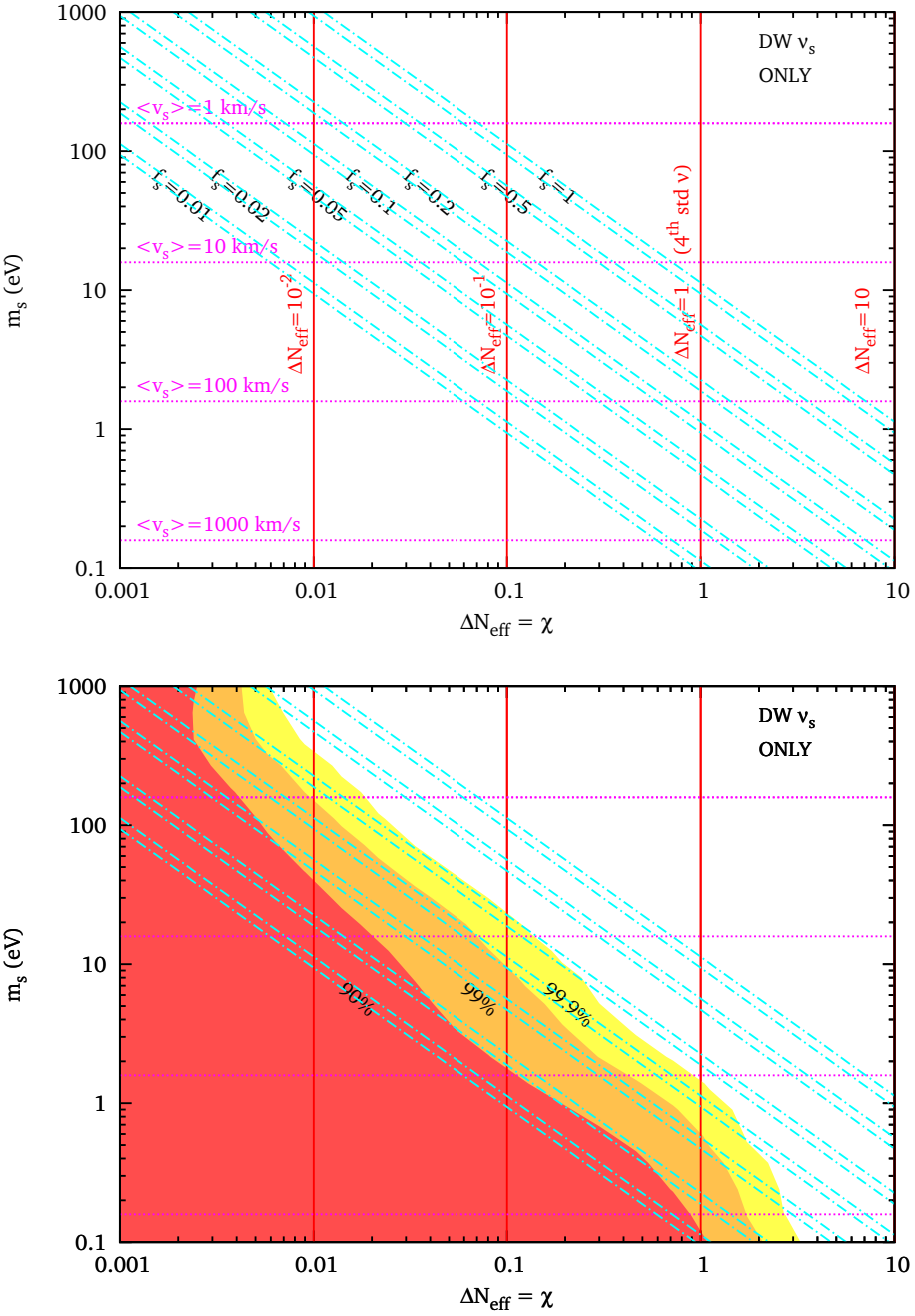

Figure 5: *(Top)* the parameter space ($\Delta N_{\rm eff}$,m_s) used for comparison with Cirelli & Strumia in the particular case of DW relics. The thin bands delimited by blue/dot-dashed lines show regions of equal f_s (assuming $\omega_{\rm dm} = 0.11 \pm 0.01$); the magenta/dotted lines correspond to fixed values of the velocity dispersion today; horizontal red/solid lines to fixed $\Delta N_{\rm eff}$. *(Bottom)* same with, in addition, the regions allowed at the 90%, 99% and 99.9% C.L. by our cosmological data set, in a Bayesian analysis with flat priors on $\log_{10}(\Delta N_{\rm eff})$ and $\log_{10}(m_s)$ within the displayed range.

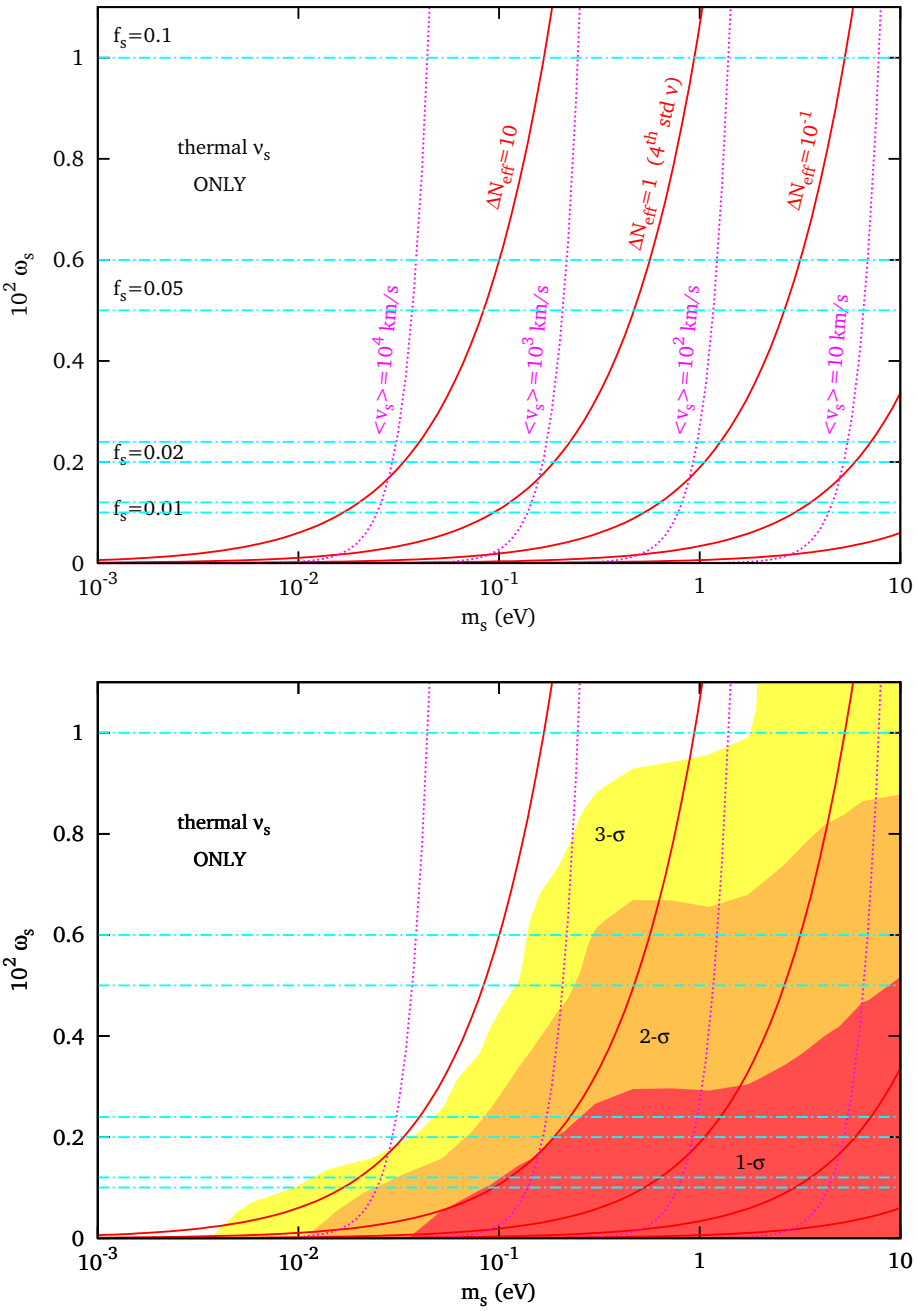

Figure 6: *(Top)* the parameter space (m_s,ω_s) used for comparison with Dodelson, Melchiorri & Slosar in the particular case of thermal relics. The thin bands delimited by blue/dot-dashed lines show regions of equal f_s (assuming $\omega_{\rm dm} = 0.11 \pm 0.01$); the magenta/dotted lines correspond to fixed values of the velocity dispersion today; horizontal red/solid lines to fixed $\Delta N_{\rm eff}$. *(Bottom)* same with, in addition, the regions allowed at the 68.3% (1σ), 95.4% (2σ) and 99.7% (3σ) C.L. by our cosmological data set, in a Bayesian analysis with flat priors on $\log_{10}(m_s)$ and ω_s within the displayed range.

5.3 Current constraints on the leptonic asymmetry, PRD 86, 023517 (2012)

CERN-PH-TH-2012-089, IFIC/12-28, LAPTH-018/12

Cosmological lepton asymmetry with a nonzero mixing angle θ_{13}

Emanuele Castorina,[1] Urbano França,[2] Massimiliano Lattanzi,[3] Julien Lesgourgues,[4,5,6] Gianpiero Mangano,[7] Alessandro Melchiorri,[8] and Sergio Pastor[2]

[1] *SISSA, Via Bonomea 265, 34136, Trieste, Italy*
[2] *Instituto de Física Corpuscular (CSIC-Universitat de València), Apdo. 22085, 46071 Valencia, Spain*
[3] *Dipartimento di Fisica G. Occhialini, Università Milano-Bicocca and INFN, Sezione di Milano-Bicocca, Piazza della Scienza 3, I-20126 Milano, Italy*
[4] *CERN, Theory Division, CH-1211 Geneva 23, Switzerland*
[5] *Institut de Théorie des Phénomènes Physiques, EPFL, CH-1015 Lausanne, Switzerland*
[6] *LAPTH (CNRS-Université de Savoie), B.P. 110, F-74941 Annecy-le-Vieux Cedex, France*
[7] *INFN, Sezione di Napoli, Complesso Univ. Monte S. Angelo, Via Cintia, I-80126 Napoli, Italy*
[8] *Physics Department and INFN, Università di Roma La Sapienza, Ple Aldo Moro 2, 00185, Rome, Italy*

(Dated: June 26, 2012)

While the baryon asymmetry of the Universe is nowadays well measured by cosmological observations, the bounds on the lepton asymmetry in the form of neutrinos are still significantly weaker. We place limits on the relic neutrino asymmetries using some of the latest cosmological data, taking into account the effect of flavor oscillations. We present our results for two different values of the neutrino mixing angle θ_{13}, and show that for large θ_{13} the limits on the total neutrino asymmetry become more stringent, diluting even large initial flavor asymmetries. In particular, we find that the present bounds are still dominated by the limits coming from Big Bang Nucleosynthesis, while the limits on the total neutrino mass from cosmological data are essentially independent of θ_{13}. Finally, we perform a forecast for COrE, taken as an example of a future CMB experiment, and find that it could improve the limits on the total lepton asymmetry approximately by up to a factor 6.6.

PACS numbers: 98.80.-k, 14.60.Pq. 26.35.+c, 98.70.Vc, 98.80.Es

I. INTRODUCTION

Quantifying the asymmetry between matter and antimatter of the Universe is crucial for understanding some of the particle physics processes that might have taken place in the early Universe, at energies much larger than the ones that can be reached currently in particle accelerators. Probes of the anisotropies of the cosmic microwave background (CMB) together with other cosmological observations have measured the cosmological baryon asymmetry η_b to the percent level thanks to very precise measurements of the baryon density [1]. For the lepton asymmetries, while they are expected to be of the same order of the baryonic one due to sphaleron effects that equilibrate both asymmetries, it could be the case that other physical processes lead instead to leptonic asymmetries much larger than η_b (see, *e.g.*, [2–4]), with consequences for the early Universe phase transitions [5], cosmological magnetic fields [6], and the dark matter relic density [7–9]. Neutrino asymmetries are also bound to be nonzero in the presence of neutrino isocurvature perturbations, like those generated by curvaton decay [10–12]. Those large neutrino asymmetries could have been imprinted in the cosmological data [13, 14], and although the limits on such asymmetries have been improving over the last years, current constraints are still many orders of magnitude weaker than the baryonic measurement.

On the other hand, thanks to the neutrino oscillations the initial primordial flavor asymmetries are redistributed among the active neutrinos before the onset of Big Bang Nucleosynthesis (BBN) [15–17], which makes the knowledge of the oscillation parameters important for correctly interpreting the limits on such asymmetries. Nowadays all of those parameters are accurately measured (see *e.g.* [18, 19]), with the exception of the mixing angle θ_{13} that only recently started to be significantly constrained. In fact, several neutrino experiments over the last year gave indications of nonzero values for $\sin^2\theta_{13}$ [20–22], and recently the Daya Bay reactor experiment claimed a measurement of $\sin^2(2\theta_{13}) = 0.092 \pm 0.016(\text{stat.}) \pm 0.005(\text{syst.})$ at 68% C.L. [23], excluding a zero value for θ_{13} with high significance. The same finding has been also reported by the RENO Collaboration [24], $\sin^2(2\theta_{13}) = 0.113 \pm 0.013(\text{stat.}) \pm 0.019(\text{syst.})$ (68% C.L.).

Finally, yet another important piece of information for reconstructing the neutrino asymmetries in the Universe is the measured value of the relativistic degrees of freedom in the early universe, quantified in the so-called effective number of neutrinos, $N_{\rm eff}$. In the case of the three active neutrino flavors with zero asymmetries and a standard thermal history, its value is the well-known $N_{\rm eff} \simeq 3.046$ [25], but the presence of neutrino asymmetries can increase that number while still satisfying the BBN constraints [26]. Interestingly enough, recent CMB data has consistently given indications of $N_{\rm eff}$ higher than the standard value: recently the Atacama Cosmology Telescope (ACT) [27] and the South Pole Telescope (SPT) [28, 29] have found evidence for $N_{\rm eff} > 3.046$ at 95% C. L., making the case for extra relativistic degrees

of freedom stronger (see also [30]). It should however be kept in mind that other physical processes, like *e.g.* the contribution from the energy density of sterile neutrinos [31, 32] or of gravitational waves [33], could also lead to a larger value for $N_{\rm eff}$.

Some recent papers have analyzed the impact of neutrino asymmetries with oscillations on BBN [26, 34, 35], mainly because data on light element abundances dominate the current limits on the asymmetries. Some studies using CMB data can be found in the literature (see for instance [36–38] for limits on the degeneracy parameters ξ_ν using the WMAP data and [39] for the effect of the primordial Helium fraction in a Planck forecast), but our paper improves on that in two directions. First, we used for our analysis the neutrino spectra in the presence of asymmetries after taking into account the effect of flavor oscillations. Second, we checked the robustness of our results comparing the analysis of CMB and BBN data with a more complete set of cosmological data, including in particular supernovae Ia (SNIa) data [40], the measurement of the Hubble constant from the Hubble Space Telescope (HST) [41], and the Sloan Digital Sky Survey (SDSS) data on the matter power spectrum[42]. While current CMB measurements and the other datasets are not expected to improve significantly the constraints on the asymmetries, they constrain the sum of the neutrino masses, giving a more robust and general picture of the cosmological parameters.

Our goals in this work is twofold: first, we constrain the neutrino asymmetries and the sum of neutrino masses for both zero and nonzero values of θ_{13} using some of the latest cosmological data to obtain an updated and clear idea of the limits on them using current data; second, we perform a forecast of the constraints that could be achievable with future CMB experiments, taking as an example the proposed mission COrE[1] [43]. Given that current constraints are basically dominated by the BBN constraints, we use our forecast to answer the more general question of whether future CMB experiments can be competitive with the BBN bounds.

This paper is organized as follows. Initially, we briefly review in Sec. II the dynamics of the neutrino asymmetries prior to the BBN epoch. With those tools in hand, we proceed to study in Sec. III the impact on cosmological observables of the neutrino asymmetries for two values of the mixing angle θ_{13} using current cosmological data. We then step towards the future and describe in Sec. IV our forecast for the experiment COrE, where we study the potential of the future data from lensing of CMB anisotropies to constrain some of the cosmological parameters (in particular, neutrino asymmetries and the sum of the neutrino masses) with great precision. Finally, in Sec. V we draw our conclusions.

[1] http://www.core-mission.org

II. EVOLUTION OF COSMOLOGICAL NEUTRINOS WITH FLAVOR ASYMMETRIES

The dynamics of the neutrino distribution functions in the presence of flavor asymmetries and neutrino oscillations in the early Universe has been discussed in detail in the literature [26, 34, 35], and here we will only briefly review its main features and its consequences for the late cosmology.

We assume that flavor neutrino asymmetries, η_{ν_α}, were produced in the early Universe. At large temperatures frequent weak interactions keep neutrinos in equilibrium thus, their energy spectrum follows a Fermi-Dirac distribution with a chemical potential μ_{ν_α} for each neutrino flavor. If $\xi_\alpha \equiv \mu_{\nu_\alpha}/T$ is the degeneracy parameter, the asymmetry is given by

$$\eta_{\nu_\alpha} \equiv \frac{n_{\nu_\alpha} - n_{\bar{\nu}_\alpha}}{n_\gamma} = \frac{1}{12\zeta(3)}\left[\pi^2\xi_\alpha + \xi_\alpha^3\right] . \qquad (1)$$

Here n_{ν_α} ($n_{\bar{\nu}_\alpha}$) denotes the neutrino (antineutrino) number density, n_γ is the photon number density, and $\zeta(3) = 1.20206$.

As usual, we will write the radiation energy density of the Universe in terms of the parameter $N_{\rm eff}$, the effective number of neutrinos, as

$$\rho_r = \rho_\gamma \left[1 + \frac{7}{8}\left(\frac{4}{11}\right)^{4/3} N_{\rm eff}\right] , \qquad (2)$$

with $N_{\rm eff} = 3.046$ the value in the standard case with zero asymmetries and no extra relativistic degrees of freedom [25]. Assuming that equilibrium holds for the neutrino distribution functions, the presence of flavor asymmetries leads to an enhancement

$$\Delta N_{\rm eff} = \frac{15}{7}\sum_{\alpha=e,\mu,\tau}\left[2\left(\frac{\xi_\alpha}{\pi}\right)^2 + \left(\frac{\xi_\alpha}{\pi}\right)^4\right] . \qquad (3)$$

Note that a neutrino degeneracy parameter of order $\xi_\alpha \gtrsim 0.3$ is needed in order to have a value of $\Delta N_{\rm eff}$ at least at the same level of the effect of non-thermal distortions discussed in [25]. This corresponds to $\eta_{\nu_\alpha} \sim \mathcal{O}(0.1)$. On the other hand, the primordial abundance of ^{4}He depends on the presence of an electron neutrino asymmetry and sets a stringent BBN bound on η_{ν_e} which does not apply to the other flavors, leaving a total neutrino asymmetry of order unity unconstrained [44, 45]. However, this conclusion relies on the absence of effective neutrino oscillations that would modify the distribution of the asymmetries among the different flavors before BBN.

The evolution of the neutrino asymmetries in the epoch before BBN with three-flavor neutrino oscillations is found by solving the equations of motion for 3×3 density matrices of the flavor neutrinos as described in [46, 47], including time-dependent vacuum and matter terms, both from background $e^\pm$ and neutrinos, as well as the collision integrals from neutrino weak interactions.

TABLE I: Cosmological and neutrino parameters.

Type	Symbol	Meaning	Uniform Prior
Primary	$\Omega_b h^2$	Baryon density	$(0.005, 0.1)$
Cosmological	$\Omega_{dm} h^2$	Dark matter density[a]	$(0.01, 0.99)$
Parameters	τ	Optical depth to reionization	$(0.01, 0.8)$
	$100\theta_s$	Angular scale of the sound horizon at the last scattering	$(0.5, 10)$
	n_s	Scalar index of the power spectrum	$(0.5, 1.5)$
	$\log\left[10^{10} A_s\right]$	Scalar amplitude of the power spectrum [b]	$(2.7, 4)$
Neutrino	m_1(eV)	Mass of the lightest neutrino [c]	$(0, 1)$
Parameters	η_ν	Total asymmetry at $T = 10$ MeV	$(-0.8, 0.8)$
	$\eta^{\rm in}_{\nu_e}$	Initial electron neutrino asymmetry at $T = 10$ MeV	$(-1.2, 1.2)$
Derived	h	Reduced Hubble constant[d]	-
Parameters	$\Delta N_{\rm eff}$	Enhancement to the standard effective number of neutrinos[e]	-

[a] Also includes neutrinos.
[b] at the pivot wavenumber $k_0 = 0.05$ Mpc^{-1}.
[c] We assume here normal hierarchy.
[d] $H_0 = 100h$ km s^{-1} Mpc^{-1}.
[e] $N_{\rm eff} = 3.046$.

This was done under certain approximations in refs. [15–17], where it was shown that neutrino oscillations are indeed effective before the onset of BBN. Therefore, the total lepton asymmetry is redistributed among the neutrino flavors and the BBN bound on η_{ν_e} can be translated into a limit on $\eta_\nu = \eta_{\nu_e} + \eta_{\nu_\mu} + \eta_{\nu_\tau}$, unchanged by oscillations and constant until electron-positron annihilations, when it decreases due to the increase in the photon number density.

The temperature at which flavor oscillations become effective is important not only to establish η_{ν_e} at the onset of BBN, but also to determine whether weak interactions with e^+e^- can still keep neutrinos in good thermal contact with the primeval plasma. Oscillations redistribute the asymmetries among the flavors, but only if they occur early enough interactions would preserve Fermi-Dirac spectra for neutrinos, in such a way that the degeneracies ξ_α are well defined for each η_{ν_α} and the relation in Eq. (3) remains valid. This the case of early conversions of muon and tau neutrinos, since oscillations and collisions rapidly equilibrate their asymmetries at $T \simeq 15$ MeV [15]. Therefore one can assume the initial values $\eta^{\rm in}_{\nu_\mu} = \eta^{\rm in}_{\nu_\tau} \equiv \eta^{\rm in}_{\nu_x}$, leaving as free parameters $\eta^{\rm in}_{\nu_e}$ and the total asymmetry $\eta_\nu = \eta^{\rm in}_{\nu_e} + 2\eta^{\rm in}_{\nu_x}$.

If the initial values of the flavor asymmetries $\eta^{\rm in}_{\nu_e}$ and $\eta^{\rm in}_{\nu_x}$ have opposite signs, neutrino conversions will tend to reduce the asymmetries which in turn will decrease $N_{\rm eff}$. But if flavor oscillations take place at temperatures close to neutrino decoupling this would not hold and an extra contribution of neutrinos to radiation is expected with respect to the value in Eq. (3), as emphasized in [26] and shown in Fig. 1, where the $N_{\rm eff}$ isocontours for non-zero mixing are compared with those obtained from the frozen neutrino distributions taking into account the effect of flavor oscillations [34]. One can see that oscillations efficiently reduce $N_{\rm eff}$ for neutrino asymmetries with respect to the initial values from Eq. (3).

The evolution of the neutrino and antineutrino distribution functions with non-zero initial asymmetries, from $T = 10$ MeV until BBN, has been calculated in [26, 34]. Here we use the final numerical results for these spectra in a range of values for $\eta^{\rm in}_{\nu_e}$ and η_ν as an input for our analysis, described in the next Section. Note that an analysis in terms of the degeneracy parameters ξ_α as done for instance in [38] is no longer possible. We adopt the best fit values for the neutrino oscillation parameters quoted in [18], assuming a normal hierarchy of the neutrino masses, except for the mixing angle θ_{13}, for which we will adopt two distinct values: $\theta_{13} = 0$ and $\sin^2\theta_{13} = 0.04$. The latter is close to the upper limit placed by the Daya Bay [23] and RENO [24] experiments on this mixing angle (with a best-fit value of $\sin^2\theta_{13} = 0.024$ and $\sin^2\theta_{13} = 0.029$, respectively), and is used as an example to understand the cosmological implications of a nonzero θ_{13}. Moreover, since the flavor asymmetries equilibrate for large values of this mixing angle, the cosmological effects are similar for $\sin^2\theta_{13} \gtrsim 0.02$, as in the case of an inverted hierarchy for a broad range of θ_{13} values (see, for instance, Fig. 4 of Ref. [35]). As for the case $\theta_{13} = 0$, though it seems presently disfavoured with a high statistical significance after the Daya Bay and RENO results, we have decided to include it for comparison.

III. COSMOLOGICAL CONSTRAINTS ON NEUTRINO PARAMETERS

Having set the basic framework for the calculation of the neutrino distribution functions in the presence of asymmetries and for different θ_{13}, we can now proceed to investigate its cosmological effects.

In order to constrain the values of the cosmological

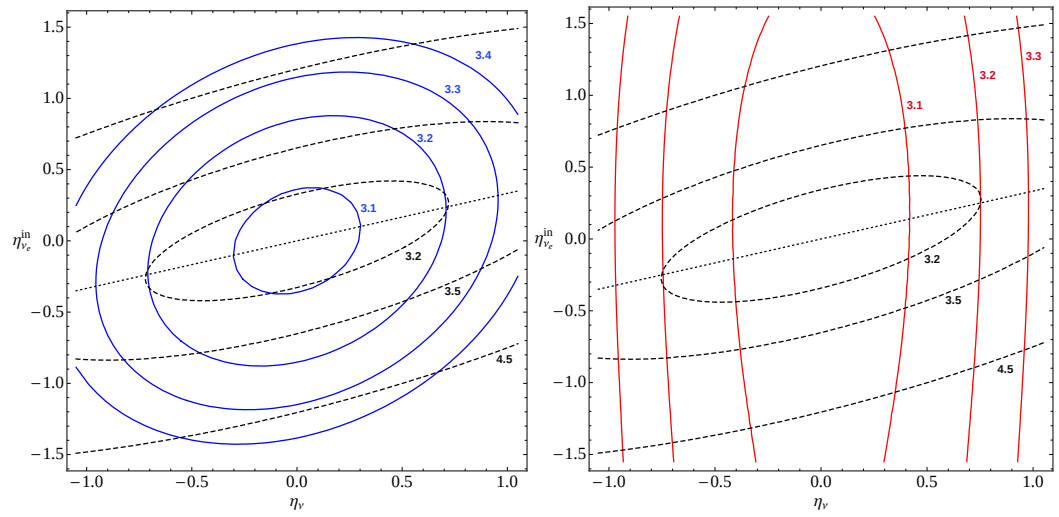

FIG. 1: Final contribution of neutrinos with primordial asymmetries to the radiation energy density. The isocontours of $N_{\rm eff}$ on the plane $\eta^{\rm in}_{\nu_e}$ vs. η_ν, including flavor oscillations, are shown for two values of $\sin^2\theta_{13}$: 0 (blue solid curves, left panel) and 0.04 (red solid curves, right panel) and compared to the case with zero mixing (dashed curves). The dotted line corresponds to $\eta_\nu = \eta_{\nu_x}$ $(x = \mu, \tau)$, where one expects oscillations to have negligible effects.

neutrino asymmetries, we compare our results to the observational data. In particular, we use a modified version of the CAMB code[2] [48] to evolve the cosmological perturbations and obtain the CMB and matter power spectra in the presence of non-zero neutrino asymmetries in the neutrino distribution functions. We checked that the spectra computed by our modified CAMB version are consistent up to high accuracy with those obtained with CLASS [49], that incorporates the models considered here in its public version. This version of CAMB is interfaced with the Markov chain Monte Carlo package CosmoMC[3] [50] that we use to sample the parameter space and obtain the posterior distributions for the parameters of interest.

We derive our constraints in the framework of a flat ΛCDM model with the three standard model neutrinos and purely adiabatic initial conditions. The parameters we use are described in Table I as well as the range of the flat priors used. As can be seen, six of them are the standard ΛCDM cosmological parameters, and we add to those three new parameters, namely the mass of the lightest neutrino mass eigenstate m_1 (the other two masses are calculated using the best fit for Δm^2_{21} and Δm^2_{31} obtained in [18], assuming normal hierarchy) and the two neutrino asymmetries we mentioned earlier, $\eta^{\rm in}_{\nu_e}$ and η_ν. The values of the effective degeneracy parameters ξ_α after BBN[4], needed by CAMB, are pre-calculated as a function of the asymmetries (following the method described in the previous section) over a grid in $(\eta^{\rm in}_{\nu_e}, \eta_\nu)$ and stored on a table, used for interpolation during the Monte Carlo run.

A comment on the parameterization is in order. It is a standard practice in cosmological analyses to parameterize the neutrino masses via $\Omega_\nu h^2$ or equivalently $f_\nu \equiv \Omega_\nu/\Omega_{dm}$, and from that (assuming that neutrinos decoupled at equilibrium) derive the sum of neutrino masses, which are taken to be degenerate. The presence of lepton asymmetries dramatically changes this simple scheme. Now the neutrino number density is a complicated function of the η's obtained from a non-equilibrium distribution function. When f_ν is used, any effect related to the way in which the total neutrino density is shared among the different mass eigenstates is completely lost. In that sense, the parameterization used in this paper looks more physically motivated since energy densities of neutrinos are constructed from two fundamental quantities, namely their phase space distributions and their masses.

The most basic dataset that we consider only consists of the WMAP 7-year temperature and polarization anisotropy data. We will refer to it simply as "WMAP". The likelihood is computed using the the WMAP likelihood code publicly available at the LAMBDA web-

[2] `http://camb.info/`
[3] `http://cosmologist.info/cosmomc/`
[4] The neutrino distribution functions can be parameterized by Fermi-Dirac-like functions with an effective ξ_α and temperature T_α [34], which are related to the first two moments of the distribution, the number density and energy density.

site[5]. We marginalize over the amplitude of the Sunyaev-Zel'dovich signal.

In addition to the WMAP data, we also include the BBN measurement of the ^{4}He mass fraction Y_p from the data collection analysis done in [51], in the form of a Gaussian prior

$$Y_p = 0.250 \pm 0.003 \quad (1\sigma)\,. \tag{4}$$

Indeed, some authors have recently reported a larger central value, $Y_p \sim 0.257$ [52–54], with quite different uncertainty determinations. In [55] using a Markov chain Monte Carlo technique already exploited in [54], the primordial value of ^{4}He decreased again to $Y_p = 0.2534 \pm 0.0083$, which is compatible at 1σ with (4). We will not use these results in our analysis, but we will comment on their possible impact in the following. We also note that in [56] a robust upper bound $Y_p < 0.2631$ (95 % C.L.) has been derived based on very weak assumptions on the astrophysical determination of ^{4}He abundance, namely that the minimum effect of star processing is to keep constant the helium content of a low-metallicity gas, rather than increase it, as expected. As we will show, the measurement of Y_p currently dominates the constraints on the asymmetries: if we were to conservatively allow for larger uncertainties on that measurement, like for example those reported in [55], our constraints from present data would correspondingly be weakened. Moreover, we decided not to use the Deuterium measurements since at the moment they are not competitive with Helium for constraining the asymmetries (see, *e.g.*, Fig. 6 of Ref. [34]), although there are recent claims that they could place strong constraints on $N_{\rm eff}$ at the level of $\Delta N_{\rm eff} \simeq \pm 0.5$ [57]. This is a very interesting perspective but at the moment, Deuterium measurements in different QSO absorption line systems show a significant dispersion, much larger than the quoted errors.

The dataset that uses both WMAP 7-year data and the determination of the primordial abundance of Helium as in (4) will be referred to as "WMAP+He". Measurements of Y_p represent the best "leptometer" currently available, in the sense that they place the most stringent constraints on lepton asymmetries for a given baryonic density [58]. The ^{4}He mass fraction depends on the baryonic density, the electron neutrino degeneracy parameter and the effective number of neutrino families. Thus, in order to consistently implement the above determination of Y_p in our Monte Carlo analysis, we compute $\Delta N_{\rm eff}$ and ξ_e coming from the distribution functions calculated with the asymmetries (as explained in the previous section) and store them on a table. During the CosmoMC run, we use this table to obtain by interpolation the values $\Delta N_{\rm eff}$ and ξ_e corresponding to given values of the asymmetries (which are the parameters actually used in the Monte Carlo), and finally to obtain Y_p as a function of $\Delta N_{\rm eff}$, ξ_e and $\Omega_b h^2$. Notice that this approach is slightly less precise than the one used in Refs. [34, 35], where a full BBN analysis was performed, but this approximation should suffice for our purposes, especially taking into account that we will be comparing BBN limits on the asymmetries with the ones placed by other cosmological data, that as we shall see are far less constraining. In any case, we have checked that the agreement between the interpolation scheme and the full BBN analysis is at the percent level.

We derive our constraints from parallel chains generated using the Metropolis-Hastings algorithm. For a subset of the models, we have also generated chains using the slice sampling method, in order to test the robustness of our results against a change in the algorithm. We use the Gelman and Rubin R parameter to evaluate the convergence of the chains, demanding that $R - 1 < 0.03$. The one- and two-dimensional posteriors are derived by marginalizing over the other parameters.

Our results for the cosmological and neutrino parameters from the analysis are shown in Table II, while Fig. 2 shows the marginalized one-dimensional probability distributions for the lightest neutrino mass, the initial electron-neutrino asymmetry, and the total asymmetry, for the different values of θ_{13}. Notice that the posterior for $\eta^{\rm in}_{\nu_e}$ (middle panel) is still quite large at the edges of the prior range. This happens also for both the $\eta^{\rm in}_{\nu_e}$ and η_ν posteriors obtained using only the WMAP data (not shown in the figure). Since the priors on these parameters do not represent a real physical constraint (as in the case $m_\nu > 0$), but just a choice of the range to explore, we refrain from quoting 95% credible intervals in these cases, as in order to do this one would need knowledge of the posterior in all the region where it significantly differs from zero. However, it is certain that the *actual* 95% C.I. includes the one that one would obtain using just part of the posterior (as long as this contains the peak of the distribution). If we do this, we obtain constraints that are anyway much worse than those from BBN. Finally, we also stress that if a larger experimental determination of Y_p or measurements with larger uncertainities were used, as those reported in [52–54], BBN would show a preference for larger values of $N_{\rm eff}$ as well.

Concerning the neutrino asymmetries, shown in the middle and right panels of Fig. 2, we notice that while the initial flavor asymmetries remain highly unconstrained by current data, the total asymmetry constraint improves significantly for $\theta_{13} \neq 0$. This result agrees with previous results from BBN-only studies [34, 35], and it is a result of the equilibration of flavor asymmetries when θ_{13} is large (see, *e.g.*, Fig. 5 of Ref. [34]). When the flavors equilibrate in the presence of a nonzero mixing angle ($\sin^2\theta_{13} = 0.04$ in our example) the total asymmetry is distributed almost equally among the different flavors, leading to a final asymmetry $\eta^{\rm fin}_{\nu_e} \approx \eta^{\rm fin}_{\nu_x} \approx \eta_\nu/3$ (where $x = \mu, \tau$). Hence, the fact that the BBN prior requires $\eta^{\rm fin}_{\nu_e} \approx 0$ for the correct abundance of primordial Helium (see Fig. 3) leads to a strong constraint on the constant

[5] `http://lambda.gsfc.nasa.gov/`

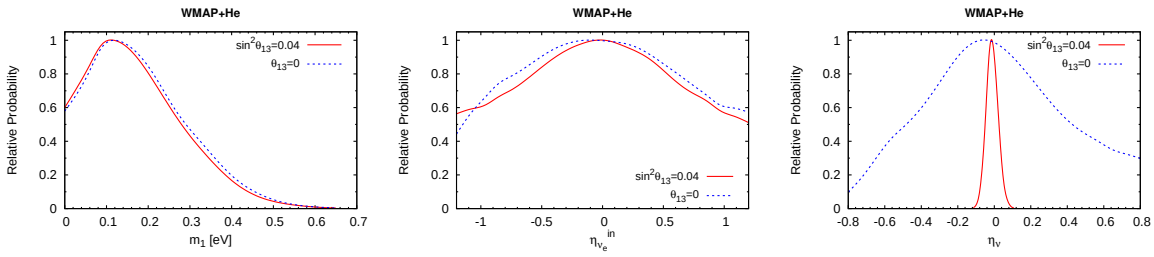

FIG. 2: One-dimensional posterior probability density for m_1, $\eta^{\rm in}_{\nu_e}$, and η_ν for the WMAP+He dataset.

TABLE II: 95% C.L. constraints on cosmological parameters for the WMAP and WMAP+He datasets.

Parameter	WMAP		WMAP+He	
	$\sin^2\theta_{13}=0$	$\sin^2\theta_{13}=0.04$	$\sin^2\theta_{13}=0$	$\sin^2\theta_{13}=0.04$
$100\ \Omega_b h^2$	$2.20^{+0.14}_{-0.12}$	$2.20^{+0.13}_{-0.12}$	2.20 ± 0.12	2.20 ± 0.12
$\Omega_{dm} h^2$	0.118 ± 0.016	$0.117^{+0.017}_{-0.016}$	0.119 ± 0.017	0.117 ± 0.016
τ	$0.085^{+0.029}_{-0.026}$	$0.085^{+0.030}_{-0.027}$	$0.085^{+0.030}_{-0.027}$	$0.085^{+0.029}_{-0.027}$
$100\theta_s$	1.0387 ± 0.0063	$1.0389^{+0.0069}_{-0.0063}$	$1.0381^{+0.054}_{-0.053}$	$1.0387^{+0.0053}_{-0.0054}$
n_s	0.953 ± 0.032	$0.953^{+0.032}_{-0.033}$	$0.955^{+0.034}_{-0.035}$	$0.952^{+0.031}_{-0.032}$
$\log\left[10^{10} A_s\right]$	$3.064^{+0.080}_{-0.082}$	$3.062^{+0.080}_{-0.079}$	$3.068^{+0.081}_{-0.078}$	$3.062^{+0.073}_{-0.075}$
m_1 (eV)	≤ 0.39	≤ 0.38	≤ 0.38	≤ 0.38
$\eta^{\rm in}_{\nu_e}$	– [a]	– [a]	– [a]	– [a]
η_ν	– [a]	– [a]	$[-0.64; 0.72]$	$[-0.071; 0.054]$
h	$0.652^{+0.084}_{-0.083}$	$0.653^{+0.081}_{-0.082}$	$0.656^{+0.084}_{-0.081}$	$0.650^{+0.078}_{-0.081}$
$\Delta N_{\rm eff}$	≤ 0.32	≤ 0.16	≤ 0.43	≤ 0.03

[a] The 95% confidence region is not well-defined in these cases because the posterior does not vanish at the end of the prior range (see e.g. the middle panel of Fig. 2). See discussion in the text.

total asymmetry, $-0.071 \leq \eta_\nu \leq 0.054$ (95% C.L.).

On the other hand, since the constraints come most from the distortion in the electron neutrino distribution function, when $\theta_{13} = 0$ (and therefore there is less mixing) the direct relation between $\eta^{\rm fin}_{\nu_e}$ and η_ν is lost. In this case, the total asymmetry could still be large, even if the final electron neutrino asymmetry is small, as significantly asymmetries can still be stored on the other two flavors, leading to a constraint an order of magnitude weaker than the previous case, $-0.64 \leq \eta_\nu \leq 0.72$ (95% C.L.). As expected, this is reflected on the allowed ranges for $\Delta N_{\rm eff}$, as shown in Fig. 4: while for $\theta_{13} = 0$ the $\Delta N_{\rm eff} \simeq 0.5$ are still allowed by the data, nonzero values of this mixing angle reduce the allowed region in the parameter space by approximately an order of magnitude in both $\Delta N_{\rm eff}$ and η_ν.

We confirmed in our analysis that the constraints on the asymmetry are largely dominated by the BBN prior at present. This is shown in Fig. 5, where we compare the results of our analysis with a more complete dataset (which we refer to as ALL) that includes distance measurements of SNIa from the SDSS compilation [40] and the HST determination of the Hubble constant H_0 [41], as well as data on the power spectrum of the matter density field, as reconstructed from a sample of Luminous Red Galaxies of the SDSS Seventh Data Release [42]. This is due to the fact that other cosmological data constrain the asymmetries via their effect on increasing $N_{\rm eff}$, and currently the errors on the measurement of the effective number of neutrinos [1, 27–29] are significantly weaker than our prior on Y_p, eq. (4)[6]. The fact that bounds on leptonic asymmetries are dominated by the BBN prior (i.e. by ^{4}He data) is also confirmed by the similarity of our bounds on (η_ν, $\eta^{\rm in}_{\nu_e}$) with those of [35]. Note that the limits reported in [35] sound weaker, because they are frequentist bounds obtained by cutting the parame-

[6] On the other hand, these other cosmological data sets have an impact on other parameters like e.g. the neutrino mass. But since in this work we are primarily interested in bounding the asymmetries, we prefer to stick to the robust WMAP+He data set. In that way, our results are not contaminated by possible systematic uncertainties in the other data. Actually, the inclusion of all external datasets (in particular, of SNIa together with H_0) reveals a conflict between them, leading to a bimodal posterior probability for $\Omega_{dm} h^2$ and to a preference for $m_1 > 0$ at 95% C.L.

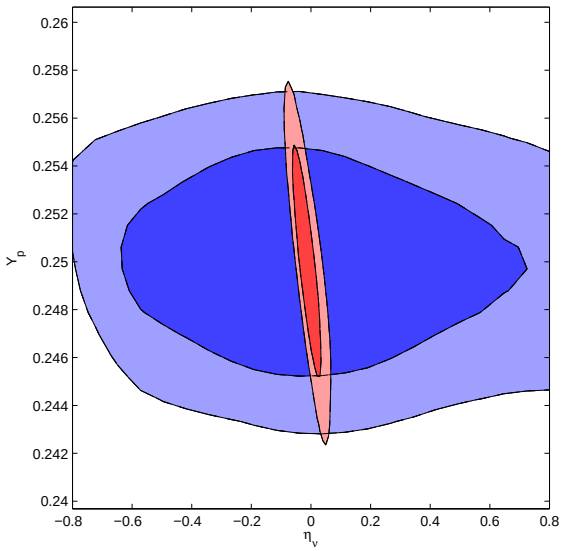

FIG. 3: 68% and 95% confidence regions in total neutrino asymmetry η_ν vs. the primordial abundance of Helium Y_p plane for $\theta_{13} = 0$ (blue) and $\sin^2\theta_{13} = 0.04$ (red), from the analysis of the WMAP+He dataset. Notice the much stronger constraint for the nonzero mixing angle due to the faster equilibration of flavor asymmetries.

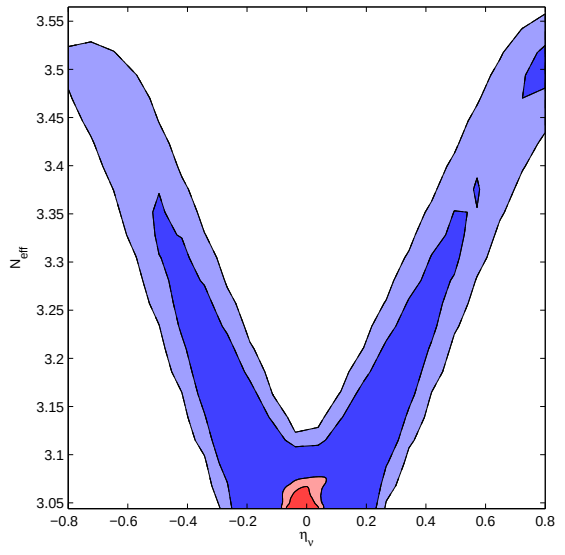

FIG. 4: Two-dimensional 68% and 95% confidence regions in the (η_ν, $N_{\rm eff}$) plane from the analysis of the WMAP+He dataset, for $\theta_{13} = 0$ (blue) and $\sin^2\theta_{13} = 0.04$ (red). Even for zero θ_{13} the data seem to favor $N_{\rm eff}$ around the standard value $N_{\rm eff} = 3.046$.

ter probability at $\Delta\chi^2 = 6.18$, i.e. they represent 95% bounds on joint two-dimensional parameter probabilities (in the Gaussian approximation). The one-dimensional 95% confidence limits, corresponding to $\Delta\chi^2 = 4$, are smaller and very close to the results of the present paper. We also checked that using our codes and data sets, we obtain very similar results when switching from Bayesian to frequentist confidence limits.

We conclude this section noting that the current constraints on the sum of neutrino masses are robust under a scenario with lepton asymmetries, as those extra degrees-of-freedom do not correlate with the neutrino mass. On the other hand, to go beyond the BBN limits on the asymmetries more precise measurements of $N_{\rm eff}$ are clearly needed, and in the next section we forecast the results that could be achievable with such an improvement using COrE as an example of future CMB experiments.

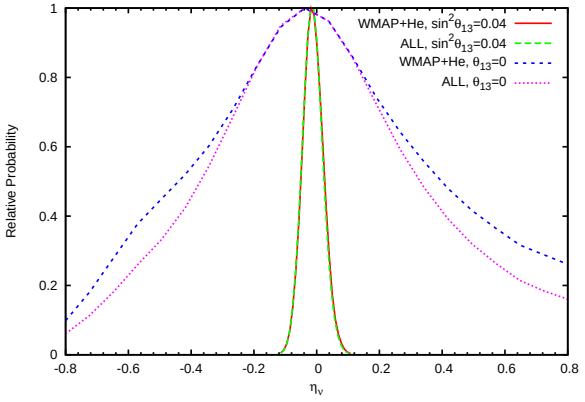

FIG. 5: One-dimensional posterior probability density for η_ν comparing the WMAP+He and the ALL datasets. As mentioned in the text, the constraints on the total asymmetry do not improve significantly with the inclusion of other cosmological datasets, as they are mainly driven by the determination of the primordial Helium abundance.

IV. FORECAST

Given that the current constraints on the lepton asymmetries are dominated by their effect on the primordial production of light elements, one can ask whether future cosmological experiments can improve over the current limits imposed by BBN. With that goal in mind, we take as an example a proposed CMB experiment, COrE (Cosmic Origins Explorer) [43], designed to detect the primordial gravitational waves and measure the CMB gravitational lensing deflection power spectrum on all linear scales to the cosmic variance limit. The latter is of special interest for this work, as the CMB lensing is expected to probe with high sensitivity the absolute neutrino masses and $N_{\rm eff}$ [59].

We used the package FuturCMB[7] in combination with CAMB and CosmoMC for producing mock CMB data, and fit it with a likelihood based on the potential sensitivity of COrE. We include, also in this case, the information coming from present measurements of the Helium fraction, encoded in the Gaussian prior (4). We consider five of COrE's frequency channels, ranging from 105 to 225 GHz, with the specifications given in [43] and reported for convenience in Table III, and assume an observed fraction $f_{\rm sky} = 0.65$. We do not consider other channels as they are likely to be foreground dominated. We take a maximum multipole $\ell_{\rm max} = 2500$. In our analysis, we have assumed that the uncertainties associated to the beam and foregrounds have been properly modeled and removed, so that we can only consider the statistical uncertainties. Those are optimistic assumptions, as under realistic conditions systematic uncertainties will certainly play an important role. In that sense, our results represent an illustration of what future CMB experiments could ideally achieve.

Frequency [GHz]	$\theta_{\rm fwhm}$ [arcmin]	σ_T [μK]	σ_P [μK]
105	10.0	0.268	0.463
135	7.8	0.337	0.583
165	6.4	0.417	0.720
195	5.4	0.487	0.841
225	4.7	0.562	0.972

TABLE III: Experimental specifications for COrE [43]. For each channel, we list the channel frequency in GHz, the FWHM in arcminutes, the temperature (σ_T) and polarization (σ_P) noise per pixel in μK.

We use CMB lensing information in the way described in [60], assuming that the CMB lensing potential spectrum will be extracted from COrE maps with a quadratic estimator technique.

For the forecast we adopt the fiducial values for the cosmological parameters shown in Table IV for both cases of θ_{13} discussed previously. The two sets of fiducial values correspond to the best-fit models of the WMAP+He dataset for the two values of θ_{13}. In the case of the neutrino mass, since the likelihood is essentially flat between 0 and 0.2 eV, we have chosen to take $m_1 = 0.02$ eV. This is below the expected sensitivity of COrE and should thus be essentialy equivalent to the case where the lightest neutrino is massless.

The sensitivities on the neutrino parameters for COrE are shown in Fig. 6 for the two values of θ_{13}. As expected for the sum of the neutrino masses, the constraints are significantly better than the current ones, and could in principle start probing the minimal values guaranteed by flavor oscillations [59]. Note that our forecast error for m_1 differs slightly from the one presented in [43], most probably because the forecasts in this reference are based on the Fisher matrix approximation. But our main goal in this section is to discuss how COrE observations will help improving the limits on the asymmetries discussed previously, that are basically dominated by the available measurements of the ^{4}He abudance. The right panel of Fig. 6 shows the forecasted posterior probability distribution for η_ν, and the marginalized constraints for it are listed in Table V for both values of θ_{13}; in particular, the vertical lines of the right panel show the 95% C.L. limits obtained from the full BBN analysis of Ref. [35]. Comparing the values from Tables II and V one can see that an experiment like COrE would improve current 95% limits on the total leptonic asymmetry by nearly a factor 6.6 ($\theta_{13} = 0$) and 1.6 ($\sin^2\theta_{13} = 0.04$), competitive over the constraints from ^{4}He abundance only. It should be noted that the error bars on the primordial abundances are very difficult to be reduced due to systematic errors on astrophysical measurements [51], and therefore it is feasible that CMB experiments will be an important tool in the future to improve the constraints on the asymmetries. Notice however that, since the CMB is insensitive to the sign of the η's, BBN measurements will still be needed in order to break this degeneracy.

Finally, in Fig. 7 we show the COrE sensitivity on the asymmetries in the plane η_ν vs. $\eta_{\nu_e}^{\rm in}$ compared to the constraints of Sec. III obtained using current data and to the full BBN analysis of Ref. [35]. Notice that in the case $\theta_{13} = 0$ the constraints of the previous section are quite less constraining than the ones coming from the full BBN analysis because we are not using deuterium data, known to be important to close the contours on the asymmetries

TABLE IV: Fiducial values for the cosmological parameters for the COrE forecast.

Parameter	Fiducial Value ($\sin^2\theta_{13} = 0$)	Fiducial Value ($\sin^2\theta_{13} = 0.04$)
$\Omega_b h^2$	0.0218	0.0224
$\Omega_{dm} h^2$	0.121	0.118
τ	0.0873	0.0865
h	0.709	0.705
n_s	0.978	0.968
$\log\left[10^{10} A_s\right]$	3.12	3.08
m_1 (eV)	0.02	0.02
$\eta_{\nu_e}^{\rm in}$	0	0
η_ν	0	0

TABLE V: 95% confidence intervals for the neutrino parameters with COrE.

Parameter	$\sin^2\theta_{13} = 0$	$\sin^2\theta_{13} = 0.04$
m_1 (eV)	< 0.049	< 0.048
$\eta_{\nu_e}^{\rm in}$	$[-0.20; 0.20]$	$[-0.25; 0.24]$
η_ν	$[-0.12; 0.09]$	$[-0.048; 0.030]$

[7] http://lpsc.in2p3.fr/perotto/

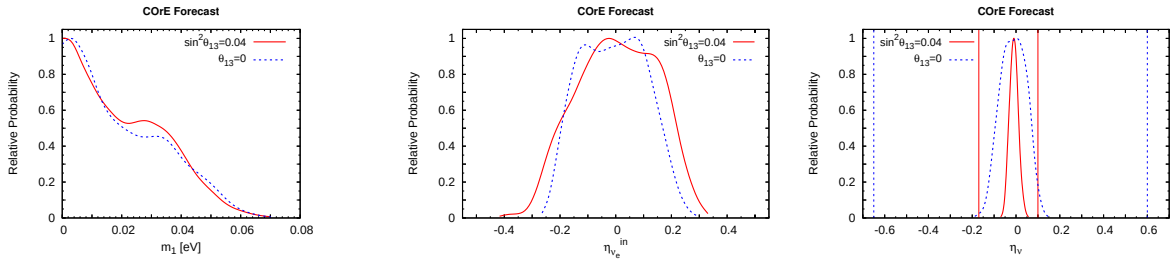

FIG. 6: One-dimensional probability distribution function for m_1 and η_ν for COrE forecast. The middle panel shows that an experiment like COrE could start constrain the initial electron neutrino asymmetry. The vertical lines on the right panel show the current 95% C.L. limits obtained in the previous section. The errors on the asymmetries are improved by approximately a factor 6.6 or 1.6 for $\theta_{13} = 0$ and $\sin^2\theta_{13} = 0.04$, respectively, compared to the results shown in Fig. 2.

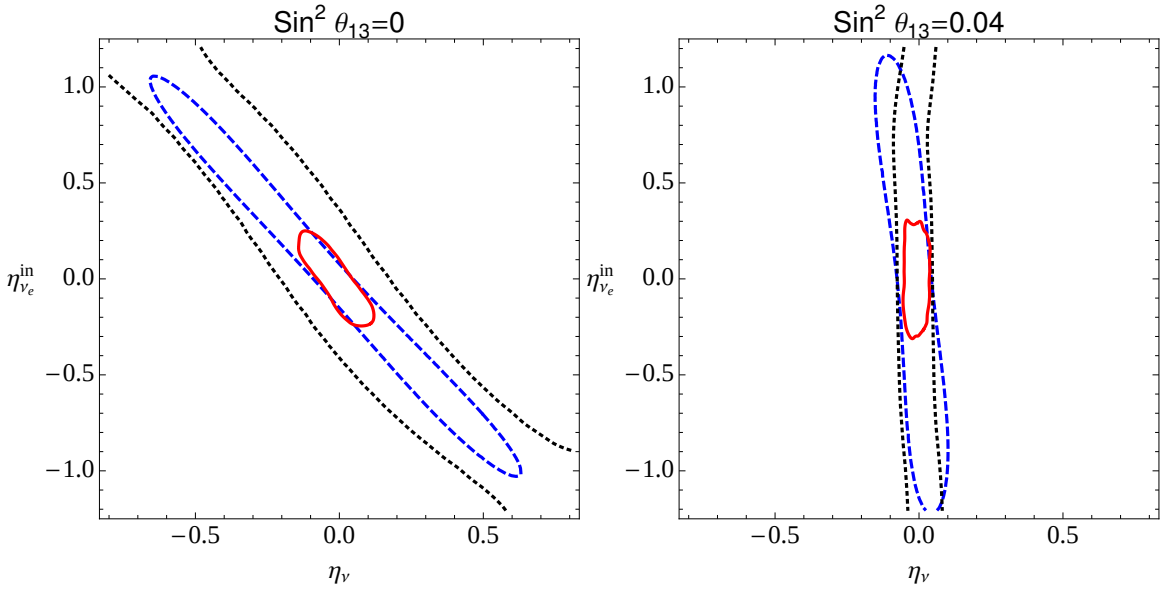

FIG. 7: The 95% C.L. contours on the η_ν vs. $\eta^{\rm in}_{\nu_e}$ plane from our analysis with current data (WMAP+He dataset, black dotted) compared to the results of the BBN analysis of Ref. [35] (blue dashed) and with the COrE forecast (red solid).

plane, especially for small values of θ_{13} [34]. Moreover, future CMB experiments have the potential to reduce the allowed region, dominating the errors in this analysis.

In summary, an experiment like COrE is capable of improving the constraints on the lepton asymmetries by up to a factor 6.6 on the total and/or flavor asymmetries depending on the value of the mixing angle θ_{13}. In addition to that, such an experiment would also constrain other cosmological parameters (in particular the sum of the neutrino masses) with significant precision, providing yet another step towards the goal of accurately measuring the properties of the Universe.

V. CONCLUSIONS

Understanding the physical processes that took place in the early Universe is a crucial ingredient for deciphering the physics at energies that cannot be currently probed in terrestrial laboratories. In particular, since the origin of the matter-antimatter is still an open question in cosmology, it is important to keep an open mind for theories that predict large lepton asymmetries. In that case, constraining total and flavor neutrino asymmetries using cosmological data is a way to test and constrain some of the possible particle physics scenarios at epochs earlier than the BBN.

For that, we initially used current cosmological data

to constrain not only the asymmetries, but also to understand the robustness of the cosmological parameters (and the limits on the sum of the neutrino masses) for two different values of the mixing angle θ_{13} to account for the evidences of a nonzero value for this angle. Our results confirm the fact that at present the limits on the cosmological lepton asymmetries are dominated by the abundance of primordial elements generated during the BBN, in particular the abundance of ^{4}He, currently the most sensitive "leptometer" available.

However, future CMB experiments might be able to compete with BBN data in what concerns constraining lepton asymmetries, although BBN will always be needed in order to get information on the sign of the η's. We took as an example the future CMB mission COrE, proposed to measure with unprecedent precision the lensing of CMB anisotropies, and our results indicate that it has the potential to significantly improve over current constraints while, at the same time placing limits on the sum of the neutrino masses that are of the order of the neutrino mass differences.

Finally, we notice that for the values of θ_{13} measured by the Daya Bay and RENO experiments the limits on the cosmological lepton asymmetries and on its associated effective number of neutrinos are quite strong, so that lepton asymmetries cannot increase $N_{\rm eff}$ significantly above 3.4. Under those circumstances, if the cosmological data (other than BBN) continues to push for large values of $N_{\rm eff}$, new pieces of physics such as sterile neutrinos will be necessary to explain that excess.

Acknowledgments

We thank Srdjan Sarikas for providing some of the data used in Figs. 1 and 7. The work of AM was supported by the PRIN-INAF grant "Astronomy probes fundamental physics" and by the Italian Space Agency through the ASI contract Euclid- IC (I/031/10/0). GM acknowledges support by the *Instituto Nazionale di Fisica Nucleare* I.S. FA51 and the PRIN 2010 "Fisica Astroparticellare: Neutrini ed Universo Primordiale" of the Italian *Ministero dell'Istruzione, Università e Ricerca*. The work of ML is supported by Ministero dell'Istruzione, dell'Universit e della Ricerca (MIUR) through the PRIN grant "Matter-antimatter asymmetry, Dark Matter and Dark Energy in the LHC era" (contract number PRIN 2008NR3EBK-005). SP and UF were supported by the Spanish grants FPA2008-00319, FPA2011-22975 and Multidark CSD2009-00064 (MINECO) and PROMETEO/2009/091 (Generalitat Valenciana), and by the EC contract UNILHC PITN-GA-2009-237920. UF acknowledges the support of the I3P-CSIC fellowship and of EPLANET. This research was also supported by a Spanish-Italian MINECO-INFN agreement, refs. AIC10-D-000543 and AIC-D-2011-0689. Finally, EC acknowledges the hospitality of CERN while working on this paper.

[1] E. Komatsu *et al.* [WMAP Collaboration], Astrophys. J. Suppl. **192**, 18 (2011).
[2] A. Casas, W. Y. Cheng and G. Gelmini, Nucl. Phys. B **538**, 297 (1999) [hep-ph/9709289].
[3] J. March-Russell, H. Murayama, and A. Riotto, JHEP **9911**, 015 (1999) [hep-ph/9908396].
[4] J. McDonald, Phys. Rev. Lett. **84**, 4798 (2000) [hep-ph/9908300].
[5] D.J. Schwarz and M. Stuke, JCAP **0911**, 025 (2009) [arXiv:0906.3434].
[6] V. B. Semikoz, D. D. Sokoloff and J. W. F. Valle, Phys. Rev. D **80**, 083510 (2009).
[7] X. -D. Shi and G. M. Fuller, Phys. Rev. Lett. **82**, 2832 (1999) [astro-ph/9810076].
[8] M. Laine and M. Shaposhnikov, JCAP **0806**, 031 (2008) [arXiv:0804.4543 [hep-ph]].
[9] M. Stuke, D. J. Schwarz and G. Starkman, JCAP **1203**, 040 (2012) [arXiv:1111.3954 [astro-ph.CO]].
[10] D. H. Lyth, C. Ungarelli and D. Wands, Phys. Rev. D **67**, 023503 (2003).
[11] C. Gordon, K. A. Malik, Phys. Rev. D **69** , 063508 (2004).
[12] E. Di Valentino, M. Lattanzi, G. Mangano, A. Melchiorri and P. Serpico, Phys. Rev. D **85**, 043511 (2012) [arXiv:1111.3810 [astro-ph.CO]].
[13] J. Lesgourgues and S. Pastor, Phys. Rev. D **60**, 103521 (1999).
[14] J. Lesgourgues and S. Pastor, Phys. Rept. **429**, 307 (2006).
[15] A. D. Dolgov, S. H. Hansen, S. Pastor, S. T. Petcov, G. G. Raffelt and D. V. Semikoz, Nucl. Phys. B **632**, 363 (2002) [hep-ph/0201287].
[16] Y.Y.Y. Wong, Phys. Rev. D **66**, 025015 (2002) [arXiv:hep-ph/0203180].
[17] K.N. Abazajian, J.F. Beacom and N.F. Bell, Phys. Rev. D **66**, 013008 (2002) [arXiv:astro-ph/0203442].
[18] T. Schwetz, M. Tortola and J. W. F. Valle, New J. Phys. **13**, 063004 (2011).
[19] G. L. Fogli, E. Lisi, A. Marrone, A. Palazzo and A. M. Rotunno, Phys. Rev. D **84**, 053007 (2011) [arXiv:1106.6028 [hep-ph]].
[20] K. Abe *et al.* [T2K Collaboration], Phys. Rev. Lett. **107**, 041801 (2011).
[21] P. Adamson *et al.* [MINOS Collaboration], Phys. Rev. Lett. **107**, 181802 (2011) [arXiv:1108.0015 [hep-ex]].
[22] Y. Abe *et al.* [DOUBLE-CHOOZ Collaboration], Phys. Rev. Lett. **108**, 131801 (2012) [arXiv:1112.6353 [hep-ex]].
[23] F. P. An *et al.* [DAYA-BAY Collaboration], Phys. Rev. Lett. **108**, 171803 (2012) [arXiv:1203.1669 [hep-ex]].
[24] J. K. Ahn *et al.* [RENO Collaboration], Phys. Rev. Lett. **108**, 191802 (2012) [arXiv:1204.0626 [hep-ex]].
[25] G. Mangano, G. Miele, S. Pastor, T. Pinto, O. Pisanti and P. D. Serpico, Nucl. Phys. B **729**, 221 (2005) [hep-ph/0506164].
[26] S. Pastor, T. Pinto and G. G. Raffelt, Phys. Rev. Lett.

102, 241302 (2009).
[27] J. Dunkley *et al.*, [ACT Collaboration], Astrophys. J. **739**, 52 (2011) [arXiv:1009.0866 [astro-ph.CO]].
[28] R. Keisler *et al.*, [SPT Collaboration], Astrophys. J. **743**, 28 (2011) [arXiv:1105.3182 [astro-ph.CO]].
[29] B. A. Benson *et al.*, [SPT Collaboration], arXiv:1112.5435 [astro-ph.CO].
[30] M. Archidiacono, E. Calabrese and A. Melchiorri, Phys. Rev. D **84**, 123008 (2011) [arXiv:1109.2767 [astro-ph.CO]].
[31] E. Giusarma, M. Corsi, M. Archidiacono, R. de Putter, A. Melchiorri, O. Mena and S. Pandolfi, Phys. Rev. D **83**, 115023 (2011) [arXiv:1102.4774 [astro-ph.CO]].
[32] J. Hamann, S. Hannestad, G. G. Raffelt and Y. Y. Y. Wong, JCAP **1109**, 034 (2011) [arXiv:1108.4136 [astro-ph.CO]].
[33] I. Sendra and T. L. Smith, Phys. Rev. D **85**, 123002 (2012) [arXiv:1203.4232 [astro-ph.CO]].
[34] G. Mangano, G. Miele, S. Pastor, O. Pisanti and S. Sarikas, JCAP **1103**, 035 (2011)
[35] G. Mangano, G. Miele, S. Pastor, O. Pisanti and S. Sarikas, Phys. Lett. B **708**, 1 (2012).
[36] M. Lattanzi, R. Ruffini and G. V. Vereshchagin, Phys. Rev. D **72**, 063003 (2005) [astro-ph/0509079].
[37] L. A. Popa and A. Vasile, JCAP **0806**, 028 (2008) [arXiv:0804.2971 [astro-ph]].
[38] M. Shiraishi, K. Ichikawa, K. Ichiki, N. Sugiyama and M. Yamaguchi, JCAP **0907**, 005 (2009).
[39] J. Hamann, J. Lesgourgues and G. Mangano, JCAP **0803**, 004 (2008) [arXiv:0712.2826 [astro-ph]].
[40] R. Kessler *et al.* Astrophys. J. Suppl. **185**, 32 (2009) [arXiv:0908.4274 [astro-ph.CO]].
[41] A. G. Riess *et al.*, Astrophys. J. **699**, 539 (2009) [arXiv:0905.0695 [astro-ph.CO]].
[42] B. A. Reid *et al.*, Mon. Not. Roy. Astron. Soc. **404**, 60 (2010) [arXiv:0907.1659 [astro-ph.CO]].
[43] F. R. Bouchet *et al.* [The COrE Collaboration], arXiv:1102.2181 [astro-ph.CO].
[44] H.S. Kang and G. Steigman, Nucl. Phys. B **372**, 494 (1992).
[45] S.H. Hansen, G. Mangano, A. Melchiorri, G. Miele and O. Pisanti, Phys. Rev. D **65**, 023511 (2002) [arXiv:astro-ph/0105385].
[46] G. Sigl and G. Raffelt, Nucl. Phys. B **406**, 423 (1993).
[47] B. H. J. McKellar and M. J. Thomson, Phys. Rev. D **49**, 2710 (1994).
[48] A. Lewis, A. Challinor and A. Lasenby, Astrophys. J. **538**, 473 (2000) [astro-ph/9911177].
[49] D. Blas, J. Lesgourgues and T. Tram, JCAP **1107**, 034 (2011) [arXiv:1104.2933 [astro-ph.CO]].
[50] A. Lewis and S. Bridle, Phys. Rev. D **66**, 103511 (2002) [astro-ph/0205436].
[51] F. Iocco, G. Mangano, G. Miele, O. Pisanti and P. D. Serpico, Phys. Rept. **472**, 1 (2009).
[52] Y. I. Izotov and T. X. Thuan, Astrophys. J. **710**, L67 (2010) [arXiv:1001.4440 [astro-ph.CO]].
[53] E. Aver, K. A. Olive and E. D. Skillman, JCAP **1005**, 003 (2010) [arXiv:1001.5218 [astro-ph.CO]].
[54] E. Aver, K. A. Olive and E. D. Skillman, JCAP **1103**, 043 (2011) [arXiv:1012.2385 [astro-ph.CO]].
[55] E. Aver, K. A. Olive and E. D. Skillman, JCAP **1204**, 004 (2012) [arXiv:1112.3713 [astro-ph.CO]].
[56] G. Mangano and P. D. Serpico, Phys. Lett. B **701**, 296 (2011) [arXiv:1103.1261 [astro-ph.CO]].
[57] M. Pettini and R. Cooke, arXiv:1205.3785 [astro-ph.CO].
[58] P. D. Serpico and G. G. Raffelt, Phys. Rev. D **71**, 127301 (2005) [astro-ph/0506162].
[59] J. Lesgourgues, L. Perotto, S. Pastor and M. Piat, Phys. Rev. D **73**, 045021 (2006) [astro-ph/0511735].
[60] L. Perotto, J. Lesgourgues, S. Hannestad, H. Tu and Y. Y. Y. Wong, JCAP **0610**, 013 (2006) [astro-ph/0606227].

5.4 Current bounds from Planck, sections 6.3, 6.4 from arXiv:1303.5076

Astronomy & Astrophysics manuscript no. draft˙p1011
December 16, 2013

Planck 2013 results. XVI. Cosmological parameters

Planck Collaboration: P. A. R. Ade[93], N. Aghanim[65], C. Armitage-Caplan[99], M. Arnaud[79], M. Ashdown[76,6], F. Atrio-Barandela[19], J. Aumont[65], C. Baccigalupi[92], A. J. Banday[102,10], R. B. Barreiro[72], J. G. Bartlett[1,74], E. Battaner[105], K. Benabed[66,101], A. Benoît[63], A. Benoit-Lévy[26,66,101], J.-P. Bernard[102,10], M. Bersanelli[38,55], P. Bielewicz[102,10,92], J. Bobin[79], J. J. Bock[74,11], A. Bonaldi[75], J. R. Bond[9], J. Borrill[14,96], F. R. Bouchet[66,101], M. Bridges[76,6,69], M. Bucher[1], C. Burigana[54,36], R. C. Butler[54], E. Calabrese[99], B. Cappellini[55], J.-F. Cardoso[80,1,66], A. Catalano[81,78], A. Challinor[69,76,12], A. Chamballu[79,16,65], R.-R. Chary[62], X. Chen[62], H. C. Chiang[30,7], L.-Y Chiang[68], P. R. Christensen[88,41], S. Church[98], D. L. Clements[61], S. Colombi[66,101], L. P. L. Colombo[25,74], F. Couchot[77], A. Coulais[78], B. P. Crill[74,89], A. Curto[6,72], F. Cuttaia[54], L. Danese[92], R. D. Davies[75], R. J. Davis[75], P. de Bernardis[37], A. de Rosa[54], G. de Zotti[50,92], J. Delabrouille[1], J.-M. Delouis[66,101], F.-X. Désert[58], C. Dickinson[75], J. M. Diego[72], K. Dolag[104,84], H. Dole[65,64], S. Donzelli[55], O. Doré[74,11], M. Douspis[65], J. Dunkley[99], X. Dupac[44], G. Efstathiou[69], F. Elsner[66,101], T. A. Enßlin[84], H. K. Eriksen[70], F. Finelli[54,56], O. Forni[102,10], M. Frailis[52], A. A. Fraisse[30], E. Franceschi[54], T. C. Gaier[74], S. Galeotta[52], S. Galli[66], K. Ganga[1], M. Giard[102,10], G. Giardino[45], Y. Giraud-Héraud[1], E. Gjerløw[70], J. González-Nuevo[72,92], K. M. Górski[74,106], S. Gratton[76,69], A. Gregorio[39,52], A. Gruppuso[54], J. E. Gudmundsson[30], J. Haissinski[77], J. Hamann[100], F. K. Hansen[70], D. Hanson[85,74,9], D. Harrison[69,76], S. Henrot-Versillé[77], C. Hernández-Monteagudo[13,84], D. Herranz[72], S. R. Hildebrandt[11], E. Hivon[66,101], M. Hobson[6], W. A. Holmes[74], A. Hornstrup[17], Z. Hou[32], W. Hovest[84], K. M. Huffenberger[28], A. H. Jaffe[61], T. R. Jaffe[102,10], J. Jewell[74], W. C. Jones[30], M. Juvela[29], E. Keihänen[29], R. Keskitalo[23,14], T. S. Kisner[83], R. Kneissl[43,8], J. Knoche[84], L. Knox[32], M. Kunz[18,65,3], H. Kurki-Suonio[29,48], G. Lagache[65], A. Lähteenmäki[2,48], J.-M. Lamarre[78], A. Lasenby[6,76], M. Lattanzi[36], R. J. Laureijs[45], C. R. Lawrence[74], S. Leach[92], J. P. Leahy[75], R. Leonardi[44], J. León-Tavares[46,2], J. Lesgourgues[100,91], A. Lewis[27], M. Liguori[35], P. B. Lilje[70], M. Linden-Vørnle[17], M. López-Caniego[72], P. M. Lubin[33], J. F. Macías-Pérez[81], B. Maffei[75], D. Maino[38,55], N. Mandolesi[54,5,36], M. Maris[52], D. J. Marshall[79], P. G. Martin[9], E. Martínez-González[72], S. Masi[37], M. Massardi[53], S. Matarrese[35], F. Matthai[84], P. Mazzotta[40], P. R. Meinhold[33], A. Melchiorri[37,57], J.-B. Melin[16], L. Mendes[44], E. Menegoni[37], A. Mennella[38,55], M. Migliaccio[69,76], M. Millea[32], S. Mitra[60,74], M.-A. Miville-Deschênes[65,9], A. Moneti[66], L. Montier[102,10], G. Morgante[54], D. Mortlock[61], A. Moss[94], D. Munshi[93], J. A. Murphy[87], P. Naselsky[88,41], F. Nati[37], P. Natoli[36,4,54], C. B. Netterfield[21], H. U. Nørgaard-Nielsen[17], F. Noviello[75], D. Novikov[61], I. Novikov[88], I. J. O'Dwyer[74], S. Osborne[98], C. A. Oxborrow[17], F. Paci[92], L. Pagano[37,57], F. Pajot[65], D. Paoletti[54,56], B. Partridge[47], F. Pasian[52], G. Patanchon[1], D. Pearson[74], T. J. Pearson[11,62], H. V. Peiris[26], O. Perdereau[77], L. Perotto[81], F. Perrotta[92], V. Pettorino[18], F. Piacentini[37], M. Piat[1], E. Pierpaoli[25], D. Pietrobon[74], S. Plaszczynski[77], P. Platania[73], E. Pointecouteau[102,10], G. Polenta[4,51], N. Ponthieu[65,58], L. Popa[67], T. Poutanen[48,29,2], G. W. Pratt[79], G. Prézeau[11,74], S. Prunet[66,101], J.-L. Puget[65], J. P. Rachen[22,84], W. T. Reach[103], R. Rebolo[71,15,42], M. Reinecke[84], M. Remazeilles[75,65,1], C. Renault[81], S. Ricciardi[54], T. Riller[84], I. Ristorcelli[102,10], G. Rocha[74,11], C. Rosset[1], G. Roudier[1,78,74], M. Rowan-Robinson[61], J. A. Rubiño-Martín[71,42], B. Rusholme[62], M. Sandri[54], D. Santos[81], M. Savelainen[29,48], G. Savini[90], D. Scott[24], M. D. Seiffert[74,11], E. P. S. Shellard[12], L. D. Spencer[93], J.-L. Starck[79], V. Stolyarov[6,76,97], R. Stompor[1], R. Sudiwala[93], R. Sunyaev[84,95], F. Sureau[79], D. Sutton[69,76], A.-S. Suur-Uski[29,48], J.-F. Sygnet[66], J. A. Tauber[45], D. Tavagnacco[52,39], L. Terenzi[54], L. Toffolatti[20,72], M. Tomasi[55], M. Tristram[77], M. Tucci[18,77], J. Tuovinen[86], M. Türler[59], G. Umana[49], L. Valenziano[54], J. Valiviita[48,29,70], B. Van Tent[82], P. Vielva[72], F. Villa[54], N. Vittorio[40], L. A. Wade[74], B. D. Wandelt[66,101,34], I. K. Wehus[74], M. White[31], S. D. M. White[84], A. Wilkinson[75], D. Yvon[16], A. Zacchei[52], and A. Zonca[33]

(Affiliations can be found after the references)

December 16, 2013

ABSTRACT

Abstract: This paper presents the first cosmological results based on *Planck* measurements of the cosmic microwave background (CMB) temperature and lensing-potential power spectra. We find that the *Planck* spectra at high multipoles ($\ell \gtrsim 40$) are extremely well described by the standard spatially-flat six-parameter ΛCDM cosmology with a power-law spectrum of adiabatic scalar perturbations. Within the context of this cosmology, the *Planck* data determine the cosmological parameters to high precision: the angular size of the sound horizon at recombination, the physical densities of baryons and cold dark matter, and the scalar spectral index are estimated to be $\theta_* = (1.04147 \pm 0.00062) \times 10^{-2}$, $\Omega_b h^2 = 0.02205 \pm 0.00028$, $\Omega_c h^2 = 0.1199 \pm 0.0027$, and $n_s = 0.9603 \pm 0.0073$, respectively (Note that in this abstract we quote 68% errors on measured parameters and 95% upper limits on other parameters.) For this cosmology, we find a low value of the Hubble constant, $H_0 = (67.3 \pm 1.2)\,\mathrm{km\,s^{-1}\,Mpc^{-1}}$, and a high value of the matter density parameter, $\Omega_m = 0.315 \pm 0.017$. These values are in tension with recent direct measurements of H_0 and the magnitude-redshift relation for Type Ia supernovae, but are in excellent agreement with geometrical constraints from baryon acoustic oscillation (BAO) surveys. Including curvature, we find that the Universe is consistent with spatial flatness to percent level precision using *Planck* CMB data alone. We use high-resolution CMB data together with *Planck* to provide greater control on extragalactic foreground components in an investigation of extensions to the six-parameter ΛCDM model. We present selected results from a large grid of cosmological models, using a range of additional astrophysical data sets in addition to *Planck* and high-resolution CMB data. None of these models are favoured over the standard six-parameter ΛCDM cosmology. The deviation of the scalar spectral index from unity is insensitive to the addition of tensor modes and to changes in the matter content of the Universe. We find an upper limit of $r_{0.002} < 0.11$ on the tensor-to-scalar ratio. There is no evidence for additional neutrino-like relativistic particles beyond the three families of neutrinos in the standard model. Using BAO and CMB data, we find $N_{\rm eff} = 3.30 \pm 0.27$ for the effective number of relativistic degrees of freedom, and an upper limit of 0.23 eV for the sum of neutrino masses. Our results are in excellent agreement with big bang nucleosynthesis and the standard value of $N_{\rm eff} = 3.046$. We find no evidence for dynamical dark energy; using BAO and CMB data, the dark energy equation of state parameter is constrained to be $w = -1.13^{+0.13}_{-0.10}$. We also use the *Planck* data to set limits on a possible variation of the fine-structure constant, dark matter annihilation and primordial magnetic fields. Despite the success of the six-parameter ΛCDM model in describing the *Planck* data at high multipoles, we note that this cosmology does not provide a good fit to the temperature power spectrum at low multipoles. The unusual shape of the spectrum in the multipole range $20 \lesssim \ell \lesssim 40$ was seen previously in the *WMAP* data and is a real feature of the primordial CMB anisotropies. The poor fit to the spectrum at low multipoles is not of decisive significance, but is an "anomaly" in an otherwise self-consistent analysis of the *Planck* temperature data.

Key words. Cosmology: observations – Cosmology: theory – cosmic microwave background – cosmological parameters

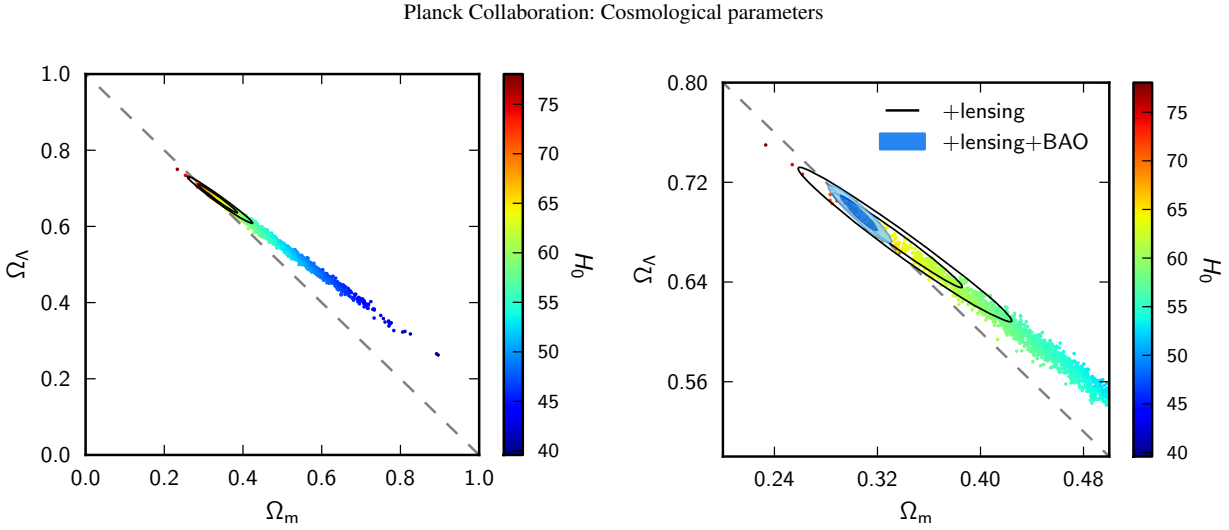

Fig. 25. The *Planck*+WP+highL data combination (samples; colour-coded by the value of H_0) partially breaks the geometric degeneracy between Ω_m and Ω_Λ due to the effect of lensing in the temperature power spectrum. These limits are significantly improved by the inclusion of the *Planck* lensing reconstruction (black contours). Combining also with BAO (right; solid blue contours) tightly constrains the geometry to be nearly flat.

Inflationary models that allow a large number of e-foldings predict that our Universe should be very accurately spatially flat[38]. Nevertheless, by introducing fine tunings it is possible to construct inflation models with observationally interesting open geometries (e.g., Linde 1995; Bucher et al. 1995; Linde 1999) or closed geometries (Linde 2003). Even more speculatively, there has been interest in models with open geometries from considerations of tunnelling events between metastable vacua within a "string landscape" (Freivogel et al. 2006). Observational limits on spatial curvature therefore offer important additional constraints on inflationary models and fundamental physics.

CMB temperature power spectrum measurements suffer from a well-known "geometrical degeneracy" (Bond et al. 1997; Zaldarriaga et al. 1997). Models with identical primordial spectra, physical matter densities and angular diameter distance to the last scattering surface, will have almost identical CMB temperature power spectra. This is a near perfect degeneracy (see Fig. 25) and is broken only via the integrated Sachs-Wolfe (ISW) effect on large angular scales and gravitational lensing of the CMB spectrum (Stompor & Efstathiou 1999). The geometrical degeneracy can also be broken with the addition of probes of late time physics, including BAO, Type Ia supernova, and measurement of the Hubble constant (e.g., Spergel et al. 2007).

Recently, the detection of the gravitational lensing of the CMB by ACT and SPT has been used to break the geometrical degeneracy, by measuring the integrated matter potential distribution. ACT constrained $\Omega_\Lambda = 0.61 \pm 0.29$ (68% CL) in Sherwin et al. (2011), with the updated analysis in Das et al. (2013) giving $\Omega_K = -0.031 \pm 0.026$ (68% CL) (Sievers et al. 2013). The SPT lensing measurements combined with seven year *WMAP* temperature spectrum improved this limit to $\Omega_K = -0.0014 \pm 0.017$ (68 % CL) (van Engelen et al. 2012).

With *Planck* we detect gravitational lensing at about 26σ through the 4-point function (Sect. 5.1 and Planck Collaboration XVII 2013). This strong detection of gravitational lensing allows us to constrain the curvature to percent level precision using observations of the CMB alone:

$$100\Omega_K = -4.2^{+4.3}_{-4.8} \quad (95\%;\ \textit{Planck}\text{+WP+highL}); \tag{67a}$$

$$100\Omega_K = -1.0^{+1.8}_{-1.9} \quad (95\%;\ \textit{Planck}\text{+lensing + WP+highL}). \tag{67b}$$

These constraints are improved substantially by the addition of BAO data. We then find

$$100\Omega_K = -0.05^{+0.65}_{-0.66} \quad (95\%;\ \textit{Planck}\text{+WP+highL+BAO}), \tag{68a}$$

$$100\Omega_K = -0.10^{+0.62}_{-0.65} \quad (95\%;\ \textit{Planck}\text{+lensing+WP +highL+BAO}). \tag{68b}$$

These limits are consistent with (and slightly tighter than) the results reported by Hinshaw et al. (2012) from combining the nine-year *WMAP* data with high resolution CMB measurements and BAO data. We find broadly similar results to Eqs. (68a) and (68b) if the Riess et al. (2011) H_0 measurement, or either of the SNe compilations discussed in Sect. 5.4, are used in place of the BAO measurements.

In summary, there is no evidence from *Planck* for any departure from a spatially flat geometry. The results of Eqs. (68a) and (68b) suggest that our Universe is spatially flat to an accuracy of better than a percent.

6.3. Neutrino physics and constraints on relativistic components

A striking illustration of the interplay between cosmology and particle physics is the potential of CMB observations to constrain the properties of relic neutrinos, and possibly of additional light relic particles in the Universe (see e.g., Dodelson et al. 1996; Hu et al. 1995; Bashinsky & Seljak 2004; Ichikawa et al. 2005; Lesgourgues & Pastor 2006; Hannestad 2010). In the following subsections, we present *Planck* constraints on the mass of ordinary (active) neutrinos assuming no extra relics, on the density of light relics assuming they all have negligible masses, and finally on models with both light massive and massless relics.

[38] The effective curvature within our Hubble radius should then be of the order of the amplitude of the curvature fluctuations generated during inflation, $\Omega_K \sim O(10^{-5})$.

6.3.1. Constraints on the total mass of active neutrinos

The detection of solar and atmospheric neutrino oscillations proves that neutrinos are massive, with at least two species being non-relativistic today. The measurement of the absolute neutrino mass scale is a challenge for both experimental particle physics and observational cosmology. The combination of CMB, large-scale structure and distance measurements already excludes a large range of masses compared to beta-decay experiments. Current limits on the total neutrino mass $\sum m_\nu$ (summed over the three neutrino families) from cosmology are rather model dependent and vary strongly with the data combination adopted. The tightest constraints for flat models with three families of neutrinos are typically around 0.3 eV (95% CL; e.g., de Putter et al. 2012). Since $\sum m_\nu$ must be greater than approximately 0.06 eV in the normal hierarchy scenario and 0.1 eV in the degenerate hierarchy (Gonzalez-Garcia et al. 2012), the allowed neutrino mass window is already quite tight and could be closed further by current or forthcoming observations (Jimenez et al. 2010; Lesgourgues et al. 2013).

Cosmological models, with and without neutrino mass, have different primary CMB power spectra. For observationally-relevant masses, neutrinos are still relativistic at recombination and the unique effects of masses in the primary power spectra are small. The main effect is around the first acoustic peak and is due to the early integrated Sachs-Wolfe (ISW) effect; neutrino masses have an impact here even for a fixed redshift of matter–radiation equality (Lesgourgues & Pastor 2012; Hall & Challinor 2012; Hou et al. 2012; Lesgourgues et al. 2013). To date, this effect has been the dominant one in constraining the neutrino mass from CMB data, as demonstrated in Hou et al. (2012). As we shall see here, the *Planck* data move us into a new regime where the dominant effect is from gravitational lensing. Increasing neutrino mass, while adjusting other parameters to remain in a high-probability region of parameter space, increases the expansion rate at $z \gtrsim 1$ and so suppresses clustering on scales smaller than the horizon size at the non-relativistic transition (Kaplinghat et al. 2003; Lesgourgues et al. 2006). The net effect for lensing is a suppression of the CMB lensing potential and, for orientation, by $\ell = 1000$ the suppression is around 10% in power for $\sum m_\nu = 0.66$ eV.

Here we report constraints assuming three species of degenerate massive neutrinos. At the level of sensitivity of *Planck*, the effect of mass splittings is negligible, and the degenerate model can be assumed without loss of generality.

Combining the *Planck*+WP+highL data, we obtain an upper limit on the summed neutrino mass of

$$\sum m_\nu < 0.66\,\mathrm{eV} \quad (95\%;\ \textit{Planck}\text{+WP+highL}). \tag{69}$$

The posterior distribution is shown by the solid black curve in Fig. 26. To demonstrate that the dominant effect leading to the constraint is gravitational lensing, we remove the lensing information by marginalizing over A_L[39]. We see that the posterior broadens considerably (see the red curve in Fig. 26) to give

$$\sum m_\nu < 1.08\,\mathrm{eV} \quad [95\%;\ \textit{Planck}\text{+WP+highL}\ (A_\mathrm{L})], \tag{70}$$

taking us back close to the value of 1.3 eV (for $A_\mathrm{L} = 1$) from the nine-year *WMAP* data (Hinshaw et al. 2012), corresponding to the limit above which neutrinos become non-relativistic before recombination. (The resolution of *WMAP* gives very little sensitivity to lensing effects.)

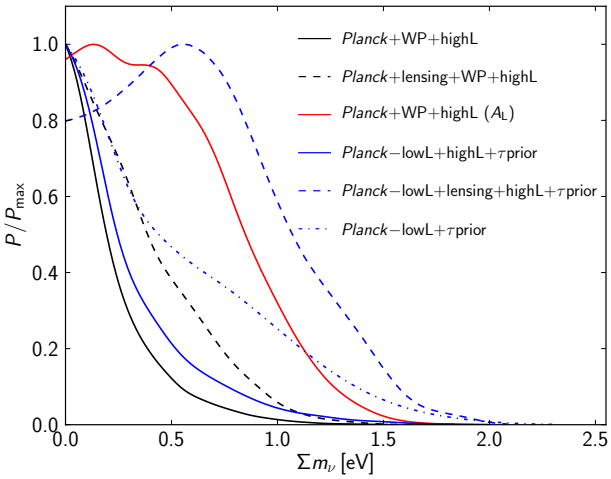

Fig. 26. Marginalized posterior distributions for $\sum m_\nu$ in flat models from CMB data. We show results for *Planck*+WP+highL without (solid black) and with (red) marginalization over A_L, showing how the posterior is significantly broadened by removing the lensing information from the temperature anisotropy power spectrum. The effect of replacing the low-ℓ temperature and (*WMAP*) polarization data with a τ prior is shown in solid blue (*Planck*−lowL+highL+τprior) and of further removing the high-ℓ data in dot-dashed blue (*Planck*−lowL+τprior). We also show the result of including the lensing likelihood with *Planck*+WP+highL (dashed black) and *Planck*−lowL+highL+τprior (dashed blue).

As discussed in Sect. 5.1, the *Planck*+WP+highL data combination has a preference for high A_L. Since massive neutrinos suppress the lensing power (like a low A_L) there is a concern that the same tensions which drive A_L high may give artificially tight constraints on $\sum m_\nu$. We can investigate this issue by replacing the low-ℓ data with a prior on the optical depth (as in Sect. 5.1) and removing the high-ℓ data. Posterior distributions with the τ prior, and additionally without the high-ℓ data, are shown in Fig. 26 by the solid blue and dot-dashed blue curves, respectively. The constraint on $\sum m_\nu$ does not degrade much by replacing the low-ℓ data with the τ prior only, but the degradation is more severe when the high-ℓ data are also removed: $\sum m_\nu < 1.31$ eV (95% CL).

Including the lensing likelihood (see Sect. 5.1) has a significant, but surprising, effect on our results. Adding the lensing likelihood to the *Planck*+WP+highL data combination *weakens* the limit on $\sum m_\nu$,

$$\sum m_\nu < 0.85\,\mathrm{eV} \quad (95\%;\ \textit{Planck}\text{+lensing+WP+highL}), \tag{71}$$

as shown by the dashed black curve in Fig. 26. This is representative of a general trend that the *Planck* lensing likelihood favours larger $\sum m_\nu$ than the temperature power spectrum. Indeed, if we use the data combination *Planck*−lowL+highL+τprior, which gives a weaker constraint from the temperature power spectrum, adding lensing gives a best-fit away from zero ($\sum m_\nu = 0.46$ eV; dashed blue curve in Fig. 26). However, the total χ^2 at the best-fit is very close to that for the best-fitting base model (which, recall, has one massive neutrino of mass 0.06 eV), with the improved fit

[39] The power spectrum of the temperature anisotropies is predominantly sensitive to changes in only one mode of the lensing potential power spectrum (Smith et al. 2006). It follows that marginalizing over the single parameter A_L is nearly equivalent to marginalizing over the full amplitude and shape information in the lensing power spectrum as regards constraints from the temperature power spectrum.

to the lensing data ($\Delta\chi^2 = -2.35$) being cancelled by the poorer fit to high-ℓ CMB data ($\Delta\chi^2 = -2.15$). There are rather large shifts in other cosmological parameters between these best-fit solutions corresponding to shifts along the acoustic-scale degeneracy direction for the temperature power spectrum. Note that, as well as the change in H_0 (which falls to compensate the increase in $\sum m_\nu$ at fixed acoustic scale), n_s, ω_b and ω_c change significantly keeping the *lensed* temperature spectrum almost constant. These latter shifts are similar to those discussed for A_L in Sect. 5.1, with non-zero $\sum m_\nu$ acting like $A_L < 1$. The lensing power spectrum $C_\ell^{\phi\phi}$ is lower by 5.4% for the higher-mass best fit at $\ell = 400$ and larger below $\ell \approx 45$ (e.g. by 0.6% at $\ell = 40$), which is a similar trend to the residuals from the best-fit minimal-mass model shown in the bottom panel of Fig. 12. Planck Collaboration XVII (2013) explores the robustness of the $C_\ell^{\phi\phi}$ estimates to various data cuts and foreground-cleaning methods. The first ($\ell = 40$–85) bandpower is the least stable to these choices, although the variations are not statistically significant. We have checked that excluding this bandpower does not change the posterior for $\sum m_\nu$ significantly, as expected since most of the constraining power on $\sum m_\nu$ comes from the bandpowers on smaller scales. At this stage, it is unclear what to make of this mild preference for high masses from the 4-point function compared to the 2-point function. As noted in Planck Collaboration XVII (2013), the lensing measurements from ACT (Das et al. 2013) and SPT (van Engelen et al. 2012) show similar trends to those from *Planck* where they overlap in scale. With further *Planck* data (including polarization), and forthcoming measurements from the full 2500 deg^2 SPT temperature survey, we can expect more definitive results on this issue in the near future.

Apart from its impact on the early-ISW effect and lensing potential, the total neutrino mass affects the angular-diameter distance to last scattering, and can be constrained through the angular scale of the first acoustic peak. However, this effect is degenerate with Ω_Λ (and so the derived H_0) in flat models and with other late-time parameters such as Ω_K and w in more general models (Howlett et al. 2012). Late-time geometric measurements help in reducing this "geometric" degeneracy. Increasing the neutrino masses at fixed θ_* increases the angular-diameter distance for $0 \le z \le z_*$ and reduces the expansion rate at low redshift ($z \lesssim 1$) but increases it at higher redshift. The spherically-averaged BAO distance $D_V(z)$ therefore increases with increasing neutrino mass at fixed θ_*, and the Hubble constant falls; see Fig. 8 of Hou et al. (2012). With the BAO data of Sect. 5.2, we find a significantly lower bound on the neutrino mass:

$$\sum m_\nu < 0.23\,\mathrm{eV} \quad (95\%;\ \textit{Planck}\text{+WP+highL+BAO}). \tag{72}$$

Following the philosophy of this paper, namely to give higher weight to the BAO data compared to more complex astrophysical data, we quote the result of Eq. (72) in the abstract as our most reliable limit on the neutrino mass. The ΛCDM model with minimal neutrino masses was shown in Sect. 5.3 to be in tension with recent direct measurements of H_0 which favour higher values. Increasing the neutrino mass will only make this tension worse and drive us to artificially tight constraints on $\sum m_\nu$. If we relax spatial flatness, the CMB geometric degeneracy becomes three-dimensional in models with massive neutrinos and the constraints on $\sum m_\nu$ weaken considerably to

$$\sum m_\nu < \begin{cases} 0.98\,\mathrm{eV} & (95\%;\ \textit{Planck}\text{+WP+highL}) \\ 0.32\,\mathrm{eV} & (95\%;\ \textit{Planck}\text{+WP+highL+BAO}). \end{cases} \tag{73}$$

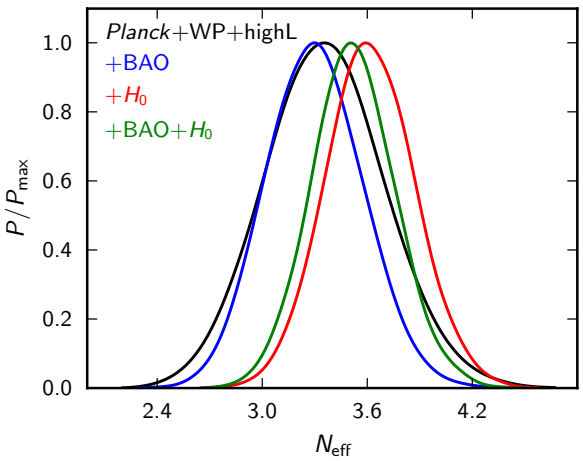

Fig. 27. Marginalized posterior distribution of $N_{\rm eff}$ for *Planck*+WP+highL (black) and additionally BAO (blue), the H_0 measurement (red), and both BAO and H_0 (green).

6.3.2. Constraints on $N_{\rm eff}$

As discussed in Sect. 2, the density of radiation in the Universe (besides photons) is usually parameterized by the effective neutrino number $N_{\rm eff}$. This parameter specifies the energy density when the species are relativistic in terms of the neutrino temperature assuming exactly three flavours and instantaneous decoupling. In the Standard Model, $N_{\rm eff} = 3.046$, due to non-instantaneous decoupling corrections (Mangano et al. 2005).

However, there has been some mild preference for $N_{\rm eff} > 3.046$ from recent CMB anisotropy measurements (Komatsu et al. 2011; Dunkley et al. 2011; Keisler et al. 2011; Archidiacono et al. 2011; Hinshaw et al. 2012; Hou et al. 2012). This is potentially interesting, since an excess could be caused by a neutrino/anti-neutrino asymmetry, sterile neutrinos, and/or any other light relics in the Universe. In this subsection we discuss the constraints on $N_{\rm eff}$ from *Planck* in scenarios where the extra relativistic degrees of freedom are effectively massless.

The physics of how $N_{\rm eff}$ is constrained by CMB anisotropies is explained in Bashinsky & Seljak (2004), Hou et al. (2011) and Lesgourgues et al. (2013). The main effect is that increasing the radiation density at fixed θ_* (to preserve the angular scales of the acoustic peaks) and fixed $z_{\rm eq}$ (to preserve the early-ISW effect and so first-peak height) increases the expansion rate before recombination and reduces the age of the Universe at recombination. Since the diffusion length scales approximately as the square root of the age, while the sound horizon varies proportionately with the age, the angular scale of the photon diffusion length, θ_D, increases, thereby reducing power in the damping tail at a given multipole. Combining *Planck*, *WMAP* polarization and the high-ℓ experiments gives

$$N_{\rm eff} = 3.36^{+0.68}_{-0.64} \quad (95\%;\ \textit{Planck}\text{+WP+highL}). \tag{74}$$

The marginalized posterior distribution is given in Fig. 27 (black curve). The result in Eq. (74) is consistent with the value of $N_{\rm eff} = 3.046$ of the Standard Model, but it is important to aknowledge that it is difficult to constrain $N_{\rm eff}$ accurately using CMB temperature measurements alone. Evidently, the nominal mission data from *Planck* do not strongly rule out a value as high as $N_{\rm eff} = 4$.

Increasing $N_{\rm eff}$ at fixed θ_* and $z_{\rm eq}$ necessarily raises the expansion rate at low redshifts too. Combining CMB with distance measurements can therefore improve constraints (see Fig. 27) although for the BAO observable $r_{\rm drag}/D_{\rm V}(z)$ the reduction in both $r_{\rm drag}$ and $D_{\rm V}(z)$ with increasing $N_{\rm eff}$ partly cancel. With the BAO data of Sect. 5.2, the $N_{\rm eff}$ constraint is tightened to

$$N_{\rm eff} = 3.30^{+0.54}_{-0.51} \quad (95\%;\ \textit{Planck}{+}{\rm WP}{+}{\rm highL}{+}{\rm BAO}). \tag{75}$$

Our constraints from CMB alone and CMB+BAO are compatible with the standard value $N_{\rm eff} = 3.046$ at the $1\,\sigma$ level, giving no evidence for extra relativistic degrees of freedom.

Since $N_{\rm eff}$ is positively correlated with H_0, the tension between the *Planck* data and direct measurements of H_0 in the base ΛCDM model (Sect. 5.3) can be reduced at the expense of high $N_{\rm eff}$. The marginalized constraint is

$$N_{\rm eff} = 3.62^{+0.50}_{-0.48} \quad (95\%;\ \textit{Planck}{+}{\rm WP}{+}{\rm highL}{+}H_0). \tag{76}$$

For this data combination, the χ^2 for the best-fitting model allowing $N_{\rm eff}$ to vary is lower by 5.3 than for the base $N_{\rm eff} = 3.046$ model. The H_0 fit is much better, with $\Delta\chi^2 = -4.4$, but there is no strong preference either way from the CMB. The low-ℓ temperature power spectrum does weakly favour the high $N_{\rm eff}$ model ($\Delta\chi^2 = -1.4$) – since $N_{\rm eff}$ is positively correlated with $n_{\rm s}$ (see Fig. 24) and increasing $n_{\rm s}$ reduces power on large scales – as does the rest of the *Planck* power spectrum ($\Delta\chi^2 = -1.8$). The high-ℓ experiments mildly disfavour high $N_{\rm eff}$ in our fits ($\Delta\chi^2 = 1.9$). Further including the BAO data pulls the central value downwards by around $0.5\,\sigma$ (see Fig. 27):

$$N_{\rm eff} = 3.52^{+0.48}_{-0.45} \quad (95\%;\ \textit{Planck}{+}{\rm WP}{+}{\rm highL}{+}H_0{+}{\rm BAO}). \tag{77}$$

The χ^2 at the best-fit for this data combination ($N_{\rm eff} = 3.48$) is lower by 4.2 than the best-fitting $N_{\rm eff} = 3.046$ model. While the high $N_{\rm eff}$ best-fit is preferred by *Planck*+WP ($\Delta\chi^2 = -3.1$) and the H_0 data ($\Delta\chi^2 = -3.3$ giving an acceptable $\chi^2 = 1.8$ for this data point), it is disfavoured by the high-ℓ CMB data ($\Delta\chi^2 = 2.0$) and slightly by BAO ($\Delta\chi^2 = 0.5$). We conclude that the tension between direct H_0 measurements and the CMB and BAO data in the base ΛCDM can be relieved at the cost of additional neutrino-like physics, but there is no strong preference for this extension from the CMB damping tail.

Throughout this subsection, we have assumed that all the relativistic components parameterized by $N_{\rm eff}$ consist of ordinary free-streaming relativistic particles. Extra radiation components with a different sound speed or viscosity parameter (Hu 1998) can provide a good fit to pre-*Planck* CMB data (Archidiacono et al. 2013), but are not investigated in this paper.

6.3.3. Simultaneous constraints on $N_{\rm eff}$ and either $\sum m_\nu$ or $m^{\rm eff}_{\nu,\,\rm sterile}$

It is interesting to investigate simultaneous contraints on $N_{\rm eff}$ and $\sum m_\nu$, since extra relics could coexist with neutrinos of sizeable mass, or could themselves have a mass in the eV range. Joint constraints on $N_{\rm eff}$ and $\sum m_\nu$ have been explored several times in the literature. These two parameters are known to be partially degenerate when large-scale structure data are used (Hannestad & Raffelt 2004; Crotty et al. 2004), but their impact in the CMB is different and does not lead to significant correlations.

Joint constraints on $N_{\rm eff}$ and $\sum m_\nu$ are always model-dependent: they vary strongly with assumptions about how the total mass is split between different species (and they would also be different for models in which massive species have chemical potentials or a non-thermal phase-space distribution). We present here *Planck* constraints for two different models and describe the scenarios that motivate them.

First, as in the previous subsection we assume that the three active neutrinos share a mass $m_\nu = \sum m_\nu/3$, and may coexist with extra massless species contributing to $N_{\rm eff}$. In this model, when $N_{\rm eff}$ is greater than 3.046, $\Delta N_{\rm eff} = N_{\rm eff} - 3.046$ gives the density of extra massless relics with arbitrary phase-space distribution. When $N_{\rm eff} < 3.046$, the temperature of the three active neutrinos is reduced accordingly, and no additional relativistic species are assumed. In this case, the CMB constraint is

$$\left.\begin{aligned} N_{\rm eff} &= 3.29^{+0.67}_{-0.64} \\ \textstyle\sum m_\nu &< 0.60\,{\rm eV} \end{aligned}\right\} \quad (95\%;\ \textit{Planck}{+}{\rm WP}{+}{\rm highL}). \tag{78}$$

These bounds tighten somewhat with the inclusion of BAO data, as illustrated in Fig. 28; we find

$$\left.\begin{aligned} N_{\rm eff} &= 3.32^{+0.54}_{-0.52} \\ \textstyle\sum m_\nu &< 0.28\,{\rm eV} \end{aligned}\right\} \quad (95\%;\ \textit{Planck}{+}{\rm WP}{+}{\rm highL}{+}{\rm BAO}). \tag{79}$$

We see that the joint constraints do not differ very much from the bounds obtained when introducing these parameters separately. The physical effects of neutrino masses and extra relativistic relics are sufficiently different to be resolved separately at the level of accuracy of *Planck*.

In the second model, we assume the existence of one massive sterile neutrino, in addition to the two massless and one massive active neutrino of the base model. The active neutrino mass is kept fixed at 0.06 eV. In particle physics, this assumption can be motivated in several ways. For example, there has recently been renewed interest in models with one light sterile neutrino in order to explain the MiniBoone anomaly reported in Aguilar-Arevalo et al. (2012), as well as reactor and Gallium anomalies (Giunti et al. 2013). The statistical significance of these results is marginal and they should not be over-interpreted. However, they do motivate investigating a model with three active neutrinos and one heavier sterile neutrino with mass $m_{\rm sterile}$. If the sterile neutrino were to thermalize with the same temperature as active neutrinos, this model would have $N_{\rm eff} \approx 4$.

Since we wish to be more general, we assume that the extra eigenstate is either: (i) thermally distributed with an arbitrary temperature $T_{\rm s}$; or (ii) distributed proportionally to active neutrinos with an arbitrary scaling factor $\chi_{\rm s}$ in which the scaling factor is a function of the active–sterile neutrino mixing angle. This second case corresponds the Dodelson-Widrow scenario (Dodelson & Widrow 1994). The two cases are in fact equivalent for cosmological observables and do not require separate analyses (Colombi et al. 1996; Lesgourgues et al. 2013). Sampling the posterior with flat priors on $N_{\rm eff}$ and $m_{\rm sterile}$ would not be efficient, since in the limit of small temperature $T_{\rm s}$, or small scaling factor $\chi_{\rm s}$, the mass would be unbounded. Hence we adopt a flat prior on the "effective sterile neutrino mass" defined as $m^{\rm eff}_{\nu,\,\rm sterile} \equiv (94.1\omega_{\nu,\,\rm sterile})\,{\rm eV}$[40]. In the case of a thermally-distributed sterile neutrino, this parameter is related to the true mass via

$$m^{\rm eff}_{\nu,\,\rm sterile} = (T_{\rm s}/T_\nu)^3 m^{\rm thermal}_{\rm sterile} = (\Delta N_{\rm eff})^{3/4} m^{\rm thermal}_{\rm sterile}\,. \tag{80}$$

[40] The factor of 94.1 eV here is the usual one in the relation between physical mass and energy density for non-relativistic neutrinos with physical temperature T_ν.

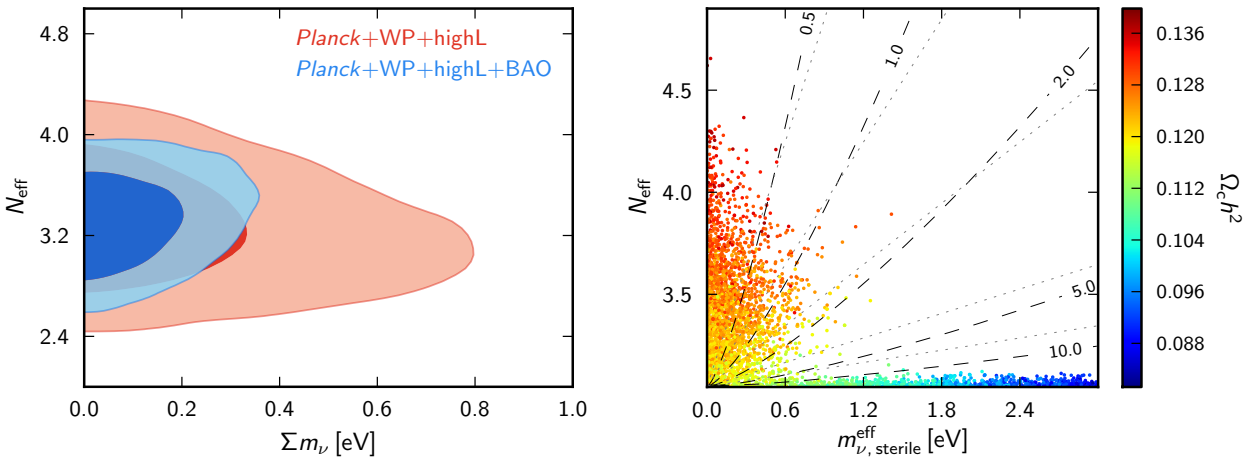

Fig. 28. *Left*: 2D joint posterior distribution between $N_{\rm eff}$ and $\sum m_\nu$ (the summed mass of the three active neutrinos) in models with extra massless neutrino-like species. *Right*: Samples in the $N_{\rm eff}$–$m^{\rm eff}_{\nu,\,\rm sterile}$ plane, colour-coded by $\Omega_c h^2$, in models with one massive sterile neutrino family, with effective mass $m^{\rm eff}_{\nu,\,\rm sterile}$, and the three active neutrinos as in the base ΛCDM model. The physical mass of the sterile neutrino in the thermal scenario, $m^{\rm thermal}_{\rm sterile}$, is constant along the grey dashed lines, with the indicated mass in eV. The physical mass in the Dodelson-Widrow scenario, $m^{\rm DW}_{\rm sterile}$, is constant along the dotted lines (with the value indicated on the adjacent dashed lines). Note the pile up of points at low values of $N_{\rm eff}$, caused because the sterile neutrino component behaves like cold dark matter there, introducing a strong degeneracy between the two components, as described in the text.

Here, recall that $T_\nu = (4/11)^{1/3} T_\gamma$ is the active neutrino temperature in the instantaneous-decoupling limit and that the effective number is defined via the energy density, $\Delta N_{\rm eff} = (T_{\rm s}/T_\nu)^4$. In the Dodelson-Widrow case the relation is given by

$$m^{\rm eff}_{\nu,\,\rm sterile} = \chi_{\rm s} m^{\rm DW}_{\rm sterile}\,, \tag{81}$$

with $\Delta N_{\rm eff} = \chi_{\rm s}$. For a thermalized sterile neutrino with temperature T_ν (i.e., the temperature the active neutrinos would have if there were no heating at electron-positron annihilation), corresponding to $\Delta N_{\rm eff} = 1$, the three masses are equal to each other.

Assuming flat priors on $N_{\rm eff}$ and $m^{\rm eff}_{\nu,\,\rm sterile}$ with $m^{\rm eff}_{\nu,\,\rm sterile} < 3\,$eV, we find the results shown in Fig. 28. The physical mass, $m^{\rm thermal}_{\rm sterile}$ in the thermal scenario is constant along the dashed lines in the figure and takes the indicated value in eV. The physical mass, $m^{\rm DW}_{\rm sterile}$, in the Dodelson-Widrow scenario is constant on the dotted lines. For low $N_{\rm eff}$ the physical mass of the neutrinos becomes very large, so that they become non-relativistic well before recombination. In the limit in which the neutrinos become non-relativistic well before any relevant scales enter the horizon, they will behave exactly like cold dark matter, and hence are completely unconstrained within the overall total constraint on the dark matter density. For intermediate cases where the neutrinos become non-relativistic well before recombination they behave like warm dark matter. The approach to the massive limit gives the tail of allowed models with large $m^{\rm eff}_{\nu,\,\rm sterile}$ and low $N_{\rm eff}$ shown in Fig. 28, with increasing $m^{\rm eff}_{\nu,\,\rm sterile}$ being compensated by decreased $\Omega_c h^2$ to maintain the total level required to give the correct shape to the CMB power spectrum.

For low $m^{\rm eff}_{\nu,\,\rm sterile}$ and $\Delta N_{\rm eff}$ away from zero the physical neutrino mass is very light, and the constraint becomes similar to the massless case. The different limits are continuously connected, and given the complicated shape seen in Fig. 28 it is clearly not appropriate to quote fully marginalized parameter constraints that would depend strongly on the assumed upper limit on $m^{\rm eff}_{\nu,\,\rm sterile}$. Instead we restrict attention to the case where the physical mass is $m^{\rm thermal}_{\rm sterile} < 10\,$eV, which roughly defines the region where (for the CMB) the particles are distinct from cold or warm dark matter. Using the *Planck*+WP+highL (abbreviated to CMB below) data combination, this gives the marginalized one-parameter constraints

$$\left.\begin{array}{r} N_{\rm eff} < 3.91 \\ m^{\rm eff}_{\nu,\,\rm sterile} < 0.59\,{\rm eV} \end{array}\right\} \quad (95\%;\ {\rm CMB\ for}\ m^{\rm thermal}_{\rm sterile} < 10\,{\rm eV})\,. \tag{82}$$

Combining further with BAO these tighten to

$$\left.\begin{array}{r} N_{\rm eff} < 3.80 \\ m^{\rm eff}_{\nu,\,\rm sterile} < 0.42\,{\rm eV} \end{array}\right\} \quad (95\%;\ {\rm CMB{+}BAO\ for}\ m^{\rm thermal}_{\rm sterile} < 10\,{\rm eV})\,. \tag{83}$$

These bounds are only marginally compatible with a fully thermalized sterile neutrino ($N_{\rm eff} \approx 4$) with sub-eV mass $m^{\rm thermal}_{\rm sterile} \approx m^{\rm eff}_{\nu,\,\rm sterile} < 0.5\,$eV that could explain the oscillation anomalies. The above contraints are also appropriate for the Dodelson-Widrow scenario, but for a physical mass cut of $m^{\rm DW}_{\rm sterile} < 20\,$eV.

The thermal and Dodelson-Widrow scenarios considered here are representative of a large number of possible models that have recently been investigated in the literature (Hamann et al. 2011; Diamanti et al. 2012; Archidiacono et al. 2012; Hannestad et al. 2012).

6.4. Big bang nucleosynthesis

Observations of light elements abundances created during big bang nucleosynthesis (BBN) provided one of the earliest precision tests of cosmology and were critical in establishing the existence of a hot big bang. Up-to-date accounts of nucleosynthesis are given by Iocco et al. (2009) and Steigman (2012). In the standard BBN model, the abundance of light elements (parameterized by $Y_{\rm P}^{\rm BBN} \equiv 4n_{\rm He}/n_{\rm b}$ for helium-4 and $y_{\rm DP}^{\rm BBN} \equiv 10^5 n_{\rm D}/n_{\rm H}$

for deuterium, where n_i is the number density of species i)[41] can be predicted as a function of the baryon density ω_b, the number of relativistic degrees of freedom parameterized by N_{eff}, and of the lepton asymmetry in the electron neutrino sector. Throughout this subsection, we assume for simplicity that lepton asymmetry is too small to play a role at BBN. This is a reasonable assumption, since *Planck* data cannot improve existing constraints on the asymmetry[42]. We also assume that there is no significant entropy increase between BBN and the present day, so that our CMB constraints on the baryon-to-photon ratio can be used to compute primordial abundances.

To calculate the dependence of Y_P^{BBN} and y_{DP}^{BBN} on the parameters ω_b and N_{eff}, we use the accurate public code `PArthENoPE` (Pisanti et al. 2008), which incorporates values of nuclear reaction rates, particle masses and fundamental constants, and an updated estimate of the neutron lifetime ($\tau_n = 880.1$ s; Beringer et al. 2012). Experimental uncertainties on each of these quantities lead to a theoretical error for $Y_P^{BBN}(\omega_b, N_{eff})$ and $y_{DP}^{BBN}(\omega_b, N_{eff})$. For helium, the error is dominated by the uncertainty in the neutron lifetime, leading to[43] $\sigma(Y_P^{BBN}) = 0.0003$. For deuterium, the error is dominated by uncertainties in several nuclear rates, and is estimated to be $\sigma(y_{DP}^{BBN}) = 0.04$ (Serpico et al. 2004).

These predictions for the light elements can be confronted with measurements of their abundances, and also with CMB data (which is sensitive to ω_b, N_{eff}, and Y_P). We shall see below that for the base cosmological model with $N_{eff} = 3.046$ (or even for an extended scenario with free N_{eff}) the CMB data predict the primordial abundances, under the assumption of standard BBN, with smaller uncertainties than those estimated for the measured abundances. Furthermore, the CMB predictions are consistent with direct abundance measurements.

6.4.1. Observational data on primordial abundances

The observational constraint on the primordial helium-4 fraction used in this paper is $Y_P^{BBN} = 0.2534 \pm 0.0083$ (68% CL) from the recent data compilation of Aver et al. (2012), based on spectroscopic observations of the chemical abundances in metal-poor H II regions. The error on this measurement is dominated by systematic effects that will be difficult to resolve in the near future. It is reassuring that the independent and conservative method presented in Mangano & Serpico (2011) leads to an upper bound for Y_P^{BBN} that is consistent with the above estimate. The recent measurement of the proto-Solar helium abundance by Serenelli & Basu (2010) provides an even more conservative upper bound, $Y_P^{BBN} < 0.294$ at the $2\,\sigma$ level.

For the primordial abundance of deuterium, data points show excess scatter above the statistical errors, indicative of systematic errors. The compilation presented in Iocco et al. (2009), based on data accumulated over several years, gives $y_{DP}^{BBN} = 2.87 \pm 0.22$ (68% CL). Pettini & Cooke (2012) report an accurate deuterium abundance measurement in the $z = 3.04984$ low-metallicity damped Ly α system in the spectrum of QSO SDSS J1419+0829, which they argue is particularly well suited to deuterium abundance measurements. These authors find $y_{DP}^{BBN} = 2.535 \pm 0.05$ (68% CL), a significantly tighter constraint than that from the Iocco et al. (2009) compilation. The Pettini-Cooke measurement is, however, a single data point, and it is important to acquire more observations of similar systems to assess whether their error estimate is consistent with possible sources of systematic error. We adopt a conservative position in this paper and compare both the Iocco et al. (2009) and the Pettini & Cooke (2012) measurements to the CMB predictions

We consider only the ^{4}He and D abundances in this paper. We do not discuss measurements of ^{3}He abundances since these provide only an upper bound on the true primordial ^{3}He fraction. Likewise, we do not discuss lithium. There has been a long standing discrepancy between the low lithium abundances measured in metal-poor stars in our Galaxy and the predictions of BBN. At present it is not clear whether this discrepancy is caused by systematic errors in the abundance measurements, or has an "astrophysical" solution (e.g., destruction of primordial lithium) or is caused by new physics (see Fields 2011, for a recent review).

6.4.2. *Planck* predictions of primordial abundances in standard BBN

We first restrict ourselves to the base cosmological model, with no extra relativistic degrees of freedom beyond ordinary neutrinos (and a negligible lepton asymmetry), leading to $N_{eff} = 3.046$ (Mangano et al. 2005). Assuming that standard BBN holds, and that there is no entropy release after BBN, we can compute the spectrum of CMB anisotropies using the relation $Y_P(\omega_b)$ given by `PArthENoPE`. This relation is used as the default in the grid of models discussed in this paper; we use the `CosmoMC` implementation developed by Hamann et al. (2008). The *Planck*+WP+highL fits to the base ΛCDM model gives the following estimate of the baryon density,

$$\omega_b = 0.02207 \pm 0.00027 \quad (68\%;\ \textit{Planck}\text{+WP+highL}), \tag{84}$$

as listed in Table 5. In Fig. 29, we show this bound together with theoretical BBN predictions for $Y_P^{BBN}(\omega_b)$ and $y_{DP}^{BBN}(\omega_b)$. The bound of Eq. (84) leads to the predictions

$$Y_P^{BBN}(\omega_b) = 0.24725 \pm 0.00032, \tag{85a}$$

$$y_{DP}^{BBN}(\omega_b) = 2.656 \pm 0.067, \tag{85b}$$

where the errors here are 68% and include theoretical errors that are added in quadrature to those arising from uncertainties in ω_b. (The theoretical error dominates the total error in the case of Y_P.)[44] For helium, this prediction is in very good agreement

[41] Observations of the primordial abundances are usually reported in terms of these number ratios. For helium, Y_P^{BBN} differs from the mass fraction Y_P, used elsewhere in this paper, by 0.5% due to the binding energy of helium. Since the CMB is only sensitive to Y_P at the 10% level, the distinction between definitions based on the mass or number fraction is ignored when comparing helium constraints from the CMB with those from observational data on primordial abundances.

[42] A primordial lepton asymmetry could modify the outcome of BBN only if it were very large (of the order of 10^{-3} or bigger). Such a large asymmetry is not motivated by particle physics, and is strongly constrained by BBN. Indeed, by taking into account neutrino oscillations in the early Universe, which tend to equalize the distribution function of three neutrino species, Mangano et al. (2012) derived strong bounds on the lepton asymmetry. CMB data cannot improve these bounds, as shown by Castorina et al. (2012); an exquisite sensitivity to N_{eff} would be required. Note that the results of Mangano et al. (2012) assume that N_{eff} departs from the standard value only due to the lepton asymmetry. A model with both a large lepton asymmetry and extra relativistic relics could be constrained by CMB data. However, we will not consider such a contrived scenario in this paper.

[43] Serpico et al. (2004) quotes $\sigma(Y_P^{BBN}) = 0.0002$, but since that work, the uncertainty on the neutron lifetime has been re-evaluated, from $\sigma(\tau_n) = 0.8$ s to $\sigma(\tau_n) = 1.1$ s (Beringer et al. 2012).

[44] Note that, throughout this paper, our quoted CMB constraints on all parameters do not include the theoretical uncertainty in the BBN relation (where used).

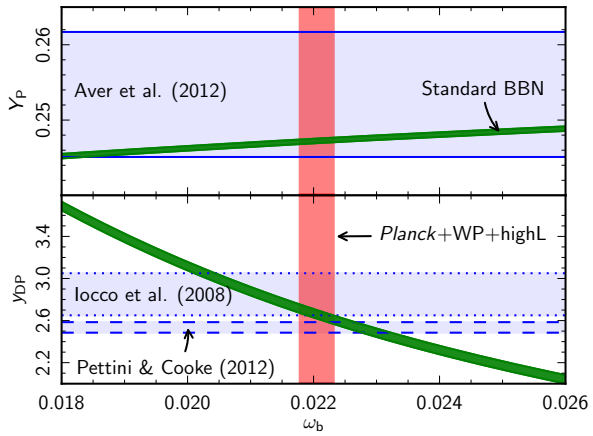

Fig. 29. Predictions of standard BBN for the primordial abundance of ^{4}He (top) and deuterium (bottom), as a function of the baryon density. The width of the green stripes corresponds to 68% uncertainties on nuclear reaction rates. The horizontal bands show observational bounds on primordial element abundances compiled by various authors, and the red vertical band shows the *Planck*+WP+highL bounds on ω_b (all with 68% errors). BBN predictions and CMB results assume $N_{eff} = 3.046$ and no significant lepton asymmetry.

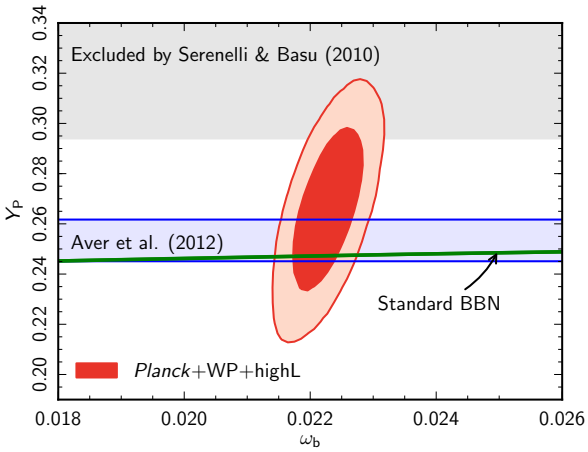

Fig. 30. Constraints in the ω_b–Y_P plane from CMB and abundance measurements. The CMB constraints are for *Planck*+WP+highL (red 68% and 95% contours) in ΛCDM models with Y_P allowed to vary freely. The horizontal band shows observational bounds on ^{4}He compiled by Aver et al. (2012) with 68% errors, while the grey region at the top of the figure delineates the conservative 95% upper bound inferred from Solar helium abundance by Serenelli & Basu (2010). The green stripe shows the predictions of standard BBN for the primordial abundance of ^{4}He as a function of the baryon density (with 68% errors on nuclear reaction rates). Both BBN predictions and CMB results assume $N_{eff} = 3.046$ and no significant lepton asymmetry.

with the data compilation of Aver et al. (2012), with an error that is 26 times smaller. For deuterium, the CMB+BBN prediction lies midway between the best-fit values of Iocco et al. (2009) and Pettini & Cooke (2012), but agrees with both at approximately the $1\,\sigma$ level. These results strongly support standard BBN and show that within the framework of the base ΛCDM model, *Planck* observations lead to extremely precise predictions of primordial abundances.

6.4.3. Estimating the helium abundance directly from *Planck* data

In the CMB analysis, instead of fixing Y_P to the BBN prediction, $Y_P^{BBN}(\omega_b)$, we can relax any BBN prior and let this parameter vary freely. The primordial helium fraction has an influence on the recombination history and affects CMB anisotropies mainly through the redshift of last scattering and the diffusion damping scale (Hu et al. 1995; Trotta & Hansen 2004; Ichikawa & Takahashi 2006; Hamann et al. 2008). Extending the base ΛCDM model by adding Y_P as a free parameter with a flat prior in the range $[0.1, 0.5]$, we find

$$Y_P = 0.266 \pm 0.021 \quad (68\%;\ \textit{Planck}\text{+WP+highL}). \tag{86}$$

Constraints in the Y_P–ω_b plane are shown in Fig. 30. This figure shows that the CMB data have some sensitivity to the helium abundance. In fact, the error on the CMB estimate of Y_P is only 2.7 times larger than the direct measurements of the primordial helium abundance by Aver et al. (2012). The CMB estimate of Y_P is consistent with the observational measurements adding further support in favour of standard BBN.

6.4.4. Extension to the case with extra relativistic relics

We now consider the effects of additional relativistic degrees of freedom on photons and ordinary neutrinos (obeying the standard model of neutrino decoupling) by adding N_{eff} as a free parameter. In the absence of lepton asymmetry, we can predict the BBN primordial abundances as a function of the two parameters ω_b and N_{eff}.

Figure 31 shows the regions in the ω_b–N_{eff} plane preferred by primordial abundance measurements, and by the CMB data if the standard BBN picture is correct. The regions allowed by the abundance measurements are defined by the χ^2 statistic

$$\chi^2(\omega_b, N_{eff}) \equiv \frac{[y(\omega_b, N_{eff}) - y_{obs}]^2}{\sigma^2_{obs} + \sigma^2_{theory}}\,, \tag{87}$$

where $y(\omega_b, N_{eff})$ is the BBN prediction for either Y_P^{BBN} or y_{DP}^{BBN}, the quantity y_{obs} is the observed abundance, and the two errors in the denominator are the observational and theoretical uncertainties. Figure 31 shows the edges of the 68% preferred regions in the ω_b–N_{eff} plane, given by $\chi^2 = \chi^2_{min} + 2.3$.

For the CMB data, we fit a cosmological model with seven free parameters (the six parameters of the base ΛCDM model, plus N_{eff}) to the *Planck*+WP+highL data, assuming that the primordial helium fraction is fixed by the standard BBN prediction $Y_P^{BBN}(\omega_b, N_{eff})$. Figure 31 shows the joint 68% and 95% confidence contours in the ω_b–N_{eff} plane. The preferred regions in this plane from abundance measurements and the CMB agree remarkably well. The CMB gives approximately three times smaller error bars than primordial abundance data on both parameters.

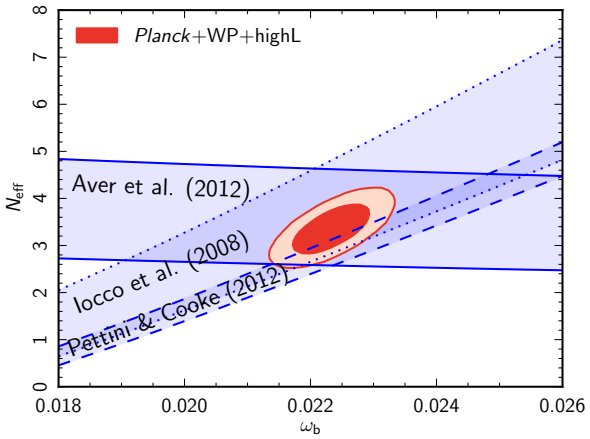

Fig. 31. Constraints in the $\omega_{\rm b}$–$N_{\rm eff}$ plane from the CMB and abundance measurements. The blue stripes shows the 68% confidence regions from measurements of primordial element abundances assuming standard BBN: ^{4}He bounds compiled by Aver et al. (2012); and deuterium bounds complied by Iocco et al. (2009) or measured by Pettini & Cooke (2012). We show for comparison the 68% and 95% contours inferred from *Planck*+WP+highL, when $N_{\rm eff}$ is left as a free parameter in the CMB analysis (and $Y_{\rm P}$ is fixed as a function of $\omega_{\rm b}$ and $N_{\rm eff}$ according to BBN predictions). These constraints assume no significant lepton asymmetry.

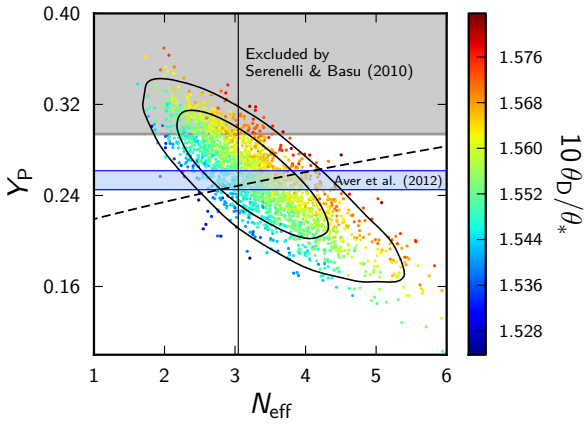

Fig. 32. 2D joint posterior distribution for $N_{\rm eff}$ and $Y_{\rm P}$ with both parameters varying freely, determined from *Planck*+WP+highL data. Samples are colour-coded by the value of the angular ratio $\theta_{\rm D}/\theta_*$, which is constant along the degeneracy direction. The $N_{\rm eff}$–$Y_{\rm P}$ relation from BBN theory is shown by the dashed curve. The vertical line shows the standard value $N_{\rm eff} = 3.046$. The region with $Y_{\rm P} > 0.294$ is highlighted in grey, delineating the region that exceeds the $2\,\sigma$ upper limit of the recent measurement of initial Solar helium abundance (Serenelli & Basu 2010), and the blue horizontal region is the 68% confidence region from the Aver et al. (2012) compilation of ^{4}He measurements.

We can derive constraints on $N_{\rm eff}$ from primordial element abundances *and* CMB data together by combining their likelihoods. The CMB-only confidence interval for $N_{\rm eff}$ is

$$N_{\rm eff} = 3.36 \pm 0.34 \quad (68\%;\ \textit{Planck}{+}\text{WP}{+}\text{highL}). \tag{88}$$

When combined with the data reported respectively by Aver et al. (2012), Iocco et al. (2009), and Pettini & Cooke (2012), the 68% confidence interval becomes

$$N_{\rm eff} = \begin{cases} 3.41 \pm 0.30, & Y_{\rm P}\ \text{(Aver et al.)}, \\ 3.43 \pm 0.34, & y_{\rm DP}\ \text{(Iocco et al.)}, \\ 3.02 \pm 0.27, & y_{\rm DP}\ \text{(Pettini and Cooke)}. \end{cases} \tag{89}$$

Since there is no significant tension between CMB and primordial element results, all these bounds are in agreement with the CMB-only analysis. The small error bar derived from combining the CMB with the Pettini & Cooke (2012) data point shows that further deuterium observations combined with *Planck* data have the potential to pin down the value of $N_{\rm eff}$ to high precision.

6.4.5. Simultaneous constraints on both $N_{\rm eff}$ and $Y_{\rm P}$

In this subsection, we discuss simultaneous constraints on both $N_{\rm eff}$ and $Y_{\rm P}$ by adding them to the six parameters of the base ΛCDM model. Both $N_{\rm eff}$ and $Y_{\rm P}$ have an impact on the damping tail of the CMB power spectrum by altering the ratio $k_{\rm D}^{-1}/r_*$, where $k_{\rm D}^{-1}$ is the photon diffusion length at last scattering and r_* is the sound horizon there. There is thus an approximate degeneracy between these two parameters along which the ratio is nearly constant. The extent of the degeneracy is limited by the characteristic phase shift of the acoustic oscillations that arises due to the free streaming of the neutrinos (Bashinsky & Seljak 2004). As discussed by Hou et al. (2011), the early ISW effect also partly breaks the degeneracy, but this is less important than the effect of the phase shifts.

The joint posterior distribution for $N_{\rm eff}$ and $Y_{\rm P}$ from the *Planck*+WP+highL likelihood is shown in Fig. 32, with each MCMC sample colour-coded by the value of the observationally-relevant angular ratio $\theta_{\rm D}/\theta_* \propto (k_{\rm D} r_*)^{-1}$. The main constraint on $N_{\rm eff}$ and $Y_{\rm P}$ comes from the precise measurement of this ratio by the CMB, leaving the degeneracy along the constant $\theta_{\rm D}/\theta_*$ direction. The relation between $N_{\rm eff}$ and $Y_{\rm P}$ from BBN theory is shown in the figure by the dashed curve[45]. The standard BBN prediction with $N_{\rm eff} = 3.046$ is contained within the 68% confidence region. The grey region is for $Y_{\rm P} > 0.294$ and is the $2\,\sigma$ conservative upper bound on the primordial helium abundance from Serenelli & Basu (2010). Most of the samples are consistent with this bound. The inferred estimates of $N_{\rm eff}$ and $Y_{\rm P}$ from the *Planck*+WP+highL data are

$$N_{\rm eff} = 3.33^{+0.59}_{-0.83} \quad (68\%;\ \textit{Planck}{+}\text{WP}{+}\text{highL}), \tag{90a}$$

$$Y_{\rm P} = 0.254^{+0.041}_{-0.033} \quad (68\%;\ \textit{Planck}{+}\text{WP}{+}\text{highL}). \tag{90b}$$

With $Y_{\rm P}$ allowed to vary, $N_{\rm eff}$ is no longer tightly constrained by the value of $\theta_{\rm D}/\theta_*$. Instead, it is constrained, at least in part, by the impact that varying $N_{\rm eff}$ has on the phase shifts of the acoustic oscillations. As discussed in Hou et al. (2012), this effect explains the observed correlation between $N_{\rm eff}$ and θ_*, which is shown in Fig. 33. The correlation in the ΛCDM+$N_{\rm eff}$ model is also plotted in the figure showing that the $N_{\rm eff}$–$Y_{\rm P}$ degeneracy combines with the phase shifts to generate a larger dispersion in θ_* in such models.

[45] For constant $N_{\rm eff}$, the variation due to the uncertainty in the baryon density is too small to be visible, given the thickness of the curve.

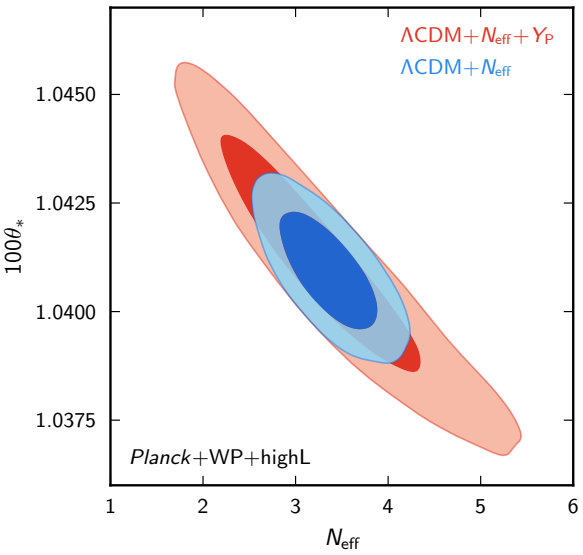

Fig. 33. 2D joint posterior distribution between $N_{\rm eff}$ and θ_* for ΛCDM models with variable $N_{\rm eff}$ (blue) and variable $N_{\rm eff}$ and $Y_{\rm P}$ (red). Both cases are for *Planck*+WP+highL data.

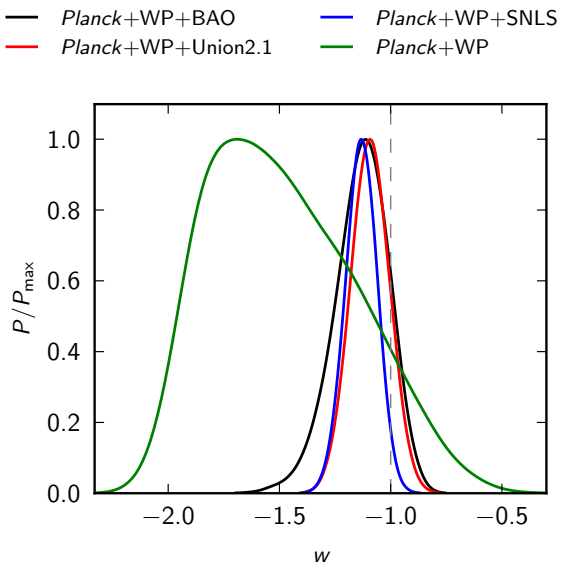

Fig. 34. Marginalized posterior distributions for the dark energy equation of state parameter w (assumed constant), for *Planck*+WP alone (green) and in combination with SNe data (SNSL in blue and the Union2.1 compilation in red) or BAO data (black). A flat prior on w from −3 to −0.3 was assumed and, importantly for the CMB-only constraints, the prior $[20, 100]\,{\rm km\,s^{-1}\,Mpc^{-1}}$ on H_0. The dashed grey line indicates the cosmological constant solution, $w = -1$.

6.5. Dark energy

A major challenge for cosmology is to elucidate the nature of the dark energy driving the accelerated expansion of the Universe. Perhaps the most straightforward explanation is that dark energy is a cosmological constant. An alternative is dynamical dark energy (Wetterich 1988; Ratra & Peebles 1988; Caldwell et al. 1998), usually based on a scalar field. In the simplest models, the field is very light, has a canonical kinetic energy term and is minimally coupled to gravity. In such models the dark energy sound speed equals the speed of light and it has zero anisotropic stress. It thus contributes very little to clustering. We shall only consider such models in this subsection.

A cosmological constant has an equation of state $w \equiv p/\rho = -1$, while scalar field models typically have time varying w with $w \geq -1$. The analysis performed here is based on the "parameterized post-Friedmann" (PPF) framework of Hu & Sawicki (2007) and Hu (2008) as implemented in `camb` (Fang et al. 2008b,a) and discussed earlier in Sect. 2. This allows us to investigate both regions of parameter space in which $w < -1$ (sometimes referred to as the "phantom" domain) and models in which w changes with time.

Figure 34 shows the marginalized posterior distributions for w for an extension of the base ΛCDM cosmology to models with constant w. We present results for *Planck*+WP and in combination with SNe or BAO data. (Note that adding in the high-ℓ data from ACT and SPT results in little change to the posteriors shown in Fig. 34.) As expected, the CMB alone does not strongly constrain w, due to the two-dimensional geometric degeneracy in these models. We can break this degeneracy by combining the CMB data with lower redshift distance measures. Adding in BAO data tightens the constraints substantially, giving

$$w = -1.13^{+0.24}_{-0.25} \quad (95\%;\ \textit{Planck}{+}\text{WP}{+}\text{BAO}), \tag{91}$$

in good agreement with a cosmological constant ($w = -1$). Using supernovae data leads to the constraints

$$w = -1.09 \pm 0.17 \quad (95\%;\ \textit{Planck}{+}\text{WP}{+}\text{Union2.1}), \tag{92a}$$

$$w = -1.13^{+0.13}_{-0.14} \quad (95\%;\ \textit{Planck}{+}\text{WP}{+}\text{SNLS}), \tag{92b}$$

The combination with SNLS data favours the phantom domain ($w < -1$) at $2\,\sigma$, while the Union2.1 compilation is more consistent with a cosmological constant.

If instead we combine *Planck*+WP with the Riess et al. (2011) measurement of H_0, we find

$$w = -1.24^{+0.18}_{-0.19} \quad (95\%;\ \textit{Planck}{+}\text{WP}{+}H_0), \tag{93}$$

which is in tension with $w = -1$ at more than the $2\,\sigma$ level.

The results in Eqs. (91–93) reflect the tensions between the supplementary data sets and the *Planck* base ΛCDM cosmology discussed in Sect. 5. The BAO data are in excellent agreement with the *Planck* base ΛCDM model, so there is no significant preference for $w \neq -1$ when combining BAO with *Planck*. In contrast, the addition of the H_0 measurement, or SNLS SNe data, to the CMB data favours models with exotic physics in the dark energy sector. These trends form a consistent theme throughout this section. The SNLS data favours a lower Ω in the ΛCDM model than *Planck*, and hence larger dark energy density today. The tension can be relieved by making the dark energy fall away faster in the past than for a cosmological constant, i.e., $w < -1$.

The constant w models are of limited physical interest. If $w \neq -1$ then it is likely to change with time. To investigate this we consider the simple linear relation in Eq. (4), $w(a) = w_0 + w_a(1 - a)$, which has often been used in the literature (Chevallier & Polarski 2001; Linder 2003). This parameterization approximately captures the low-redshift behaviour of light, slowly-rolling minimally-coupled scalar fields (as long as they do not contribute significantly to the total energy density at early times) and avoids the complexity of scanning a large number of possible potential shapes and initial conditions. The dynamical

physics comes almost entirely from the astrophysical data sets. It is up to the reader to decide how to interpret such results, but it is simplistic to assume that all astrophysical data sets have accurately quantified estimates of systematic errors. We have therefore tended to place greater weight on the CMB and BAO measurements in this paper rather than on more complex astrophysical data.

Our overall conclusion is that the *Planck* data are remarkably consistent with the predictions of the base ΛCDM cosmology. However, the mismatch with the temperature spectrum at low multipoles, evident in Figs. 1 and 39, and the existence of other "anomalies" at low multipoles, is possibly indicative that the model is incomplete. The results presented here are based on a first, and relatively conservative, analysis of the *Planck* data. The 2014 data release will use data obtained over the full mission lifetime of *Planck*, including polarization data. It remains to be seen whether these data, together with new astrophysical data sets and CMB polarization measurements, will offer any convincing evidence for new physics.

Acknowledgements. The development of *Planck* has been supported by: ESA; CNES and CNRS/INSU-IN2P3-INP (France); ASI, CNR, and INAF (Italy); NASA and DoE (USA); STFC and UKSA (UK); CSIC, MICINN and JA (Spain); Tekes, AoF and CSC (Finland); DLR and MPG (Germany); CSA (Canada); DTU Space (Denmark); SER/SSO (Switzerland); RCN (Norway); SFI (Ireland); FCT/MCTES (Portugal); and PRACE (EU). A description of the *Planck* Collaboration and a list of its members, including the technical or scientific activities in which they have been involved, can be found at http://www.sciops.esa.int/index.php?project=planck&page=Planck_Collaboration. We thank the referee for a comprehensive and helpful report. We also thank Jean-Philippe Uzan for his contributions to Sect. 6.8. We additionally acknowledge useful comments on the first version of this paper from a large number of scientists who have helped improve the clarity of the revised version. We mention specifically Jim Braatz, John Carlstrom, Alex Conley, Raphael Flauger, Liz Humphreys, Adam Reiss, Beth Reid, Uros Seljak, David Spergel, Mark Sullivan, and Reynald Pain.

References

Abazajian, K. N., Adelman-McCarthy, J. K., Agüeros, M. A., et al. 2009, ApJS, 182, 543, arXiv:0812.0649

Acquaviva, V., Baccigalupi, C., & Perrotta, F. 2004, Phys. Rev. D, 70, 023515, arXiv:astro-ph/0403654

Addison, G. E., Dunkley, J., Hajian, A., et al. 2012a, ApJ, 752, 120, arXiv:1108.4614

Addison, G. E., Dunkley, J., & Spergel, D. N. 2012b, MNRAS, 427, 1741, arXiv:1204.5927

Aguilar-Arevalo, A. et al. 2012, arXiv:1207.4809

Albrecht, A. & Steinhardt, P. J. 1982, Phys. Rev. Lett., 48, 1220

Ali-Haimoud, Y., Grin, D., & Hirata, C. M. 2010, Phys.Rev., D82, 123502, arXiv:1009.4697

Ali-Haimoud, Y. & Hirata, C. M. 2011, Phys.Rev., D83, 043513, arXiv:1011.3758

Amanullah, R., Lidman, C., Rubin, D., et al. 2010, ApJ, 716, 712, arXiv:1004.1711

Amblard, A., Cooray, A., Serra, P., et al. 2011, Nature, 470, 510, arXiv:1101.1080

Anderson, L., Aubourg, E., Bailey, S., et al. 2012, Mon. Not. Roy. Astron. Soc., 427, 3435, arXiv:1203.6594

Archidiacono, M., Calabrese, E., & Melchiorri, A. 2011, Phys.Rev., D84, 123008, arXiv:1109.2767

Archidiacono, M., Giusarma, E., Melchiorri, A., & Mena, O. 2012, Phys.Rev., D86, 043509, arXiv:1206.0109

Archidiacono, M., Giusarma, E., Melchiorri, A., & Mena, O. 2013, arXiv:1303.0143

Audren, B., Lesgourgues, J., Benabed, K., & Prunet, S. 2012, arXiv:1210.7183

Avelino, P., Martins, C., & Rocha, G. 2000, Phys. Rev. D, **62**, 123508, arXiv:astro-ph/0008446

Aver, E., Olive, K. A., & Skillman, E. D. 2012, JCAP, 1204, 004, arXiv:1112.3713

Balbi, A., Ade, P., Bock, J., et al. 2000, ApJ, 545, L1

Bardeen, J. M., Steinhardt, P. J., & Turner, M. S. 1983, Phys. Rev. D, 28, 679

Bashinsky, S. & Seljak, U. 2004, Phys. Rev. D, 69, 083002, arXiv:astro-ph/0310198

Basko, M. M. & Polnarev, A. G. 1980, MNRAS, 191, 207

Bassett, B. A., Tsujikawa, S., & Wands, D. 2006, Rev. Mod. Phys., 78, 537, arXiv:astro-ph/0507632

Battaglia, N., Bond, J. R., Pfrommer, C., & Sievers, J. L. 2012, ApJ, 758, 75, arXiv:1109.3711

Battaglia, N., Bond, J. R., Pfrommer, C., Sievers, J. L., & Sijacki, D. 2010, ApJ, 725, 91

Baumann, D. 2009, ArXiv e-prints, arXiv:0907.5424

Baumann, D., Jackson, M. G., Adshead, P., et al. 2009, in American Institute of Physics Conference Series, Vol. 1141, American Institute of Physics Conference Series, ed. S. Dodelson, D. Baumann, A. Cooray, J. Dunkley, A. Fraisse, M. G. Jackson, A. Kogut, L. Krauss, M. Zaldarriaga, & K. Smith , 10–120

Becker, G. D., Bolton, J. S., Haehnelt, M. G., & Sargent, W. L. W. 2011, MNRAS, 410, 1096, arXiv:1008.2622

Benjamin, J., Van Waerbeke, L., Heymans, C., et al. 2013, MNRAS, 431, 1547, arXiv:1212.3327

Bennett, C. L., Halpern, M., Hinshaw, G., et al. 2003, ApJS, 148, 1, arXiv:astro-ph/0302207

Bennett, C. L., Hill, R. S., Hinshaw, G., et al. 2011, ApJS, 192, 17, arXiv:1001.4758

Bennett, C. L., Larson, D., Weiland, J. L., et al. 2012, ArXiv e-prints, arXiv:1212.5225

Benson, B. A., de Haan, T., Dudley, J. P., et al. 2013, ApJ, 763, 147, arXiv:1112.5435

Beringer, J. et al. 2012, Phys.Rev., D86, 010001

Bertschinger, E. 1995, arXiv:astro-ph/9506070

Betoule, M., Marriner, J., Regnault, N., et al. 2013, A&A, 552, A124, arXiv:1212.4864

Beutler, F., Blake, C., Colless, M., et al. 2011, MNRAS, 416, 3017, arXiv:1106.3366

Blake, C., Kazin, E. A., Beutler, F., et al. 2011, MNRAS, 418, 1707, arXiv:1108.2635

Blas, D., Lesgourgues, J., & Tram, T. 2011, JCAP, 1107, 034, arXiv:1104.2933

Bonamente, M., Joy, M. K., LaRoque, S. J., et al. 2006, ApJ, 647, 25, arXiv:astro-ph/0512349

Bond, J. R. & Efstathiou, G. 1987, MNRAS, 226, 655

Bond, J. R., Efstathiou, G., & Tegmark, M. 1997, MNRAS, 291, L33, arXiv:astro-ph/9702100

Boyle, L. A., Steinhardt, P. J., & Turok, N. 2004, Phys. Rev. D, 69, 127302, arXiv:hep-th/0307170

Braatz, J., Reid, M., Kuo, C.-Y., et al. 2013, in IAU Symposium, Vol. 289, IAU Symposium, ed. R. de Grijs, 255–261

Brandenberger, R. 2012, ArXiv e-prints, arXiv:1204.6108

Bridle, S. L., Lewis, A. M., Weller, J., & Efstathiou, G. 2003, MNRAS, 342, L72, arXiv:astro-ph/0302306

Brown, I. & Crittenden, R. 2005, Phys.Rev., D72, 063002, arXiv:astro-ph/0506570

Bucher, M., Goldhaber, A. S., & Turok, N. 1995, Nuclear Physics B Proceedings Supplements, 43, 173, arXiv:hep-ph/9501396

Busca, N. G., Delubac, T., Rich, J., et al. 2012, ArXiv e-prints, arXiv:1211.2616

Calabrese, E., de Putter, R., Huterer, D., Linder, E. V., & Melchiorri, A. 2011, Phys. Rev. D, 83, 023011, arXiv:1010.5612

Calabrese, E., Hlozek, R. A., Battaglia, N., et al. 2013, ArXiv e-prints, arXiv:1302.1841

Calabrese, E., Slosar, A., Melchiorri, A., Smoot, G. F., & Zahn, O. 2008, Phys. Rev. D, 77, 123531, arXiv:0803.2309

Caldwell, R., Dave, R., & Steinhardt, P. J. 1998, Phys.Rev.Lett., 80, 1582, arXiv:astro-ph/9708069

Caldwell, R. R., Dave, R., & Steinhardt, P. J. 1998, Ap&SS, 261, 303

Caldwell, R. R., Doran, M., Mueller, C. M., Schafer, G., & Wetterich, C. 2003, Astrophys.J., 591, L75, arXiv:astro-ph/0302505

Caprini, C., Finelli, F., Paoletti, D., & Riotto, A. 2009, JCAP, 0906, 021, arXiv:0903.1420

Carlstrom, J. E., Holder, G. P., & Reese, E. D. 2002, ARA&A, 40, 643, arXiv:astro-ph/0208192

Castorina, E., Franca, U., Lattanzi, M., et al. 2012, Phys.Rev., D86, 023517, arXiv:1204.2510

Chen, X.-L. & Kamionkowski, M. 2004, Phys. Rev., D70, 043502, arXiv:astro-ph/0310473

Chevallier, M. & Polarski, D. 2001, International Journal of Modern Physics D, 10, 213, arXiv:gr-qc/0009008

Chiang, H. C., Ade, P. A. R., Barkats, D., et al. 2010, ApJ, 711, 1123, arXiv:0906.1181

Chluba, J. & Thomas, R. M. 2011, MNRAS, 412, 748, arXiv:1010.3631

Chluba, J., Vasil, G., & Dursi, L. 2010, MNRAS, 407, 599, arXiv:1003.4928

Cole, S., Percival, W. J., Peacock, J. A., et al. 2005, MNRAS, 362, 505, arXiv:astro-ph/0501174
Colombi, S., Dodelson, S., & Widrow, L. M. 1996, Astrophys.J., 458, 1, arXiv:astro-ph/9505029
Conley, A., Guy, J., Sullivan, M., et al. 2011, ApJS, 192, 1, arXiv:1104.1443
Conley, A., Sullivan, M., Hsiao, E. Y., et al. 2008, ApJ, 681, 482, arXiv:0803.3441
Cooray, A. & Sheth, R. 2002, Phys. Rep., 372, 1, arXiv:astro-ph/0206508
Courbin, F., Chantry, V., Revaz, Y., et al. 2011, A&A, 536, A53, arXiv:1009.1473
Creminelli, P. & Senatore, L. 2007, JCAP, 0711, 010, arXiv:hep-th/0702165
Crittenden, R., Bond, J. R., Davis, R. L., Efstathiou, G., & Steinhardt, P. J. 1993, Physical Review Letters, 71, 324, arXiv:astro-ph/9303014
Crittenden, R. G., Coulson, D., & Turok, N. G. 1995, Phys. Rev. D, 52, 5402, arXiv:astro-ph/9411107
Crotty, P., Lesgourgues, J., & Pastor, S. 2004, Phys.Rev., D69, 123007, arXiv:hep-ph/0402049
Das, S., Louis, T., Nolta, M. R., et al. 2013, ArXiv e-prints, arXiv:1301.1037
Das, S., Sherwin, B. D., Aguirre, P., et al. 2011, Physical Review Letters, 107, 021301, arXiv:1103.2124
de Bernardis, P., Ade, P. A. R., Bock, J. J., et al. 2000, Nature, 404, 955, arXiv:astro-ph/0004404
de Putter, R., Mena, O., Giusarma, E., et al. 2012, ApJ, 761, 12, arXiv:1201.1909
Diamanti, R., Giusarma, E., Mena, O., Archidiacono, M., & Melchiorri, A. 2012, arXiv:1212.6007
Dodelson, S., Gates, E., & Stebbins, A. 1996, Astrophys.J., 467, 10, arXiv:astro-ph/9509147
Dodelson, S. & Widrow, L. M. 1994, Physical Review Letters, 72, 17, arXiv:hep-ph/9303287
Doran, M. & Robbers, G. 2006, JCAP, 0606 (2006) 026
Doran, M., Schwindt, J.-M., & Wetterich, C. 2001, Phys.Rev., D64, 123520, arXiv:astro-ph/0107525
Dunkley, J., Calabrese, E., Sievers, J., et al. 2013, ArXiv e-prints, arXiv:1301.0776
Dunkley, J., Hlozek, R., Sievers, J., et al. 2011, ApJ, 739, 52, arXiv:1009.0866
Efstathiou, G. 2004, MNRAS, 349, 603, arXiv:astro-ph/0307515
Efstathiou, G. 2006, MNRAS, 370, 343, arXiv:astro-ph/0601107
Efstathiou, G. & Bond, J. R. 1999, MNRAS, 304, 75, arXiv:astro-ph/9807103
Efstathiou, G. & Migliaccio, M. 2012, MNRAS, 423, 2492, arXiv:1106.3208
Eisenstein, D. J. & Hu, W. 1998, ApJ, 496, 605, arXiv:astro-ph/9709112
Eisenstein, D. J., Seo, H.-J., Sirko, E., & Spergel, D. N. 2007, ApJ, 664, 675, arXiv:astro-ph/0604362
Eisenstein, D. J., Zehavi, I., Hogg, D. W., et al. 2005, ApJ, 633, 560, arXiv:astro-ph/0501171
Erben, T., Hildebrandt, H., Miller, L., et al. 2013, MNRAS, 433, 2545, arXiv:1210.8156
Eriksen, H. K., Jewell, J. B., Dickinson, C., et al. 2008, ApJ, 676, 10, arXiv:0709.1058
Evoli, C., Pandolfi, S., & Ferrara, A. 2013, MNRAS, 433, 1736, arXiv:1210.6845
Fang, W., Hu, W., & Lewis, A. 2008a, Phys.Rev., D78, 087303, arXiv:0808.3125
Fang, W., Wang, S., Hu, W., et al. 2008b, Phys.Rev., D78, 103509, arXiv:0808.2208
Fields, B. D. 2011, Annual Review of Nuclear and Particle Science, 61, 47, arXiv:1203.3551
Finelli, F., Paci, F., & Paoletti, D. 2008, Phys.Rev., D78, 023510, arXiv:0803.1246
Finkbeiner, D. P., Davis, M., & Schlegel, D. J. 1999, ApJ, 524, 867, arXiv:astro-ph/9905128
Finkbeiner, D. P., Galli, S., Lin, T., & Slatyer, T. R. 2012, Phys.Rev., D85, 043522, arXiv:1109.6322
Fixsen, D. 2009, Astrophys.J., 707, 916, arXiv:0911.1955
Forero, D., Tortola, M., & Valle, J. 2012, arXiv:1205.4018
Freedman, W. L., Madore, B. F., Gibson, B. K., et al. 2001, ApJ, 553, 47, arXiv:astro-ph/0012376
Freedman, W. L., Madore, B. F., Scowcroft, V., et al. 2012, ApJ, 758, 24, arXiv:1208.3281
Freivogel, B., Kleban, M., Rodríguez Martínez, M., & Susskind, L. 2006, Journal of High Energy Physics, 3, 39, arXiv:hep-th/0505232
Galli, S., Iocco, F., Bertone, G., & Melchiorri, A. 2009, Phys.Rev., D80, 023505, arXiv:0905.0003
Galli, S., Iocco, F., Bertone, G., & Melchiorri, A. 2011, Phys.Rev., D84, 027302, arXiv:1106.1528
Gasperini, M. & Veneziano, G. 1993, Astroparticle Physics, 1, 317, arXiv:hep-th/9211021
Gelman, A. & Rubin, D. 1992, Statistical Science, 7, 457
Giesen, G., Lesgourgues, J., Audren, B., & Ali-Haimoud, Y. 2012, JCAP, 1212, 008, arXiv:1209.0247
Giovannini, M. 2004, Phys.Rev., D70, 123507, arXiv:astro-ph/0409594
Giovannini, M. 2007, PMC Phys., A1, 5, arXiv:0706.4428
Giovannini, M. & Kunze, K. E. 2008, Phys.Rev., D77, 063003, arXiv:0712.3483
Giunti, C., Laveder, M., Li, Y., & Long, H. 2013, Phys.Rev., D87, 013004, arXiv:1212.3805
Gonzalez-Garcia, M., Maltoni, M., Salvado, J., & Schwetz, T. 2012, JHEP, 1212, 123, arXiv:1209.3023
Grin, D. & Hirata, C. M. 2010, Phys.Rev., D81, 083005, arXiv:0911.1359
Grishchuk, L. P. 1975, Sov. Phys. JETP, 40, 409
Guth, A. H. 1981, Phys. Rev. D, 23, 347
Guth, A. H. & Pi, S. Y. 1982, Phys. Rev. Lett., 49, 1110
Guy, J., Astier, P., Baumont, S., et al. 2007, A&A, 466, 11, arXiv:astro-ph/0701828
Guy, J., Sullivan, M., Conley, A., et al. 2010, A&A, 523, A7, arXiv:1010.4743
Hall, A. C. & Challinor, A. 2012, MNRAS, 425, 1170, arXiv:1205.6172
Hamann, J., Balbi, A., Lesgourgues, J., & Quercellini, C. 2009, JCAP, 0904, 011, arXiv:0903.0382
Hamann, J., Hannestad, S., Raffelt, G. G., & Wong, Y. Y. 2011, JCAP, 1109, 034, arXiv:1108.4136
Hamann, J., Lesgourgues, J., & Mangano, G. 2008, JCAP, 0803, 004, arXiv:0712.2826
Hamimeche, S. & Lewis, A. 2008, Phys. Rev. D, 77, 103013, arXiv:0801.0554
Hannestad, S. 1999, Phys. Rev. D, **60**, 023515, arXiv:astro-ph/9810102
Hannestad, S. 2010, Prog.Part.Nucl.Phys., 65, 185, arXiv:1007.0658
Hannestad, S. & Raffelt, G. 2004, JCAP, 0404, 008, arXiv:hep-ph/0312154
Hannestad, S., Tamborra, I., & Tram, T. 2012, JCAP, 1207, 025, arXiv:1204.5861
Hanson, D., Challinor, A., Efstathiou, G., & Bielewicz, P. 2011, Phys. Rev. D, 83, 043005, arXiv:1008.4403
Hasselfield, M., Hilton, M., Marriage, T. A., et al. 2013, ArXiv e-prints, arXiv:1301.0816
Hawking, S. W. 1982, Phys. Lett., B115, 295
Heymans, C., Grocutt, E., Heavens, A., et al. 2013, MNRAS, 432, 2433, arXiv:1303.1808
Heymans, C., Van Waerbeke, L., Miller, L., et al. 2012, MNRAS, 427, 146, arXiv:1210.0032
Hinshaw, G., Larson, D., Komatsu, E., et al. 2012, ArXiv e-prints, arXiv:1212.5226
Hinshaw, G., Spergel, D. N., Verde, L., et al. 2003, ApJS, 148, 135, arXiv:astro-ph/0302217
Hirata, C. M. 2008, Phys.Rev., D78, 023001, arXiv:0803.0808
Hirata, C. M. & Switzer, E. R. 2008, Phys. Rev., D77, 083007, arXiv:astro-ph/0702144
Hlozek, R., Dunkley, J., Addison, G., et al. 2012, ApJ, 749, 90, arXiv:1105.4887
Holtzman, J. A., Marriner, J., Kessler, R., et al. 2008, AJ, 136, 2306, arXiv:0908.4277
Hou, Z., Keisler, R., Knox, L., Millea, M., & Reichardt, C. 2011, ArXiv e-prints, arXiv:1104.2333
Hou, Z., Reichardt, C. L., Story, K. T., et al. 2012, ArXiv e-prints, arXiv:1212.6267
Howlett, C., Lewis, A., Hall, A., & Challinor, A. 2012, JCAP, 1204, 027, arXiv:1201.3654
Hu, W. 1998, Astrophys.J., 506, 485, arXiv:astro-ph/9801234
Hu, W. 2001, Phys. Rev. D, 64, 083005, arXiv:astro-ph/0105117
Hu, W. 2008, Phys.Rev., D77, 103524, arXiv:0801.2433
Hu, W. & Sawicki, I. 2007, Phys.Rev., D76, 104043, arXiv:0708.1190
Hu, W., Scott, D., Sugiyama, N., & White, Martin J., . 1995, Phys.Rev., D52, 5498, arXiv:astro-ph/9505043
Hu, W. & Sugiyama, N. 1996, Astrophys.J., 471, 542, arXiv:astro-ph/9510117
Hu, W. & White, M. 1996, ApJ, 471, 30, arXiv:astro-ph/9602019
Hu, W. & White, M. 1997, ApJ, 479, 568, arXiv:astro-ph/9609079
Hu, W. & White, M. J. 1997, Phys.Rev., D56, 596, arXiv:astro-ph/9702170
Humphreys, E. M. L., Reid, M. J., Moran, J. M., Greenhill, L. J., & Argon, A. L. 2013, ApJ, 775, 13, arXiv:1307.6031
Hutsi, G., Chluba, J., Hektor, A., & Raidal, M. 2011, Astron.Astrophys., 535, A26, arXiv:1103.2766
Ichikawa, K., Fukugita, M., & Kawasaki, M. 2005, Phys.Rev., D71, 043001, arXiv:astro-ph/0409768
Ichikawa, K. & Takahashi, T. 2006, Phys.Rev., D73, 063528, arXiv:astro-ph/0601099
Iocco, F., Mangano, G., Miele, G., Pisanti, O., & Serpico, P. D. 2009, Phys.Rept., 472, 1, arXiv:0809.0631
James, F. 2004, `http://seal.web.cern.ch/seal/documents/minuit/mnusersguide.pdf`
Jedamzik, K., Katalinic, V., & Olinto, A. V. 1998, Phys.Rev., D57, 3264, arXiv:astro-ph/9606080
Jimenez, R., Kitching, T., Pena-Garay, C., & Verde, L. 2010, JCAP, 1005, 035, arXiv:1003.5918

Jones, M. E., Edge, A. C., Grainge, K., et al. 2005, MNRAS, 357, 518, arXiv:astro-ph/0103046
Kamionkowski, M., Kosowsky, A., & Stebbins, A. 1997, Phys. Rev. D, 55, 7368, arXiv:astro-ph/9611125
Kaplinghat, M., Knox, L., & Song, Y.-S. 2003, Phys.Rev.Lett., 91, 241301, arXiv:astro-ph/0303344
Kaplinghat, M., Scherrer, R., & Turner, M. 1999, Phys. Rev. D, **60**, 023516, arXiv:astro-ph/9810133
Kazanas, D. 1980, ApJ, 241, L59
Keisler, R., Reichardt, C. L., Aird, K. A., et al. 2011, ApJ, 743, 28, arXiv:1105.3182
Kesden, M., Cooray, A., & Kamionkowski, M. 2003, Phys. Rev. D, 67, 123507, arXiv:astro-ph/0302536
Kessler, R., Becker, A. C., Cinabro, D., et al. 2009, ApJS, 185, 32, arXiv:0908.4274
Khoury, J., Ovrut, B. A., Steinhardt, P. J., & Turok, N. 2001, Phys. Rev., D64, 123522
Kilbinger, M., Fu, L., Heymans, C., et al. 2013, MNRAS, 430, 2200, arXiv:1212.3338
Knox, L. 1995, Phys. Rev. D, 52, 4307, arXiv:astro-ph/9504054
Knox, L. & Turner, M. S. 1994, Physical Review Letters, 73, 3347, arXiv:astro-ph/9407037
Komatsu, E. & Seljak, U. 2002, MNRAS, 336, 1256, arXiv:astro-ph/0205468
Komatsu, E., Smith, K. M., Dunkley, J., et al. 2011, ApJS, 192, 18, arXiv:1001.4538
Kosowsky, A., Kahniashvili, T., Lavrelashvili, G., & Ratra, B. 2005, Phys.Rev., D71, 043006, arXiv:astro-ph/0409767
Kosowsky, A. & Loeb, A. 1996, Astrophys.J., 469, 1, arXiv:astro-ph/9601055
Kosowsky, A., Milosavljevic, M., & Jimenez, R. 2002, Phys. Rev., D66, 063007, arXiv:astro-ph/0206014
Kosowsky, A. & Turner, M. S. 1995, Phys. Rev. D, 52, 1739
Kowalski, M., Rubin, D., Aldering, G., et al. 2008, ApJ, 686, 749, arXiv:0804.4142
Landau, S. & Scóccola, C. 2010, Astron. Astrophys., **517**, A62, arXiv:1002.1603
Lesgourgues, J. 2011a, arXiv:1104.2932
Lesgourgues, J. 2011b, arXiv:1104.2934
Lesgourgues, J., Mangano, G., Miele, G., & Pastor, S. 2013, Neutrino Cosmology (Cambridge: Cambridge Univ. Press)
Lesgourgues, J. & Pastor, S. 2006, Phys.Rept., 429, 307, arXiv:astro-ph/0603494
Lesgourgues, J. & Pastor, S. 2012, Adv.High Energy Phys., 2012, 608515, arXiv:1212.6154
Lesgourgues, J., Perotto, L., Pastor, S., & Piat, M. 2006, Phys.Rev., D73, 045021, arXiv:astro-ph/0511735
Lesgourgues, J. & Tram, T. 2011, JCAP, 1109, 032, arXiv:1104.2935
Lewis, A. 2004, Phys.Rev., D70, 043518, arXiv:astro-ph/0403583
Lewis, A. 2008, Phys. Rev., D78, 023002, arXiv:0804.3865
Lewis, A. 2013, Phys.Rev., D87, 103529, arXiv:1304.4473
Lewis, A. & Bridle, S. 2002, Phys. Rev., D66, 103511, arXiv:astro-ph/0205436
Lewis, A. & Challinor, A. 2006, Phys. Rep., 429, 1, arXiv:astro-ph/0601594
Lewis, A., Challinor, A., & Lasenby, A. 2000, Astrophys. J., 538, 473, arXiv:astro-ph/9911177
Lewis, A., Weller, J., & Battye, R. 2006, Mon.Not.Roy.Astron.Soc., 373, 561, arXiv:astro-ph/0606552
Liddle, A. R. & Lyth, D. H. 2000, Cosmological inflation and large-scale structure (Cambridge University Press)
Linde, A. 1995, Physics Letters B, 351, 99, arXiv:hep-th/9503097
Linde, A. 1999, Phys. Rev. D, 59, 023503, arXiv:hep-ph/9807493
Linde, A. 2003, J. Cosmology Astropart. Phys., 5, 2, arXiv:astro-ph/0303245
Linde, A. 2008, Lect. Notes Phys., 738, 1, arXiv:0705.0164 [hep-th]
Linde, A. D. 1982, Phys. Lett., B108, 389
Linde, A. D. 1983, Phys. Lett., B129, 177
Linder, E. V. 2003, Physical Review Letters, 90, 091301, arXiv:astro-ph/0208512
Lyth, D. H. 1984, Physics Letters B, 147, 403
Lyth, D. H. & Riotto, A. 1999, Phys. Rept., 314, 1
Ma, C.-P. & Bertschinger, E. 1995, Astrophys. J., 455, 7, arXiv:astro-ph/9506072
Mack, A., Kahniashvili, T., & Kosowsky, A. 2002, Phys.Rev., D65, 123004, arXiv:astro-ph/0105504
Mandelbaum, R., Slosar, A., Baldauf, T., et al. 2013, MNRAS, 432, 1544, arXiv:1207.1120
Mangano, G., Miele, G., Pastor, S., & Peloso, M. 2002, Phys.Lett., B534, 8, arXiv:astro-ph/0111408
Mangano, G., Miele, G., Pastor, S., et al. 2005, Nucl.Phys., B729, 221, arXiv:hep-ph/0506164
Mangano, G., Miele, G., Pastor, S., Pisanti, O., & Sarikas, S. 2012, Phys.Lett., B708, 1, arXiv:1110.4335
Mangano, G. & Serpico, P. D. 2011, Phys.Lett., B701, 296, arXiv:1103.1261
Mapelli, M., Ferrara, A., & Pierpaoli, E. 2006, Mon. Not. Roy. Astron. Soc., 369, 1719, arXiv:astro-ph/0603237
Martins, C., Melchiorri, A., Rocha, G., & Trotta, R. e. a. 2004, Phys. Lett. B, **585**, 29, arXiv:astro-ph/0302295
Mehta, K. T., Cuesta, A. J., Xu, X., Eisenstein, D. J., & Padmanabhan, N. 2012, MNRAS, 427, 2168, arXiv:1202.0092
Menegoni, E., Galli, S., Bartlett, J., Martins, C., & Melchiorri, A. 2009, Phys. Rev. D, **80**, 087302, arXiv:0909.3584
Millea, M., Doré, O., Dudley, J., et al. 2012, ApJ, 746, 4, arXiv:1102.5195
Mortonson, M. J., Dvorkin, C., Peiris, H. V., & Hu, W. 2009, Phys. Rev. D, 79, 103519, arXiv:0903.4920
Mukhanov, S. 2007, Journal of Physics A Mathematical General, 40, 6561
Mukhanov, V. F. & Chibisov, G. V. 1981, JETP Letters, 33, 532
Murphy, M. T., Webb, J., & Flambaum, V. 2003, Mon. Not. Roy. Astron. Soc., **345**, 609, arXiv:astro-ph/0306483
Nakashima, M., Ichikawa, K., Nagata, R., & Yokoyama, J. 2010, JCAP, **1001**, 030, arXiv:0810.1098
Nakashima, M., Nagata, R., & Yokoyama, J. 2008, Prog. Theor. Phys., **120**, 1207, arXiv:0810.1098
Namikawa, T., Hanson, D., & Takahashi, R. 2012, ArXiv e-prints, arXiv:1209.0091
Natarajan, A. 2012, Phys.Rev., D85, 083517, arXiv:1201.3939
Neal, R. M. 2005, arXiv:math.ST/0502099
Oguri, M. 2007, ApJ, 660, 1, arXiv:astro-ph/0609694
Okamoto, T. & Hu, W. 2003, Phys. Rev. D, 67, 083002, arXiv:astro-ph/0301031
Padmanabhan, N. & Finkbeiner, D. P. 2005, Phys. Rev., D72, 023508, arXiv:astro-ph/0503486
Padmanabhan, N., Xu, X., Eisenstein, D. J., et al. 2012, MNRAS, 427, 2132, arXiv:1202.0090
Paoletti, D. & Finelli, F. 2011, Phys.Rev., D83, 123533, arXiv:1005.0148
Paoletti, D. & Finelli, F. 2012, arXiv:1208.2625, arXiv:1208.2625,
Paoletti, D., Finelli, F., & Paci, F. 2009, Mon.Not.Roy.Astron.Soc., 396, 523, arXiv:0811.0230
Peebles, P. J. E. 1968, ApJ, 153, 1
Peebles, P. J. E., Page, Jr., L. A., & Partridge, R. B. 2009, Finding the Big Bang (Cambridge University Press)
Peiris, H. V., Komatsu, E., Verde, L., et al. 2003, ApJS, 148, 213, arXiv:astro-ph/0302225
Penzias, A. A. & Wilson, R. W. 1965, ApJ, 142, 419
Percival, W. J., Reid, B. A., Eisenstein, D. J., et al. 2010, MNRAS, 401, 2148, arXiv:0907.1660
Percival, W. J. et al. 2002, Mon.Not.Roy.Astron.Soc., 337, 1068, arXiv:astro-ph/0206256
Perlmutter, S., Aldering, G., Goldhaber, G., et al. 1999, ApJ, 517, 565, arXiv:astro-ph/9812133
Pettini, M. & Cooke, R. 2012, arXiv:1205.3785
Pettorino, V., Amendola, L., & Wetterich, C. 2013, ArXiv e-prints, arXiv:1301.5279
Pisanti, O., Cirillo, A., Esposito, S., et al. 2008, Comput.Phys.Commun., 178, 956, arXiv:0705.0290
Planck Collaboration. 2005, ESA publication ESA-SCI(2005)/01, arXiv:astro-ph/0604069
Planck Collaboration. 2013, *Planck* intermediate results: The multi-frequency and multi-scale CIB anisotropy (in preparation)
Planck Collaboration ES. 2013, The Explanatory Supplement to the Planck 2013 results (ESA)
Planck Collaboration I. 2013, Submitted to A&A, [arXiv:astro-ph/1303.5062]
Planck Collaboration II. 2013, Submitted to A&A, [arXiv:astro-ph/1303.5063]
Planck Collaboration III. 2013, Submitted to A&A, [arXiv:astro-ph/1303.5064]
Planck Collaboration IV. 2013, Submitted to A&A, [arXiv:astro-ph/1303.5065]
Planck Collaboration IX. 2013, Submitted to A&A, [arXiv:astro-ph/1303.5070]
Planck Collaboration V. 2013, Submitted to A&A, [arXiv:astro-ph/1303.5066]
Planck Collaboration VI. 2013, Submitted to A&A, [arXiv:astro-ph/1303.5067]
Planck Collaboration VII. 2013, Submitted to A&A, [arXiv:astro-ph/1303.5068]
Planck Collaboration VIII. 2013, Submitted to A&A, [arXiv:astro-ph/1303.5069]
Planck Collaboration X. 2013, Submitted to A&A, [arXiv:astro-ph/1303.5071]
Planck Collaboration XI. 2013, In preparation
Planck Collaboration XII. 2013, Submitted to A&A, [arXiv:astro-ph/1303.5072]
Planck Collaboration XIX. 2013, Submitted to A&A, [arXiv:astro-ph/1303.5079]
Planck Collaboration XV. 2013, Submitted to A&A, [arXiv:astro-ph/1303.5075]
Planck Collaboration XVII. 2013, Submitted to A&A, [arXiv:astro-ph/1303.5077]
Planck Collaboration XVIII. 2011, A&A, 536, A18
Planck Collaboration XVIII. 2013, Submitted to A&A, [arXiv:astro-ph/1303.5078]
Planck Collaboration XX. 2013, Submitted to A&A, [arXiv:astro-ph/1303.5080]

Planck Collaboration XXI. 2013, Submitted to A&A, [arXiv:astro-ph/1303.5081]
Planck Collaboration XXII. 2013, Submitted to A&A, [arXiv:astro-ph/1303.5082]
Planck Collaboration XXIII. 2013, Submitted to A&A, [arXiv:astro-ph/1303.5083]
Planck Collaboration XXIV. 2013, Submitted to A&A, [arXiv:astro-ph/1303.5084]
Planck Collaboration XXIX. 2013, Submitted to A&A, [arXiv:astro-ph/1303.5089]
Planck Collaboration XXV. 2013, Submitted to A&A, [arXiv:astro-ph/1303.5085]
Planck Collaboration XXVI. 2013, Submitted to A&A, [arXiv:astro-ph/1303.5086]
Planck Collaboration XXVII. 2013, Submitted to A&A, [arXiv:astro-ph/1303.5087]
Planck Collaboration XXVIII. 2013, Submitted to A&A, [arXiv:astro-ph/1303.5088]
Planck Collaboration XXX. 2013, Submitted to A&A, [arXiv:astro-ph/1309.0382]
QUIET Collaboration, Araujo, D., Bischoff, C., et al. 2012, ApJ, 760, 145, arXiv:1207.5034
Ratra, B. & Peebles, P. J. E. 1988, Phys. Rev., D37, 3406
Regnault, N., Conley, A., Guy, J., et al. 2009, A&A, 506, 999, arXiv:0908.3808
Reichardt, C. L., de Putter, R., Zahn, O., & Hou, Z. 2012, ApJ, 749 (2012) L9, arXiv:1110.5328
Reichardt, C. L., Shaw, L., Zahn, O., et al. 2012, ApJ, 755, 70, arXiv:1111.0932
Reichardt, C. L., Stalder, B., Bleem, L. E., et al. 2013, ApJ, 763, 127, arXiv:1203.5775
Reid, B. A., Percival, W. J., Eisenstein, D. J., et al. 2010, MNRAS, 404, 60, arXiv:0907.1659
Reid, M. J., Braatz, J. A., Condon, J. J., et al. 2012, ArXiv e-prints, arXiv:1207.7292
Riess, A. G., Filippenko, A. V., Challis, P., et al. 1998, AJ, 116, 1009, arXiv:astro-ph/9805201
Riess, A. G., Macri, L., Casertano, S., et al. 2011, Astrophys.J., 730, 119, arXiv:1103.2976
Riess, A. G., Strolger, L.-G., Casertano, S., et al. 2007, ApJ, 659, 98, arXiv:astro-ph/0611572
Rocha, G., Trotta, R., Martins, C., & Melchiorri, A. e. a. 2004, Mon. Not. Roy. Astron. Soc., **32**, 20, arXiv:astro-ph/0309211
Rubino-Martin, J. A., Chluba, J., Fendt, W. A., & Wandelt, B. D. 2009, arXiv:0910.4383
Ryu, D., Schleicher, D. R., Treumann, R. A., Tsagas, C. G., & Widrow, L. M. 2012, Space Sci.Rev., 166, 1, arXiv:1109.4055
Sandage, A., Tammann, G. A., Saha, A., et al. 2006, ApJ, 653, 843, arXiv:astro-ph/0603647
Sato, K. 1981, MNRAS, 195, 467
Schmittfull, M. M., Challinor, A., Hanson, D., & Lewis, A. 2013, Phys.Rev., D88, 063012, arXiv:1308.0286
Seager, S., Sasselov, D. D., & Scott, D. 2000, Astrophys. J. Suppl., 128, 407, arXiv:astro-ph/9912182
Sehgal, N., Bode, P., Das, S., et al. 2010, ApJ, 709, 920
Seljak, U. 1997, ApJ, 482, 6, arXiv:astro-ph/9608131
Seljak, U. & Zaldarriaga, M. 1996, Astrophys. J., 469, 437, arXiv:astro-ph/9603033
Serenelli, A. M. & Basu, S. 2010, ApJ, 719, 865, arXiv:1006.0244
Serpico, P. D., Esposito, S., Iocco, F., et al. 2004, JCAP, 0412, 010, arXiv:astro-ph/0408076
Seshadri, T. & Subramanian, K. 2009, Phys.Rev.Lett., 103, 081303, arXiv:0902.4066
Shafieloo, A. & Souradeep, T. 2008, Phys. Rev. D, 78, 023511, arXiv:0709.1944
Shaw, J. R. & Chluba, J. 2011, MNRAS, 415, 1343, arXiv:1102.3683
Shaw, J. R. & Lewis, A. 2010, Phys.Rev., D81, 043517, arXiv:0911.2714
Shaw, J. R. & Lewis, A. 2012, Phys.Rev., D86, 043510, arXiv:1006.4242
Shaw, L. D., Nagai, D., Bhattacharya, S., & Lau, E. T. 2010, ApJ, 725, 1452
Sherwin, B. D., Dunkley, J., Das, S., et al. 2011, Physical Review Letters, 107, 021302, arXiv:1105.0419
Shull, J. M. & van Steenberg, M. E. 1985, ApJ, 298, 268
Sievers, J. L., Hlozek, R. A., Nolta, M. R., et al. 2013, ArXiv e-prints, arXiv:1301.0824
Slatyer, T. R., Padmanabhan, N., & Finkbeiner, D. P. 2009, Phys.Rev., D80, 043526, arXiv:0906.1197
Slosar, A., Iršič, V., Kirkby, D., et al. 2013, ArXiv e-prints, arXiv:1301.3459
Smith, K. M., Hu, W., & Kaplinghat, M. 2006, Phys. Rev. D, 74, 123002, arXiv:astro-ph/0607315
Smith, R. E. et al. 2003, Mon. Not. Roy. Astron. Soc., 341, 1311, arXiv:astro-ph/0207664
Smoot, G. F., Bennett, C. L., Kogut, A., et al. 1992, ApJ, 396, L1
Smoot, G. F., Gorenstein, M. V., & Muller, R. A. 1977, Physical Review Letters, 39, 898
Spergel, D. N., Bean, R., Doré, O., et al. 2007, ApJS, 170, 377, arXiv:astro-ph/0603449
Spergel, D. N., Verde, L., Peiris, H. V., et al. 2003, ApJS, 148, 175, arXiv:astro-ph/0302209
Srianand, R., Chand, H., Petitjean, P., & Aracil, B. 2004, Phys. Rev. Lett., **92**, 121302, arXiv:astro-ph/0402177
Srianand, R., Chand, H., Petitjean, P., & Aracil, B. 2007, Phys. Rev. Lett., **99**, 239002, arXiv:0711.1742
Starobinsky, A. A. 1979, ZhETF Pis ma Redaktsiiu, 30, 719
Starobinsky, A. A. 1982, Phys. Lett., B117, 175
Steigman, G. 2012, arXiv:1208.0032
Stompor, R. & Efstathiou, G. 1999, MNRAS, 302, 735, arXiv:astro-ph/9805294
Story, K. T., Reichardt, C. L., Hou, Z., et al. 2012, ArXiv e-prints, arXiv:1210.7231
Subramanian, K. 2006, Astron.Nachr., arXiv:astro-ph/0601570
Subramanian, K. & Barrow, J. D. 1998, Phys.Rev., D58, 083502, arXiv:astro-ph/9712083
Sugiyama, N. 1995, ApJS, 100, 281, arXiv:astro-ph/9412025
Sullivan, M., Guy, J., Conley, A., et al. 2011, ApJ, 737, 102, arXiv:1104.1444
Suyu, S. H., Auger, M. W., Hilbert, S., et al. 2013, ApJ, 766, 70, arXiv:1208.6010
Suyu, S. H., Treu, T., Blandford, R. D., et al. 2012, ArXiv e-prints, arXiv:1202.4459
Suzuki, N., Rubin, D., Lidman, C., et al. 2012, ApJ, 746, 85, arXiv:1105.3470
Switzer, E. R. & Hirata, C. M. 2008, Phys. Rev., D77, 083006, arXiv:astro-ph/0702143
Takahashi, R., Sato, M., Nishimichi, T., Taruya, A., & Oguri, M. 2012, arXiv:1208.2701
Tewes, M., Courbin, F., Meylan, G., et al. 2013, A&A, 556, A22, arXiv:1208.6009
Thacker, C., Cooray, A., Smidt, J., et al. 2012, ArXiv e-prints, arXiv:1212.2211
Trac, H., Bode, P., & Ostriker, J. P. 2011, ApJ, 727, 94, arXiv:1006.2828
Trivedi, P., Subramanian, K., & Seshadri, T. 2010, Phys.Rev., D82, 123006, arXiv:1009.2724
Trotta, R. & Hansen, S. H. 2004, Phys. Rev., D69, 023509, arXiv:astro-ph/0306588
Tucci, M. & Toffolatti, L. 2012, ArXiv e-prints, arXiv:1204.0427
Uzan, J.-P. 2003, Rev. Mod. Phys., **75**, 403, arXiv:hep-ph/0205340
Uzan, J.-P. 2011, Living Rev. Rel., **14**, 2, arXiv:1009.5514
Valdes, M., Evoli, C., & Ferrara, A. 2010, Mon.Not.Roy.Astron.Soc., 404, 1569, arXiv:0911.1125
van Engelen, A., Keisler, R., Zahn, O., et al. 2012, arXiv:1202.0546
Verde, L. & Peiris, H. 2008, JCAP, 7, 9, arXiv:0802.1219
Verde, L. & Spergel, D. N. 2002, Phys. Rev. D, 65, 043007, arXiv:astro-ph/0108179
Webb, J., Murphy, M., Flambaum, V., & Dzuba, V. e. a. 2001, Phys. Rev. Lett., 87, 091301, arXiv:astro-ph/0012539
Wetterich, C. 1988, Nucl. Phys., B302, 668
Wetterich, C. 2004, Phys.Lett., B594, 17, arXiv:astro-ph/0403289
Widrow, L. M. 2002, Rev.Mod.Phys., 74, 775, arXiv:astro-ph/0207240
Widrow, L. M., Ryu, D., Schleicher, D. R., et al. 2012, Space Sci.Rev., 166, 37, arXiv:1109.4052
Wilks, A. S. S. 1938, Ann.Math.Statist., 1, 60
Wong, W. Y., Moss, A., & Scott, D. 2008, MNRAS, 386, 1023, arXiv:0711.1357 [astro-ph]
Zaldarriaga, M. & Seljak, U. 1997, Phys. Rev. D, 55, 1830, arXiv:astro-ph/9609170
Zaldarriaga, M., Seljak, U., & Bertschinger, E. 1998, Astrophys.J., 494, 491, arXiv:astro-ph/9704265
Zaldarriaga, M., Spergel, D. N., & Seljak, U. 1997, ApJ, 488, 1, arXiv:astro-ph/9702157
Zeldovich, Y. B., Kurt, V. G., & Syunyaev, R. A. 1969, Soviet Journal of Experimental and Theoretical Physics, 28, 146
Zhang, L., Chen, X.-L., Lei, Y.-A., & Si, Z.-G. 2006, Phys. Rev., D74, 103519, arXiv:astro-ph/0603425

Appendix A: Comparison of the *Planck* and *WMAP*-9 base ΛCDM cosmologies

The parameters for the base ΛCDM cosmology derived from *Planck* differ from those derived from *WMAP*-9. In this appendix, we address the question of whether the parameter shifts

5.5 Non-resonantly produced sterile neutrino dark matter, PRL 97, 071301 (2006)

Can sterile neutrinos be ruled out as warm dark matter candidates?

Matteo Viel,[1,2] Julien Lesgourgues,[3] Martin G. Haehnelt,[1] Sabino Matarrese,[4,5] Antonio Riotto[6]
[1] *Institute of Astronomy, Madingley Road, Cambridge CB3 0HA, United Kingdom*
[2] *INAF - Osservatorio Astronomico di Trieste, Via G.B. Tiepolo 11, I-34131 Trieste, Italy*
[3] *Laboratoire d'Annecy-le-vieux de Physique Théorique LAPTH, BP110, F-74941 Annecy-le-vieux Cedex, France*
[4] *Dipartimento di Fisica "G. Galilei", Università di Padova, Via Marzolo 8, I-35131 Padova, Italy*
[5] *INFN, Sezione di Padova, Via Marzolo 8, I-35131 Padova, Italy*
[6] *CERN, Theory Division, CH 1211, Geneva 23, Switzerland*
(Dated: February 4, 2008)

We present constraints on the mass of warm dark matter (WDM) particles from a combined analysis of the matter power spectrum inferred from the Sloan Digital Sky Survey Lyman-α flux power spectrum at $2.2 < z < 4.2$, cosmic microwave background data, and the galaxy power spectrum. We obtain a lower limit of $m_{\rm WDM} \gtrsim 10$ keV (2σ) if the WDM consists of sterile neutrinos and $m_{\rm WDM} \gtrsim 2$ keV (2σ) for early decoupled thermal relics. If we combine this bound with the constraint derived from x-ray flux observations in the Coma cluster, we find that the allowed sterile neutrino mass is ~ 10 keV (in the standard production scenario). Adding constraints based on x-ray fluxes from the Andromeda galaxy, we find that dark matter particles cannot be sterile neutrinos, unless they are produced by a nonstandard mechanism (resonant oscillations, coupling with the inflaton) or get diluted by some large entropy release.

PACS numbers: 98.80.Cq

Introduction. Warm dark matter (WDM) has been advocated in order to solve some apparent problems of standard cold dark matter (CDM) scenarios at small scales (see [1] and references therein), namely: the excess of galactic satellites, the cuspy and high density of galactic cores, the large number of galaxies filling voids. Moreover, recent observational results suggest that the shape of the Milky Way halo is spherical [2] and cannot easily be reproduced in CDM models. All these problems would be alleviated if the dark matter (DM) is made of warm particles, whose effect would be to suppress structures below the Mpc scale. Detailed studies of the dynamics of the Fornax dwarf spheroidal galaxy suggest shallower cores than predicted by numerical simulations of CDM models and put an upper limit on the mass of a putative WDM particle [3]. One of the most promising WDM candidate is a sterile (right-handed) neutrino with a mass in the keV range, which could explain the pulsar velocity kick [4], help in reionizing the universe at high redshift [5], and emerge from many particle physics models with grand unification (e.g. [6, 7]). Because of a small, non-zero mixing angle between active and sterile flavor states, X-ray flux observations can constrain the abundance and decay rate of such DM particles. The Lyman-α absorption caused by neutral hydrogen in the spectra of distant quasars is a powerful tool for constraining the mass of a WDM particle since it probes the matter power spectrum over a large range of redshifts down to small scales. In a previous work, [8] used the LUQAS sample of high resolution quasar absorption spectra to set a lower limit of 2 keV for the sterile neutrino mass. More recently, exploiting the small statistical errors and the large redshift range of the SDSS Lyman-α forest data, Seljak et al. [9] found a lower limit of 14 keV. If the latter result is correct, a large fraction of the sterile neutrino parameter space can be ruled out (assuming that all the DM is made of sterile neutrinos); together with constraints from X-ray fluxes, this discards the possibility that DM consists of sterile neutrinos produced by non-resonant active-sterile neutrino oscillations [6] (still, they could be produced by resonant oscillations caused by a large leptonic asymmetry in the early Universe [10], or considerably diluted by some large entropy release [9, 10, 11], or generated in a radically different manner, e.g. from their coupling with the inflaton [12]). More recently, some joint analyses of the SDSS flux power spectrum and the WMAP year three data [13] have been presented in [14, 15] for standard ΛCDM models. The authors of [14] found some moderate disagreement between the inferred power spectrum amplitudes. Instead, from an independent analysis of the SDSS data [16], the authors of [15] find good agreement in their joint analysis. Here, we extend the analysis of [16] to constrain the mass of WDM particles.

Data sets and Method. We use here the SDSS Lyman-α forest data of McDonald et al. [17], which consist of 3035 quasar spectra with low resolution ($R \sim 2000$) and low signal-to-noise spanning a wide range of redshifts ($z = 2.2 - 4.2$). The data set differs substantially from the LUQAS and C02 samples used [8], which contain mainly high resolution, high signal-to-noise spectra at $z \sim 2.5$. More precisely, we use the 132 flux power spectrum measurements $P_F(k, z)$ that span 11 redshift bins and 12 $k-$wavenumbers in the range $0.00141 < k$ (s/km)< 0.01778 (roughly corresponding to scales of 5-50 comoving Mpc). It is not straightforward to model the flux power spectrum of the Lyman-α forest for given cosmological parameters, and accurate numerical simulations are required. McDonald et al. [17] modelled the flux

power spectrum using a large number of Hydro Particle Mesh simulations [18], calibrated with a few small-box-size full hydrodynamical simulations. Here, instead, we model the flux power spectrum using a Taylor expansion around a best fitting model: this allows a reasonably accurate prediction of the flux power spectrum for a large range of parameters, based on a moderate number of full hydrodynamical simulations [19]. The method has been first introduced in Ref. [16] and we refer to this work for further details. The fiducial flux power spectrum has been extracted from simulations of 60 h^{-1} comoving Mpc and 2×400^3 gas and DM particles (gravitational softening 2.5 h^{-1} kpc) corrected for box size and resolution effects. We performed a number of additional hydrodynamical simulations with a box size of 20 h^{-1} comoving Mpc and with 2×256^3 gas and DM particles (grav. soft. 1 h^{-1} kpc) for a WDM model with a sterile neutrino of mass $m_s = 1, 4, 6.5$ keV, to calculate the flux power spectrum with respect to changes of the WDM particle mass. We have checked the convergence of the flux power spectrum on the scales of interests using additional simulations with 2×256^3 gas and DM particles and box sizes of 10 h^{-1} Mpc (grav. soft. 0.5 h^{-1} kpc). We then used a modified version of the code CosmoMC [20] to derive the parameter likelihoods from the combination of the Lyman-α data with Cosmic Microwave Background (CMB) and galaxy power spectrum data, from WMAP [13], ACBAR [21], CBI [22], VSA [23] and 2dF [24]. In total, we used a set of 29 parameters: 7 cosmological parameters; 1 parameter describing a free light-to-mass bias for the 2dF galaxy power spectrum; 6 parameters describing the thermal state of the Intergalactic Medium (parametrization of the gas temperature-gas density relation $T = T_0(z)(1+\delta)^{\gamma(z)-1}$ as a broken power law at $z = 3$ in the two astrophysical parameters $T_0(z)$ and $\gamma(z)$); 2 parameters describing the evolution of the effective optical depth with redshift (slope and amplitude at $z = 3$); 1 parameter which accounts for the contribution of damped Lyman-α systems and 12 parameters modelling the resolution and the noise properties (see [25]). We applied moderate priors to the thermal history to mimic the observed thermal evolution as in [26], but the final results in terms of sterile neutrino mass are not affected by this.

Results. We assume the Universe to be flat, with no tensor or neutrino mass contributions. We further note that adding CMB and large scale structure data has very little effect on the results for $m_{\rm s}$, since the free-streaming effect of WDM particles is visible only on the scales probed by the Lyman-α flux power spectrum[36].

In Figure 1 we show the 2-dimensional marginalized likelihoods for the most important cosmological and astrophysical parameters: σ_8, n_s, $\Omega_{\rm m}$ and the effective optical depth amplitude measured at $z = 3$, $\tau^A_{\rm eff}$, all plotted as a function of the parameter (1 keV)/$m_{\rm s}$. The constraints on $m_{\rm s}$ get stronger for the Lyman-α forest data

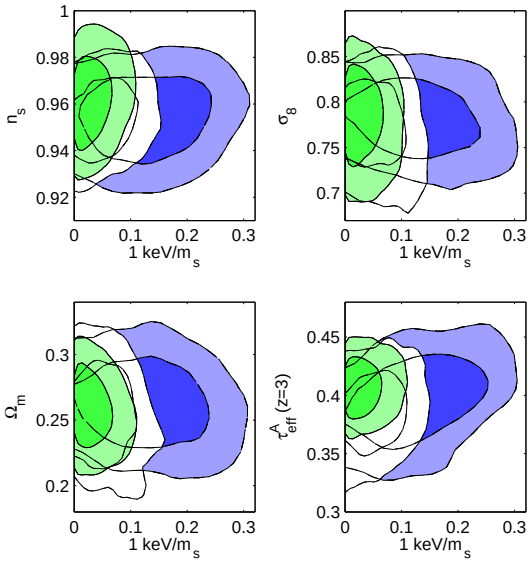

FIG. 1: 2-dimensional marginalized likelihoods (68% and 95% confidence limits) for $n_s, \sigma_8, \Omega_{\rm m}$ and the effective optical depth at $z = 3$, using the SDSS data at $z \leq 4.2$ (left, green), $z \leq 3.6$ (middle, white) and $z \leq 3.2$ (right, blue).

in the highest redshift bins. To demonstrate this we plot the likelihood contours for data in three different redshift ranges: $z \leq 3.2$ (blue), $z \leq 3.6$ (white) and $z \leq 4.2$ (green), which is the whole data set. The constraints improve by a factor almost 3 (2) for the whole data set compared to the $z \leq 3.2$ ($z \leq 3.6$) subsamples. At high redshifts, the mean flux level is lower and the flux power spectrum is closer to the linear prediction making the SDSS data points very sensitive to the free-streaming effect of WDM [9]. We find no strong degeneracies between $m_{\rm s}$ and the other parameters, showing that the signature of a WDM particle in the Lyman-α flux power is very distinct, and that other considered cosmological and astrophysical parameters cannot mimic its effect.

In Figure 2 we show the 1-dimensional marginalized likelihoods for (1 keV)/$m_{\rm s}$ for several redshift ranges. The 2σ lower limits for the sterile neutrino mass are: 3.9, 8.3, 8.1, 8.6, 10.3 keV for $z \leq 3.2, 3.4, 3.6, 3.8, 4.2$, respectively. The corresponding limits for an early decoupled thermal relic are: 0.9, 1.7, 1.6, 1.7, 1.9 keV (see [8] for the correspondence between the two cases). Also shown (dotted black line) is the constraint obtained in [8] using the LUQAS and C02 samples [26, 29]. The SDSS data improve the constraint from the high resolution data at $z \sim 2.5$ by a factor 5. This is mainly due to the extension to higher redshift where the flux power spectrum is most sensitive to the effect of WDM. The smaller statistical errors of the flux power spectrum and the coverage of a substantial range in redshift help to break some of the degeneracies between astrophysical and cosmological pa-

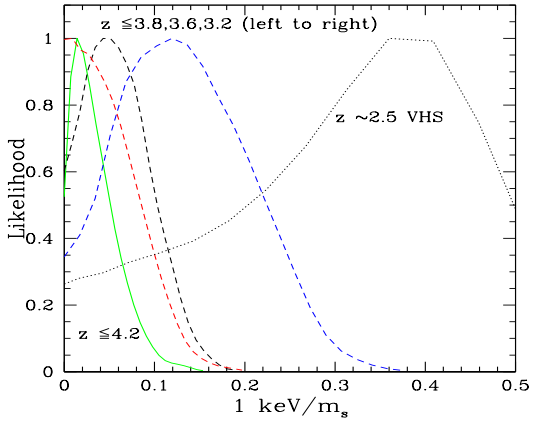

FIG. 2: 1-dimensional marginalized likelihoods for the parameter (1 keV)/m_s for the SDSS Lyman-α data for the redshift ranges $z \leq 3.2, 3.6, 3.8, 4.2$ and the VHS [26] data.

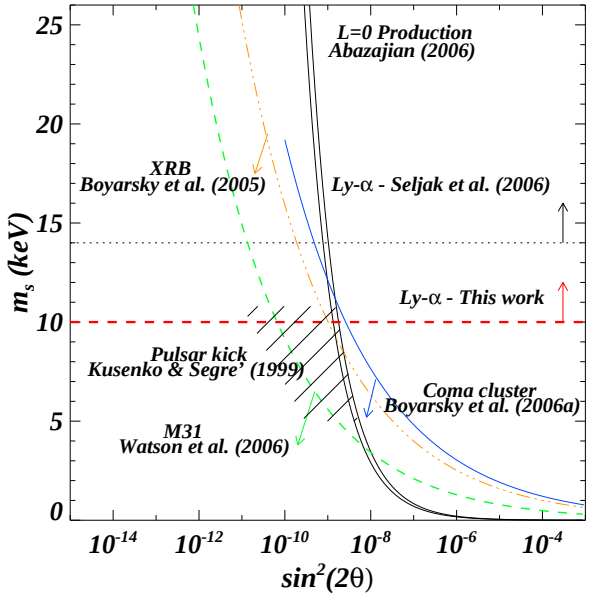

FIG. 3: This plot summarizes some of the parameter space constraints (at the 95% C.L.) for the sterile neutrino models, assuming that they constitute the dark matter. Limits are explained in the text.

rameters and also contribute to the improvement. Our independent analysis confirms the limits found in [9] for the SDSS Lyman-α data and a small sample of high resolution data that also extends to high redshift. Note, however, that our lower limit for essentially the same data set is ∼30% smaller (indeed, when using only SDSS Lyman-α data, Ref. [9] obtains $m_s > 12$ keV (2σ), which includes a 10% correction caused by the non-thermal momentum distribution of sterile neutrinos [28]: so, for the assumption made here, they would get $m_s > 13$ keV).

Discussion. In Figure 3 we summarize a number of current constraints for sterile neutrinos in the (m_s, $\sin^2 2\theta$) plane, where θ is the vacuum 2×2 mixing angle between active and sterile neutrinos [30]. We show the limits obtained from different types of X-ray observations: X-ray diffuse background (XRB, orange curve, [31]); flux from the Coma cluster (blue curve, [32]); and finally, flux from the Andromeda galaxy (M31) halo (95% C.L., green dashed curve, [33]). In addition, we plot the Lyman-α constraints obtained in this work (red dashed) and in [9] (black dotted). The region which can explain observed pulsar kicks [4] is shown as the hatched area. Finally, according to [7], sterile neutrinos produced from non-resonant oscillations (i.e., in absence of significant leptonic asymmetry, $L = 0$) with a density $\Omega_{\rm DM} = 0.23 \pm 0.04$ should lie between the two black solid curves (the computation in [7] is based on simplifying assumptions concerning the QCD phase transition; the effect of hadronic corrections is currently under investigation [34] and could shift the allowed region in the (m_s, $\sin^2 2\theta$) plane). If all these constraints are correct, then there is no room for sterile neutrinos as DM candidates in the standard case. Models in which the decay of massive particles release some entropy and dilutes the dark matter by a factor S can alleviate the tension between the Lyman-α and X-ray bounds [11], but a very large S is needed [9, 10]. As mentioned in the introduction, the sterile neutrino remains a viable WDM candidate for alternative production mechanisms (e.g. resonant oscillations with $L \neq 0$, or coupling with the inflaton). Recently, Ref. [10] questioned the results based on the LMC and Milky Way because of uncertainties in modelling the dark matter distribution; and also those based on detecting emission lines in cluster spectra [32], which used a fixed phenomenological model for X-ray emission (not shown in the figure but 30% more constraining than [31]). If these observational constraints are inaccurate, then a sterile neutrino mass in the range $9 \lesssim m_s$ (keV) $\lesssim 11.5$ and $\sin^2 2\theta \sim 2 \times 10^{-9}$ would be marginally consistent with the XRB bound and the Lyman-α forest data, but it is strongly excluded by the robust limit obtained by Ref. [33] (which is very conservative, since the bound quoted as 2σ by the authors requires a signal a few times larger than the background). The corresponding emission line for such a decaying sterile neutrino would be at $E \sim 5.5$ keV (close to, or possibly contaminated by, the recently discovered Chromium line [35]). If instead all X-ray constraints are correct, but the two recent Lyman-α forest constraints are not accurate, then a mass of $m_s \sim 2$ keV is still possible and compatible with the robust and conservative lower limit from [8]. It would also satisfy the requirement from the dynamical analysis of the Fornax dwarf galaxies [3]. However, the latter

possibility appears unlikely. Even if the highest redshift bins of the SDSS Lyman-α forest data were affected by not yet considered systematic errors the analysis of the data with $z \leq 3.2$ still gives a lower limit of about ~ 3.5 keV (see [33]). Appealing to an insufficient resolution of the hydrodynamical simulations would also not help, since an increase in resolution could only increase the flux power spectrum at small scales and raise the lower limits. We have furthermore checked explicitly that this is not the case and that other possible effects on the flux power have a different signature than that of WDM. A potentially big improvement on the quality of the constraints from Lyman-α forest data could be achieved by an analysis of a large set of high-redshift, high-resolution data to extend the measurement of the flux power spectrum at high redshift to smaller scales. This would, however, also require accurate modelling of the thermal history and the contribution of associated metal absorption to the small scale flux power spectrum.

Acknowledgements. Simulations were done at the UK Cosmology Supercomputer Center in Cambridge funded by PPARC, HEFCE and Silicon Graphics/Cray Research. We thank A. Lewis for technical help and K. Abazajian, S. Hansen, A. Kusenko, J. Sanders, M. Shaposhnikov and C. Watson for useful comments.

[1] P. Bode, J. P. Ostriker and N. Turok, Astrophys. J. **556**, 93 (2001); B. Moore, T. Quinn, F. Governato, J. Stadel and G. Lake, Mon. Not. Roy. Astron. Soc. **310**, 1147 (1999); V. Avila-Reese, P. Colin, O. Valenzuela, E. D'Onghia and C. Firmani, Astrophys. J. **559**, 516 (2001).

[2] M. Fellhauer *et al.*, arXiv:astro-ph/0605026.

[3] L. E. Strigari, J. S. Bullock, M. Kaplinghat, A. V. Kravtsov, O. Y. Gnedin, K. Abazajian and A. A. Klypin, arXiv:astro-ph/0603775; T. Goerdt, B. Moore, J. I. Read, J. Stadel and M. Zemp, Mon. Not. Roy. Astron. Soc. **368**, 1073 (2006); F. J. Sanchez-Salcedo, J. Reyes-Iturbide and X. Hernandez, arXiv:astro-ph/0601490.

[4] A. Kusenko and G. Segre, Phys. Lett. B **396**, 197 (1997); Phys. Rev. D **59**, 061302(R) (1999).

[5] M. Mapelli and A. Ferrara, Mon. Not. Roy. Astron. Soc. **364**, 2 (2005); P. L. Biermann and A. Kusenko, Phys. Rev. Lett. **96**, 091301 (2006); M. Mapelli, A. Ferrara and E. Pierpaoli, arXiv:astro-ph/0603237.

[6] P. J. E. Peebles, Astrophys. J. **258**, 415 (1982); K. A. Olive and M. S. Turner, Phys. Rev. D **25**, 213 (1982); S. Dodelson and L. M. Widrow, Phys. Rev. Lett. **72**, 17 (1994); X. Shi and G. M. Fuller, Phys. Rev. Lett. **82**, 2832 (1999) M. Drees and D. Wright, arXiv:hep-ph/0006274; A. D. Dolgov and S. H. Hansen, Astropart. Phys. **16**, 339 (2002); K. Abazajian, G. M. Fuller and M. Patel, Phys. Rev. D **64**, 023501 (2001).

[7] K. Abazajian, Phys. Rev. D **73**, 063513 (2006).

[8] M. Viel, J. Lesgourgues, M. G. Haehnelt, S. Matarrese and A. Riotto, Phys. Rev. D **71**, 063534 (2005).

[9] U. Seljak, A. Makarov, P. McDonald and H. Trac, arXiv:astro-ph/0602430.

[10] K. Abazajian and S. M. Koushiappas, arXiv:astro-ph/0605271.

[11] T. Asaka, A. Kusenko and M. Shaposhnikov, arXiv:hep-ph/0602150.

[12] M. Shaposhnikov and I. Tkachev, arXiv:hep-ph/0604236; M. Shaposhnikov, arXiv:hep-ph/0605047.

[13] D. N. Spergel *et al.*, arXiv:astro-ph/0603449; G. Hinshaw *et al.*, arXiv:astro-ph/0603451; L. Page *et al.*, arXiv:astro-ph/0603450.

[14] U. Seljak, A. Slosar and P. McDonald, arXiv:astro-ph/0604335.

[15] M. Viel, M. G. Haehnelt and A. Lewis, arXiv:astro-ph/0604310.

[16] M. Viel and M. G. Haehnelt, Mon. Not. Roy. Astron. Soc. **365**, 231 (2006).

[17] P. McDonald *et al.*, Astrophys. J. Suppl. **163**, 80 (2006).

[18] N. Y. Gnedin and L. Hui, Mon. Not. Roy. Astron. Soc. **296**, 44 (1998); M. Viel, M. G. Haehnelt and V. Springel, Mon. Not. Roy. Astron. Soc. **367**, 1655 (2006).

[19] V. Springel, Mon. Not. Roy. Astron. Soc. **364**, 1105 (2005).

[20] A. Lewis and S. Bridle, Phys. Rev. D **66**, 103511 (2002); CosmoMC home page: `http://www.cosmologist.info`

[21] C. l. Kuo *et al.* [ACBAR collaboration], Astrophys. J. **600**, 32 (2004).

[22] A. C. S. Readhead *et al.*, Astrophys. J. **609**, 498 (2004).

[23] C. Dickinson *et al.*, Mon. Not. Roy. Astron. Soc. **353**, 732 (2004).

[24] S. Cole *et al.* [The 2dFGRS Collaboration, Mon. Not. Roy. Astron. Soc. **362**, 505 (2005).

[25] P. McDonald *et al.*, Astrophys. J. **635**, 761 (2005).

[26] M. Viel, M. G. Haehnelt and V. Springel, Mon. Not. Roy. Astron. Soc. **354**, 684 (2004).

[27] S. Colombi, S. Dodelson and L. M. Widrow, Astrophys. J. **458**, 1 (1996); S. H. Hansen, J. Lesgourgues, S. Pastor and J. Silk, Mon. Not. Roy. Astron. Soc. **333**, 544 (2002).

[28] K. Abazajian, Phys. Rev. D **73**, 063506 (2006)

[29] T. S. Kim, M. Viel, M. G. Haehnelt, R. F. Carswell and S. Cristiani, MNRAS, **347**, 355 (2004); R. A. C. Croft *et al.*, Astrophys. J. **581**, 20 (2002).

[30] Abazajian K., Fuller G.M. and Tucker W.H., Astrophys. J. **562**, 593 (2001).

[31] A. Boyarsky, A. Neronov, O. Ruchayskiy and M. Shaposhnikov, arXiv:astro-ph/0512509.

[32] A. Boyarsky, A. Neronov, O. Ruchayskiy and M. Shaposhnikov, arXiv:astro-ph/0603368.

[33] C. R. Watson, J. F. Beacom, H. Yuksel and T. P. Walker, arXiv:astro-ph/0605424.

[34] T. Asaka, M. Laine and M. Shaposhnikov, arXiv:hep-ph/0605209.

[35] N. Werner *et al.*, arXiv:astro-ph/0512401.

[36] in this work, the linear matter power spectrum is computed under the assumption that the sterile neutrino phase-space distribution is equal to that of active neutrinos multiplied by a suppression factor [8, 27]. Deviations from this first-order approximation were computed in [28], but typically these corrections lower m_s bounds by only 10% [9].

5.6 Resonantly produced sterile neutrino dark matter, PRL 102, 201304 (2009)

CERN-PH-TH/2008-234, LAPTH-1290/08

Realistic sterile neutrino dark matter with keV mass does not contradict cosmological bounds

Alexey Boyarsky[a,b], Julien Lesgourgues[c,d,e], Oleg Ruchayskiy[d], Matteo Viel[f,g]
[a] *ETHZ, Zürich, CH-8093, Switzerland*
[b] *Bogolyubov Institute for Theoretical Physics, Kiev 03680, Ukraine*
[c] *PH-TH, CERN, CH-1211 Geneve 23, Switzerland*
[d] *École Polytechnique Fédérale de Lausanne, FSB/ITP/LPPC, BSP, CH-1015, Lausanne, Switzerland*
[e] *LAPTH, Université de Savoie, CNRS, B.P.110, F-74941 Annecy-le-Vieux Cedex, France*
[f] *INAF – Osservatorio Astronomico di Trieste, Via G.B. Tiepolo 11, I-34131 Trieste, Italy*
[g] *INFN – National Institute for Nuclear Physics, Via Valerio 2, I-34127 Trieste, Italy*
(Dated: December 17, 2008)

Previous fits of sterile neutrino dark matter models to cosmological data assumed a peculiar production mechanism, which is not representative of the best-motivated particle physics models given current data on neutrino oscillations. These analyses ruled out sterile neutrino masses smaller than 8-10 keV. Here we focus on sterile neutrinos produced resonantly. We show that their cosmological signature can be approximated by that of mixed Cold plus Warm Dark Matter (CWDM). We use recent results on ΛCWDM models to show that for each mass ≥ 2 keV, there exists at least one model of sterile neutrino accounting for the totality of dark matter, and consistent with Lyman-α and other cosmological data. Resonant production occurs in the framework of the νMSM (the extension of the Standard Model with three right-handed neutrinos). The models we checked to be allowed correspond to parameter values consistent with neutrino oscillation data, baryogenesis and all other dark matter bounds.

The sterile neutrino is a very interesting Dark Matter candidate [1, 2, 3, 4, 5, 6]. The existence of sterile neutrinos (right-handed or gauge singlet) is one of the most simple and natural explanations of the observed flavor oscillations of active neutrinos. It was observed long ago that such particles can be produced in the Early Universe through oscillations with active neutrinos [1]. For any mass (above ~ 0.4 keV, which is a universal lower bound on any fermionic Dark Matter (DM) particle, see [7] and references therein) sterile neutrinos produced in this way can end up with a correct relic density [1, 2, 4, 8, 9, 10].

A single right-handed neutrino would be unable to explain the two observed mass splittings between Standard Model (SM) neutrinos. Moreover, should this neutrino play the role of DM, its mixing with active neutrinos would be too small for explaining the observed flavor oscillations [6, 11]. However, in presence of three right-handed neutrinos (one for each SM flavor), active neutrino mass splittings and DM may be explained at the same time [6]. Moreover, the mass of each sterile neutrino can be chosen below the electroweak scale and additionally explain the matter-antimatter asymmetry of the Universe (baryogenesis) [6]. These observations motivated a lot of recent efforts for developing this model, called the νMSM [8, 12, 13, 14, 15, 16], and for constraining sterile neutrino DM [17, 18, 19].

Because of its mixing with flavor neutrinos, this DM particle has a small probability of decaying into an active neutrino and a photon of energy $E = m_s/2$ [20], producing a monochromatic line in the spectrum of DM dominated objects. The corresponding photons flux depends on the sterile neutrino mass m_s and mixing angle θ as $F \sim \theta^2 m_s^5$. For each value of the mass and of other parameters in the model (see below), the angle θ is fixed by the requirement of a correct DM abundance. Combining this constraint with bounds on decay lines in astrophysical spectra allows to put an *upper* limit on the mass of DM sterile neutrinos [3, 5, 17, 18, 19].

Within the νMSM, the relation between m_s, θ and the DM abundance can be affected by the presence of a *lepton asymmetry* (an excess of leptons over anti-leptons). In this case, the production of sterile neutrinos may be of the resonant type [2]. The lepton asymmetry required for this mechanism to be effective is several orders of magnitude larger than the baryon asymmetry $\eta_B \sim 10^{-10}$. In many models of baryogenesis (for a review see e.g. [21]), both asymmetries are of the same order, because they are generated above the electroweak scale and sphaleron processes equalize them. Instead, in the νMSM, the lepton asymmetry is generated below the electroweak scale, when sphaleron processes are not active anymore [9]. As a result, it can be as large as the upper limit imposed by Big Bang Nucleosynthesis (BBN) and other cosmological constraints (see e.g. [22] and refs. therein). Such a large lepton asymmetry is consistent with generic values of the parameters of the νMSM, satisfying current data on neutrino oscillations, cosmological requirements (baryogenesis, BBN constraints) and particle physics constraints [23]. So, resonant production (RP) is a natural way of producing sterile neutrino DM in the νMSM. At the same time, most previous constrains on sterile neutrino DM assumed non-resonant production (NRP) [1, 8].

In the NRP case, the comparison of X-ray bounds [17,

18, 19] with constraints on DM relic abundance [8] gives an *upper bound* $m_s^{\rm NRP} \leq 4$ keV on the DM sterile neutrino mass. In the more effective RP scenario, smaller mixing angles are required and the corresponding bound is much weaker: $m_s^{\rm RP} \lesssim 50$ keV [10].

The most robust *lower bound* on the DM mass comes from the analysis of the phase space density of compact objects, e.g. dwarf spheroidals of the Milky Way halo. The universal Gunn-Tremaine bound [24] can be made stronger if one assumes a particular primordial phase-space distribution function. For NRP sterile neutrinos, this leads to $m_s^{\rm NRP} > 1.8$ keV, while for RP particles the bound is weaker: $m_s^{\rm RP} > 1$ keV [7].

An interesting property of sterile neutrino DM with keV mass is that it falls in the Warm Dark Matter (WDM) category. Lyman-α (Ly-α) forest observations in quasar spectra provide strong *lower bounds* on the mass of DM sterile neutrinos produced with the NRP mechanism [25, 26, 27]. The analysis of SDSS Ly-α data led to $m_s^{\rm NRP} > 13$ keV in Ref. [26], or $m_s^{\rm NRP} > 10$ keV in [25]. In [27] these bounds were revisited using the same SDSS Ly-α data (combined with WMAP5 [28]), but paying special attention to the interpretation of statistics in the parameter extraction, and to possible systematic uncertainties. It was shown that a conservative (frequentist, 3-σ) lower bound is $m_s^{\rm NRP} > 8$ keV. The Ly-α method is still under development, and there is a possibility that some of the related physical processes are not yet fully understood. However, at this moment, it is difficult to identify a source of uncertainty that could give rise to systematic errors affecting the result by more than 30%. Even with such an uncertainty, the possibility to have all DM in the form of NRP sterile neutrinos is ruled out by the comparison of Ly-α results with X-ray upper bounds [27].

In the RP case, Ly-α bounds have not been derived yet. However, in Ref. [27], a ΛCWDM model – containing a mixture of WDM (in the form e.g. of NRP sterile neutrinos) and Cold Dark Matter (CDM) – was analyzed. Below we will show that although the phase-space distribution of RP sterile neutrinos does not coincide exactly with such mixed models, some results can be inferred from the ΛCWDM analysis. In particular, we will show that for each mass ≥ 2 keV, there is at least one value of the lepton asymmetry for which the RP sterile neutrino model is fully consistent with Ly-α and other cosmological data (this value of the lepton asymmetry is natural within the νMSM).

Spectra of RP sterile neutrino. DM production in the RP scenario occurs in two stages [2, 10]. In presence of a lepton asymmetry, the conditions for resonant oscillations (related to the intersection of dispersion curves for active and sterile neutrinos) are fulfilled for temperatures of few hundred MeV. Later, at $T \sim 150\,(m_s^{\rm RP}/{\rm keV})^{1/3}$ MeV, non-resonant production takes place. As a result, the primordial velocity distribution of sterile neutrinos contains a narrow resonant (*cold*) component and a non-resonant (*warm*) one. Its exact form can be computed by taking into account the expansion of the Universe, the interaction of neutrinos with the content of the primeval plasma and the changes in the lepton asymmetry resulting from DM production. In this work, we used the spectra computed in Ref. [10].

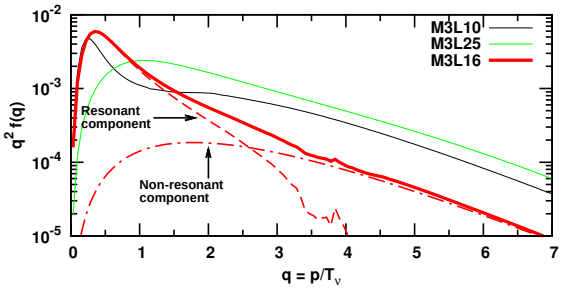

FIG. 1: Characteristic form of the RP sterile neutrino distribution function for $m_s^{\rm RP} = 3$keV and various values of the lepton asymmetry parameter L_6. The spectrum for $L_6 = 16$ (red solid line) is shown together with its resonant (dashed) and non-resonant (dashed-dotted) components. All these spectra have the same shape for $q \gtrsim 3$.

Characteristic forms of the spectra are shown in Fig. 1. They are expressed as a function of the comoving momentum $q \equiv p/T_\nu$ (T_ν being the temperature of active neutrinos), and depend on the lepton asymmetry parameter [9] $L_6 \equiv 10^6 (n_{\nu_e} - n_{\bar{\nu}_e})/s$ (s being the entropy density). In rest of this work, the notation M2L25 would refer to a model with $m_s^{\rm RP} = 2$ keV and $L_6 = 25$. The shape of the non-resonant distribution tail depends on the mass, but not on L_6. For $q \gtrsim 3$, the distribution is identical to a rescaled NRP spectrum [8] with the same mass (red dashed-dotted line on Fig. 1). We call this rescaling coefficient the *warm component fraction* $f_{\rm NRP}$. For the few examples shown in Fig. 1, the M3L16 models corresponds to $f_{\rm NRP} \simeq 0.12$, M3L10 to $f_{\rm NRP} \simeq 0.53$ and M3L25 to $f_{\rm NRP} \simeq 0.60$. The maximum of $q^2 f(q)$ for the NRP component occurs around $q \approx 1.5 - 2$. We define the *cold component* to be the remaining contribution: its distribution is given by the difference between the full spectrum and the rescaled NRP one (red dashed line on Fig. 1), and peaks around $q_{\rm res} \sim 0.25 - 1$. Its width and height depend on L_6 and $m_s^{\rm RP}$.

The DM clustering properties can be characterized qualitatively by the particle's *free-streaming horizon* (see e.g. [27] for definition), proportional to its average velocity $\langle q \rangle / m$. In the RP case, the dependence of the average momentum $\langle q \rangle$ on $m_s^{\rm RP}$ and L_6 is not monotonic. For a given mass, the RP model departing most from an NRP model is the one with the smallest $\langle q \rangle$ (i.e., with the most significant cold component). For each mass, there is indeed a value of L_6 minimizing $\langle q \rangle$, such that $\langle q \rangle_{min} \approx 0.3 \langle q \rangle_{\rm NRP}$ (cf. [10]). This minimum corresponds to lepton asymmetries that are likely to be generated within the νMSM. For instances, for $m_s^{\rm RP} = 2$, 3 or 4 keV, the spectra with the smallest average momentum

are M2L25, M3L16 and M4L12, all having $f_{\rm NRP} \lesssim 0.2$.

For a quantitative analysis, we computed the power spectrum of matter density perturbations $P_{\rm RP}(k,z)$ for these models. The standard software (i.e. CAMB [29]) is not immediately appropriate for this purpose, as it only treats massive neutrinos with a Fermi-Dirac primordial distribution. To adapt it to the problem at hand, we modified CAMB so that it could take arbitrary spectra as input data files. We analyzed the spacing in momentum space needed in order to obtain precise enough results, and implemented explicit computations of distribution momenta in CAMB. We cross-checked our results by modifying another linear Boltzmann solver – CMBFAST [30], implementing a treatment of massive neutrinos with arbitrary *analytic* distribution function.

To separate the influence of primordial velocities on the evolution of density perturbations from that of cosmological parameters, it is convenient to introduce the transfer function (TF) $T(k) \equiv \left[P_{\rm RP}(k)/P_{\Lambda{\rm CDM}}(k)\right]^{1/2}$. Figure 2 shows the transfer function of the models M3L16 and M4L12. The TF becomes smaller than one above the wave number associated with the free-streaming horizon today, $k_{\rm FSH} \approx 0.5\,(m_s^{\rm RP}/1\,{\rm keV})\,h\,{\rm Mpc}^{-1}$ (c.f. [27]). We see that for a large range of k values above $k_{\rm FSH}$, roughly $k \lesssim 5\,k_{\rm FSH}$, the transfer function $T_{\rm RP}(k)$ is very close to $T_{\Lambda{\rm CWDM}}(k)$ for the same mass and warm component fraction $F_{\rm WDM} = f_{\rm NRP}$. On smaller scales, $T_{\rm RP}(k)$ decreases faster, since the cold component of RP sterile neutrinos also has a non-negligible free-streaming scale. For all values of the mass studied in this work, $m_s^{\rm RP} \geq 2$ keV, the discrepancy appears above 5 $h/$ Mpc (vertical line in Fig. 2), i.e. above the maximum scale in the three-dimensional power spectrum to which current Ly-α data are sensitive. Hence, for the purpose of constraining RP sterile neutrinos with Ly-α data, it is possible to use the results obtained in the ΛCWDM case. In Ref. [27], we presented the results of a WMAP5 plus SDSS Ly-α data analysis for ΛCWDM models with $m_s^{\rm RP} \geq 5$ keV. In Fig.3, we show the Bayesian credible region for the mass and the warm component fraction, now extended till $m_s^{\rm NRP} = 2$ keV [34].

Fig. 2 demonstrates that for the models M3L16 and M4L12, the function $T_{\rm RP}(k)$ lies above $T_{\Lambda{\rm CWDM}}(k)$ for the same masses and $F_{\rm WDM} = 0.2$ (at least, in the range of wave numbers probed by Ly-α data): so, it can only be in better agreement with cosmological data. We checked that the same is true for M2L25. However, ΛCWDM models with $m_s^{\rm RP} = 2, 3, 4$ keV and $F_{\rm WDM} = 0.2$ are within the 2-σ contour of Fig. 3. We conclude that M2L25, M3L16 and M4L12 are clearly allowed by the data. For larger mass (and still minimal $\langle q \rangle$), the free-streaming horizon is smaller, and agreement with observations can only become easier. Therefore, we see that for each mass $m_{\rm RP} \gtrsim 2$ keV there exists *at least* one value of the lepton asymmetry for which RP sterile neutrinos are perfectly compatible with WMAP5 and SDSS Ly-α data.

Fig. 4 shows the range of masses and mixing angles consistent with constraints from phase-space density [7]

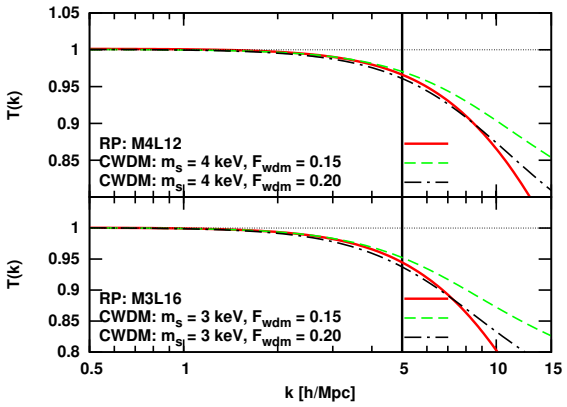

FIG. 2: TFs for the models M4L12 (top) and M3L16 (bottom), together with CWDM spectra for the same mass and $F_{\rm WDM} \simeq 0.15$ or 0.2.

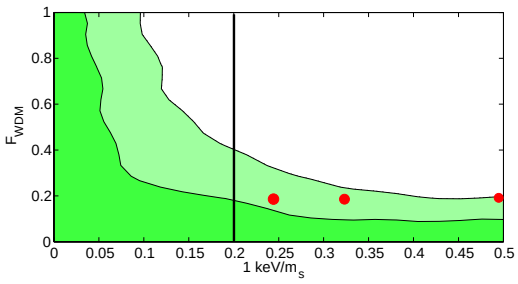

FIG. 3: 1 and 2-σ bounds from WMAP5 and SDSS Ly-α data on ΛCWDM parameters. Red points correspond to approximations for the models M4L12, M3L16, M2L25. Results to the left of black vertical lines were already reported in [27].

(left shaded region), from X-rays [17, 19] (upper right corner, shaded in red) and providing the correct DM abundance (curves between the lines "NRP" and L_6^{max}: from top to bottom $L_6 = 8, 12, 16, 25, 70, 250$). The black dashed line shows approximately the RP models with minimal $\langle q \rangle$ for each mass, i.e., the family of models with the largest cold component. We have seen that all black filled circles along this line and with $m_s^{\rm RP} \geq 2$ keV are compatible with Ly-α bounds. In addition, those with $m_s^{\rm RP} \leq 4$ keV are also compatible with X-ray bounds (this conclusion does not change with the new results of Ref. [31]). Note that above 4 keV, Ly-α data allows increasingly high WDM fractions, so that agreement with both Ly-α and X-ray bounds can be maintained with larger values of L_6. This is very clear e.g. for the models M10L25, M10L16 and M10L12, allowed by X-ray data (open circles on Fig.4), and consistent with Ly-α data since for $m_s^{\rm RP} = 10$ keV, up to 100% of WDM is allowed at the 2-σ level (c.f. Fig.3).

In conclusion, we showed in this work that sterile neutrino DM with mass $\geq$ 2keV is consistent with all existing

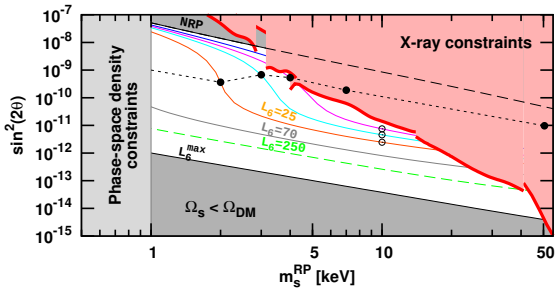

FIG. 4: Region of masses and mixing angles for RP sterile neutrinos consistent with existing constraints.

constraints. A sterile neutrino with mass ~ 2 keV is an interesting WDM candidate, as it may affect structure formation on galactic scales. This range of masses and corresponding mixing angles is important for laboratory and astrophysical searches.

To determine the precise shape of the allowed parameter range (which may continue below 2 keV, see Fig. 4), one should perform specific hydrodynamical simulations in order to compute the flux power spectrum on a grid of $(m_s^{\rm RP}, L_6)$ values, and compare with Ly-α data. We leave this for future work.

The νMSM does not require new particles apart from the three sterile neutrinos. Extensions of this model may include a scalar field providing Majorana masses to sterile neutrinos via Yukawa couplings [32, 33]. Then, sterile neutrino DM can also be produced by the decay of this scalar field, and also contain a cold and a warm component. We expect a similar range of masses and mixing angles to be allowed by Ly-α data. The quantitative analysis of this model is also left for future work.

Acknowledgments. We thank A. Kusenko, M. Laine, M. Shaposhnikov, S. Sibiryakov for useful discussions. J.L. acknowledges support from the EU network "UniverseNet" (MRTN-CT-2006-035863). O.R. was supported by the Swiss Science Foundation.

[1] S. Dodelson and L. M. Widrow, Phys. Rev. Lett. **72**, 17 (1994).
[2] X.-d. Shi and G. M. Fuller, Phys. Rev. Lett. **82**, 2832 (1999).
[3] A. D. Dolgov and S. H. Hansen, Astropart. Phys. **16**, 339 (2002).
[4] K. Abazajian, G. M. Fuller, and M. Patel, Phys. Rev. D **64**, 023501 (2001).
[5] K. Abazajian, G. M. Fuller, and W. H. Tucker, ApJ **562**, 593 (2001).
[6] T. Asaka, S. Blanchet, and M. Shaposhnikov, Phys. Lett. **B631**, 151 (2005); T. Asaka and M. Shaposhnikov, Phys. Lett. B **620**, 17 (2005).
[7] A. Boyarsky, O. Ruchayskiy, and D. Iakubovskyi, 0808.3902 (2008).
[8] T. Asaka, M. Laine, and M. Shaposhnikov, JHEP **01**, 091 (2007).
[9] M. Shaposhnikov, JHEP **08**, 008 (2008).
[10] M. Laine and M. Shaposhnikov, JCAP **6**, 31 (2008).
[11] A. Boyarsky, A. Neronov, O. Ruchayskiy, and M. Shaposhnikov, JETP Letters pp. 133–135 (2006).
[12] M. Shaposhnikov, Nucl. Phys. **B763**, 49 (2007).
[13] D. Gorbunov and M. Shaposhnikov, JHEP **10**, 015 (2007).
[14] F. L. Bezrukov and M. Shaposhnikov, Phys. Lett. **B659**, 703 (2008).
[15] M. Shaposhnikov and D. Zenhausern, 0809.3395 (2008).
[16] M. E. Shaposhnikov and I. I. Tkachev, 0811.1967 (2008).
[17] A. Boyarsky et al., Phys. Rev. Lett. **97**, 261302 (2006).
[18] S. Riemer-Sørensen, S. H. Hansen, and K. Pedersen, ApJ **644**, L33 (2006); C. R. Watson, J. F. Beacom, H. Yuksel, and T. P. Walker, Phys. Rev. **D74**, 033009 (2006); K. N. Abazajian et al., Phys. Rev. D **75**, 063511 (2007); H. Yuksel, J. F. Beacom, and C. R. Watson, Phys. Rev. Lett. **101**, 121301 (2008).
[19] A. Boyarsky, J. Nevalainen, and O. Ruchayskiy, A&A **471**, 51 (2007); A. Boyarsky, D. Iakubovskyi, O. Ruchayskiy, and V. Savchenko, MNRAS **387**, 1361 (2008); A. Boyarsky, D. Malyshev, A. Neronov, and O. Ruchayskiy, MNRAS **387**, 1345 (2008).
[20] P. B. Pal and L. Wolfenstein, Phys. Rev. **D25**, 766 (1982); V. D. Barger, R. J. N. Phillips, and S. Sarkar, Phys. Lett. **B352**, 365 (1995).
[21] S. Davidson, E. Nardi, and Y. Nir, Phys. Rept. **466**, 105 (2008).
[22] P. D. Serpico and G. G. Raffelt, Phys. Rev. **D71**, 127301 (2005).
[23] M. Daum et al., Phys. Rev. Lett. **85**, 1815 (2000).
[24] S. Tremaine and J. E. Gunn, Phys. Rev. Lett. **42**, 407 (1979).
[25] M. Viel et al., Phys. Rev. Lett. **97**, 071301 (2006).
[26] U. Seljak, A. Makarov, P. McDonald, and H. Trac, Phys. Rev. Lett. **97**, 191303 (2006).
[27] A. Boyarsky, J. Lesgourgues, O. Ruchayskiy, and M. Viel, 0812.0010 (2008).
[28] J. Dunkley et al. (WMAP), 0803.0586 (2008).
[29] A. Lewis, A. Challinor, and A. Lasenby, ApJ **538**, 473 (2000).
[30] U. Seljak and M. Zaldarriaga, ApJ **469**, 437 (1996).
[31] M. Loewenstein, A. Kusenko and P. L. Biermann, 0812.2710 (2008).
[32] M. Shaposhnikov and I. Tkachev, Phys. Lett. **B639**, 414 (2006)
[33] A. Kusenko, Phys. Rev. Lett. **97**, 241301 (2006); K. Petraki and A. Kusenko, Phys. Rev. **D77**, 065014 (2008).
[34] Thermal velocities of NRP neutrinos may become important below 5 keV [27]. To be conservative, this mass region was excluded from the results of [27], but we put it back here. We see that 1 and 2σ contours become nearly horizontal for $m \lesssim 5$ keV (c.f. Fig. 3). We do not expect thermal velocities to affect this conclusion. For detailed bounds on RP sterile neutrinos, we plan to explore the precise dependence of N-body simulation results on thermal velocities elsewhere.

Acknowledgements

First, I would like to thank my referees and jury members for the time they spent on this application. Besides, my work on neutrino cosmology is the result of collaboration and friendship with many people. I would like to thank especially Sergio, who was the first to attract my interest on this tropic; Matteo, whithout whom I wouldn't have jumped into the Lyman-alpha data business; Gianpiero, the instigator and the soul of our the book; François, who urged me to write CLASS and letted me join Planck; Thomas, who was essential to the writing of CLASS; as well as Alessandro, Alexei, Andrew, Benjamin, Cornelius, Diego, Emanuele, Enrique, Huitzu, Jan, Joe, Laurence, Marco, Mario, Martin, Massi, Michel, Oleg, Patrick, Rino, Sabino, Simeon, Simon, Steen I, Steen II, Toni, Urbano, Wessel, Yvonne.